

Characterization of metal organic frameworks of interest for gas adsorption/separation applications

Présentée le 31 janvier 2020

à la Faculté des sciences de base
Laboratoire des matériaux inorganiques fonctionnels
Programme doctoral en chimie et génie chimique

pour l'obtention du grade de Docteur ès Sciences

par

Mehrdad ASGARI

Acceptée sur proposition du jury

Prof. B. Smit, président du jury
Prof. W. L. Queen, directrice de thèse
Prof. C. Brown, rapporteur
Dr M. Nachtegaal, rapporteur
Prof. K. Agrawal, rapporteur

“Now this is not the end. It is not even the beginning of the end. But it is, perhaps, the end of the beginning.”

-Winston Churchill

Acknowledgements

Now that I am at the end of my PhD studies, I should take advantage of this moment to thank all of the people that have contributed so as I can come this way.

First of all, I am sincerely thanking **Professor Wendy Queen** for the opportunity that she provided for me to work under her supervision, in the area I like. The support and the direction that I received from her made me a better and more methodological scientist. She was always ready to help me in my academic and personal life in Sion, for which I am very thankful to her. Thank you **Wendy**!

I should also thank the president, and the reviewers of my thesis for the fact that they accepted to review my thesis. I thank **Prof. Berend Smit**, **Prof. Kumar Agrawal**, **Prof. Craig Brown**, and **Dr. Maarten Nachtegaal**, for being a part of the reviewing committee of my PhD thesis.

In addition, a big thank you to our great secretary, Miss **Laure Dayer**, for being very helpful with all the administrative tasks. Thank you **Laure**!

I should also thank my current and the previous groupmates in LFIM, without whom coming this way would have been much more difficult. In this regards, I should name **Dr. Safak Bulut**, **Dr. Olga Trukhina**, **Dr. Li Peng**, **Dr. Shuliang Yang**, **Dr. Jordi Espin**, **Dr. Pierre Dapsens**, **Mr. Daniel Sun**, **Mr. Ilia Kochetygov**, **Mr. Vikram Karve**, **Miss Anita Justin**, **Mr. Hassan Abedini**, **Mr. Mohammad Andalibi**, **Mr. Martin Watt Coull**, **Mr. Till Schertenleib**, **Mr. Guanchu Lu**, **Mr. Zhaoyan Sun**, **Mr. Matthieu Porchet**, **Miss Sandrine Chuard**, **Mr. Abbas Jamali**, **Mr. Daniel Doeller**, **Mr. Washington S. Reeder**, and all those whose name may have been missed out. I really appreciate all of the help that you gave me this time. I enjoyed my time with you and will be forever grateful for your support during this key phase of my scientific career!

I also thank **all of my friends at EPFL Valais** at different groups whose name I cannot bring in just this one page. But I thank everyone including the supervisors, secretaries and the group members at LMER, LAS, LSMO, LNCE, GMF, LEPA, GEM and IPESE. In this regard, I should especially thank **Seyed Mohamad Moosavi**, **Seryio Saris** and **Senja Barthel Dominique** for fruitful discussions.

I also should thank the direction and all the staff members in EPFL Valais. In this regard, I should thank the director, Mr. **Marc-Andre Berclaz**, the responsables at the chemical store, **Laurent Seydoux** and **Annabelle Coquoz**, the responsible person at the electronic workshop, **Patrick Favre**, the responsible persons at the mechanical workshop, **Stephane Voeffray** and **Robin Cyril deleze**, the responsables at the IT, **Cedric Passerini**, **Jean Perruchoud**, and **Filipe**

Martins, and all those whose name have been missed out, without the help of whom our research couldn't be done.

And finally a special thanks to my family:

To my wife, Fatemeh Rahimian, who supported me sincerely during the past few years. She has been standing next to me and supporting me as a strong pillar and has helped me to improve in every aspect. I love you and will always be grateful for your support **Fatemeh!**

To my lovely parents, Jahandar Asgari and Maryam Sadeghi, who have beared a lot efforts to raise me and grow me and have taught me the value of being genuine. Thanks dad! Thanks mom! I hope I can follow you!

To my younger sister, Mehrnoosh Asgari, who has always brought vivacity and energy to our house! Thanks for your passion!

To my grandparents, my uncles (here I cannot overlook mentioning **Jahangir Asgari**, who has been also supporting me like a strong pillar in the life), my aunts, my cousins, and all of my friends and relatives who have been staying in my heart and will stay there forever.

Thank you all!

Abstract

Metal-Organic Frameworks (MOFs) are a class of porous materials that are applicable in many energy and environmentally relevant areas, due to their unique features including unprecedented internal surface areas and easy chemical tunability. Gas separation and storage are among the most important applications for which MOFs have been extensively studied. Considering the large number of potential MOFs that can be accessed, through a combination of numerous metal clusters and organic linkers, determining the relationship between their structural features (such as pore size and shape and chemical functionalities) and corresponding gas adsorption properties is of utmost importance. In this regard, *in-situ* characterization, especially diffraction, can be advantageous.

MOFs can offer high crystallinity, and so their structure can readily be characterized via diffraction. In addition, due to the presence of metal ions, and predefined molecular building blocks, which exhibit multiple chemical moieties, the potential energy surface for a guest molecule within a MOF cavity possesses multiple minima that correspond to well-defined adsorption sites with varying binding energies. This makes diffraction the most direct way to probe static site-specific binding properties.

Given this, the focus of this work is on understanding the structure-derived function of MOFs of interest in gas separation/storage applications. To do this, standard adsorption experiments are coupled with *in-situ* diffraction techniques. The latter is able to reveal the location and orientation of adsorbed guest species inside the framework, provide insights into the framework response to varying pressure, temperature, and atmosphere, and allow one to determine the relative differences in binding energy between neighboring adsorption sites. The aforementioned information can then be used to rationalize the relationship between different physiochemical features of a given framework and their performance in an adsorption process. In addition to establishing structure-property relations for the usage of MOFs, the obtained experimental results are used to corroborate those calculated by DFT methods, providing a stress test for computational methods aimed at predicting the structures and properties of hypothetical MOFs.

The first chapter of this thesis, the introduction, offers a brief review of different characterization methods for studying gas adsorption/separation applications in MOFs. Although the focus of this chapter is on carbon dioxide capture as the application, these characterization methods are also used to study other adsorption processes. The next three chapters, chapters 2-4, present several prominent MOF families that are of interest in hydrogen storage and carbon dioxide capture applications. These case studies demonstrate how using *in-situ* diffraction techniques coupled with adsorption measurements and DFT calculations can be used to gain molecular level insight into how small molecules bind inside the selected MOF structures. Further, these structure-property correlation studies are able to help unveil how altering MOF building blocks, such as metals and ligands, gives rise to enhanced or diminished adsorption properties. The last chapter, chapter 5, is a study of the response of an activated MOF to varying temperature; in this chapter various structural motions, which are responsible for a large negative thermal expansion (NTE), are elucidated.

Overall, the work in this thesis is aimed at showing how the gas adsorption properties are linked with the chemical and physical make-up of the MOF. It is hoped that efforts like this one can provide the insight necessary for the eventual deliberate design of new or the optimization of existing MOFs that offer unprecedented performance in important energy-related applications such as hydrogen storage and carbon-dioxide capture.

Keywords: metal-organic frameworks, structure-property relationship study, *in-situ* diffraction, gas adsorption, chemical separation, and gas storage.

Abstrakt

Metallorganische Gerüstverbindungen (engl. Metal-Organic Frameworks, MOFs) sind eine Klasse poröser Materialien, die in vielen energie- und umweltrelevanten Gebieten Einsatz finden. Dies ist ihren einmaligen Eigenschaften wie ihrer beispiellos grossen inneren Oberfläche zu verdanken sowie der Möglichkeit sie leicht chemisch massschneiden zu können. Die Trennung und Speicherung von Gasen gehören zu den bedeutendsten Anwendungen, für die MOFs eingehend untersucht worden sind. Da durch die Vielzahl an Kombinationen der Metallcluster und organischen Verbindungsstücken eine ausgesprochen grosse Zahl von MOFs potentiell hergestellt werden kann, ist es von äusserster Bedeutung den Zusammenhang zwischen ihren strukturellen Merkmalen (wie Grösse und Form der Poren oder ihrer chemischen Funktionalität) und ihrer jeweiligen Gasadsorption zu bestimmen. In dieser Hinsicht kann es vorteilhaft sein *in-situ* Charakterisierungen, insbesondere *in-situ* Diffraktion, durchzuführen.

Da MOFs kristallin sind, kann ihre Struktur mit *in-situ* Diffraktionstechniken direkt charakterisiert werden. Durch das Vorhandensein von Metallionen sowie molekularer Bausteine, die aus mehreren chemischen Einheiten bestehen, weist die Potentialhyperfläche eines Gastmoleküls mehrere Minima auf, die wohldefinierten Positionen mit verschiedenen Adsorptionsenergien entsprechen. Dies macht Diffraktion die direkteste Methode zur Untersuchung statischer ortsspezifischer Bindungseigenschaften. Aufgrund dessen, der Schwerpunkt dieser Arbeit liegt auf dem Verständnis der strukturellen Eigenschaften der untersuchten MOFs in Hinblick auf die Abtrennung von Gasen und ihre Lagerung. Dieses Verständnis wird durch die Kombination von Standardexperimenten zur Bestimmung des Adsorptionsverhaltens mit thermodynamischen Berechnungen und *in-situ* Charakterisierungstechniken, insbesondere mit *in-situ* Diffraktion, erlangt.

Die *in-situ* Diffraktionstechniken werden sowohl verwendet um die räumliche Position und Ausrichtung der adsorbierten Gasmoleküle innerhalb des Gerüsts zu bestimmen, als auch um die Reaktion des Gerüsts auf Gastmoleküle unter sich änderndem Druck, Temperatur und Umgebung zu untersuchen. Die mit den oben genannten Methoden erhaltenen Einsichten werden verwendet um Zusammenhänge zwischen verschiedenen physiochemischen Eigenschaften der Gerüste und ihres Adsorptionsverhalten aufzudecken.

Zusätzlich zu dem Aufstellen von Zusammenhängen zwischen strukturellen

Eigenschaften und dem Verhalten der Materialien mit Hinblick auf ihre Verwendung werden die erzielten Ergebnisse mit den Vorhersagen verglichen, die mit auf Dichtefunktionaltheorie beruhenden Methoden gemacht werden können. Dies ermöglicht es die rechnerischen Methoden zu testen, die in der Lage sind um die Form und Eigenschaften von hypothetische MOFs vorherzusagen.

Im ersten Kapitel dieser Arbeit, d.h. in der Einleitung, geben wir einen kurzen Überblick über verschiedene Charakterisierungsmethoden zur Untersuchung von Anwendungen zur Gasadsorption und -trennung unter Verwendung von MOFs. Obwohl der Schwerpunkt dieses Kapitels auf der Abscheidung von Kohlenstoffdioxid liegt, können die meisten der Methoden zur Charakterisierung auch zur Untersuchung anderer Adsorptionsprozesse verwendet werden. In den folgenden drei Kapiteln, d.h. Kapitel 2-4, präsentieren wir mehrere prominente MOF-Familien, die für Anwendungen im Bereich Wasserstoffspeicherung und Kohlenstoffdioxidabscheidung interessant sind. Diese Fallstudien zeigen, wie mithilfe einer Kombination von *in-situ*-Diffraktionstechniken, Adsorptionsmessungen und DFT-Berechnungen Einblicke auf molekularer Ebene wie kleine Moleküle an die MOF-Struktur gebunden sind. Darüber hinaus können diese Struktur-Eigenschafts-Korrelationsstudien Aufschluss darüber geben, wie die Veränderung von MOF-Bausteinen wie Metallen und Liganden zu verbesserten oder verminderten Adsorptionseigenschaften führt. Das letzte Kapitel, Kapitel 5, beinhaltet eine Fallstudie, in der die Reaktion eines aktivierten Gerüsts auf Temperatur untersucht wird und in der die für die Dichteanomalie verantwortlichen strukturellen Bewegungen des betrachteten Gerüsts identifiziert werden.

Insgesamt soll in dieser Arbeit gezeigt werden, wie die Gasadsorptionseigenschaften mit der chemischen und physikalischen Zusammensetzung des MOF zusammenhängen. Man hofft, dass solche Bemühungen die notwendigen Erkenntnisse für das rationale Design neuer oder die Optimierung bestehender MOFs liefern können, die in wichtigen energiebezogenen Anwendungen wie der Speicherung von Wasserstoff und der Abscheidung von Kohlendioxid eine beispiellose Leistung bieten.

Stichwörter: Metallorganische Gerüstverbindungen, Struktur-Eigenschafts Beziehungen, *in-situ* Diffraktion, Gas Adsorption, Chemische Separation, und Gasspeicherung.

Table of Contents

ACKNOWLEDGEMENTS	V
ABSTRACT	VII
ABSTRAKT	IX
TABLE OF CONTENTS	XI
LIST OF ABBREVIATIONS AND SYMBOLS	XVII
CHAPTER 1- AN INTRODUCTION ON CHARACTERIZATION OF METAL-ORGANIC FRAMEWORKS (MOFS) FOR GAS ADSORPTION APPLICATIONS	1
1.1. INTRODUCTION	1
1.1.1 <i>The importance of carbon dioxide capture</i>	2
1.1.2 <i>Conventional industrial process of carbon capture and limitations: liquid amines</i>	4
1.1.3 <i>Metal-organic frameworks and their synthesis</i>	4
1.1.4 <i>CCS technologies and MOF requirements</i>	6
1.1.5 <i>Molecule specific</i>	10
1.2 UNDERSTANDING THE ADSORPTION PROPERTIES OF MOFS	10
1.2.1 <i>Single component Isotherms</i>	11
1.2.2 <i>Multicomponent adsorption</i>	14
1.2.3 <i>Experimental breakthrough</i>	15
1.2.4 <i>In-situ Characterization</i>	16
1.3 MOFS FOR POST-COMBUSTION CAPTURE	30
1.3.1 <i>Necessary framework properties for CO₂ capture</i>	30
1.3.2 <i>Assessing MOFs for CO₂/N₂ separations</i>	31
1.3.3 <i>MOFs with open metal coordination sites (OMCs)</i>	33
1.3.4 <i>MOFs containing Lewis basic sites</i>	37
1.3.5 <i>Stability and competitive binding in the presence of H₂O</i>	42
1.4 MOFS FOR PRE-COMBUSTION CAPTURE	45
1.4.1 <i>Advantages of Pre-combustion capture</i>	45
1.4.2 <i>Necessary framework properties for CO₂ capture</i>	46
1.4.3 <i>Potential MOF candidates for CO₂/H₂ separations</i>	48
1.5 MOFS FOR OXY-FUEL COMBUSTION CAPTURE	51
1.5.1 <i>Necessary framework properties for O₂/N₂ separations</i>	51
1.5.2 <i>Biological inspiration for O₂/N₂ separations in MOFs</i>	53
1.5.3 <i>Potential MOF candidates for O₂/N₂ separations</i>	54
1.6 FUTURE PERSPECTIVES AND OUTLOOK	56
CHAPTER 2- AN EXPERIMENTAL AND COMPUTATIONAL STUDY OF CO ₂ ADSORPTION IN THE SODALITE-TYPE M-BTT (M = CR, MN, FE, CU) METAL-ORGANIC FRAMEWORKS FEATURING OPEN METAL SITES	59

2.1	INTRODUCTION	59
2.2	EXPERIMENTAL SECTION.....	61
2.2.1	<i>Materials and methods</i>	61
2.2.2	<i>Synthesis</i>	61
2.2.3	<i>Adsorption Measurements</i>	61
2.2.4	<i>Structural Analysis</i>	62
2.2.5	<i>Periodic Density Functional Theory Calculations</i>	63
2.2.6	<i>Grand Canonical Monte Carlo Simulations</i>	64
2.3	RESULTS AND DISCUSSION	64
2.3.1	<i>CO₂ adsorption properties</i>	64
2.3.2	<i>Characterization of multi-site CO₂ adsorption in M-BTT</i>	66
2.3.3	<i>Comparison with Previous Computational Work</i>	71
2.4	CONCLUSIONS.....	72
CHAPTER 3- AN <i>IN-SITU</i> NEUTRON DIFFRACTION AND DFT STUDY OF HYDROGEN ADSORPTION IN A SODALITE-TYPE METAL–ORGANIC FRAMEWORK, CU-BTTRI		73
3.1	INTRODUCTION	73
3.2	EXPERIMENTAL SECTION	74
3.2.1	<i>Synthesis of H₃BTTRI ligand</i>	74
3.2.2	<i>Synthesis of Cu-BTTRI</i>	74
3.2.3	<i>Activation of Cu-BTTRI</i>	75
3.2.4	<i>SEM-EDX characterization</i>	75
3.2.5	<i>In-situ neutron diffraction experiments</i>	75
3.2.6	<i>In-situ synchrotron X-ray experiments</i>	75
3.2.7	<i>Rietveld analysis</i>	76
3.2.8	<i>Quantum computational calculation methods</i>	76
3.3	RESULTS AND DISCUSSION.....	77
3.3.1	<i>Characterization of Cu-BTTRI framework</i>	77
3.3.2	<i>Hydrogen adsorption properties</i>	78
3.3.3	<i>D₂ binding sites</i>	80
3.4	CONCLUSIONS.....	85
CHAPTER 4- UDERSTANDING HOW LIGAND FUNCTIONALIZATION INFLUENCES CO₂ AND N₂ ADSORPTION IN A SODALITE MOF.....		87
4.1	INTRODUCTION	87
4.2	EXPERIMENTAL SECTION.....	89
4.2.1	<i>Synthesis of Cu-BTTRI</i>	89
4.2.2	<i>Standard adsorption isotherm measurements</i>	89
4.2.3	<i>In situ neutron diffraction</i>	89
4.2.4	<i>In situ synchrotron X-ray diffraction</i>	90
4.2.5	<i>Electronic structure simulation details</i>	91
4.3	RESULTS AND DISCUSSION.....	92

4.3.1	Characterization of the Cu-BTtri framework	92
4.3.2	Standard adsorption isotherms and isosteric heat of adsorption for CO ₂ and N ₂	92
4.3.3	The location of adsorption sites for CO ₂ and N ₂	94
4.3.4	Evolution of lattice parameters and guest occupancies as a function of temperature ...	100
4.3.5	Transient breakthrough simulations in fixed bed adsorbers	101
4.4	CONCLUSIONS.....	106
CHAPTER 5- LARGE ANISOTROPIC NEGATIVE THERMAL EXPANSION IN CU-TDPAT METAL-ORGANIC FRAMEWORK: AN <i>IN-SITU</i> X-RAY DIFFRACTION STUDY		109
5.1	INTRODUCTION	109
5.2	RESULTS AND DISCUSSIONS.....	111
CHAPTER 6- CONCLUSION AND FUTURE WORK		117
6.1	ACHIEVED RESULTS	117
6.1.1	Preparation of the required hardware, software and experimental methods	117
6.1.2	Information obtained from structure-property relationship studies	118
6.1.3	Synergy of theory and experiments	119
6.2	FUTURE WORKS.....	119
6.2.1	Evaluation of the adsorbents in real-world chemical separation applications.....	120
6.2.2	Extending the structure-property relationship studies to other chemical applications...	120
CHAPTER 7- APPENDIX.....		121
7.1	APPENDIX TO CHAPTER 2	121
7.1.1	Gas adsorption measurements	121
7.1.2	Pore Volume calculations based on the adsorption data for nitrogen at 77 K.....	122
7.1.3	Surface area calculations based on the N ₂ adsorption data at 77 K.....	123
7.1.4	Fitting M-BTT CO ₂ adsorption isotherms	124
7.1.5	References for the appendix to chapter 2.....	145
7.2	APPENDIX TO CHAPTER 3	146
7.2.1	SEM image of Cu-BTtri sample.....	146
7.2.2	The reported structure of Cu-BTtri.	147
7.2.3	The EDX spectra for Cu-BTtri.....	148
7.2.4	Rietveld refinement of the activated framework (neutron diffraction data).....	149
7.2.5	Rietveld refinement of the activated framework (synchrotron x-ray diffraction pattern).....	151
7.2.6	Cu-BTtri structure refined based on the synchrotron data.....	152
7.2.7	Gas adsorption measurements.....	153
7.2.8	Pore Volume calculations based on the adsorption data for nitrogen at 77 K.....	154
7.2.9	Surface area calculations based on the N ₂ adsorption data at 77 K.....	154
7.2.10	Fitting Cu-BTtri hydrogen adsorption isotherms.....	155
7.2.11	Calculating Isosteric heats of adsorption.....	157
7.2.12	Rietveld refinement of the framework loaded with 0.36 D ₂ /Cu ²⁺ (neutron diffraction data)	159

7.2.13	<i>Rietveld refinement of the framework loaded with 3.11 D₂/Cu²⁺ (neutron diffraction data)</i>	161
7.2.14	<i>Comparing adsorption sites with Cu-BTT</i>	163
7.2.15	<i>Isosurfaces of the charge density plots</i>	165
7.2.16	<i>References for the appendix to chapter 3</i>	166
7.3	APPENDIX TO CHAPTER 4	167
7.3.1	<i>XRD pattern of Cu-BTTRI sample</i>	167
7.3.2	<i>Gas adsorption measurements</i>	168
7.3.3	<i>Pore Volume calculations based on the adsorption data for nitrogen at 77 K</i>	169
7.3.4	<i>Surface area calculations based on the N₂ adsorption data at 77 K</i>	169
7.3.5	<i>Fitting Cu-BTTRI CO₂ and N₂ adsorption isotherms</i>	171
7.3.6	<i>Isosurfaces of the charge density plots for CO₂ adsorption sites</i>	179
7.3.7	<i>Isosurfaces of the charge density plots for N₂ adsorption sites</i>	181
7.3.8	<i>Rietveld refinement of the framework loaded with 0.40 CO₂/Cu²⁺ (neutron diffraction data)</i>	182
7.3.9	<i>Rietveld refinement of the framework loaded with 1.25 CO₂/Cu²⁺ (neutron diffraction data)</i>	184
7.3.10	<i>Rietveld refinement of the framework loaded with 1.60 CO₂/Cu²⁺ (neutron diffraction data)</i>	186
7.3.11	<i>Rietveld refinement of the framework loaded with 0.33 N₂/Cu²⁺ (neutron diffraction data)</i>	188
7.3.12	<i>Rietveld refinement of the framework loaded with 2.19 N₂/Cu²⁺ (neutron diffraction data)</i>	190
7.3.13	<i>Rietveld refinement of the framework loaded with 1.09 CO₂/Cu²⁺ (synchrotron diffraction data)</i>	192
7.3.14	<i>Fitting of unary isotherm data for transient breakthrough simulations</i>	194
7.3.15	<i>References for the appendix to chapter 4</i>	195
7.4	APPENDIX TO CHAPTER 5	196
7.4.1	<i>Synchrotron powder X-ray diffraction pattern of Cu-TDPAT at 100K</i>	196
7.4.2	<i>Synchrotron powder X-ray diffraction pattern of Cu-TDPAT at 500K</i>	197
7.4.3	<i>Synchrotron single crystal X-ray diffraction pattern of Cu-TDPAT at 100 K</i>	198
7.4.4	<i>Sequential LeBail refinement</i>	199
7.4.5	<i>Fitting of the lattice parameters and unit cell volume by 2nd degree polynomial</i>	203
7.4.6	<i>Lattice parameters from Single Crystal diffraction</i>	208
7.4.7	<i>Naming of the atoms in the asymmetric unit of Cu-TDPAT</i>	211
7.4.8	<i>The fold angle between the azine ring (N4, C26, N5, C27, N6, and C25) and the benzene ring (C15, C16, C17, C18, C13, and C14)</i>	212
7.4.9	<i>Benzene rings rotating around the paddlewheel planes</i>	213
7.4.10	<i>Paddlewheels twisting</i>	217
7.4.11	<i>Change in the Cu-Cu distance</i>	223
7.4.12	<i>References for the appendix to chapter 5</i>	229

REFERENCES	231
CURRICULUM VITAE	263
PUBLICATION LIST	267

List of abbreviations and symbols

°	degree
ΔQ	separation potential
δ	chemical shift
μmol	micromole
Å	Ångström
ad	adeninate
atz	aminotriazole
BDC-NH ₂	2-amino-1,4-benzenedicarboxylate
BET	Brunauer-Emmett-Teller method
bptc	biphenyl-3, 3', 5,5'-tetracarboxylate
BTB	benzene-1,3,5 tribenzoate
BTT ³⁻	1,3,5-benzenetristetrazolate
btc ³⁻	1,3,5-benzenetricarboxylate
1,4-BDC	1,4-benzenedicarboxylate
°C	degree Celsius
CCS	Carbon Capture and Storage
CP	Cross Polarization
DEF	Diethylformamide
DFT	density functional theory
DMA	Dimethylacetamide
DMF	Dimethylformamide
dobpdc ⁴⁻	4,4'-dioxido-3,3'-biphenyldicarboxylate
DRIFTS	Diffuse reflectance infrared Fourier transform spectroscopy
DSC	differential scanning calorimetry
esu	statcoulomb centimeter
g/gr	gram
GCMC	grand canonical monte carlo
H ₃ BTP	(1,3,5-tris-1H-pyrazol-4-yl)benzene
H ₃ BTTri	1,3,5-tri(1H-1,2,3-triazol-4-yl)benzene)

INS	inelastic neutron scattering
IR	infrared spectroscopy
J	Joule
K	Kelvin
L	Liter
M	molar (mol.L ⁻¹)
m	meter
m ² /g	square meter per gram
MAS	magic-angle-spinning
MD	molecular dynamics
MeOH	Methanol
mg	milligram
min	minutes
mL	milliliter
mmol	mill mole
mol	mole
MW	molecular weight
MIL100(Fe)/Fe-BTC/ Basolite® F300	[Fe(1,3,5-benzenetricarboxylate)]
MIL-53/Basolite® A100	[Al(OH)(1,4-benzenedicarboxylate)]
MIL-53(Cr)	Cr(OH)(1,4-BDC)
MIL	Material des Instituts Lavoisier
MIL-101(Cr)	Cr ₃ O(1,4-BDC) ₃ (H ₂ O) ₂ X, where X = F ⁻ or NO ³⁻
mmen	N,N'-dimethylethylenediamine
MOF-177/Basolite® 7377	Zn ₄ O(1,3,5-benzenetribenzoate) ₂]]
M-MOF-74/CPO-27-M/M2(dhtp)	M ₂ (dobdc)
MOF	metal-organic framework
NEXAFS	near edge x-ray absorption fine structure
NIST	national institute of standards and technology
nm	nanometer
NMR	nuclear magnetic resonance
NOTT-300	Al ₂ (OH) ₂ (bptc)
NTE	negative thermal expansion
OMS	open metal site

OMC	open metal coordination site
ox	oxalate
PEI	polyethyleneimine
ppm	parts per million
PSA	pressure swing adsorption
QENS	quasielastic neutron scattering
Q_{st}	Isosteric heat of adsorption
SIFSIX	hexafluorosilicate
STP	standard temperature and pressure
STY	Space Time Yield
T	temperature
TDPAT	(2,4,6-tris(3,5-dicarboxylphenylamino)- 1,3,5-triazine)
TSA	temperature swing adsorption
UFF	universal force field
VASP	Vienna ab-initio simulation package
vdW	van der Waals
VSA	vacuum swing adsorption
XAS	X-Ray absorption spectroscopy
XRD	X-ray diffraction
ZIF-8/ Basolite® Z1200	[Zn(2-methylimidazole) ₂]

Note: additional abbreviations for specific compounds are defined within the thesis.

Chapter 1

An introduction on characterization of Metal-Organic Frameworks (MOFs) for gas adsorption applications¹

1.1. Introduction

In this chapter, we briefly review the literature of metal-organic frameworks (MOFs) for gas adsorption/capture applications. Later on, in the next chapters, we will employ the techniques and tools that are mentioned in this chapter for the study of physiochemical properties of MOFs. Although, in this chapter, we mostly focus on the most important and frequent separation application which MOFs have been used in, i.e. CO₂ capture/separation, most of the techniques that are explained here can be extended to other separation applications, namely hydrogen storage, which will be discussed later in chapter 3.

We hope that this chapter can introduce the basics of the important characterization tools for the study of MOF properties, especially in chemical separation applications.

¹ This chapter is based on published the book chapter: Asgari, Mehrdad, and Wendy L. Queen. "Carbon Capture in Metal–Organic Frameworks." *Materials and Processes for CO₂ Capture, Conversion, and Sequestration* (2018): 1. M. A. has screened literature, read the corresponding articles, reports, theses, and books. He has also written the book chapter.

1.1.1 The importance of carbon dioxide capture

Carbon dioxide, an important chemical gas found in the atmosphere, is critical for the continuation of life on earth. This molecule is required for photosynthesis that fuels plants, which serve as the main source of food for all humans and animals and further produces oxygen that is essential for human respiration.¹ Studies have shown that a small accumulation of CO₂ in the atmosphere is necessary to warm earth to a level where glaciation is inhibited, producing an environment where plant and animal life can thrive.² However, there is recent evidence that human activity related to energy production is generating an abundance of CO₂ in the atmosphere that can no longer be balanced by earth's natural cycles, an act that is expected to confront mankind with serious environmental problems in the future. Since CO₂ is the most abundantly produced greenhouse gas (Figure 1-1),³ it is directly implemented in global warming. It is predicted that if the negligent release of CO₂ persists, it could have detrimental effects on our environment that include: melting ice caps, rising sea levels, strong changes in weather patterns, ocean acidification, ozone layer depletion, poor air quality, and desertification; all of these things could lead to the potential demise of the human, plant, and animal life making CO₂ mitigation an urgent need⁴⁻⁵.

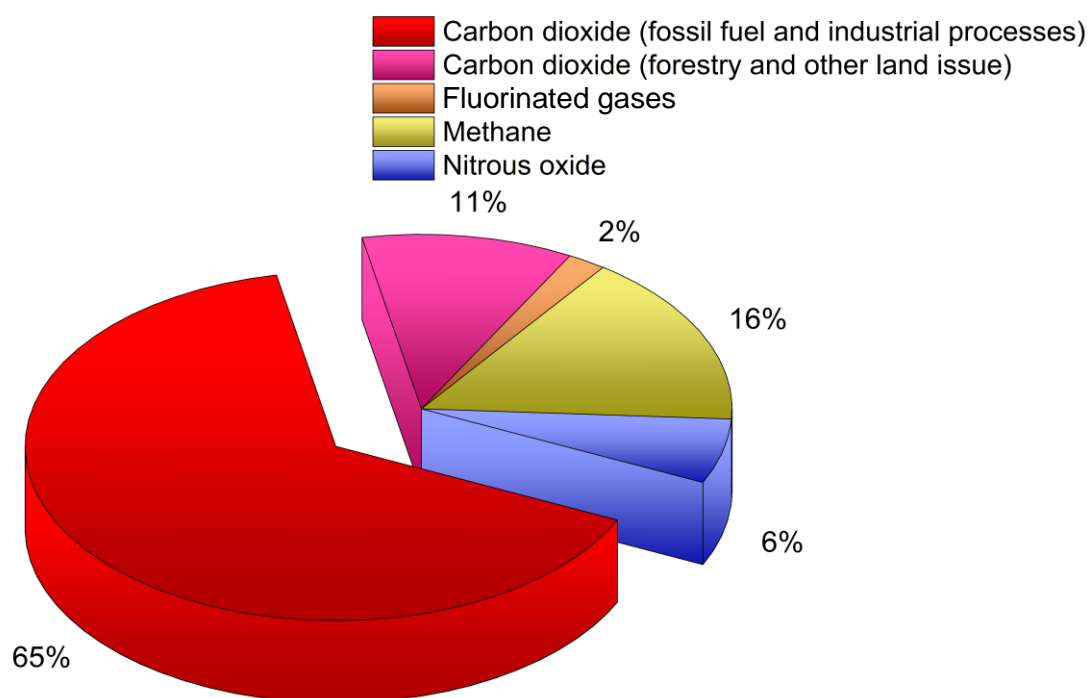


Figure 1-1 The contribution of different constituent in the greenhouse gas emission. Data is taken from reference³.

Eighty percent of the world's energy is currently supplied by the combustion of carbon-based fossil fuels,⁶ an anthropogenic activity that has led to steady increase in atmospheric CO₂ levels. Since the beginning of the industrial revolution in the 1750s, atmospheric CO₂

concentration has increased from 280 ppm⁷ to above 400 ppm in March of 2015⁸⁻⁹. While the best remediation method is to transition from traditional carbon-based fuels to clean energy sources, like wind and solar, energy transitions are historically slow.⁹ As such, it is projected that the use of fossil fuels will continue for years to come, requiring the development of materials that can remediate the effects of CO₂ through direct carbon capture and sequestration (CCS) and/or conversion of this greenhouse gas into value added chemicals and fuels. While CO₂ capture directly from air is considered to be an unfeasible task, carbon capture from large point sources, such as coal- or gas-fired power plants, could be realized. Currently 42% of the world's CO₂ emissions come from production of electricity and heat¹⁰ and it is anticipated that approximately 80 to 90% of these emissions could be eliminated with the implementation of adequate CCS technology¹¹. CCS is a three-step process that includes the capture of CO₂ and its transport to sites where it is subsequently stored. While the processes of storage and transport are well-developed technologies, the actual implementation of capture process on a global scale is still constrained by the development of an adequate gas separation technology. Thus, the discovery of new materials with high separation ability is a pertinent obstacle that must be overcome.

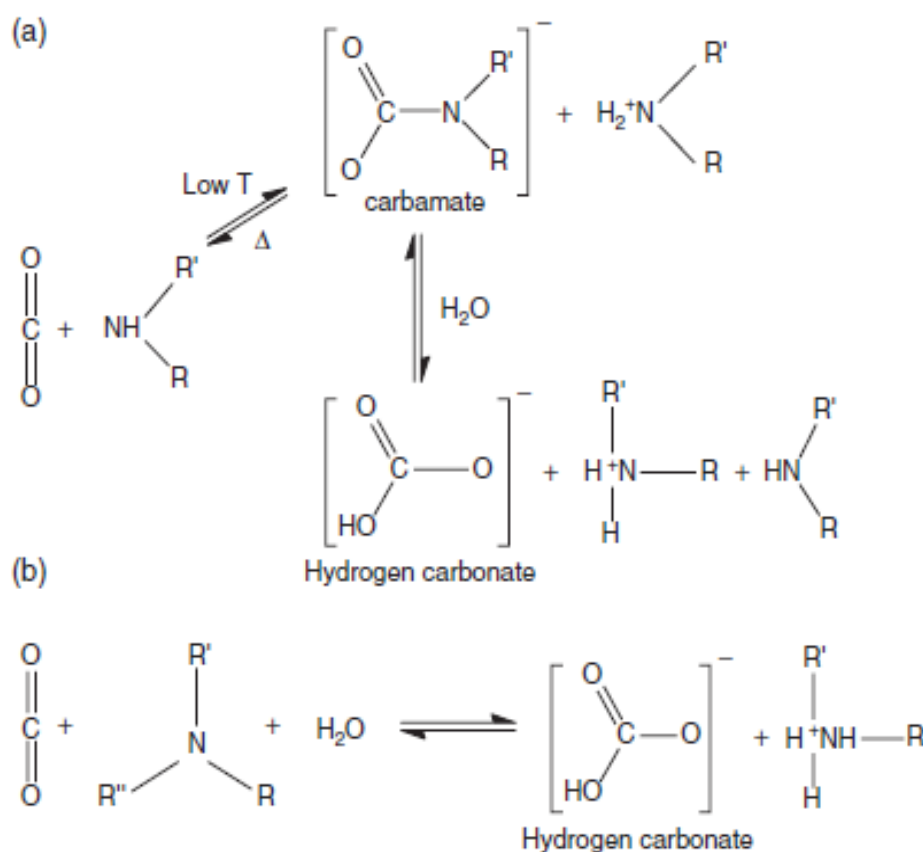


Figure 1-2 Reaction scheme for carbon dioxide with a (a) primary, secondary or (b) tertiary amine.

1.1.2 Conventional industrial process of carbon capture and limitations: liquid amines

The most mature capture technology, which has been around since the 1930s, includes aqueous alkanolamine-based scrubbers.¹² These chemical absorbents feature an amine functionality that undergoes a nucleophilic attack on the carbon of the CO₂ molecule (Figure 1-2) to form either a carbamate (in the case of primary or secondary amines) or a bicarbonate species (in the case of tertiary amines).¹³ While amine scrubbers are highly selective in the capture of CO₂ relative to other components in a gas stream, operate well at low partial pressures, and can be readily included into existing infrastructure at power plants, they have several limitations that inhibit their implementation on scales large enough for post-combustion carbon capture.¹⁴ The materials are quite corrosive to sources of containment requiring their dilution with water to concentrations ranging from 20 to 40 wt% of the amine.¹⁵ The high heat capacities of the aqueous-amine solutions combined with high adsorption enthalpies of CO₂, approaching -100 kJ/mol, creates a large parasitic energy cost for the subsequent release of CO₂. While the strength of CO₂ binding can be tuned to some degree with amine substitution (1° > 2° > 3°, i.e. monoethanolamine, diethanolamine or triethanolamine)¹³, the regeneration process typically requires temperatures that range from 120 to 150 °C.¹⁶⁻¹⁸ The instability of the materials at these temperatures leads to a slow decomposition and hence decrease in the materials performance with subsequent absorption cycles. Given all of these problems, this technology, which has already been employed in hundreds of plants worldwide for CO₂ removal from natural gas, hydrogen, and other gases, requires that approximately 30% of the energy produced from a power plant be put back into the carbon-capture process¹². It is projected that solid adsorbent materials with lower heat capacities might cut the energy consumption assumed from the current carbon capture technology considerably.¹⁹ For this to be realized, much further work is required to design porous solid adsorbents that show (i) high stability in the presence of various components in the gas stream, particularly water, (ii) high selectivity and adsorption capacity, (iii) low-cost, (iv) reversibility, and (v) scale ability²⁰. To date, there are several classes of porous adsorbents studied for applications related to carbon capture including zeolites, activated carbons, and covalent organic frameworks; however, all of these materials suffer quite significantly from a minimal adsorption capacity and/or low selectivity.^{19, 21-25}

1.1.3 Metal-organic frameworks and their synthesis

One materials solution to the aforementioned carbon-capture problem is a relatively new class of porous adsorbents known as metal-organic frameworks (MOFs), which are constructed by metal-ions or metal-ion clusters linked together by organic ligands (Figure 1-3).²⁶⁻²⁷ Since the discovery that these materials can exhibit permanent porosity in the late 1990s²⁸, they have rapidly moved to the forefront of materials research. Looking at publications related to carbon dioxide adsorption in MOFs, one can see a significant increase in the number since 2005, with over 500 publications in 2015 alone.²⁹ This is in part due to their unprecedented internal surface areas,

up to $7000 \text{ m}^2/\text{g}$ ³⁰, which allows the adsorption of significant amount of guest species. Further, the molecular nature of the predefined organic linkers offers a modular approach to their design (Figure 1-3). Through judicious selection of the building blocks, MOF structures can be chemically tuned for a variety of environmentally relevant applications such as gas storage and separation, sensing, and catalysis.³¹⁻³⁹ MOFs have become particularly attractive due to recent reports of materials with high capacities and selectivities for the adsorption of various guest molecules.⁴⁰⁻⁴¹ Currently MOFs hold several world records related to small molecule adsorption that include: (i) surface area ³⁰, (ii-iii) room-temperature hydrogen ⁴² and methane storage⁴³, and (iv) carbon-dioxide storage capacity.⁴⁴ The facile chemical tunability of MOFs is their primary advantage relative to other more traditional porous adsorbents such as activated carbons and zeolites. Further their highly crystalline nature combined with a nonhomogenous van der Waals potential energy landscape on the internal MOF surface dictates that incoming guest molecules bind in well-defined positions and orientations; this allows diffraction techniques to be used to readily unveil their site-specific binding properties. Understanding the structure-function allows one to tune the properties of existing materials or rationally design new materials with specified function.

MOFs are typically synthesized using a combination of metal salts and ligands *via* standard hydrothermal or solvothermal methods; reactions are usually carried out inside of sealed vessels or using schlenk line techniques with reaction times that range from hours to days. The aforementioned methodologies are typically limited to small-scale reactions, from mg to g size

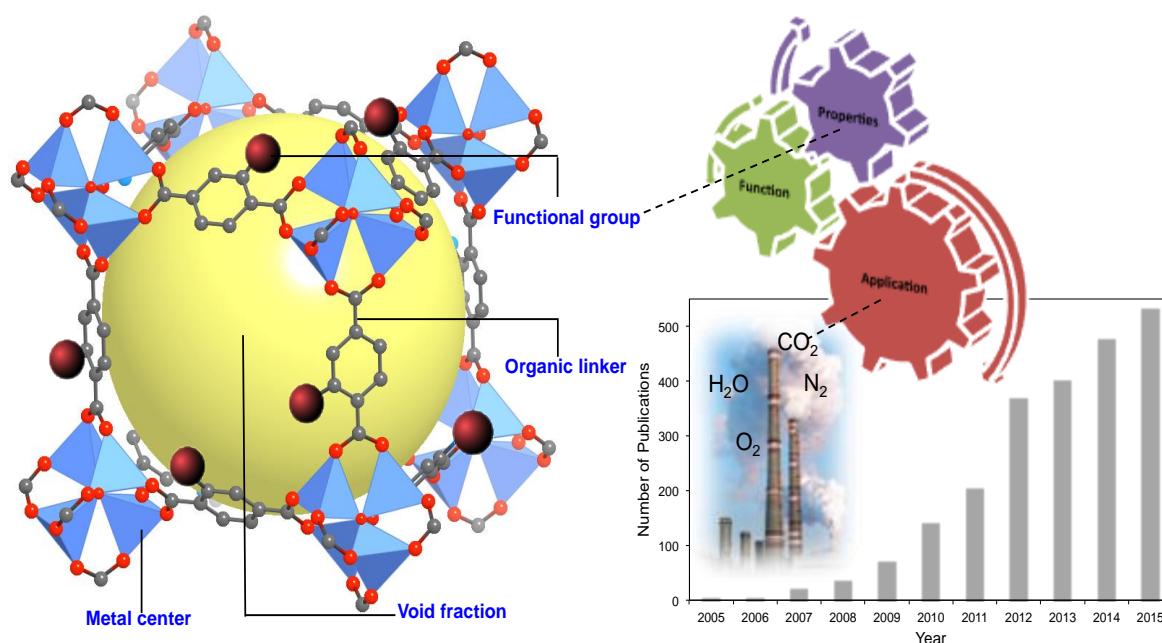


Figure 1-3 (left) Ball and stick model of a MOF, MOF-5 or $\text{Zn}_4\text{O}(\text{1,4-benzendicarboxylate})_3$ ²⁷, showing the modular nature of the frameworks, which can be used to tune MOF properties for the selective binding of gas molecules, making the materials of particular interest in applications related to carbon capture. (right) The number of publications related to “CO₂ adsorption” and “metal-organic frameworks” from 2005 to 2015 is significantly increasing; the data was obtained from the Thomas Reuters ISI web of knowledge.²⁹

yields, making them only suitable for standard laboratory based characterization. To reduce the energy requirements associated with these traditional procedures, recent efforts have been made to search for reaction conditions necessary to produce MOFs at room-temperature; however many of these methods involve non-aqueous solvents such as DEF, DMF, and ETOH.⁴⁵ Given this, more recent efforts have been made to develop MOF syntheses in water, an effort that makes industrial production of these materials more feasible.⁴⁶⁻⁴⁷ Other research has abandoned the more traditional forms of laboratory based techniques and moved towards more innovative methods to assist in materials scale-up; some examples of non-traditional techniques include microwave⁴⁸, mechanochemical methods⁴⁹⁻⁵⁰ (such as solvent-free neat grinding or extrusion), continuous flow reactions⁵¹⁻⁵², and spray drying⁵³. Of these techniques the highest space time yields (STY, kg per m³ per day), a process parameter that is used to determine industrial profitability, is reported for the mechanochemical extrusion methods developed by James *et al.*; these methods have remarkable STY values that range between 1 and 3 orders of magnitude greater than those for other methods, a result of the absence or near absence of solvent and high reaction rates. Further, it should be noted that the reported surface areas and pore volumes for the as-prepared materials are similar to those produced on small scales.⁵⁰⁻⁵¹ The latter is an important note because many reports show that surface areas and CO₂ adsorption properties suffer quite significantly in the scale-up procedure.⁵⁴

While industrial scale synthesis of MOFs is currently limited to a handful of iconic frameworks, it is expected to become a developing trend as companies like BASF have shown proof of concept for the production of MOFs on large scales⁵⁵⁻⁵⁷ using green synthetic methods (in aqueous media). These materials, targeted for applications related to on-board storage in natural gas and hydrogen powered vehicles, are currently available under the trade name Basolite® and include a few eminent frameworks such as HKUST-1 (Basolite® C300 or [Cu₃(1,3,5-benzenetricarboxylate)₂]), MIL-53 (Basolite® A100 or [Al(OH)(1,4-benzenedicarboxylate)]), ZIF-8 (Basolite® Z1200 or [Zn(2-methylimidazole)₂]), and Fe-BTC (Basolite® F300 or [Fe(1,3,5-benzenetricarboxylate)]), and MOF-177 (Basolite® 7377 or Zn₄O(1,3,5-benzenetribenzoate)₂).⁵⁸⁻⁶⁰ The most critical parameters that must be considered for the industrial scale-up of MOFs have been recently identified as the following: (i) the cost of raw material per kg of obtained MOF (ii) the amount of MOF produced per m³ of reaction mixture per day, (iii) conditions required for reaction agitation during synthesis, (iv) length of time required and amount of solvent required for sample filtration and (v) washing conditions necessary for drying (activating) prepared solids.⁶¹

1.1.4 CCS technologies and MOF requirements

Growing energy demands related to continued population growth and the industrialization of developing countries, like China, imposes the need for the continued combustion of fossil fuels, including coal, natural gas, and oil.⁶²⁻⁶³ Considering that carbon capture from air is not a feasible task, capture at large point sources is certainly one of the best-case scenarios to significantly reduce global CO₂ emissions despite the tremendous effort that is

required. It is projected that global reserves of coal, which has the highest carbon content and is responsible for 43% of CO₂ emissions from fuel combustion⁶⁴, will last over 110 years at the

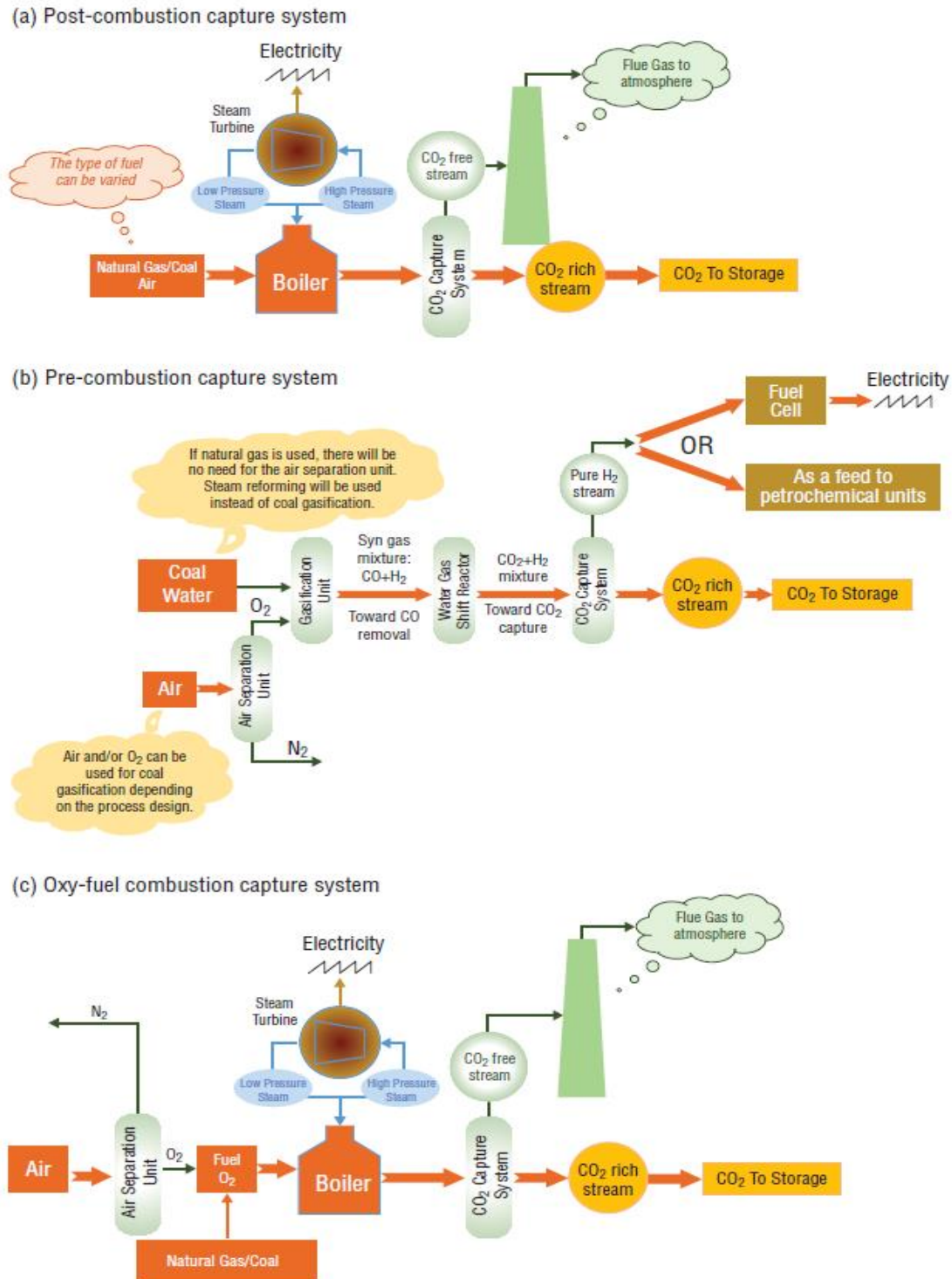


Figure 1-4 Schemes for the 3 different carbon capture technologies including (a) post-combustion capture, (b) pre-combustion capture, and (c) oxy-fuel combustion capture.

current production rate.⁶⁵ For comparison, oil reserves are projected to exist for the next 40-55 years.⁶⁵⁻⁶⁷

Currently there are three existing chemical processes used for the combustion of fossil fuels at large point sources such as coal and gas-fired power plants. These three processes, which include: (i) post-combustion capture, (ii) pre-combustion capture, and (iii) oxy-fuel combustion capture, result in the need for a collection of separation materials capable of operating at different temperatures and pressures and offer selective adsorption for several different gas mixtures (Table 1-1). The three processes are briefly described below.

(i) Post-combustion capture at a coal-fired power plant (Figure 1-4a) involves the separation of CO₂ from flue gas (1 bar) that consists primarily of CO₂ (13-15% by volume) N₂ (70-76%), H₂O (5-7%), O₂ (2-15%) and other minor contaminants like SO_x and NO_x. Flue gas is generated after the combustion of fuel in air.⁶⁸ The high N₂ content in air lends to flue gas mixtures with low-partial pressures of CO₂; as such, the selectivity for CO₂/N₂ is one of the most critical factors considered in the selection of a separation material. As in the case of the liquid amine based scrubbers, finding a balance between CO₂ selectivity and binding affinity in MOFs is necessary. Very high CO₂ binding energies on the sorbents affords high regeneration energies significantly reducing power plant efficiency.⁶⁹

(ii) Pre-combustion capture (Figure 1-4b) involves the separation of CO₂ from H₂ prior to the combustion process and hence zero carbon emission afterwards. In this process coal undergoes gasification to produce a syngas that typically consists of CO, CO₂, H₂ and H₂O. Afterwards the syngas is reacted with steam in a process called the water-gas shift reaction to form CO₂ (15-34%), H₂ (35-45%) with small amounts CO, H₂S, and N₂. It should be noted that there is also a significant amount of water present in the flue gas stream after the water-gas shift reaction. However, much of the water could be removed using existing technologies. From this point, the separation is carried out to remove CO₂ producing a nearly pure H₂ fuel that is then combusted to form water. This separation is significantly easier, relative to post-combustion capture, due to the higher partial pressures and concentrations of CO₂, approximately 5-40 bar and up to 34% CO₂, respectively, making the consideration for the separation medium a bit more versatile to include, solid adsorbents, liquid absorbents, and membranes.⁷⁰⁻⁷¹

(iii) As the final alternative, rather than using air for the combustion of fossil fuels, oxy-fuel combustion (Figure 1-4c) involves a separation of O₂ from air before the combustion process. Post-separation this technology involves a nearly pure feed of O₂ (purity usually > 95%) that is then used in the combustion step eliminating the need for the separation of CO₂ and N₂ later. The problems with this separation is that it is currently limited to energetically unfavorable distillation as most adsorbents designed to date, such as lithium-containing zeolites, only show limited selectivity of N₂ over O₂ giving rise to gas mixtures with inadequate purity levels.⁷² After combustion, the final gas mixture has CO₂ (72-85%) with some amount of water (6-7%) that can easily be condensed giving rise to CO₂ capture rates higher than 95%, a feat not yet achieved by

pre-combustion and post-combustion capture separations. Compared with aforementioned processes utilizing N_2 rich air for combustion, the formation of NO_x is largely inhibited due to the initial removal of N_2 ; this will allow for a significantly smaller NO_x removal than in typical power plants.

Table 1-1 Typical composition of gas for 3 carbon capture technologies

Molecules and conditions	Post-combustion ^{*T[23, 62-68]} by volume		Pre-combustion ^{*[23, 69, 70]} by volume		Oxyfuel ^{*[71, 72]} by volume
	Natural Gas	Coal	Natural Gas	Coal	Air purification ^{**}
CO ₂	3-9 %	13-15%	15-25%	26-34%	400 ppm
N ₂	70-76%	73-77%	trace	0.3-2.2%	78 %
H ₂ O	7-18%	5-7%	--	18-38%	--
H ₂	--	--	70-80%	35-45%	0.5 ppm
CH ₄	--	--	3-6%	--	-
O ₂	2-15%	3-4%	--	--	21%
H ₂ S	--	--	--	0.1-0.2%	--
SO ₂	--	800 ppm	--	--	--
SO ₃	--	10 ppm	--	-	--
HCl	--	100 ppm	--	trace	--
Hg	--	1 ppb	--	--	--
CO	200-300 ppm	20-50 ppm	1-3%	0.5-0.6%	--
NO _x	10-300 ppm	500 ppm	--	--	0.3 ppm
Ne	--	--	--	--	18 ppm
Kr	--	--	--	--	1 ppm
Xe	--	--	--	--	0.087 ppm
Ar	--	--	--	0.04%	0.9%
Temperature	40-75 °C	40-75 °C	40 °C	40 °C	25 °C
Pressure	1 bar	1 bar	5-40 bar	5-40 bar	1 atm

For the aforementioned carbon capture cases, there are 3 potential processes for regeneration after adsorbent bed saturation including (i) Temperature Swing Adsorption (TSA), Pressure Swing Adsorption (PSA), and Vacuum Swing Adsorption (VSA). TSA is a process where the temperature of the bed will be increased (likely using heat from the power plant) post saturation allowing desorption of the small molecules from the surface of the adsorbent. The resulting pressure increase drives the adsorbate out of the bed, and once no further desorption is observed at the target temperature, a purge gas can additionally be run through the bed to push out additional adsorbate. Subsequently the bed can be cooled and additional adsorption cycles can be run. On the other hand, PSA and VSA processes entail lowering the pressure from which adsorption takes place to permit removal of the surface bound guests. For PSA, the inlet valve, where high-pressure gas is allowed to flow into the bed, is simply closed allowing the pressure inside the bed to approach atmospheric pressure. Albeit similar, VSA entails lowering the bed pressure below atmospheric. The low partial pressure of CO₂ in post-combustion capture makes TSA the most plausible method for bed regeneration, as it would be energetically unfeasible to expand the bed or pull vacuum on such a large volume of gas. Considering pre-combustion capture

involves high-pressure flue gas it is much more feasible to employ PSA for the regeneration method.

Considering the parameters for these capture technologies and their subsequent regeneration methods are not easily modified, it is necessary to design adsorbents with all of these parameters in mind. As MOFs are the most chemically tunable adsorbent available, they offer unmatched opportunity to find the necessary balance between various parameters such as binding energies and densities of adsorption sites, capacities, and selectivities, which influence the ability to achieve high working capacities and low-regeneration energies. The final decision related to which adsorbent should be applied to the carbon capture process should be taken after a detailed evaluation of the technical performance and assessment of economic feasibility. Such an evaluation is imperative for implementation of carbon capture processes on a global scale.

1.1.5 Molecule specific

The elevated temperature at which carbon capture is carried out, combined with low boiling points (Table 1-2) of many of the small molecules in flue gas and air makes cryogenic distillations, carried out on scales large enough for CCS, energetically unfeasible; hence, large energy savings could be realized with the use of solid adsorbents that function at much higher temperatures. When working to design adsorbent materials capable of separating gases, one must first consider the differences in the physical properties of the molecules of interest. For physisorptive type interactions, the separation process relies on guest molecules having small disparities in their physical properties that include polarizability, quadrupole moment, and dipole moment. For most of the components in flue gas and air, the values for these aforementioned physical properties are listed in Table 1-2. While some important differences exist for instance between CO₂ and N₂, regarding the nature of their intermolecular interactions and their chemical reactivity, these differences are minimal and necessitate the careful design of carbon capture materials that exhibit strong, molecule specific chemical interactions on their internal surface.

1.2 Understanding the Adsorption Properties of MOFs

There are a variety of techniques used to assess MOFs for CO₂ capture applications. These include single component adsorption isotherms, breakthrough analysis, multicomponent adsorption and a host of *in-situ* techniques. Several studies have shown that pairing many characterization methods, particularly adsorption, with *in-situ* characterization can provide molecular level insight into the adsorption process giving direct evidence of the structural components that give rise to enhanced or diminished properties.⁷³ There is hope that in-depth experimental efforts like these can provide the insight necessary for the eventual deliberate design of new MOF for energetically favorable carbon capture technologies.

Table 1-2 Chemical properties of small molecules involved in carbon capture

Molecules	Normal boiling point (K)	Kinetic diameter ^{*[63]}	Quadrupole moment ^{*[63]}	Dipole moment ^{**}	Polarizability ^{***[40]}
CO ₂	195 (Sublimation)	3.3	43.0	0	29.1
N ₂	77.35	3.64	15.2	0	17.4
H ₂ O	373.15	2.64	--	18.5	14.5
H ₂	20.27	2.89	6.62	0	8.04
CH ₄	111.66	3.76	0	0	25.9
O ₂	90.17	3.46	3.9	0	15.8
H ₂ S	212.84	3.62	--	9.78	37.8
SO ₂	263.13	4.11	--	16.3	37.2
HCl	188.15	3.34	38.0	11.1	26.3
CO	81.66	3.69	25.0	1.1	19.5
NO	121.38	3.49	--	1.59	17.0
NO ₂	302.22	--	--	3.16	30.2
Ne	27.07	2.82	0	0	3.96
Kr	119.74	3.66	0	0	24.8
Xe	165.01	4.05	0	0	40.4
Ar	87.27	3.54	0	0	16.4

*The numbers are expressed with the following unit: 10^{-27} esu⁻¹ cm⁻¹. **The numbers are expressed with the following unit: 10^{-19} esu⁻¹ cm⁻¹. ***The numbers are expressed with the following unit: (10^{-25} cm³)

1.2.1 Single component Isotherms

Nitrogen adsorption isotherms, collected at 77 K and up to 1 bar, are typically used to first assess the pore volume, pore size distribution and surface area of as-prepared MOF materials. Subsequently, adsorption isotherms can also be used to further assess a materials performance related to carbon capture processes. For this, the isotherms are collected using carbon dioxide (or other small molecules) as probes. These experiments are typically carried out using commercially available equipment at temperatures ranging from 25 to 40 °C and from low-pressures up to 50 bar. It should be noted that these measurements provide insight into a materials (i) adsorption capacity, (ii) selectivity, and (iii) enthalpy of adsorption.⁶² These three metrics will be briefly discussed below.

Adsorption capacity

Adsorption capacity is expressed gravimetrically or volumetrically as the amount of adsorbed CO₂ per unit volume or mass of adsorbent, respectively. While reports of gravimetric capacity are more predominate throughout the literature, it is equally important to look at the volumetric properties of materials as it dictates the required volume of the adsorbent bed and both parameters also influence the efficiency with which the materials can be regenerated. It was recently shown that MOF-177, a high surface area adsorbent (BET surface area > 4500 m² per

gram of adsorbent), exhibits a volumetric capacity at room temperature and 35 bar of 320 cm³ (STP) /cm³, a value that is over nine times larger than the quantity of CO₂ that can be stored in the same empty container without the MOF.⁷⁴ More often than not, high surface areas lead to high capacities in the high pressure regime, while low pressure adsorption measurements, < 1 bar, are more strongly impacted by the strength and density of the binding sites (Figure 1-5). It should be noted that high pressure CO₂ adsorption isotherms are important for pre-combustion capture while low-pressure, typically not higher than 1 bar are more relevant for post-combustion capture.

Small molecule selectivity

Selectivity can be kinetic in nature, based on size exclusion of molecules of varying size, or thermodynamic in nature, and based on significant differences in interaction energies on the internal MOF surface. It can be seen from Table 1-2 that the kinetic diameter of the small molecules of interest for carbon capture, CO₂/N₂, CO₂/H₂, and O₂/N₂, are all less than 4 Å. Considering these issues and that MOF pores sizes are more often than not above 4 Å, kinetic based selectivities become problematic. Instead the gas separations are based on thermodynamics. Therefore chemists must take other physical and chemical characteristics into consideration when designing separation materials.

The selectivity factor (S), is simply calculated using the following equation (1-1), where q represents the amount adsorbed of each gas and p represents the partial pressure of each gas. While this factor is a good way to compare different materials, it is not a real selectivity because it is calculated from single component isotherms where the gas molecules are not actually competing for adsorption sites.

$$S = \frac{q_1/q_2}{p_1/p_2} \quad Eq. (1 - 1)$$

Another method commonly used for predicting selectivities from single component isotherms is using the Ideal Adsorbed Solution Theory (IAST) developed by Meyers and Prausnitz.⁷⁵ For this method, single component isotherms are used to predict the adsorption equilibria for gas mixtures. The adsorption isotherms are collected for two gases at the relevant temperature and they are mathematically fit to extract the mole fraction of each species in the adsorbed phase. While the method is not extensively reviewed here it is becoming more visible throughout MOF literature due to the difficulty in acquiring multicomponent adsorption isotherms.⁷⁶ The validity of IAST estimations for the systems of CO₂/CH₄, CO₂/H₂, CH₄/H₂, and CO₂/N₂ mixtures in a variety of MOFs (MgMOF-74, MOF-177, and BTP-COF) and zeolites (FAU, LTA, MFI, and CHA) has been established in literature.⁷⁷⁻⁸⁰ While it is true that IAST theory can be utilized in many cases to give a relatively accurate estimation of the selectivity of different compounds relative to each other, there are some cases where the accuracy of estimated selectivities is questionable. A recent study of Cessford *et al.* investigated the applicability of IAST

to a variety of MOFs with varying structural features and also for a variety of small molecules with differing sizes, shapes, and polarities. The results, which were directly compared with GCMC (grand canonical Monte Carlo) simulations, showed that IAST has difficulty in predicting accurate selectivities when the adsorbates have large differences in size and shape or the MOF framework exhibits heterogeneities such as large variations in cavities or pore sizes.⁸¹

Isosteric heat of adsorption

Isosteric heat of adsorption ($-Q_{st}$) is an important parameter that gives an indication of the affinity of a MOF towards a specific small molecule. Often defined, as the average enthalpy of adsorption at constant coverage, it can give further insight into the energy required for the molecules subsequent release, a crucial point to be considered for lowering the overall energy consumption in carbon capture processes. Although a high isosteric heat implies stronger binding of the guest molecule to the surface, large values also indicate a larger amount of energy for the subsequent release of the guest molecule upon regeneration of the adsorbent. And so, chemists are constantly striving to find a balance where a small molecule binds strong (and selectively) enough to give large amounts of high purity gas after the separation, but weak enough so that the materials can be easily regenerated.

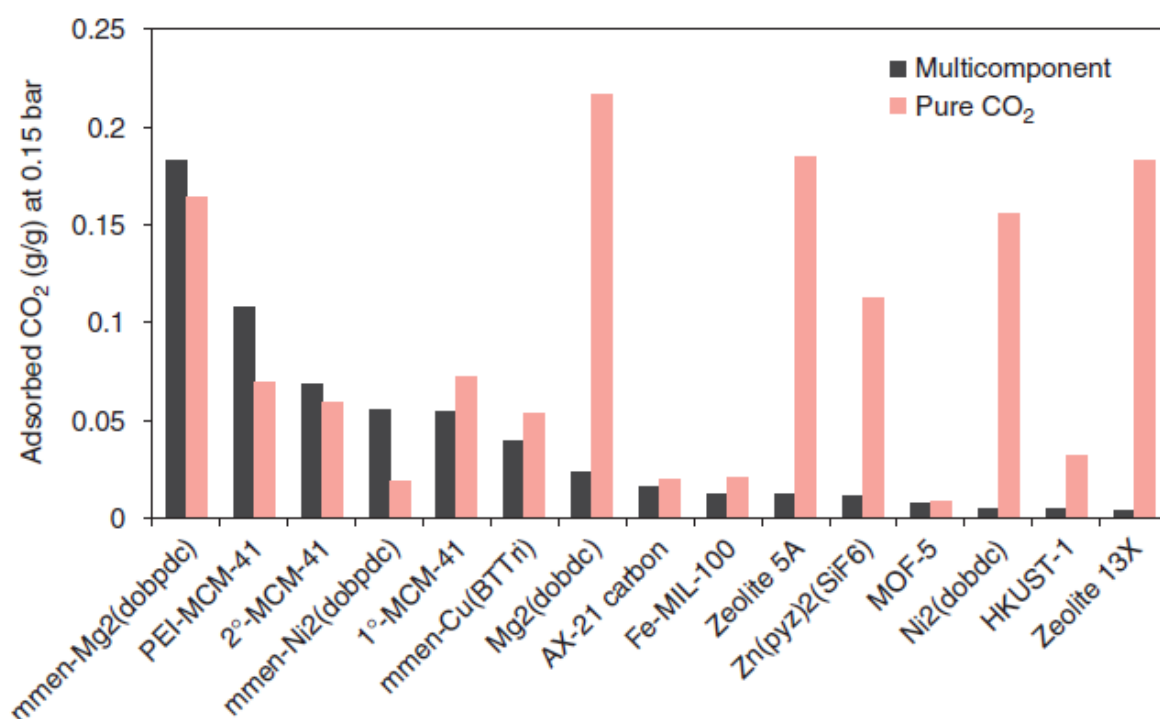


Figure 1-5 Comparison of CO₂ adsorption in 15 different framework materials in a single component isotherm, (pure CO₂) or a multicomponent mixture consisting of CO₂, N₂, and H₂O. Experiments were carried out at 40 °C and at equilibrium. The pressures for the multicomponent mixture include N₂ between 0.679 and 0.698 bar, CO₂ between 0.113 and 0.178, and H₂O between .01 and .029 bar with the total pressures ranging from 0.821 and 0.890 bar. For the equilibrium pressure refer to reference.⁸⁷

$$(\ln P)_N = -\left(Q_{st}/R\right)(1/T) + C \quad \text{Eq. (1-2)}$$

To calculate the isosteric heat, first single component adsorption isotherms are collected for at least two temperatures (or more) usually within 10 to 15 K of one another. These isotherms are then fit using a high order polynomial such as the single or dual site Langmuir model to formulate an expression representative of the adsorption isotherm.^{64, 82} Then the $(\ln P)$ is plotted as a function of $1/T$. From the Claussius Clapeyron⁸³, equation (1-2), (where P = pressure, R = universal gas constant, T = temperature, and C = is a constant), the isosteric heat of adsorption can be determined

A second method for determining the isosteric heat is using a virial type equation (1-3) shown below, which is first used to again model the adsorption isotherm. Afterwards, the isosteric heat can be extracted using equation (1-4).⁸³

$$\ln(P) = \ln(n) + \left(\frac{1}{T}\right) * \sum_{i=0}^m a_i n^i + \sum_{j=0}^k b_j n^j \quad \text{Eq. (1-3)}$$

$$Q_{st} = -R \sum_{i=1}^m a_i n^i \quad \text{Eq. (1-4)}$$

The biggest advantage of this calculation method lies in the fact that the isosteric heat can be obtained by the direct derivation of the equation (1-3). However, it should be noted that the first method, using the dual site Langmuir model, is particularly good for accurately fitting data that has a combination of both strong and weak adsorption sites. Without a proper fit to the adsorption isotherm, inaccurate determination of isosteric heats will likely be the result. This is apparent throughout the literature where the same MOF can have markedly different reported values for isosteric heats. A few examples include HKUST-1 whose isosteric heats range from 15 to 35 kJ/mol⁸⁴⁻⁸⁵ and Mg₂(dobdc) whose isosteric heats range from 39 to 47 kJ/mol⁸⁶⁻⁸⁷. This inconsistency in reported results could be related to improper activations, varied sample quality, or issues regarding the method chosen to determine the low-coverage isosteric heat. In these cases, theory capable of accurately determining enthalpies of adsorption can be quite useful for experimentalists to gauge the quality of their results.⁷³

1.2.2 Multicomponent adsorption

A more realistic, yet somewhat experimentally intractable method to assess the performance of a material for carbon-capture applications is through multicomponent adsorption isotherms. While single component isotherms are readily accessible using commercially available equipment, multicomponent adsorption measurements are time consuming, require customized equipment, and pose challenges regarding data analysis. Binary adsorption measurements in MOFs were first carried out in 2009 by Férey *et al.*⁸⁸ who measured the co-adsorption in a mixture

of CO₂/CH₄ in a flexible framework known as MIL-53(Cr)⁸⁹ (also known as Cr(OH)(1,4-BDC) where 1,4-BDC = 1,4-benzenedicarboxylate, MIL = Material des Instituts Lavoisier). Since this time other studies have been limited to a few other systems⁹⁰ exposed to binary mixtures and none of these reports assess CO₂/N₂ mixtures. However, in 2015, Mason *et al.* reported multicomponent adsorption carried out in ternary mixtures of CO₂/N₂/H₂O at temperatures of 298 K and 313 K in 15 iconic frameworks that include MOFs, zeolites, activated carbons, and mesoporous silica.⁷⁶ The amount of CO₂ adsorbed in these materials in the CO₂/N₂/H₂O mixtures at 40 °C can be seen in Figure 1-5. This gas mixture was meant to assess materials performance in a mixture of the main components found in post-combustion flue gas. It can be seen that the amount of CO₂ adsorbed in the single (pure) component isotherms varies quite significantly from the multicomponent measurements, likely due to water competing for CO₂ adsorption sites in the series of materials. For these measurements, Mason *et al.* used a custom built high-throughput analyzer capable of measuring 28 different samples and as many as 8 different gases including H₂O. This instrument is the first reported to be capable of performing high-throughput multicomponent adsorption measurements at equilibrium.⁷⁶

1.2.3 Experimental breakthrough

Considering post-combustion capture will consist of flue gas flowing through a packed bed of adsorbent, breakthrough measurements are a good way to prove the feasibility of MOFs' performance in more application relevant environments. A typical breakthrough apparatus consists of a gas mixing system, a column where the sample is packed, and a detector, which usually consists of a gas chromatograph and/or mass spectrometer. A known gas mixture is flowed through the fixed adsorbent bed and the detector is used to monitor the downstream gas composition as a function of time. As the gas flows through the bed, certain components in the gas stream will break through the bed at different times. The idea is that the gases with the lowest affinity for the MOF surface passes through the bed more rapidly. As such, from a practical point of view, the best adsorbent is the one that exhibits a long breakthrough time for the small molecule of interest, while exhibiting a short breakthrough time for the other components in the gas stream. In this case, the adsorption bed will have longevity, passing undesired gases through very quickly, while capturing the component of interest. At some point, once the adsorbent bed becomes saturated with the targeted molecule, the composition of the effluent downstream will match the initial composition of the gas feed.

Typically breakthrough experiments are carried out at room-temperature and slightly above.⁹¹⁻⁹² Thus far in the MOF literature several MOFs have been studied in multicomponent streams, such as CO₂/N₂,⁹³ CO₂/N₂/H₂O,⁹⁴⁻⁹⁶ CO₂/H₂O,⁹⁷ and CO₂/N₂/O₂.⁹⁸ Most of the reported studies are only relevant to post-combustion carbon capture or natural gas sweetening applications. While breakthrough experiments are relatively straightforward, due to variations in the MOF particle size, the density of the packed bed, and flow rates of the gas mixture, there are

often difficulties in using this method to get an accurate comparison between different materials. As such, breakthrough curves are often instead simulated.⁹⁹

1.2.4 *In-situ* Characterization

As in the case of carbon capture, most practical applications for MOFs are reliant on interactions with guest species. Knowing the nature of these interactions is essential to interpret the properties of existing frameworks, and this knowledge can be used to inform the design of new materials with specified function. As such, a number of *in-situ* techniques including single crystal and powder diffraction,^{63, 100-101} infrared spectroscopy (IR)¹⁰², Raman spectroscopy¹⁰³⁻¹⁰⁴, nuclear magnetic resonance (NMR)¹⁰⁵⁻¹⁰⁷, x-ray absorption spectroscopy (XAS)¹⁰⁸, inelastic neutron scattering (INS)^{64, 109-111}, and quasiclastic neutron scattering (QENS)¹¹²⁻¹¹³ have been employed to investigate the static and dynamic properties of various small molecules in MOFs. These techniques can be used to provide pertinent information on how and where guest molecules bind, on the nature of the electronic environment around the adsorption site, and also how the molecules move throughout the material. As an example, a powder x-ray diffraction cell and single crystal x-ray diffraction cells are shown in Figures 1-6 and 1-7. For most *in-situ* experiments customized gas cells are integrated with a gas-dosing manifold that is able to deliver a predetermined amount of gas to an activated sample, which is then heated or

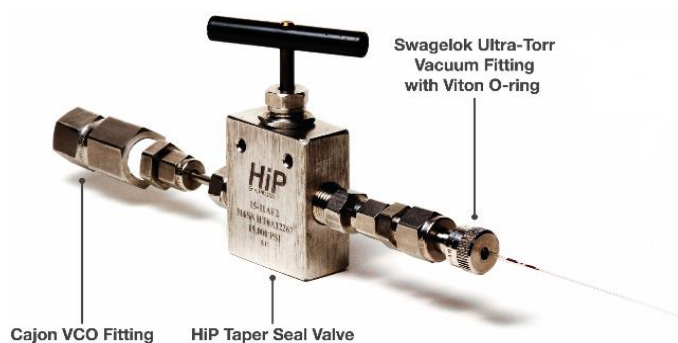


Figure 1-6 Custom built *in-situ* gas cell used for synchrotron powder x-ray diffraction.

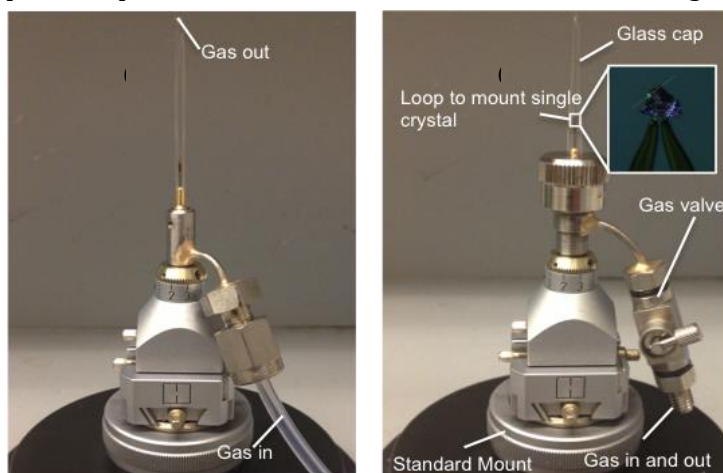


Figure 1-7- A customized gas cell designed for SXR. The cells can be used for (a) flow through or (b) gas dosing.

cooled to the temperature regime of interest. For measurements focused on obtaining static structural information, usually temperatures below 100 K are used in order to eliminate dynamic disorder associated with the surface bound molecules. For spectroscopic measurements used to unveil dynamic properties like diffusion, researchers typically work at higher temperatures where these dynamic modes are activated.¹⁰⁶ Recent work has also been focused on studying

materials under more application relevant environments at higher pressures and temperatures and many of these studies are intent on unveiling information related to mechanical stability or framework flexibility.¹¹⁴ The most predominate forms of characterization throughout the MOF literature are briefly reviewed below. While all of these techniques have their limitations, when combined, they can provide a complete experimental picture of the adsorption process and its effect on the structure of the materials.

Crystallographic techniques

Due to their crystalline nature, MOFs have a nonhomogeneous van der Waals potential energy landscape that dictates how incoming guest molecules arrange themselves on the internal framework surface. This makes diffraction the most direct way to probe static site-specific binding properties of MOFs, and it is a particularly powerful tool when paired with adsorption isotherms. In addition to providing the location and orientation of surface bound guest species, diffraction techniques can be used to unveil a host of information such as the relative difference in binding energy between neighboring adsorption sites. The latter is done through sequential dosing type experiments, where diffraction data is collected after the sample has been dosed with increasing amounts of gas, allowing one to see an increasing number of sites populated with higher gas doses. Of course, this information is gained under the assumption that sites with the strongest binding energy are populated first. Further, diffraction is used to probe the structural response of materials under more application relevant environments with varying pressures and temperatures that are required for various gas storage and separation applications, providing information on the framework flexibility and mechanical stability.¹¹⁵ Last this technique can

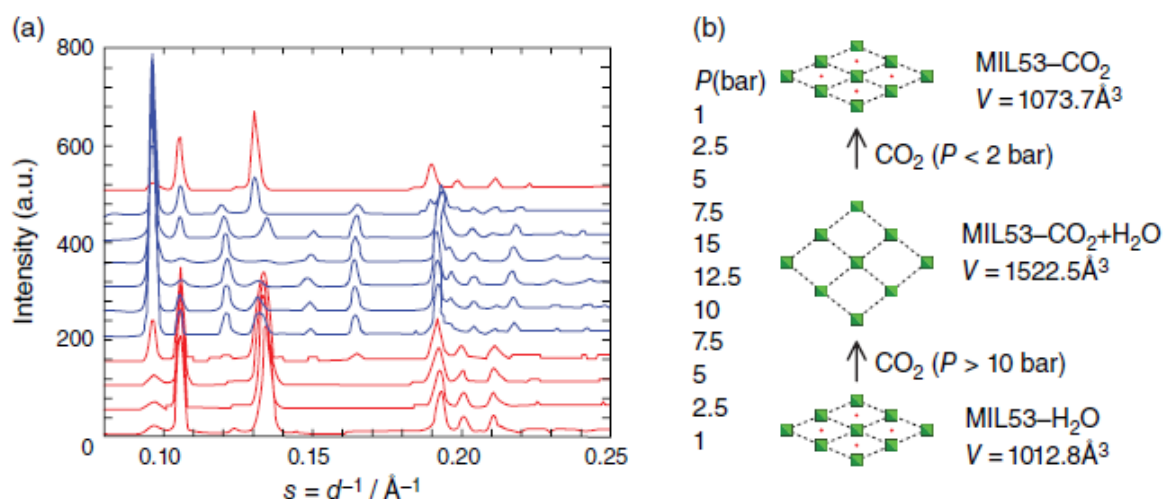


Figure 1-8 (a) The illustration of structural change of hydrated MIL-53(Cr) unveiled using *in situ* X-ray powder diffraction carried out as a function of CO₂ pressure; (b) Schematic diagram of corresponding breathing behavior of MIL-53(Cr) as a function of pressure. This image is reproduced from reference [140] with permission from WILEY-VCH Verlag GmbH & Co. KGaA, Weinheim.

provide valuable insight in the nature of host-guest interactions.¹¹⁶ While most metal-organic

frameworks are dominated by weak van der Waals interactions and typically exhibit host-guest distances above 3 Å, many reports have shown that the presence of highly reactive, electron deficient open metal coordination sites (OMCs) can create strong electrostatic type interactions with small guest molecules; these are often depicted by shorter framework-guest distances ranging from 2 to 3.0 Å. In some instances there are much stronger chemisorptive type interactions where there is charge transfer between the MOF and guest species, leading to structural changes at the adsorption site and/or small molecule.⁷² For chemisorptive interactions, diffraction data usually reveals very short distances between the host framework and guest species. Further, when compared to those of the unbound species, small molecule activation can give rise to significant changes in bond distances and/or angles that can easily be seen in diffraction data.⁷² All of this information cannot easily be determined from *in-situ* spectroscopic techniques, which do not easily provide a direct visualization of surface bound guest species. Crystallographic investigations of a variety of small molecules, such as CO,¹¹⁷ N₂,⁷² CO₂,^{63, 101, 118-119} H₂O,¹²⁰ O₂,^{72, 121-122} NO,¹²³ and H₂,^{121, 124-125}, have been carried out for a number of MOFs of interest for carbon capture applications.

One of the first crystallographic studies of CO₂ adsorption in a MOF was carried out on a breathing framework known as Cr-MIL-53⁸⁹ that is made up of Cr(III)O₆ nodes with 1,4-benzodicarboxylic acid struts. The framework pores undergo expansion and compression as a function of changing pressure. *In-situ* powder diffraction carried out on the hydrated-MIL-53 under various CO₂ pressures was used to understand the structural evolution (Figure 1-8a).^{119, 126} Prior to the introduction of CO₂ the material exhibits a narrow pore phase¹²⁷, which is maintained up to a pressure of approximately 5 bar, where there is co-existence of both a narrow pore and large pore phase. At 15 bar there is complete conversion to the large pore phase (Figure 1-8b). In this structural transition the unit cell increases by over 30% from 1012.8 Å³ for the hydrated analog to 1522.5 Å³ after CO₂ loading. While the narrow pore material adsorbs minimal CO₂ the structural phase transition opens up a significant amount of accessible surface area depicted as a step in the CO₂ adsorption isotherm.¹²⁸

Most crystallographic reports in the MOF literature include either neutron or x-ray powder diffraction¹²⁹⁻¹³⁰, while only a few studies have used single crystal methods.⁶³ Although the data obtained by single crystal diffraction is more complete and hence can give more structural detail, the technical aspects of the experiment is more difficult. MOF single crystals often experience a decrease in the quality with sample activation. There are also inherent limitations in MOF chemistry, due to weak coordination type bonding that renders metal-ligand interactions quite labile, which can inhibit the growth of sizeable single crystals for structural analysis. Hence, there is a bottleneck in the field related to isolating the reactions conditions necessary for single crystal growth. Further, due to the extremely small sample size, very minor leaks in gas dosing equipment can cause contamination and hence problems in the final data refinement. This is particularly a problem for MOFs with OMCs, which typically bind water relatively strong compared to CO₂ and other small molecules of interest for post-combustion

carbon capture. As such, *in-situ* neutron or synchrotron x-ray powder diffraction, which requires significantly larger samples sizes (gram or milligram scale for neutrons and x-rays, respectively), are more straightforward. For powder neutron or x-ray experiments activated samples are loaded into either a vanadium sample can or glass/kapton capillary, respectively (Figure 1-6). After data collection, Fourier difference analysis, followed by subsequent Rietveld refinement is used to elucidate CO₂ locations and orientations (Figure 1-9a).⁶³ Figure 1-9b shows 3 adsorption sites identified in Cu₂(dobdc) (dobdc⁴⁻ = 2,5-dioxido-1,4-benzenedicarboxylate) with site I bound at the OMC as determined by neutron powder diffraction. The plot of the diffraction data (Figure 1-9c) shows an excellent match with the final structural model.⁶³ While crystallographic tools have been

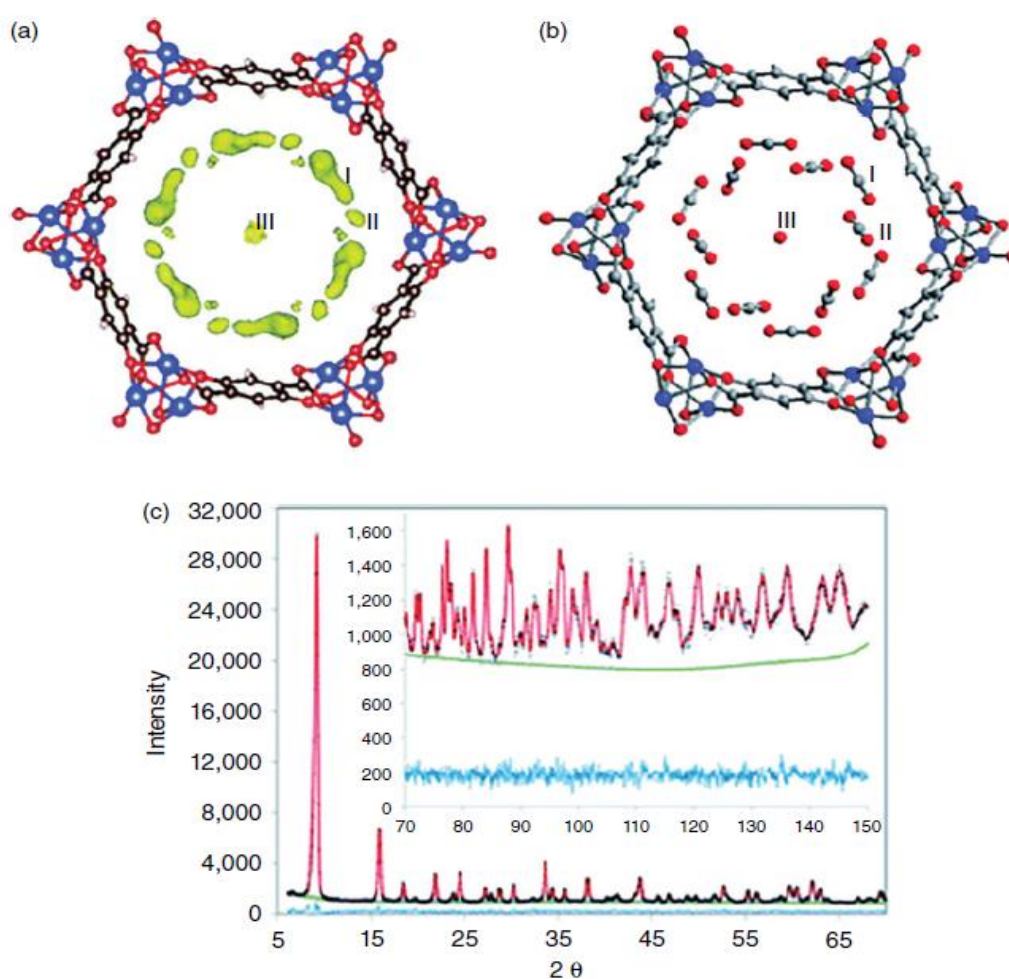


Figure 1-9 (a) Fourier difference map revealing excess scattering density in Cu₂(dobdc) that results from CO₂ adsorption in the framework channel. The excess scattering for site II becomes more apparent with the inclusion of site I atoms in the model. (b) A ball and stick model of the finalized structure of Cu₂(dobdc) showing 3 CO₂ adsorption sites (determined from Rietveld analysis). (c) NPD data from Cu₂(dobdc) (10 K) after dosing with 0.5 CO₂ per Cu²⁺. The green line, crosses, and red line represent the background, experimental, and calculated diffraction patterns, respectively. The blue line represents the difference between experimental and calculated patterns. This image is reproduced from reference⁶³ with permission from the Royal Society of Chemistry.

used in the characterization of a number of MOF systems, there are also a few limitations to be considered. The time and position averaged diffraction data can suffer from static or dynamic disorder that inhibits the elucidation of fine structural detail associated with small molecule bond distances and angles.⁶³ Further crystallographic problems can arise due to poor crystalline quality and improper sample handling or activation.

Spectroscopic techniques

IR, Raman, and INS

While PXRD can be used to probe the static structure of materials, IR, Raman, and INS are often used to look at local vibrations and rotations of guest species throughout MOF materials. These spectroscopic tools are highly sensitive to molecular interactions in the frameworks. As such, they can also be used to indirectly probe binding configurations, binding enthalpies, and loading levels. However, this information is usually extracted from peak shifts, broadening, or intensities and so interpretation should proceed with caution. There are many false assumptions throughout the literature that peak shifts, which are very sensitive to the coordination environment around the adsorption site, are directly correlated with the adsorption enthalpy. Last, the integrated spectral intensities are often assumed to correlate with loading level. While this can hold true in some instances, sometimes intermolecular interactions can strongly influence the peak intensities as highlighted in a recent study H_2 adsorption in $Mg_2(\text{dobdc})$ of Nijem *et al.*¹³¹ They found that high H_2 loadings resulted in a counterintuitive decrease in IR intensity due to a decrease in the effective charge of H_2 at the OMC.

There are 3 vibrational modes associated with CO_2 , the asymmetric stretching mode, $\nu_3 = 2349\text{ cm}^{-1}$ and bending $\nu_2 = 667\text{ cm}^{-1}$, mode are IR-active, while the symmetric stretching mode, $\nu_1 = 1388\text{ cm}^{-1}$, is IR-inactive.¹³²⁻¹³³ If there is significant polarization of the surface bound molecules, as in the case of OMCs, the IR -active modes offer a way to probe the nature of the CO_2 framework interaction. Dietzel *et al.* carried out one of the earliest *in-situ* IR studies on $Ni_2(\text{dobdc})$ framework to unveil the nature of the CO_2 interaction with the Ni^{2+} -OMC.¹⁰¹ They observed several bands associated with the CO_2 adsorption that were assigned to the CO_2 in an end-on orientation at the OMC, an observation that agreed well with *in-situ* diffraction experiments. The ν_3 mode was slightly red shifted by 8 cm^{-1} with respect to the gas phase, a result of the charge transfer between the lone-pair of electrons on the CO_2 to the OMC. They additionally observed a combination mode of $\nu_3 + \nu_{M-O}$, where ν_{M-O} is the stretching mode of the $Ni^{2+}-(O)CO_2$ adduct. The position of ν_{M-O} was determined to be 67 cm^{-1} , a value that is comparable to the expected value of approximately 70

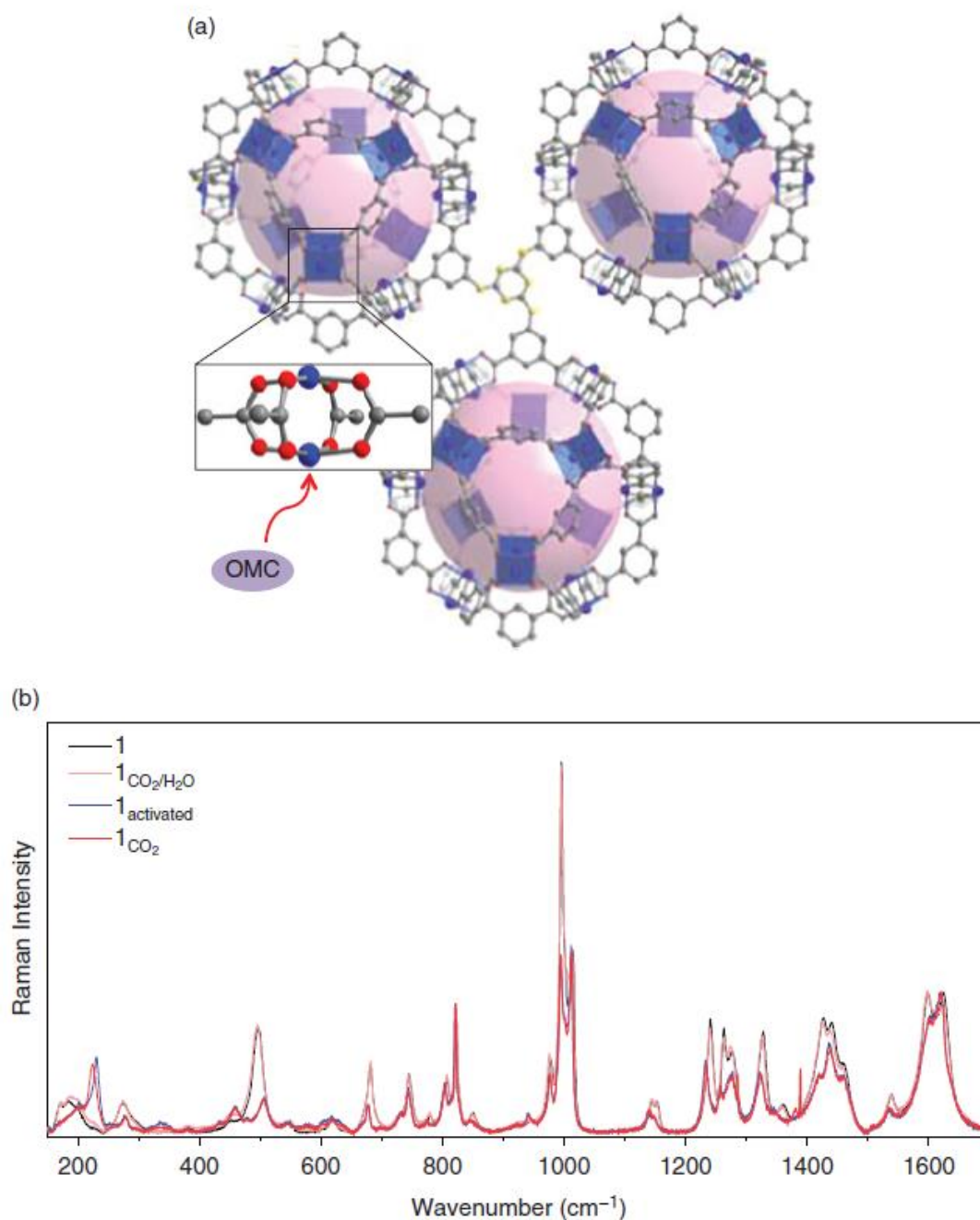


Figure 1-10 (a) Ball and stick model of Cu-TDPAT that shows interconnected cuboctahedral building units, consisting of Cu-paddlewheels and isophthalate ligands. The pink balls represent void space. Cu, C, O are represented by blue, grey, and red spheres, respectively. (b) Full Raman spectra of as-synthesized Cu-TDPAT (black), Cu-TDPAT treated with H₂O saturated CO₂ (pink), activated Cu-TDPAT (blue), and activated Cu-TDPAT treated with pure CO₂ gas (red). Figure 9b is reproduced with permission from ref¹⁵⁰ with permission from the Royal Society of Chemistry.

cm⁻¹. Further there was observation of the aforementioned bending mode. While it is expected to be doubly degenerate, a doublet was instead observed at 659 and 651 cm⁻¹. This observation was

used to support bending of the CO₂ molecule at the OMCs observed in the diffraction data. It should also be noted that the CO₂ angle found in the diffraction studies carried out in this work was 162(3)°, ¹⁰¹ a huge deviation from the expected linear geometry. Later studies showed that this unexpected bending was due to a misinterpretation of the time and position averaged diffraction data and that the CO₂ angle should not deviate greatly from 180°. ⁶³

Since this initial work, IR and Raman have both become highly active tools for the characterization of many MOFs. Valenzano *et al.* used variable temperature IR data to obtain the enthalpy and entropy of adsorption for CO₂ adsorbed at the OMC in Mg₂(dobdc). The calculated enthalpy of adsorption was estimated to be -47 kJ/mol, which agreed very well with previously reported values obtained from adsorption isotherms. ¹³⁴ An additional *in-situ* IR study of CO₂ adsorption was carried out in the rht-type MOF known as Cu-TDPAT ¹³⁵ (Cu-TDPAT = [Cu₃(TDPAT)(H₂O)₃]·10H₂O·5DMA and TDPAT = 2,4,6-tris(3,5-dicarboxylphenylamino)-1,3,5-triazine), a framework that consists of Cu paddlewheel clusters and triazine ligands (Figure 1-10a). CO₂ adsorption studies show not only high carbon dioxide uptake (0.072 grams of CO₂ per gram of MOF at 0.15 bar and 298 K) ¹³⁶, but also high CO₂ to N₂ selectivity (34.2 determined *via* IAST). An *in-situ* IR study carried out on the Cu-TDPAT framework, which exhibits both Lewis acidic OMCs and Lewis basic amine functionality on the triazine linker, gives evidence of two strong adsorption sites. ¹³⁷ A follow up study of Lockard *et al.* monitored certain Raman active vibrational frequencies associated with the metal-containing building unit, the ligand, and surface bound CO₂ (Figure 1-10b). ¹³⁸ They were able to monitor a Cu-Cu stretching mode in the paddlewheel, revealing that the Cu-Cu interaction became stronger with dehydration and with CO₂ loading, implying a shorter Cu-Cu distance. Additional Raman active modes were used to show a rearrangement of the linker configuration to becoming more planar and hence less strained upon activation, which was verified using DFT simulations of the Raman spectra. Further the Raman-active CO₂ vibrational modes gave additional insight into the presence of two strong adsorption sites, one associated with the metal and one associated with the triazine linker. After poisoning the OMC with the addition of water, and effectively blocking that adsorption site, the linker reverts back to a nonplanar configuration, enhancing the Lewis basicity of the linker. The latter, in turn, enhances the CO₂ interaction with the Lewis base functionality, an observation that is consistent with theoretical work that predicts that the selectivity for CO₂ over N₂ will be enhanced in a wet gas streams. ¹³⁵

In-situ DRIFTS (Diffuse reflectance infrared Fourier transform spectroscopy) studies were utilized to study CO₂ adsorption in mmen-CuBTTri (Cu-BTTri = H₃[(Cu₄Cl)₃(BTTri)₈(mmen)₁₂] ¹³⁹ and mmen: N,N'-dimethylethylenediamine), ¹⁴⁰ which is one of the best MOF-candidates discovered to date for energy efficient post-combustion carbon capture. ¹⁴¹ The idea was to mimic the chemical reactivity observed in liquid amine scrubbers through the appendage of alkyl amines to the OMC on the internal MOF surface. After dosing the mmen-CuBTTri framework with CO₂, there is disappearance of a peak at 3283 cm⁻¹, which is related to the N-H stretching mode. There is also an emergence of several other peaks that were unobserved before the introduction of CO₂.

These significant changes in the spectrum have been attributed to the formation of zwitterionic carbamates or carbamic acid, which are the expected species *via* chemisorption of CO₂ to the amine functional groups.

Last, recent work of Wright *et al.* showed that synchrotron based IR microspectroscopy with polarized IR light could be used to determine the orientation of adsorbed CO₂ molecules, the CO₂ loading level, and the enthalpy of adsorption in single crystals of a small pore amine-containing MOF, Sc₂(BDC-NH₂)₃, (BDC-NH₂= 2-amino-1,4-benzenedicarboxylate).¹⁴² The measurements, collected during CO₂ uptake at partial pressures of 0.025 bar to 0.2 bar at 298 K to 393 K (Figure 1-11), have 100-fold higher photon flux density relative to lab sources. Further, this technique yields a large improvement in the signal-to-noise ratio so that high quality direction-dependent polarized IR spectra can be measured for anisotropic crystals. As such, in this study, measurements could be done at extremely low CO₂ coverage of ~0.1 mmol / g, which is equivalent to a site occupancy of 1.5%. This value is within the error of what can be measured by diffraction experiments and certainly outside the regime of what can be seen with most other *in-situ* techniques. While it was not shown in this study, due to the high rate of CO₂ diffusion at the temperatures probed, it is suggested that the technique could be used to elucidate CO₂

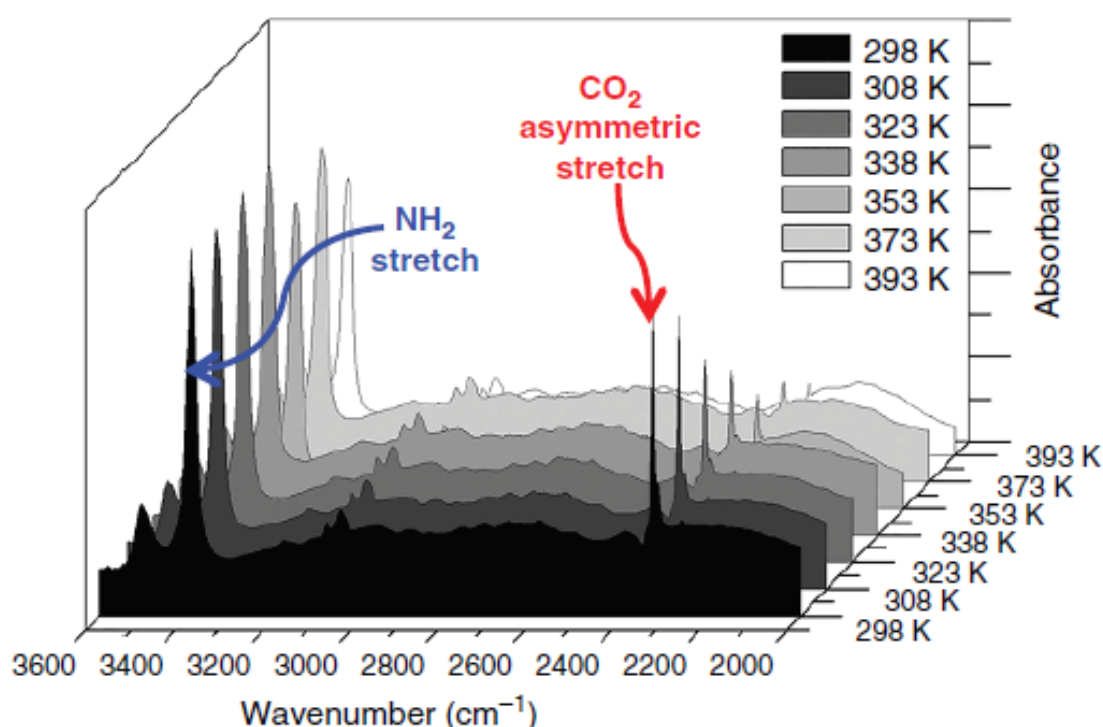


Figure 1-11 Series of spectra taken from an isobar from a single site of a single Sc₂(BDC-NH₂)₃ crystal. As temperature increases the magnitude of the adsorbed CO₂ asymmetric stretch (red arrow) at 2335 cm⁻¹ wavenumbers decreases relative to the NH₂ stretching modes, one of which is shown with a blue arrow. This figure is reproduced from reference¹⁵⁴ with permission from WILEY-VCH Verlag GmbH & Co. KGaA, Weinheim.

diffusivities. This can be done by following the temporal and spatial variations over a single crystal.¹⁴²

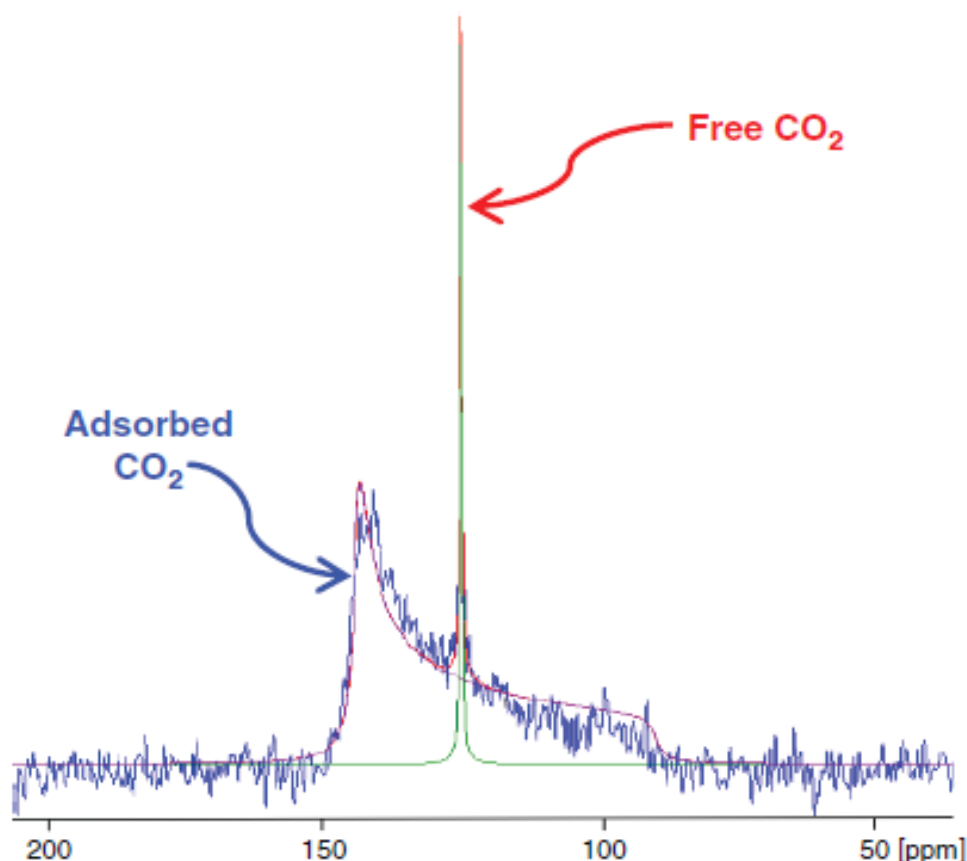


Figure 1-12 ^{13}C NMR spectrum of DUT-8(Ni) pressurized with 9.5 bar carbon dioxide measured at 237 K. Note that the initially closed structure opens during the adsorption experiment at temperature-dependent gate-opening pressure (ca. 5 bar at 237 K) whereas it remains open during desorption down to 1 bar (hysteresis). (Blue: experimental spectrum, green: simulated gas phase signal, magenta: simulated signal of adsorbed CO_2 ; red: Sum of the simulated signals.) This figure is reproduced from reference¹⁶⁷ with permission from MDPI – open access publishing.

It should be noted that while Raman and IR have been used extensively due to their sensitivity to CO_2 and several other small molecules of interest, INS, a technique that does not suffer from selection rules, rarely has been used to study materials for carbon capture applications. The reason is that the incoherent scattering cross sections for C, O, and N are weak relative to those of H.¹⁴³ As such, these studies require long measurement times. Further, for INS measurements, data are first collected for the activated framework. This is followed by data collection for the framework loaded with gas, and the spectrum of the bare framework is then subtracted from the spectrum obtained for the CO_2 loaded sample. Given the data subtraction, when possible frameworks should be deuterated in order to lower the contribution of the framework H atoms in the background spectrum. Further, in cases where CO_2 binds very strongly

and causes significant changes in the unit cell parameters, this can shift the framework phonon frequencies. These two problems were highlighted in an INS study of CO₂ adsorption Mg₂(dobdc). Despite framework deuteration, Queen *et al.* could still see no convincing indication of vibrational modes associated with framework adsorbed CO₂. The difference spectrum instead revealed negative and positive intensities, indicating significant shifts in the framework modes upon CO₂ adsorption. This was further verified by neutron powder diffraction, which showed a significant reduction in unit cell volume from the bare framework to the CO₂ dosed one. Both softening and hardening of the vibrational modes are observed, likely due to the inverse effect CO₂ adsorption has on the lengths of the *a/b* and *c*-axes, as supported by the diffraction data.⁶³

NMR

In-situ NMR, a powerful technique that can be used to complement diffraction studies, locally probes the nuclear spins present in the sample, and hence the local environment around

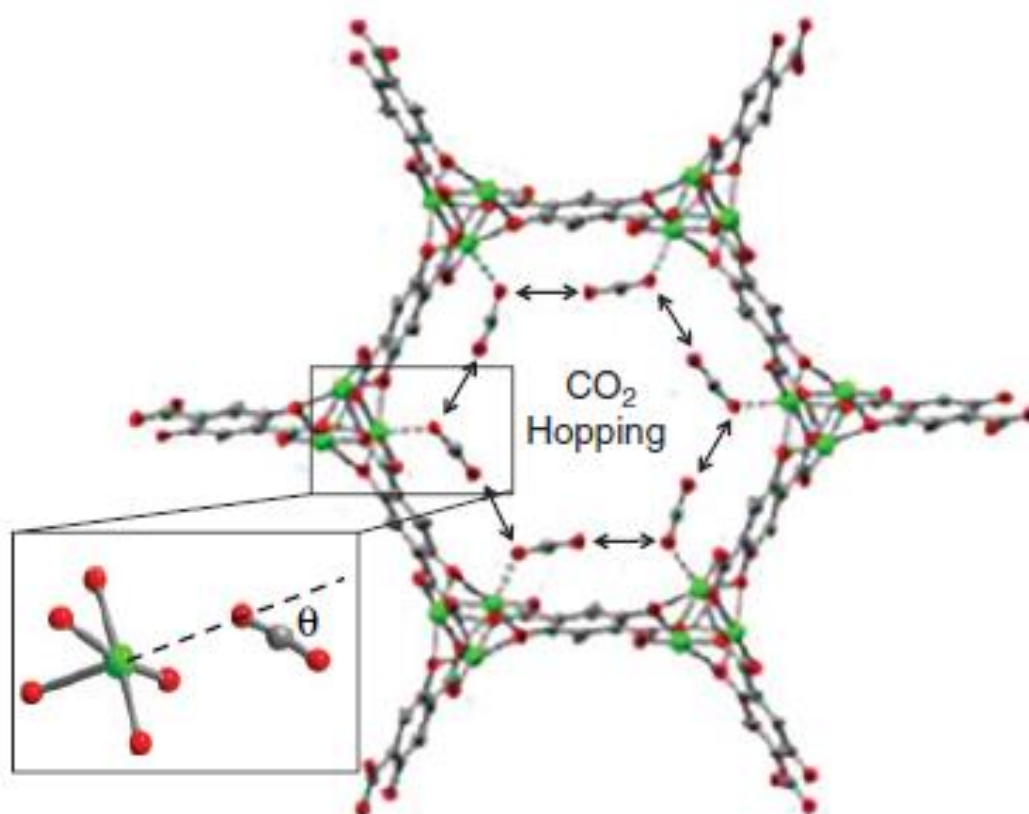


Figure 1-13 Ball and stick model of Mg₂(dobdc) with CO₂ adsorbed at the open metal site, as determined by NPD. The arrows represent the CO₂-hopping mechanism proposed by molecular simulations used to interpret NMR data. The higher-magnification view represents the fixed rotation angle, θ . The green, red, and grey spheres represent Mg, O, and C, respectively. This figure is reproduced from reference⁸³ with permission from WILEY-VCH Verlag GmbH & Co. KGaA, Weinheim.

each atom. This technique, which does not require any long-range order, can provide binding configurations, information on adsorption induced framework flexibility, as well as the dynamic properties of imbibed guest molecules throughout the frameworks (in the millisecond regime). While the number of studies is growing, *in situ* NMR experiments reported to date for the elucidation of host-guest interactions are few in number. To the best of our knowledge *in-situ* studies have been carried out with the following adsorbates including Xe¹⁴⁴, CO₂^{106, 145}, H₂¹⁴⁶⁻¹⁴⁸, H₂O^{146, 149}, NH₃¹⁵⁰ and hydrocarbons¹⁵¹⁻¹⁵². It is thought that the lack in utilization of *in-situ* NMR is due to the lack of accessible instruments, difficulty in data interpretation, and probe restrictions. It has been shown that CO₂ adsorption in frameworks can result in anisotropic or restricted motions of CO₂. As such, the ¹³C NMR signals exhibit characteristic line shapes that in turn allow determination of information pertaining to the motion of the adsorbed molecules,¹⁵³ such as rotational axes of surface bound CO₂. These characteristic line shapes were observed in *in-situ* ¹³C NMR spectra of CO₂ adsorbed in Ni₂(2,6-ndc)₂(dabco) or DUT-8 (2,6-ndc = 2,6-naphthalenedicarboxylate, dabco = 1,4-diazabicyclo[2.2.2]octane)¹⁵⁴ (Figure 1-12), a MOF that exhibits a gate opening effect at a characteristic pressure of 5 bar. Below this pressure, the only signal observed in the NMR is from unbound CO₂ at 335 ppm; however, at higher pressures the framework pops open and a broad signal is observed with a characteristic shape due to chemical shift anisotropy, $\Delta\alpha\vartheta$ of 52 ppm. From this data the tilt angle, θ , defined as the angle between the symmetry axis and the rotational axis, can be calculated using the following equation:

$$\Delta\alpha\vartheta = \Delta \left(\frac{3 \cos^2\theta - 1}{2} \right) \quad \text{Eq. (1 - 5)}$$

The tilt angle determined for DUT-8(Ni) was calculated to be 49(2)^o.¹⁵⁵ Following this study, a similar effort was made by Kong *et al.* to elucidate the CO₂ adsorption behavior in Mg₂(dobdc).¹⁰⁶ This study is briefly described in the next section; however, an image showing the determined θ value for CO₂ in Mg₂(dobdc) is shown in Figure 1-13.

QENS

The use of quasielastic neutron scattering (QENS), often combined with molecular dynamics simulations, has on several occasions been used to understand diffusive properties of small molecules in MOFs. One thing to note for QENS is that the incoherent scattering cross section is minimal for many elements other than H and so in the case of CO₂, collective motions of molecules are measured rather than diffusivities of individual molecules that are measured for H₂ and CH₄, for instance.^{113, 156-157} Most QENS studies are used to extract three parameters, the self-diffusivity (D_s), which describes the diffusion of individual molecules, the transport diffusivity (D_t), which describes the mass transport that is induced in the presence of a gradient, and the corrected diffusivity (D_o) which is related to the transport diffusivity *via* a thermodynamic correction factor that is calculated from the experimental adsorption isotherm. When looking at many industrial applications regarding separations, particularly membrane separations, where there might be mass transport in non-equilibrium environments, the transport diffusivity

becomes very important and so it is necessary to assess these terms separately. Because the scattering from CO₂ is coherent in nature, the transport diffusivity is probed. Compared to NMR, QENS measures fast diffusive motions on time scales ranging from 10¹⁰ to 10¹³ sec⁻¹. Further, the distances over which the diffusive properties are observed is well defined and variable, typically the distances range from 2 to 100 Å for QENS, while in NMR the time scales are long, in the millisecond regime and as such, so are the distances (microns).

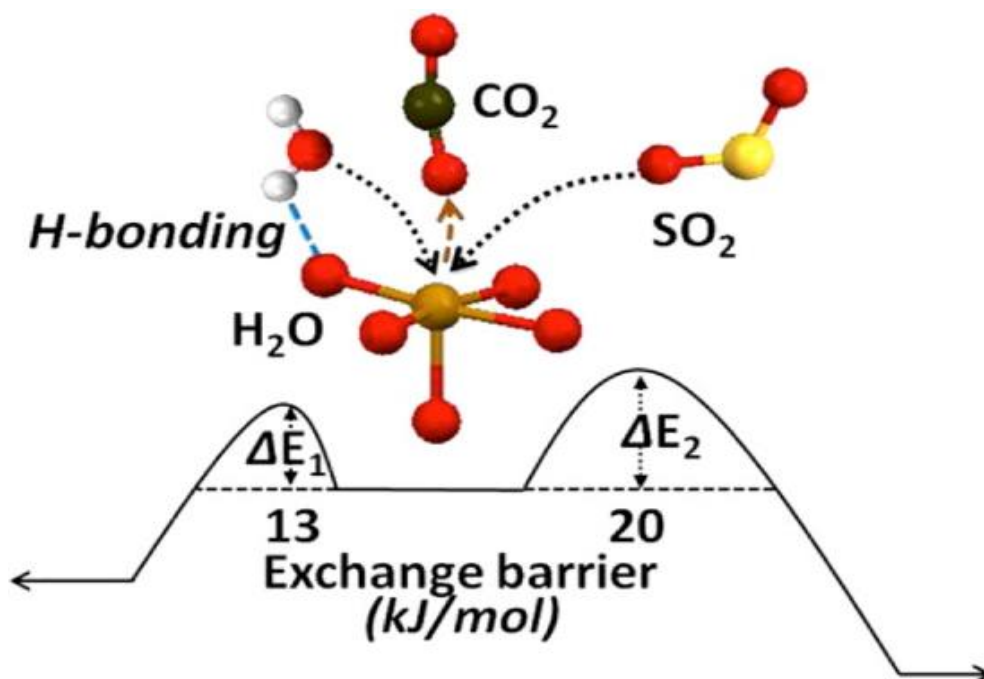


Figure 1-14 Ball and stick model of the OMC in M₂(dobdc) with CO₂ being displaced by either H₂O or SO₂ and their energy barriers to activation. M²⁺, O, C, H, and S are represented by orange, red, great, white, and yellow spheres, respectively. This figure is reproduced from reference¹⁷³ with permission from the American Chemical Society.

One of the first QENS studies of CO₂ adsorption in a MOF was carried out by Maurin *et al.* in MIL-47(V) or VO(1,4-BDC) (1,4-BDC = 1,4-benzenedicarboxylate)¹⁵⁸ to extract the aforementioned three diffusivity parameters over a wide range of loadings. They found that while D_s and D_o decrease as a function of loading, that D_t shows a non-monotonous response that is rationalized to be the result of intermolecular CO₂ interactions that deviate from the behavior expected for an ideal gas. They show that the MD-QENS study is able to probe the transport diffusivity in MOFs, a method, which can be applied to understand the dynamics associated with industrially relevant gas mixtures.¹⁵⁸ Since this time, the diffusivity of H₂ and CO₂ in the small pore Zr-based MOF MIL-140A(Zr) has been evaluated using the MD-QENS technique to determine the self-diffusivities of H₂, and the corrected and transport diffusivities of CO₂ as single components and also in a binary mixture. Of these two guests, H₂, with its smaller kinetic diameter, was shown to diffuse through the narrow triangular channel of MIL-140A(Zr) at a significantly faster rate than CO₂ at the same temperature. In the binary mixture, H₂ is still faster, but it shows a slightly

slower self-diffusivity, while CO₂ gets a bit faster. Despite these slight changes, there is still a significant difference in the observed diffusivities in the binary mixture, suggesting that this material might be a good candidate for kinetic based separations of CO₂ and H₂.¹⁵⁹⁻¹⁶⁰

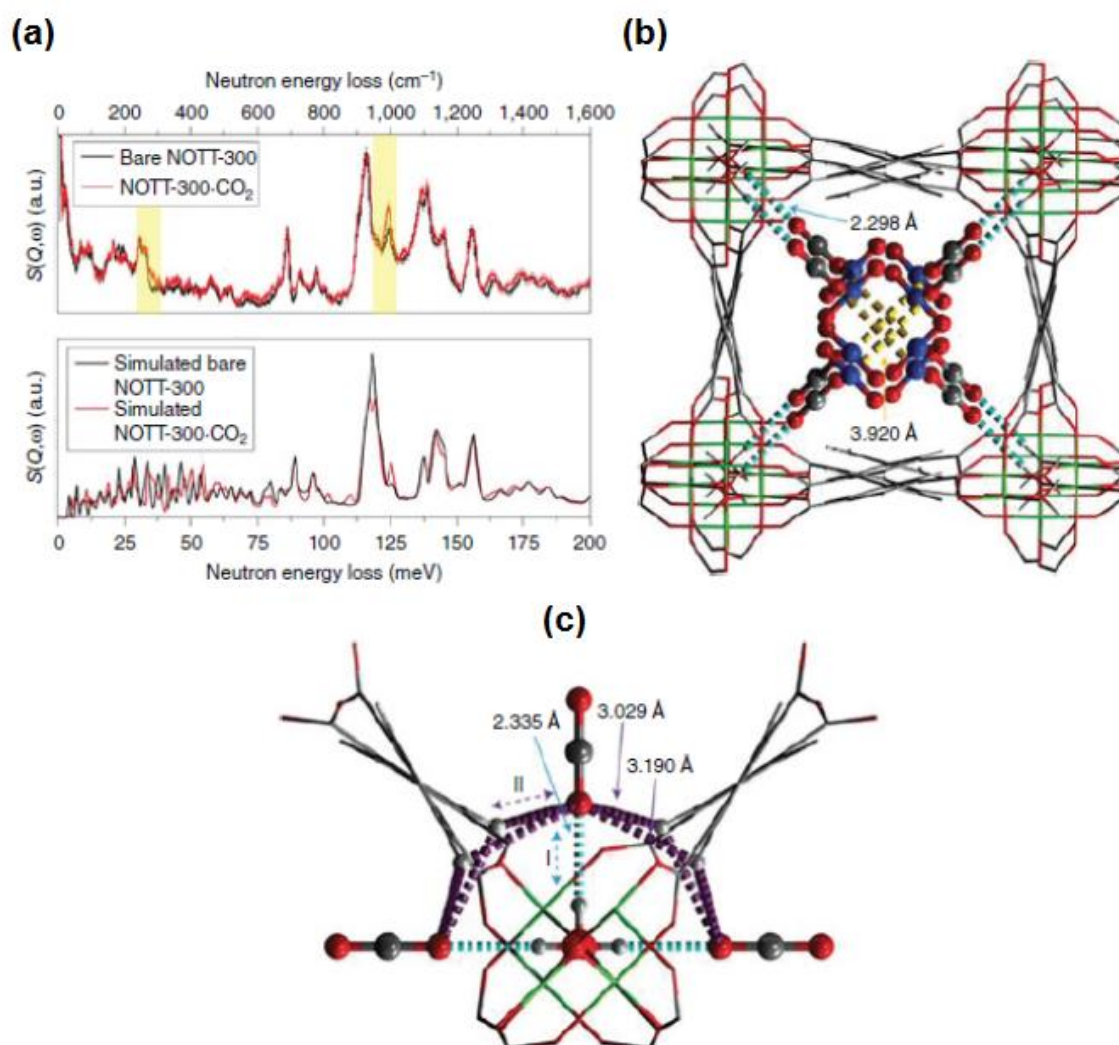


Figure 1-15 (a) Experimental and simulated INS spectra for the CO₂-loaded Al(OH)₂(bptc). The yellow bars highlight the position of peak I and II. (b) Wire view of the Al(OH)₂(bptc) obtained using PXRD analysis. There are two identified CO₂ adsorption sites in the pore channel are represented by a ball-and-stick model. Site I (with the grey carbon) was determined by INS/DFT and verified via powder x-ray diffraction and site II (with a blue carbon) was determined by powder x-ray diffraction. The dipole interaction between neighboring CO₂(I,II) molecules is highlighted in orange. (c) Detailed view of the interactions between MOF -OH and -CH groups with CO₂ molecules in a pocket-like cavity (determined by DFT simulation). The modest hydrogen bond between O(δ^-) of CO₂ and H(δ^+) from the Al-OH moiety is highlighted in cyan. The weak cooperative hydrogen-bond interactions between O(δ^-) of CO₂ and H(δ^+) from -CH are highlighted in purple. Each O(δ^-) centre therefore interacts with five different H(δ^+) centres. Framework aluminium, carbon, oxygen, and hydrogen are represented by green, grey, red, and white, respectively. This figure is reproduced from reference¹⁷⁴ with permission from Macmillan Publishers Limited.

Computational aid for data interpretation

While spectroscopic tools, as a means to assess small molecule interactions in MOFs, are generally accepted, because of the aforementioned reasons data interpretation should proceed with caution. When relevant, it is helpful to utilize theoretical tools capable of incorporating vdW interactions to reduce error in data interpretation. There are several examples throughout the literature where computational tools have proven essential to interpret spectra. This was highlighted by the work of Lin *et al*¹⁰⁷ who used molecular simulations to reproduce chemical shift anisotropy (CSA) powder patterns of ^{13}C NMR, work that was proven to be essential for the interpretation of diffusive motions of CO_2 in $\text{Mg}_2(\text{dobdc})$. In this study the NMR measurements of CO_2 adsorbed $\text{Mg}_2(\text{dobdc})$ ¹⁰⁶ revealed a distinct CSA powder pattern, which at the time was interpreted to be the result of a uniaxial rotation with a fixed rotation angle θ that ranged from 56° to 69° (at temperatures from 200 K to 400 K). However, a more recent study used molecular simulations to probe the free-energy landscape of CO_2 in $\text{Mg}_2(\text{dobdc})$ under conditions similar to those used in the NMR study. The Monte Carlo simulations indicated that NMR signature was instead the result of a molecular-hopping motion between metals within the crystallographic *ab* plane (Figure 1-14). This study implies that the dynamics of CO_2 within $\text{Mg}_2(\text{dobdc})$ were more complex than originally expected.¹⁰⁷

X-ray absorption spectroscopy (XAS), an element specific technique used to probe changes in the electronic environments with the adsorption or desorption of guest species, is highly sensitive yet difficult to interpret without the help of theory. Near edge x-ray absorption fine structure (NEXAFS) was used to probe the Mg K-edge first in the activated $\text{Mg}_2(\text{dobdc})$, and then again with the DMF and CO_2 bound to the open Mg^{2+} site. Spectra were simulated using DFT and then compared with the experimental spectra. This theoretical analysis proved necessary to understand the variations in the local electronic environment around the OMC from the activated MOF to the one with surface bound molecules.¹⁰⁸ Using *in-situ* XAS (x-ray absorption spectroscopy), a similar study was carried out to study CO_2 adsorption around the OMC in Cu-TDPAT.¹³⁸ The constant edge position at 8990 eV has confirmed the oxidation state of the Cu^{2+} throughout the adsorption and desorption process. In addition, the activated framework was exposed to both water and carbon dioxide, and due to the fact that the edge feature intensity for the CO_2 dosed framework was between that of H_2O loaded and activated one, it has been concluded that the interaction of the OMC with the CO_2 molecule is not as strong as that of water, giving a strong indication that in a competitive environment, water would preferentially bind over CO_2 .

More recently, Chabal *et al* used *in-situ* IR combined with *ab initio* simulations to investigate competitive binding of small molecules in $\text{M}_2(\text{dobdc})$ where $\text{M} = \text{Mg}, \text{Co}, \text{and Ni}$.¹⁶¹ They investigated the displacement of CO_2 with several molecules including H_2O , NH_3 , SO_2 , NO , NO_2 , N_2 , O_2 , and CH_4 . They found, despite the higher binding energy of SO_2 , NO_2 , and NO ($\sim 70\text{--}90$ kJ/mol), that H_2O and NH_3 ($\sim 60\text{--}80$ kJ/mol) are the only molecules able to sufficiently displace the CO_2 (38

to 48 kJ/mol for the 3 metals). They used DFT simulations to evaluate the energy barrier associated with CO₂ displacement by H₂O and SO₂. They found the energy barrier to be approximately 13 and 20 kJ/mol, for H₂O and SO₂, respectively. The calculations revealed that, instead of differences in binding energies, the kinetic barrier for this exchange is dictated by the interaction of the second guest molecule (in this case H₂O or SO₂) with the MOF ligands. Hydrogen bonding between the H₂O and oxygen on the organic linker facilitate the positioning of the H₂O oxygen atom toward the metal center (Figure 1-14). These interactions reduce the exchange barrier for the CO₂ displacement by H₂O. In contrast, the SO₂ instead interact with the benzene ring that is more distant from the metal center, an occurrence that hinders the exchange process. To the best of our knowledge this is the first *in-situ* work that provides insight into competitive co-adsorption.¹⁶¹

Due to the aforementioned problems with negligible incoherent scattering cross sections of many of the elements of interest for CO₂ capture, many INS studies actually pair DFT-based calculations to aid in understanding the host-guest interactions. For instance, Al₂(OH)₂(bptc) (where bptc = biphenyl-3, 3', 5,5'-tetracarboxylate alternatively known as NOTT-300), shows relatively high CO₂ uptake with a value of 2.64 mmol / gram of MOF at 0.15 bar and 298 K and minimal uptake of CH₄, N₂, Ar, O₂, or H₂.¹⁶² INS, paired with DFT derived simulations of the INS spectrum, was used as the primary method for characterization of the surface bound CO₂, a process that was then validated *via* powder x-ray diffraction. The sample was loaded with 1.0 CO₂ per formula unit, and the INS data revealed an increase in the intensity of two peaks located at 30 meV and 125 meV. Further, peaks above 100 meV were shifted to higher energy indicative of a hardening of the framework modes with CO₂ adsorption (Figure 1-15a). The DFT-derived INS spectrum showed very good agreement with the experimental one and indicated that the preferential CO₂ adsorption site was located in an end-on orientation approximately 2.33 Å from the framework hydroxyl group. This implies that moderate H-bonding interactions were responsible for the observed CO₂ adsorption properties (Figure 1-15b, c). The low energy peak in the INS spectrum was assigned to a wagging mode of the -OH that was induced by the presence of CO₂, while the higher energy peak was assigned to the wagging mode of four aromatic C-H bonds that are found adjacent to the surface bound CO₂. This work shows that pairing DFT and INS made it possible to visualize the binding mechanism of CO₂ and gain necessary insight into the high CO₂ absorption properties of the framework at low-pressures. Additionally, the low H₂ uptake for this material was rationalized using the same methodology.¹⁶²

1.3 MOFs for post-combustion capture

1.3.1 Necessary framework properties for CO₂ capture

Maximizing the framework adsorption capacity (both volumetric and gravimetric) and selectivity of CO₂ at low pressures and in the presence of other components in the flue gas stream is of principal importance to post-combustion carbon capture. As shown in Table 1-1, this process

is carried out at a pressure of ≈ 1 bar with CO_2 volumes that range from 3 to 15% depending on the fuel source and at temperatures between 40 and 75 °C. As such, absorbents used for post-combustion capture must show high CO_2 adsorption capacity at partial pressures less than 0.15 bar, a property that can be positively influenced by designing frameworks with high densities of strong adsorption sites. Other properties required for post-combustion capture include the ease of regeneration (likely to occur between temperatures of 100 to 200 °C in a TSA process), rapid diffusion of gases through the adsorbent, and long-term stability of materials under application relevant conditions. While it is considered difficult to design materials to meet all of these criteria, the facile structural tunability of MOFs offer an unprecedented opportunity to target new materials with tunable interactions for the energy-efficient capture of CO_2 .

Knowledge of the fundamental differences in the physical properties and reactivity of CO_2 and N_2 has aided the design of multiple frameworks that exhibit strong CO_2 adsorption in the low-pressure regime that is of interest for post-combustion carbon capture.¹⁶³ For example, Table 1-2 shows that CO_2 has higher polarizability ($\text{CO}_2 = 29.1 \times 10^{-25} \text{ cm}^3$; $\text{N}_2 = 17.4 \times 10^{-25} \text{ cm}^3$) and quadrupole moment ($\text{CO}_2 = 43.0 \times 10^{-27} \text{ esu}^{-1} \text{ cm}^{-1}$; $\text{N}_2 = 15.2 \times 10^{-27} \text{ esu}^{-1} \text{ cm}^{-1}$) compared to N_2 . As such, the introduction of structural components that exhibit high charge densities on the framework surface can be used to polarize incoming CO_2 molecules and hence manipulate both the selectivity and the adsorption capacity at low pressures.¹⁶⁴ As an alternative, CO_2 is also known to be susceptible to attack by nucleophiles as demonstrated with the aforementioned liquid amine based scrubbers. Chemisorptive interactions, achieved *via* Lewis base functionality appended on the internal MOF surface is also becoming a common trend in MOF chemistry.¹⁶⁵⁻¹⁶⁸

1.3.2 Assessing MOFs for CO_2/N_2 separations

The most common method to assess applicability of MOFs in post-combustion flue gas capture is through the assessment of CO_2 and N_2 single component isotherms collected between 293 and 313 K at pressures up to 1 bar.²³ From extraction of isosteric heats obtained from variable temperature adsorption data and analysis of the CO_2 uptake in the low-pressure regime, one can gain immediate insight into the materials affinity for CO_2 , its potential regarding adsorption capacity, and the potential ease of regeneration. It should be noted that, compared to many reports in the literature, flue gas will be introduced to the adsorbent at temperatures ranging from 50 to 75 °C and then released at temperatures that range from 100 to 200 °C. As such, there is a clear need in the literature for materials assessment at significantly higher temperatures. This fact was highlighted in a recent report by Mason *et al.* which show assessment of CO_2 and N_2 adsorption in two MOF frameworks, $\text{Mg}_2(\text{dobdc})$ and MOF-177, at temperatures ranging from 20 to 200 °C. With this work, they report a methodology to assess the performance of materials in a likely scenario using temperature swing adsorption.

Given the partial pressures of CO_2 and N_2 in the flue gas of a coal-fired power plant, MOF selectivities reported in the literature for CO_2 over N_2 are usually calculated using the molar ratio of the CO_2 uptake at pressures of 0.15 bar over the N_2 uptake at 0.75 bar. It should be considered

that the significantly larger quadrupole moment of CO₂ over N₂ will lead to an overestimated N₂ adsorption in MOFs that contain highly polarizing adsorption sites because CO₂ will preferentially bind to strong adsorption sites and hence reduce the actual amount of adsorbed N₂ in a binary mixture. While this molar ratio method is the simplest way to calculate selectivity, it has been shown in a recent report by Mason *et al.* that the obtained values cannot be taken too literally. In assessment of CO₂ adsorption isotherms of Mg₂(dobdc) between 40 and 60 °C they show an unrealistic increase in selectivity for CO₂ over N₂ demonstrating the importance of using IAST¹⁶⁹ to calculate the selectivities for MOFs containing strong adsorption sites.⁹⁹

One very important metric for assessing a material for post-combustion carbon capture applications is the isosteric heat of adsorption, $-Q_{st}$. The $-Q_{st}$ at low-coverage is indicative of the strength of binding of the strongest adsorption site and strongly influences the low-pressure adsorption capacity and selectivity of MOFs and further influences their ability to undergo regeneration.¹⁷⁰⁻¹⁷¹ Figure 1-16 shows the CO₂ adsorption capacity and isosteric heats for a number of frameworks in the low-pressure regime of interest for post-combustion capture.^{63, 84, 99, 102, 140, 172-179} It should be noted that because the density of adsorption sites is not taken into account in this image, the strength of the adsorption site does not correlate very well with the low-pressure capacity. However, for the high surface area materials with no polarizing surface functionality, such as MOF-177, the adsorption capacity is only 6 mg of CO₂ per g of adsorbent and the isosteric heat is 14 kJ/mol, while Mg₂(dobdc), a material with much stronger adsorption sites due to the presence of exposed metal cations (43.5 kJ/mol) and a modest BET surface area of only 1200 m² per g of adsorbent, takes up 290 mg CO₂ per g of adsorbent at 0.15 bar and 298K. This shows that surface area has minimal impact in the low-pressure adsorption properties. Further, it can be seen in Figure 1-16, that the strongest binding sites for CO₂, (hence the highest $-Q_{st}$ values) are related to frameworks with alkyl amine based functionality or highly polarizing open-metal coordination sites (OMCs). These two structural components have been used quite extensively throughout MOF chemistry to enhance the overall low-pressure CO₂ adsorption properties.

1.3.3 MOFs with open metal coordination sites (OMCs)

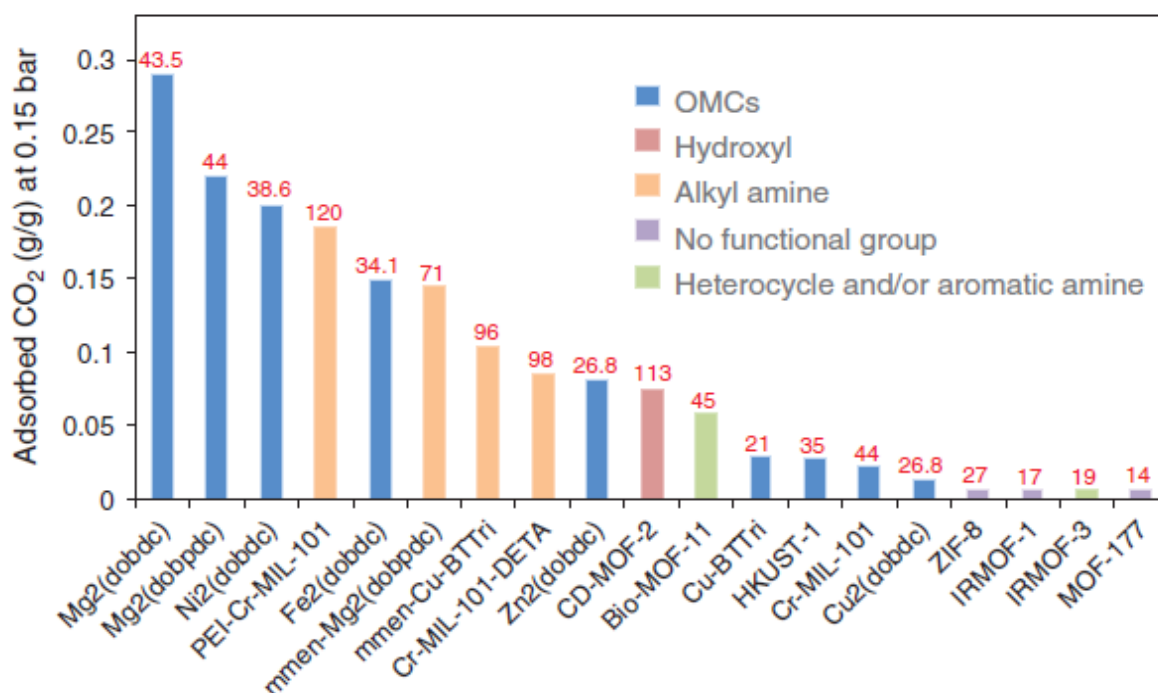


Figure 1-16 CO₂ adsorption at 0.15 bar, the pressure relevant for post-combustion capture. It should be noted that all for the data presented was obtained from isotherms collected at 298K with the exception of HKUST-1 and Cr-MIL-101 and Cr-MIL-101-DETA, which were collected at 293 and 296 K, respectively. The values in red represent the low-coverage experimental isosteric heats of adsorption, $-Q_{st}$.^{63, 96, 111, 114, 152, 184-191}

In most reported MOFs, weak van der Waals (vdW) forces are the dominant interactions between the framework and incoming guests; however, recent work has shown that an effective strategy to increase the surface packing density of adsorbates is through the generation of MOFs that contain high concentrations of open metal coordination sites (OMCs).¹⁸⁰ The incorporation of highly reactive, electron deficient OMCs into frameworks can also enhance both binding energy and selectivity and permit charge transfer between the framework and surface bound guest species^{72, 116}, a property of much interest for the conversion of small molecules into other useable products. While many of the frameworks with OMCs have been discovered serendipitously,²⁶ there are emerging methodologies for their controlled introduction including the incorporation of metalloligands¹⁸¹ and using synthetic protocols where metal clusters containing OMCs are used *ab initio*.⁸⁶ In all of these cases, the frameworks form with solvent remaining in the channels and in the metal coordination sphere. Post-synthetic treatment of the materials with a combination of heat and vacuum, a process called activation, can liberate the solvent molecules from the framework, and if the MOF porosity is maintained, the newly generated OMCs are available for guest inclusion.

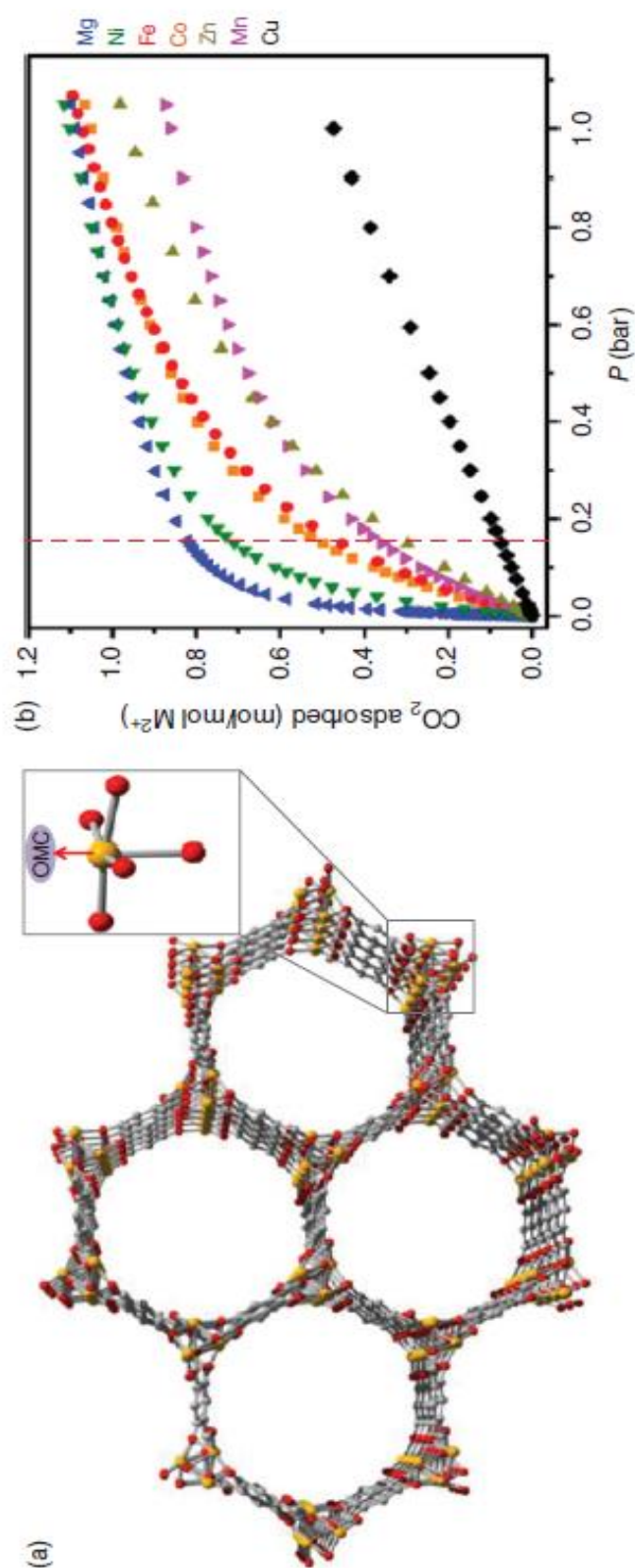


Figure 1-17 (a) Ball and stick model of $M_2(\text{dobdc})$ showing open metal coordination sites (OMCs). Orange, red, and grey spheres represent metals, oxygen, and carbon, respectively. (b) Excess CO_2 adsorption isotherms collected for the $M_2(\text{dobdc})$ series at 298 K showing variability in the low-pressure adsorption properties with metal substitution. The red line, located at 0.15 bar, represents a pressure relevant to post-combustion flue gas capture in a coal-fired power plant.⁶³

Figure 1-16 shows the low-pressure adsorption capacity for several MOFs at 0.15 bar and 298K. Those highlighted in blue are the adsorption capacities for MOFs with OMCs while those highlighted in purple are frameworks dominated by weak vdW type interactions.⁸⁶ It can easily be seen from this plot that the electron deficient OMCs, which strongly polarize incoming CO₂, lend to significantly higher adsorption at low pressures of interest for post-combustion carbon capture. It should also be noted that while OMCs provide strong interactions allowing CO₂ adsorption at higher temperatures and lower pressures than typically used for energy-consuming cryogenic distillation processes, the adsorbate-adsorbent interactions are often weak relative to the formation of chemical bonds, providing facile release of the molecules during the regeneration step of a separation process.⁸⁶

One of the most well-studied OMC-containing MOFs to date is M₂(dobdc), alternatively known as M-MOF-74, CPO-27-M, or M₂(dhtp) where M = Mg, Mn, Fe, Co, Ni, Cu, or Zn and dobdc⁴⁻ = 2,5-dioxido-1,4-benzenedicarboxylate (Figure 1-17a).^{87, 93, 100-101, 123, 182-184} The framework consists of 1-D honeycomb like channels that are constructed by metal oxide chains interlinked by dobdc⁴⁻ ligands. The significance of this framework is related to the interesting adsorption properties that derive from the existence of unique structural features. For instance, upon solvent removal, M₂(dobdc) offers one of the highest densities of OMCs of any framework discovered to date. It also undergoes chemical substitution with a wide range of first-row transition metals. The extent of the metal substitution is only rivaled by a few MOF families such as M-BTT (BTT³⁻ = 1,3,5-benzenetristetrazolate), where M = Cr, Mn, Fe, Co, Ni, or Cu,^{121, 185-188} and M₃(btc)₂(btc³⁻ = 1,3,5-benzenetricarboxylate), where M = Cr, Fe, Ni, Cu, Zn, Mo, or Ru¹⁸⁹⁻¹⁹⁴.

The high concentration of electron deficient OMCs in Mg₂(dobdc) leads to an unprecedented adsorption at low-pressures of ≈ 0.29 g CO₂ per g MOF (0.15 bar and 298 K) and an isosteric heat of -43.5 kJ/mol.⁶³ The low-pressure adsorption is still the highest reported to date. Multiple *in-situ* techniques including NMR, IR, EXAFS, and *in-situ* diffraction have shown that the high-initial isosteric heat is directly related to the presence of OMCs.^{63, 106, 108, 131, 134} Rietveld analysis of neutron powder diffraction data followed by subsequent Fourier difference analysis has revealed CO₂ is bound to Mg²⁺ in an end-on orientation that is angled with respect to the framework surface, a direct result of secondary vdW interactions between the CO₂ and ligand atoms (Figure 1-13). The high isosteric heat is reflected in the ability of the CO₂ molecule to get close to the framework with short Mg-CO₂ distances approaching ≈ 2.3 Å.¹⁹⁵ Britt *et al.* also showed a facile release of CO₂ in Mg₂(dobdc) at a moderate temperature of 80 °C. Later, Mason *et al.* calculated the working capacity for the material to be approximately 17.6 wt% with a temperature swing process from 40 °C (at 0.15 bar CO₂) to 200 °C. This value is much higher than MOF-177, a material without strong adsorption sites, which has a negative working capacity at all evaluated temperatures.

It has recently been demonstrated that chemical substitution of the framework metals offers tunability with regard to the CO₂ adsorption properties, Figure 1-17b. The low-coverage isosteric heats show the following trend: (Cu < Zn < Mn < Fe < Co < Ni < Mg) for the M₂(dobdc)

series, one that does not correlate with the expected ionic radii or Irving Williams series.⁶³ A first principles study of Yu *et al* show that the trend is instead dictated by the effective nuclear charge seen by the CO₂ as it approaches the OMC.¹⁹⁶ Much additional theoretical work has been focused on predicting the structures and properties of this family of compounds. The wide range of chemical substitution and vast amount of experimental data provides a platform to test the efficacy and accuracy of developing computational methods in slightly varying chemical environments.⁷³ On the experimental side, in addition to metal substitution, recent efforts have been made to elongate the framework ligands to tune the pore size. Deng *et al.* have constructed an isorecticular series of MOFs that contain expanded versions of the linker with as many as 11 additional benzene rings giving rise to pore diameters as large as 98 Å.⁴⁴

Another iconic framework that has been the subject of a large number of CO₂ adsorption studies throughout the literature is Cu₃(BTC)₂ (alternatively known as HKUST-1 or Cu-BTC), which has a cubic structure that consists of copper-containing paddlewheels, Cu₂(COO)₄, interlinked by BTC³⁻ ligands. This material is shown to have an isosteric heat of –35.0 kJ/mol with a modest CO₂ uptake less than 15.4 wt% at 0.15 bar and 25 °C.⁸⁵ This value is significantly lower than Mg₂(dobdc) due to a lower density of OMCs and the smaller charge density of the Cu²⁺ cation. This work was followed by Arnold *et al.*, which performed CO₂ adsorption studies on the M₃(BTC)₂ analogs that are capable of maintaining their permanent porosity post-activation. They found the following trend for isosteric heats of adsorption: Ni > Ru > Cu > Mo ≈ Cr, which range from –36.8 to –26.7 kJ/mol. However, it should be noted that the OMC on the Ni analog is incapable of undergoing complete activation and instead is blocked by coordinated guest molecules including H₂O and MeNH₂. As such, it is thought that Coulombic interactions occurring between the surface bound CO₂ and guest molecules could be the culprit for the high isosteric heat.¹⁹⁴ This is further supported by a recent study of Snurr *et al.* that show that slightly hydrated variations of Cu₃(BTC)₂ show improvements in the low pressure CO₂ adsorption capacity and zero-coverage isosteric heats of adsorption when compared to the completely activated framework.¹¹¹ Framework families like the aforementioned ones that undergo a broad range of chemical substitution provide a mechanism for tuning the adsorption properties (Figure 1-17b) while retaining the same structural motif. These types of in depth studies offer an unprecedented opportunity to gain insight into the structure derived function of MOFs, knowledge that is necessary to understand how to design new candidates with optimized properties for post-combustion capture applications.

1.3.4 MOFs containing Lewis basic sites

Much work has been focused on functionalizing the surface of MOFs with a variety of functional groups that, unlike the Lewis acidic OMCs, can additionally function as electron donating Lewis bases. This work has primarily been focused on (i) the generation of framework ligands with strongly polarizing functional groups and/or heterocycles and the (ii) appendage or infusion of MOFs with Lewis base containing substituents that lend to chemisorptive interactions. The nature of the framework- CO_2 interaction, whether it be physisorption or chemisorption, respectively, is dictated by the type of the functional group.

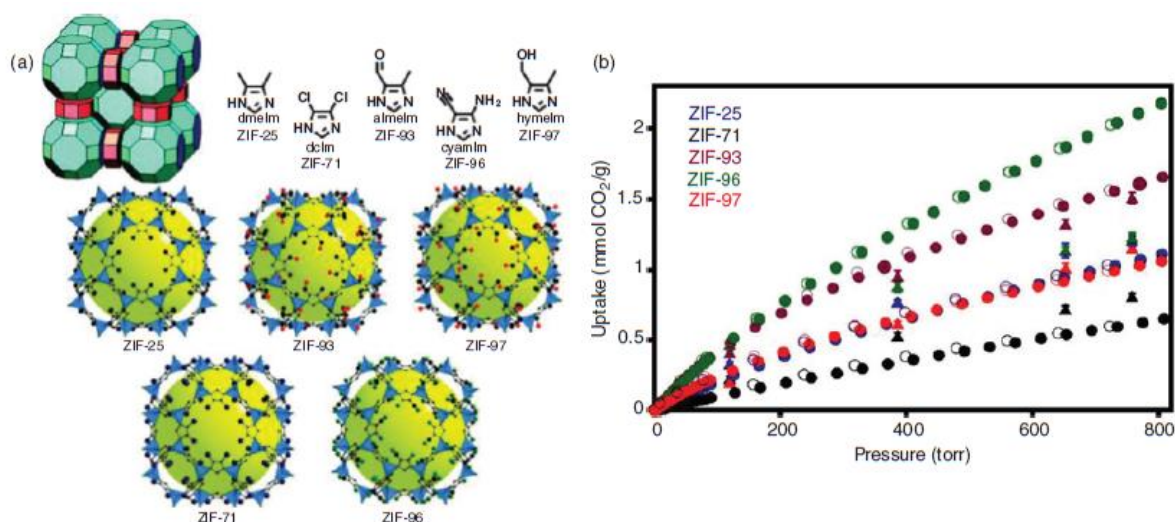


Figure 1-18 (a) Isotropical series of RHO Zeolitic Imidazolate frameworks with varying functionality and (b) experimental (circles) and theoretical (triangles) excess CO_2 adsorption isotherms collected at 298K for the RHO ZIF series. This image is reproduced from reference²⁰⁹ with permission from the American Chemical Society.

(i) *strongly polarizing ligands for physisorption*: The quadrupole moment of CO_2 can become polarized by the existence of dipole moments from a variety of framework functionality. This dipole moment can be generated for instance by the introduction of heterocycles in the organic ligand or through direct functionalization of the ligand with a variety of chemical groups including amine, hydroxyl, thio, cyano, and halides. The idea is that the stronger polarizing the functionality, the stronger the interaction with CO_2 . This effort is highlighted in the Zeolitic imidazolate frameworks (ZIFs), a class of MOFs that have zeolite-based topologies; ZIFs are generally described by a formula, $\text{M}(\text{Im})_2$, that is similar to their zeolite counterparts $\text{Al}(\text{SiO}_2)$ where the Si nodes and oxygen bridges are replaced by metal cations and imidazolate ligands, respectively. Due to their high porosity and chemical and thermal stability, they have been investigated for carbon capture applications. A variety of ZIF topologies with varying functionality on the imidazole ligands have been prepared. Figure 1-18a for instance shows the introduction of various functional groups into the RHO ZIF framework family reported by Yaghi and co-workers. It is reported that the improved CO_2 adsorption of the amine functionalized ZIF-96 relative to the others (Figure 1-18b), is likely

due to a combination of two effects: a large contribution arising from electrostatic interactions, due to the asymmetric functionalization, and strong vdW interactions arising from the polarizability of the functional groups.¹⁹⁷ While this framework family shows some tunability in the CO₂ adsorption properties, the low-pressure adsorption is moderate leaving little room for potential applications in post-combustion carbon capture. As a significant improvement, An *et al.* introduced Bio-MOF-11 (also known as Co₂(ad)₂(CO₂CH₃)₂·2DMF·0.5H₂O where ad = adeninate) whose structure consists of Co²⁺ paddlewheels capped with two acetate ligands and interlinked by 2 heterocyclic adeninate ligands, which have amine-based functionality.¹⁹⁸ This MOF has a high initial isosteric heat of adsorption of -45 kJ/mol and an impressive selectivity of 75:1 for CO₂:N₂ calculated from the molar ratios of CO₂ and N₂ uptake at 298 K. While these values are very impressive, it should be noted that the isosteric heat drops off rapidly with higher loading and stabilizes around -35 kJ/mol, likely due to the rapid saturation of strong adsorption sites. As a result, the low pressure CO₂ adsorption has a modest value of ≈ 5.8 wt% at 0.15 bar. While this value is significantly improved from the aforementioned ZIFs and any reported framework containing aromatic amines, it is well-below many of the OMC-containing MOFs (Figure 1-16) and frameworks made with alkylamine functionality.¹⁹⁸ However, a follow up study of Chen *et al.* report molecular simulation studies on Bio-MOF-11. They show that, relative to other nanoporous adsorbents including MOFs and zeolites, this framework has one of the highest CO₂/N₂ selectivities, and it is even slightly enhanced in the presence of water, a factor that makes the material of high interest for post-combustion

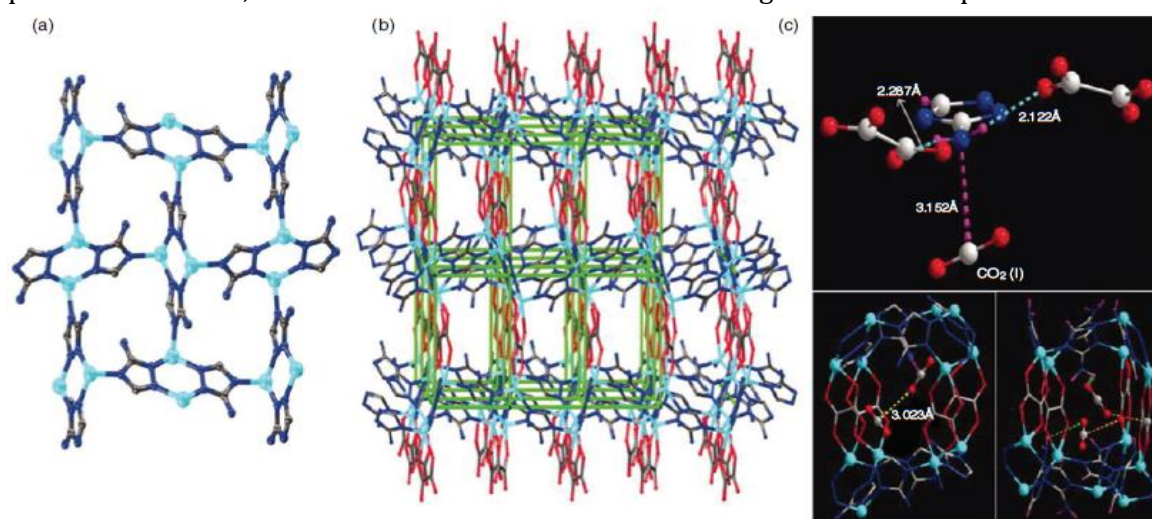


Figure 1-19 (a) Partial structure showing Zn-atz layer that is made up of Zn₂ dimers rotated by 90° with respect to each other. (b) Ball and stick model of the Zn₂(atz)(ox) structure formed from Zn-atz layers that are pillared by the oxalate units. (c) Single crystal x-ray structure of CO₂ binding in Zn₂(atz)(ox) at 173 K. (c) (top) The amine group of Atz ligand is shown bound to CO₂(I) and (bottom) The H atoms of the amine group form H-bonds to the oxalate O atoms, directing the N lone pair toward the C atom of the CO₂ molecule. (bottom) The CO₂ molecules are found in a cavity with short intermolecular distances (CO₂-I and CO₂-II). There are secondary interactions between the CO₂-I and Ox (drawn in orange). Zn, N, O, C, and H are represented by cyan, blue, red, grey and purple spheres, respectively. This figure is reproduced from reference²¹² with permission AAS.

capture applications. They further attribute the preferential adsorption of CO₂ to the presence of pyrimidine and amino Lewis basic adsorption sites.¹⁹⁹

More recently Woo and co-workers used *in-situ* single crystal diffraction to provide the first observation of CO₂ binding to an amine in Zn₂(C₂O₄)(C₂N₄H₃)₂•(H₂O)_{0.5} (alternatively known as Zn₂(atz)(ox) where atz = aminotriazole and ox = oxalate, Figure 1-19),²⁰⁰ which features an isosteric heat of -40.8 kJ/mol and low-pressure capacity of 13.6 at 0.15 bar and 22 °C.²⁰¹ This MOF has two crystallographically distinct CO₂ adsorption sites. The first is located near the free amine group, while the second adsorption site is near the oxalate, both with distances above 3 Å. The intermolecular CO₂ distances imply strong intermolecular interactions. Using this experimental work combined with molecular simulation studies, they concluded that the observed CO₂ adsorption properties are a combination of appropriate pore size, strong interaction between CO₂ and functional groups on the pore surface, and intermolecular interactions between neighboring CO₂ molecules.²⁰⁰

(ii) *lewis bases for chemisorption*: Amines do not only polarize CO₂, in many instances they can strongly and selectively bind CO₂ *via* chemisorptive interactions. Considering the

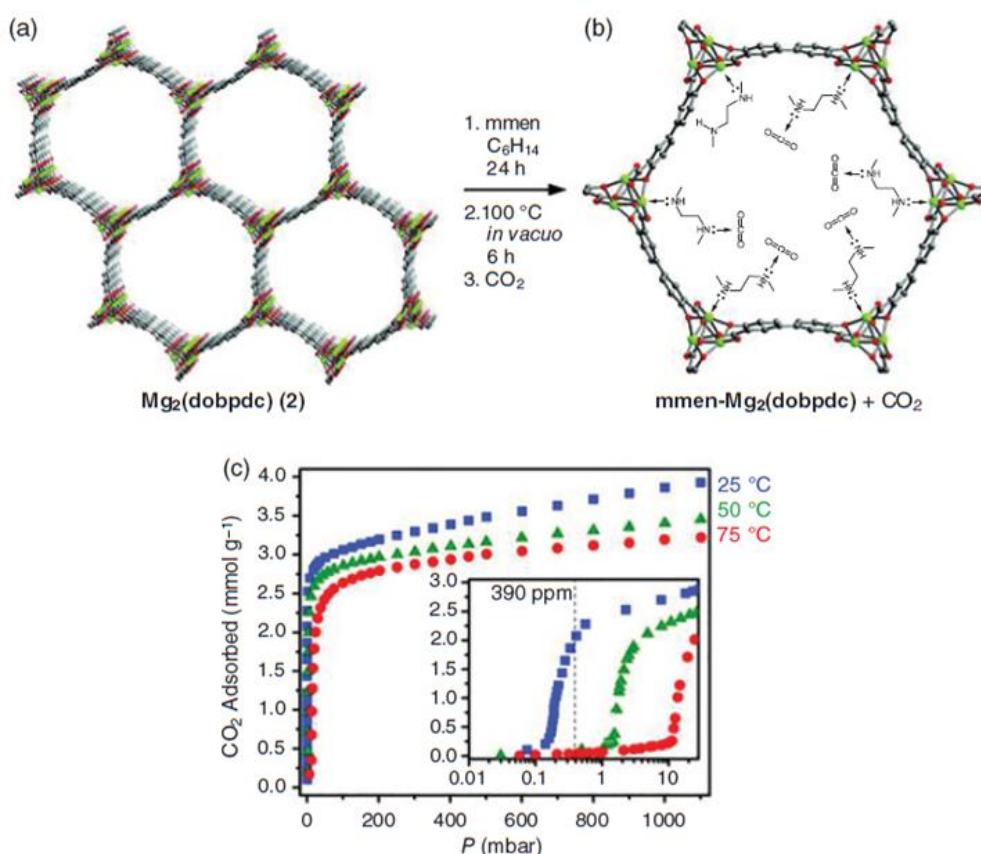


Figure 1-20 Ball and stick model of (a) Mg₂(dobpdc) and (b) mmen-Mg₂(dobpdc) and (c) excess CO₂ adsorption isotherms for mmen-Mg₂(dobpdc) at various temperatures showing a sharp step at 0.39 mbar (the partial pressure of CO₂ in air) that is shifted with temperature. Image is reproduced with permission from the American Chemical Society.¹⁸⁵

lower heat capacity of solid adsorbents compared to the liquid amine based scrubbers, which are already implemented industrially for various CO₂ separations, it seems feasible that decorating the surface of MOFs with pendant alkylamines could lower regeneration energies, and hence give rise to an overall energy penalty that is closer to the projected thermodynamic minimum (projected to be about 11% energy penalty).²⁰² Recent work in the MOF field has been focused on either appending alkylamines to the internal surface of MOFs *via* OMCs or through impregnation of MOF frameworks with polymers, such as polyethyleneimine.

The first report of post-synthetic appendage of small molecules to OMCs was carried out by Hwang *et al* who appended ethylenediamine to Cr³⁺ sites in the MIL-101 framework (alternatively known as Cr₃O(1,4-BDC)₃(H₂O)₂X, where X = F⁻ or NO₃⁻).²⁰³ While the targeted application was Knoevenagel condensation catalysis, several works reported since are focused solely on post-combustion carbon capture. The first report of an amine-appended MOF for flue gas separation was by McDonald *et al.* in 2011. At 25 °C mmen-CuBTTri (mmen = *N,N'*-dimethylethylenediamine and H₃BTTri = 1,3,5-tri(1*H*-1,2,3-triazol-4-yl)benzene) adsorbs 0.105 g CO₂ per g MOF with an IAST selectivity of 327, a direct result of the high isosteric heat of CO₂ adsorption, which was calculated to be -96 kJ / mol at zero coverage (-Q_{st} for Cu-BTTri = 21 kJ/mol). In addition to this, *in-situ* IR spectra gave evidence of the formation of a zwitterionic carbamate species indicative of a chemisorptive interaction. Despite the large initial isosteric heat of adsorption, the CO₂ uptake was also fully reversible and the framework could be easily regenerated at 50 °C, enabling a cycling time of just 27 min and no loss of capacity over the course of 72 adsorption/desorption cycles tested.¹⁴⁰ Later, Hu *et al.* appended several amines to the surface of Cr-MIL-101 and showed a 3-fold enhancement of the low pressure CO₂ adsorption properties compared to the bare framework (from .022 to .085 g CO₂ / g MOF at 0.15 bar and 23 °C). The isosteric heats of CO₂ adsorption increased from -44 kJ/mol¹⁰² to -98 kJ/mol and the selectivity of the amine-based analog again showed nearly no N₂ uptake at 296 K leading to a very high selectivity factor for CO₂/N₂.¹⁷⁴ More recently Lin *et al.* reported polyethyleneimine (PEI) infused Cr-MIL-101. Although the surface area and pore volume of MIL-101 decreased significantly with a 100 wt% PEI loading (BET surface areas range from 3125 to 608 m²/g), there is a dramatic enhancement in the CO₂ adsorption capacity at 0.15 bar that ranges from 0.0145 to 0.185 g CO₂ per g MOF at 25 °C, respectively (Figure 1-16). Further, at 50 °C, a temperature more relevant to post-combustion capture, the adsorption capacity is still 0.150 g CO₂ per g of 100 wt% PEI-Cr-MIL-101.

In 2012, McDonald *et al.* reported mmen-appendage to Mg₂(dobpdc) (dobpdc⁴⁻ = 4,4'-dioxido-3,3'-biphenyldicarboxylate) (Figure 20a, b), which showed 0.088 g CO₂ / g MOF at 0.39 mbar (298 K) and 0.138 g/g at 0.15 bar (at 40 °C), conditions relevant to CO₂ capture from air and flue gas, respectively.¹⁷³ The material also shows excellent performance in the presence

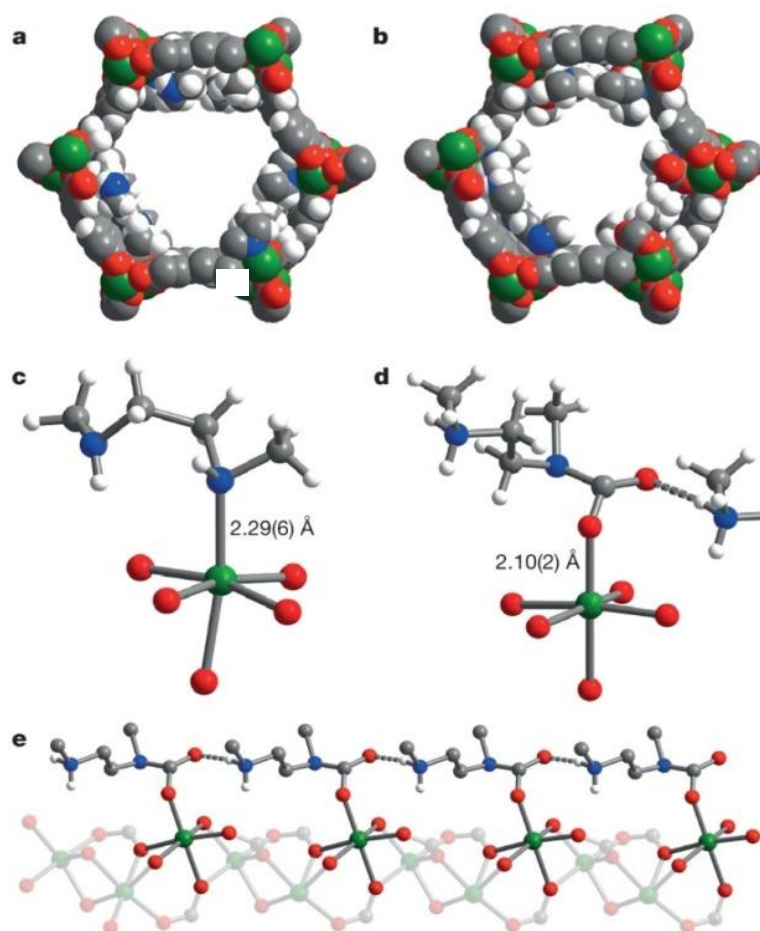


Figure 1-21 Space-filling models of the solid-state structures of (a) mmen-Mn₂(dobpdc) and (b) CO₂-mmen-Mn₂(dobpdc) at 100 K. Portions of the crystal structures for mmen-Mn₂(dobpdc) (c) before and (d) after CO₂ adsorption, as determined from synchrotron powder X-ray diffraction data. The latter shows CO₂ insertion between the amine and Mn metal. (e) A portion of the crystal structure shows the formation of an ammonium carbamate chain along the MOF pore. Green, grey, red, blue and white spheres represent Mn, C, O, N and H atoms, respectively; some H atoms are omitted for clarity. Image is reproduced with permission from Nature Publishing Group.²²⁰

of water²⁰⁴. Adsorption/desorption cycling experiments, carried out *via* TGA, demonstrate that mmen-Mg₂(dobpdc) can be repeatedly regenerated (at 150 °C under N₂ flow) after many 15 minute exposures to simulated flue gas. The working capacity, calculated to be 0.11 g CO₂ per g of MOF, corresponds to a total CO₂ removal of 98%.¹⁷³ With DSC (differential scanning calorimetry), the authors further estimated that regeneration would require approximately 2.34 MJ of energy to release 1 kg of CO₂ from mmen-Mg₂(dobpdc) compared to the 3.6 to 4.5 MJ energy requirement for the state of the art MEA scrubbers.²⁰⁵⁻²⁰⁷ Later, in 2015, this study was extended to append mmen onto the internal surface of multiple M₂(dobpdc) analogs (where M= Mg, Mn, Fe, Ni, Co, and Zn). They show significant tunability in the steep steps observed in the adsorption isotherm. Using a combination of IR, synchrotron x-ray diffraction, and computational studies they were able to reveal the origin of the sharp adsorption step in

the isotherm (Figure 1-20c) is the result of a cooperative insertion process in which CO₂ molecules insert into metal-amine bonds, inducing a reorganization of the amines into well-ordered chains of ammonium carbamate (Figure 1-21a-e). As a consequence, large CO₂ separation capacities can be achieved with small temperature swings, and regeneration energies appreciably lower than achievable with state-of-the-art aqueous amine solutions become feasible.²⁰⁸

Beyond alkyl amine containing frameworks, there are few examples of other Lewis base functionality in MOFs that lend to chemisorptive type interactions with CO₂. Recently, Gassensmith and co-workers reported the synthesis of a MOF constructed by γ -cyclodextrin linked together by alkali metals such as Rb (CD-MOF-2).¹⁴⁵ The ligand in this MOF, which is decorated with free hydroxyl groups, is a natural product produced from starch. Further, the MOF can be prepared readily in green solvents such as water using slow evaporation methods. While this material was not assessed for room-temperature N₂ adsorption, it shows extremely high uptake of CO₂ at very low-partial pressures indicative of very strong binding. As such, solid-state cross-polarization magic-angle-spinning (CP/MAS) ¹³C NMR spectroscopy was used to monitor the material before and after exposure to CO₂. Upon introduction of CO₂, CD-MOF-2 shows a new peak at 158 ppm that was interpreted as the formation of carbonic acid functionality, due to a direct interaction between the CO₂ and surface hydroxyls. This additional resonance was also accompanied by chemical shifts of other signature peaks in the MOF supporting the hypothesis that a chemical reaction was occurring. Later, calorimetry revealed a zero coverage differential enthalpy of CO₂ adsorption equal to approximately -113.5 kJ/mol at 25 °C. This value quickly dropped to around -65.4 kJ/mol binding event, which was attributed to less reactive hydroxyls and then another plateau at -40.1 kJ/mol that was attributed to physisorptive type interactions. It should be noted that the strongest binding sites appear to be irreversible; however this only reduces the capacity slightly with cycling.²⁰⁹

1.3.5 Stability and competitive binding in the presence of H₂O

One of the major drawbacks for the utilization of MOFs in many applications is the widespread belief that they are unstable in the presence of water, a result of many reports that show frameworks that break down due to hydrolysis. While these materials do exhibit coordination type bonding, that is considered to be weaker than that of their covalent counterparts, there have been many MOFs synthesized to date that exhibit water stability.²¹⁰ This effort has been driven by the need for materials that maintain high performance in wet environments, such as post-combustion flue gas separations. While the amount of water present in a flue gas stream could be reduced, it is energetically costly and complete removal is likely unfeasible.²¹¹ As such, many synthetic strategies have been taken to provide water stable materials. These methodologies include the use of high oxidation state metals, multidentate ligands, metal nodes with large coordination numbers, MOF modification with hydrophobic ligands, guests or polymers, and the use of ligands with limited acidity, like pyrazoles and imidazoles.^{210, 212-219}

While many of the azole-based ligands can bind metals with similar geometries as carboxylates, the higher Lewis basicity creates stronger metal-ligand bonds improving both thermal and chemical stability. It is expected that MOF stability will increase with increasing pKa to give the following stability trend: pyrazole > imidazole > triazole > tetrazole. A recent report of Long *et al* reveals the synthesis of a new pyrazolate framework, $\text{Ni}_3(\text{BTP})_2$ (H_3BTP =1,3,5-tris-1H-pyrazol-4-yl)benzene), which exhibits stability in boiling water for 14 days with varying pH levels that range from 2 to 14.²¹⁵ Later, *in-situ* IR studies revealed weak

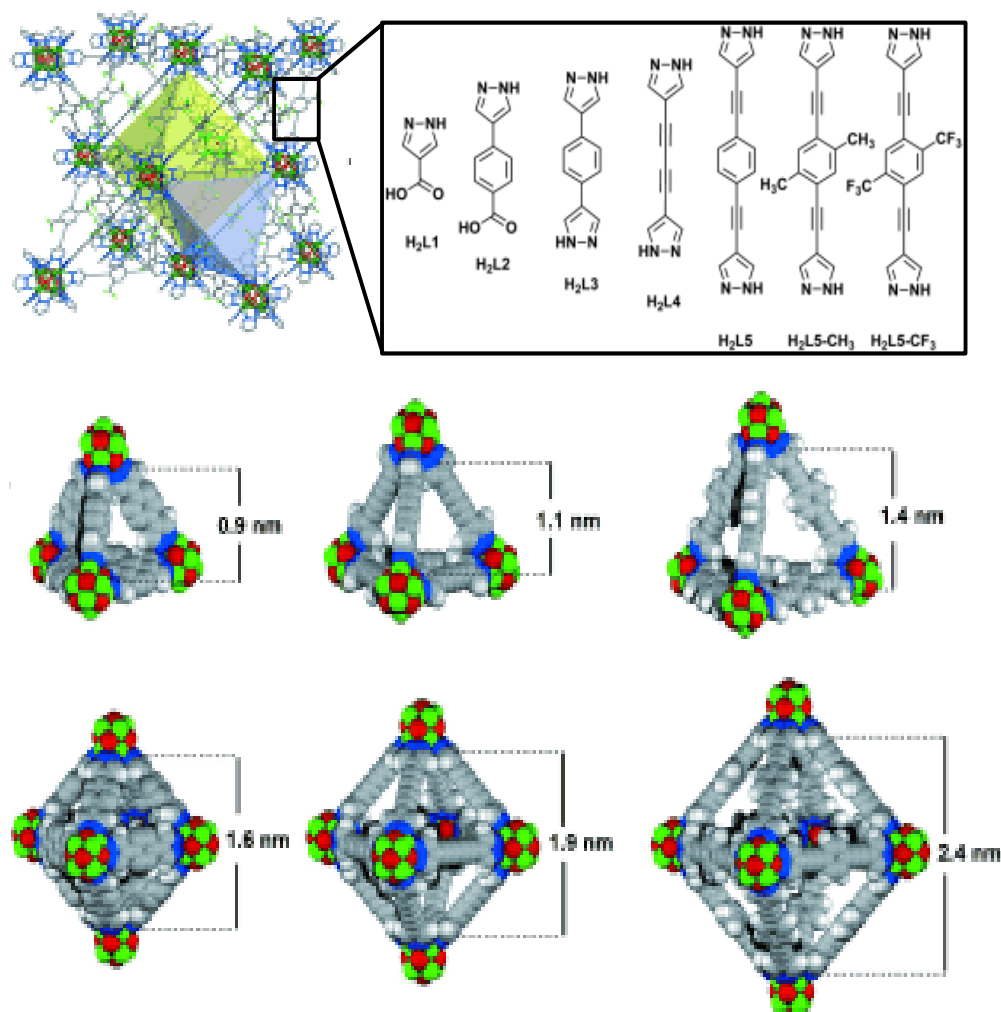


Figure 1-22 (a) The crystal structure of $[\text{Ni}_8(\text{OH})_4(\text{H}_2\text{O})_2(\text{L5-CF}_3)_6]_n$ viewed as a combination of n octahedral (yellow polyhedron) and $2n$ tetrahedral (gray polyhedron) cavities. (b) Pyrazolate-based ligands used in the synthesis of the $[\text{Ni}_8(\text{OH})_4(\text{H}_2\text{O})_2(\text{L})_6]_n$ MOFs. $\text{H}_2\text{L1}$ =1H-pyrazole-4-carboxylic acid, $\text{H}_2\text{L2}$ = 4-(1H-pyrazole-4-yl)benzoic acid, $\text{H}_2\text{L3}$ = 4,4'-benzene-1,4'-diylbis(1H-pyrazole), $\text{H}_2\text{L4}$ = 4,4'-buta-1,3-diyne-1,4'-diylbis(1H-pyrazole), $\text{H}_2\text{L5}$ = 4,4'-(benzene-1,4'-diyl)diethyne-2,1'-diylbis(1H-pyrazole), and $\text{H}_2\text{L5-R}$ (R=methyl, trifluoromethyl). (c) View of the tetrahedral (top) and octahedral (bottom) cages found in the crystal structures of $[\text{Ni}_8(\text{OH})_4(\text{H}_2\text{O})_2(\text{L3})_6]_n$ (left), $[\text{Ni}_8(\text{OH})_4(\text{H}_2\text{O})_2(\text{L4})_6]_n$ (middle), and $[\text{Ni}_8(\text{OH})_4(\text{H}_2\text{O})_2(\text{L5})_6]_n$ (right), and the corresponding metric descriptors. Ni, N, C, O, and F and H are depicted as green, blue, grey, red, and white spheres, respectively. Image is reproduced from reference²³⁵ with permission of WILEY-VCH Verlag GmbH & Co. KGaA, Weinheim.

interactions of $\text{Ni}_3(\text{BTP})_2$ with CO , CO_2 , and H_2 . It is proposed that the pyrazolate ligand forces the Ni^{2+} into a diamagnetic low-spin state with a large energy barrier to transition from low-spin to high-spin of 75 kJ/mol, a value derived from *ab-initio* molecular modeling.²²⁰ This low-spin state might also inhibit the interaction of the metal with water and hence add to the overall framework stability. While this study has focused on improving the strength of the metal-ligand bond other studies have added hydrophobic functionality to framework ligands such as $-\text{CH}_3$, $-\text{CF}_3$, and $-\text{F}$.²²¹⁻²²² A later study of Navarro et al reports construction of an isorecticular series of MOFs denoted as $[\text{Ni}_8(\text{OH})_4(\text{H}_2\text{O})_2(\text{L})_6]_n$ where L = a series of azolate ligands with increasing levels of hydrophobicity shown in Figure 1-22. Moreover, the length and functionalization of the linkers impact on the pore size as well as on the fine tuning of the surface polarity and the incorporation of trifluoroalkyl groups gives rise to a significant enhancement in the hydrophobicity and an overall improvement in hydrolytic stability. Although this study was mostly focused on overcoming problems related to the adsorption of harmful volatile organics in wet environments, these same principles can be applied to MOFs for various gas separation applications.²²³

While the aforementioned studies worked to improve hydrolytic stability and hydrophobicity in the initial framework design, others have utilized post-synthetic modifications to manipulate these parameters. A recent report demonstrated that the encapsulation of HKUST-1 into polystyrene microspheres not only improved the hydrolytic stability of the framework, but additionally allowed retention of most of the CO_2 uptake capacity after exposure of the composite to 80% relative humidity at 27 °C for 1 month.²²² This is a significant achievement considering that HKUST-1 readily decomposes in the presence of water, which coordinates to the Cu-OMC on the paddlewheel cluster, promoting hydrolysis of the metal-ligand bond and hence framework degradation.²²⁴

For MOFs that exhibit highly charged functionality on their internal surface, such as OMCs, water will compete for adsorption sites with CO_2 and in most cases water will win this battle due to an existing dipole moment. As such, even if MOFs are deemed water stable, their separation performance must still be assessed in wet multicomponent streams or at minimum after exposure to water vapor. While $\text{Mg}_2(\text{dobdc})$ is currently the best performing MOF at ambient pressure and dry conditions, it cannot be used for the capture of CO_2 under flue gas conditions due to diminished adsorption properties in the presence of water. In a study of Matzger *et al*, the breakthrough performance of a series of $\text{M}_2(\text{dobdc})$ (where $\text{M} = \text{Zn}, \text{Ni}, \text{Co}$, and Mg) MOFs were evaluated in dry streams of $\text{CO}_2:\text{N}_2$ (0.16 bar and 0.84 bar, respectively) after exposure to relative humidity levels that range from 0 to 70%. For $\text{Mg}_2(\text{dobdc})$, after exposure to 70% RH and subsequent thermal regeneration, only about 16% of the initial CO_2 capacity was recovered. While the other metal-analogs experienced less of a performance decline, it is clear that in the event that water does not cause framework decomposition, it will be in competition for the OMCs and with further cycling the materials will become saturated.⁹⁴ Subsequent removal of water adsorbed at the OMCs can often be energy intensive, requiring high heat and vacuum. This work was additionally supported by a recent study of Mason *et al*,

which carried out multicomponent adsorption studies of several MOFs in $\text{CO}_2/\text{N}_2/\text{H}_2\text{O}$ mixtures. It was found that for every OMC containing MOF studied, that the low-pressure CO_2 adsorption capacity decreased significantly compared to the capacities in pure streams of CO_2 (Figure 1-5).⁷⁶ To alleviate this problem, appending amines to the OMCs, which are known to preferentially bind CO_2 , even in the presence of water, can be a useful solution. Given that the amine appended frameworks are likely hydrophilic due to the high concentration of functional groups that readily form hydrogen bonding interactions, it also promotes water adsorption inside of the MOF that could inadvertently induce structural changes or simply decreasing overall capacity. As such, there is still a need to assess the separation ability of many amine-appended frameworks in wet streams.²²⁵ However, it should be noted that the aforementioned study of Mason *et al*, also probed several alkyl amine-containing frameworks using multicomponent adsorption. For every amine-containing MOF studied, the decreases in the CO_2 adsorption capacities are minimal in the presence of water (Figure 1-5). Even in some cases, a slight increase can be observed upon introducing water.

Recently, an alternative strategy for achieving water stability was reported by Cohen *et al*, who introduced polyMOFs, which are constructed by ligands with long hydrophobic polymeric chains. Some of these polyMOF materials are shown to exhibit relatively high CO_2 sorption with minimal N_2 sorption, making them promising materials for CO_2/N_2 separations. Although the parent MOFs are generally unstable to water, the polyMOFs demonstrated excellent water stability due to the hydrophobic polymer, as well as the cross-linking of the polymer chains within the MOF. Further, the polyMOFs exhibit minimal change in their CO_2 adsorption properties before and after water exposure.²²⁶ While many of the studies focused on enhancing water stability and assessing the performance of MOFs in wet environments are still in their infancy, this work has already led to significant improvements in materials performance providing optimism towards the eventual implementation of MOFs in various energy relevant gas separations.

1.4 MOFs for pre-combustion capture

1.4.1 Advantages of Pre-combustion capture

Pre-combustion capture, which primarily involves the separation of CO_2 from H_2 and a few other impurities, has several advantages over other carbon capture technologies. First, the separation is carried out at high pressure ranging from 5-40 bar⁷¹ with much higher CO_2 concentrations. As a result, it will be less energy intensive to regenerate the material. The high pressure allows implementation of a PSA type regeneration process where the pressure is simply dropped to atmospheric eliminating the need to heat the material through temperature swing process, as in post-combustion capture. Further, the actual separation of CO_2 from H_2 is significantly easier due to much larger disparities in their chemical properties such as polarizability and quadrupole moment for CO_2/H_2 compared to CO_2/N_2 and O_2/N_2 in post-combustion and oxy-fuel processes (Table 1-2). These differences provide much higher selectivity for CO_2 over H_2 in solid adsorbents allowing the separation to be done using a purely

physisorptive process. All of these added benefits could allow a more rapid development of separation materials and their subsequent implementation into industrial separations.

Currently the separation of CO₂ and H₂ is already carried out on extremely large scales worldwide, 50 million tons per year, for the purification of H₂, which is used primarily in the production of ammonia and various hydrocarbons.²²⁷ This process is typically carried out via PSA with solid adsorbents such as activated carbons or zeolites.⁶² While the process is still too energetically inefficient to make pre-combustion capture economically viable, significant improvements in the efficiency of solid adsorbents for the separation of CO₂/H₂ could render the technology workable on a large scale or provide further energy savings in existing hydrogen purification infrastructure world-wide. It is projected that a 10% energy savings in already implemented hydrogen purification industries would be the equivalent of closing 18 coal-fired power plants.⁷⁷ The already existing infrastructure for hydrogen purification and the scale with which this separation is already carried out, implies that the implementation of pre-combustion capture could be expedited relative to post-combustion and oxy-fuel technologies.

1.4.2 Necessary framework properties for CO₂ capture

Most of the energy expended in the separation of CO₂ and H₂ is related to mass transport of the gas and PSA regeneration process. As such, much energy savings could be realized through an improvement in the selectivity and working capacity of the solid adsorbent. Working capacity is defined as the difference between the amount of gas adsorbed at the flue gas stream pressure and the amount of gas adsorbed at the regeneration pressure. High gravimetric and volumetric working capacity lowers the amount of material required and/or size of the fixed bed for the separation and hence also lowers the overall energy input for the PSA regeneration process.

Other factors to be considered when selecting materials for pre-combustion capture should include their long term stability and that their separation properties are maintained in the presence of other minor impurities in a flue gas stream such as CO, H₂O, and H₂S. While there are many studies assessing the hydrolytic stability of MOFs previously mentioned, little is known about their behavior in H₂S. Only a few studies are included in the literature, in one of these Eddaoudi *et al.* show that SIFSIX-3-Ni (SIFSIX = hexafluorosilicate) metal-organic framework has high selectivity for CO₂ and is stable in the presence of H₂S²²⁸. Further, De Weireld *et al* have studied H₂S adsorption in a series of MIL-frameworks. They show that two MOFs, including MIL-53(Al, Cr) and MIL-47(V), maintain their methane adsorption properties after H₂S treatment, whereas MIL-100 and MIL-101 show significant decreases in their CH₄ adsorption capacities.²²⁹

Considering our limited ability to tune the pore size, pore shape, and surface functionality of activated carbons and zeolites, it is expected that only minor improvements can be made regarding their efficiency of the separation could be realized. Indeed, MOFs already offer record-breaking capacity for CO₂ adsorption in the pressure regime of interest

for pre-combustion capture.^{74, 93, 230-232} To date, the highest high pressure carbon dioxide adsorption belongs to NU-11 with the absolute uptake of 856 cm³ per gram of MOF at 30 bar and 25 °C. Further, the facile structural tunability of MOFs can allow significant improvements in binding strength of CO₂ and hence the selectivity of CO₂ over H₂. Last, their unprecedented

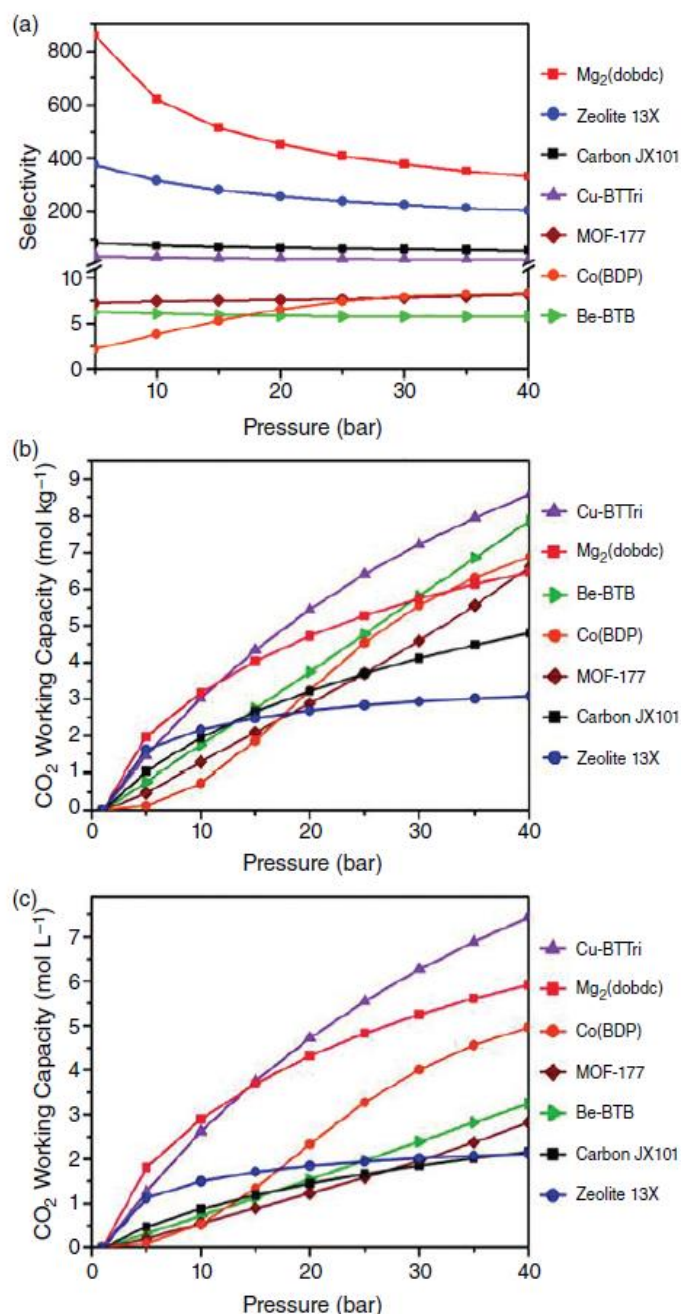


Figure 1-23 IAST-calculated (a) selectivity and (b) gravimetric and (c) volumetric CO₂ working capacities for an 80:20 H₂/CO₂ mixture at 40 °C for the metal-organic frameworks MOF-177, Be-BTB, Co(BDP), Cu-BTTri, and Mg₂(dobdc), the activated Carbon JX101 and zeolite 13X. This image is reproduced from reference⁸⁸ with permission from the American Chemical Society.

internal surface areas, a factor of strong importance for high-pressure separations, offer significant promise with regard to this separation.^{77, 233-237}

1.4.3 Potential MOF candidates for CO₂/H₂ separations

To date, while there are a number of studies looking at high-pressure CO₂ adsorption (up to 50 bar) in MOFs, there are very few studies focused specifically on assessing their properties for hydrogen purification or pre-combustion capture. Currently more work is needed to assess the properties of existing frameworks and in turn gain more insight into the structural features that give rise to enhanced separation ability of CO₂/H₂ in MOFs. For the most part, current CO₂/H₂ studies are limited to a few frameworks and are based on the use of single component CO₂ and H₂ adsorption isotherms to estimate the separation ability of the MOFs in question.

The first experimental study of MOFs for CO₂:H₂ separations by PSA was carried out by Herm *et al.* This work features single component adsorption isotherms for a series of 5 MOFs, which are further compared to state of the art separation materials including zeolite 13X and activated carbon JX101.⁷⁷ The MOF series was comprised of two with OMCs yet modest surface areas, including Mg₂(dobdc) (1800 m²/g)⁶² and Cu-BTTri (1750 m²/g),¹³⁹ two frameworks with high surface areas yet no polarizing functionality, including MOF-177 (4690 m²/g)²³² and Be-BTB (4400 m²/g, BTB = benzene-1,3,5 tribenzoate),⁴² and one flexible framework, Co-BDP (2030 m²/g, BDP = 1,4benzenedipyrozoate).²³⁸ Single component adsorption isotherms were collected for H₂ and CO₂ at pressures up to 40 bar and 40 °C and then IAST was used to estimate the materials behaviors in a binary mixtures of 80:20 or 60:40 H₂:CO₂. It was revealed that the materials with highly polarizing functionality on their internal surface such as the OMC-containing MOFs and zeolite 13X yielded much higher selectivities, between 75 and 859. This was also true of the carbon and was rationalized based on the small pores and overlapping van der Waals potential. Although, the MOFs with high surface areas and no polarizing functionality show appreciable CO₂ uptake at high pressures compared to the other materials assessed, they have shown inadequate selectivities significantly less than 10 (Figure 1-23a) limiting their performance in an actual separation process. In addition to selectivities, the gravimetric and volumetric working capacities were also estimated from IAST (Figure 1-23 b,c). Further, if we only consider the MOF with the highest selectivity, Mg₂(dobdc), the gravimetric and volumetric working capacities climb to 6.4 and 5.9 mmol CO₂ per gram of MOF, respectively. It is suggested that if the separations are carried out in the high pressure regime with Mg₂(dobdc) replacing zeolite 13X, then the mass and volume of the required adsorbent would be decreased by a factor of 2 and 2.7, respectively. From this study it shows that while materials with high surface areas can have high adsorption capacities, adsorbents with polarizing functional groups lend to higher CO₂:H₂ selectivities and enhanced performance with regard to working capacity. This study is further the proof of the concept that MOFs can indeed potentially outperform the state of the art materials.⁷⁷

In light of the previous work, Vaidhyanathan *et al* began working with small framework ligands for the synthesis of ultramicroporous MOFs.²³⁷ They were inspired by the knowledge that OMCs are susceptible to poisoning by even trace amounts of water. As such, they began to look at a small pore material without OMCs, Ni-(4-pyridylcarboxylate)₂ (Figure 1-24a) that might lend to overlapping van der Waals potential and hence high selectivities as in the case of the aforementioned carbon. This Ni-MOF exhibits a cubic framework with ultramicropores ranging from 3.5 to 4.8 Å, labeled as I – IV in Figure 1-24a. High pressure adsorption isotherms, collected up to 10 bar at 40 °C, were used to calculate the IAST selectivities and capacities for a 1 to 10 bar PSA process. The results show that the selectivities of the material is 285 and 230 for 20:80 and 40:60 CO₂:H₂ mixtures, respectively, and despite a modest surface area (945 m²/g) that the gravimetric capacity is relatively high, 3.95 mmol

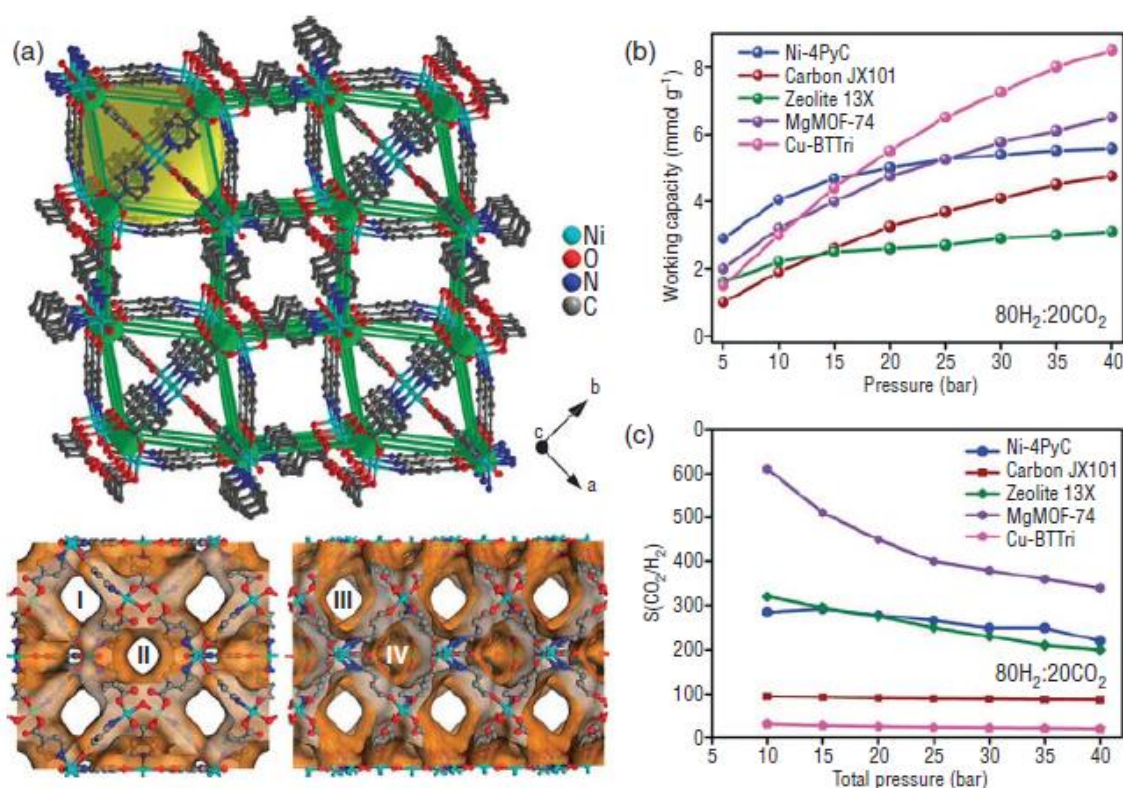


Figure 1-24 Structure of Ni-(4-pyridylcarboxylate)₂ obtained from single-crystal x-ray structure green, Ni dimers reduced to one node. The green cones trace the six-connected distorted cubic arrangement formed by collapsing the Ni dimers to nodes and the PyC linkers as lines. The yellow ball represents the cages in the structure. Below the structure is the Connolly surface diagram. The channels labeled I and III are interconnected and run along the *a* and *c* axes, respectively, whereas the channel labeled II propagate along the *c* axis. IV represents the cages, which are lined with terminal water molecules in addition to the ligand groups. (b) IAST working capacities and (c) selectivity characteristics. from an 20:80 mixture of CO₂:H₂ at 40 °C for a 1 to 10 bar PSA process. Comparison of the H₂/CO₂ selectivity of Ni-(4-pyridylcarboxylate)₂ is compared to other known MOFs and industrial sorbents determined under the same conditions. Data for activated carbon JX101, zeolite 13X, MgMOF-74, and Cu-BTTri are taken from the study of Herm *et al.* in reference.⁸⁸ This image is reproduced from reference²⁴⁹ with permission from AAS.

per gram of MOF (Figure 1-24b). While the selectivities are lower than $\text{Mg}_2(\text{dobdc})$, they are similar to those observed for zeolite 13X. Further, the gravimetric working capacity bests all materials analyzed by Herm *et al* (at 10 bar) and more importantly $\text{Ni}-(4\text{-pyridylcarboxylate})_2$ is shown to retain its CO_2 adsorption properties after exposure to H_2O . Last, the CO_2 self-diffusivities ($3 \times 10^{-9} \text{ m}^2 / \text{s}$) were determined to be as much as 2 times higher than zeolite 13X and comparable to the top performing CO_2 adsorbing MOFs.²³⁷

Other experimental studies have included one by Chen *et al* that form a NbO type MOF referred to as UTSA-40 ($1630 \text{ m}^2/\text{g}$, also known as $[\text{Cu}_2(\text{L})(\text{H}_2\text{O})_2] \cdot 6\text{DMF} \cdot 2\text{H}_2\text{O}$ where $\text{L} = 6,6\text{-Dichloro-2,2-diethoxy-1,1'-binaphthyl-4,4-di(5-isophthalic acid)}$) that consists of a tetracarboxylate ligand and dicopper paddlewheel cluster. The authors found that the material outperforms several traditional zeolites, and while the performance is lower than two OMC-containing MOFs, including $\text{Mg}_2(\text{dobdc})$ ⁶² and Cu-TDPAT ¹³⁶, this framework has a significantly lower energy cost for regeneration.²²⁵

One weakness in many of the aforementioned studies is the lack of assessment of the materials performance in the presence of other impurities in the flue gas stream such as H_2O , H_2S , CO , and CH_4 (the latter in the case of methane reforming). The adsorption behavior of each impurity can vary widely in MOFs as it is dictated by the pore size, shape, and surface functionalization. It is expected for instance that H_2O , H_2S , and/or CO could poison the OMCs and block the adsorption of CO_2 . While most of the water could be removed by condensation or other adsorbents placed in route to the fixed bed intended for CO_2/H_2 separation, it is likely that all of these impurities cannot be removed from the flue gas stream. As such, a more thorough assessment of materials performance in multicomponent streams is needed. Ideally a study would include both the adsorption properties in the multicomponent gas stream containing all potential impurities. The best way to test these properties is *via* experimental or simulated breakthrough curves. Because experimental breakthrough analysis containing very minor impurities or mixtures of more than 2 or 3 components can be extremely time consuming or in some cases experimentally intractable, Krishna *et al.* have used computational methods to simulate breakthrough curves for a number of MOFs, zeolites, and carbons in the tertiary mixture, $\text{CO}_2/\text{CH}_4/\text{H}_2$, and their binary combinations.²³⁹ Their study revealed the utility of breakthrough simulations for MOFs and further implied that $\text{Mg}_2(\text{dobdc})$ was the top performer of the materials tested under dry conditions. As such, this work was followed by an experimental one of Herm *et al* for validation of the computational methods.²⁴⁰ For this, breakthrough curves were generated for $\text{Mg}_2(\text{dobdc})$ in several multicomponent streams including CO_2/CH_4 , CH_4/H_2 , and $\text{CO}_2/\text{CH}_4/\text{H}_2$.²⁴⁰ The experiment not only validated the aforementioned simulations, but also showed that this MOF additionally outperformed zeolite 13X for all three-gas mixtures. Later, Wu *et al* simulated several MOFs and zeolites in quaternary mixtures including $\text{CO}_2/\text{CO}/\text{CH}_4/\text{H}_2$ and identified a new pre-combustion capture candidate, Cu-TDPAT ²⁴¹ and then Banu *et al* carried out simulations for a quinary mixture including $\text{CO}_2/\text{CO}/\text{CH}_4/\text{H}_2/\text{N}_2$ for a series of four Zr-containing MOFs.²⁴²

The results of these studies suggest that MOFs with small pores and open metal-sites, or other sources of charged functionality could be used to achieve both high selectivity and working capacity necessary to improve the efficiency of the CO₂:H₂ separation. However, considering the few number of data points, more work is needed to screen a large number of existing MOFs with varying structural features to gain more clarity related to their structure-derived function. Studies of this kind will provide insight into how to find the intricate balance between strength of CO₂ adsorption and high working capacity. Additionally, while it is clear that MOFs have a high potential to outperform the state of the art zeolites or activated carbons, more understanding of MOF properties in flue gas mixtures containing minor impurities must be obtained.

1.5 MOFs for Oxy-fuel combustion capture

1.5.1 *Necessary framework properties for O₂/N₂ separations*

The implementation of oxy-fuel combustion in the power industry is limited by an adequate, low-cost gas separation technology for the separation of O₂ from air. Currently air purification, which predominately involves the separation of O₂ from N₂, is most widely carried out *via* cryogenic distillation; while it provides high purity O₂ (99%), due to very low boiling points of O₂ and N₂ (-196 and -183 °C for N₂ and O₂, respectively), it also poses a large energy and economic cost for execution on the scale that is necessary for CCS. As such, other technologies have been studied; these included various adsorbents like zeolites and activated carbons and membrane-based separations. All of these aforementioned technologies can be implemented, they are limited to processes that can utilize O₂ at a purity level that is less than 94%, a direct result of limited selectivity for N₂ over O₂.⁶² The development of adsorbent materials that exhibit higher selectivities (lending to O₂ purity levels > 95%) and are also operational at ambient temperature and pressure could afford significant energy savings. Compared to post-combustion and pre-combustion technologies, the capture step for an oxy-fuel process is relatively easy using existing condensation protocol to isolate CO₂ (55 to 65 wt%) from water (25 to 35 wt%) after the combustion process.²⁴³ As such, existing power plants could be easily retrofitted to accommodate this process, which has shown capture rates of CO₂ on the order 95%, a value significantly higher than pre- or post-combustion capture technologies.²⁴⁴ In addition to easy implementation, the O₂ stream used for combustion in an oxy-fuel process is first diluted with CO₂ to a partial pressure of approximately 0.21 bar to control the flame temperature, an act that limits the formation of NO_x impurities.²⁴⁵

The most difficult part of the oxy-fuel process is generating large quantities of nearly pure O_2 ²⁴⁶ from air whose main component is N_2 . As such separation materials must show high selectivities and capacities for O_2 in the pressure and temperature regime of interest, which is approximately 0.2 bar and 25 °C. The modularity of MOFs makes them ideal candidates for this separation; however, compared to CO_2 and N_2 discussed in the previous section, O_2 and N_2 have even smaller disparities in their physical properties including kinetic diameter, quadrupole moment, polarizability, and boiling point creating a challenge for the design of adsorbents. Looking at Table 1-2, the polarizability and quadrupole moment of N_2 is slightly higher than O_2 making most framework materials like MOFs and zeolites with highly

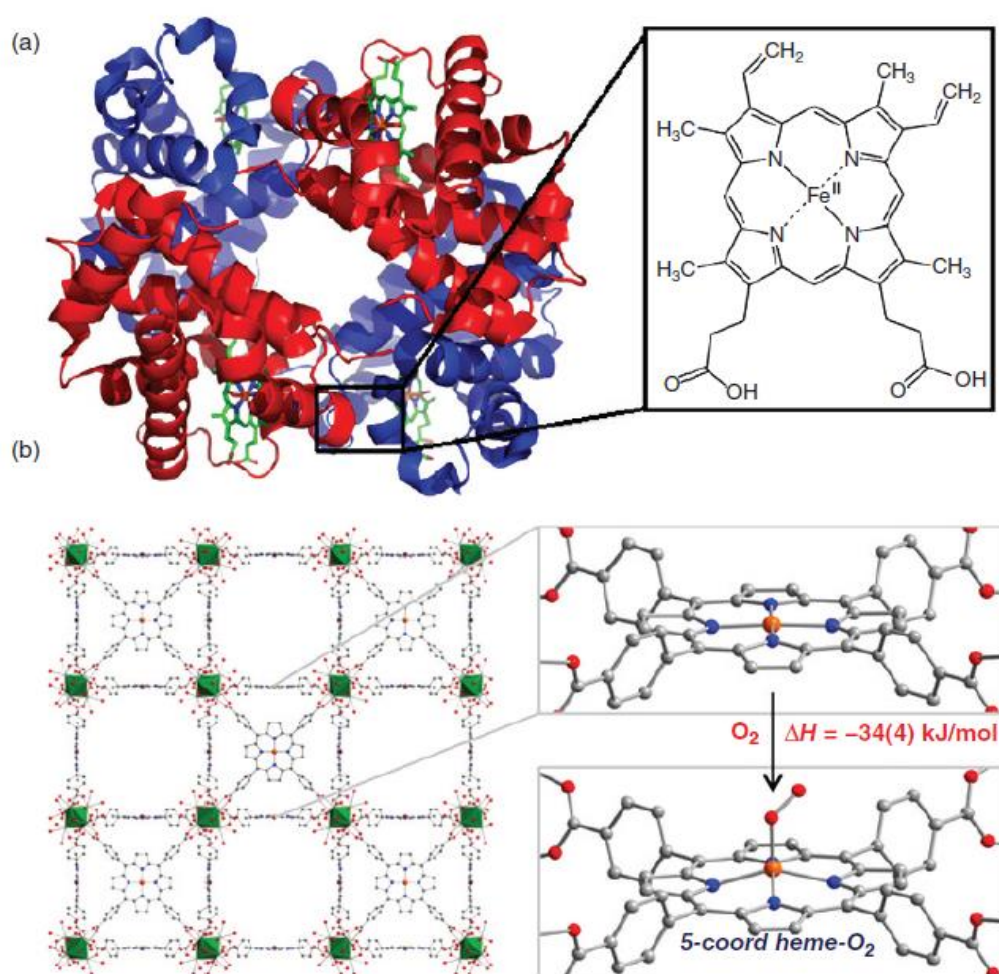


Figure 1-25 (a) Heme-based metaloprotein and (b) PCN-224-Fe (left), which forms PCN-224-Fe- O_2 at -78 °C (right). The structure consists of Zr_6 clusters interlinked by TCPP ligands (where TCPP = tetrakis(4-carboxyphenyl)porphyrin). Green octahedra represent Zr atoms; Fe, N, O, and C atoms are represented by orange, blue, red, and gray spheres, respectively. The distances and angles for PCN-224-Fe- O_2 are Fe-O 1.79(1), O-O 1.15(4), Fe...N4 plane 0.526(2), Fe-O-O 118(4), N-Fe-O 104(1). Image is reproduced from reference²⁶¹ with permission from the American Chemical Society.

polarizing adsorption sites only slightly more selective for N_2 over O_2 . This will cause the selectivities and hence resulting O_2 purity to be quite low. As such, recent efforts in MOF chemistry are instead focused on the differences in the chemical properties of O_2 and N_2 . Of these two small molecules, O_2 exhibits a significantly higher electron affinity than N_2 making redox active MOFs that might give rise to a reversible electron transfer to O_2 of great interest for oxy-fuel combustion.

1.5.2 Biological inspiration for O_2/N_2 separations in MOFs

Knowledge of the reactivity of O_2 with transition metal complexes is not new as this property is exploited in heme containing metalloproteins that are responsible for transport and storage of O_2 in mammalian systems. Heme species, also known as porphyrins, are a group of heterocycles composed of four modified pyrrole subunits with Fe^{2+} bound in the center (Figure 1-25a). Much research has been dedicated to producing synthetic molecular complexes that can mimic the reversible O_2 binding observed in nature;⁶² however, these molecular species have a strong propensity to react and combine upon formation of the metal- O_2 complex making them highly difficult to isolate.²⁴⁷ The instability of the mononuclear species has prompted the development of porphyrin-based supports that provide isolation of the reactive species to inhibit their decomposition and allow experimental observation of the porphyrin- O_2 adduct.²⁹ While observation of this species has been limited to spectroscopic evidence at low temperature, recent work of Harris *et al.* used a heme based Zr-MOF, PCN-224²⁴⁸, to give the first crystallographic evidence of a 5-coordinate heme- O_2 adduct (Figure 1-25b).²⁴⁹ Relative to their molecular counterparts, MOFs contain immobilized, separated active

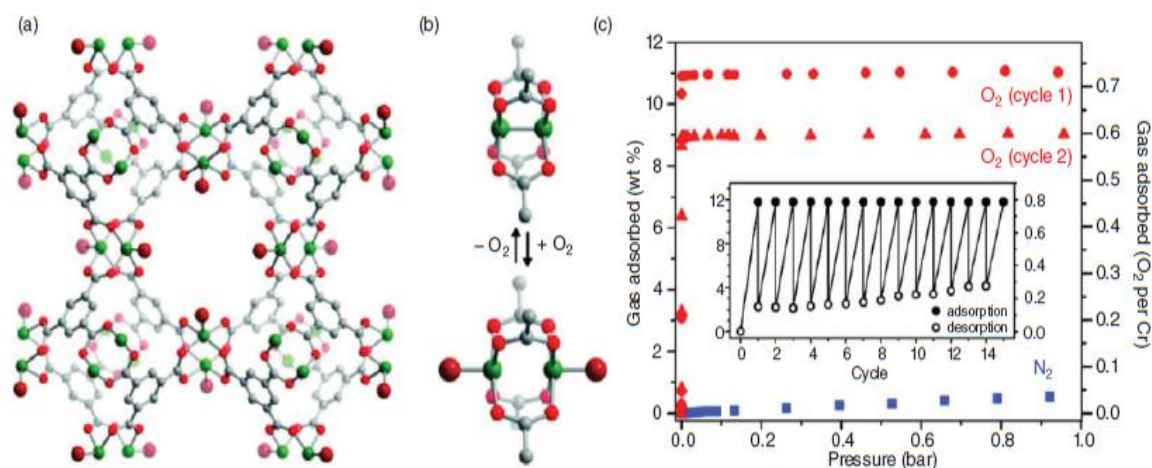


Figure 1-26 (a) Ball and stick model of O_2 adsorbed $\text{Cr}_3(\text{BTC})_2$ and (b) close-up view of the activated and O_2 adsorbed Cr-paddlewheel where the large red spheres represent bound O_2 molecules. The structures were obtained from Rietveld refinement of powder neutron diffraction data. (c) Uptake of O_2 and N_2 by $\text{Cr}_3(\text{BTC})_2$ at 298 K. The compound saturates with O_2 at ~ 2 mbar but shows little affinity for N_2 . Upon evacuation, the O_2 isotherms reveal reduced capacity. The inset shows O_2 adsorption in $\text{Cr}_3(\text{BTC})_2$ over 15 consecutive cycles at 25 °C. Desorption was carried out by heating at 50 °C under vacuum for 48 h. Image is reproduced from reference²⁰³ with permission from the American Chemical Society.

sites and offer facile structural tunability allowing control over important metrics such as O_2 binding enthalpy and as such adsorption capacity and regeneration conditions. Further, given their highly crystalline nature, crystallography techniques can be used to further unveil their structure-derived function. As such, MOFs provide an ideal platform to study O_2 adsorption and separation.

1.5.3 Potential MOF candidates for O_2/N_2 separations

While studies related to O_2 adsorption are still limited, over the last few years there have been several reports that show O_2 adsorption in redox active OMC-containing MOFs. These materials are thus far limited to a few SBUs constructed by metals such as Cr^{2+} , Fe^{2+} , and Ti^{3+} , all of which have a propensity to undergo redox activity in the presence of oxygen. One of the first studies of O_2/N_2 adsorption in a redox active MOF was carried out on $Cr_3(BTC)_2$ ($BTC^{3-} = 1,3,5$ benzenetri-carboxylate) (Figure 1-26a, b).¹⁹¹ The material, which is isostructural the aforementioned HKUST-1 and has a BET surface area of $1810\text{ m}^2/\text{g}$, displayed both a high O_2 loading capacity and high selectivity, ≈ 22 , for binding O_2 ($0.73\text{ mmol/g } O_2$ at 0.21 bar) over N_2 ($0.033\text{ mmol/g } N_2$ at 0.78 bar) at $25\text{ }^\circ\text{C}$; however, the material showed a significant loss in capacity with cycling (Figure 1-26c).¹⁹¹

More recently, these authors studied O_2 and N_2 adsorption in a redox active $Fe_2(dobdc)^{72}$ (Figure 1-27a), which has a BET surface area of $1360\text{ m}^2/\text{g}$ and features a hexagonal array of one dimensional channels lined with coordinatively unsaturated Fe^{2+} OMCs. Single component gas adsorption isotherms collected at 298 K indicate that this framework binds O_2 preferentially over N_2 (Figure 1-27c); however there is an irreversible capacity of 9.3 wt\% , corresponding to the adsorption of $0.5\text{ } O_2$ molecule per Fe^{2+} -OMC. Upon cooling the material to 211 K , O_2 uptake becomes fully reversible and the capacity increases to 18.2 wt\% , a value that corresponds to the adsorption of one O_2 molecule per Fe^{2+} -OMC. Several techniques, including Mössbauer spectroscopy, infrared spectroscopy, and neutron powder diffraction were used to investigate this crossover from the physisorption (211 K) to the chemisorption regime where O_2 adsorption becomes irreversible. All characterization pointed to a partial charge transfer from Fe^{2+} to O_2 at low temperature and a complete charge transfer to form Fe^{3+} and O_2^{2-} at room temperature. Rietveld analyses of powder neutron diffraction data confirms this interpretation, revealing O_2 bound to Fe in a symmetric side-on configuration with an O–O distance of $1.25(1)\text{ \AA}$ at low temperature, labeled as site I in Figure 1-27b. This value is only slightly elongated compared to the distance found in a free O_2 species ($1.2071(1)\text{ \AA}$).²⁵⁰ Neutron diffraction carried out after the exposure of $Fe_2(dobdc)$ to O_2 at room-temperature reveals a different structure with the O_2 species is in a slipped side-on mode with O–O distance of $1.6(1)\text{ \AA}$ (Figure 1-27b), a value that is consistent with a two electron reduction of O_2 to a peroxide species. These measurements were also unveiled two secondary adsorption sites at low temperatures labeled as II and III in Figure 1-27a. Simulated breakthrough curves, which were calculated *via* single-component gas adsorption isotherms and IAST indicate that the material should be capable of the high-capacity separation of O_2

from air at temperatures as high as 226 K, well above the current temperatures employed in cryogenic distillation.⁷²

$\text{Cr}_3(\text{BTC})_2$ and $\text{Fe}_2(\text{dobdc})$, are representative members of large isostructural framework families that have been synthesized with a wide number of transition metal cations ($\text{M}_3(\text{btc})_2$ where $\text{M} = \text{Cr, Fe, Ni, Cu, Zn, Mo, or Ru}$ ¹⁸⁹⁻¹⁹⁴ and $\text{M}_2(\text{dobdc})$ where $\text{M} = \text{Mg, Mn, Fe, Co, Ni, Cu, or Zn}$.^{87, 93, 100-101, 123, 182-184}). Despite this, no other materials in the framework families have shown utility in the separation of O_2 from N_2 . As such, recent work of Bloch *et al.* have explored a new framework family known as M-BTT with the sodalite type structure, $\text{M}_3[(\text{M}_4\text{Cl})_3(\text{BTT})_8]_2$. While the aforementioned MOF family has also been synthesized with a variety of M^{2+} OMCs (M-BTT here $\text{M} = \text{Mn, Fe, Co, Cu, Cd}$); only the most recently synthesized Cr^{2+} analog (with a BET surface area of $2300 \text{ m}^2/\text{g}$) shows utility in O_2/N_2 separations (Figure 1-28a).¹²¹ The single component adsorption isotherms indicated a high selectivity for O_2 over N_2 as the material has a reasonably high O_2 uptake of 7.01 wt% at 0.2 bar and 298 K and a low adsorption capacity for N_2 , which is less than 0.6 wt% at 0.8 bar and 298 K (Figure 1-28b). Consistent with the significantly higher O_2 capacity compared to N_2 , the material exhibits an isosteric heat of -65 kJ/mol and -15.3 kJ/mol for O_2 and N_2 , respectively. IAST calculations reveal that the material has a selectivity factor greater than 2500 under conditions necessary for O_2 separation from air. As shown in Figure 1-28b, Cr-BTT displays only a moderate capacity loss after the first adsorption/ desorption cycle, with a decreased uptake from 7.01 wt% to 5.6 wt%. After the second cycle the capacity drops a bit further to 4.6 wt% but then

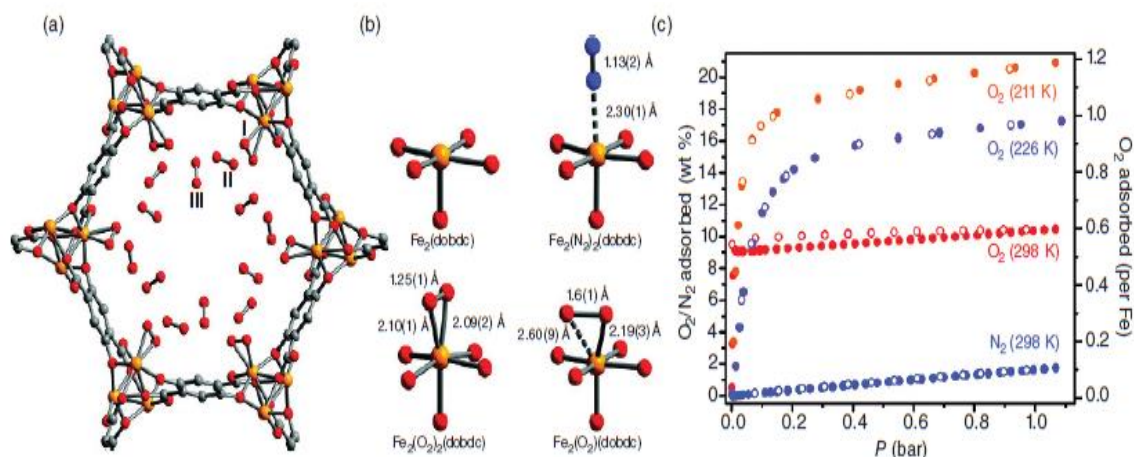


Figure 1-27 Ball and stick model showing the partial structure of O_2 adsorbed in $\text{Fe}_2(\text{dobdc})$ with 3 O_2 adsorption sites, labeled as I-III. Site I is bound in a side-on fashion at the Fe-OMC. (b) shows a close-up view of the Fe-OMC after activation and then after dosing with N_2 and O_2 . The structures are for samples under vacuum (upper left), dosed with N_2 at 100 K (upper right), dosed with O_2 at 100 K (lower left), and dosed with O_2 at 298 K (lower right). All structures were determined *via* Rietveld analysis of neutron powder diffraction data. Orange, blue, and red spheres represent Fe, N, and O atoms, respectively. All diffraction data were collected below 10 K. (c) Adsorption isotherms collected for $\text{Fe}_2(\text{dobdc})$ at 211 (orange), 226 (purple), 298 K (red) and N_2 adsorption at 298 K (blue). Filled and open circles represent adsorption and desorption, respectively. Image is reproduced from reference⁸² with permission from the American Chemical Society.

appears to plateau for the next 13 consecutive cycles. Despite this slight loss in capacity, the material shows rapid adsorption/desorption and a reversible capacity of 4.6 wt%. While the capacity loss is not yet fully understood, several *in-situ* techniques were employed to understand O₂ binding mechanism. Infrared spectroscopy and neutron diffraction were again used to show experimental evidence of the electron transfer to form a Cr³⁺ superoxide species. The diffraction data is consistent with what was observed in the IR spectrum, showing an end-on coordination of the guest species and a Cr–O₂ distance of 1.84(2) Å, a value that is in excellent agreement with other previously reported Cr³⁺–superoxo species (1.876(4) Å).²⁵¹ As observed in the case of Fe₂(dobdc), the O–O distance is slightly elongated to 1.26(2) compared to free O₂, consistent with the formation of a superoxide. Further, Cr–N and Cr–Cl distances decrease from 2.064(3) Å and 2.57(2) Å to 2.026(4) Å and 2.52(2) Å, upon oxidation from Cr²⁺ to Cr³⁺, respectively.¹²¹

All of the aforementioned work demonstrates the importance of having redox active OMCs in MOFs for selective separations of O₂ over N₂. While this work is dependent on existing framework families that can undergo metal substitution, there is a lot of room for further MOF development for air purification through the use of (i) metaloligands, which may offer a way to post-synthetically decorate MOF surfaces with under coordinated metals or (ii) through the infusion or appendage of other metal-containing small molecules on the internal surface of MOFs. A proof of concept for redox active MOF-composites was highlighted by Zhang *et al.*, which infused a well-known Cr-MIL-101 with the redox active Fe²⁺ containing ferrocene molecule.²⁵² Heating the material above 350 °C led to a transformation of the ferrocene into maghemite nanoparticles rendering a composite MOF materials that exhibited a high selectivity for O₂ over N₂. Experimental breakthrough obtained using a custom-built apparatus equipped with a residual gas analyzer (in a gas mixture of 0.21% O₂ and 0.79% N₂) showed N₂ breakthrough within a minute, while O₂ required 40 minutes. At any rate, MOFs offer an unprecedented opportunity to tailor make materials with controlled capacities, selectivities, and regeneration energies.²⁵²

1.6 Future perspectives and outlook

The previous sections have highlighted some of the recent progress made in the advancement of MOFs towards carbon captures applications. While we have confirmed that there are a number of frameworks currently available for the efficient separation of CO₂/N₂, O₂/N₂, and CO₂/H₂, there are still a number of factors that need to be addressed for their eventual implementation. More understanding of how MOF materials function in wet environments and in the presence of other minor impurities present in gas streams is a necessity. To achieve this, it will require experimentalists to characterize the materials in more application relevant environments as in multicomponent adsorption and breakthrough analysis. Further, on-going work should pay more attention to the temperatures and pressures necessary for the varying applications as these two factors vary a great deal throughout the literature, making it difficult on some occasions to gain an accurate comparison between two differing materials. Also, there are a number of reports that show disparities in measured

values for various properties ranging from surface areas, adsorption capacities, selectivities, and isosteric heats. As such, more emphasis should be placed on sample quality and efforts should be made to understand how varying reaction conditions affect the crystallization and hence subsequent framework properties.

Once the more fundamental problems are addressed it is expected that MOF chemistry will naturally gravitate away from the synthesis of new materials and look towards addressing more engineering related issues. Some of these areas include: (i) material scale-up and cost

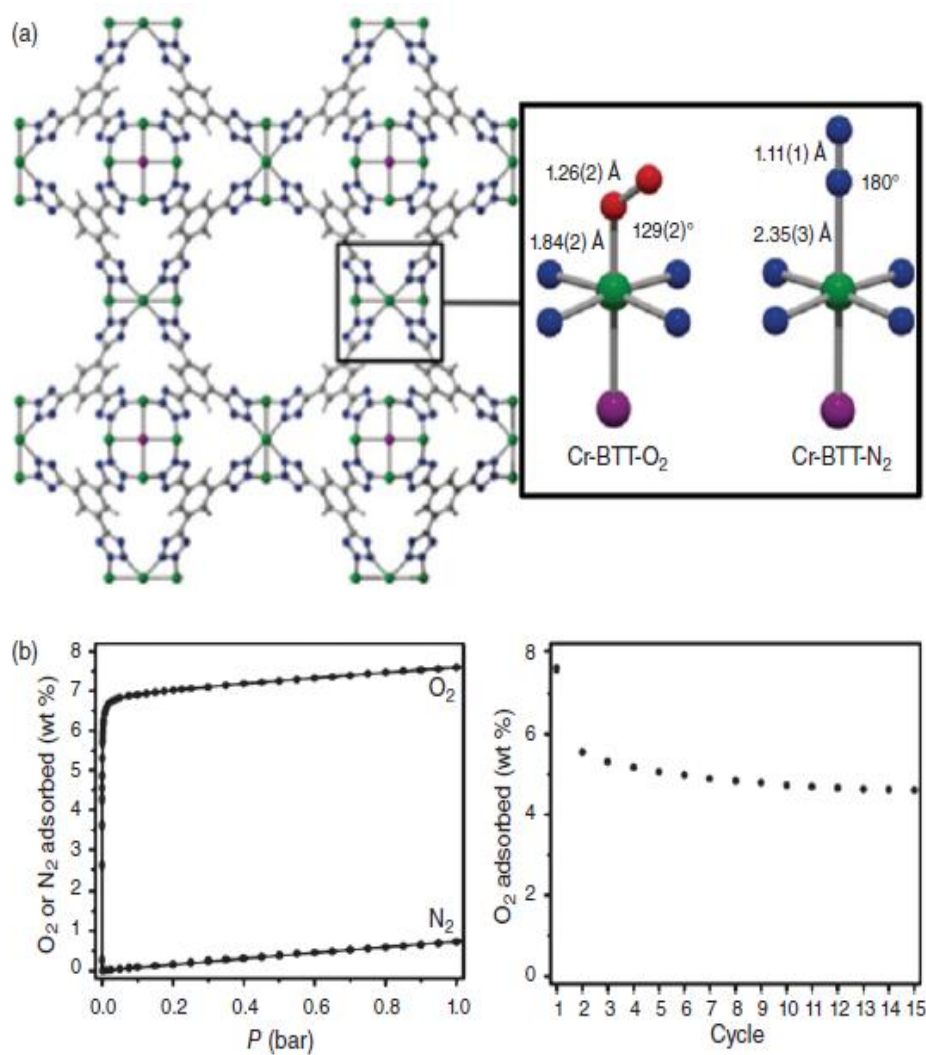


Figure 1-28 (a) ball and stick model of Cr-BTT and the first coordination spheres for the Cr centers within O₂- and N₂-dosed Cr-BTT as determined from Rietveld analysis of powder neutron diffraction data. Atom colors: Cr dark green, Cl purple, O red, N blue. Values in parenthesis give the estimated standard deviation in the final digit of the number. (b) Excess O₂ and N₂ adsorption isotherms collected for Cr-BTT at 298 K; the solid lines represent Langmuir–Freundlich fits to the data. Bottom: Uptake of O₂ at 200 mbar in Cr-BTT over 15 cycles at 298 K. Adsorption experiments were performed over 30 min and desorption was carried out by placing the sample under a dynamic vacuum at 423 K for 30 min. Image is reproduced from reference¹³³ with permission of WILEY-VCH Verlag GmbH & Co. KGaA, Weinheim.

analysis, (ii) nanostructuring materials for pelletization, (iii) the impact of pelletization on MOF performance, (iv) assessing their performance over many adsorption/desorption cycles, and (v) accurate determination of the energy penalty associated with MOF regeneration. While we know that the parasitic energy cost of liquid amine scrubbers is approximately 30%, to the best of our knowledge there are no thorough studies addressing the energy penalty and economic cost related to MOF adsorbents and so it is a necessity for the future. It is assumed throughout the literature that these materials will have better performance due to lower heats capacities, but a number of factors must be considered. For instance there is not a lot of information pertaining to MOF thermal conductivity,²⁵³ a parameter that dictates the efficiency of the adsorbent bed and the duration of the regeneration cycle of a TSA capture process. In the same regard, there are just a few studies addressing the desorption of CO₂ *via* PSA in any great detail either.

While it is not discussed to a large extent throughout this chapter, it should be noted that there are a number of developing computational tools that might allow accurate structure and property prediction in MOFs.²⁵⁴ Advancements in this area could provide experimentalists with target frameworks that will perform well in predefined gas mixtures and hence deliver these materials more rapidly to industry.²⁵⁵ Though progress has been made through cooperative work between theoreticians and experimentalists to understanding MOF–small molecule interactions, the rate at which theoretical tools are being actively used to provide optimized MOF targets remains slow. One challenge for instance is the difficulty of developing synthetic pathways toward a specific structure containing the desired building blocks or the inability to predict structural changes that occur with adsorption. While these challenges are large, the partnership between experimentalists and theoreticians is becoming more prevalent throughout the literature and hence significant progress has been made in the area.⁷³ As such, we are confident that computational tools, including high throughput screening methods, could push MOF chemistry past the era of largely serendipitous discoveries and allow for engineering porous media for solving specific problems.

Given the huge scientific progress made in the last 10 years within MOF research, we have an optimistic outlook on MOF chemistry for their eventual implementation in a wide number of energetically relevant gas separations. Unprecedented internal surface areas, facile structural tunability, and the ease with which MOFs readily undergo post-synthetic modification, clearly distinguishes this class of materials from other porous counterparts. It is demonstrated throughout the literature that MOFs offer a unique opportunity for controlled design, allowing one to find the intricate balance necessary between a variety of properties such as selectivity, gravimetric and volumetric working capacity, regeneration energy, and framework stability, making them likely candidates for future carbon capture technologies.

Chapter 2

An experimental and computational study of CO₂ adsorption in the sodalite-type M-BTT (M = Cr, Mn, Fe, Cu) metal–organic frameworks featuring open metal sites²

2.1 Introduction

Rising levels of atmospheric CO₂ are heavily implicated in global warming and predominantly result from the combustion of carbon-based fuels, which has steadily increased since the industrial revolution.²⁵⁶ Carbon dioxide levels recently surpassed an alarming level of 400 ppm,²⁵⁷ and given the expectation that the transition to clean, renewable energies will continue to progress slowly,²⁰ the quest for new carbon capture technologies has moved to the forefront of scientific research.²⁵⁸ At present, widespread implementation of the most prominent capture technology, namely liquid amine-based scrubbers, is limited by the high regeneration energies associated with using these materials in a post-combustion CO₂ capture process. It has been alternatively proposed that solid adsorbents, which exhibit both lower heat capacities and heats of adsorption, could reduce this parasitic energy cost considerably by requiring far less heat for regeneration.^{62, 259}

Metal–organic frameworks are a broad class of solid adsorbents consisting of metal ions linked by organic ligands to form porous, crystalline arrays, and are being intensively

² This chapter is based on the published article: Asgari, M., Jawahery, S., Bloch, E.D., Hudson, M.R., Flacau, R., Vlaisavljevich, B., Long, J.R., Brown, C.M. and Queen, W.L. "An experimental and computational study of CO₂ adsorption in the sodalite-type M-BTT (M= Cr, Mn, Fe, Cu) metal–organic frameworks featuring open metal sites." *Chemical science* 9.20 (2018): 4579-4588. M. A. has analyzed the data and has written the paper.

investigated for various energy-relevant applications, including gas storage, gas separation, and catalysis. These materials possess significant advantages over other solid adsorbents, including unprecedented internal surface areas, impressive structural diversity, and facile chemical tunability. Given the numerous permutations of potential linker and metal combinations, a vast number of frameworks are accessible in principle; however, to identify and better tune the properties of any framework for a target application, such as CO₂ capture, it is essential to first understand structure-derived function. One powerful approach is the study of isostructural families of frameworks differing only in the identity of the metal ion.^{194, 260-261} For example, we have previously shown that a combined experimental and theoretical approach can afford important insights into the factors influencing CO₂ adsorption in the M₂(dobdc) (M = Mg, Mn, Fe, Co, Ni, Cu, Zn; dobdc⁴⁻ = 2,5-dioxido-1,4 benzenedicarboxylate) series of frameworks.²⁶² However, a lingering practical challenge to conduction of such structure-property relationship studies is the need for reliable experimental adsorption and *in-situ* diffraction data for a group of isostructural frameworks, which is often not available for many frameworks of interest.

One such family is the sodalite-type series M-BTT (M = Cr, Mn, Fe, Co, Ni, Cu, Cd; BTT³⁻ = 1,3,5-benzenetristetrazolate),²⁶³⁻²⁶⁷ with a general formula of [(M₄Cl)₃(BTT)₈]³⁻. The framework crystallizes in the cubic *Pm*–*3m* spacegroup (no. 221) and features truncated, octahedral cages built up of six [M₄Cl]⁷⁺ units and eight [BTT]³⁻ ligands that are further interlinked to form an anionic, porous, three-dimensional network (Fig. 2-1). This material is somewhat unique among metal-organic frameworks in that it readily undergoes chemical substitution with a number of first row transition metals and has a high density of open metal sites that are accessible after heating the as-synthesized material under dynamic vacuum to remove coordinated solvent. These properties are exhibited by only a few other known framework families, namely M₂(dobdc)^{72, 87, 100, 182-184, 268-271}, M₂(dobpdc) (M = Mg, Mn, Fe, Co, Ni, Zn; dobpdc⁴⁻ = 4,4'-dioxidobiphenyl-3,3'-dicarboxylate),²⁷² M₂Cl₂(bbta) (H₂bbta = 1H,5H-benzo(1,2-d:4,5-d') bistriazole) and M₂Cl₂(btdd) (H₂btdd = bis(1H-1,2,3-triazolo[4,5-b],[4',5'-i])dibenzo[1,4]dioxin),²⁷³ M₂(*m*-dobdc) (M = Mg, Mn, Fe, Co, Ni; *m*-dobdc⁴⁻ = 4,6-dioxido-1,3-benzenedicarboxylate),²⁷⁴ and M₃(btc)₂ (M = Cr, Cu, Zn, Mo, Ru; btc³⁻ = 1,3,5-benzene tricarboxylate).^{192, 275-277}

The open metal sites of the M-BTT family have been shown previously to increase the surface packing density of hydrocarbon adsorbates,²⁷⁸ to exhibit strong and selective binding of framework guests,^{164, 265, 267, 279} and also to provide a pathway to achieve charge transfer between frameworks and guest species,²⁸⁰ a desirable property for using metal-organic frameworks for the conversion of small molecules into value-added chemicals.²⁸¹ Most relevant to this study, the open metal sites can improve CO₂ uptake at low-pressures, which is a property of interest for flue gas separations in post-combustion capture technologies.^{62, 282} The M-BTT family thus stands as an important system for experimental examination of the role of metal identity on CO₂ adsorption and subsequent identification and validation of computational tools useful in varying chemical environments.

Herein, we present a comprehensive experimental and computational investigation of CO₂ adsorption in M-BTT (M = Cr, Mn, Fe, Cu) analogs, using *in situ* powder neutron diffraction and DFT calculations in tandem. Powder neutron diffraction reveals for the first time a molecular level view of CO₂ adsorption in M-BTT and facilitates rationalization of experimental CO₂ adsorption isotherms. The experimentally obtained binding distances and enthalpies are further used to benchmark and evaluate the results of DFT calculations on M-BTT, as reported in this work and a previous study.¹⁶⁴ Ultimately, it is expected that the insights gained will inform how existing and hypothetical frameworks can be most efficiently screened for CO₂ adsorption applications.

2.2 Experimental section

2.2.1 Materials and methods

The Fe-BTT²⁶⁵ and Cu-BTT²⁶⁴ frameworks were synthesized as previously reported.

2.2.2 Synthesis

Cr-BTT: Anhydrous chromium(II) chloride (1.1 g, 9.0 mmol), 1,4-H₃BTT (0.71 g, 3.6 mmol), DMF (300 mL) and triflic acid (3.2 mL 3.6 mmol) were added to a 500-mL Schlenk flask. The reaction mixture was heated at 393 K and stirred for 72 h to afford a light brown precipitate. The solid was collected by filtration and washed with 100 mL of DMF to yield 2.0 g (91%) of Cr-BTT. A sample of this compound (1.9 g, 3.3 mmol) was soaked in 100 mL of DMF at 393 K for 24 h after which the solvent was decanted, and the solid was then soaked in 100 mL of methanol at 343 K for 24 h. The methanol exchange was repeated three times, and the solid was collected by filtration to yield 1.3 g (87%) of Cr-BTT·MeOH as a tan powder. A sample of this compound was fully desolvated by heating under dynamic vacuum (< 10 μbar) at 433 K for 24 h to yield Cr-BTT as a light tan powder.

Mn-BTT: The synthesis of Mn-BTT was carried out according to the previously published procedure, with slight modification.²⁶³ In order to produce large quantities of the material for neutron diffraction experiments, the synthesis was scaled to a 500-mL autoclave bottle. Additionally, in order to maximize surface area, solvent was removed by decanting rather than filtration prior to activation.

It is important to mention that the M-BTT compounds in activated form can sometimes detonate upon exposure to air. As such, these materials should be handled with caution and in small quantities.

2.2.3 Adsorption Measurements

Ultra-high purity-grade (99.999% purity) helium, nitrogen, and carbon dioxide were used for all gas adsorption isotherm measurements. Adsorption data were collected at pressures ranging from 0 to 1.1 bar using a commercial Micromeritics ASAP 2020.²⁸³ Samples were transferred under a N₂ atmosphere to preweighed analysis tubes that were capped with

a Transeal. The samples were first evacuated on the activation station until the outgas rate was less than 3 mbar per min. The evacuated analysis tubes and samples were then carefully transferred to an electronic balance and weighed to determine the mass of the sample (typically 100–200 mg) after activation. For cryogenic measurements, the tube was immersed in liquid N₂, covered with an isothermal jacket, and transferred back to the analysis port of the gas adsorption instrument. The outgas rate was again confirmed to be less than 3 mbar per min. Langmuir surface areas and pore volumes were determined from N₂ adsorption isotherms measured in a 77-K liquid N₂ bath, and were calculated using the Micromeritics software assuming a value of 16.2 Å² for the molecular cross-sectional area of N₂. For CO₂ adsorption measurements, data were collected at temperatures ranging from 25 to 45 °C using a Micromeritics recirculating dewar connected to a Julabo F32-MC isothermal bath.

2.2.4 Structural Analysis

High-resolution powder neutron diffraction experiments were carried out on M-BTT (M = Cr, Mn, Fe, Cu) using BT1 at the National Institute of Standards and Technology (NIST) Center for Neutron Research (NCNR). All measurements were carried out on activated samples of ~0.8 g. At NIST, samples were activated while heating under dynamic vacuum and then transferred into a He purged glove-box, loaded into a vanadium can equipped with a gas loading valve, and sealed using an indium O-ring. Powder neutron diffraction data were collected using a Ge(311) monochromator with an in-pile 60 collimator corresponding to a wavelength of 2.0780 Å. The samples were loaded onto a closed cycle refrigerator and then data were collected at 10 K. After data collection on the activated framework, CO₂ was then loaded into each framework by first warming the samples to room temperature and then exposing them to a pre-determined amount of gas. Upon reaching an equilibrium pressure at the loading temperature, the sample was then slowly cooled (at a rate of 1 K/min) to ensure complete adsorption of the CO₂, and data was then collected again at 10 K. It should be noted that the activation procedure for Mn-BTT was not successful in extracting all of the solvent molecules from the material. This is consistent with previous reports, which reveal that solvent remains coordinated to 83% of the open metal sites after activation.²⁶³ Considering the low occupancy of CO₂ at the Mn²⁺ sites and high occupancy of solvent, *in situ* experiments were not pursued for this sample.

Additional high-resolution neutron diffraction data were collected on the C2 diffractometer at Chalk River Laboratories at the Canadian Neutron Beam Center using a 1.2-g sample of Cr-BTT. The sample preparation and data collection of the bare and CO₂-loaded framework were carried out using procedures similar to those described above. A wavelength of 2.3704 Å was used to collect data from ~2.8° to 117° in 2θ. For this experiment, the gas loading apparatus designed for the top-loading, closed cycle refrigerator was not equipped with line heaters, and, because of this, cold zones caused the CO₂ to freeze in the gas line before complete adsorption could be achieved. As such, loadings higher than 0.5 CO₂ per Cr metal were not achieved and data were recollected at NIST. However, we note that results from the

refinements of the bare structure and low CO₂ loading are similar to those obtained at NIST (see Appendix, Table S2-7 and S2-8 and Fig. S2-22).

Powder neutron diffraction data were analyzed using the Rietveld method, as implemented in EXPGUI/GSAS.²⁸⁴⁻²⁸⁵ The M-BTT models were based on those previously determined,^{264-265, 267} with the scale-factor and unit cell allowed to vary. Fourier difference methods were employed to locate residual solvent, extra-framework cations, and the adsorbed CO₂ molecules in the structures of the activated bare materials.

X-ray diffraction data were also collected on Fe-BTT on 17-BM-B at the Advanced Photon Source at Argonne National Laboratory. The unactivated sample was loaded into a 1.0-mm borosilicate capillary that was then placed in a custom designed gas cell. The capillary was mounted onto the goniometer head at 17-BM and centered in the beam. The sample was then placed under dynamic vacuum, inserted in a N₂ stream that was slowly heated to 150 °C where it was held for 2 h. Post-activation, the sample was gradually cooled to room temperature and then dosed with a small amount of He exchange gas. The sample was then further cooled to 100 K at a rate of 2 K/min where it was held for 30 min prior to data measurement to allow for temperature equilibration. The data were collected using a Si (111) monochromator ($\lambda = 0.61072$ Å, $\Delta E/E = 1.5 \times 10^{-4}$). It should be noted that while efforts to activate the sample *in situ* succeeded in removing some of the methanol from the framework channels, they were unsuccessful at removing any of the methanol coordinated to the metal sites. Rietveld analysis was carried out on the data to elucidate the positions of extra-framework cations. Due to the inability to completely desolvate the framework at the synchrotron, data collection on the CO₂-adsorbed samples were not pursued.

2.2.5 Periodic Density Functional Theory Calculations

Periodic density functional theory (DFT) calculations were employed to compute first-principles CO₂ binding energies using the Vienna Ab initio Simulation Package (VASP).²⁸⁶ To correctly model noncovalent interactions between CO₂ and the framework, the dispersion corrected functional rev-vdW-DF2+U was employed.²⁸⁷⁻²⁸⁸ The Hubbard *U* parameter is needed to model valence *d* electrons during adsorption and has been shown to be particularly important for frameworks with open-metal sites.²⁸⁹⁻²⁹⁰ The Hubbard *U* values in this work were based on values determined for the M₂(dobdc) series: 6.1, 6.5, and 10.4 eV for Cr, Fe, and Cu, respectively.²⁹¹ Based on the results of Poloni *et al.*,¹⁶⁴ all metal centres are treated as high spin with antiferromagnetic ordering between metal centers. A plane wave basis set with a cutoff of 800 eV and PAW pseudopotentials were used.²⁹² Atomic positions and lattice constants were optimized for bare frameworks without CO₂ with forces on each atom converged to 2×10^{-2} eV/Å. The atomic positions and lattice constants of the bare frameworks were optimized starting from the experimentally refined structures, and extra-framework cations were incorporated in order to balance the anionic framework charge. For Cu-BTT, the DFT relaxation included the experimentally observed Cu⁺ extra-framework cation which has a Cl and water molecule coordinated to it (described below in more detail, shown in Figure 2-

3, and S2-23). For Cr-BTT and Fe-BTT, sodium cations were included in the tetrazolate cages, which corresponds more closely to their experimentally observed cation positions (shown in Figure S2-21). The placement of extra-framework cations in this work benefits from new diffraction data while previous studies by Poloni *et al.*^{164, 293} placed the sodium cations coordinated to nitrogen atoms on two adjacent tetrazole ligands. Geometry optimizations of the bare framework allowed for the relaxation of all atoms, both in the framework and extra-framework cations, and the lattice constants. After relaxing the framework structure, the positions of CO₂ molecules were relaxed starting from their positions in the experimental structure keeping the framework atoms fixed using the so-called rigid framework approximation. The CO₂ binding enthalpies were calculated using harmonic vibrational frequencies (obtained for CO₂ and the corresponding open metal site). Atomic positions for bound and unbound CO₂ were optimized at the same level of theory as the framework. Point charges were assigned to framework atoms using the REPEAT scheme and the electrostatic potential generated by DFT for use in our simulations.²⁹⁴

2.2.6 Grand Canonical Monte Carlo Simulations

Grand Canonical Monte Carlo (GCMC) simulations were performed using the RASPA molecular simulation software²⁹⁵ to compute room temperature CO₂ and 77-K N₂ isotherms. Total cycle numbers of 100,000 and 20,000 (evenly split between equilibrium and sampling cycles) were employed for the room temperature CO₂ isotherms and 77-K N₂ isotherms, respectively. Interactions between CO₂ molecules and between N₂ molecules were modelled with the TraPPE force field.²⁹⁶ Framework atoms were assigned interaction parameters using the Universal Force Field (UFF), and CO₂-framework interactions were determined using Lorentz-Berthelot mixing rules.²⁹⁷

2.3 Results and discussion

2.3.1 CO₂ adsorption properties

Low-pressure CO₂ adsorption isotherms were collected for M-BTT (M = Cr, Mn, Fe, Cu) at 298, 308, and 318 K. At 298 K and pressures below 0.1 bar, the isotherms exhibit a steep initial rise that is indicative of highly polarizing adsorption sites, a phenomenon often observed for frameworks with coordinatively-unsaturated metals.^{93, 136, 145, 262} The adsorption isotherm for Fe-BTT is the steepest of all the analogues, indicating a strong interaction with CO₂ at low surface coverage, which is an area of interest for post-combustion flue gas capture.

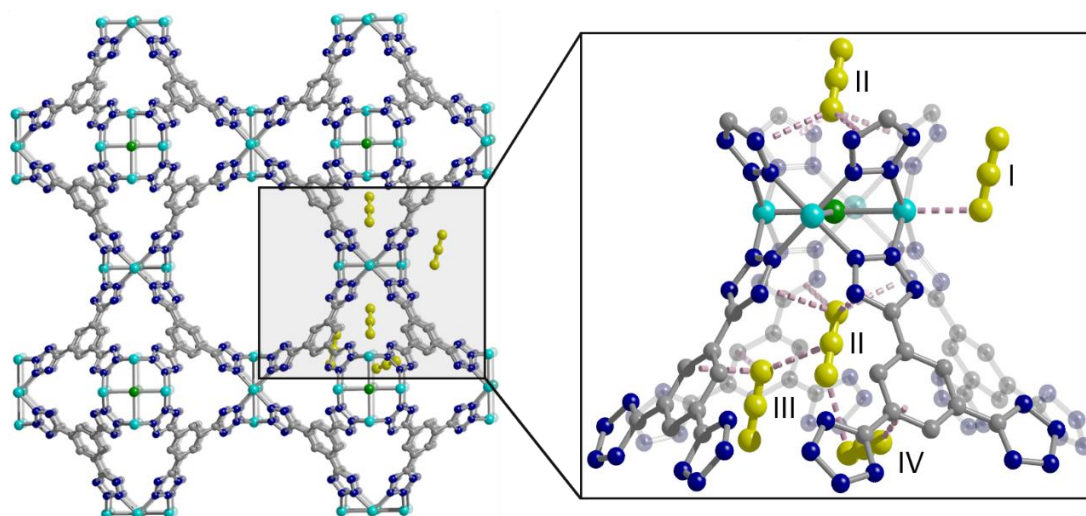


Figure 2-2 Structure of a portion of the Cu-BTT framework, as determined from Rietveld analysis of high-resolution powder neutron diffraction data (left), and an expanded view of the four different CO₂ adsorption sites within the framework (right). Cyan, grey, blue, and green spheres represent Cu, C, N, and Cl atoms, respectively, and yellow ball-and-stick models represent CO₂; H atoms and charge balancing cations are omitted for clarity. At site I, the Cu–O distance is 2.60(3) Å while other nearest-neighbour CO₂–framework and CO₂–CO₂ interactions are dominated by van der Waals forces and range approximately from 2.95 to 3.44 Å.

To gain a quantitative estimation of binding strength, we calculated isosteric heats (Q_{st}) of CO₂ adsorption, which afford a measure of the average binding energy at constant coverage and can be determined by fitting the adsorption isotherms with a dual-site Langmuir-Freundlich equation (Fig. S2-3 to S2-6). The calculated zero-coverage isosteric heats (Table 2-1) range from 30.7 kJ/mol to 51.2 kJ/mol with the trend Fe > Mn > Cr > Cu. Consistent with previous studies of the M₂(dobdc) (M = Mg, Mn, Fe, Co, Cu, Zn) frameworks, the observed isosteric heats cannot be rationalized based upon ionic radii alone.^{196, 262} A computational study of the M₂(dobdc) series by Yu *et al.* revealed that the electrostatic interactions are likely dictated by nuclear screening effects that cause variations in the

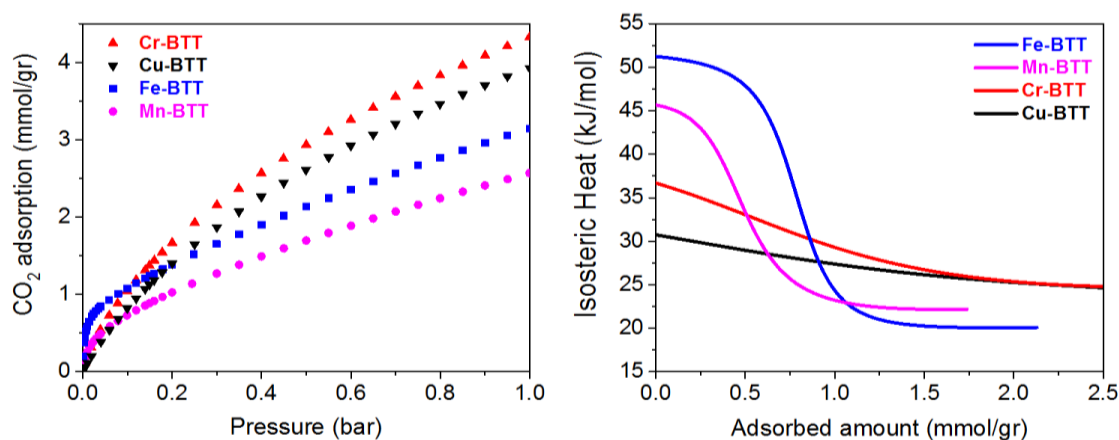


Figure 2-1 (left) Excess CO₂ adsorption isotherms obtained at 298 K for various M-BTT analogs. (right) Isosteric heats of adsorption, Q_{st} , plotted as a function of CO₂ loading

effective charge experienced by the CO₂ at the open metal site.¹⁹⁶ Computational work conducted both in this study on M-BTT frameworks (M = Cr, Fe, Cu) and an earlier work by Poloni *et al.* supports the experimentally observed trend in binding energy (Fe > Cr > Cu).¹⁶⁴

Upon increasing the CO₂ loading, a rapid drop is observed in the isosteric heat for Fe- and Mn-BTT, likely indicating that a portion of the primary adsorption sites are blocked by residual solvent molecules. Indeed, previous *in situ* structural studies of D₂ adsorption in this series of frameworks revealed a significant number of metal sites are blocked by solvent molecules that cannot be removed using standard activation procedures.^{263, 265} Rietveld refinement of the neutron diffraction data collected in this study on the bare Cr-BTT, Fe-BTT, and Cu-BTT frameworks post-activation revealed that ~23%, ~65%, and ~17% of the open metal sites, respectively, are blocked by coordinated solvent. Therefore, the overall trend for the number of available open metal sites follows the order Cu ≈ Cr > Fe > Mn, consistent with what has been previously reported.^{263, 265, 267} The smaller number of available open metal sites in Mn-BTT causes the isosteric heat to drop faster than that of the Fe-analog (Fig. 2-2), while the larger number of available open metal sites in Cu-BTT and Cr-BTT can be used to rationalize their higher overall capacity for CO₂ at 1 bar, despite their lower zero-coverage isosteric heat of CO₂ adsorption (Table 2-1).

2.3.2 Characterization of multi-site CO₂ adsorption in M-BTT

We used high-resolution neutron diffraction to elucidate the CO₂ adsorption behavior of the M-BTT frameworks, excluding Mn-BTT, due to the difficulty of removing a sufficient amount of coordinated solvent from the metal sites. With the general chemical formula [(M₄Cl)₃(BTT)₈]³⁻, M-BTT requires extra-framework metal cations to balance anionic charge. Although the positions of the extra-framework cations for Cr-BTT could not be determined due to a low coherent scattering neutron cross section, Cu cations were found in a slightly distorted trigonal planar environment coordinated by two N atoms of the tetrazolate ring

Table 2-1 Experimental and computed data for CO₂ adsorbed at site I in M-BTT.^a Distances and angles are listed in Å and degrees, respectively

M ²⁺	Isotherm		DFT (rev-vdW-DF2+U)				Diffraction Data		
	SA (m ² /g)	-Q _{st} (kJ/mol)	-H _b (kJ/mol)	M-O(CO ₂) ^b	N...C ^c	O-C-O ^d	M-O(CO ₂)	N...C ^c	O-C-O
Cr	1820	36.7	36.6	2.625	2.914	176.7	2.66(4)	3.04(2)	176(2)
Mn ^e	2050	45.6	-	-	-	-	-	-	-
Fe	1700	51.2	51.7	2.301	3.019	174.4	2.36(3)	3.00(3)	180(4)
Cu	1700	30.7	29.4	2.567	3.041	177.1	2.60(3)	3.01(1)	177(1)

^aExperimentally-determined surface areas (SA), zero-coverage isosteric heats of adsorption (-Q_{st}), and select geometric parameters for surface bound CO₂ are presented; computed enthalpies of adsorption (-H_b) and select geometric parameters are included for comparison. Values in parentheses indicate one standard deviation.

^bDistance from the metal center to the bound oxygen of CO₂.

^cDistance between carbon of bound CO₂ and the nearest tetrazole nitrogen.

^dIntramolecular angle of bound CO₂.

^eDue to the challenge of removing all solvent molecules bound to the open Mn²⁺ sites, data collection using neutron powder diffraction and DFT calculations on Mn-BTT were not pursued.

(1.97(3) Å) and a Cl⁻ (2.51(6) Å) (Fig. 2-3). This coordination geometry is indicative of the presence of a reduced Cu¹⁺ ion with an occupancy that charge balances the Cu-BTT framework to suggest an overall composition of Cu₆[(Cu₄Cl)₃(BTT)₈]Cl₃ for fully activated Cu-BTT.²⁹⁸⁻²⁹⁹ For Fe-BTT, the extra-framework cations are found directly above the Cl-centered [Fe₄Cl]⁷⁺ cluster at a Cl...Fe distance of 4.4(1) Å (Fig. S2-21). A small amount of excess scattering density was also observed in the axial position of the Cu²⁺ cations found in the [Cu₄Cl]⁷⁺ cluster of Cu-BTT, supporting the evidence for incomplete activation noted above. In this case, the excess scattering density appears to be a single atom, likely due to water adsorption, and hence is modelled as a single oxygen at an occupancy of 0.17(2) and a distance of 2.17(6) Å from the Cu²⁺ site. A similar procedure was carried out to model excess scattering density in Cr- and Fe-BTT (Tables S2-6 and S2-10).

Following structure determination of the activated materials, the samples were dosed with ~0.5 CO₂ per framework M²⁺ and the analysis was repeated. For all analogs, the primary adsorption site consists of CO₂ bound in an end-on configuration at the M²⁺ cation (Fig. 2-1), confirming the presence of strong electrostatic interactions indicated by the high initial isosteric heats of adsorption. The M²⁺–O(CO₂) distances range from 2.36(3) Å for Fe-BTT to 2.60(3) Å for Cu-BTT. While Cr-BTT binds CO₂ more strongly than Cu-BTT, the similar M²⁺–O(CO₂) distances in both analogs can be rationalized based on the larger ionic radii of Cr compared to Cu.

Secondary van der Waals interactions between the CO₂ carbon atoms and the nitrogen atoms on the nearest tetrazole ring in each framework (located at a C...N distance of ~3 Å) lead to M–O–C(CO₂) angles ranging from 106(1)° for Cu-BTT to 116(2)° for Fe-BTT. DFT angles are overestimated for this parameter at 127.5° for Cu-BTT and 134.0° for Fe-BTT, but the trend between the metals is consistent with the experiment. Fe-BTT has the strongest binding energy and the largest angle. The computed angle for Cr-BTT is 126.3°, so Cr and Cu have

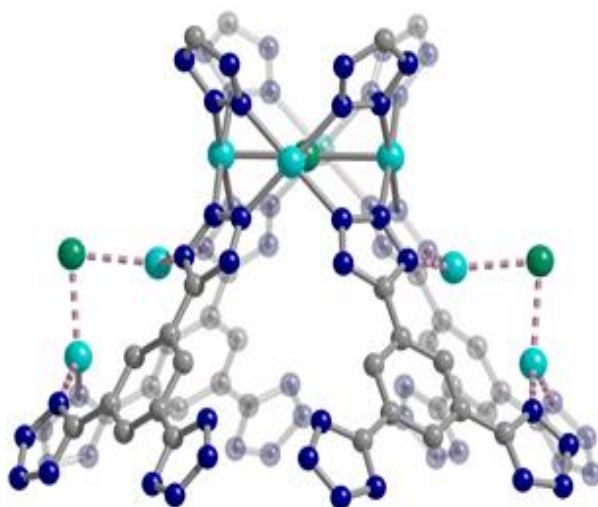


Figure 2-3 High-resolution neutron powder diffraction structure of Cu-BTT showing the extra-framework Cu⁺ cations that bridge N atoms of the tetrazolate ligand. Cyan, grey, blue, and green spheres represent Cu, C, N, and Cl atoms, respectively; H atoms are omitted for clarity.

similar binding angles despite Cr having a stronger binding energy; however, in the case of Cu, the presence of an extra-framework cation in the main adsorption cage could also influence the CO₂ orientation. The intramolecular CO₂ angles show minimal deviation from the expected linear geometry. While these angles are in good agreement with DFT calculations (Table 2-1) and indicate that there is little electronic activation of the bound CO₂ molecule, nothing can be said about the trend in the CO₂ angles due to the error associated with the diffraction experiment. The binding enthalpies and geometries of CO₂ in M-BTT (M = Cr, Fe, Cu) were also determined by periodic DFT calculations, and the results are presented in Tables 2-1 and 2-2. The theoretical site I CO₂ binding energies (Table 2-1) are in excellent agreement with experimentally-determined zero-coverage isosteric heats of adsorption, importantly capturing the observed experimental trend. The theoretical M–O(CO₂) distances for site I (Table 2-1) in the Cr- and Cu-BTT frameworks are also in near perfect agreement with the experiment (differing by < 0.04 Å) and within the range of the standard deviation (Fig. 2-4 and Fig. S2-20). The theoretical site I M–O(CO₂) distance in Fe-BTT is also in excellent agreement with experiment (differing by < 0.06 Å). When considering the margin of error associated with the diffraction experiment (\approx 0.03-0.04 Å), there is almost no difference between the computationally and experimentally determined metal–oxygen distances for CO₂ binding in Cr-, Fe-, or Cu-BTT. We note that the calculated M–O(CO₂) distances are also in much better agreement with experiment than those previously predicted for the M-BTT series,¹⁶⁴ which show deviations up to \sim 0.2 Å (the values reported previously use a different flavour of DFT and different positions for extra-framework cations). While the calculated trend in M–O(CO₂) binding distances (Cr \approx Cu > Fe) presented here corresponds with the one observed experimentally, the Cr–O(CO₂) bond distance is slightly longer than the Cu–O(CO₂) distance despite the stronger Cr–CO₂ binding energy. This is likely due to the aforementioned difference in the ionic radii of Cu²⁺ and Cr²⁺. Note that previous work by Poloni *et al.* reported that this distance correlated with binding strength; however, their calculated Cu–O(CO₂) distance was only 0.005 Å longer than Cr–O(CO₂) and therefore is also in good agreement with experiment.

Upon increasing the CO₂ loading from 0.5 to 1.5 CO₂ per M²⁺, three additional, weaker adsorption sites become populated (Fig. 2-1). In the case of Mn- and Fe-BTT, the significant drop in their isosteric heats of CO₂ adsorption (Fig. 2-2. (right)) indicates that preference for site I persists to room temperature. In contrast, the relatively flat nature of the isosteric heats of adsorption for Cr- and Cu-BTT implies similar binding energies for the different binding sites at room temperature, an observation that is supported by the predicted binding enthalpies of sites I and II determined via DFT calculations (Tables 2-1 and 2-2). A comparison of the DFT-derived CO₂ binding energies for sites I and II provides further valuable insight into the behavior of the framework adsorption isotherms. While the binding energy of CO₂ at site I depends strongly on metal identity, the binding strength at site II appears to be nearly independent of the metal. Indeed, the DFT binding strengths of CO₂ at site II (Table 2-2) vary by only 2 kJ/mol across the frameworks studied. Given that the M-BTT frameworks are isostructural, it is perhaps unsurprising that CO₂ should adsorb with similar binding energies

at secondary adsorption sites. The DFT results are further supported by the similar isosteric heat values extracted for the frameworks at higher surface coverage (Fig. 2-2).

The secondary CO₂ adsorption site in Cu-BTT (Fig. 2-1) is rotationally disordered above the [Cu₄Cl]⁷⁻ cluster. The closest oxygen atom of carbon dioxide bound at this site is approximately 3.27 Å from the Cl⁻ and 3.44 Å from the center of the tetrazolate ring, distances that are in agreement with what is expected based on the van der Waals radii of oxygen and chlorine. Interestingly, the extra-framework cations in Fe-BTT also reside just above the Cl⁻ anion in the [M₄Cl]⁷⁻ cluster and partially block the secondary adsorption site in this structure. In addition to the blocking of a large number of primary adsorption sites due to solvent molecules, the positioning of this cation may also influence the significant drop observed in the Q_{st} for Fe-BTT relative to Cr- and Cu-BTT. As was the case for CO₂ bound at site I, the DFT calculated binding geometries for CO₂ at site II match well with the experimentally-determined values (Table 2-2). The largest deviation was observed for Cr-BTT, for which the DFT calculations revealed a Cl⁻⋯O(CO₂) distance that is ~0.1 Å longer than that observed experimentally. The experimentally and theoretically determined structures for Cu-BTT are overlaid in Fig. 2-4 (see also Fig. S2-20).

At site III, CO₂ is rotationally disordered between two carbon atoms of the BTT³⁻ linker and located at a C⋯O distance of ~3.27 Å from the framework wall. Although this site is twice as abundant as site II, the adsorption of CO₂ at site III is expected to be weaker given its lower occupation observed via *in situ* neutron diffraction. It should be noted that while the CO₂ molecules located at sites III and IV are somewhat disordered, the intermolecular CO₂ distances for these two sites are shorter than those of the closest CO₂-framework distances. It may be that the population of site II helps to stabilize the population of these two additional adsorption sites, an observation that is supported by a pronounced plateau in Q_{st} at higher loadings (Fig. 2-2). It is also possible that CO₂ molecules located at sites III and IV afford additional stabilization to CO₂ molecules located at site II (Fig. 2-1), in a manner similar to that suggested in an earlier study on CH₄ binding in the metal-organic framework Cu₃(btc)₂.³⁰⁰

Table 2-2 Experimental and computed binding enthalpies and geometries (DFT) for site II CO₂. Distances and angles are listed in Å and degrees, respectively.

	$-H_b$ (kJ/mol)	O⋯Cl ^a	O–C–O ^b	O⋯Cl ^a	O–C–O ^b
Cr	26.6	3.303	179.1	3.17(3)	179(6)
Fe	24.5	3.237	179.7	3.38(2)	179(7)
Cu	26.8	3.300	179.4	3.27(2)	179(8)

^a Theoretical and computed bond distances describe the distance between the oxygen atom in CO₂ and the chlorine atom in the center of the cluster.

^b The intramolecular O–C–O angle of the CO₂ molecule.

Positional disorder in the CO₂ molecules bound at sites III and IV precluded periodic DFT analysis, and therefore we turned to force fields to quantify any stabilizing influence of neighboring CO₂ molecules on the adsorbed gas at these positions. For this analysis, we arranged the site III and IV CO₂ molecules at their experimental unit cell positions around site II CO₂ with the DFT-determined binding geometry. We found the strength of the interaction between site II and site III CO₂ molecules to be -4.58, -3.13, and -3.26 kJ/mol for Cu-, Cr-, and Fe-BTT, respectively. Interactions between CO₂ located at site II and site IV were found to be smaller, although of the same order of magnitude. Considering the magnitude of the CO₂ binding enthalpies at site II (Table 2-2), it is expected that interactions with CO₂ molecules at sites III and IV are unlikely to have a large impact on the site II binding enthalpy. However, the CO₂ molecules at sites III and IV exhibit weaker interactions with the framework compared to that of site II and may be primarily stabilized by interactions with the closest site II molecule.

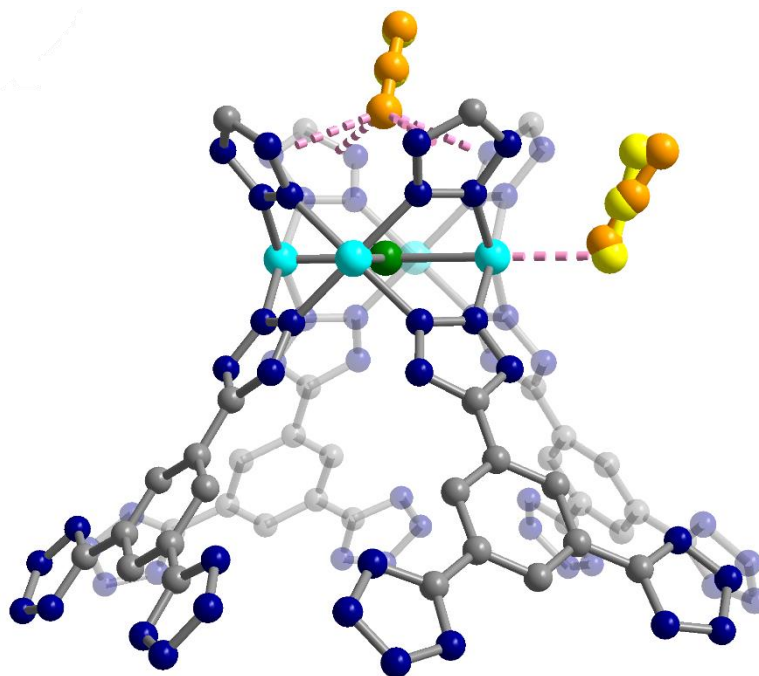


Figure 2-4 Structure of Cu-BTT showing the primary (site I, right) and secondary (site II, top) CO₂ adsorption sites, as identified by *in situ* powder neutron diffraction and DFT calculations (yellow and orange ball-and-stick representations, respectively). Cyan, grey, blue, and green spheres represent Cu, C, N, and Cl atoms, respectively; H atoms are omitted for clarity.

Because the strength of CO₂ binding at site I is dependent on the identity of the framework metal and the binding strength at site II is not, the theoretical difference between the site I and site II binding energies follows the same trend across the M-BTT series as the site I binding energy (Fe > Cr > Cu). DFT calculations show that CO₂ binds more strongly at site I than site II in Fe-, Cr-, and Cu-BTT by 27.2, ~10, and 2.6 kJ/mol, respectively. The higher binding strength at site I is supported by the higher experimentally observed site I occupancy at low CO₂ loadings in diffraction experiments. We note that while an energy difference as small as ~3 kJ/mol is enough to distinguish sites I and II and lead to sequential occupation of adsorption sites at 10 K, at room temperature there is enough thermal energy such that there is no strongly preferred adsorption site. A similar phenomenon has been observed for CH₄

binding in $\text{Cu}_3(\text{btc})_2$ using powder neutron diffraction, wherein thermodynamic preference for a given binding site at 150 K is lost at higher temperatures.³⁰⁰ Room-temperature CO_2 adsorption isotherms for Cr-, Fe- and Cu-BTT plotted on semi-log and logarithmic axes are shown in Figs. S2-18 and S2-19. On a semi-log scale, Cr- and Cu-BTT exhibit Langmuir-type CO_2 adsorption behavior, while in Fe-BTT CO_2 appears to bind most strongly at low pressures. This latter observation is supported by DFT calculations, which predict the largest difference in site I and II binding energies for Fe-BTT. The combined theoretical and experimental work presented here suggests that differences in binding energy of > 20 kJ/mol may be needed to observe a truly sequential loading of different binding sites in room temperature adsorption isotherms.

2.3.3 Comparison with Previous Computational Work

It is of interest to compare the DFT results obtained here to previous computational work by Poloni *et al.*, which examined CO_2 adsorption at the primary site in M-BTT for both existing and hypothetical analogs.¹⁶⁴ The results in the previous work¹⁶⁴ were obtained using atomic orbital basis sets and a PBE+D2+U van der Waals corrected functional, whereas this work used a plane wave basis set and the rev-vdW-DF2+U functional. Additionally, the two studies differ in the placement of the extra-framework cations. Both of these factors will contribute to differences in the geometric parameters and binding energies reported in the two studies; however, overall trends can be examined.

In particular, the site I binding energies and trend in $\text{M}-\text{O}(\text{CO}_2)$ distances reported previously are in good agreement both with those in this work and with the experimental isosteric heats of adsorption. This supports the conclusion that the interaction with the M^{2+} cation dominates and this site is not particularly sensitive to the position of the framework cation. On the other hand, the site I binding geometries from this study more closely match the diffraction results. For example, the $\text{M}-\text{O}(\text{CO}_2)$ binding distances at the primary adsorption sites were on average 0.045 Å closer to the experimental values compared to those reported previously. Our distances are slightly shorter than experiment while those of Poloni *et al.* are slightly longer. This could be due to the fact that the rev-vdW-DF2 functional was reparametrized specifically to improve bond distances while maintaining good binding energies; however, functional dependence in this system has not been systematically examined. The previous study also observed that stronger CO_2 binding correlated with deviations from the expected linear geometry of CO_2 and shorter distances between the tetrazole nitrogen and the CO_2 carbon. In the diffraction results presented here, neither of these trends is observed. Although our DFT calculations started from the experimental structure, we observe the same trend in CO_2 bending as Poloni *et al.* Moreover, the distance between the tetrazole nitrogen and CO_2 carbon shows no clear dependence on the binding energy and the trend between the metals is different in the experiment ($\text{Cr} > \text{Cu} > \text{Fe}$), our calculations ($\text{Cu} > \text{Fe} > \text{Cr}$), and those of Poloni *et al.* ($\text{Cu} > \text{Cr} > \text{Fe}$). However, both experiment and Poloni *et al.* report the shortest N-C distance for the strongest binding metal. Additionally, in our calculations for Fe-BTT sodium migrated closer to Cl than the experimentally observed

Fe cation. It is possible that the location and identity of the extra framework Fe cations has an impact on the CO₂ binding geometry.

The diffraction data presented in this work has created the opportunity for a future benchmarking study to determine the influence of different DFT functionals on the accurate prediction of CO₂ adsorption properties in the M-BTT framework series. Relative differences between Cr- and Fe-BTT structures computed in this work compared to the previous study may have to do with the placement of sodium cations, the respective choices of functional, and the choices in the level-of-theory. Furthermore, the specific identity of the extra-framework cations may play an important role in counterbalancing intra-framework forces. For example, DFT studies exploring whether extra-framework cations with different ionic radii and partial charge could occupy different sites based on steric effects, which has been suggested in the literature,³⁰¹ have not been performed.

2.4 Conclusions

We have demonstrated that *in situ* neutron diffraction can provide insights into how to optimize existing metal–organic frameworks for CO₂ adsorption (e.g., via metal substitution) while also providing detailed structural information that can be used to validate computational methods aimed at predicting the behavior of metal–organic frameworks with open metal sites. Indeed, in this study, calculated CO₂ binding energies and geometries were in good agreement with the experimental results, and such validation of computational approaches for adsorption applications opens the door to predicting the behavior of synthesized and even hypothetical metal–organic frameworks.

The foregoing results also provide experimental evidence that the strength of adsorption at the open metal site in the M-BTT series can be rationalized based on metal identity, including the partial charge on the electropositive M²⁺ cations. This observation is confirmed by both prior computational work and the results of DFT calculations presented here.¹⁶⁴ DFT calculations also suggest that the heat of adsorption at site II is not dependent on metal identity. Strong CO₂ adsorbents, like Fe-BTT, display sequential adsorption behaviour, which could potentially be exploited for applications such as CO₂ conversion. This study shows the need for combined experimental and computational studies capable of predicting framework properties, a process that might eventually allow the rapid identification of target materials for CO₂ capture, as well as a host of other applications.

Chapter 3

An *in-situ* neutron diffraction and DFT study of hydrogen adsorption in a sodalite-type metal–organic framework, Cu-BTTri³

3.1 Introduction

Metal-Organic Frameworks (MOFs), a class of porous, crystalline materials, have received intense attention over the last few decades in a variety of fields coupled to gas storage,³⁰²⁻³⁰⁶ gas and liquid separations,^{36, 307-309} catalysis,^{38, 310} sensing,³¹¹ drug delivery,³¹² etc. Among these applications, gas storage has been intensely studied in MOFs;³¹³ this is largely owed to their unprecedented internal surface areas and pore volumes, combined with the ease of decorating internal surface area with high densities of strong adsorption sites.^{21, 282, 314} These attractive features result in high capacities for the capture of a variety of small guest molecules such as hydrogen.³¹⁵⁻³¹⁶ When compared to other porous adsorbents, MOFs can offer higher storage capacities,³¹⁷ and in some cases boast hydrogen storage densities that exceed what can be achieved through pure compression.^{316, 318-319} While more than 70,000 MOF structures have been reported in literature to date,³²⁰ few of these have been experimentally screened to determine their applicability in hydrogen storage. As such, studies focused on providing knowledge of how the MOF structure influences storage properties are needed. Studies of this kind not only deepen our chemical understanding of adsorption

³ This chapter is based on the published article: Asgari, M., Semino, R., Schouwink, P., Kochetygov, I., Trukhina, O., Tarver, J.D., Bulut, S., Yang, S., Brown, C.M., Ceriotti, M. and Queen, W.L. "An In-Situ Neutron Diffraction and DFT Study of Hydrogen Adsorption in a Sodalite-Type Metal–Organic Framework, Cu-BTTri." *European Journal of Inorganic Chemistry* 2019.8 (2019): 1147-1154. M. A. has synthesized the material, performed the experiments, analyzed the data and written the paper.

phenomena,⁷³ but will hopefully promote the development of computational methods able to rapidly and accurately predict the performance of existing and hypothetical materials towards hydrogen gas storage.³²¹⁻³²²

One family of MOFs which has shown promising performance for hydrogen storage is the M-BTT ($\text{BTT}^{3-} = 1,3,5\text{-benzenetristetrazolate}$ where $M = \text{Cr, Mn, Fe, Co, Ni, Cu, Cd}$) series of frameworks.^{264-265, 313, 323-324} This framework family can be substituted with a variety of metals and ligands (BTT^{3-} vs $\text{BTTri}^{3-} = 1,3,5\text{-benzenetristriazolate}$ or $\text{BTP}^{3-} = 1,3,5\text{-benzenetrispyrazolate}$), thus altering the chemical environment inside the MOF pore all while keeping the same structural motif.^{139, 220, 325-326} Further, upon solvent removal, many of these materials exhibit open-metal coordination sites, a structural feature known to increase the surface packing density of hydrogen,³²⁷ and give rise to high isosteric heats of hydrogen adsorption (Q_{st}).^{64, 265, 272, 313, 328} The latter is required to enhance adsorption capacities at higher temperature, which is desirable for storage on-board vehicles. Given this, herein we report *in-situ* neutron diffraction experiments,^{64, 72, 262, 329} which are used to unveil the intimate details of hydrogen adsorption in a highly stable, crystalline MOF, known as Cu-BTTri. In this work we also report the correct structure for the activated Cu-BTTri framework, and location of four D_2 adsorption sites within the gas dosed material, for the first time. In addition, the experimental data is used to validate Density Functional Theory (DFT) methods, used to predict the location and binding energy of the guest hydrogen species. A good agreement with the experiment implies that this theoretical approach can be applied to simulations of similar systems, thus potentially helping lay the basis for the rapid computational screening of hydrogen adsorption properties of both existing and hypothetical MOF structures in the future.

3.2 Experimental Section

3.2.1 Synthesis of H_3BTTri ligand

The H_3BTTri ligand has been synthesized according to the reported method in the literature.¹³⁹

3.2.2 Synthesis of Cu-BTTri

The Cu-BTTri framework has been synthesized according to the reported method in the literature¹³⁹ with minor modifications. 225 mg of H_3BTTri ligand was dissolved in 40 ml of DMF in a 100 ml glass jar with the plastic cap. 383 mg of solid $\text{CuCl}_2 \cdot 2\text{H}_2\text{O}$ was also introduced into the jar. After that, 50 droplets of the five times diluted concentrated HCl and 10 ml of water were added to the solution. Then, the cap was sealed and placed in the oven to be heated at 100 °C for 72 hours. Subsequently, the jar was taken out of the oven and was filtered while hot and then washed 3 times with hot DMF and 3 times with MeOH. Then, the sample was dried to yield between 200-250 mg of the product in the form of a purple powder.

3.2.3 Activation of Cu-BTtri

To do the solvent exchange, the sample was placed in a cellulose thimble and then underwent soxhlet extraction for 24 hours. Then, the sample was inserted into the sample tubes, sealed and kept under vacuum for 3 hours. Subsequently, the sample was heated to 180 °C over 3 hours and kept at 180 °C for 16 hours to yield the activated product in a form of brown product.

3.2.4 SEM-EDX characterization

SEM analysis was performed on a FEI Teneo at an accelerating voltage of 1.00 kV and a beam current of 100 pA. SEM images were acquired with an in-column (Trinity) detector. SEM-EDX elemental maps were acquired using a beam current of ~ 400 pA and accelerating voltage of 10 kV.

3.2.5 In-situ neutron diffraction experiments

High-resolution neutron powder diffraction (NPD) experiments were carried out on the Cu-BTtri sample using BT1 at the National Institute of Standards and Technology (NIST) Center for Neutron Research (NCNR). All measurements were carried out on activated samples of ≈ 0.8 g. At NIST, samples were activated while heating under dynamic vacuum and then transferred into a He purged glove-box, loaded into a vanadium can equipped with a gas loading valve, and sealed using an indium O-ring. NPD data were collected using a Ge(311) monochromator with an in-pile 60 collimator corresponding to a wavelength of 2.0728 Å. The sample was loaded onto a closed cycle refrigerator (CCR) and then data was collected at 10 K. After data collection on the activated framework, D₂ with two different dosing levels of 0.36 D₂/Cu²⁺ and 3.11 D₂/Cu²⁺ were then loaded into the sample cell. To do this, the sample was firstly heated to room temperature and then exposed to a pre-determined amount of gas. Upon reaching an equilibrium pressure at the loading temperature, the sample was then slowly cooled (1 K per minute) to ensure complete adsorption of the D₂ and then data was collected again at 10 K. The collected powder diffraction pattern at reduced temperature has been used for further Rietveld analysis. The Rietveld analysis has been done using Topas 5 software.³³⁰

3.2.6 In-situ synchrotron X-ray experiments

Bare sample was measured at the Swiss-Norwegian Beamlines (BM31) at the European Synchrotron Radiation Facility (ESRF) in Grenoble, France. A custom built *in-situ* diffraction powder cell, which was mountable on the goniometer, was used for *in-situ* variable temperature synchrotron X-ray diffraction experiments. An oxford cryostream 700 system with the working temperature of 80-500 K has been used to keep the temperature of the sample (the zone covered the X-ray beam width) at the desired temperature. The nozzle of the cryostream was tried to be located close enough so as the precision of the temperature will be guaranteed. Data were collected using a MAR 2D image detector and the wavelength was adjusted to be 0.5008 Å. The azimuthal integration of raw images was performed with the

program Bubble. Profile fits (Le Bail analysis) and Rietveld refinements of the powder diffraction patterns were performed using EXPGUI/GSAS.

3.2.7 *Rietveld analysis*

All diffraction pattern data were analysed using the Rietveld method as implemented in Topas 5 (for the case of neutron diffraction experiments) and EXPGUI/GSAS (for the case of synchrotron experiment).^{285, 330-331} The activated Cu-BTTri model was refined with most structural and peak profile parameters free to vary. Atomic displacement parameters (ADPs) for atoms with the same identity were constrained to be the same throughout the refinement process. Fourier difference analysis, applied to data obtained from D₂ adsorbed samples, was then employed to locate the adsorbed molecules in the frameworks. The obtained CIF file for the structures refined by Rietveld analysis against powder diffraction data has been uploaded to CCDC data base with the CCDC number of 1872064-1872067. The number associated with each structure has been written in the SI above the crystallographic table for each structure.

3.2.8 *Quantum computational calculation methods*

Binding energies, structural details and charge distribution were obtained from DFT calculations, under the generalized gradient approximation by Perdew, Burke and Ernzerhof (PBE functional).³³² All calculations were performed by using the PWscf (Plane-Wave Self-Consistent Field) package from the Quantum Espresso³³³ suite of codes. We used the following ultra soft pseudopotentials³³⁴ extracted from <http://materialscloud.org/sssp> : Cu_pbe_v1.2.uspp.F.UPF, C_pbe_v1.2.uspp.F.UPF, H.pbe-rrkjus_psl.0.1.UPF and N.pbe.theos.UPF. The former two were generated using Vanderbilt code³³⁵ and the latter two using the “atomic” code by A. Dal Corso.³³⁶ We employed kinetic energy cutoffs for wave functions and charge density and potential of 55 and 660 Ry respectively. All calculations were performed for the Γ point of the Brillouin zone, due to the large size of the MOF (228 atoms in the unit cell). Spin-polarized calculations were performed to take into account the most stable spin state for Cu-BTTri, which was found to be antiferromagnetic. Following previous work¹⁶⁴ where other chemically similar MOFs including Cu-BTT were studied, dispersion corrections were considered under the Grimme-D2 scheme³³⁷.

We took as a starting point the experimental configuration for Cu-BTTri, and then allowed the structure to relax while keeping the cell parameters fixed to experimental values (tests allowing the cell parameters to change were also carried out and have shown very small changes of 1-3% in volume). Subsequently, several calculations were set, each of them containing one gas molecule adsorbed in a different site of the MOF. We took as initial configurations those found in the experiment and allowed them to relax, again without changing the cell parameters. Binding energies were computed as the difference between the energy of the MOF/gas binary complex and the sum of the energies of MOF and gas molecule.

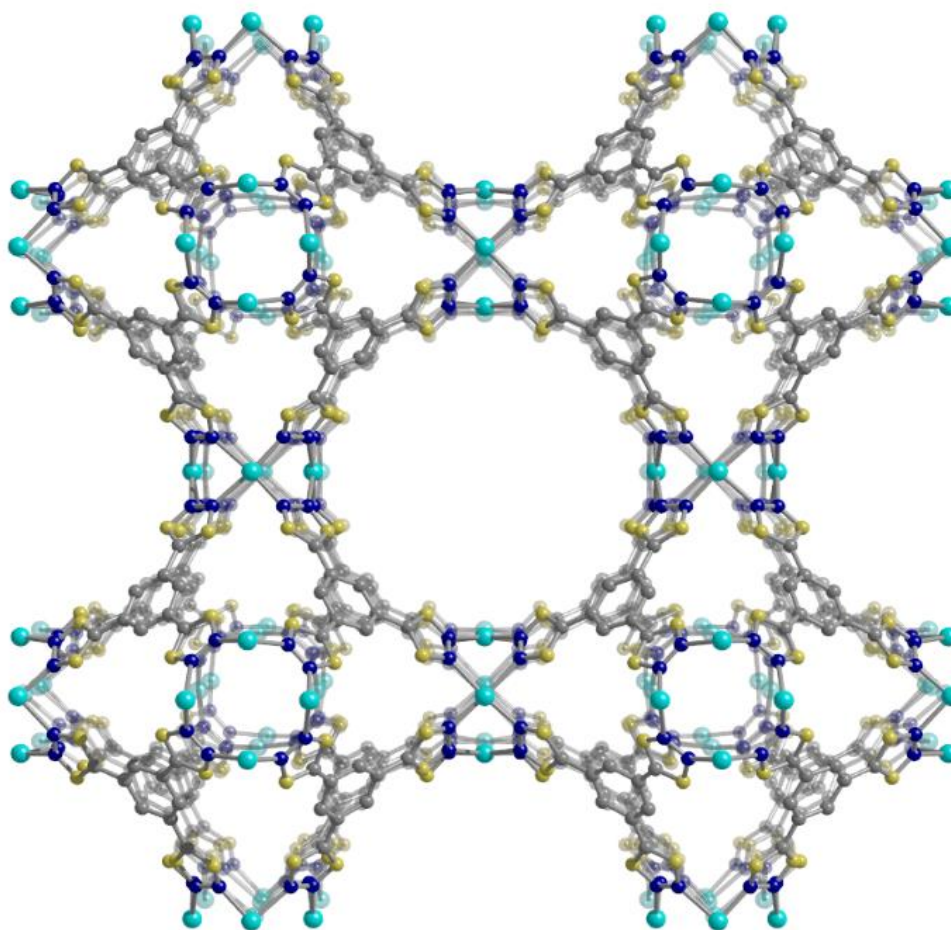


Figure 3-1 A ball and stick model of the Cu-BTtri structure obtained from Rietveld analysis of powder neutron diffraction data. Cu, N, and C atoms are represented by cyan, blue, and grey spheres, respectively. Yellow spheres represent sites mixed with both C and N. Hydrogen atoms are excluded for clarity.

3.3 Results and Discussion

3.3.1 Characterization of Cu-BTtri framework

The H₃BTtri ligand and corresponding Cu-BTtri framework were synthesized using reported procedures that were slightly modified (see the Appendix). A scanning electron microscope (SEM) was used to assess the size and morphology of the crystallites, Figure S3-1. The octahedral shape is consistent with the cubic crystal system reported for this material. However, the single crystal size, which is well below 5 μm , inhibits standard single crystal diffraction studies. Due to this limitation, no experimental report of the single crystal structure of Cu-BTtri can be found in the literature. In the original report of Cu-BTtri,¹³⁹ the powder x-ray diffraction data was compared to the simulated powder pattern obtained from its ligand substituted counterpart, Cu-BTT²⁶⁴ and assumed to have the following chemical formula: H₃[(Cu₄Cl)₃(BTtri)₈].¹³⁹ In order to check this, neutron powder diffraction data was first

collected on the desolvated Cu-BTTri structure, and Rietveld analysis was carried out using the previously reported composition as a starting point. However, this previously reported structure¹³⁹, shown in Figure S3-2, did not provide a satisfying fit to the experimental neutron diffraction data obtained in this study. As such, the occupancy of the charge balancing chlorine anions were varied. Interestingly, a good fit could only be achieved by removing Cl⁻ anions from the centre of the [Cu₄Cl]⁷⁻ clusters giving rise to a neutral framework with the following composition: Cu₃(BTTri)₂. (Figure S3-4) To corroborate this finding, the sample was characterized by EDX analysis, which shows no chlorine (Figure S3-3, Table S3-1) further supporting the new Cl⁻ free structural model, Figure 3-1. Cu-BTTri crystallizes in a cubic *Fm-3c* space group (no. 226) and features square [Cu₄]⁸⁺ clusters that are interlinked by triangular [BTTri]³⁻ ligands to form a sodalite-type framework with a 3-dimensional pore network. The triazole groups of the ligand show rotational disorder resulting in refined partial occupancies of carbon and nitrogen on positions 3 and 5 of the triazolate rings (Table S3-1). It is noted that this structure was further confirmed via Rietveld analysis carried out on synchrotron X-ray diffraction data also collected on an activated sample of Cu-BTTri. Due to the minimal difference in the X-ray atomic scattering factor for C and N, rotational disorder on the triazole group was neglected. Additionally, hydrogen atoms were excluded during refinement of the structural model. The resulting fit (Figure S3-5) is satisfactory and additionally confirms the absence of any chlorine species in the activated framework (Figure S3-6 and TableS3-2).

Surface area and pore volume analysis was carried out on the activated sample via N₂ adsorption isotherms measured at 77 K (Figure S3-7). The resulting BET surface area and pore volume for this sample are 1950 m²/g and 0.8 cm³/g, respectively. These values are slightly higher than those obtained from the ligand substituted counterpart, Cu-BTT, which were reported to be 1760 m²/g and 0.7 cm³/g, respectively. Unlike Cu-BTTri, the Cu-BTT framework, has extra charge-balancing cations in its framework and Cl⁻ anions centered in the face of the copper cluster. The material has the following chemical formula: Cu₆[(Cu₄Cl)₃(BTT)₈]Cl₃. The absence of extra Cu²⁺ and Cl⁻ ions in the Cu-BTTri structure allows the pores to become more accessible and hence will likely alter the performance of this material in various host-guest chemistries.

3.3.2 Hydrogen adsorption properties

The low-pressure hydrogen adsorption isotherms were collected for Cu-BTTri at variable temperatures in order to evaluate hydrogen uptake, Figure 3-2a. Further, the isosteric heat of hydrogen adsorption was extracted from the data obtained at 140 K and 159 K using the Clausius-Clapeyron equation, Figure 3-2b. A relatively steep slope in the adsorption isotherm for hydrogen is indicative of the presence of strongly polarizing open Cu²⁺ sites. We have compared the low-pressure hydrogen adsorption for Cu-BTTri (measured at 77 K) to its ligand substituted counterpart, Cu-BTT, and see that hydrogen adsorption at low pressures is lower in Cu-BTTri than Cu-BTT (Figure S3-9). Considering that low-pressure hydrogen adsorption is dictated strongly by the potential energy landscape on the internal framework surface,³³⁸ the origin of this difference can often be determined via structural analysis.³³⁹⁻³⁴⁰ It

was hypothesized that the lower H_2 adsorption observed in Cu-BTTri likely originates from the absence of the extra Cu^{2+} cations and Cl^- anions observed in Cu-BTT, or the weaker Lewis acidity of Cu^{2+} , which results from the higher pK_a of the BTTri³⁻ ligand. However, the initial isosteric heat of adsorption (Q_{st}) for Cu-BTTri, Figure 3-2b, is ~ 10.5 kJ/mol, a value that is slightly higher than the one previously reported for Cu-BTT, ~ 9.5 kJ/mol.³¹³ This indicates that changing the ligand does not strongly influence the binding energy of the first adsorption site.³¹³ Also, the geometry of the cluster coupled with the structural differences of the framework raises the zero coverage isosteric heat of Cu-BTTri with respect to another Cu^{2+} containing MOF known as Cu-BTC (BTC= benzene-1,3,5-tricarboxylate), which has a paddlewheel-like cluster and a moderate zero coverage isosteric heat of hydrogen adsorption

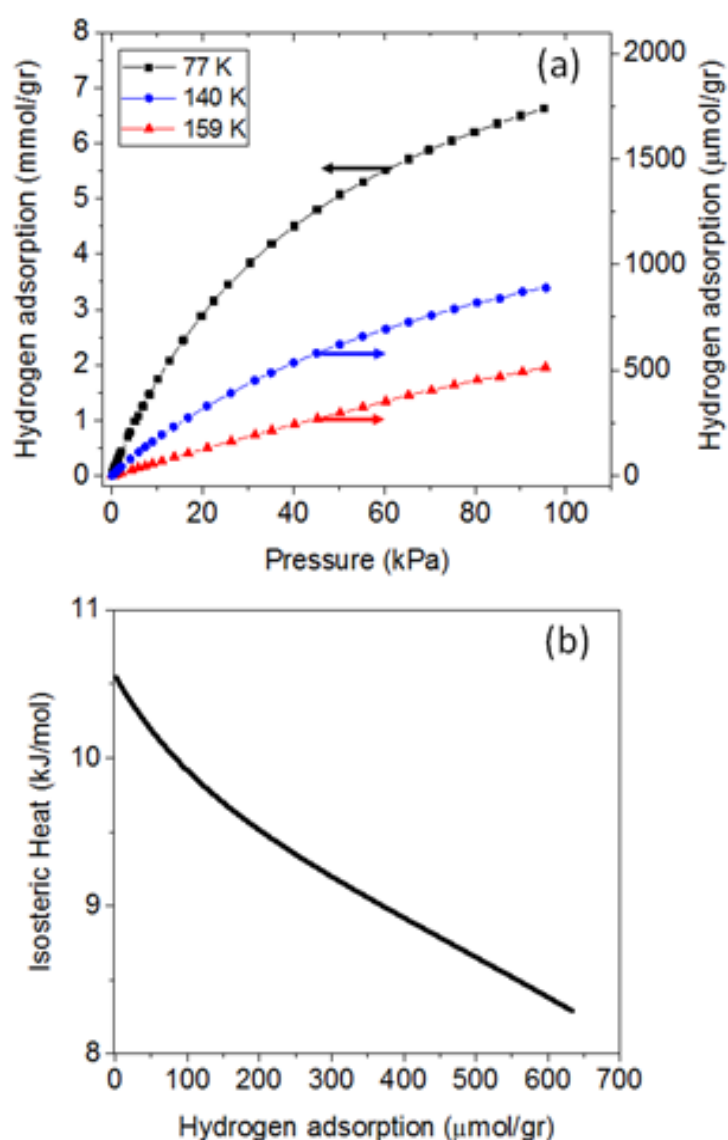


Figure 3-2- (a) Hydrogen adsorption isotherms in Cu-BTTri collected at 77 K, 140 K, and 159 K. (b) Enthalpy of adsorption of H_2 in Cu-BTTri, extracted by Clausius-Clapeyron equation.

of ~ 6.6 kJ/mol.³⁴¹ A similar trend was reported for Cr-BTT and Cr-BTC, with Cr-BTT showing a higher Q_{st} .³¹³

3.3.3 D_2 binding sites

Following refinement of the structural model associated with the activated material, the sample was dosed with 0.36 and 3.11 D_2 per Cu^{2+} , and neutron powder diffraction data were subsequently collected at 10 K. Rietveld analysis followed by subsequent Fourier difference analysis allowed determination of the location of the adsorbed D_2 molecules. The D_2 molecules were modelled as single atoms due to quantum mechanical rotations that make the molecules almost spherical.³⁴² Fractional atomic coordinates, occupancies, and isotropic displacement parameters of the refined structures are shown in Tables S3-4 and S3-5.

From these data, four adsorption sites were identified with the two of them only being present at the higher loading. The location of these four adsorption sites inside the structure are shown in Figure 3-3. The site with the highest occupancy (0.13(1) and 0.47(1) D_2 at the loading of 0.36 D_2 per Cu^{2+} and 3.11 D_2 per Cu^{2+} , respectively) is presumed to be the primary adsorption site, and is located at the open Cu^{2+} cation, Figure 3-3. This site is disordered between two D_2 molecules produced by the mirror plane. The vicinity of the disordered D_2 molecules with the distance of 0.74(9) Å yields in the maximum possible occupancy of 0.5 for the D_2 molecules in this adsorption site, which means that the primary adsorption site is almost fully occupied at 3.11 D_2 per Cu^{2+} loading. The location of $D_2(I)$ confirms our initial assumption that the high initial isosteric heat results from relatively strong interaction between the metal node and D_2 . The Cu^{2+} - $D_2(I)$ distance is 2.73(4) Å, which is significantly longer than the value observed for Cu^{2+} - $D_2(I)$ in Cu-BTT or Cu-BTC, 2.47 Å and 2.4 Å, respectively.²⁶⁴ The longer Cu- $D_2(I)$ distance likely arises due to the higher electron donating effect of the BTTri ligand compared to BTT,³⁴³ making the Cu^{2+} nodes in Cu-BTTri weaker Lewis acids.²²⁰ Also, DFT calculations (see Table 3-1) were used to predict the location of the primary adsorption site, $D_2(I)$, which resulted in a distance of 2.65 Å from the Cu^{2+} . Considering the standard deviation for the experimental data, the difference between the DFT and experiment is considered to be negligible.

Despite the significantly longer Cu^{2+} - $D_2(I)$ distances observed in Cu-BTTri over Cu-BTT, its zero-coverage isosteric heat (10.5 kJ/mol) is slightly higher than that of Cu-BTT (9.5 kJ/mol). This anomaly is confirmed by DFT calculations (Table 3-1). To better understand the aforementioned differences in Q_{st} , additional secondary interactions between the $D_2(I)$ molecule and the framework must be considered. There are two additional host-guest interactions in Cu-BTTri observed between $D_2(I)$ and the framework. The first and more relevant one is the hydrogen-hydrogen interaction between the hydrogen of the triazole ring and $D_2(I)$ [$D_2(I) \cdots H - C = 2.6(1)$ Å]. This type of van der Waals interaction is previously observed in MOFs,^{339, 344} and should not be confused with dihydrogen bonding, a form of hydrogen bonding with a hydridic hydrogen that plays the role of the base atom.³⁴⁵ The hydrogen-hydrogen interaction seen in Cu-BTTri, cannot exist in Cu-BTT due to extra nitrogen

atom on the tetrazole ring.²⁶⁴ It is thought that this strong, secondary interaction is likely responsible for the aforementioned disorder around the $D_2(I)$ site, which could pull the molecule off the mirror plane in Cu-BTTri. (Figure S3-12) It is noted that this disorder is expectedly not observed for Cu-BTT. The second interaction to be considered is the van der Waals interaction between $D_2(I)$ and the nitrogen atoms of the triazole ring (Figure 3-3). The distances between $D_2(I)$ and the nitrogen lies within the range of 3.3-3.7 Å, which is reminiscent of weak van der Waals interactions.³⁴⁶ For Cu-BTTri, the $D_2(I)$ -N interaction is stronger than in Cu-BTT because the triazole nitrogen are stronger electron donors.³⁴³ Therefore, although it is true that the open Cu^{2+} has a major overall contribution to the affinity of the $D_2(I)$ molecules to the framework, the two aforementioned secondary interactions likely compensate for the slightly weaker Lewis acidity of the metal ion in Cu-BTTri giving rise to an overall higher Q_{st} .

The second adsorption site is found between the hydrogen of the benzene ring [$D_2(II) \cdots H - C = 2.67(9)$ Å] and those of two neighbouring triazole rings ($[D_2(II) \cdots H - C = 2.8(1)$ Å] and $[D_2(II) \cdots H - C = 3.0(1)$ Å]). The nature of this type of hydrogen-hydrogen interaction is similar to that of the primary adsorption sites. In addition, this site is further stabilized by van der Waals interactions between $D_2(II)$ and the benzene ring [$D_2(II) \cdots C = 3.44(6)$ Å] as well as the nitrogen atoms of two neighbouring triazole rings ($[D_2(II) \cdots N = 3.44(6)$ Å] and $[D_2(II) \cdots N = 3.73(5)$ Å]). Moreover, the short $D_2 - D_2$ distances [$D_2(II) \cdots D_2(I) = 2.76(8)$ Å], imply that the secondary site is likely stabilized by the primary adsorption site. The occupancies of $D_2(II)$ goes from 0.04(1) to 0.45(1) at loadings of 0.36 D_2/Cu^{2+} and 3.11 D_2 per Cu^{2+} . It is noted that the secondary adsorption site previously observed in Cu-BTT is found directly above the Cl^- in the $[Cu_4Cl]^{7+}$ cluster (Figure S3-13). The lack of this anion inhibits population of this site in Cu-BTTri (Figure 3-3). It is likely that the absence of this relatively strong binding site also lends to its lower hydrogen uptake (Figure S3-9).

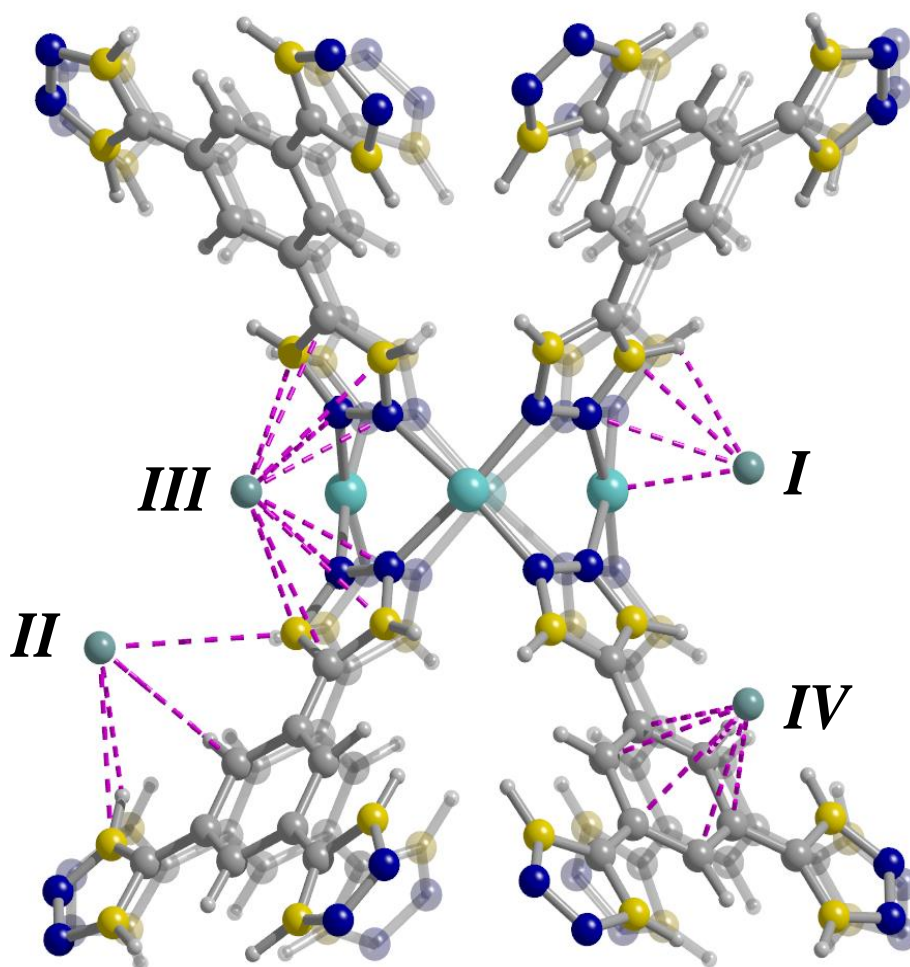


Figure 3-3 A Ball and stick model of the Cu-BTTRI framework dosed with 3.11 D_2/Cu^{2+} . The Cu, C, N, and H are denoted as cyan, grey, blue, and white spheres, respectively. Yellow spheres represent mixed sites containing both C and N. The pink dotted lines represent nearest neighbor interactions.

The third adsorption site appears in a pocket located between two neighbouring triazole rings, with distances that range from $[D_2(III) \cdots N = 3.33(4) \text{ \AA}], [D_2(III) \cdots N = 3.36(3) \text{ \AA}], [D_2(III) \cdots N/C = 3.47(5) \text{ \AA}], [D_2(III) \cdots N/C = 3.59(3) \text{ \AA}],$ and $[D_2(III) \cdots C = 3.62(4) \text{ \AA}]$. A similar position has previously been observed for Cu-BTT and Fe-BTT.²⁶⁵ This adsorption site is not visible in diffraction data collected at 0.36 D_2/Cu^{2+} loading, but is almost fully occupied at the 3.11 D_2 per Cu^{2+} loading.

The quaternary adsorption site in Cu-BTTRI is located in the large pore of the framework facing the benzene rings with an approximate distance of 3 \AA from the plane of the benzene rings. This site has an occupancy of 0.19(2) D_2 .

Interestingly, it can be concluded that there are overlapping potential energy fields, which strongly influence the total binding energy of the hydrogen adsorption sites in Cu-BTTRI. For the gases with permanent multipoles, such as CO₂, binding energy can often be defined largely by one key electrostatic interaction, and hence can vary significantly upon modifying the metal identity for instance.³²³ However, if the metal cluster is kept the same, the interaction energy between CO₂ and the framework do not often vary to a large extent upon varying ligands and pore geometry.³⁴⁷⁻³⁴⁸ For molecules without permanent multipoles, the multiplicity of the interactions is a governing factor that causes the formation of adsorption sites in particular regions of the host structure. Moreover, secondary van der Waals interactions are often comparable to the electrostatic interaction between the guest and host, and as in this case, can be used to compensate for decreases in Lewis acidity of metal sites. The multiplicity of weak van der Waals interactions and their influence on adsorption sites has also previously been reported for other gases with no dipole or quadrupole moment, like xenon and krypton.³⁴⁹⁻³⁵¹

Table 3-1 Experimental and computed data for D₂ adsorption sites in Cu-BTTRI framework.

	Overall	Site I		Site II		Site III		Site IV	
	-Q _{st} (kJ/mol)	-H ₂ (kJ/mol)	Cu-D(H)	D(H)-N	-H ₂ (kJ/mol)	D(H)-H	-H ₂ (kJ/mol)	D(H)-N	-H ₂ (kJ/mol) D-benzene
Experimental	10.5	-	2.73(4)	3.34 (5)	-	2.67(9)	-	3.33(4)	- ≈ 3 Å
DFT	-	10.0	2.65	3.14	3.0	2.87	4.9	3.1	3.0 ≈ 3 Å

The location of sites II-IV were also studied by means of DFT calculations. The shortest D₂-framework distances obtained computationally and experimentally are shown in Table 3-1. The DFT methods reveal only slightly elongated distances, up to ~0.2 Å, when compared to the experimental results. This work confirms the validity of the chosen computational method in the accurate prediction of secondary binding sites.

In order to gather further insight into the D₂ binding energies PBE-D2 DFT calculations were performed. For this, the bare Cu-BTTRI and the D₂ molecule were allowed to relax, while the cell parameters were kept constant. The energy of the resulting relaxed structures was computed by a single point calculation, and the binding energies were then extracted as follows:

$$E_{\text{binding}} = E_{\text{CuBTTRI}+\text{D}_2} - E_{\text{CuBTTRI}} - E_{\text{D}_2} \quad \text{Eq. (3 - 1)}$$

The resulting values are shown in Table 3-1. Note that even though we present positive values for convention, the DFT results were in fact negative, which indicates the stability of the complex with respect to the Cu-BTTRI and D₂ alone. The value obtained for the primary adsorption site, D₂(I), is 10 kJ/mol, and is in excellent agreement with the experimental zero coverage isotheric heat of adsorption, 10.5 kJ/mol. These observations validate the DFT method employed in this study, and previous studies of Poloni et al¹⁶⁴, which utilized the same method to predict the nature of CO₂ binding in the isostructural series of M-BTT MOFs. The overall binding energy for the three secondary sites is smaller than D₂(I), which is consistent with the observations made from the diffraction data, which reveals that site I is predominately occupied first.

The calculated binding energies for sites I-IV are also listed in Table 3-1. Based on the observed occupancies in the diffraction data, we predict the following trend in binding energies: $D_2(I) > D_2(II) > D_2(III) > D_2(IV)$; however, it is noted that the DFT results imply that $D_2(III) > D_2(II)$. This is likely because the calculations only take into account D_2 -framework interactions, excluding any intermolecular interactions between neighboring D_2 molecules. As such, it is thought that site II is further stabilized by the primary adsorption site increasing the actual binding energy of $D_2(II)$ compared to that predicted by DFT. Despite this, the calculated binding energies can also help justify the relatively sharp drop in the isosteric heat of adsorption plotted as a function of D_2 loading, Figure 3-2b. While an energy difference as small as ≈ 3 kJ/mol is sufficient to cause a sequential occupation of adsorption sites at 10 K, at higher temperatures, where adsorption isotherms are collected, it is likely that multiple sites are simultaneously populated.³²³

In order to obtain more detailed insight into the nature of the interactions, we also computed the charge density difference induced by D_2 binding in each adsorption site. For this, we took the sum of the self-consistent densities for the empty Cu-BTTRI framework and an isolated D_2 molecule and then subtracted that from the self-consistent density for the Cu-BTTRI+ D_2 . Plots for two isosurfaces representing the charge density differences are shown in Figure S3-14, which shows that in all sites the charge density of the molecule becomes polarized by the interactions with the framework. Furthermore, for $D_2(I)$, the interaction mostly occurs through the polarization of the open metal site, as is expected. For $D_2(II)$, the imidazole and phenyl moieties of the framework are both polarized, and for $D_2(III)$ the main component of the density distortion involves the imidazole moiety. Finally, for $D_2(IV)$ the charge density difference reveals a sigma-pi interaction between the molecule and the phenyl ring. These observations corroborate what was discussed above based on the distances obtained by Rietveld analyses. While charge density differences give an indication of the parts of the framework that are most perturbed by the interaction with the D_2 molecule, they do not necessarily directly indicate the sign and magnitude of the interactions. Given this, decomposition of the binding energies into the contribution given by the PBE functional (which includes electrostatics and short-range exchange-correlation effects) and those given by the van der Waals interactions, were additionally computed using the Grimme-D2 method, Table 3-2.

Table 3-2- Contributions to the binding energies for all adsorption sites

Site No.	E_{PBE} (kJ/mol)	$E_{\text{Dispersion-D2}}$ (kJ/mol)
1	-0.490	-9.516
2	-0.064	-2.905
3	-0.185	-4.677
4	1.116	-4.152

Even though the E_{PBE} is the most stabilizing for $\text{D}_2(\text{I})$, relative to the others, this decomposition suggests that the van der Waals interactions are the dominant factors in the D_2 -CuBTTri binding, and determine both the ordering and the overall magnitude of the binding energies. This observation is consistent with the low quadrupole moment of the D_2 molecule, $\Theta_{zz} = 0.39$,³⁵² and sheds light into the seemingly counter-intuitive observation that the overall experimental zero coverage isosteric heat of adsorption for Cu-BTTri is slightly larger than that observed for Cu-BTT (10.5 versus 9.5 kJ/mol, respectively) despite that the latter has a stronger Lewis acid site. Interestingly, the other M-BTT frameworks, including Fe-BTT, Cr-BTT and Mn-BTT, also show similarities in the isosteric heat of adsorption for the primary adsorption site, ranging from 10.0 to 11.9 kJ/mol. The small effect of metal substitution on the binding energy of the first adsorption site in the M-BTT family is also indicative of the strong role that the van der Waals interactions play at the primary adsorption site.

3.4 Conclusions

In this work, we have demonstrated the importance of using *in-situ* diffraction techniques to gain intimate insight into small molecule binding in MOFs. We have shown an accurate structure for Cu-BTTri, which is a critical element required should computational methods be employed to screen this MOF for targeted applications. We have also identified the location of four D_2 adsorption sites in Cu-BTTri and compared our results to those previously reported for a ligand substituted counterpart, Cu-BTT. We show that the DFT method used in this work successfully models hydrogen adsorption sites with minimal deviation from the experimental results. The validation of this computational approach opens the door to predict the adsorption behaviour of existing and even hypothetical MOFs.

The identification of the adsorption sites has provided critical insight into the relative impact that different structural elements have on the observed hydrogen adsorption properties of Cu-BTTri. The roles that the open metal site and other secondary van der Waals interactions, like hydrogen-hydrogen interactions, play in the adsorption properties has been assessed using the results of diffraction experiments, and confirmed computationally by an energy-decomposition analysis. We emphasize the contribution by van der Waals interactions plays a crucial role in determining the binding energy, and the ranking of different sites. This critical insight could lead to methods to enhance H_2 binding energies towards those required for room temperature storage (>15 kJ/mol).³²⁴

Chapter 4

Understanding how ligand functionalization influences CO₂ and N₂ adsorption in a sodalite MOF⁴

4.1 Introduction

Since the industrial revolution, the combustion of carbon based fuels has led to a significant rise in atmospheric CO₂ levels, one of the main causes of global warming.³⁵³ During the last few years, the concentration of atmospheric CO₂ has surpassed a record value of 400 ppm.³⁵⁴ This, combined with a slow transition to clean, renewable energy sources, has brought a sense of urgency towards the design of new porous solid adsorbents^{62, 76, 355-356} able to capture CO₂ from a variety of gas mixtures, such as post-combustion flue gas.²⁰

One possible solution to this problem, is the use of membranes based on a class of porous crystalline materials known as Metal Organic Frameworks (MOFs), which consist of metal-ions or metal-ion clusters that are interlinked by organic ligands. These unique materials offer unprecedented internal surface area and easy chemical tunability, allowing chemists to readily adjust their adsorption properties.^{62, 282, 305, 314} Due to the presence of metal

⁴ This chapter is based on the written article: " Understanding how ligand functionalization influences CO₂ and N₂ adsorption in a sodalite MOF." Mehrdad Asgari, Rocio Semino, Pascal Schouwink, Ilia Kochetygov, Jacob D. Tarver, Olga Trukhina, Rajamani Krishna, Craig M. Brown, Michelle Ceriotti, and Wendy Queen To be submitted, 2019. M. A. has synthesized the material, performed the experiments, analyzed the data and written the paper.

ions, and of molecular building blocks that exhibit multiple chemical moieties, the potential energy surface for a guest molecule within a MOF cavity possesses multiple minima, that correspond to well-defined interaction sites with different adsorption energies.³⁵⁷ Considering this, these materials offer a unique opportunity to gain direct insight into their structure-derived function using X-ray and neutron diffraction techniques. Such insights would make it possible to pinpoint the structural features that enhance or diminish the adsorption properties. Diffraction data provides direct insight into binding mechanisms, reveals the relative differences in binding energies between neighboring adsorption sites, and delivers understanding of how the local framework structure changes as a function of external stimuli, such as temperature or pressure. Further, such data can be additionally employed to validate computational methods meant to predict the structural features and the properties associated with host-guest interactions.⁶ This validation process is necessary for the eventual deployment of simulation tools that can accurately predict the adsorption properties of hypothetical MOF structures, a process that might allow for the rapid identification of target materials having optimal properties for important gas separations, such as CO₂ capture. Once validated, simulations provide further insight into the nature of the host-guest interactions.

MOFs bearing azole containing ligands are becoming increasingly prevalent in the literature.³⁵⁸⁻³⁵⁹ Their popularity is associated with strong metal-nitrogen bonds, a phenomenon that often leads to higher chemical and thermal stability when compared to their carboxylate counterparts.^{139, 360} One prevalent example of a family of azole frameworks is M-BTT (M = Mg, Ca, Ti, V, Cr, Mn, Fe, Co, Ni, Cu, and Zn; BTT³⁻ = 1,3,5-benzenetristetrazolate), which has the following general formula: $[(M_4Cl_x)_3(BTT)_8]^{y-}$ (x=0 or 1; y=0 or -3).³²³ The MOF features truncated, octahedral cages constructed by six $[M_4Cl_x]^{(8-x)+}$ units and eight $[BTT]^{3-}$ ligands that are interlinked to form a porous, three-dimensional sodalite-based network. In addition to their high stability, this family of frameworks possesses a high density of open metal coordination sites (OMCs), which are capable of forming strong interactions with small molecules such as CO₂; thus, the adsorption properties of the framework are readily modified by altering the metal identity. Given this, in previous work, we employed *in situ* diffraction techniques, combined with density functional theory to rationalize how metal-substitution influences the CO₂ adsorption properties of several isostructural M-BTT (M = Fe, Mn, Cu, Cr) frameworks.³²³ In addition to varying metals, the tetrazole ligand can also be replaced with a triazole or pyrazole (BTT³⁻ vs BTTri³⁻ = 1,3,5-benzenetristriazole or BTP³⁻ = 1,3,5-benzenetrispyrazolate) forming similar sodalite architectures;^{139, 220, 323, 325-326} however, the resulting materials show dissimilar adsorption properties, due to the distinct structural features that are induced by the ligand selection. Given that the aforementioned sodalite MOFs can undergo extensive chemical substitution and often exhibit exceptional crystallinity, they are interesting cases for *in situ* diffraction studies.¹³⁹ We have previously shown that the substitution of the BTT³⁻ ligand with BTTri³⁻ causes a change in the structure of the metal cluster and the framework charge, and eliminates the existence of charge-balancing cations and anions in the channel of Cu-BTTri.³⁶¹ In the current work, we extend this study to unveil how ligand substitution influences the CO₂ and N₂ adsorption properties of Cu-BTTri

compared to Cu-BTT. For this, both single component N₂ and CO₂ adsorption isotherms and *in situ* diffraction techniques, coupled with DFT calculations are used. The diffraction results unveil the structures of the CO₂ and N₂ adsorbed Cu-BTTri framework, providing molecular level insight into how the presence of the triazole influences the CO₂ adsorption isotherms. The characterization of the structure and adsorption properties of the different sites can be used to validate a computational framework aimed at predicting the structures and CO₂ adsorption properties of MOFs, which can then be used to extract analytical insights on the adsorbate-framework interactions. Finally, transient breakthrough simulations are used to provide insight into the performance of the Cu-BTT and Cu-BTTri for CO₂/N₂ separation under dry, post-combustion flue gas conditions. This work links the structural parameters of two Cu-containing frameworks to the CO₂ and N₂ adsorption properties, which influence the materials overall performance for post-combustion flue gas separations. This structure-property rationalization is very much sought after to design MOFs that are tailored for such separations.

4.2 Experimental section

4.2.1 Synthesis of Cu-BTTri

The H₃BTTri ligand was first synthesized following a procedure that was reported previously in the literature.¹³⁹ Subsequently, Cu-BTTri was synthesized, solvent exchanged and activated following a procedure reported previously by us.³⁶¹

4.2.2 Standard adsorption isotherm measurements

For gas adsorption isotherms, UHP-grade (99.999% purity) helium, nitrogen, and carbon dioxide were used for all measurements at pressures that ranged from 0 to 1 bar using a commercial BELSORP-max instrument. The sample was transferred to pre-weighed analysis tubes that were capped with a Transeal. The sample was first evacuated on the activation station based on the program described in the literature.¹³⁹ The evacuated analysis tube containing the sample was then carefully transferred to an electronic balance and reweighed to determine the mass of the activated sample (typically ranging 50 mg – 200 mg). Then, the tube was transferred to the BELSORP-max. N₂ adsorption isotherms were collected at 77 K and BET surface areas and pore volumes were calculated assuming a value of 16.2 Å² for the molecular cross-sectional area of N₂. In addition, N₂ adsorption isotherms were measured at temperatures ranging from 278-298 K. For CO₂, standard adsorption isotherms were measured using a commercial water bath dewar vessel connected to a Julabo F32-MC isothermal bath at temperatures ranging from 278-318 K.

4.2.3 In situ neutron diffraction

High-resolution neutron powder diffraction (NPD) experiments were carried out on the Cu-BTTri sample using BT1 at the National Institute of Standards and Technology (NIST) Center for Neutron Research (NCNR). All measurements were carried out on activated samples of ≈ 0.8 g. At NIST, the sample was first activated via heating under dynamic vacuum

at 450 K and then transferred into a He purged glove-box, loaded into a vanadium can equipped with a gas loading valve, and sealed using an indium O-ring. NPD data were collected using a Ge(311) monochromator with an in-pile 60 collimator corresponding to a wavelength of 2.0728 Å. The sample was loaded onto a closed cycle refrigerator (CCR) and then data was collected at 10 K. After data collection on the activated framework, CO₂ and N₂ with different dosing levels were then loaded into the pores. The dosing levels used for CO₂ include 0.40, 1.25, and 1.60 CO₂ per Cu²⁺, while for N₂ the loading levels were 0.33 and 2.19 N₂ per Cu²⁺. For data collection, the samples were first exposed to a pre-determined amount of gas at room temperature. Upon reaching an equilibrium pressure, the sample was then slowly cooled (1 K per minute) to ensure complete adsorption of the CO₂ and N₂, and then data was recollected at 10 K. The resulting diffraction patterns were assessed via Le Bail and subsequent Rietveld analysis. To locate the CO₂ or N₂ molecules, Fourier difference maps were used to unveil excess scattering density in the MOF channels.

4.2.4 *In situ* synchrotron X-ray diffraction

Bare and CO₂-loaded Cu-BTTri samples were measured at the Swiss-Norwegian Beamline (SNBL, BM01) at the European Synchrotron Radiation Facility (ESRF) in Grenoble, France. A custom-built *in situ* diffraction powder cell was designed to mount directly on the goniometer head. Before the measurements, a sample of Cu-BTTri was activated at 180 °C for 24 hours. Then, both the sample and the *in situ* powder cell were placed into an Ar-filled glove box. Afterwards, a capillary was loaded with 2 mg of activated sample that was attached directly to the *in situ* cell, and then sealed using a valve. The *in situ* cell was subsequently removed from the glove box and mounted on the goniometer head for data collection ranging from 190 K to 290 K. An Oxford Cryostream 700 with working temperature of 80-500 K was used to maintain the desired temperature. Data were collected using a DECTRIS PILATUS 2M detector and the wavelength was adjusted at 0.67522 Å. The sample to detector distance was set at 339 mm and the measurement time was varying between 20 s and 40 s. After data collection of the bare framework from 190 K to 290 K, the *in situ* cell was attached to a custom-built gas dosing manifold that is equipped with a turbo pump and pressure gauges. The Ar was evacuated from the cell, and next, the sample was dosed with 12.5 torr of CO₂ pressurized with He to the ambient pressure. The cooling rates in all experiments were 2 K per minute. The azimuthal integration of raw images was performed with the Bubble software.³⁶² Further, Le Bail analysis and Rietveld refinements of the acquired powder diffraction patterns were performed using TOPAS 5.³³⁰ The CIF files for the structure of the guest loaded frameworks based on the Rietveld analysis have been produced by Topas and uploaded to CCDC database. The table of the atomic parameters corresponding to the bare and loaded structures have been also attached to SI. It should be noted that, for the gas loaded structures, the standard deviation errors related to the occupancy of guest species have been produced based on the least squares matrix of Topas. While this is the standard procedure for the calculation of the errors associated with the occupancies in Rietveld analysis, the actual errors can deviate from the reported values.

Sequential Le Bail fitting and Rietveld analysis was carried out on the variable temperature X-ray diffraction data that ranged from 190 K to 290 K for the activated sample, and the samples dosed with CO₂ or N₂. After initial analysis on the data set collected at the lowest temperature (190 K), the crystal structure obtained from Rietveld refined was used as starting model for subsequent, sequential Le Bail/Rietveld analysis.

4.2.5 *Electronic structure simulation details*

Binding energies, structural details and charge distribution were obtained from DFT calculations, under the generalized gradient approximation by Perdew, Burke and Ernzerhof (PBE functional).³³² All calculations were performed by using the PWscf (Plane-Wave Self-Consistent Field) package from the Quantum Espresso³³³ suite of codes. We used the following ultra soft pseudopotentials³³⁴ extracted from <http://materialscloud.org/sssp> : Cu_pbe_v1.2.uspp.F.UPF, O_pbe_v1.2.uspp.F.UPF, C_pbe_v1.2.uspp.F.UPF, H.pbe-rrkjus_psl.0.1.UPF and N.pbe.theos.UPF. The former three were generated using Vanderbilt code³³⁵ and the latter two using the “atomic” code by A. Dal Corso.³³⁶ We employed kinetic energy cutoffs for wave functions and charge density and potential of 55 and 660 Ry respectively. All calculations were performed for the Γ point of the Brillouin zone, due to the large size of the MOF (228 atoms in the unit cell). Spin-polarized calculations were performed to take into account the most stable spin state for Cu-BTTri, which was found to be antiferromagnetic. Following previous work¹⁶⁴ where other chemically similar MOFs including Cu-BTT were studied, dispersion corrections were considered under the Grimme-D2 scheme.³³⁷ We also tested the Tkatchenko-Scheffler³⁶³ dispersion correction scheme, and the results were found to be in good agreement with those obtained by applying Grimme-D2 method (see Supporting Information).

We took as a starting point the experimental configuration for Cu-BTTri, and then allowed the nuclei to relax while keeping the cell parameters fixed to experimental values (tests allowing the cell parameters to change were also carried out and have shown very small changes of 1-3% in volume). Subsequently, several calculations were set, each of them containing one gas molecule adsorbed in a different site of the MOF. We took as initial configurations those found in the experiment and allowed atomic positions to relax, again without changing the cell parameters. Binding energies were computed as the difference between the energy of the MOF/gas binary complex and the sum of the energies of MOF and gas molecule.

4.3 Results and Discussion

4.3.1 Characterization of the Cu-BTTri framework

The Cu-BTTri framework was first synthesized using previously published procedures^{139, 361} and subsequently characterized via powder X-ray diffraction to confirm the sample purity. Synchrotron X-ray diffraction data (Figure S4-1) reveal up to a of 42° 2θ (wavelength 0.67522 \AA , $\approx 0.94 \text{ \AA}$ d-spacing) confirm that the sample has exceptional crystallinity, a prerequisite for *in situ* diffraction studies. The BET surface area and the pore volume for Cu-BTTri were calculated based on the nitrogen adsorption isotherm collected at 77 K (Figure S4-2) to be $1850 \text{ m}^2/\text{g}$ and $0.88 \text{ cm}^3/\text{g}$, which is consistent with the originally reported values for this material.¹³⁹

We recently determined that Cu-BTTri,³⁶¹ which crystallizes in a cubic *Fm-3c* space group (no. 226), has the following molecular formula: $\text{Cu}_3(\text{BTTri})_2$. The structure features square $[\text{Cu}_4]^{8+}$ clusters that are interlinked by triangular $[\text{BTTri}]^{3-}$ ligands to form a neutral sodalite-type framework. The structure does not fully replicate that of its ligand substituted counterpart, Cu-BTT²⁶⁴, nor the other metal substituted triazole analogs, such as Co-BTTri³²⁵ and Fe-BTTri³²⁶. Unlike these other sodalite MOFs, the Cu-BTTri structure has no chlorine at the center of the cluster. As such, the framework is neutral and hence is devoid of any extra-framework charge-balancing species inside the channel. When compared to Co- or Fe-BTTri, the difference can be justified by the stronger Jahn-Teller distortion for octahedral copper(II) complexes, which results in the elongation of the bonds in the *z*-direction. While in some cases this leads to the formation of distorted octahedral coordination environments³⁶⁴, in others it leads to a loss of *z*-bound ligands³⁶⁵⁻³⁶⁶ as is the case of Cu-BTTri. When compared to Cu-BTT, the lower basicity of the tetrazolate compared to the triazolate, likely helps to stabilize the presence of the Cl⁻ ligand. The pK_as of the triazole and tetrazole rings are approximately 13.93, and 8.23, respectively.³⁴³ The higher basicity of BTTri^{3-} implies it is also a stronger electron donor. Consequently, the Jahn-Teller effect is more pronounced for Cu-BTTri^{3-, 367} likely promoting the elimination of the chlorine in the center of square-like metal cluster. The higher ligand basicity not only influences the structural properties of the framework, it also enhances the chemical/thermal stability of Cu-BTTri over Cu-BTT, a direct result of the higher bond strength found between the Cu and the triazolate.¹³⁹

4.3.2 Standard adsorption isotherms and isosteric heat of adsorption for CO₂ and N₂

To assess the adsorption properties of Cu-BTTri, single component CO₂ adsorption isotherms were collected up to 1 bar and at temperatures ranging from 278 K to 318 K , Figure 4-1a. Interestingly, the isotherm does not exhibit a steep slope in the low-pressure regime, in contrast to what is normally observed for other MOFs having OMCs, such as M-BTT frameworks (Figure S4-3).³²³ This is likely indicative of a low zero-coverage isosteric heat of CO₂ adsorption, which was extracted from the variable temperature data using a Dual Site

Langmuir Model, followed by fitting with the Clasius-Clapeyron equation (Figure 4-1b, S4-4, and S4-5). The zero-coverage isosteric heat was determined to be 21.7 kJ/mol for Cu-BTTri, which is significantly lower than the value previously reported for Cu-BTT, 30.7 kJ/mol.³²³ This observation is not surprising, considering that BTTri is a stronger electron donor, which likely decreases the frameworks affinity for CO₂ due to Jahn-Teller effect enhancement. It is noted that, as the CO₂ loading increases in Cu-BTTri, the isosteric heat is relatively flat. This suggests that there are other, secondary adsorption sites, which have similar isosteric heats. Further, as the pressure is increased, the interactions between neighboring CO₂ could further promote an increase in the average binding energy at constant coverage.

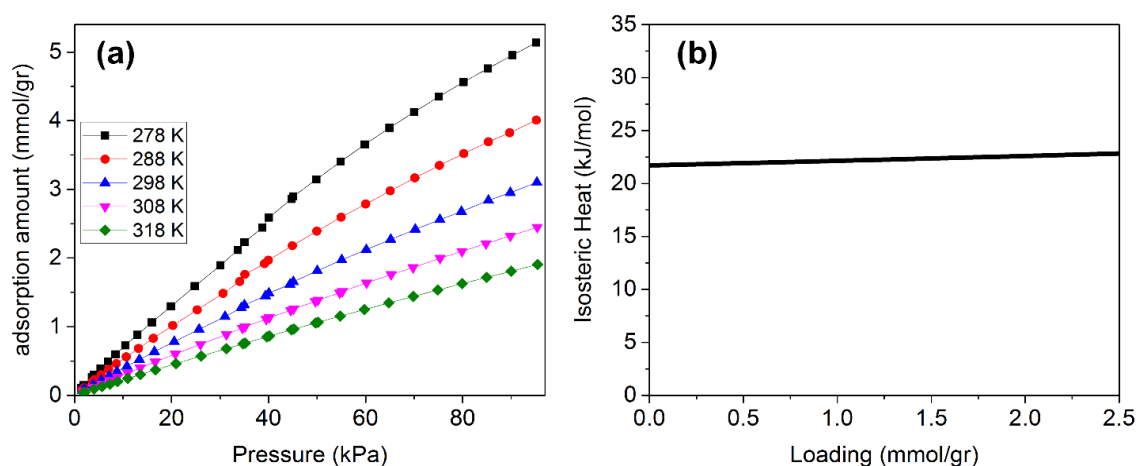


Figure 4-1 (a) The measured CO₂ adsorption isotherms for Cu-BTTri at different temperatures. (b) Calculated isosteric heat of CO₂ adsorption for Cu-BTTri

Nitrogen adsorption isotherms were also collected for Cu-BTTri (Figure S4-6) at temperatures ranging from 278 to 298 K. As expected, the amount of N₂ adsorbed in the framework is significantly less than that of CO₂, because of the lower quadrupole moment and polarizability of the N₂ compared to CO₂.³⁰⁵ The weaker interaction of N₂ with the framework is further supported by the low zero-coverage isosteric heat of N₂ adsorption, which is 12 kJ/mol (Figure S4-7). Further, when comparing the N₂ adsorption properties of Cu-BTTri and Cu-BTT at 298 K, (Figure S4-8) the triazole offers a lower total N₂ uptake. As such, the selectivity factors were calculated from isotherms collected at 298 K to be 27.8 and 20.8 for Cu-BTT and Cu-BTTri, respectively. The selectivity factor is the ratio of the quantity of CO₂ adsorbed at 0.15 bar / the quantity of N₂ adsorbed at 0.85 bar, normalized by the concentrations of both adsorbents. The chosen pressure points (0.15 bar for CO₂ and 0.85 bar for N₂) are those relevant to post-combustion flue gas capture. While Cu-BTTri offers a higher CO₂/N₂ selectivity, Cu-BTT offers an overall higher CO₂ capacity, leaving questions as to which of these frameworks would effectively perform better in a post-combustion capture process.

4.3.3 The location of adsorption sites for CO₂ and N₂

To obtain molecular level insight into CO₂ and N₂ adsorption, neutron and synchrotron X-ray powder diffraction data were collected on the activated Cu-BTTri and then again on the sample dosed with various amounts of CO₂- 0.40, 1.25, and 1.60 CO₂ per Cu²⁺. The location and orientation of CO₂ and N₂ molecules were determined via Rietveld analysis followed by subsequent Fourier difference analysis. A total of four CO₂ adsorption sites were observed inside Cu-BTTri, which are outlined in Figure 4-2. Fractional atomic coordinates, occupancies, and isotropic displacement parameters for all adsorption sites are reported in Tables S4-6 to S4-8, and then a comparison of experimental and computationally obtained binding energies and shortest framework distances are shown in Table S4-3.

The first identified CO₂ adsorption site, I, is found as expected at the OMC, Cu²⁺. The occupancies of this adsorption site are 0.21(2), 0.74(2), and 0.82(2) for loadings of 0.40, 1.25, and 1.60 CO₂ per Cu²⁺, respectively. (CO₂)O ... Cu²⁺ distances range from 2.7(1) Å to 2.96(8) Å, depending on the CO₂ loading level (Figure 4-2). This results in a distance of 3.63(7) Å between the nitrogen atom of the triazole ring and the carbon atom of the CO₂. For Cu-BTT, the distance of CO₂ to the OMC was previously reported by us to be 2.60(3) Å at a loading level of 1.56 CO₂ per Cu²⁺;³²³ this value is considerably shorter than the corresponding distance in Cu-BTTri, a direct result of the weaker electrostatic interaction between the metal site and the adsorbed CO₂ molecules (Figure S4-9). This weaker interaction is due to the reduced bonding affinity of the Cu²⁺ sites in the axial direction as a result of the more pronounced Jahn-Teller effect in Cu-BTTri compared to Cu-BTT.^{164, 262}

In order to obtain further insight into the mechanism of host-guest interactions in this framework, we took advantage of the theoretical support provided by DFT calculations. Firstly, the bare Cu-BTTri and the CO₂ molecules were allowed to relax, while the cell parameters were kept constant (see the section on Electronic structure simulation details, and the SI). The distance between the OMC and CO₂ for the computationally simulated site I is 2.96 Å, which matches well with the experimentally obtained value (Table S4-3). Moreover, the energy of the resulting relaxed structures was computed by a single point calculation, and the binding energies were then extracted as follows (Table S4-3):

$$E_{\text{binding}} = E_{\text{Cu-BTTri+CO}_2} - E_{\text{Cu-BTTri}} - E_{\text{CO}_2} \quad \text{Eq. (4 - 1)}$$

The calculated binding energy of site I is estimated to be -25.0 kJ/mol, which matches well with the aforementioned measured zero-coverage isosteric heat of adsorption, 22 kJ/mol. To unveil the main interactions responsible for the adsorption of CO₂, the charge density difference induced by CO₂ binding was also computed. For this, the sum of the self-consistent densities for the empty Cu-BTTri framework and an isolated CO₂ molecule were first determined and then subsequently subtracted from the self-consistent density for Cu-BTTri+CO₂ binary complex. Plots for two isosurfaces representing the charge density differences are shown in Figure S4-10. Based on the plot (Figure S4-10a) for site I, the main interactions responsible for the CO₂ binding predominantly originate from the OMC, while

secondary interactions take place with the nitrogen atoms in the triazole ring. The charge density differences provide a qualitative indication of the perturbations induced by the CO₂ molecule on the framework, but they do not necessarily indicate the sign and magnitude of the interactions. Therefore, to better understand the mechanism of host-guest interactions at different adsorption sites, decomposition of the binding energies into different contributions was carried out using the PBE functional; the results include electrostatics and short-range exchange-correlation effects. Further, the contributions dictated by van der Waals interactions, were additionally computed using the Grimme-D2 method, Table S4-4. For the primary adsorption site, the binding energy at the DFT-PBE level is calculated to be -7.4 kJ/mol, while van der Waals forces contribute a further -17.6 kJ/mol to the binding energy. Based on these results, it can be concluded that the van der Waals contribution is dominating.

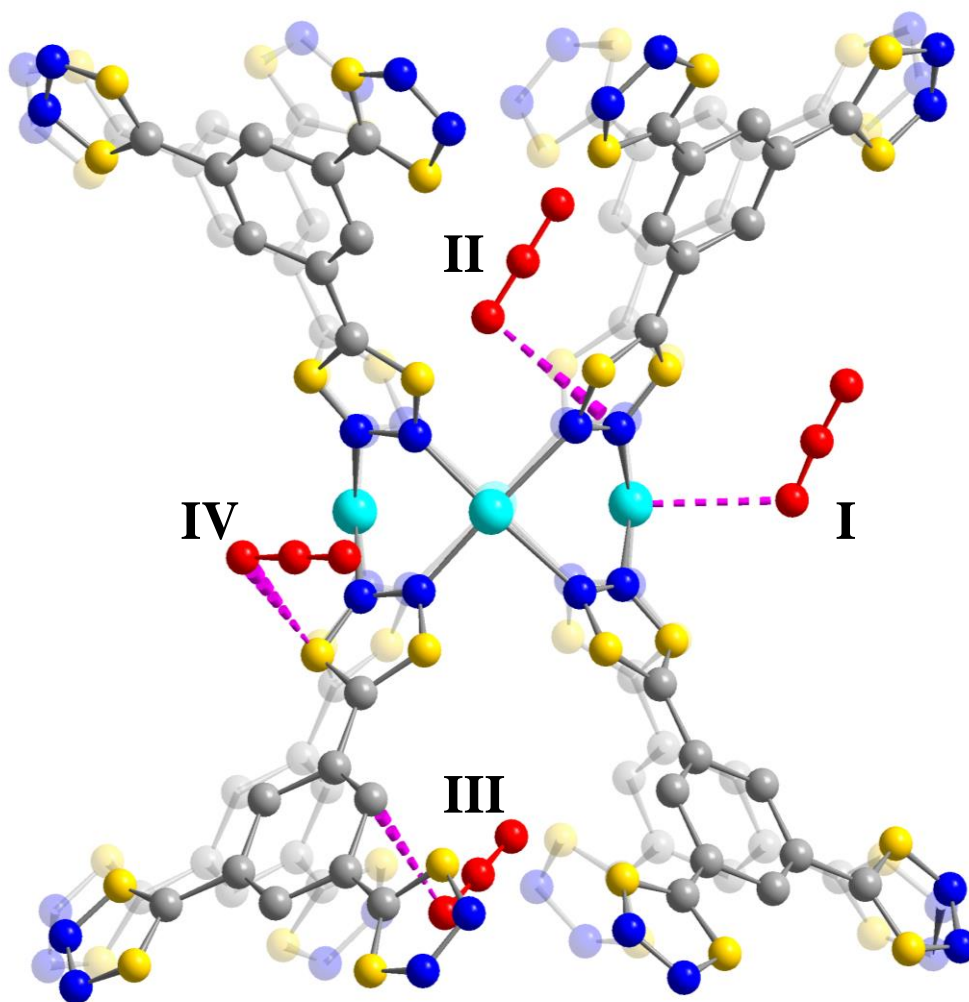


Figure 4-2 Ball and stick model of the Cu-BTTri framework dosed with 1.60 CO₂ per Cu²⁺. The adsorbed CO₂ molecules have been shown with the red color. The Cu, C, N, are denoted as cyan, grey, and blue spheres, respectively. Hydrogen atoms have been excluded for the sake of clarity. Yellow spheres represent mixed sites containing both C and N. The pink dotted lines represent nearest neighbor interactions.

Most probably, the combination of the strong electron donating ligands to the Cu^{2+} OMC lends to a considerably reduced electrostatic affinity towards the guest species when compared to Cu-BTT.^{164, 323} For other MOFs with OMCs, like HKUST-1 and MOF-74, contributions to CO_2 binding are mainly attributed to strong electrostatic interactions.¹¹⁸ For Cu-BTTri, the highly electron donating ligand can reduce the charge, and hence electrostatic contribution at the OMC.³⁶¹ It is noted that while vdW interactions are the dominant force found in Cu-BTTri, electrostatic interactions, and other terms that are well-described at the DFT-PBE level, play an important role towards the overall binding energy.

The second CO_2 adsorption site, II, located just above the metal cluster (Figure 4-2), is disordered around the 4-fold rotation axis that passes through the center of the square-like metal cluster; this static disorder is dictated by vdW interactions between this CO_2 and the ligand. The shortest distance is 3.27(4) Å, which is found between the oxygen atom of the CO_2 molecule and the nitrogen atom on the triazole ring. Within error of the experimental data, the DFT-based simulations provide a secondary adsorption site that is nearly identical to site II. The shortest framework- CO_2 distance is approximately 3.16 Å. Like site I, site II can be observed in all refined structures regardless of the CO_2 loading. The occupation of this adsorption site ranges from 0.101(6) at the loading of 0.40 CO_2 per Cu^{2+} and reaches a value of 0.67(3) at the highest loading of 1.60 CO_2 per Cu^{2+} . The fact that the occupancies for site I and II are similar indicates that the enthalpy of adsorption for these sites are also comparable, a hypothesis that is further supported by the linear isosteric heat of CO_2 adsorption obtained from Cu-BTTri (Figure 4-1b). This is confirmed by DFT calculations that yield a value of -26.5 kJ/mol for the isosteric heat of adsorption of site II, which is only 1.5 kJ/mol higher than that of site I (Table S4-3). The isosurface plot for site II confirms the interaction between the electron-rich triazole groups with the CO_2 molecule. Moreover, DFT calculations show that binding in this site is entirely due to strong vdW interactions ($E_{\text{Dispersion-D2}} = -30.3$ kJ/mol), with a repulsive interaction between the host framework and the adsorbed CO_2 at the DFT-PBE level ($E_{\text{PBE}} = +3.8$ kJ/mole, see Table S4-4). This can probably be explained by electrostatics, because both moieties, including the triazole rings and oxygen atom of the carbon dioxide molecule have a surplus of partial negative charge.

The third CO_2 adsorption site, site III, is located nearest to the benzene rings on the ligand (see Figure 4-2).³²³ The main mechanism for the stabilization of this adsorption site is through vdW interactions between the oxygen atom of the CO_2 with the carbon atoms of the benzene ring. The shortest framework distance for site III is 2.8(1) Å, which is similar to other vdW interactions found between CO_2 and other MOFs.^{143, 368-369} DFT calculations have also successfully modeled this adsorption site and predicted its binding energy to be -17.0 kJ/mol, which is lower than those calculated for site II (Table S4-4). This observed drop in binding energy is consistent with the observation that the relative occupancy of site II is significantly lower than site I and II at all CO_2 loadings evaluated. For example, at the highest loading, 1.60 CO_2 per Cu^{2+} , the occupancy of site III is 0.124(8), while site I and II are 0.82(2) and 0.67(3), respectively. Despite the lower predicted binding energy of site III, the simulated site III

binding energy might not be precise, because the DFT calculations do not take intermolecular CO₂-CO₂ interactions into account in this work. The shortest contact distance for site III is approximately 3 Å from site II CO₂ and hence, this likely implies that the adsorption is further stabilized by intermolecular CO₂(II)-CO₂(III) interactions. The importance of these intermolecular interactions also explains the very low occupancy of site III at lower CO₂ loadings. It should be noted that, unlike site I and II, there are more pronounced differences between the experimental and DFT determined location of site III CO₂ (see Table S4-3), which can be also attributed to the fact that only a single adsorbed CO₂ molecule is considered in the computational model.

The fourth adsorption site, IV, was found inside the large pore of Cu-BTTri, at the same location where the extra cations and anions were previously observed in Cu-BTT (Figure 4-2).³²³ Site IV is in close proximity to the triazole ring, with the shortest framework-CO₂ distance equal to 3.02(9) Å. This adsorption site has additional interactions with other atoms of the triazole ring with distances that range from 3-3.5 Å. The DFT-determined binding energy for site IV is -15.8 kJ/mol, is almost entirely due to vdW interactions ($E_{\text{Dispersion-D2}} = -15.8$ kJ/mol and $E_{\text{PBE}} = +0.05$ kJ/mol). The latter results from a minimal interaction with the Cu²⁺, with a distance of approximately 4.6 Å from the OMC. This is no surprise given the long distance combined with the considerably low Lewis acidity of Cu²⁺ in this structure.

In order to further understand the performance of the material for CO₂/N₂ separations in Cu-BTTri, the N₂ adsorption sites were also determined via Rietveld analysis of neutron diffraction data dosed with the 0.33 and 2.19 N₂ per Cu²⁺. This analysis has led to the elucidation of 6 adsorption sites, I-VI, Figure 4-3.

The first N₂ adsorption site is found at the OMC, with a Cu²⁺-N₂ distance of 2.74(5) Å (Figure 4-3). The occupancy of N₂ at this adsorption site is 0.145(7) and 0.326(8) at loadings of 0.33 and 2.19 N₂ per Cu²⁺, respectively. The binding energy for this adsorption site is calculated to be -11.9 kJ/mol, which is in excellent agreement with the zero-coverage isosteric heat of adsorption ($Q_{\text{st}} = 11.9$ kJ/mol) obtained from variable temperature N₂ adsorption isotherms collected from 278 K to 298 K. The contribution of vdW and DFT-PBE terms have been calculated to be -9.9 kJ/mol and -2.0 kJ/mol, respectively.

The energy decomposition based on DFT+vdW calculations can help understand better the role of the physicochemical properties of the adsorbate on the nature and extent of the host-guest interaction. While the DFT-PBE baseline involves many other terms, e.g. Pauli repulsion, exchange-correlation energy, it largely reflects electrostatic interactions between the adsorbate and the framework. For instance, in our previous work,³⁶¹ we demonstrated that DFT-PBE interactions between the OMC and D₂ molecule are responsible for less than 5% of the total binding energy, while herein this share is calculated to be approximately 17% and 31% for N₂ and CO₂, respectively (table S4-4 and S4-5). The electrostatic nature of these interactions is consistent with the relation between their magnitude, and that of the adsorbate's permanent multipoles.³⁶¹ For example, CO₂, N₂, and H₂ have quadrupole moments of 43.0*10⁻²⁷ esu⁻¹.cm⁻¹, 15.2*10⁻²⁷ esu⁻¹.cm⁻¹, and 6.6*10⁻²⁷ esu⁻¹.cm⁻¹, respectively,³⁰⁵ that

follow the same trend as the DFT-PBE binding energies of CO₂, N₂, and H₂, i.e. -7.41 kJ/mol, -1.98 kJ/mol, and -0.49 kJ/mol, respectively. For the gases with stronger permanent multipoles, tuning the charge in the framework wall can have a larger impact in the adsorption properties, while for those with weaker or no permanent multipole, the vdW interaction tends to dominate.³⁶¹ Understanding this relationship can provide insight into how to alter the structural features to optimize the adsorbate's physicochemical properties for different separations.

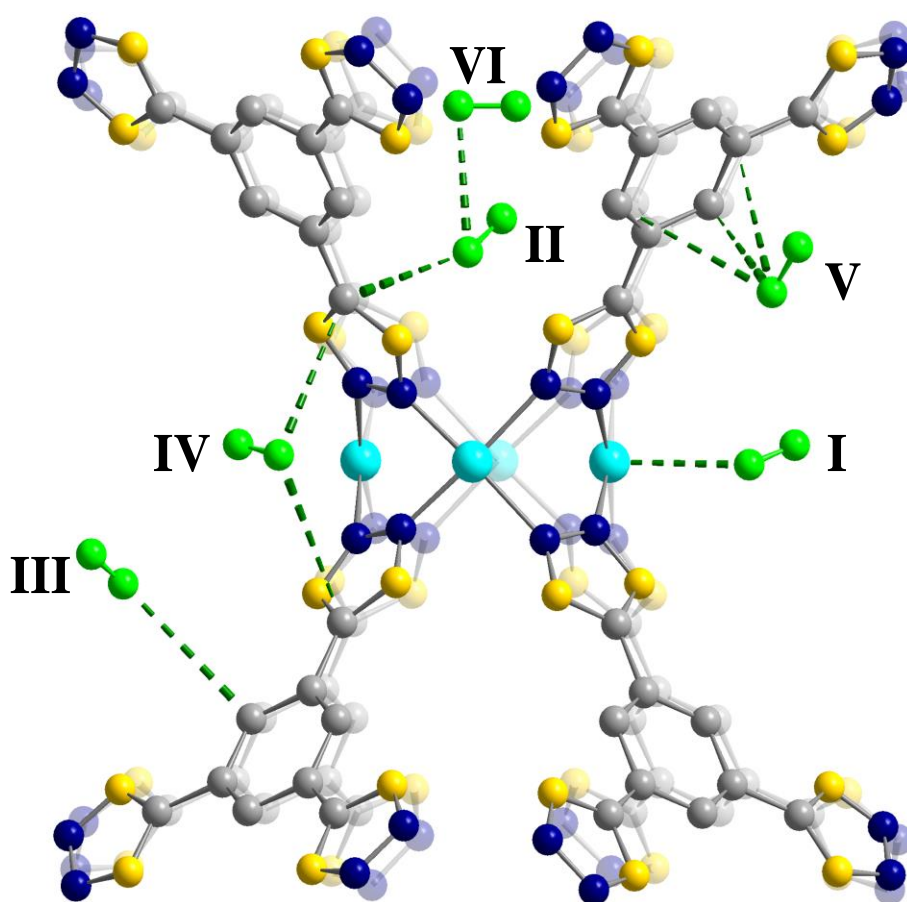


Figure 4-3 Ball and stick model of the Cu-BTTri framework dosed with 2.19 N₂/Cu²⁺. The adsorbed N₂ molecules depicted in green. The Cu, C, N, are denoted as cyan, grey, and blue spheres, respectively. Hydrogen atoms are excluded for the sake of clarity. Yellow spheres represent atomic sites that are mixed with both C and N. The green dotted lines represent nearest neighbor interactions, and have distances ranging from 2.74(5) Å to 3.67(5) Å.

The second N₂ adsorption site, II, is located just above the Cu₄⁸⁺ cluster, albeit slightly farther away from the cluster than observed for CO₂ (Figure 4-3). Like site I, site II N₂ can be detected in the data obtained from 0.33 and 2.19 N₂ per Cu²⁺ loadings with occupancies of 0.020(4), and 0.149(8), respectively. The shortest framework distance for this adsorption site, i.e. the C-N distance, is 3.21(9) Å, (Figure 4-3). This predominantly vdW interaction is further

corroborated by the calculated shares of vdW and DFT-PBE interactions as well as the charge difference isosurfaces plot (Table S4-5 and Figure S4-11). The other four N_2 adsorption sites, III to VI, only appear in the diffraction data collected at the highest N_2 loading, 2.19 N_2 per Cu^{2+} . These sites have occupancies ranging from 0.296(9) to 0.020(5) and all exhibit N_2 -framework distances greater than 3 Å with DFT calculated binding energies that range from -4.5 kJ/mol to -7.1 kJ/mol. While site VI is not found in close proximity to the framework wall, N_2 - N_2 intermolecular interactions with molecules in site II likely stabilize the last adsorption site.

Based on the above information, we can better explain the reduced N_2 adsorption of Cu-BTTri compared to Cu-BTT. By looking at the location of adsorbed N_2 molecules in the framework, we can see that all of the adsorption sites other than the first and sixth adsorption sites, are mainly interacting with carbon atoms in the ligand of Cu-BTTri. This means that the presence of the carbon atoms in the structure can be potentially effective for the adsorption of nitrogen. However, in spite of the higher carbon content of BTTri ligand compared to BTT, the nitrogen uptake of Cu-BTTri is lower than that of Cu-BTT at low pressure regimes (below 1 bar). This can be justified by the lower affinity of the first and second adsorption sites inside Cu-BTTri compared to Cu-BTT, as the low pressure adsorption regime is usually attributed to the occupation of the stronger adsorption sites. The lower affinity of the first adsorption site toward nitrogen molecules is due to the already aforementioned strong Jahn-Teller effect in the Cu-BTTri structure. Moreover, for the second adsorption site, the nitrogen atoms of triazole rings have higher partial negative charge compared to that of tetrazole groups (due to the higher basicity of triazole groups as was discussed above), causing stronger electrostatic repulsion between the adsorbed N_2 and the neighboring triazole groups as compared to tetrazole ones; thus, the second adsorption site in Cu-BTTri should also have lower binding energy compared to Cu-BTT.

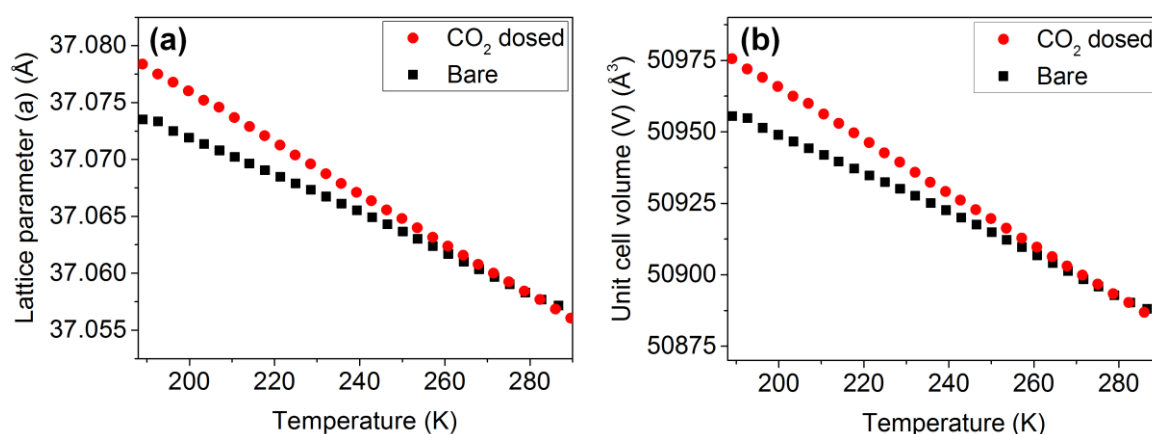


Figure 4-4 The change of (a) Lattice parameter (a) (b) unit cell volume (V) of activated Cu-BTTri with temperature.

4.3.4 Evolution of lattice parameters and guest occupancies as a function of temperature

In addition to CO₂ and N₂ binding, the bulk properties of the material, such as unit cell parameters and cell volume, were investigated as a function of temperature and gas loading level. This allows us to follow adsorption/desorption processes and better understand how the material's structure changes as a function of external stimuli. In this work, *in situ* synchrotron X-ray diffraction measurements were employed rather than neutron diffraction, in order to obtain rapid measurements using small sample sizes. First, data were collected at 100 K on a Cu-BTTri sample dosed with 12.5 torr of CO₂ (1.09 CO₂/Cu²⁺) as it was necessary to determine if the position of CO₂ could be elucidated via synchrotron X-ray diffraction. Indeed, Rietveld analysis permitted the elucidation of the same four adsorption sites (Table S4-11) as observed via neutron powder diffraction. Afterwards, variable temperature measurements were performed on the activated sample and then again on the aforementioned sample dosed with 12.5 torr of CO₂ gas. For both samples data were collected during cooling from 290 K to 190 K (rate of 2 K per minute). For the bare Cu-BTTri, see black dots in Figure 4-4, the lattice parameter a , increases from 37.0571(1) Å to 37.0735(1) Å upon cooling, which leads to an increase in cell volume by 0.13% representative of a negative thermal expansion (NTE). The average thermal expansion coefficient, α , was calculated for lattice parameter a , to be approximately -4.5 (MK)⁻¹. Albeit small, NTE was previously reported for only a few MOF structures to date.³⁷⁰⁻³⁷² This magnitude of NTE behavior for this framework is similar to what was observed for HKUST-1, a well-known MOF with the cubic crystal system, that has shown an average thermal expansion coefficient of -4.1 (MK)⁻¹.³⁷² Understanding the extent to which a material contracts or expands as a function of temperature is important to better understand how it might change throughout the course of a separation, a factor that can significantly

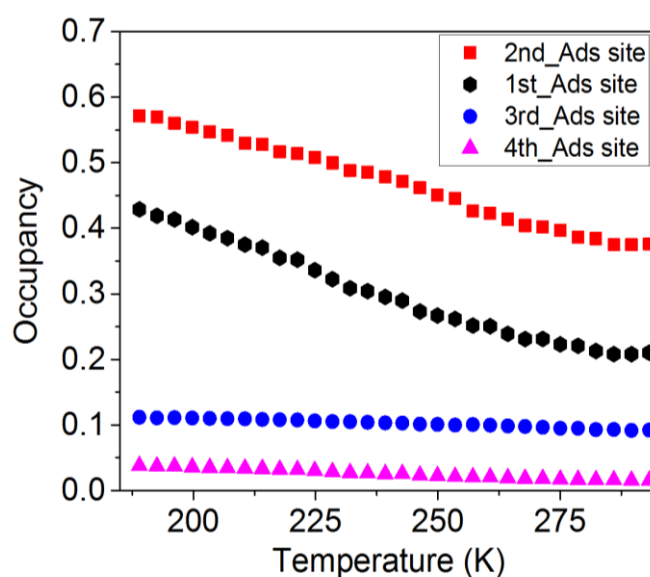


Figure 4-5 Occupation of different CO₂ adsorption sites in Cu-BTTri as a function of temperature.

impact process engineering. Interestingly, the NTE becomes even more pronounced when the sample is under 12.5 torr of CO₂. Upon decreasing the temperature from 290 K to 190 K, the lattice parameter, a , increases from 37.0560(1) Å to 37.0783(1) Å and results in a 0.18% change in the unit cell volume; this leads to a slightly larger thermal expansion coefficient, α , of -6.0 (MK)⁻¹ (Figure 4-4). The more intense NTE behavior in the presence of CO₂ gas can be attributed to the development of host-guest interactions inside the framework as a result of the higher amount of adsorbate loading by cooling the structure. Similar behavior was previously reported for Fe-MOF-74, where an increase in CO₂ dosing led to the increase in the degree of the lattice expansion for the framework.²⁶²

Subsequent to the unit cell analysis, carried out via LeBail fitting, sequential Rietveld analysis was performed on the aforementioned variable temperature diffraction data obtained from Cu-BTTri dosed with 1.09 CO₂ per Cu²⁺. The occupancies of sites I-IV are plotted as a function of temperature in Figure 4-5. While the occupancies of site III and site IV are minimal over the entire temperature regime, the occupancies of sites I and II increase significantly as the temperature is decreased, which is due to the higher isosteric heats of CO₂ adsorption, as predicted by the Van't Hoff equation.³⁷³ Further, it is noted that at these temperatures, the second adsorption site II has a higher occupancy than site I, which is counterintuitive considering the NPD data collected at 10 K shows a higher occupancy of site I. The occupancies are 0.21(1) and 0.38(1) at the highest temperature, 290 K, while the occupancies increase to 0.43(1) and 0.57(1), for site I and II respectively, at 190 K. While an energy difference as small as ≈ 3 kJ/mol is sufficient to cause a sequential occupation of adsorption sites at 10 K, at higher temperatures, where adsorption isotherms are collected, it is possible that the distribution of the occupancies are also influenced by entropic effects.³⁷⁴ Therefore, despite the higher occupancy of site II at room temperature, it is still assumed that site I is energetically favorable, and hence has a higher occupancy at temperatures approaching 0 K where entropy effects are highly attenuated.

4.3.5 Transient breakthrough simulations in fixed bed adsorbers

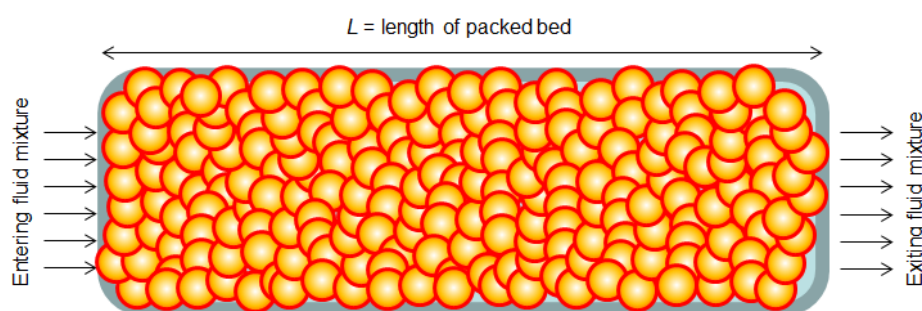


Figure 4-6 A schematic figure of a fixed bed adsorption bed for post-combustion capture process

Given that the single component adsorption isotherms imply that Cu-BTTri has a higher selectivity for CO₂ over N₂, while Cu-BTT has a higher CO₂ capacity, it was of interest to

evaluate the potential of these frameworks in a dry post-combustion capture process (see scheme in Figure 4-6). For a clear comparison, Figure 4-7(a) shows the adsorption selectivities of Cu-BTT and Cu-BTTri over the whole pressure range and Figure 4-7(b) compares the volumetric CO₂ uptake capacities of both Cu-BTT and Cu-BTTri. We note that Cu-BTT has an uptake capacity that is significantly higher than Cu-BTTri by a factor of two, despite the higher selectivity for the latter.

The typical composition of the flue gas feed is approximately 15/85 v/v CO₂/N₂ and the separations are normally carried out in fixed bed adsorbers (see schematic in Figure 4-6); such adsorbers are commonly operated in a transient mode, and the compositions of the gas phase, as well as component loadings within the crystals, vary with position and time.³⁷⁵⁻³⁷⁷ During the initial stages of the transience, the pores are gradually loaded, and only towards the end of the adsorption cycle pore saturation is attained. For a given separation task, transient breakthroughs provide a more realistic evaluation of the efficacy of a material, as they reflect the combined influence of CO₂/N₂ adsorption selectivity and CO₂ uptake capacity.³⁷⁶⁻³⁷⁷

The adsorption selectivity is defined by

$$S_{ads} = \frac{q_1/q_2}{y_1/y_2} \quad Eq. (4 - 2)$$

where the q_1 , and q_2 represent the molar loadings of CO₂(1), and N₂(2) within the MOF that is in equilibrium with a bulk fluid mixture with mole fractions y_1 , and $y_2 = 1 - y_1$. The molar loadings, also called *gravimetric uptake capacities*, are usually expressed with the units mol kg⁻¹. The component loadings are commonly calculated on the basis of unary isotherm data fits, along with the Ideal Adsorbed Solution Theory (IAST) of Myers and Prausnitz³⁷⁸ for mixture adsorption equilibrium (see the SI). The *volumetric uptake capacities* are

$$Q_1 = \rho q_1; \quad Q_2 = \rho q_2 \quad Eq. (4 - 3)$$

where ρ is the crystal framework density of the MOF, expressed in units of kg m⁻³, or kg L⁻¹.

High uptake capacities are desirable because these result in longer breakthrough times, and reduced frequency of bed regeneration. Higher values of S_{ads} are also desired because they lead to sharper breakthrough fronts and larger differences between the breakthrough times of individual constituents. If high product purities are desired, then this also demands $S_{ads} \gg 1$. Most commonly, however, high uptake capacities do not go hand-in-hand with high selectivities.^{377, 379}

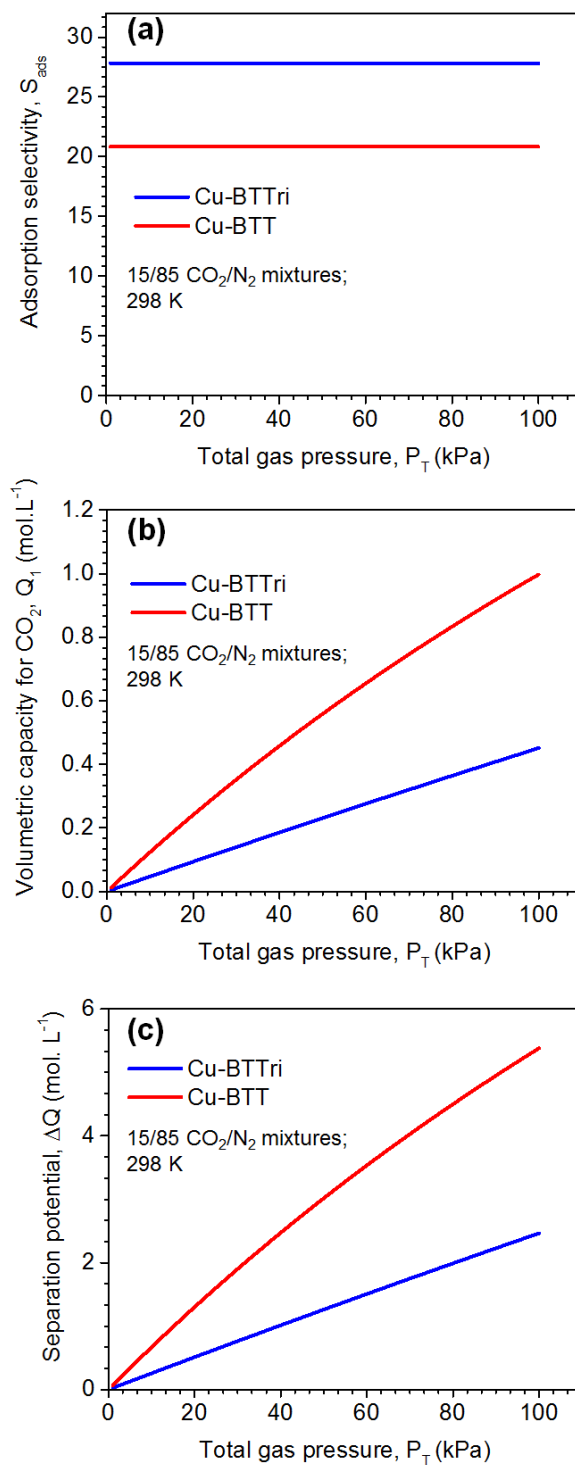


Figure 4-7 (a) Adsorption selectivity (S_{ads}) (b) Volumetric capacity for CO₂, Q_1 (c) Separation potential, ΔQ , as a function of total pressure.

In order to overcome the selectivity/capacity trade-off for these two MOFs, we adopted an approach previously developed by Krishna,³⁷⁹ which defines a *combined*

selectivity/capacity metric that is derived using the “shock wave” model for fixed bed adsorbers. The maximum achievable productivity of purified N₂ is realized when both intra-crystalline diffusion and axial dispersion effects are completely absent and the concentrations “fronts” of the fluid mixture traverse the fixed bed in the form of shock waves.³⁷⁹ For the separation of CO₂(1)/N₂(2) mixtures, the maximum achievable productivity, ΔQ , called the *separation potential*, can be calculated using the shock-wave model; the result is ³⁷⁹

$$\Delta Q = Q_1 \frac{y_2}{1 - y_2} - Q_2 \quad \text{Eq. (4 - 4)}$$

The quantity ΔQ can be described as an appropriate combination of selectivity and uptake capacity that is reflective of the separation potential for a specific adsorbent in a fixed bed.³⁷⁹ The ΔQ , expressed in mols of N₂ per L of adsorbent, represents the maximum amount of pure N₂ that can be recovered during the adsorption phase of the fixed bed separation and hence, is also indicative of the amount of CO₂ that is adsorbed on the bed until the point of breakthrough. Of course, it should be noted that if the purity of the CO₂ gas, which is released in the desorption stage, is of utmost importance, then the evaluation of the materials may be done based on the selectivity rather than separation potential.

A comparison of the separation potential, ΔQ , of Cu-BTT and Cu-BTTri for 15/85 CO₂(1)/N₂(2) mixtures at 298 K, is plotted as a function of the total pressure, p_t in Figure 4-7(c). At 100 kPa total pressure, the ΔQ is 5.4 mol.L⁻¹ for Cu-BTT and 2.7 mol L⁻¹ for Cu-BTTri. These values imply that Cu-BTT has the potential to produce twice the amount of pure N₂ as Cu-BTTri. In order to confirm the superior performance of Cu-BTT, transient breakthrough curves were also simulated for 15/85 CO₂/N₂ gas mixtures at an operating pressure of 100 kPa and 298 K using a methodology reported previously.^{376-377, 379-380} For the breakthrough simulations, the following parameter values were used: length of packed bed, $L = 0.3$ m; voidage of packed bed, $\varepsilon = 0.4$; superficial gas velocity at inlet, $u = 0.04$ m/s.

The results for the transient breakthrough simulations obtained from a fixed bed packed with (a) Cu-BTT and (b) Cu-BTTri are shown in Figure 4-8. The transient breakthrough simulation results are presented in terms of a *dimensionless* time as the x -axis, τ , defined by dividing the actual time, t , by the characteristic time, $\frac{L\varepsilon}{u}$. The y -axis represents the % CO₂ and % N₂ in the gas mixture exiting the adsorber. The time at which CO₂ “breaks through” is significantly higher for Cu-BTT, as compared to Cu-BTTri; this can be primarily ascribed to the higher CO₂ capacity of Cu-BTT, as shown in Figure 4-7(b). During the time interval indicated by $\Delta\tau$ in Figure 4-8, nearly pure N₂ can be produced. Note that the time interval $\Delta\tau$ is higher for Cu-BTT than that of Cu-BTTri by nearly a factor of two. Arbitrarily setting the minimum purity requirements for N₂ as 99.95%, we can determine the productivity of N₂ from a material balance on the adsorber. The calculated values for Cu-BTT and Cu-BTTri are, respectively, 4.3 mol L⁻¹ and 1.8 mol L⁻¹, confirming that the separations with Cu-BTT yield a significantly higher productivity of pure N₂ and thus a higher amount of CO₂ can be captured. The actual values of

the productivities for Cu-BTT and Cu-BTTri are lower than the corresponding values of ΔQ , calculated using the IAST (see Figure 4-7(c)), because of the distended nature of the transient breakthroughs in Figure 4-8.

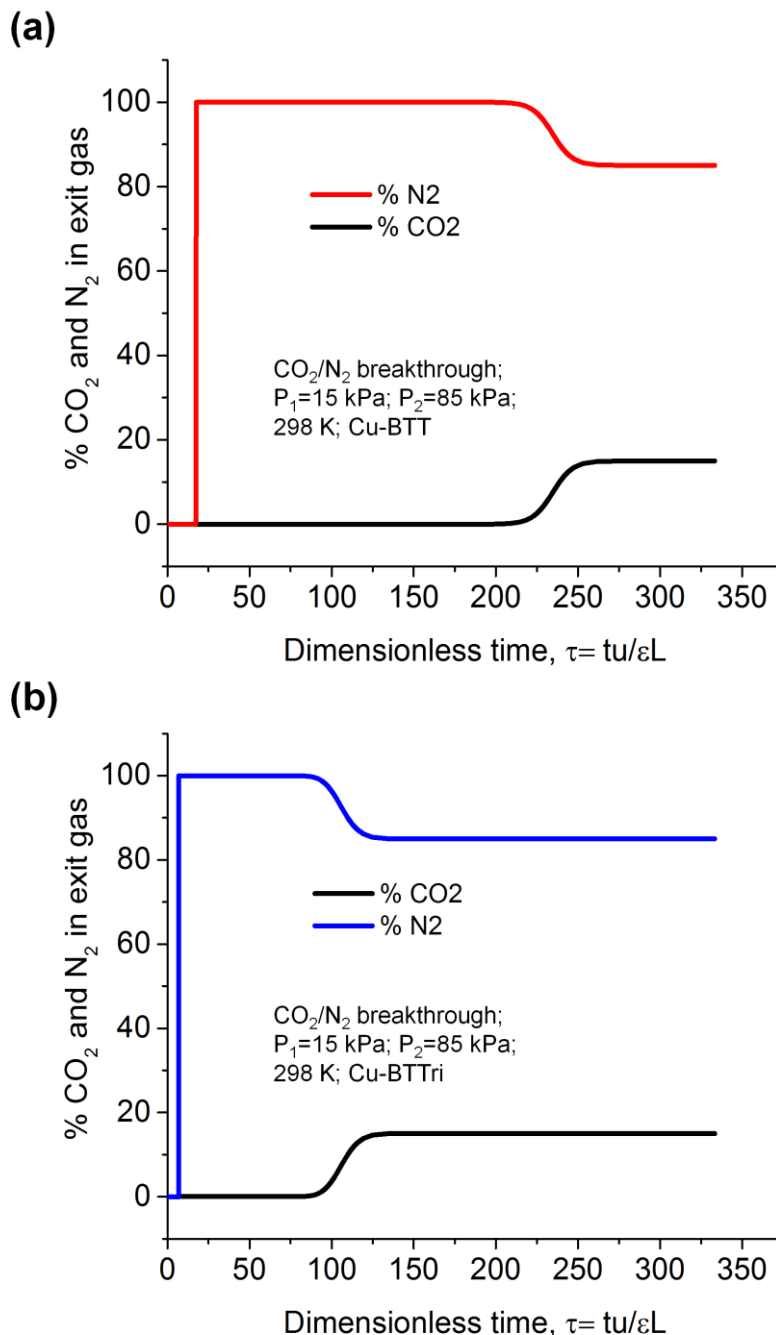


Figure 4-8 Transient CO₂ and N₂ breakthrough curves for: (a) Cu-BTT (b) Cu-BTTri frameworks

Overall, neither the adsorption capacity of the single gases nor the selectivity, S_{ads} , are a proper metric for judging the effectiveness of a specific MOF for separations in fixed bed adsorbers. Separation potential can give a better estimation of how effective a material's performance is. However, depending on the particular requirements for each case, such as CO₂

recovery, CO₂ purity or the effective amount of gas captured per mass unit of the material, the final choice might be different. For example, in the present case, for optimizing CO₂ recovery, Cu-BBT is a better option because it yields higher amount of cyclic CO₂ adsorption, due to its higher separation potential. However, if the CO₂ purity is the main target, Cu-BTTri, which shows better CO₂/N₂ selectivity would be a better choice for this separation.

4.4 Conclusion

This work presents a comprehensive study of CO₂ and N₂ adsorption in a sodalite MOF known as Cu-BTTri, which was carried out using a series of characterization tools including single component adsorption measurements, *in situ* neutron and X-ray diffraction, DFT calculations, and finally breakthrough simulations. While CO₂ and N₂ isotherms are used to assess selectivity and adsorption capacity, *in situ* diffraction is used to provide molecular level insight into the location and orientation of these two small molecules throughout the framework. As such, the diffraction technique allows further rationalization of the observed isotherms, provides a means to monitor adsorption/desorption processes, and allows one to assess changes in the framework as a function of temperature. Albeit small, both the activated and CO₂ loaded Cu-BTTri are found to exhibit a rare NTE phenomenon, with average thermal expansion coefficients of -4.5 (MK)⁻¹ and -6.0 (MK)⁻¹, respectively. In addition, DFT calculations are used to predict the binding energies and geometries of potential adsorption sites, results which are found to be in excellent agreement with those determined experimentally. To better understand the host-guest interaction at each adsorption site, the calculated binding energies were further decomposed into separate contributions from DFT-PBE (predominantly electrostatic) and van der Waals interactions.

Finally, the performance of Cu-BTTri is compared to a ligand substituted counterpart, Cu-BTT. While the sodalite structures are similar, the ligand exchange has an extreme effect on the performance of the material with regard to CO₂ and N₂ adsorption. Despite that Cu-BTTri exhibits a lower overall adsorption capacity and weaker interactions with both CO₂ and N₂, the material surprisingly offers a higher selectivity for CO₂ over N₂ compared to that of its tetrazole counterpart. These results stem from the fact that the triazolate offers a stronger Cu-ligand bond compared to the tetrazolate, and hence, significantly weakens the interactions along the z-axis, where small molecules bind, due to Jahn-Teller effect. This assumption is validated by neutron diffraction and adsorption measurements, which show elongated Cu-CO₂ distances and lower, initial isosteric heats of CO₂ adsorption, respectively. We finally compared these materials' performance in a dry, post-combustion flue gas separation. For this, the separation potential, ΔQ , of Cu-BTT and Cu-BTTri was determined, and transient breakthrough curves were simulated; it was concluded that, despite its higher selectivity for CO₂ over N₂, Cu-BTTri does not outperform Cu-BTT for the separation of interest. It was demonstrated that adsorption capacity and selectivity alone cannot be appropriate metrics to evaluate the efficiency of an adsorbent to be employed in a chosen separation.

It should be reiterated that this study is based on the thermodynamic and hydrodynamic properties of the frameworks of interest in dry post-combustion capture conditions. For the actual application of a material in such a large-scale separation, other techno-economic factors like price, long term stability/cyclability, ease of regeneration, temperature spikes during adsorption, and the influence of other minor impurities, particularly water, must also be considered.

Chapter 5

Large anisotropic negative thermal expansion in Cu-TDPAT metal-organic framework: an *in-situ* X-ray diffraction study⁵

5.1 Introduction

Most solid materials expand when heated, a phenomena that is attributed to enhanced longitudinal bond vibrations.³⁸¹ However, during the past few decades, there is mounting interest in understanding the opposite behavior,³⁸² referred to as negative thermal expansion (NTE). Albeit rare, this phenomenon has increasing importance in the engineering of systems that require precise control of volume over a wide range of temperatures, a process called controlled thermal expansion (CTE).³⁸³⁻³⁸⁷ The importance of CTE is exemplified by its use in a number of applications such as casting, molding, microchip industries, dental fillers, and many other expansion sensitive systems, like high precision optical mirrors.

In order to design new CTE processes, one must first understand the underlying principles of the NTE mechanism in various materials. NTE can have different origins, ranging

⁵ This chapter is based on the written article: "Large anisotropic negative thermal expansion in Cu-TDPAT metal-organic framework: an in-situ X-ray diffraction study." Mehrdad Asgari, Ilia Kochetygov, Hassan Abedini, and Wendy L. Queen. Submitted, 2019. M. A. has synthesized the material, performed the experiments, analyzed the data and written the paper.

from electronic and magnetic transitions to transverse atomic and molecular vibrations.³⁷² Compounds reported to exhibit vibrational NTE mostly consist of metal oxides, like ZrW_2O_8 ,³⁸⁸⁻³⁸⁹ and several classes of porous frameworks such as zeolites³⁹⁰ and cyanide-based materials³⁹¹⁻³⁹³. The origin of the NTE behavior in the aforementioned inorganic materials is often attributed to transverse “skipping rope type” vibrations of the linkers that bridge between metal clusters.³⁹⁴

Recently, NTE properties have also been reported in a few metal-organic frameworks (MOFs). MOFs are crystalline materials that contain metal-ions or metal-ion clusters as nodes and organic ligands as linkers.^{314, 323, 395} With a large number of potential building block combinations, numerous MOFs with different properties can be designed. Their vast structural versatility has led to the formation of over 88000 new frameworks,³⁹⁶ some of which offer unprecedented internal surface areas (up to $7800 \text{ m}^2/\text{g}$) and ultra large void fractions (up to 90%).^{20, 397} These properties, combined with structural flexibility, can on occasion lend to NTE behaviour. However, the higher chemical and structural complexity of MOF frameworks, when compared to other aforementioned materials, also results in a higher degree of complexity with regard to the structural dynamics.³⁹⁴ This necessitates an in-depth study of the variable temperature structural changes in MOFs.

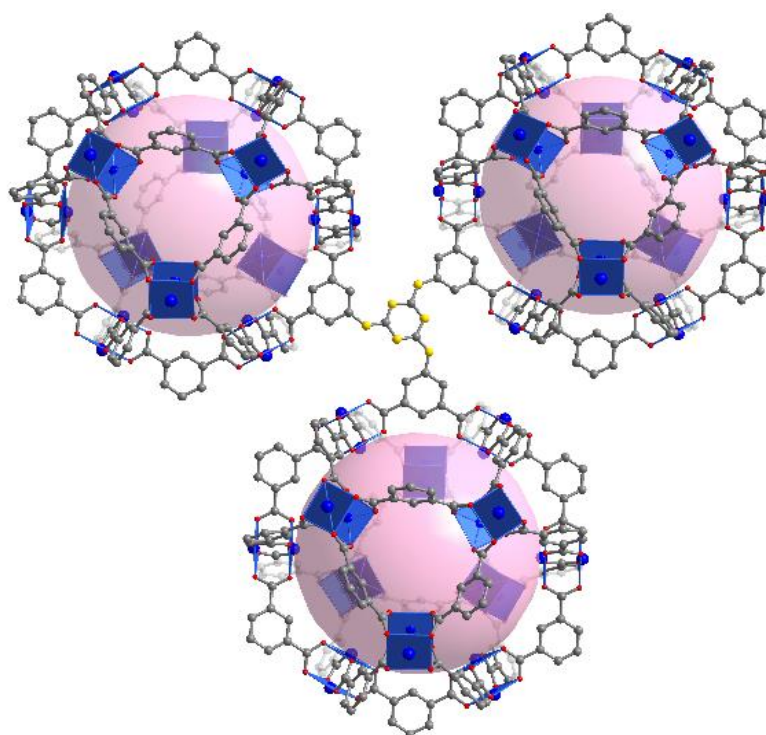


Figure 5-1 The 3D structure of Cu-TDPAT framework

Given that MOFs are highly crystalline, x-ray diffraction is a useful technique to elucidate the structural changes. While, computational techniques first hypothesized NTE in MOFs³⁷⁰ well before its experimental confirmation, a number of recent reports have demonstrated that

diffraction experiments can help elucidate new vibrational mechanisms responsible for NTE behavior.^{372, 382, 394, 398}

5.2 Results and discussions

With the desire to extend our knowledge of NTE behavior in MOFs, herein, Cu-TDPAT ($\text{Cu}_3(\text{TDPAT})$),¹³⁶ H_6TDPAT = 2,4,6-tris(3,5-dicarboxylphenylamino)-1,3,5-triazine), was selected as a case study. The framework crystallizes in the Tetragonal $I4/m$ spacegroup (no. 87) and contains $\text{Cu}_2(\text{carboxylate})_4$ “paddlewheels” that are interlinked by TDPAT⁶⁻ ligands forming a neutral, porous, three-dimensional network (Figure 5-1). During synchrotron powder x-ray diffraction experiments, this material revealed a large lattice contraction upon increasing temperature, which incited curiosity about the underlying mechanism of this uncommon behavior.

In addition to NTE, Cu-TDPAT has certain characteristics that make it attractive for a comprehensive structural study. First, this material offers exceptional adsorption capacities for a number of energetically relevant small molecules including CO_2 , CH_4 , and H_2 .¹³⁶ Further, the relatively large TDPAT⁶⁻ ligand, lends to a high degree of framework flexibility, which significantly influences the material’s gas adsorption behavior.³⁹⁹ Despite this, to date there is no knowledge regarding the origin of this flexibility. Additionally, Cu-TDPAT is highly crystalline (Figure S5-1), even after a heat treatment up to 500 K (Figure S5-2). Further, high-quality single crystals of the

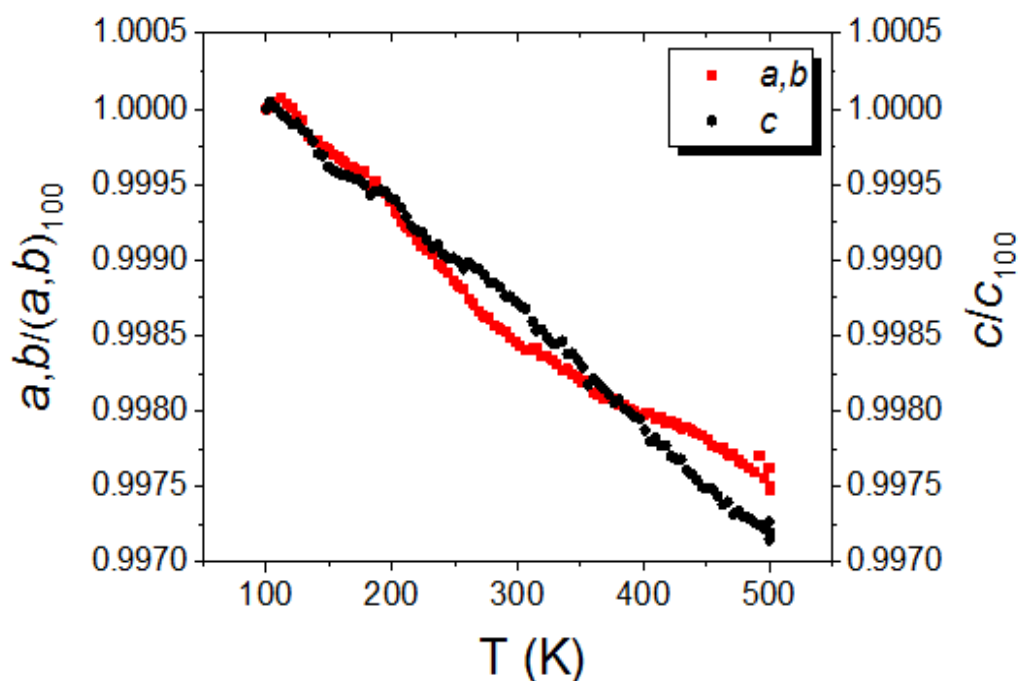


Figure 5-2 The evolution of lattice parameters (a,c) as a function of the temperature normalized by their original value at 100 K. The standard deviations are smaller than the size of the points. Therefore, cannot be shown in this graph

material are readily available (Figure S5-3), permitting the precise determination of any structural changes. Moreover, this framework contains a $\text{Cu}_2(\text{carboxylate})_4$ “paddlewheel” that is similarly observed in $\text{Cu}_3(\text{BTC})_2$ (Cu-BTC or HKUST-1; btc=1,3,5-benzenetricarboxylate) and $\text{Cu}_3(\text{btb})_2$ (Cu-BTB or MOF-14; btb=4,4',4''-benzene-1,3,5-triyl-tribenzoate).³⁷² While the NTE of Cu-BTC is significantly less pronounced than that observed in Cu-TDPAT, the NTE mechanism was still elucidated³⁷², providing us with inspiration that similar success could be achieved in the current study. Last, as in the case of Cu-BTC, Cu-BTB, and MOF-5 ($\text{Zn}_4\text{O}(\text{1,4-benzenedicarboxylate})_3$)³⁹⁸, most NTE studies are limited to the cubic crystal systems showing isotropic NTE behavior,⁴⁰⁰ making NTE studies of MOFs in lower symmetry crystal systems of interest.

To study the mechanism of NTE behavior in Cu-TDPAT, single crystal and powder synchrotron x-ray diffraction techniques were employed. The *in-situ* experiments were done in an inert environment to exclude solvation and desolvation effects. Because the framework can easily adsorb water molecules at the open metal sites, complete activation was first carried out at 150 °C for 12 hours under dynamic vacuum provided by a turbo pump, and then the sample was sealed inside of a borosilicate capillary. Before sealing, the samples were placed under 700 torr of He, as the exchange gas. To understand the temperature dependant evolution of lattice parameters, we first performed *in-situ* powder synchrotron x-ray diffraction measurements on the activated sample. The lattice parameters and the volumes of the unit cells were determined via sequential LeBail refinements of the powder diffraction data collected at temperatures ranging from 100 K to 500 K (see Table S5-1 and Figure S5-4). Both lattice parameters, a and c , show a reduction of 0.25% and 0.284%, respectively, upon heating (Figure 5-2). The temperature-dependent linear ($\alpha_l = \frac{dl}{l dT}$) and volumetric ($\alpha_v = \frac{dV}{V dT}$) thermal expansion coefficients were also calculated by fitting a second order polynomial to the plot of each lattice parameter and the unit cell volume (Figure S5-5 to Figure S5-9). The average linear thermal expansion coefficient for a and c is calculated to be -6.4 and -7.2 (MK)⁻¹, respectively. These values are significantly higher than those previously reported for the cubic Cu-BTC (-4.1 (MK)⁻¹)³⁷². Figure 5-3 shows the absolute values of the unit cell volume (left vertical axis) and the volume ratio (volume at each temperature / volume at 100 K, right vertical axis). The change of lattice parameters causes an overall 0.8% reduction in the unit cell volume (Figure 5-3), and the calculated volumetric thermal expansion coefficient ranges from -26.8 MK⁻¹ at 100 K to -13.6 MK⁻¹ at 500 K. The latter indicates that the NTE effect is significantly more pronounced at lower temperatures (see inset, Figure 5-3).

The large NTE observed for Cu-TDPAT encouraged us to unveil the mechanism via single crystal experiments. The crystals of the MOF were first inserted into a borosilicate capillary and treated under the same conditions as the aforementioned powder sample. The variable temperature single crystal diffraction experiments were carried out in the temperature range of 100 to 500 K at intervals of 25 K. The structures are available in CSD database.⁴⁰¹ The resulting lattice parameters and the unit cell volumes are shown in Figures S5-10, S5-11, and S5-12. The lattice parameters undergo changes that are similar to those observed from the powder diffraction data. Despite their similar trend, there are minor ($\sim 0.1\%$ abs. value) differences between the absolute values of lattice parameters extracted from the single crystal and powder samples, a known observation reported elsewhere.²⁶² This phenomenon can be attributed to averaging small deviations in the unit cell parameters throughout many crystallites in the powder diffraction experiment.

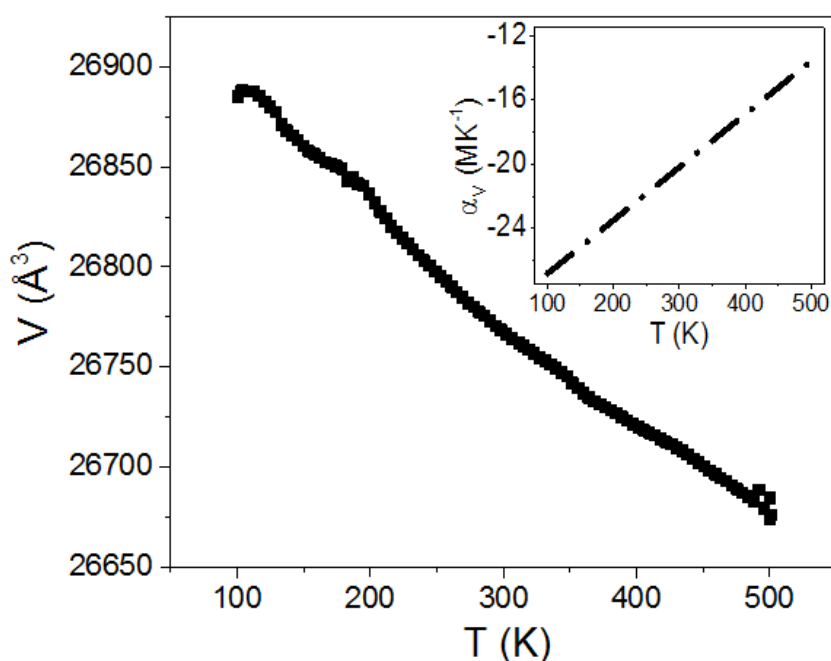


Figure 5-3 Volume of the unit cell as a function of the temperature. The standard deviations are smaller than the size of the points. (inset) Volumetric thermal expansion coefficient of Cu-TDPAT as a function of temperature, as fitted with a second order polynomial.

Inspection of the framework's structure at different temperatures, via single crystal measurements provided direct insight into the NTE mechanism. This tool was used to highlight the structural motions associated with the metal clusters and the ligands, which are responsible for the unit cell contraction. A total of three structural changes were observed from the data (Figure 5-4). First, the three benzene rings on the TDPAT⁶⁻ ligand are found to twist around the triazine ring (Figure 5-4a, Table S5-2, and Figure S5-14). The resulting increase in the fold angle (Figure S5-14) found between the benzene and the central triazine rings (bending of the ligand),

in turn, alters the longitudinal size of the ligand thus causing the unit cell contraction (Figure S5-12). Such a change is not present in Cu-BTC, due to the structural simplicity and rigidity of the BTC³⁻ ligand, which contains only one benzene ring directly connecting the carboxylates. Hence, this first observed feature helps to explain the more strongly pronounced NTE observed for Cu-TDPAT when compared to its structural counterpart, Cu-BTC. In relation to this, the observed anisotropic displacement parameters (ADPs) for atoms in the benzene rings and to a greater extent in the triazine rings, are larger in the direction perpendicular to the ring plane (Figures S5-26 and S5-27 and Tables S5-11 to S5-14). As such, in addition to the aforementioned reorientation

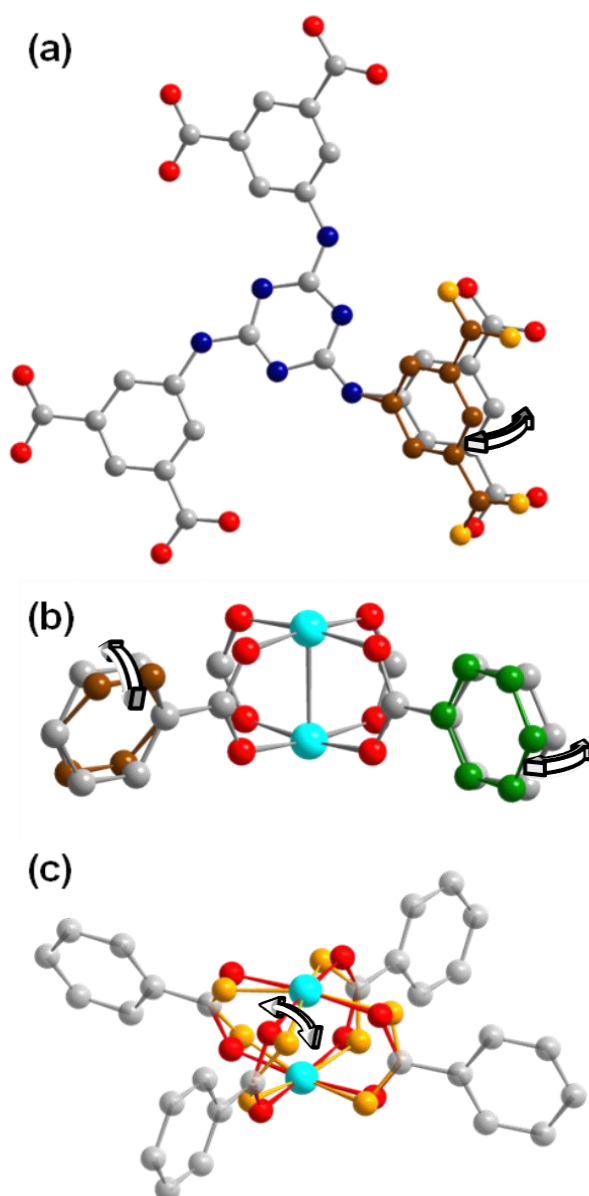


Figure 5-4 Structural motions in Cu-TDPAT responsible for the NTE effect. (a) bending of the benzene rings around the central triazine ring (b) folding and twisting of the benzene rings around paddlewheel metal clusters (c) twisting of the paddlewheel clusters

of aromatic rings inside the framework, the elongated ADPs are a further indication of the structural dynamics. For the second motion, the benzene rings (Figure 5-4b, Tables S5-3 to S5-5, and Figures S5-15 to S5-17) twist and fold around the metal building unit; both motions were similarly observed in diffraction data obtained from Cu-BTC.³⁷² The observed rotations of the benzene rings either around triazine ring (Figure 5-4a) or around the paddlewheels (Figure 5-4b) are thought to be transverse rather than longitudinal vibrational modes. Transverse modes typically have lower excitation energies and hence can be observed better at lower temperatures than their longitudinal counterparts.³⁸¹ Given that the volumetric thermal expansion coefficient of Cu-TDPAT is more pronounced at lower temperatures (Figure 5-2b), it is hypothesized that such motions are transverse in nature. Last, although the metal clusters are generally not as flexible as the bridging ligands,³⁸¹ the paddlewheel units in Cu-TDPAT also undergo a slight twisting via the rotation of the carboxylate groups (Fig. 5-4c, Tables S5-6 to S5-9, and Figures S5-18 to S5-23). This is similar to what was previously observed for Cu-BTC, thus indicating that paddlewheel metal clusters are likely prone to twist in porous frameworks despite the expected rigid nature of the metal units.

These transverse vibrational modes also induce bond libration³⁸¹ in Cu-TDPAT; this is evident by a decrease in the Cu-Cu distance from 100 K to 300 K. However, above this temperature there is a noted increase in the Cu-Cu distance, which likely indicates the onset of competitive longitudinal vibrations. This competitive effect causes a volcano-type plot for Cu-Cu distances as a function of temperature (Table S5-10, and Figures S5-24 to S5-25).

It is concluded that Cu-TDPAT's more pronounced NTE behaviour compared to Cu-BTC stems from the framework's increased structural flexibility. The ligand of the Cu-TDPAT showed several junctions where, bending, twisting and folding can happen. The bending of the ligand as well as twisting of the paddlewheel clusters together were shown to be responsible for the framework contraction. In addition to more ligand complexity, the lower symmetry of Cu-TDPAT compared to Cu-BTC, provides higher degree of structural freedom which promotes a more pronounced anisotropic NTE behaviour in Cu-TDPAT that can be observed in two different directions via relative movements of numerous structural components.

Chapter 6

Conclusion and future work

6.1 Achieved results

The achievements of this thesis are explained briefly in the following:

6.1.1 Preparation of the required hardware, software and experimental methods

Over the course of this thesis, several experimental setups, computer codes, and methodologies were developed in order to carry out detailed structural analysis of MOFs. For example, in this work, a gas dosing manifold, an *in-situ* powder and single crystal x-ray diffraction cells, and experimental protocol first had to be developed in order to conduct the structural work, which was carried out at the Swiss Norwegian Beamlines at ESRF. As such, these setups and protocols are not just important for the title study, but also for future studies to be carried out by the current group at EPFL and others throughout the world.

In addition to the developed experimental setups for the *in-situ* diffraction studies, the computer codes for the analysis of the standard adsorption isotherm data as well as *in-situ* diffraction data were also developed. Having access to this software, we can extract the thermodynamic parameters of the adsorption or obtain structural data for the variable temperature/pressure behavior of the framework under different environments.

All of the above tools and setups were used for the structure-property relationship studies.

6.1.2 Information obtained from structure-property relationship studies

The case studies described in chapters 2-5 were able to elucidate many important chemical and structural parameters that are influential on the adsorption properties of several prominent families of MOFs including sodalite structures such as M-BTT (where M=Cu,Fe, Cr, and Mn) and Cu-BTTri, as well as *rht*-type Cu-TDPAT.

In chapter 2, we showed, for the first time, a molecular level view of CO₂ adsorption in a series of isostructural MOFs known as M-BTT (where M²⁺ = Cr, Mn, Fe, and Cu and BTT³⁻ = 1,3,5-benzenetristetrazolate), which exhibit a high density of open metal sites that offer strong interactions with CO₂. *In-situ* structural studies revealed that the high initial isosteric heats of adsorption are directly correlated with the presence of the open metal sites and also provided the positions and orientations of as many as three other secondary CO₂ adsorption sites. Density functional theory calculations that include van der Waals dispersion corrections quantitatively supported the observed structural features associated with the primary and secondary CO₂ binding sites, including CO₂ position and orientation, as well as the experimentally determined isosteric heats of CO₂ adsorption. This work provided a stress test for computational tools in varying chemical environments. We believe that combined computational and experimental studies of this kind can inform the design of new MOFs with properties that are optimized for a variety of energy-related applications.

Additionally, in chapter 3, we demonstrated the importance of using *in-situ* diffraction techniques to gain intimate insight into small molecule binding in MOFs. We reported, for the first time, an accurate structure for a sodalite MOF known as Cu-BTTri. This knowledge is critical should computational methods be used to screen MOFs for targeted applications. We identified also for the first time the location of four D₂ adsorption sites in Cu-BTTri, and showed that the DFT method used in this work successfully models hydrogen adsorption sites with minimal deviation from the experimental results. The validation of this computational approach opens the door to predict the adsorption behaviour of existing and even hypothetical MOFs.

Furthermore, in chapter 4, a detailed study was conducted to understand how ligand substitution influences the CO₂ and N₂ adsorption properties of two highly crystalline sodalite MOFs known as Cu-BTT (BTT-3= 1,3,5-benzenetristetrazolate) and Cu-BTTri (BTTri-3 = 1,3,5-benzenetristriazole). The enthalpy of adsorption and observed adsorption capacities at a given pressure were significantly lower for Cu-BTTri compared to its isostructural counterpart, Cu-BTT. *In situ* X-ray and neutron diffraction, which allow visualization of the CO₂ and N₂ binding sites on the internal surface of Cu-BTTri, provided insight into understanding these subtle differences. As expected, slightly elongated distances between the open Cu²⁺ sites and surface bound CO₂ in Cu-BTTri could be explained by the fact that the triazolate ligand is a better electron donor than the tetrazolate. The more pronounced Jahn-Teller effect in Cu-BTTri led to weaker guest binding. The results of the aforementioned structural analysis were complemented by the prediction of the binding energies of CO₂ and N₂ adsorption sites by DFT calculations. In addition, variable temperature *in situ* diffraction measurements shed light on the fine structural changes of the framework and CO₂ occupancies at different adsorption sites as a function of temperature.

Finally, simulated breakthrough curves obtained for both sodalite MOFs demonstrated the materials' potential performance in dry post-combustion CO₂ capture. The simulation, which considers both framework uptake capacity and selectivity, predicted better separation performance for Cu-BTT under dry conditions. The information obtained in this work highlighted how ligand substitution can influence the adsorption properties of porous materials, and hence provided further insight in unprecedented detail into their optimization for technologically-relevant gas-separation processes.

Moreover, in chapter 5, we shed light on the mechanism of negative thermal expansion (NTE) in a lower tetragonal symmetry MOF, Cu-TDPAT, using a combination of *in situ* single crystal and powder x-ray diffraction techniques. This was done while most studies focused on NTE of MOFs are limited to cubic crystal systems, which show isotropic NTE behavior. We for the first time, revealed the structural motions that are responsible for large NTE behavior in the Cu-TDPAT, including bending, twisting and folding of a highly flexible ligand. Additionally, the NTE properties of Cu-TDPAT were compared to Cu-BTC, a framework constructed by the same copper paddlewheel building units but with a smaller, more rigid ligand.

6.1.3 Synergy of theory and experiments

The combination of theoretical and experimental studies carried out in this thesis enhanced our level of understanding of the adsorption processes in the selected MOF materials. For instance, DFT studies were used to answer experimentally intractable questions regarding the nature of the interactions between the host and guest. Using DFT, the binding energies at each adsorption site could be decomposed into interactions i) that were predominately electrostatic and those that were ii) predominately dispersive in nature. This unveiled how the local pore structure really contributes to small molecules binding. Further, both DFT and experimental work, including diffraction and adsorption studies, were employed to determine binding energies and host-guest structures of MOFs with several small molecules such as CO₂, N₂, and H₂. In all cases theory corroborated the experimental findings with regard to the strength of small molecule-MOF interactions and the location and orientation of these small molecules inside the frameworks. Overall, this work confirms the accuracy of such computational techniques and gives us hope that these tools can be employed in the future to answer more experimentally intractable questions and also to predict the best existing or hypothetical MOF for a given application. Such work might eventually alleviate the experimental bottleneck related to materials design, synthesis, and characterization by giving us a way to know, pre-experiment what the best performing material might be. This could help rapidly bring advanced materials to market.

6.2 Future works

The suggestions for the future works will be expressed in the following:

6.2.1 Evaluation of the adsorbents in real-world chemical separation applications

After linking the structural and chemical features to the adsorption properties of the frameworks, the performance of the adsorbents can be evaluated in the real-world chemical separation processes. In this regard, we have designed and constructed a breakthrough apparatus that can be used to perform multi-component adsorption measurements in a fixed adsorption bed. The capacity and selectivity of the adsorbents toward the target gas namely CO₂ in the presence of the impurities namely water, SO_x, NO_x and other interfering gases can be evaluated. Further, the capacity of the material can be measured after regeneration in a temperature swing adsorption (TSA) or pressure swing adsorption (PSA) process. This can be done after consecutive cycles which provides information about the recyclability of material, a very important parameter for the implementation of the adsorbents in the industrial processes. In addition, the effect of heat of adsorption in the temperature of bed at different cross-sections can be evaluated in the fixed bed adsorption setup. The fluctuation of the temperature across the bed, as a result of adsorption or desorption process, can significantly affect the efficiency of the adsorbents in the target chemical separation/storage process.

Overall, evaluation of the performance of the adsorbent in the experimental setups mimicking real-world applications can provide an additional puzzle piece to complement the picture of structure-property relationship for the application of interest.

6.2.2 Extending the structure-property relationship studies to other chemical applications

Considering the inclusive nature of *in-situ* diffraction studies on small molecule adsorption in MOFs, the structure-property relationship studies can be extended to other chemical adsorption/separation application than the carbon dioxide capture and hydrogen storage applications, namely hydrocarbon or noble gas separation processes. This will eventually enable finding the required chemical and structural features of the optimal adsorbent for different chemical separation processes.

In addition to the adsorption and separation, localization of the small molecules inside the structure of the porous frameworks can provide critical information in other chemical processes, for example heterogeneous catalysis. Finding the adsorption sites corresponding to the reactants and products of the reaction of interest not only can reveal the reactive sites but also can shed light on the mechanism of the catalytic reaction.

Chapter 7

Appendix

7.1 Appendix to chapter 2

7.1.1 *Gas adsorption measurements*

UHP-grade (99.999% purity) helium, nitrogen, and carbon dioxide were used for all adsorption measurements. Gas adsorption isotherms for pressures in the range 0–1 bar were measured using a Micromeritics ASAP 2020 instrument. For standard measurements in ASAP low-pressure glass sample holders, activated samples were transferred under a N₂ atmosphere to pre-weighed analysis tubes, which were capped with a Transeal. The samples were evacuated on the ASAP until the outgas rate was less than 3 µbar/min. The evacuated analysis tubes containing degassed samples were then carefully transferred to an electronic balance and weighed to determine the mass of sample (typically 100–200 mg). For cryogenic measurements, the tube was fitted with an isothermal jacket and transferred back to the analysis port of the gas adsorption instrument. The outgas rate was again confirmed to be less than 3 µbar/min. BET

surface areas and pore volumes were determined by measuring N₂ adsorption isotherms in a 77 K liquid N₂ bath and calculated, assuming a value of 16.2 Å² for the molecular cross-sectional area of N₂. Adsorption isotherms between 25 and 45°C were measured using a recirculating dewar (Micromeritics) connected to a Julabo F32-MC isothermal bath.

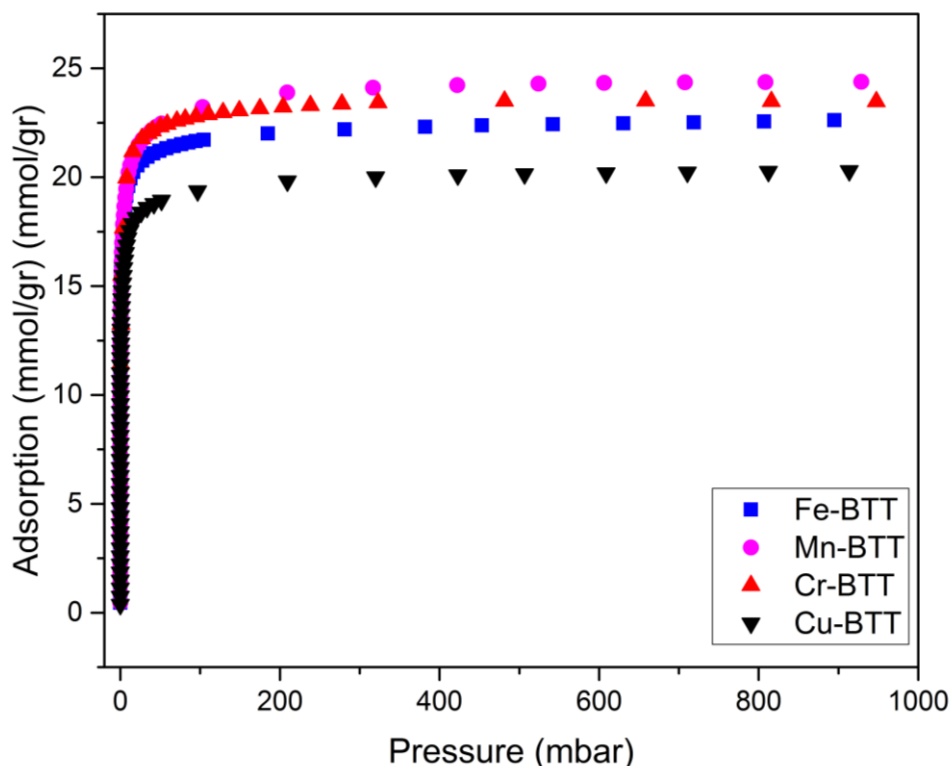


Figure S2-1. Nitrogen adsorption isotherms for M-BTT analogues collected at 77 K.

7.1.2 Pore Volume calculations based on the adsorption data for nitrogen at 77 K

As shown in Figure S2-1, the adsorption isotherm for N₂ at 77 K ceases to be a function of pressure when the pressure exceeds 200 mbar, implying that the structure has been saturated with nitrogen. Therefore, the uptake of N₂ at highest measured pressure can be considered as the full capacity of the framework for an inert small molecule, and the pore volume can then be calculated from the following formula:

$$\text{Pore Volume} = \frac{N_{N_2}^{Sat} * M_{wN_2}}{1000 * d_{liqN_2}|_{77K}} \quad \text{Eq. (S2 - 1)}$$

Where $N_{N_2}^{Sat}$ is the the amount of nitrogen adsorbed at the highest pressure point in mmol/g, M_{wN_2} is the molecular weight dinitrogen in g/mol and $d_{liqN_2}|_{77K}$ is the density of liquid nitrogen at 77 K in g/mL.

Therefore, for the M-BTT pore volumes we obtain:

$$\begin{aligned}
\text{Pore Volume}_{\text{Fe-BTT}} &= \frac{22.6 \cdot 28.013}{1000 \cdot 0.807} = 0.785 \text{ mL/g} \\
\text{Pore Volume}_{\text{Mn-BTT}} &= \frac{24.4 \cdot 28.013}{1000 \cdot 0.807} = 0.846 \text{ mL/g} \\
\text{Pore Volume}_{\text{Cr-BTT}} &= \frac{23.5 \cdot 28.013}{1000 \cdot 0.807} = 0.815 \text{ mL/g} \\
\text{Pore Volume}_{\text{Cu-BTT}} &= \frac{23.5 \cdot 28.013}{1000 \cdot 0.807} = 0.704 \text{ mL/g}
\end{aligned}$$

7.1.3 Surface area calculations based on the N_2 adsorption data at 77 K

Based on the BET theory, we have the following equation:

$$\frac{1}{N[(\frac{p_0}{p})-1]} = \frac{c-1}{N_m c} \left(\frac{p}{p_0}\right) + \frac{1}{N_m c} \quad \text{Eq. (S2 - 2)}$$

Where N is the amount of gas adsorbed in mmol/g, N_m is the monolayer adsorption in mmol/g, p is the partial pressure of N_2 and p_0 is the saturation pressure of N_2 at the measurement temperature.⁴⁰² A plot of $\frac{1}{N[(\frac{p_0}{p})-1]}$ versus $\frac{p}{p_0}$ and the best possible trendline is fit to the points on the plot. We note that points with low $(\frac{p}{p_0})$ are chosen such that the c parameter stays positive and high R^2 values are obtained. With M as the slope and I as the intersect of the plot, N_m can be obtained from the following formula:

$$N_m = \frac{1}{M+I} \quad \text{Eq. (S2 - 3)}$$

The surface area can then be obtained using the equation:

$$SA = N_m \cdot N_A \cdot CSA_{N_2} \quad \text{Eq. (S2 - 4)}$$

Where N_A is Avogadro's number and CSA_{N_2} is the cross sectional area of one N_2 molecule at 77 K (taken to be 16 \AA^2). The above calculations were carried out on the nitrogen adsorption isotherm data collected at 77 K for M-BTT; the resulting surface areas are given in Table S2-1.

Table S2-1. Surface areas for the M-BTT frameworks.

Sample	Surface Area (m^2/g)
Fe-BTT	2044.8
Mn-BTT	2078.4
Cr-BTT	1930.4
Cu-BTT	1755.9

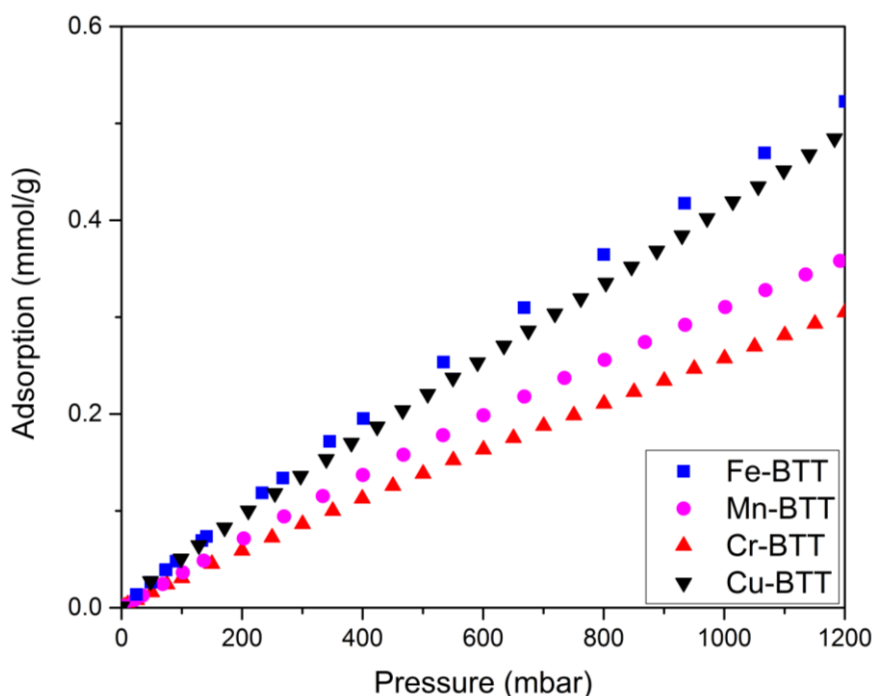


Figure S2-2. Nitrogen adsorption of M-BTT analogues at 298 K. A comparison of the N₂ uptake with CO₂ uptake at the same temperature (Figures S2-3 to S2-6) reveals selective adsorption of CO₂ over N₂, which is favorable in the context of post-combustion CO₂ capture.

7.1.4 Fitting M-BTT CO₂ adsorption isotherms

The CO₂ adsorption isotherms collected at 298, 308, and 318 K were fitted with a dual-site Langmuir model (Eq. S2-5):

$$n = \frac{q_{\text{sat},1} b_1 P}{1 + b_1 P} + \frac{q_{\text{sat},2} b_2 P}{1 + b_2 P} \quad \text{Eq. (S2 - 5)}$$

where n is adsorbed CO₂ in mmol/g, $q_{\text{sat},i}$ is the adsorption capacity for the site i , b_i is the Langmuir parameter for this site, and P is the pressure in bar. The fitted parameters for each adsorption isotherm can be found in Tables S2-2 to S2-5, and a comparison of the experimental CO₂ adsorption isotherms with the fitted dual-site Langmuir model based on the experimental data is shown in Fig. S2-3 to S2-6. The dual-site Langmuir model was chosen because of the validity of the theory behind this model for prediction of the interaction of heterogeneous surfaces with gas-phase small molecules. For porous materials that have adsorption sites of differing binding energies, a single-site Langmuir model is unable to accurately predict the adsorption behavior. The use of a dual-site Langmuir model for fitting gas adsorption isotherm data and the extraction of isosteric heats of adsorption has been reported elsewhere.^{62, 403-404}

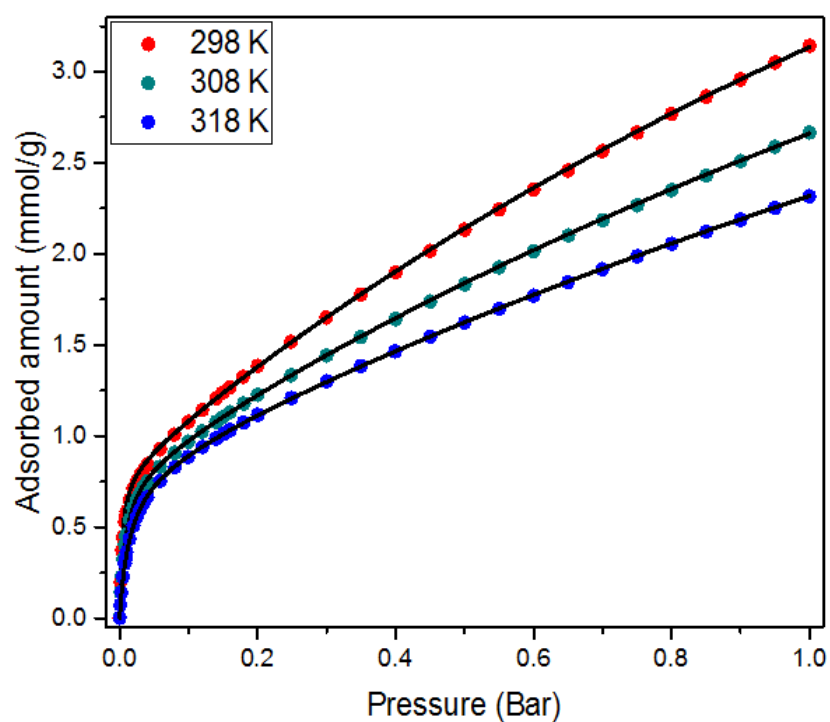


Figure S2-3. Dual-site Langmuir fits for CO₂ adsorption in Fe-BTT at 298, 308, and 318 K.

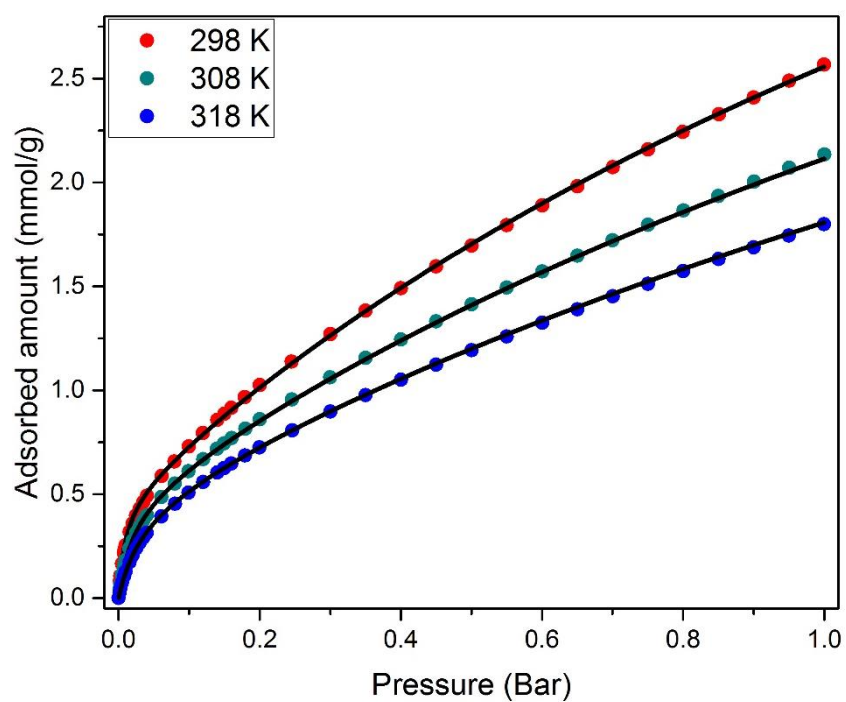


Figure S2-4. Dual-site Langmuir fits for CO₂ adsorption in Mn-BTT at 298, 308, and 318 K.

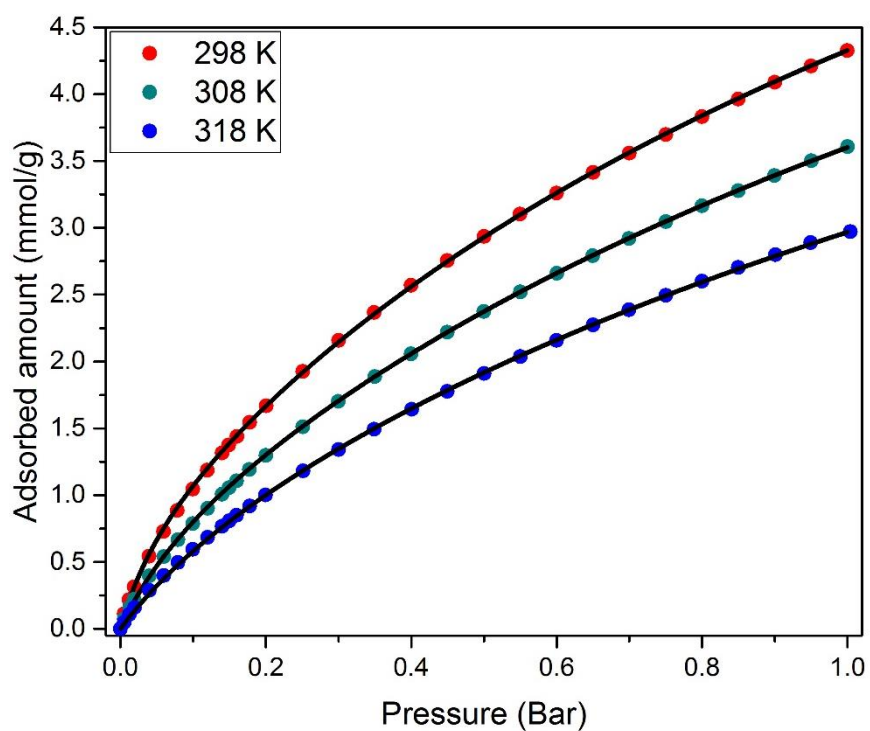


Figure S2-5. Dual-site Langmuir fits for CO₂ adsorption in Cr-BTT at 298, 308, and 318 K.

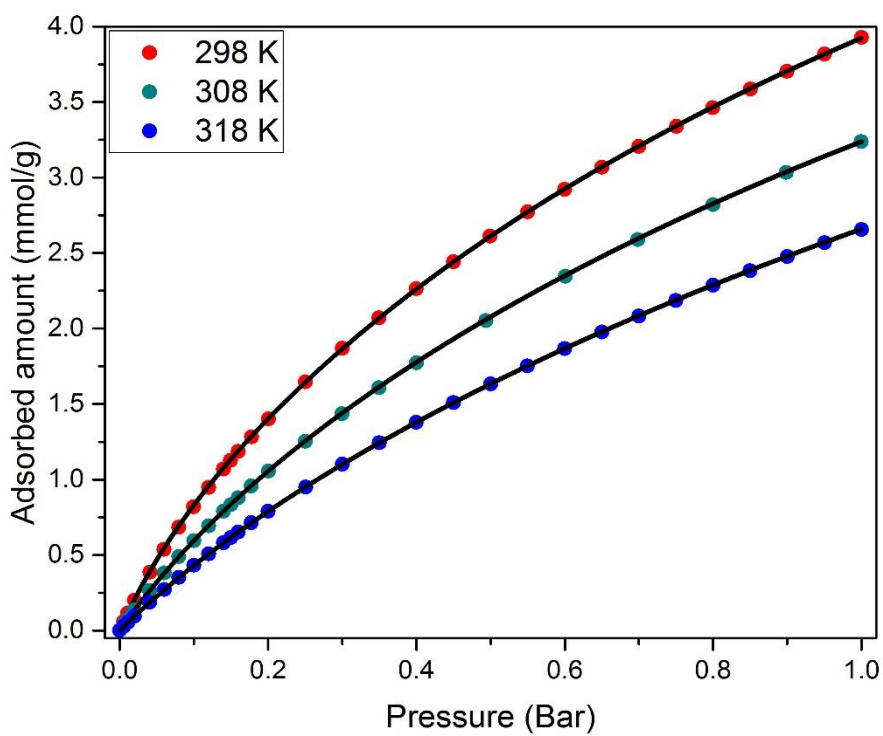


Figure S2-6. Dual-site Langmuir fits for CO₂ adsorption in Cu-BTT at 298, 308, and 318 K.

Table S2-2. Dual-site Langmuir parameters for CO₂ adsorption in M-BTT.

Framework	Temperature (K)	q_{sat1}	b_1	q_{sat2}	b_2
Fe-BTT	298	0.0008056	2.82	0.009	0.0035
	308	0.0008	1.232047	0.008278	0.002914
	318	0.000813	0.685	0.008293	0.002237
Mn-BTT	298	0.00048	1.051007	0.006683	0.004522
	308	0.0008	1.232047	0.008278	0.002914
	318	0.000813	0.685	0.008293	0.002237
Cr-BTT	298	0.00087	0.166593	0.009462	0.00589
	308	0.000773	0.102999	0.00899	0.004756
	318	0.000715	0.0565	0.00785	0.0043
Cu-BTT	298	0.000866	0.071123	0.008669	0.005748
	308	0.000877	0.038788	0.00832	0.004395
	318	0.000723	0.028083	0.00868	0.003243

Calculating Isosteric heats of adsorption

The Clausius-Clapeyron equation (Eqn. S2-6) was used to calculate the isosteric heats of adsorption, Q_{st} , for CO₂ adsorption in M-BTT analogs at 298, 308 K, and 318 K, using dual-site Langmuir-Freundlich fits.

$$(\ln P)_n = -\frac{Q_{\text{st}}}{R} \left(\frac{1}{T} \right) + C \quad \text{Eq. (S2 - 6)}$$

Where, P is the pressure in any desired unit, n is the amount adsorbed mol/g, T is the temperature in K, R is the universal gas constant kJ/mol·K, and C is a constant. The isosteric heat of adsorption, Q_{st} , was obtained from the slope of plots of $(\ln P)_n$ as a function of inverse T . The isosteric heats of adsorption as a function of CO₂ loading in M-BTT can be found in Figure 2-2 in the main text (chapter 2).

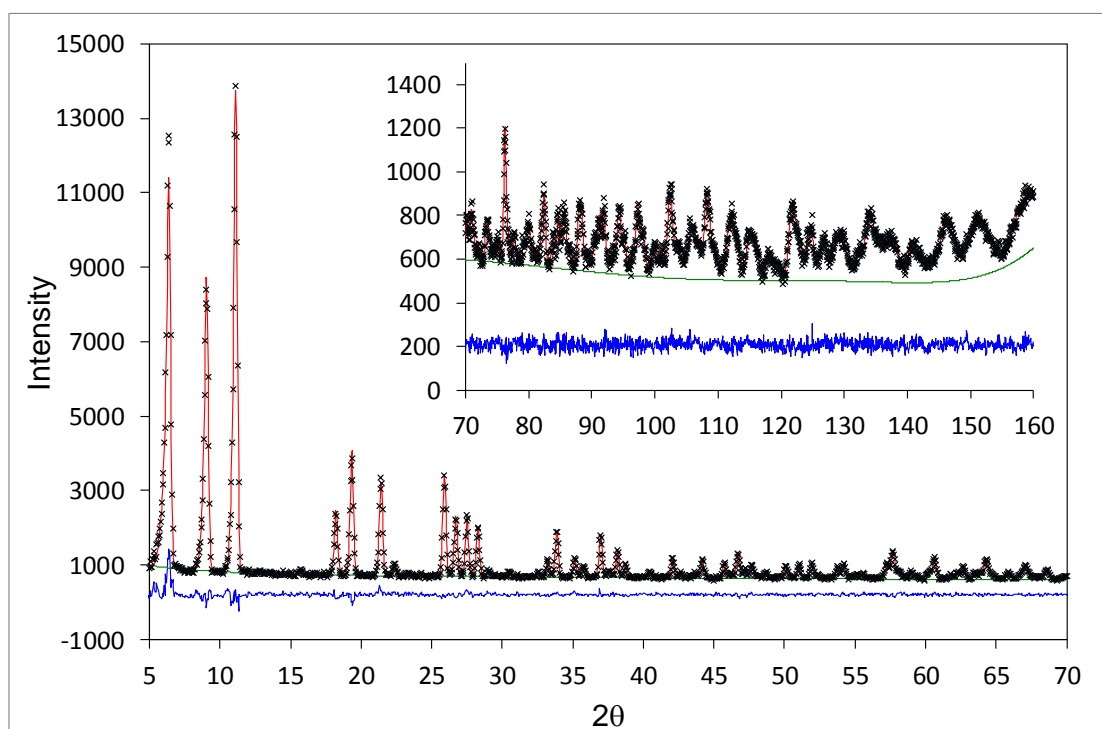


Figure S2-7. Neutron powder diffraction data collected on an activated sample of Cu-BTT at 10 K. The green line, crosses, and red line represent the background, experimental, and calculated diffraction patterns, respectively. The blue line represents the difference between experimental and calculated patterns.

Table S2-3. Fractional atomic coordinates, occupancies, and isotropic displacement parameters obtained from Rietveld refinement of the activated Cu-BTT structural model against the data presented in Figure S2-7. The optimal refinement yielded a cubic structure with *Pm-3m* space group, $a = 18.5198(4) \text{ \AA}$, and $V = 6351.9(4) \text{ \AA}^3$. Values in parentheses indicate standard deviation. Goodness-of-fit (GOF) parameters: $\chi^2 = 0.99$, $wRp = 0.0354$, $Rp = 0.0308$. (The number for corresponding CIF file in CCDC database: 1582009).

Atom	x	Y	Z	occupancy	Uiso*100 (\AA^2)
Cu1	0.1322(5)	0.5	0.0	1.0	0.010(3)
C1	0.1483(3)	0.3371(3)	-0.1483(3)	1.0	0.0063(8)
C2	0.1808(2)	0.2735(3)	-0.1808(2)	1.0	0.0063(8)
C3	0.2416(3)	0.2416(3)	-0.1492(4)	1.0	0.0063(8)
Cl1	0.0	0.5	0.0	1.0	0.045(5)
N1	0.1296(2)	0.4251(2)	-0.0787(2)	1.0	0.0102(5)
N2	0.1747(2)	0.3704(2)	-0.0892(2)	1.0	0.0102(5)
H1	0.2664(5)	0.2664(5)	-0.1027(7)	1.0	0.021(4)
Cu2	0.231(2)	0.356(3)	0.0	0.192(8)	0.06409
Os	0.250(3)	0.5	0.0	0.17(2)	0.01168
Cl2	0.366(2)	0.366(2)	0.0	0.192(8)	0.06535

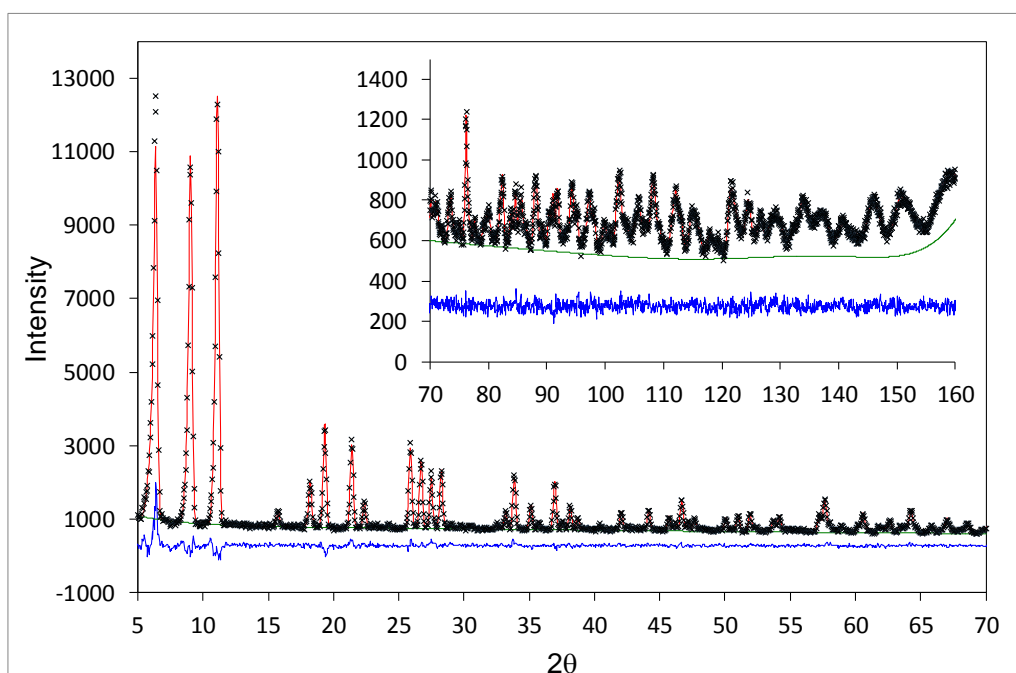


Figure S2-8. Neutron powder diffraction data collected at 10 K for a sample of Cu-BTT loaded with 0.533 CO₂ per Cu site (6.396 CO₂ per unit cell). The green line, crosses, and red line represent the background, experimental, and calculated diffraction patterns, respectively. The blue line represents the difference between experimental and calculated patterns.

Table S2-4. Fractional atomic coordinates, occupancies, and isotropic displacement parameters obtained from Rietveld refinement of the structural model for Cu-BTT (loaded with 0.533 CO₂ per Cu site) against diffraction data presented in Figure S2-8. The structure is cubic with *Pm-3m* space group, $a = 18.5295(3)$ Å, and $V = 6362.0(3)$ Å³. Values in parentheses represent standard deviation. GOF parameters: $\chi^2 = 1.01$, $wRp = 0.0354$, $Rp = 0.0305$. (The number for corresponding CIF file in CCDC database: 1582006).

Atom	x	y	Z	occupancy	Uiso*100 (Å ²)
Cu1	0.1330(5)	0.5	0	1	0.008(3)
C1	0.1477(3)	0.3374(3)	-0.1477(3)	1	0.0065(9)
C2	0.1801(2)	0.2714(3)	-0.1801(2)	1	0.0065(9)
C3	0.2420(3)	0.2420(3)	-0.1484(4)	1	0.0065(9)
Cl1	0	0.5	0	1	0.041(5)
N1	0.1294(2)	0.4254(2)	-0.0784(2)	1	0.0081(5)
N2	0.1741(2)	0.3701(2)	-0.0894(2)	1	0.0081(5)
H1	0.2657(5)	0.2657(5)	-0.1013(7)	1	0.020(4)
Cu2	0.227(1)	0.384(2)	0	0.19199	0.06409
Cl1a	0.291(1)	0.4388(6)	0	0.266(5)	0.011(6)
O1a	0.274(2)	0.5	0	0.533(9)	0.08(1)
O1b	0.312(2)	0.380(1)	0	0.266(5)	0.05(1)
Cl2	0.358(2)	0.358(2)	0	0.19199	0.06535
Os	0.2505(7)	0.5	0	0.17378	0.01168

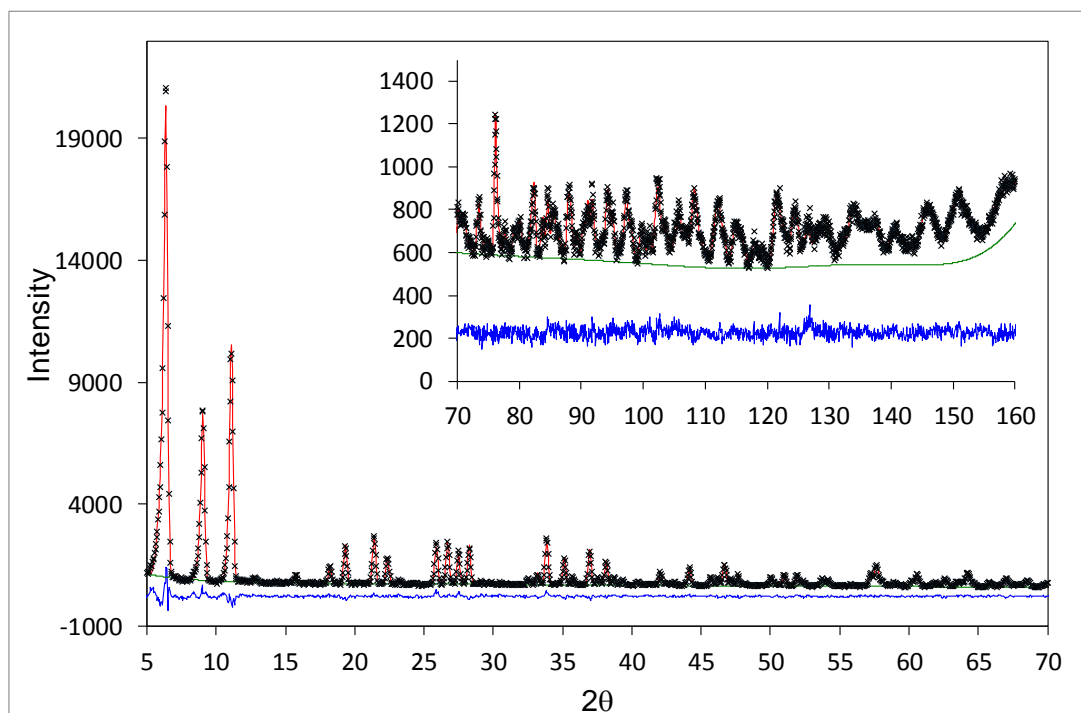


Figure S2-9. Neutron powder diffraction data collected at 10 K on a sample of Cu-BTT loaded with 1.558 CO₂ per Cu site (18.696 CO₂ per unit cell). The green line, crosses, and red line represent the background, experimental, and calculated diffraction patterns, respectively. The blue line represents the difference between experimental and calculated patterns.

Table S2-5. Fractional atomic coordinates, occupancies, and isotropic displacement parameters obtained from Rietveld refinement of the structural model for Cu-BTT loaded with 1.558 CO₂ per Cu site (18.696 CO₂ per unit cell) against diffraction data collected presented in Figure S2-9. The structure is cubic, space group *Pm-3m*, $a = 18.5323(4)$ Å, $V = 6364.8(4)$ Å³. Values in parentheses represent standard deviation. GOF parameters: $\chi^2 = 1.05$, $wRp = 0.0369$, $Rp = 0.0319$. (The number for corresponding CIF file in CCDC database: 1582007).

Atom	x	y	Z	occupancy	Uiso*100 (Å ²)
Cu1	0.1330(5)	0.5	0	1	0.016(3)
C1	0.1478(3)	0.3363(3)	-0.1478(3)	1	0.0085(8)
C2	0.1793(3)	0.2717(4)	-0.1793(3)	1	0.0085(8)
C3	0.2405(3)	0.2405(3)	-0.1474(4)	1	0.0085(8)
Cl1	0	0.5	0	1	0.061(6)
N1	0.1299(2)	0.4258(2)	-0.0778(2)	1	0.0103(5)
N2	0.1744(2)	0.3699(2)	-0.0890(2)	1	0.0103(5)
H1	0.2636(5)	0.2636(5)	-0.1014(7)	1	0.016(3)
Cu2	0.216(1)	0.328(2)	0	0.19199	0.06409
C1a	0.2915(7)	0.4389(4)	0	0.434(5)	0.03625
O1a	0.2753(8)	0.5	0	0.87(1)	0.10109
O1b	0.309(1)	0.3787(7)	0	0.434(5)	0.07825
C4a	0.095(4)	0.066(3)	0.066(3)	0.058(3)	0.04533
O4a	0.080(5)	0.023(3)	0.023(3)	0.058(3)	0.04533
O4b	0.110(3)	0.110(3)	0.110(3)	0.17(1)	0.04533
C2a	0	0.272(1)	0.036(1)	0.180(4)	0.03761
O2b	0	0.221(1)	0.072(2)	0.180(4)	0.06551
O2a	0	0.324(1)	0	0.72(2)	0.05482
C3a	0.1597(8)	0.1597(8)	0	0.33(1)	0.06602
O3a	0.0990(8)	0.173(4)	0	0.165(5)	0.04786
O3b	0.2199(8)	0.146(4)	0	0.165(5)	0.04786
Os	0.2505(8)	0.5	0	0.17378	0.01168
Cl2	0.349(2)	0.349(2)	0	0.19199	0.06535

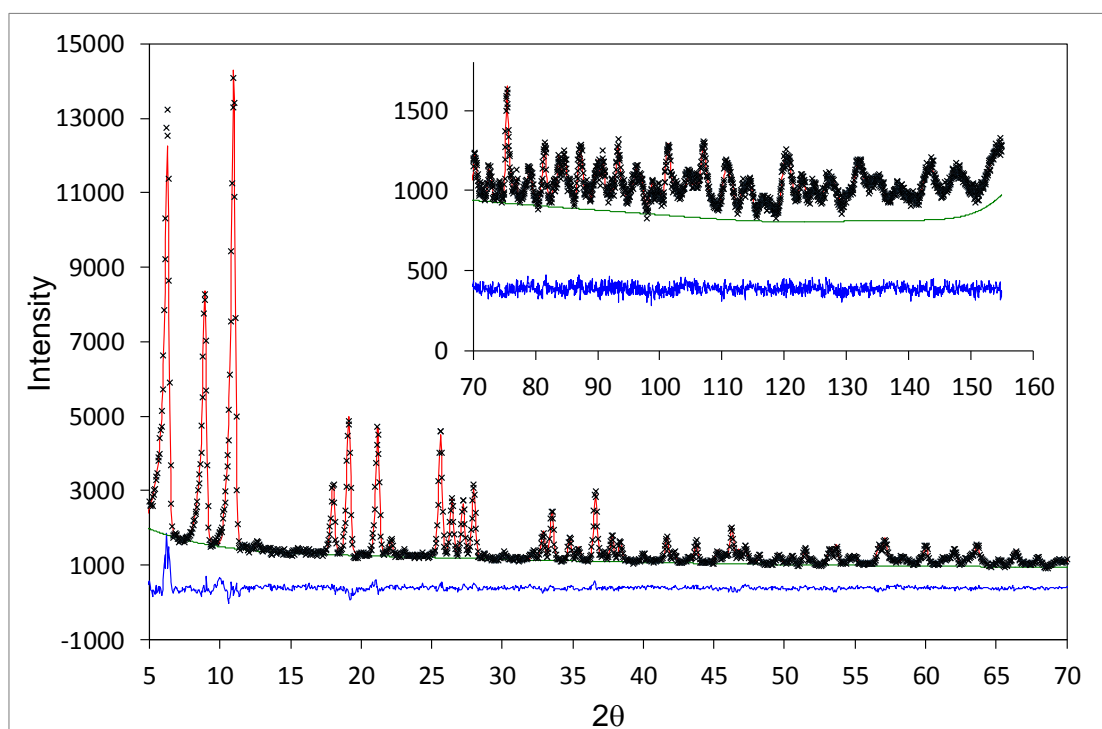


Figure S2-10. Neutron powder diffraction data collected at 10 K for an activated sample of Cr-BTT. The green line, crosses, and red line represent the background, experimental, and calculated diffraction patterns, respectively. The blue line represents the difference between experimental and calculated patterns.

Table S2-6. Fractional atomic coordinates, occupancies, and isotropic displacement parameters obtained from Rietveld refinement of the activated Cr-BTT structural model against data presented in Figure S2-10. The structure is cubic, space group $Pm\bar{3}m$, $a = 18.6689(4)$ Å, and $V = 6506.6(4)$ Å³. Values in parentheses indicate one standard deviation in the refined value. GOF parameters: $\chi^2 = 1.06$, $wRp = 0.0296$, $Rp = 0.0255$. (The number for corresponding CIF file in CCDC database: 1582001).

Atom	X	y	Z	occupancy	Uiso*100 (Å ²)
Cr1	0.136(1)	0.5	0	1	0.00605
C1	0.1494(3)	0.3365(4)	0.1494(3)	1	0.009(1)
C2	0.1817(3)	0.2737(4)	0.1817(3)	1	0.009(1)
C3	0.2435(3)	0.2435(3)	-0.1507(4)	1	0.009(1)
Cl1	0	0.5	0	1	0.032(5)
N1	0.1311(2)	0.4234(2)	0.0801(2)	1	0.0119(6)
N2	0.1750(2)	0.3694(2)	0.0909(2)	1	0.0119(6)
H1	0.2675(5)	0.2675(5)	-0.1062(7)	1	0.016(4)
Os	0.233(2)	0.5	0	0.24(2)	0.00351

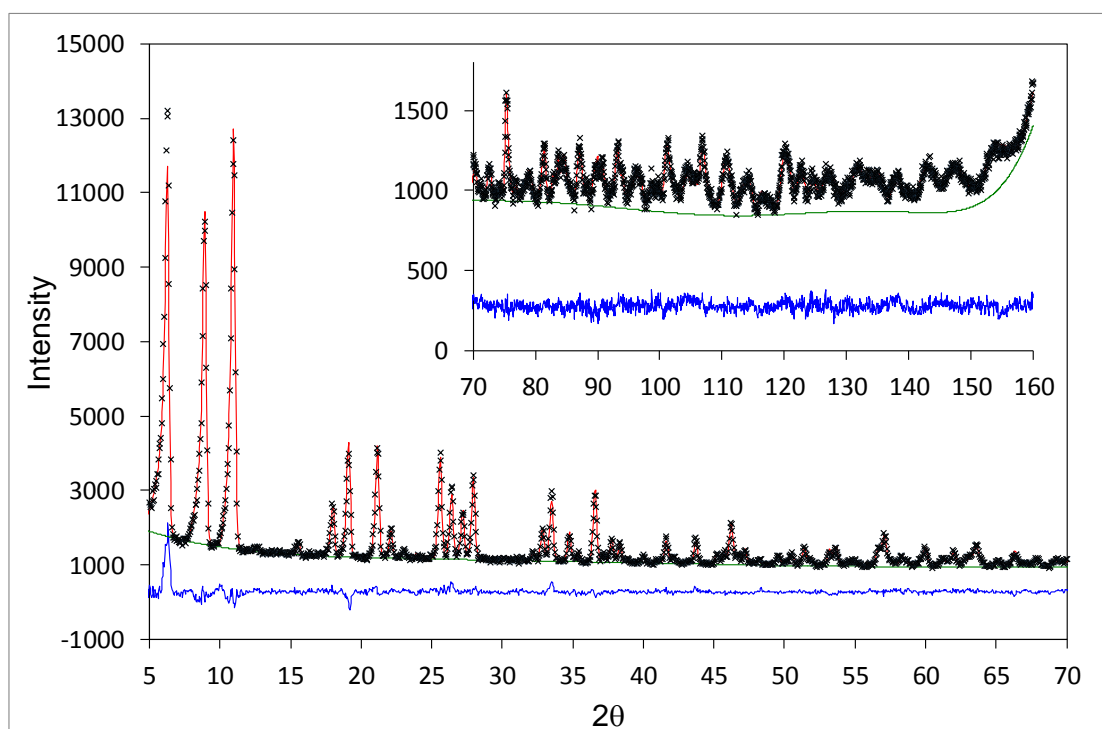


Figure S2-11. Neutron powder diffraction data collected at 10 K on a sample of Cr-BTT loaded with 0.56 CO₂ per Cr site (6.72 CO₂ per unit cell). The green line, crosses, and red line represent the background, experimental, and calculated diffraction patterns, respectively. The blue line represents the difference between experimental and calculated patterns. Data was collected at NIST.

Table S2-7. Fractional atomic coordinates, occupancies, and isotropic displacement parameters obtained from Rietveld refinement of the structural model for Cr-BTT loaded with 0.56 CO₂ per Cr site (6.72 CO₂ per unit cell) against the data presented in Figure S2-11. The structure is cubic, space group *Pm-3m*, $a = 18.6867(5)$ Å, $V = 6252.2(5)$ Å³. Values in parentheses indicate standard deviation. GOF parameters: $\chi^2 = 1.16$, $wRp = 0.0333$, $Rp = 0.0288$. (The number for corresponding CIF file in CCDC database: 1582003).

Atom	X	Y	Z	occupancy	Uiso*100 (Å ²)
Cr1	0.132(1)	0.5	0	1	0.00991
C1	0.1485(3)	0.3366(4)	-0.1485(3)	1	0.013(1)
C2	0.1806(3)	0.2713(4)	-0.1806(3)	1	0.013(1)
C3	0.2425(3)	0.2425(3)	-0.1486(5)	1	0.013(1)
Cl1	0	0.5	0	1	0.057(7)
N1	0.1301(2)	0.4231(2)	-0.0792(2)	1	0.0139(7)
N2	0.1753(3)	0.3698(2)	-0.0900(2)	1	0.0139(7)
H1	0.2662(6)	0.2662(6)	-0.1068(8)	1	0.016(5)
Os	0.230(1)	0.5	0	0.2353	0.00351
Ca	0.291(1)	0.4399(7)	0	0.277(5)	0.07288
Oa	0.275(2)	0.5	0	0.56(1)	0.08225
Ob	0.312(2)	0.382(1)	0	0.277(5)	0.07411

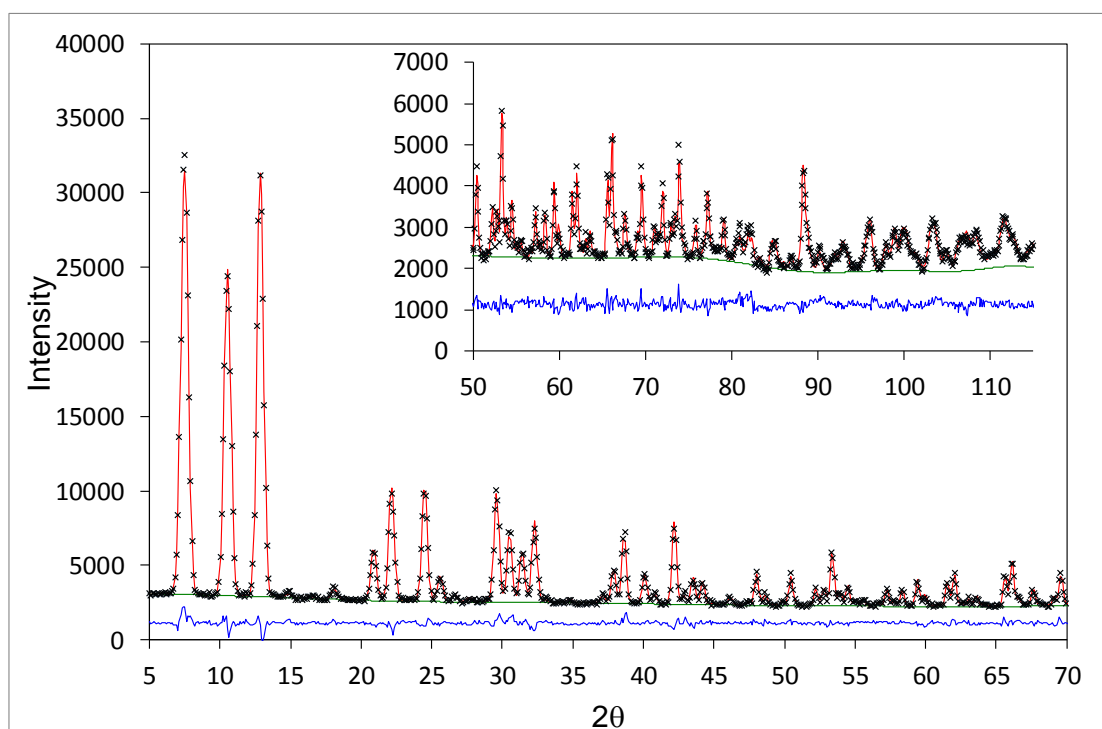


Figure S2-12. Neutron powder diffraction data collected at 10 K on Cr-BTT loaded with 0.436 CO₂ per Cr site (5.23 CO₂ per unit cell). The green line, crosses, and red line represent the background, experimental, and calculated diffraction patterns, respectively. The blue line represents the difference between experimental and calculated patterns. Data was collected at Chalk River Laboratories at the Canadian Neutron Beam Center.

Table S2-8. Fractional atomic coordinates, occupancies, and isotropic displacement parameters obtained from Rietveld refinement of the structural model for Cr-BTT loaded with 0.436 CO₂ per Cr site (5.23 CO₂ per unit cell) against the data presented in Figure S2-12. The structure is cubic, space group *Pm-3m*, $a = 18.7761(6)$ Å, $V = 6619.4(6)$ Å³. Values in parentheses indicate standard deviation. GOF parameters: $\chi^2 = 2.13$, $wRp = 0.0360$, $Rp = 0.0284$. (The number for corresponding CIF file in CCDC database: 1582004).

Atom	X	Y	Z	occ.	Uiso*100 (Å ²)
Cr1	0.134(2)	0.5	0	1	0.01(3)
C1	0.1476(5)	0.333(1)	-0.1476(5)	1	0.012(3)
C2	0.1811(5)	0.2703(6)	-0.1811(5)	1	0.012(3)
C3	0.2440(5)	0.2440(5)	-0.1484(6)	1	0.012(3)
Cl1	0	0.5	0	1	0.12(2)
N1	0.1314(3)	0.4221(3)	-0.0788(3)	1	0.010(1)
N2	0.1748(4)	0.3695(3)	-0.0924(4)	1	0.010(1)
H1	0.2635(7)	0.2635(7)	-0.1027(9)	1	0.02(1)
Os	0.233(2)	0.5	0	0.22	0.004
Ca	0.289(2)	0.4385(8)	0	0.218(5)	0.012(3)
Oa	0.277(2)	0.5	0	0.44(1)	0.018(2)
Ob	0.306(3)	0.378(1)	0	0.218(5)	0.012(2)

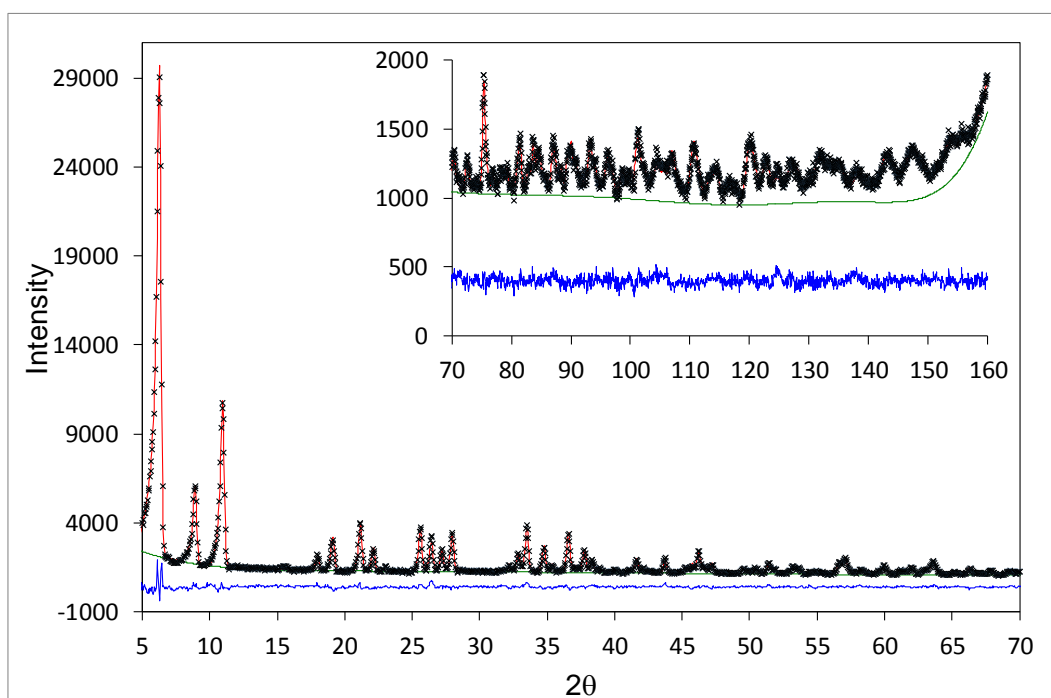


Figure S2-13. Neutron powder diffraction data collected at 10 K on Cr-BTT loaded with 1.275 CO₂ per Cr site (15.304 CO₂ per unit cell). The green line, crosses, and red line represent the background, experimental, and calculated diffraction patterns, respectively. The blue line represents the difference between experimental and calculated patterns.

Table S2-9. Fractional atomic coordinates, occupancies, and isotropic displacement parameters obtained from Rietveld refinement of the structural model for Cr-BTT loaded with 1.275 CO₂ per Cr site (15.304 CO₂ per unit cell) against data shown in Figure S2-13. The structure is cubic, space group *Pm-3m*, *a* = 18.6816(3) Å, *V* = 6520.0(4) Å³. Values in parentheses indicate standard deviation. GOF parameters: $\chi^2 = 1.18$, wRp = 0.0317, Rp = 0.0271. (The number for corresponding CIF file in CCDC database: 1582002).

Atom	x	y	Z	occupancy	Uiso*100 (Å ²)
Cr1	0.131(1)	0.5	0	1	0.00372
C1	0.1488(3)	0.3368(4)	-0.1488(3)	1	0.0111(9)
C2	0.1779(3)	0.2690(4)	-0.1778(3)	1	0.0111(9)
C3	0.2410(3)	0.2410(3)	-0.1460(5)	1	0.0111(9)
Cl1	0	0.5	0	1	0.11(1)
N1	0.1306(2)	0.4223(2)	-0.0788(2)	1	0.012(5)
N2	0.1748(2)	0.3694(2)	-0.0905(2)	1	0.012(5)
H1	0.2610(6)	0.2610(6)	-0.1040(7)	1	0.010(4)
C1a	0.2907(9)	0.4397(5)	0	0.386(6)	0.10145
O1a	0.272(1)	0.5	0	0.77(1)	0.065
O1b	0.310(2)	0.3808(9)	0	0.386(6)	0.10486
C4a	0.114(4)	0.0641(9)	0.0641(9)	0.133(5)	0.10621
O4a	0.071(4)	0.034(3)	0.034(3)	0.133(5)	0.10621
O4b	0.158(4)	0.095(3)	0.095(3)	0.133(5)	0.10621
C2a	0	0.277(2)	0.031(1)	0.187(4)	0.03831
O2b	0	0.224(2)	0.062(2)	0.187(4)	0.05208
O2a	0	0.330(2)	0	0.75(2)	0.06768
C3a	0.1656(7)	0.1656(7)	0	0.50(1)	0.0634
O3a	0.111(1)	0.193(2)	0	0.250(6)	0.0634
O3b	0.220(1)	0.137(2)	0	0.250(6)	0.0634
Os	0.229(1)	0.5	0	0.2353	0.00351

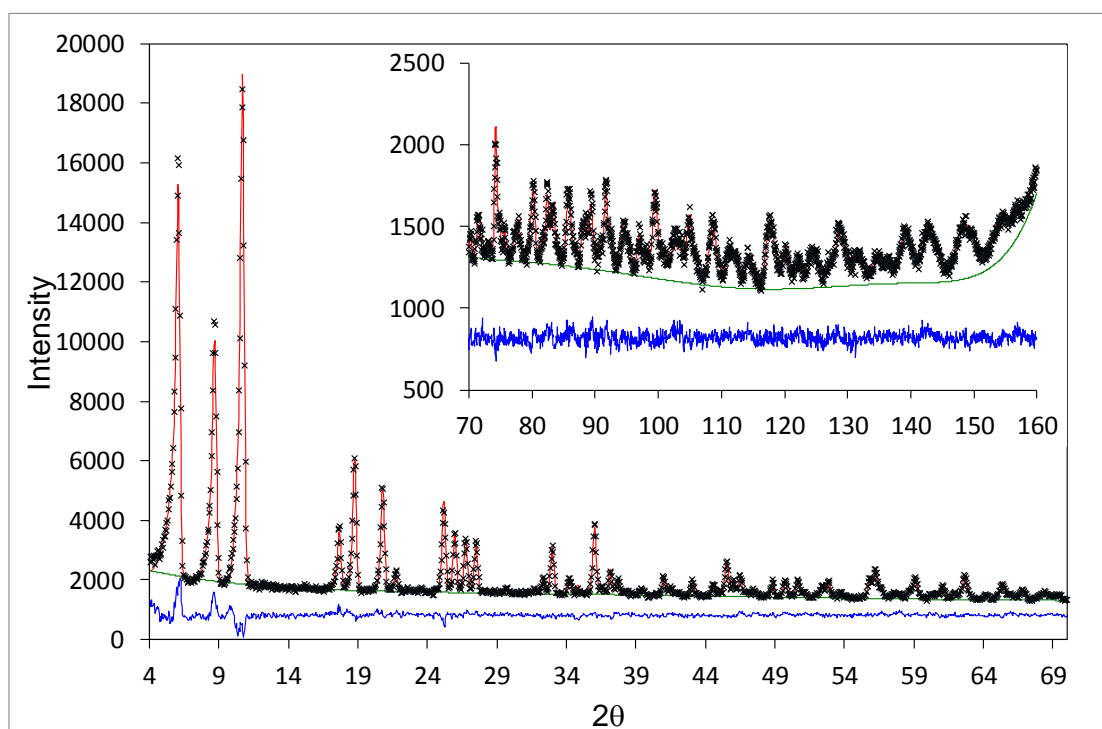


Figure S2-14. Neutron powder diffraction data obtained at 10 K on an activated sample of Fe-BTT. The green line, crosses, and red line represent the background, experimental, and calculated diffraction patterns, respectively. The blue line represents the difference between experimental and calculated patterns.

Table S2-10. Fractional atomic coordinates, occupancies, and isotropic displacement parameters obtained from Rietveld refinement of the activated Fe-BTT structural model against the data presented in Figure S2-14. The structure is cubic, space group *Pm-3m*, $a = 18.8957(4)$ Å, $V = 6746.6(5)$ Å³. Values in parentheses indicate standard deviation. GOF parameters: $\chi^2 = 1.3$, $wRp = 0.0272$, $Rp = 0.0236$. (The number for corresponding CIF file in CCDC database: 1582010).

Atom	X	y	Z	occupancy	Uiso*100 (Å ²)
Fe1	0.1343(4)	0.5	0	1	0.006(2)
C1	0.1512(3)	0.3361(5)	-0.1512(3)	1	0.019(1)
C2	0.1807(3)	0.2710(4)	-0.1807(3)	1	0.019(1)
C3	0.2419(3)	0.2419(3)	-0.1466(4)	1	0.019(1)
Cl1	0	0.5	0	1	0.007(3)
N1	0.1303(2)	0.4208(2)	-0.0816(2)	1	0.0161(7)
N2	0.1758(2)	0.3682(2)	-0.0913(2)	1	0.0161(7)
H1	0.2629(5)	0.2629(5)	-0.1069(6)	1	0.028(5)
Fe2	0.264(5)	0	0	0.18(2)	0.10(5)
Os	0.251(1)	0.5	0	0.65(2)	0.035(6)
Cs	0.303(1)	0.5	0.055(1)	0.324(9)	0.035(6)
Hsa	0.28(2)	0.5	0.0995(9)	0.324(9)	0.11(2)
Hsb	0.330(2)	0.4578(8)	0.053(2)	0.324(9)	0.11(2)

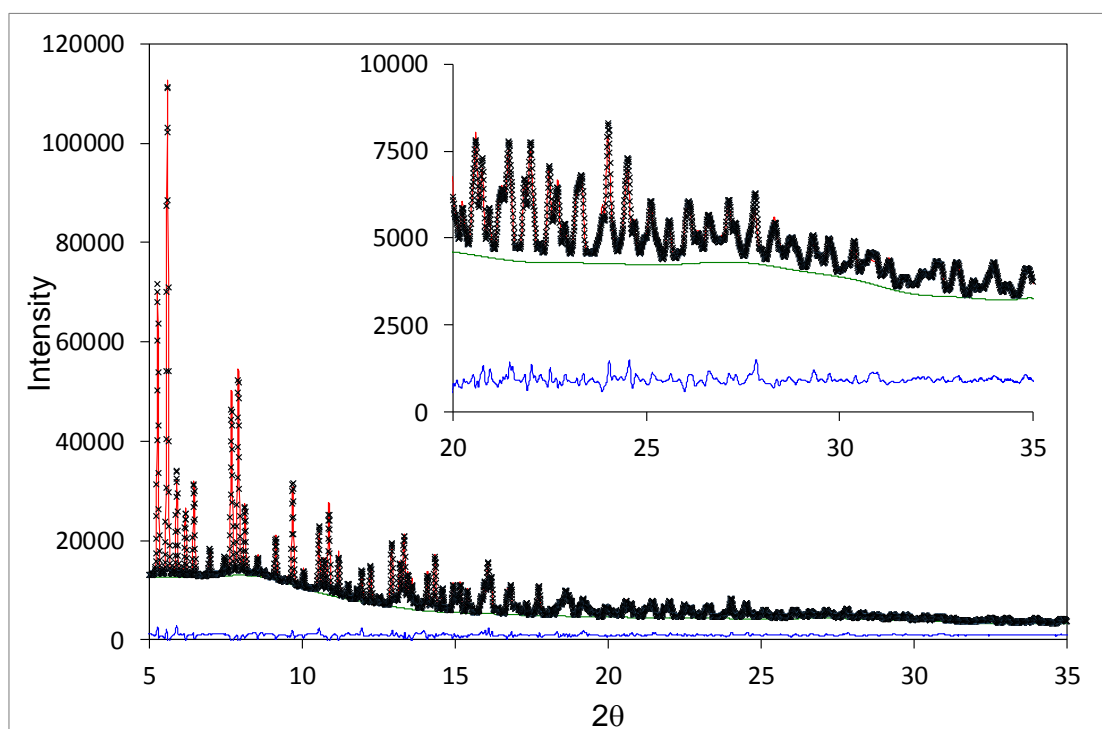


Figure S2-15. Synchrotron powder diffraction data obtained at 100 K on an activated sample of Fe-BTT. The green line, crosses, and red line represent the background, experimental, and calculated diffraction patterns, respectively. The blue line represents the difference between experimental and calculated patterns.

Table S2-11. Fractional atomic coordinates, occupancies, and isotropic displacement parameters obtained from Rietveld refinement of the activated Fe-BTT structural model against the data in Figure S2.15. The structure is cubic, space group $Pm\bar{3}m$, $a = 18.8004(1) \text{ \AA}$, $V = 6645.1(1) \text{ \AA}^3$. Values in parentheses indicate one standard deviation in the refined value. GOF parameters: $\chi^2 = 3.20$, $wRp = 0.0289$, $Rp = 0.0213$. (The number for corresponding CIF file in CCDC database: 1582005).

Atom	X	y	Z	occupancy	Uiso*100 (\AA^2)
Fe1	0.1360(1)	0.5	0	1	0.0183(4)
C1	0.1498(4)	0.3341(5)	-0.1498(4)	1	0.048(2)
C2	0.1810(4)	0.2701(4)	-0.1810(4)	1	0.048(2)
C3	0.2397(3)	0.2397(3)	-0.1468(4)	1	0.048(2)
Cl1	0	0.5	0	1	0.015(2)
N1	0.1294(1)	0.4201(2)	-0.0795(2)	1	0.019(1)
N2	0.1746(2)	0.3661(2)	-0.0920(2)	1	0.019(1)
Fe3	0.2447(24)	0	0	0.114(2)	0.28059
Os	0.2578(5)	0.5	0	1	0.09725
Cs	0.3180(6)	0.5	0.0491(7)	0.5	0.09725
Os2	0.370(3)	0.370(3)	0	0.0636(7)	0.12388
Cs2	0.4194(22)	0.4194(22)	-0.031(8)	0.0636(7)	0.12388
Os3	-0.086(5)	0	0	0.114(2)	0.28059
Fe2	0.2523(8)	0.3619(7)	0	0.127(1)	0.12388

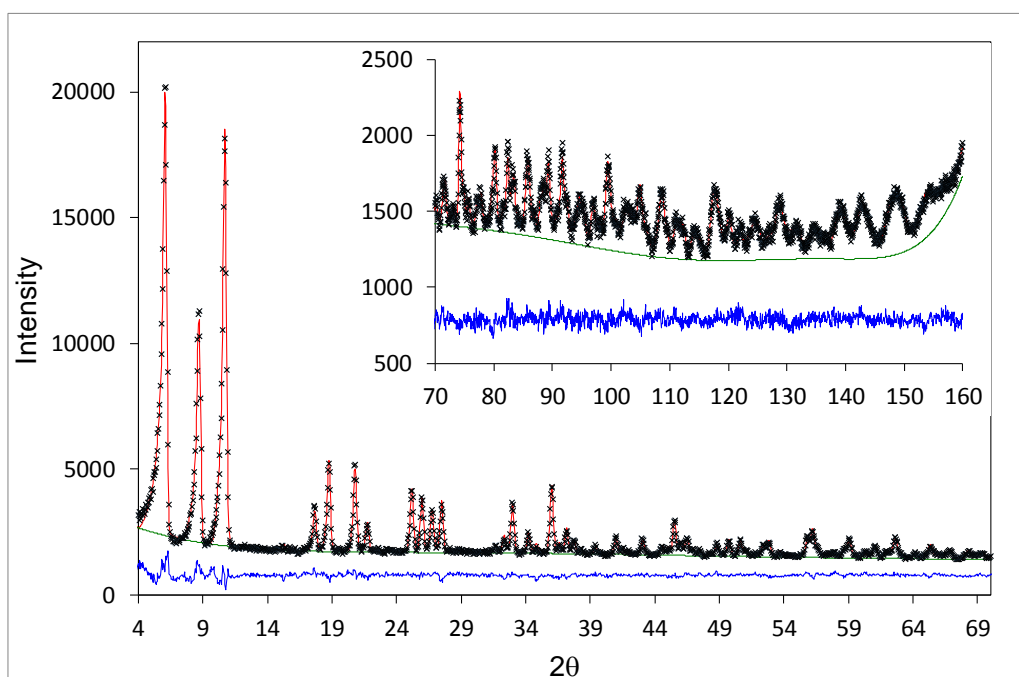


Figure S2-16. Neutron powder diffraction data obtained at 10 K on a sample of Fe-BTT loaded with 0.662 CO₂ per Fe site (7.944 CO₂ per unit cell). The green line, crosses, and red line represent the background, experimental, and calculated diffraction patterns, respectively. The difference between experimental and calculated patterns is represented as a blue line.

Table S2-12. Fractional atomic coordinates, occupancies, and isotropic displacement parameters obtained from Rietveld refinement of the structural model for Fe-BTT loaded with 0.662 CO₂ per Fe site (7.944 CO₂ per unit cell) against the data presented in Figure S2-16. The structure is cubic, space group Pm-3m, $a = 18.9005(3)$ Å, $V = 6751.8(3)$ Å³. Values in parentheses indicate standard deviation. GOF parameters: $\chi^2 = 1.12$, wRp = 0.0272, Rp = 0.0234. (The number for corresponding CIF file in CCDC database: 1582011).

Atom	x	y	Z	occupancy	Uiso*100 (Å ²)
Fe1	0.1331(4)	0.5	0	1	0.002(1)
C1	0.1517(3)	0.3369(4)	-0.1517(3)	1	0.017(1)
C2	0.1812(3)	0.2724(4)	-0.1812(3)	1	0.017(1)
C3	0.2421(3)	0.2421(3)	-0.1470(4)	1	0.017(1)
Cl1	0	0.5	0	1	0.006(4)
N1	0.1306(2)	0.4207(2)	-0.0811(2)	1	0.0148(5)
N2	0.1766(2)	0.3680(2)	-0.0918(2)	1	0.0148(5)
H1	0.2633(5)	0.2633(5)	-0.1073(6)	1	0.025(4)
Fe2	0.268(3)	0	0	0.1793	0.10322
Os	0.2482(6)	0.5	0	0.6471	0.03508
Cs	0.301(1)	0.5	0.054(1)	0.3236	0.03508
O1a	0.258(2)	0.5	0	0.36(1)	0.09(1)
O1b	0.308(3)	0.388(2)	0	0.18(5)	0.10(2)
C1a	0.285(2)	0.445(1)	0	0.18(5)	0.10(2)
Hsa	0.277(2)	0.5	0.1009(9)	0.3236	0.10908
Hsb	0.330(1)	0.4532(8)	0.049(2)	0.3236	0.10908
C2a	0	0.285(2)	0.040(2)	0.074(4)	0.09(3)
O2b	0	0.240(5)	0.081(6)	0.074(4)	0.09(3)
O2a	0	0.3308(4)	0	0.30(2)	0.07(4)
C3a	0.135(4)	0.135(4)	0	0.152(7)	0.07(2)
O3a	0.076(5)	0.118(5)	0	0.078(4)	0.07(2)
O3b	0.194(5)	0.153(5)	0	0.078(4)	0.07(2)

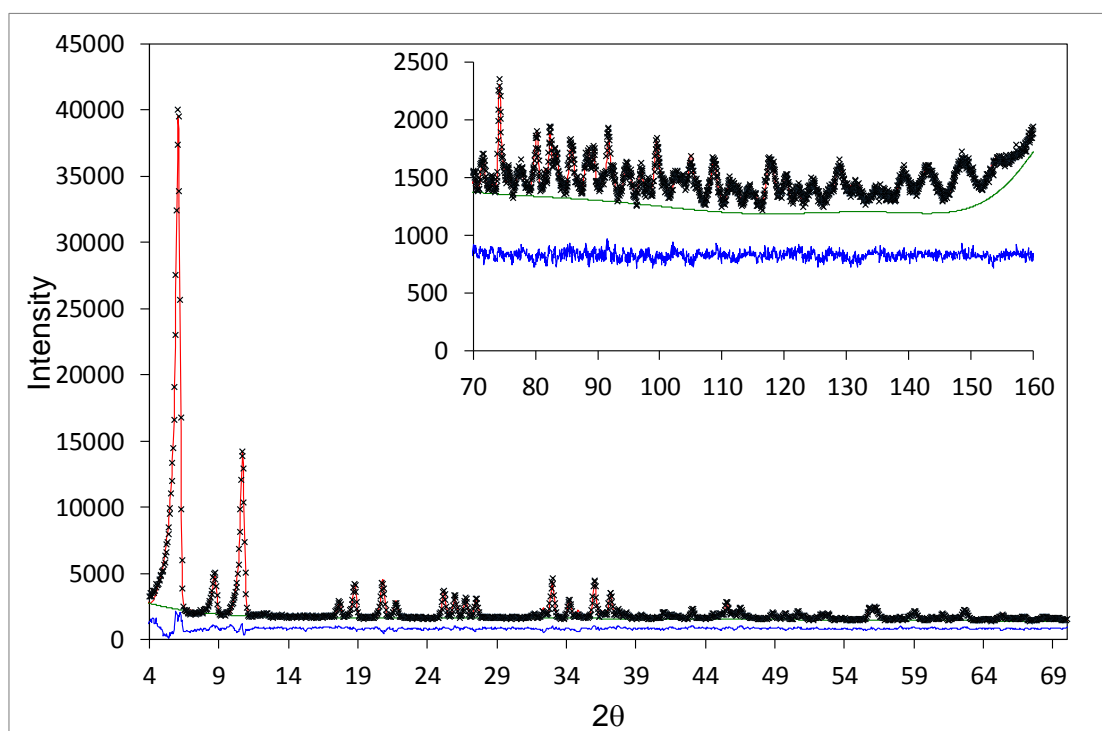


Figure S2-17. Neutron powder diffraction data obtained at 10 K on a sample of Fe-BTT loaded with 1.716 CO₂ per Fe site (20.592 CO₂ per unit cell). The green line, crosses, and red line represent the background, experimental, and calculated diffraction patterns, respectively. The blue line represents the difference between experimental and calculated patterns.

Table S2-13. Fractional atomic coordinates, occupancies, and isotropic displacement parameters obtained from Rietveld refinement of the structural model for Fe-BTT loaded with 1.716 CO₂ per Fe site (20.592 CO₂ per unit cell) against the data presented in Figure S2-17. The structure is cubic, space group *Pm-3m*, $a = 18.5952(4)$ Å, $V = 6746.1(4)$ Å³. Values in parentheses indicate standard deviation. GOF parameters: $\chi^2 = 1.56$, wRp = 0.0302, Rp = 0.0267. (The number for corresponding CIF file in CCDC database: 1582008).

Atom	X	Y	Z	occupancy	Uiso*100 (Å ²)
Fe1	0.1351(5)	0.5	0	1	0.002(2)
C1	0.1508(4)	0.3368(5)	-0.1508(4)	1	0.019(1)
C2	0.1795(4)	0.2707(5)	-0.1795(4)	1	0.019(1)
C3	0.2419(3)	0.2419(3)	-0.1473(5)	1	0.019(1)
Cl1	0	0.5	0	1	0.027(5)
N1	0.1308(3)	0.4209(3)	-0.0803(3)	1	0.0211(7)
N2	0.1752(3)	0.3665(3)	-0.0904(2)	1	0.0211(7)
H1	0.2616(6)	0.2616(6)	-0.1100(8)	1	0.026(5)
Fe2	0.2679(7)	0	0	0.1793	0.10322
Os	0.2508(7)	0.5	0	0.6471	0.03508
Cs	0.309(1)	0.5	0.047(1)	0.3236	0.03508
O1a	0.2607(8)	0.5	0	0.35765	0.09372
O1b	0.305(4)	0.385(2)	0	0.17882	0.010422
Cl1a	0.286(2)	0.444(1)	0	0.17882	0.010422
Hsa	0.291(2)	0.5	0.095(2)	0.3236	0.10908
Hsb	0.343(2)	0.460(2)	0.032(3)	0.3236	0.10908
C2a	0	0.277(1)	0.040(1)	0.205	0.015(6)
O2b	0	0.231(2)	0.080(2)	0.205	0.021(6)
O2a	0	0.321(1)	0	0.82	0.013(6)
C3a	0.1590(8)	0.1590(8)	0	0.67(1)	0.06(1)
O3a	0.099(1)	0.159(2)	0	0.33(1)	0.06(1)
O3b	0.218(1)	0.158(2)	0	0.33(1)	0.06(1)
C4a	0.101(2)	0.048(3)	0.048(3)	0.14(1)	0.06(2)
O4a	0.144(4)	0.079(2)	0.079(2)	0.14(1)	0.06(2)
O4b	0.055(2)	0.019(2)	0.019(2)	0.14(1)	0.06(2)

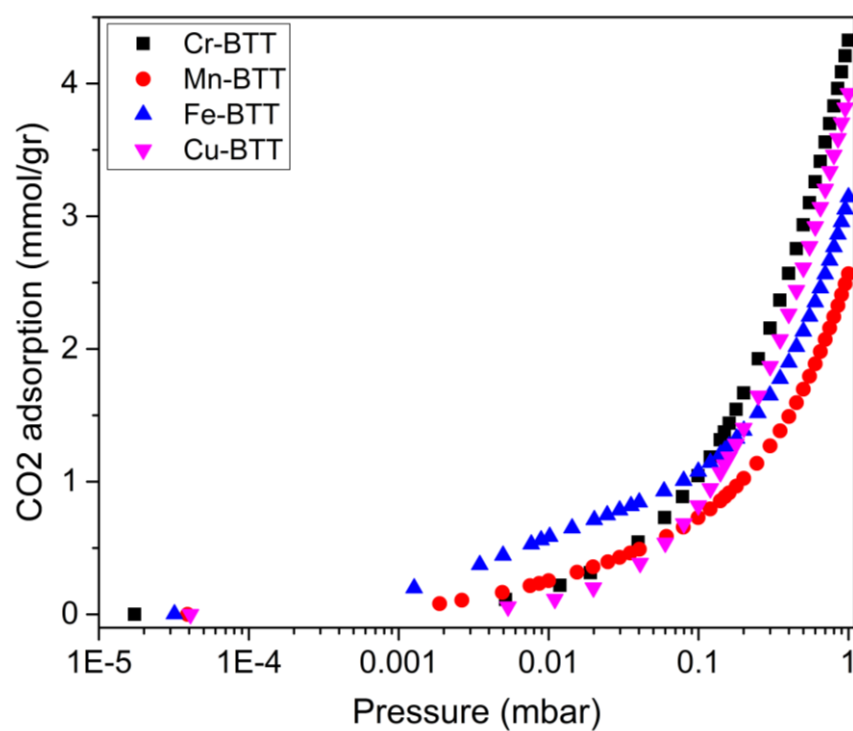


Figure S2-18. Semi-log scale plotted isotherm of CO₂ adsorption in M-BTT (M = Cr, Mn, Fe, and Cu).

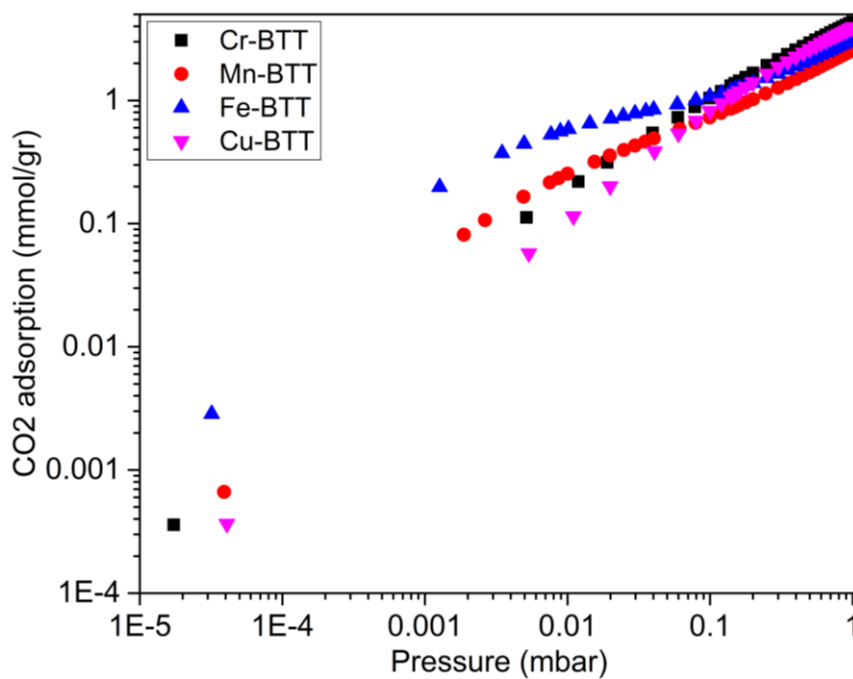


Figure S2-19. Log scale plotted isotherm of CO₂ adsorption in M-BTT (M = Cr, Mn, Fe, and Cu).

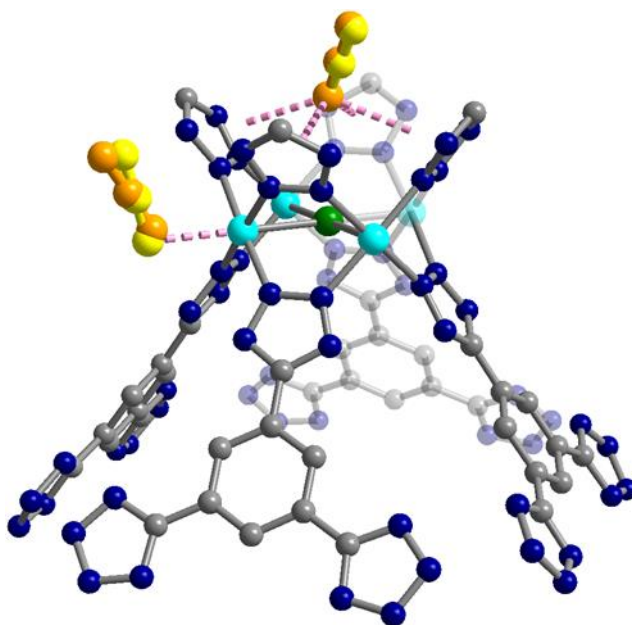


Figure S2-20. Locations of the primary and secondary CO₂ adsorption sites in Cu-BTT as determined from DFT calculations (orange ball and stick representation) and *in situ* neutron powder diffraction (yellow ball-and-stick representation). Cyan, green, blue, and gray spheres represent framework Cu, Cl, N, and C atoms, respectively; H atoms are omitted for clarity.

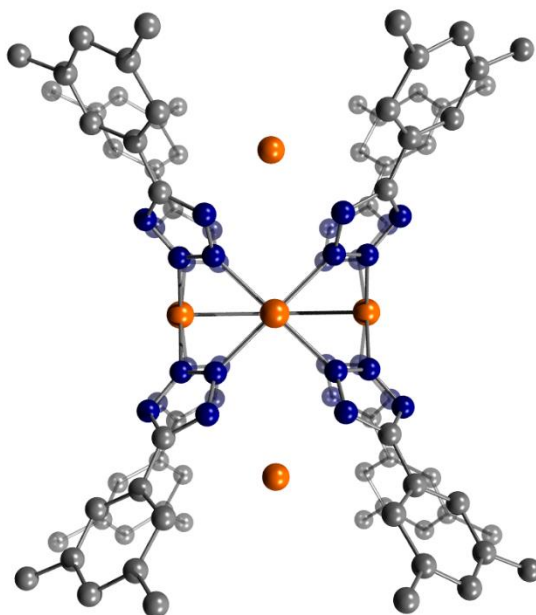


Figure S2-21. The position of extra-framework Fe cations inside Fe-BTT. Orange, blue, and grey spheres represent Fe, N, and C atoms, respectively; H atoms are omitted for clarity.

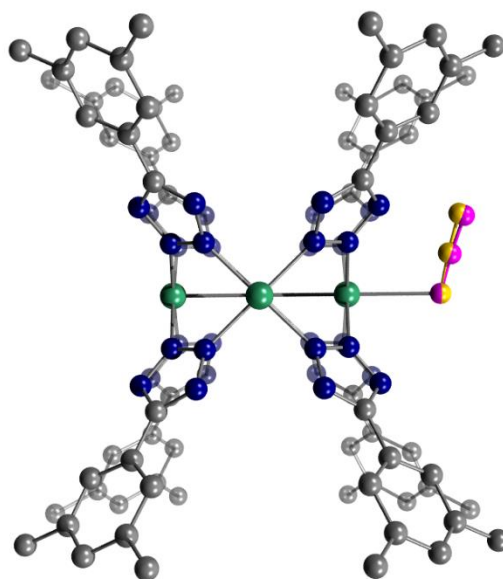


Figure S2-22. Comparison of the location of primary CO₂ adsorption sites as determined from analysis of diffraction data collected at NIST (pink ball-and-stick representation) and at the Chalk River Laboratories at the Canadian Neutron Beam Center (yellow ball-and-stick representation). Green, blue, and grey spheres represent Cr, N, and C atoms, respectively; H atoms are omitted for clarity.

7.1.5 References for the appendix to chapter 2

1. S. Brunauer, P. H. Emmett and E. Teller, *Journal of the American chemical society*, 1938, **60**, 309-319.
2. J. A. Mason, K. Sumida, Z. R. Herm, R. Krishna and J. R. Long, *Energy & Environmental Science*, 2011, **4**, 3030-3040.
3. P. M. Mathias, R. Kumar, J. D. Moyer, J. M. Schork, S. R. Srinivasan, S. R. Auvil and O. Talu, *Industrial & engineering chemistry research*, 1996, **35**, 2477-2483.
4. T. M. McDonald, D. M. D'Alessandro, R. Krishna and J. R. Long, *Chemical Science*, 2011, **2**, 2022-2028.

7.2 Appendix to chapter 3

7.2.1 SEM image of Cu-BTTri sample

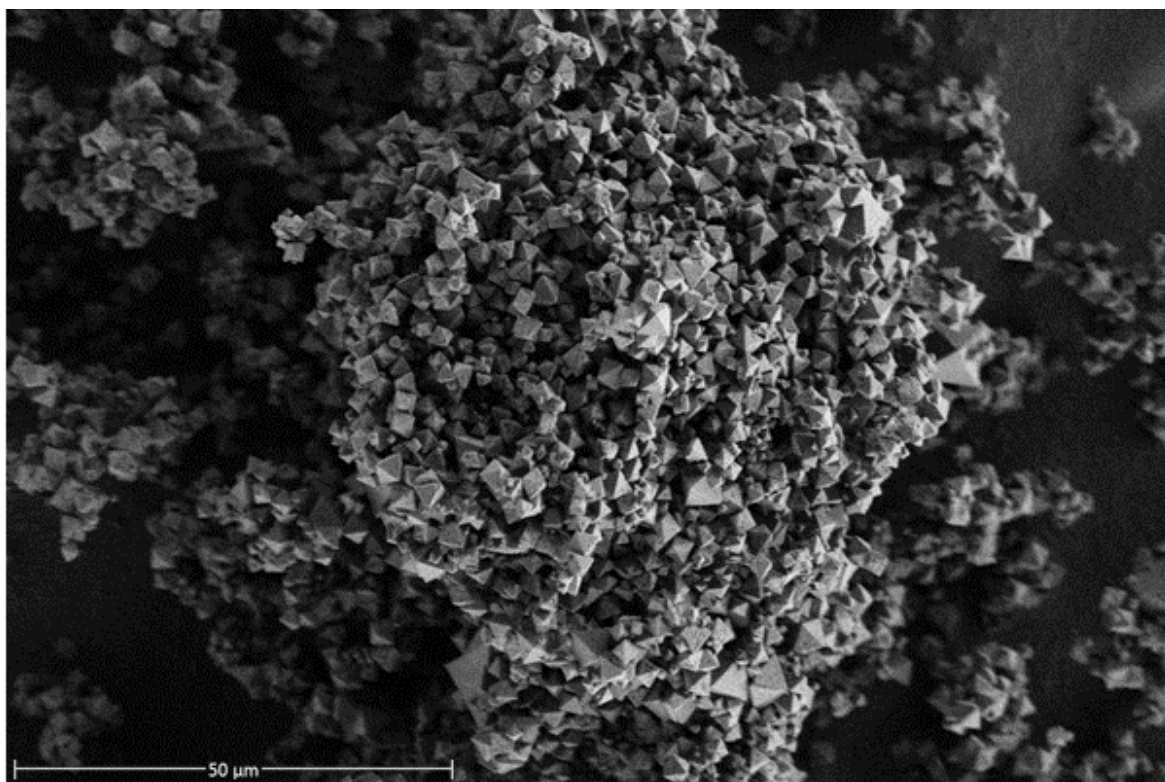


Figure S3-1. The SEM image of synthesized Cu-BTTri sample.

7.2.2 The reported structure of Cu-BTTri.

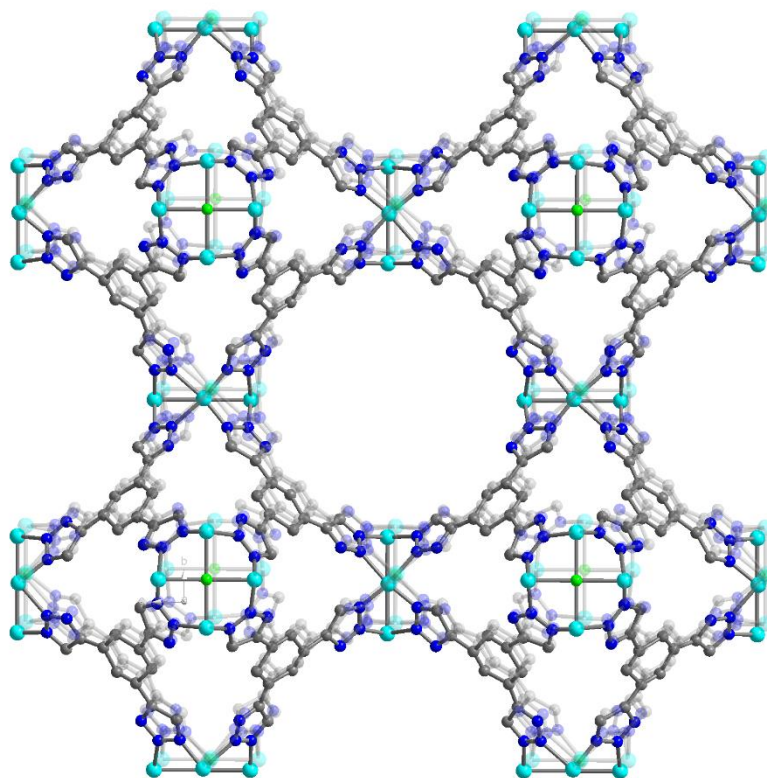


Figure S3-2. The reported structure of Cu-BTTri in the literature. Cu, Cl, N, and C atoms have been identified with cyan, green, blue and gray color. (Hydrogen atoms are excluded for clarity).

7.2.3 The EDX spectra for Cu-BTTri

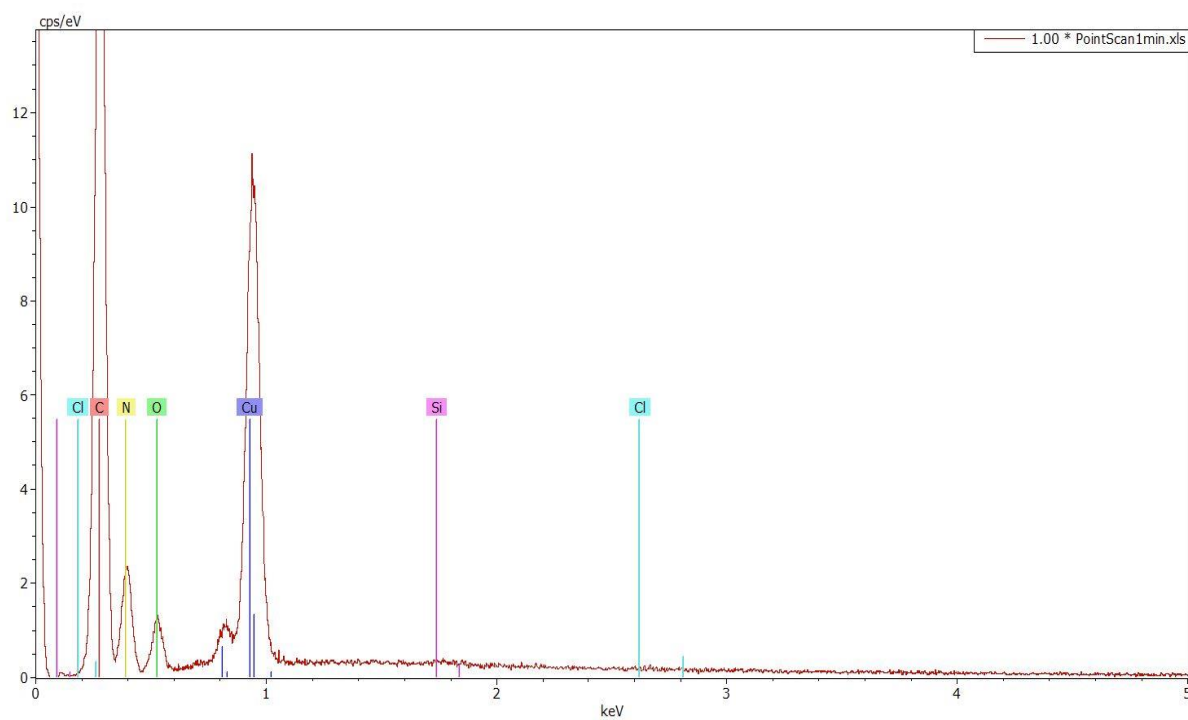


Figure S3-3. The EDX spectra for the Cu-BTTri sample.

7.2.4 Rietveld refinement of the activated framework (neutron diffraction data)

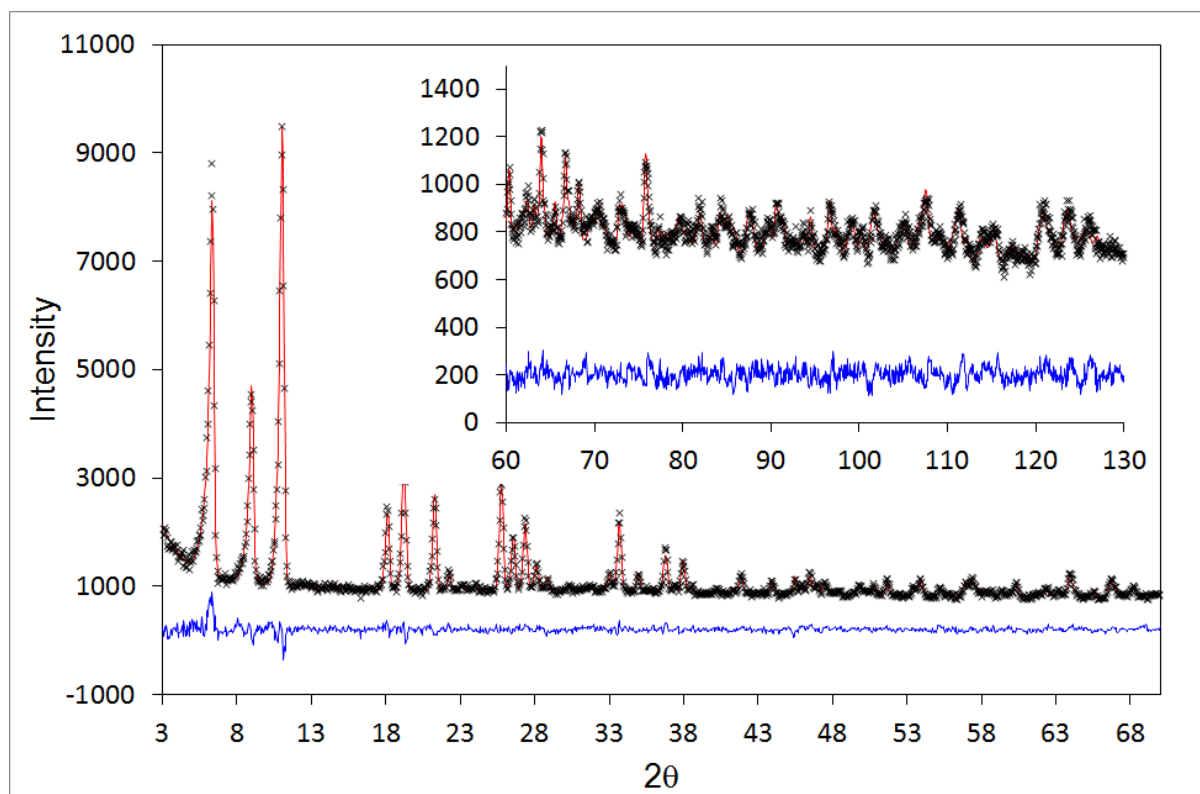


Figure S3-4. Neutron powder diffraction data collected on an activated sample of Cu-BTtri at 10 K. The crosses and red line represent the experimental and calculated diffraction patterns, respectively. The blue line represents the difference between experimental and calculated patterns.

Table S3-1. Fractional atomic coordinates, occupancies, and isotropic displacement parameters obtained from Rietveld refinement of the activated Cu-BTtri structural model against the data presented in Figure S3.7. The optimal refinement yielded a cubic structure with *Fm-3c* space group, $a = 37.128(2)$ Å, and $V = 51181(7)$ Å³. Values in parentheses indicate standard deviation. Goodness-of-fit (GOF) parameters: wRp = 0.0430, Rp = 0.0340. (The number for corresponding CIF file in CCDC database: 1872067).

Atom	x	Y	Z	occupancy	Biso (Å ²)
Cu1	0.5	0.3152(5)	0.7574(7)	1.0	0.4(5)
C1	0.3358(6)	0.6152(4)	0.3422(6)	1.0	1.4(2)
C2	0.3187(6)	0.5823(5)	0.3274(6)	1.0	1.4(2)
C3	0.3257(5)	0.6334(6)	0.3735(6)	1.0	1.4(2)
N1	0.2845(5)	0.5386(4)	0.3150(5)	1.0	2.3(1)
N2	0.3102(5)	0.5384(4)	0.2922(4)	1.0	2.3(1)
N3A	0.3313(6)	0.5667(5)	0.2958(5)	0.56(1)	2.3(1)
C1A	0.2897(7)	0.5626(6)	0.3409(7)	0.44(1)	2.3(1)
N3B	0.2897(7)	0.5626(6)	0.3409(7)	0.44(1)	2.3(1)
C1B	0.3313(6)	0.5667(5)	0.2958(5)	0.56(1)	2.3(1)
H1	0.3045(8)	0.619(1)	0.386(1)	1	2.7(7)
H1A	0.273(2)	0.573(3)	0.360(3)	0.44(1)	2.7(7)
H1B	0.356(2)	0.572(2)	0.286(2)	0.56(1)	2.7(7)

7.2.5 Rietveld refinement of the activated framework (synchrotron x-ray diffraction pattern)

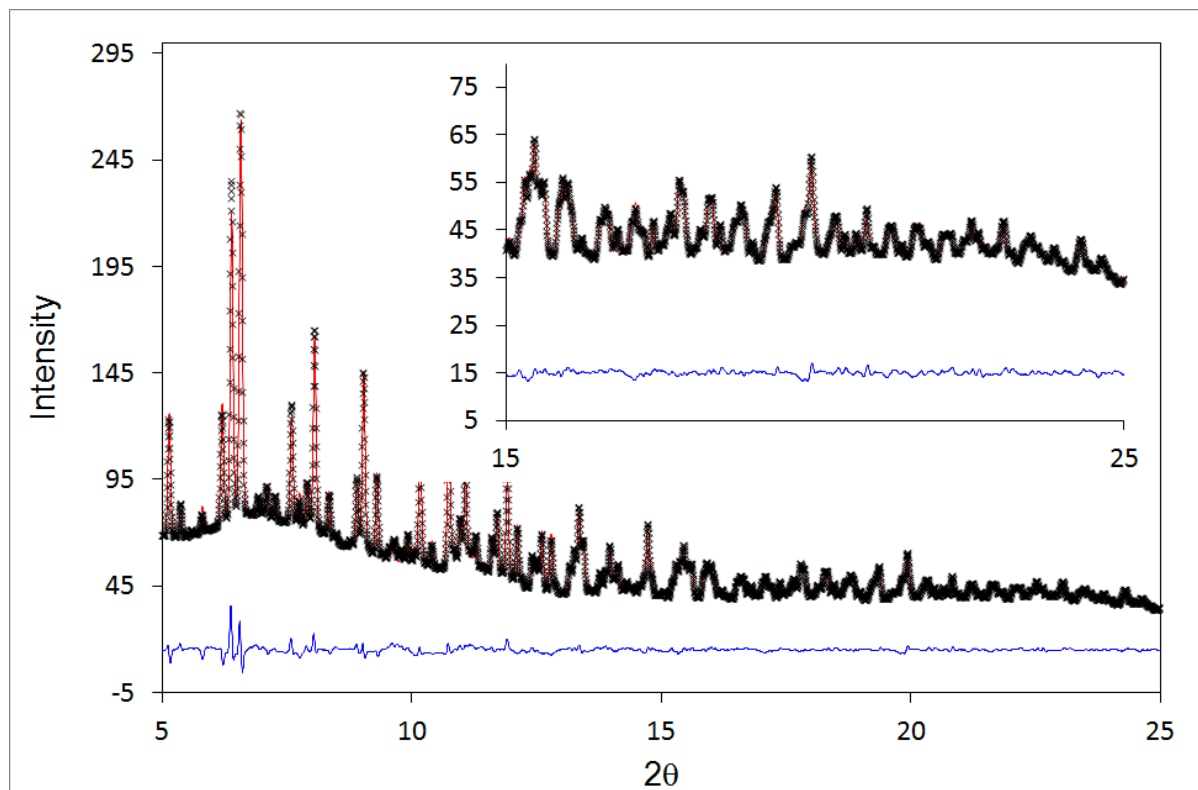


Figure S3-5. Synchrotron X-ray powder diffraction data collected on an activated sample of Cu-BTTri at 120 K ($\lambda = 0.5008 \text{ \AA}$). The crosses and red line represent the experimental and calculated diffraction patterns, respectively. The blue line represents the difference between experimental and calculated patterns.

Table S3-2. Fractional atomic coordinates, occupancies, and isotropic displacement parameters obtained from Rietveld refinement of the activated Cu-BTTri structural model against the data presented in Figure S3.4. The optimal refinement yielded a cubic structure with $Fm\text{-}3c$ space group, $a = 37.0539(5) \text{ \AA}$, and $V = 50875(2) \text{ \AA}^3$. Values in parentheses indicate standard deviation. Goodness-of-fit (GOF) parameters: $wRp = 0.0231$, $Rp = 0.0359$. (The number for corresponding CIF file in CCDC database: 1872065).

Atom	x	Y	Z	occupancy	Uiso*100 (\AA^2)
Cu1	0.24457(5)	0.5	0.31511(4)	1.0	0.64(2)
C1	0.3384(3)	0.6164(2)	0.3393(3)	1.0	2.3(1)
C2	0.3176(3)	0.5840(2)	0.3254(3)	1.0	2.3(1)
C3	0.3218(2)	0.6341(2)	0.3699(3)	1.0	2.3(1)
N1	0.2826(2)	0.5388(2)	0.3169(3)	1.0	2.3(1)
N2	0.3091(3)	0.5375(2)	0.2928(2)	1.0	2.3(1)
N3A	0.3324(3)	0.5649(3)	0.2981(2)	1.0	2.3(1)
C1A	0.2850(3)	0.5680(3)	0.3375(3)	1.0	2.3(1)

7.2.6 Cu-BTtri structure refined based on the synchrotron data

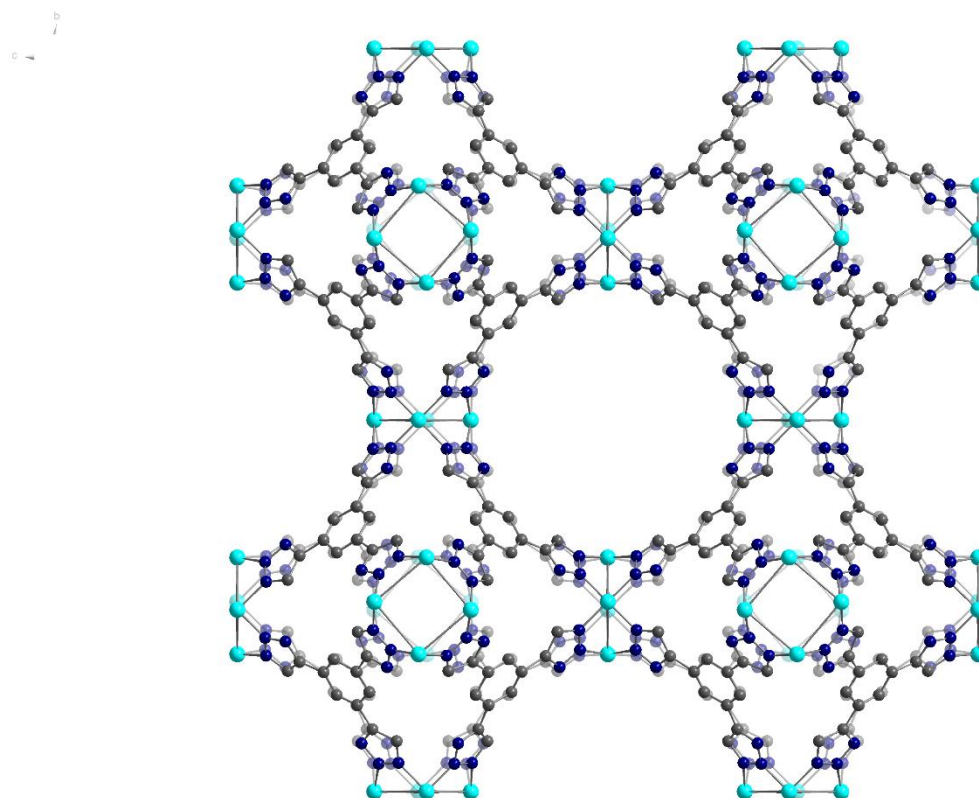


Figure S3-6. A scheme of the refined structure of activated Cu-BTtri based on the collected synchrotron x-ray diffraction pattern. Cu, N, and C atoms have been identified with cyan, blue and gray color. (Hydrogen atoms are excluded for clarity).

7.2.7 Gas adsorption measurements

UHP-grade (99.999% purity) helium, nitrogen, and hydrogen were used for all adsorption measurements. Gas adsorption isotherms for pressures in the range 0–1 bar were measured using a BELSORP-max instrument. For standard measurements in BELSORP-max, the sample was transferred to pre-weighed low pressure resistant analysis tubes, which were capped with a Transeal. The sample was evacuated and heated on the activation stages of BELSORP-max based on the desired activation program. After finishing the activation program, the evacuated analysis tubes containing degassed sample was then carefully transferred to an electronic balance and weighed to determine the mass of sample (typically 100–200 mg). For cryogenic measurements, the dewar vessel is used where is capable of keeping cryogenic baths under isolation. Then the tube was transferred to the analysis port of the gas adsorption instrument. BET surface areas and pore volumes were determined by measuring N₂ adsorption isotherms in a 77 K liquid N₂ bath and calculated, assuming a value of 16.2 Å² for the molecular cross-sectional area of N₂.

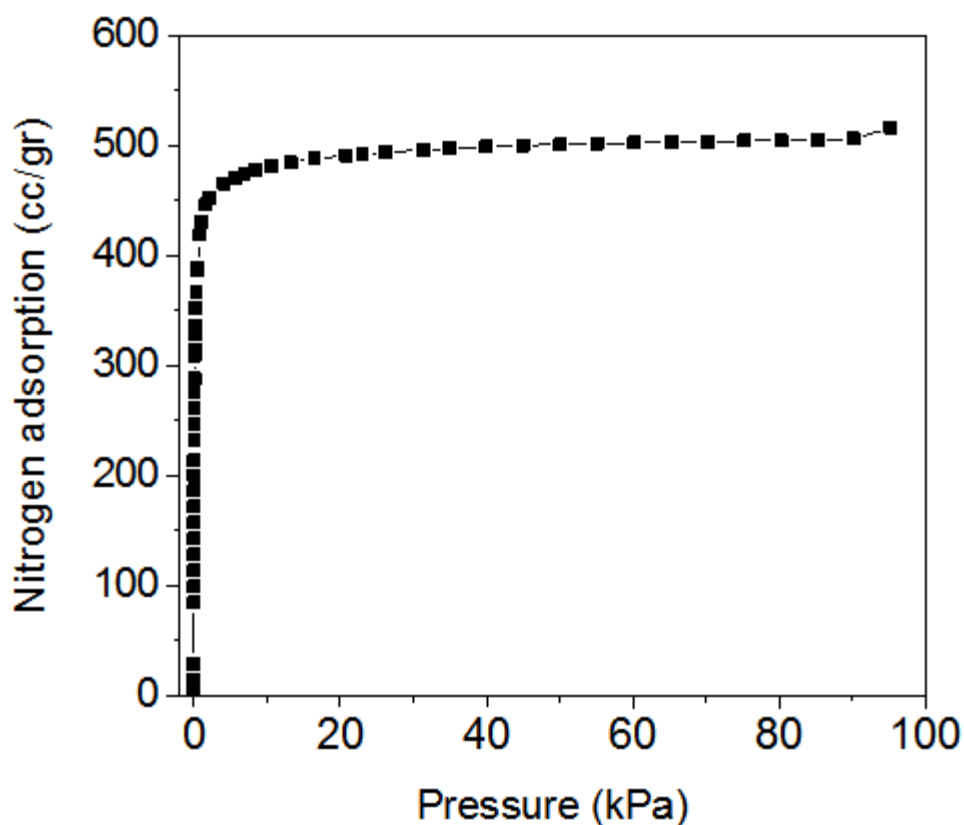


Figure S3-7. Nitrogen adsorption isotherm for Cu-BTtri collected at 77 K.

7.2.8 Pore Volume calculations based on the adsorption data for nitrogen at 77 K

As shown in Figure S3-7, the adsorption isotherm for N₂ at 77 K ceases to be a function of pressure when the pressure exceeds 200 mbar, implying that the structure has been saturated with nitrogen. Therefore, the uptake of N₂ at highest measured pressure can be considered as the full capacity of the framework for an inert small molecule, and the pore volume can then be calculated from the following formula:

$$\text{Pore Volume} = \frac{N_{N_2}^{\text{Sat}} \cdot M_{wN_2}}{1000 \cdot d_{\text{liq}N_2}|_{77K}} \quad \text{Eq. (S3 - 1)}$$

Where $N_{N_2}^{\text{Sat}}$ is the the amount of nitrogen adsorbed at the highest pressure point in mmol/g, M_{wN_2} is the molecular weight dinitrogen in g/mol and $d_{\text{liq}N_2}|_{77K}$ is the density of liquid nitrogen at 77 K in g/mL.

7.2.9 Surface area calculations based on the N₂ adsorption data at 77 K

Based on the BET theory, we have the following equation:

$$\frac{1}{N[(\frac{p_0}{p})-1]} = \frac{c-1}{N_m c} \left(\frac{p}{p_0}\right) + \frac{1}{N_m c} \quad \text{Eq. (S3 - 2)}$$

Where N is the amount of gas adsorbed in mmol/g, N_m is the monolayer adsorption in mmol/g, p is the partial pressure of N₂ and p_0 is the saturation pressure of N₂ at the measurement temperature.⁴⁰² A plot of $\frac{1}{N[(\frac{p_0}{p})-1]}$ versus $\frac{p}{p_0}$ and the best possible trendline is fit to the points on the plot. We note that points with low $\left(\frac{p}{p_0}\right)$ are chosen such that the c parameter stays positive and high R² values are obtained. With M as the slope and I as the intersect of the plot, N_m can be obtained from the following formula:

$$N_m = \frac{1}{M+I} \quad \text{Eq. (S3 - 3)}$$

The surface area can then be obtained using the following equation:

$$SA = N_m \cdot N_A \cdot CSA_{N_2} \quad \text{Eq. (S3 - 4)}$$

where N_A is Avogadro's number and CSA_{N_2} is the cross sectional area of one N₂ molecule at 77 K (taken to be 16 Å²). The above calculations were carried out on the nitrogen adsorption isotherm data collected at 77 K for Cu-BTTri; the resulting surface area has been reported in the paper.

7.2.10 Fitting Cu-BTtri hydrogen adsorption isotherms

The hydrogen adsorption isotherms collected at 140, and 159 K were fitted with a dual-site Langmuir model (Eq. S3 – 5):

$$n = \frac{abP}{1+bP} + \frac{cdP}{1+dP} \quad \text{Eq. (S3 – 5)}$$

where n is adsorbed H_2 in mmol/g, a and b are Langmuir parameter for the first adsorption site, c and d are Langmuir parameter for the second adsorption site and P is the pressure in bar. The fitted parameters for each adsorption isotherm can be found in Tables S3-3, and a comparison of the experimental H_2 adsorption isotherms with the fitted dual-site Langmuir model based on the experimental data is shown in Fig. S3-7. The dual-site Langmuir model was chosen because of the validity of the theory behind this model for prediction of the interaction of heterogeneous surfaces with gas-phase small molecules. The use of a dual-site Langmuir model for fitting gas adsorption isotherm data and the extraction of isosteric heats of adsorption has been reported elsewhere.^{62, 403-404}

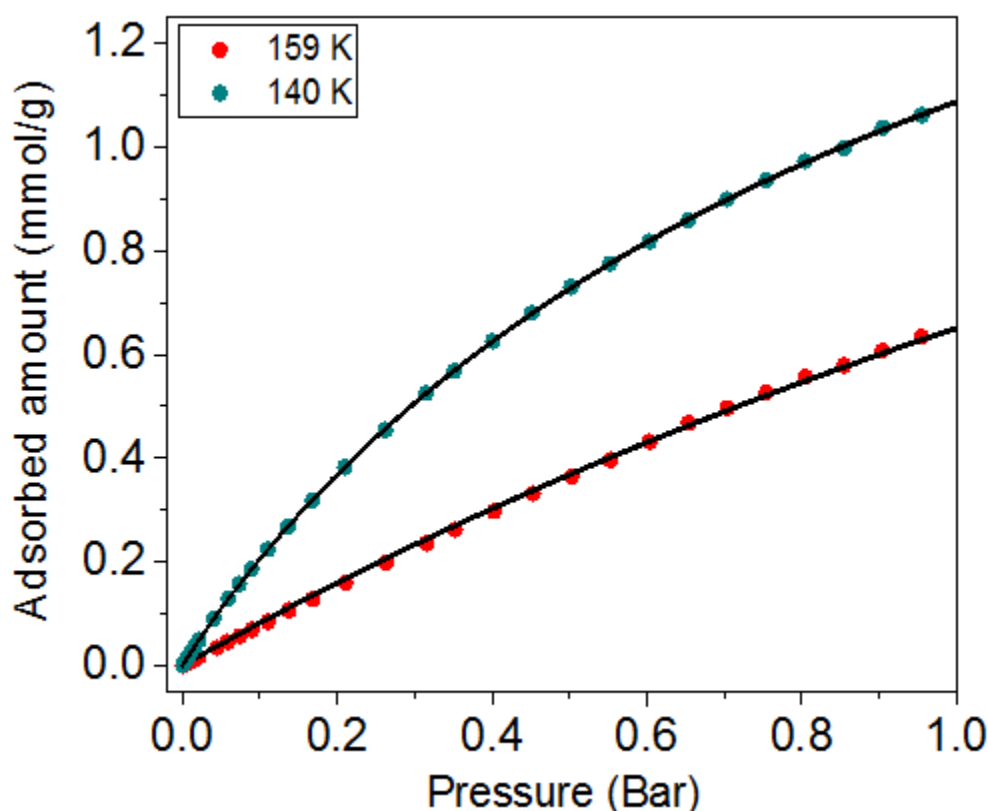


Figure S3.8. Dual-site Langmuir fits for CO₂ adsorption in Fe-BTT at 298, 308, and 318 K.

Table S3-3. Dual-site Langmuir parameters for CO₂ adsorption in M-BTT.

Framework	Temp (K)	<i>a</i>	<i>b</i>	<i>c</i>	<i>d</i>
Cu-BTTri	140	2.170E-03	9.649E-06	2.448E-05	1.451E-04
	159	2.820E-03	3.002E-06	1.001E-08	6.741E-06

7.2.11 Calculating Isosteric heats of adsorption

The Clausius-Clapeyron equation Eq. (S3 – 6) was used to calculate the isosteric heats of adsorption, Q_{st} , for H₂ adsorption in Cu-BTTri analogs at 140 K, and 159 K using dual-site Langmuir-Freundlich fits.

$$(\ln P)_n = -\frac{Q_{st}}{R} \left(\frac{1}{T} \right) + C \quad \text{Eq. (S3 – 6)}$$

Where, P is the pressure in any desired unit, n is the amount adsorbed mol/g, T is the temperature in K, R is the universal gas constant kJ/mol·K, and C is a constant. The isosteric heat of adsorption, Q_{st} , was obtained from the slope of plots of $(\ln P)_n$ as a function of inverse T . The isosteric heats of adsorption as a function of H₂ loading in Cu-BTTri can be found in Figure 3-2 in the main text (chapter 3).

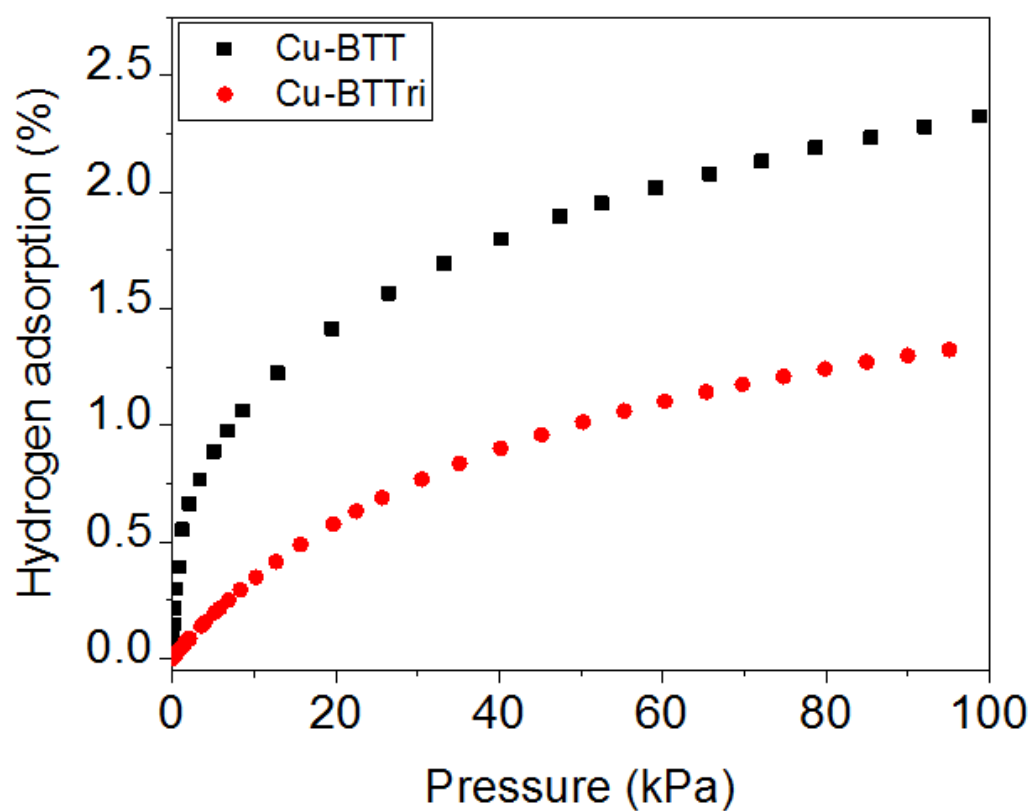


Figure S3-9. The comparison of hydrogen adsorption data for Cu-BTT and Cu-BTTri at 77K. The data for the adsorption data for Cu-BTT has been extracted from literature.²⁶⁴

7.2.12 Rietveld refinement of the framework loaded with 0.36 D_2/Cu^{2+} (neutron diffraction data)

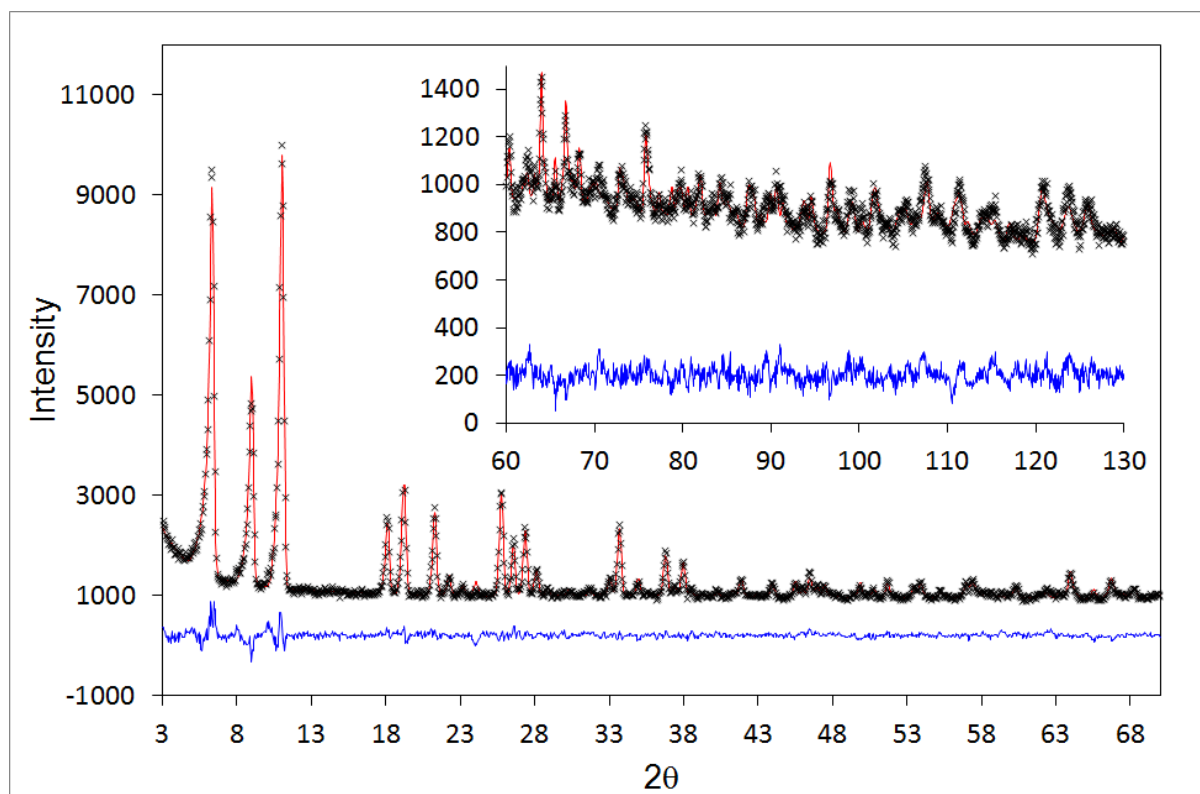


Figure S3-10. Neutron powder diffraction data collected at 10 K for a sample of Cu-BTTri loaded with 0.36 D_2 per Cu site (34.6 D_2 per unit cell). The green line, crosses, and red line represent the background, experimental, and calculated diffraction patterns, respectively. The blue line represents the difference between experimental and calculated patterns.

Table S3-4. Fractional atomic coordinates, occupancies, and isotropic displacement parameters obtained from Rietveld refinement of the structural model for Cu-BTtri loaded with 0.36 D₂ per Cu site (34.6 D₂ per unit cell) against diffraction data presented in Figure S3-10. The structure is cubic with *Pm-3m* space group, *a* = 37.105(2) Å, and *V* = 51086(7) Å³. Values in parentheses represent standard deviation. GOF parameters: wRp = 0.0426, Rp = 0.0331. (The number for corresponding CIF file in CCDC database: 1872064).

Atom	x	y	Z	occupancy	Biso (Å ²)
Cu1	0.25	0.5	0.3146(5)	1	0.4(5)
C1	0.3384(3)	0.6162(5)	0.3384(3)	1	2.9(3)
C2	0.3221(4)	0.5846(6)	0.3221(4)	1	2.9(3)
C3	0.3231(5)	0.6314(3)	0.3686(3)	1	2.9(3)
N1	0.2833(6)	0.5407(6)	0.3148(7)	1	2.9(2)
N2	0.3099(6)	0.5374(6)	0.2914(5)	1	2.9(2)
N3A	0.3320(9)	0.5654(9)	0.2934(10)	0.56	2.9(2)
C1A	0.2907(10)	0.5694(9)	0.3361(10)	0.56	2.9(2)
N3B	0.2907(10)	0.5694(9)	0.3361(10)	0.44	2.9(2)
C1B	0.3320(9)	0.5654(9)	0.2934(10)	0.44	2.9(2)
H1	0.2999(9)	0.617(2)	0.383(2)	1	3.2(8)
H1A	0.274(5)	0.576(4)	0.359(5)	0.44	3.2(8)
H1B	0.357(5)	0.571(4)	0.275(4)	0.56	3.2(8)
D1	0.239(5)	0.490(5)	0.390(2)	0.27(3)	12
D2	0.425(9)	0.697(8)	0.062(9)	0.09(2)	8

7.2.13 Rietveld refinement of the framework loaded with 3.11 D_2/Cu^{2+} (neutron diffraction data)

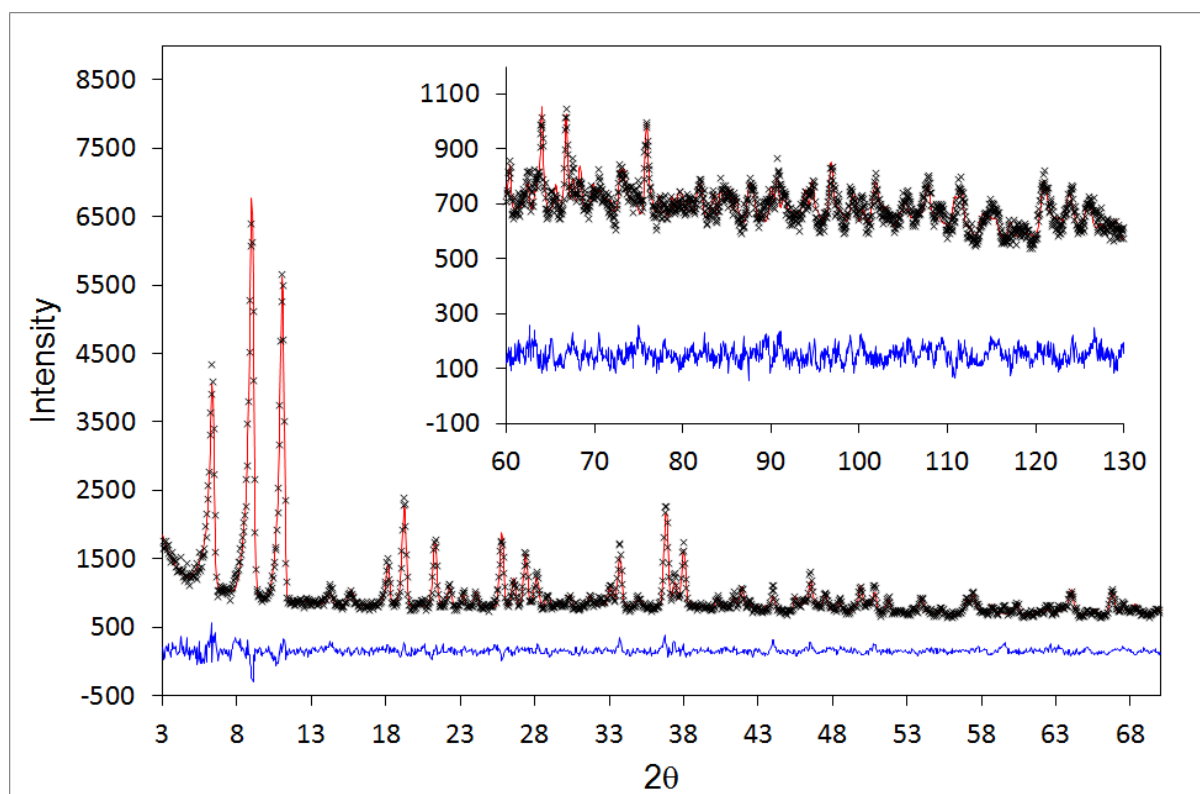


Figure S3-11. Neutron powder diffraction data collected at 10 K on a sample of Cu-BTTRI loaded with 3.11 D_2 per Cu site (299 D_2 per unit cell). The green line, crosses, and red line represent the background, experimental, and calculated diffraction patterns, respectively. The blue line represents the difference between experimental and calculated patterns.

Table S3-5. Fractional atomic coordinates, occupancies, and isotropic displacement parameters obtained from Rietveld refinement of the structural model for Cu-BTTri loaded with 3.11 D₂ per Cu site (299 D₂ per unit cell) against diffraction data collected presented in Figure S3-11. The structure is cubic, space group *Pm-3m*, *a* = 37.080(1) Å, *V* = 50982(5) Å³. Values in parentheses represent standard deviation. GOF parameters: wRp = 0.0468, Rp = 0.0369. (The number for corresponding CIF file in CCDC database: 1872066).

Atom	x	y	Z	occupancy	Uiso*100 (Å ²)
Cu1	0.25	0.5	0.3170(6)	1	0.016(3)
C1	0.3370(4)	0.6154(4)	0.3370(4)	1	2.2(2)
C2	0.3221(4)	0.5836(5)	0.3221(4)	1	2.2(2)
C3	0.3218(5)	0.6308(3)	0.3692(3)	1	2.2(2)
N1	0.2855(5)	0.5387(5)	0.3179(5)	1	2.1(1)
N2	0.3091(5)	0.5367(5)	0.2914(5)	1	2.1(1)
N3A	0.3314(6)	0.5642(7)	0.2922(7)	0.56	2.1(1)
C1A	0.2930(7)	0.5678(7)	0.3402(6)	0.56	2.1(1)
N3B	0.2930(7)	0.5678(7)	0.3402(6)	0.44	2.1(1)
C1B	0.3314(6)	0.5642(7)	0.2922(7)	0.44	2.1(1)
H1	0.3005(10)	0.6192(14)	0.3842(14)	0.44	3.2(8)
H1A	0.281(3)	0.580(3)	0.361(3)	0.44	3.2(8)
H1B	0.355(3)	0.569(3)	0.276(3)	0.56	3.2(8)
D1	0.2386(15)	0.490(2)	0.3898(9)	0.93(3)	20(2)
D2	0.4262(18)	0.6971(13)	0.0599(19)	0.90(3)	20(2)
D3	0.5	0.3611(12)	0.3542(11)	1.79(5)	12(1)
D4	0.394(6)	0.592(2)	0.398(7)	0.372(18)	7(3)

7.2.14 Comparing adsorption sites with Cu-BTT

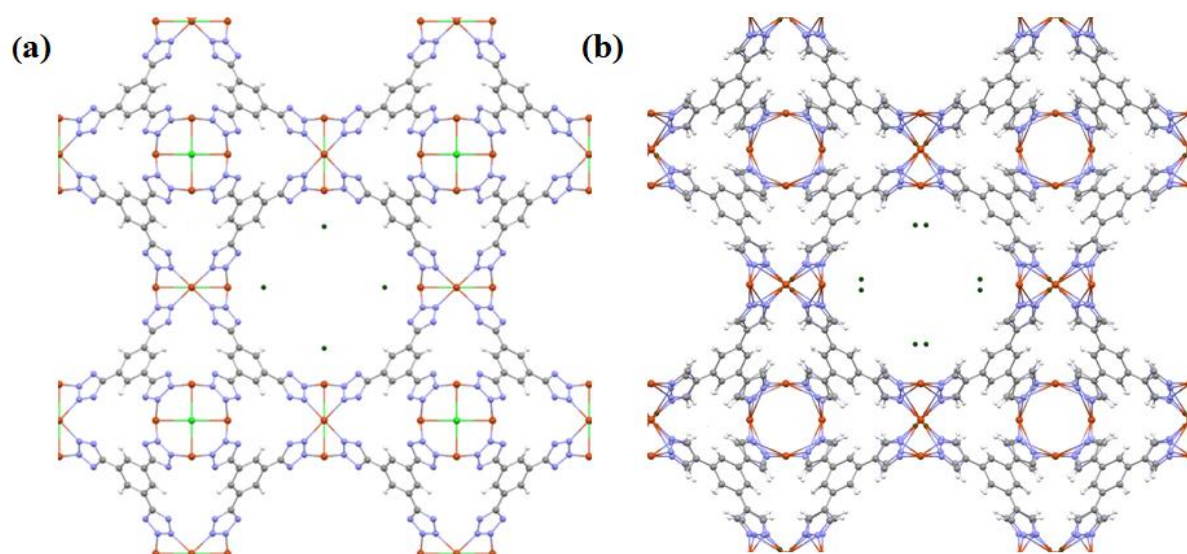


Figure S3-12. The location of primary adsorption sites in (a) Cu-BTT (b) Cu-BTTri. Cu, Cl, N, and C atoms have been identified with orange, light green, light blue and gray color. The primary adsorption sites only have been shown at the central pore. The extra cations and anions and deuterium adsorption sites in other pores have been excluded for the sake of clarity.

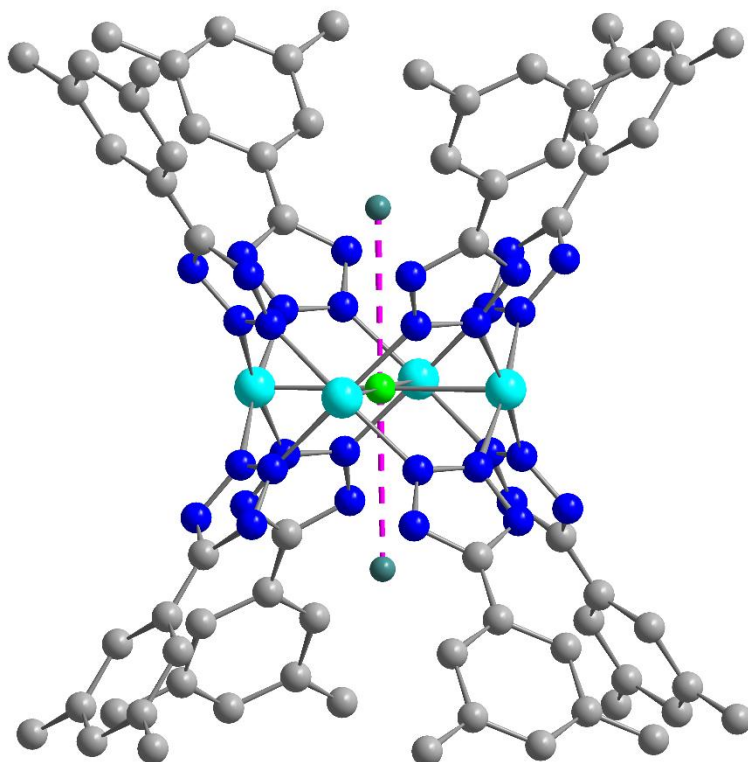


Figure S3-13. The location of secondary adsorption site in Cu-BTT framework. Cu, Cl, N, and C atoms have been identified with cyan, light green, blue and gray color. Duterium atoms have been shown above chlorine atoms with dark green color. The extra cations and anions have been excluded for clarity.

7.2.15 Isosurfaces of the charge density plots

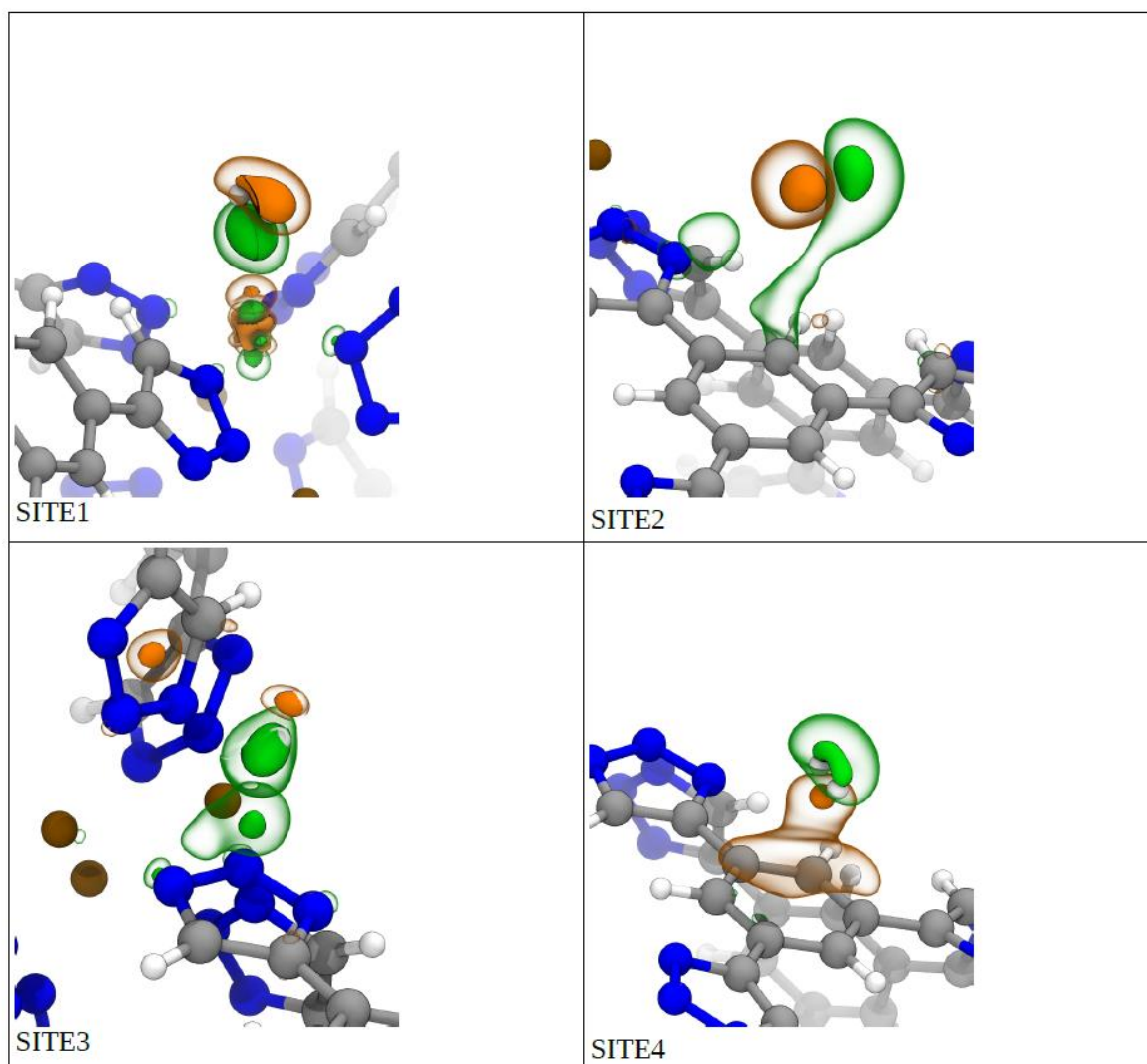


Figure S3-14. Scheme showing the four D₂ adsorption sites and two isosurfaces of the charge density (negative=green, positive=orange) that is involved in the binding to the CuBTtri.

7.2.16 References for the appendix to chapter 3

1. S. Brunauer, P. H. Emmett and E. Teller, *Journal of the American chemical society*, 1938, **60**, 309-319.
2. J. A. Mason, K. Sumida, Z. R. Herm, R. Krishna and J. R. Long, *Energy & Environmental Science*, 2011, **4**, 3030-3040.
3. P. M. Mathias, R. Kumar, J. D. Moyer, J. M. Schork, S. R. Srinivasan, S. R. Auvil and O. Talu, *Industrial & engineering chemistry research*, 1996, **35**, 2477-2483.
4. T. M. McDonald, D. M. D'Alessandro, R. Krishna and J. R. Long, *Chemical Science*, 2011, **2**, 2022-2028.
5. M. Dincă, W. S. Han, Y. Liu, A. Dailly, C. M. Brown and J. R. Long, *Angewandte Chemie International Edition*, 2007, **46**, 1419-1422.

7.3 Appendix to Chapter4

7.3.1 XRD pattern of Cu-BTTri sample

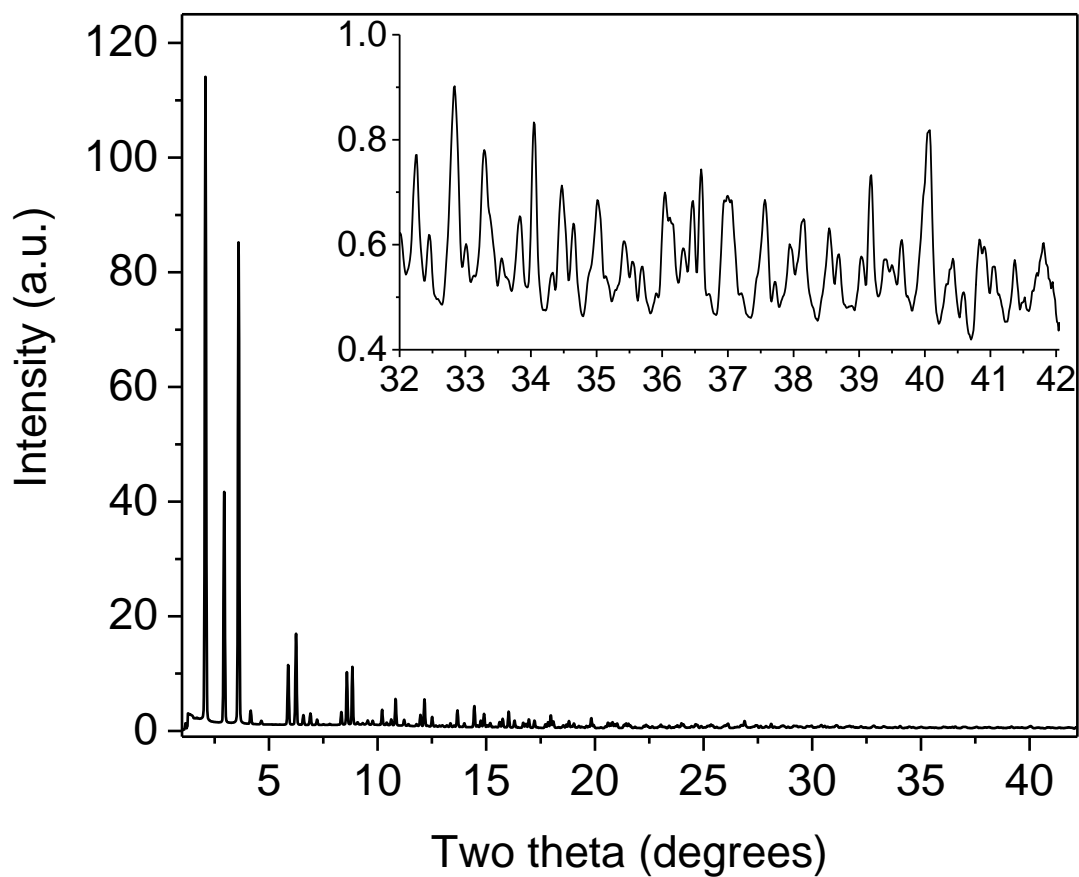


Figure S4-1. Synchrotron x-ray diffraction pattern collected on the bare Cu-BTTri in SNBL (BM01), ESRF. The wavelength is set to 0.67522 Å. The data confirms high crystallinity of the sample needed for the Rietveld analysis.

7.3.2 Gas adsorption measurements

UHP-grade (99.999% purity) helium, nitrogen, and hydrogen were used for all adsorption measurements. Gas adsorption isotherms for pressures in the range 0–1 bar were measured using a BELSORP-max instrument. For standard measurements in BELSORP-max, the sample was transferred to pre-weighed low pressure resistant analysis tubes, which were capped with a Transeal. The sample was evacuated and heated on the activation stages of BELSORP-max based on the desired activation program. After finishing the activation program, the evacuated analysis tubes containing degassed sample was then carefully transferred to an electronic balance and weighed to determine the mass of sample (typically 100–200 mg). Then the tube was transferred to the analysis port of the gas adsorption instrument. Adsorption isotherms between 5 and 45°C were measured using a recirculating dewar (Micromeritics) connected to a Julabo F32-MC isothermal bath. For cryogenic measurements, the dewar vessel is used where is capable of keeping cryogenic baths under isolation. BET surface areas and pore volumes were determined by measuring N₂ adsorption isotherms in a 77 K liquid N₂ bath and calculated, assuming a value of 16.2 Å² for the molecular cross-sectional area of N₂.

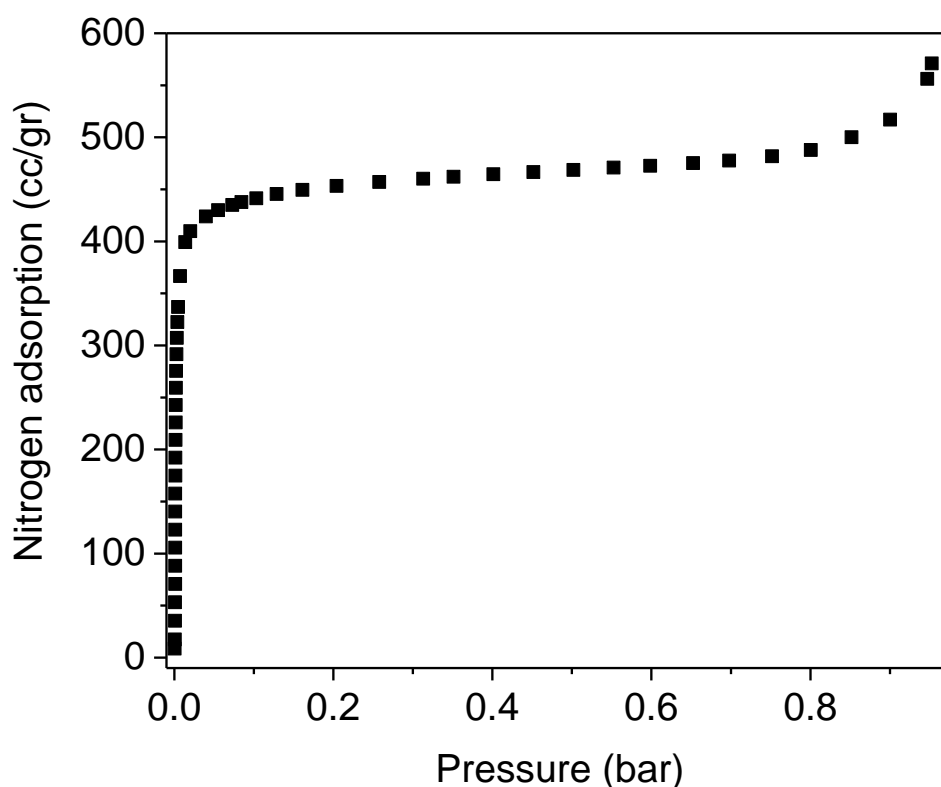


Figure S4-2. Nitrogen adsorption isotherm for Cu-BTTrI collected at 77 K.

7.3.3 Pore Volume calculations based on the adsorption data for nitrogen at 77 K

As shown in Figure S4-2, the adsorption isotherm for N₂ at 77 K ceases to be a function of pressure when the pressure exceeds 200 mbar, implying that the structure has been saturated with nitrogen. Therefore, the uptake of N₂ at highest measured pressure can be considered as the full capacity of the framework for an inert small molecule, and the pore volume can then be calculated from the following formula:

$$\text{Pore Volume} = \frac{N_{N_2}^{\text{Sat}} \cdot M_{wN_2}}{1000 \cdot d_{\text{liq}N_2}|_{77K}} \quad \text{Eq. (S4 - 1)}$$

Where $N_{N_2}^{\text{Sat}}$ is the the amount of nitrogen adsorbed at the highest pressure point in mmol/g, M_{wN_2} is the molecular weight dinitrogen in g/mol and $d_{\text{liq}N_2}|_{77K}$ is the density of liquid nitrogen at 77 K in g/mL.

7.3.4 Surface area calculations based on the N₂ adsorption data at 77 K

Based on the BET theory, we have the following equation:

$$\frac{1}{N[(\frac{p_0}{p})-1]} = \frac{c-1}{N_m c} \left(\frac{p}{p_0} \right) + \frac{1}{N_m c} \quad \text{Eq. (S4 - 2)}$$

Where N is the amount of gas adsorbed in mmol/g, N_m is the monolayer adsorption in mmol/g, p is the partial pressure of N₂ and p_0 is the saturation pressure of N₂ at the measurement temperature.⁴⁰² A plot of $\frac{1}{N[(\frac{p_0}{p})-1]}$ versus $\frac{p}{p_0}$ and the best possible trendline is fit to the points on the plot. We note that points with low $(\frac{p}{p_0})$ are chosen such that the c parameter stays positive and high R² values are obtained. With M as the slope and I as the intersect of the plot, N_m can be obtained from the following formula:

$$N_m = \frac{1}{M+I} \quad \text{Eq. (S4 - 3)}$$

The surface area can then be obtained using the following equation:

$$SA = N_m \cdot N_A \cdot CSA_{N_2} \quad \text{Eq. (S4 - 4)}$$

where N_A is Avogadro's number and CSA_{N_2} is the cross sectional area of one N₂ molecule at 77 K (taken to be 16 Å²). The above calculations were carried out on the nitrogen adsorption isotherm data collected at 77 K for Cu-BTTri; the resulting surface area has been reported in the paper.

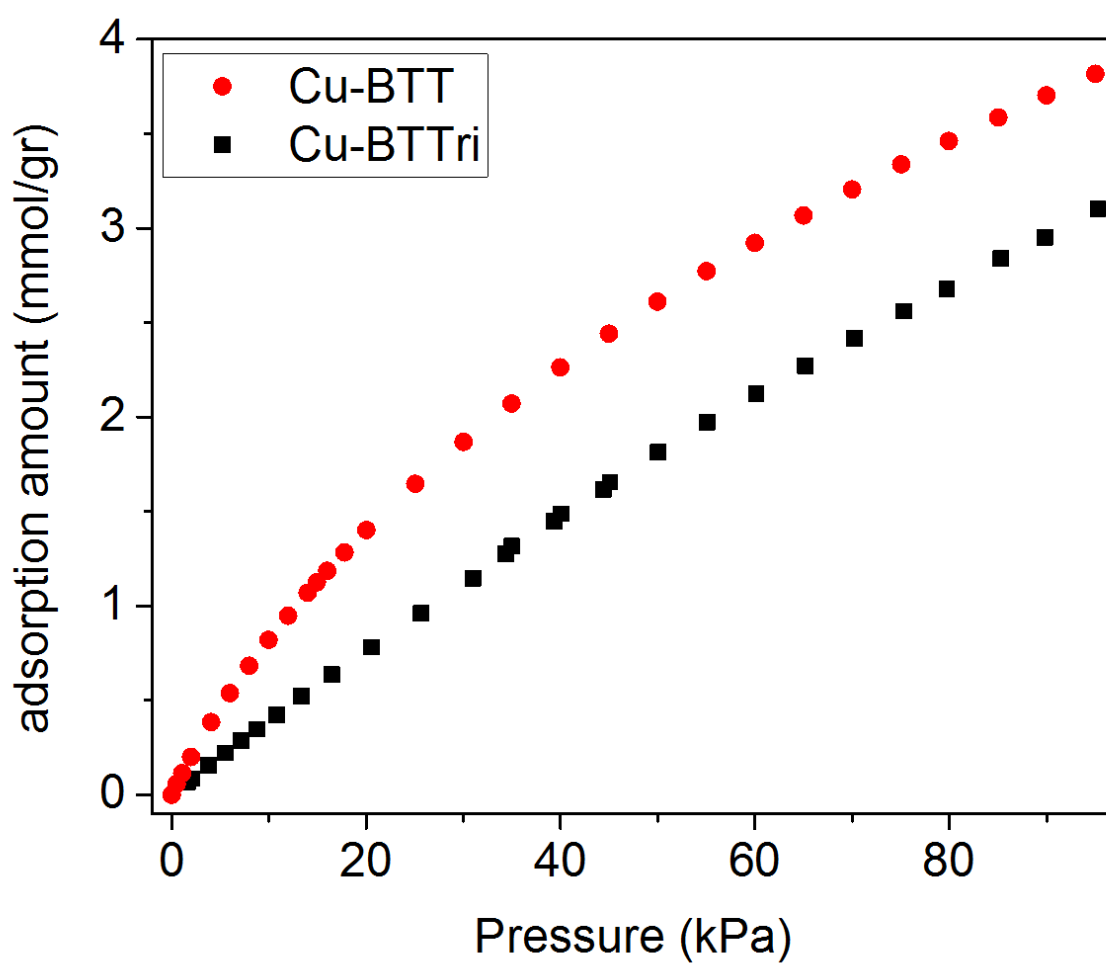


Figure S4-3. The comparison of carbon dioxide adsorption data for Cu-BTT and Cu-BTTri at 298K. The data for the adsorption data for Cu-BTT has been extracted from literature.³²³

7.3.5 Fitting Cu-BTTri CO₂ and N₂ adsorption isotherms

The CO₂ and N₂ adsorption isotherms collected at three different temperatures of 278 K, 288 K and 298 K were fitted with a dual-site Langmuir model (Eq. S4 – 5):

$$n = \frac{abP}{1+bP} + \frac{cdP}{1+dP} \quad \text{Eq. (S4 – 5)}$$

where n is the amount of CO₂ or N₂ adsorbed in mol/g, a and b are Langmuir parameter for the first adsorption site, c and d are Langmuir parameter for the second adsorption site and P is the pressure in Pa. The fitted parameters for each adsorption isotherm can be found in Tables S4-1 and S4-2 for CO₂ and N₂, respectively. The comparison of the experimental CO₂ and N₂ adsorption isotherms with the fitted dual-site Langmuir model based on the experimental data are shown in Fig. S4-4 and Fig. S4-5, respectively. The n and P have been rescaled to mmol/gr and bar in these figures, which are more common units for showing adsorption isotherms. The dual-site Langmuir model was chosen because of the validity of the theory behind this model for prediction of the interaction of heterogeneous surfaces with gas-phase small molecules. The use of a dual-site Langmuir model for fitting gas adsorption isotherm data and the extraction of isosteric heats of adsorption has been reported elsewhere.^{62, 403-404}

Calculating Isosteric heats of adsorption

The Clausius-Clapeyron equation (Eqn. S4-6) was used to calculate the isosteric heats of adsorption, Q_{st} , for CO₂ and N₂ adsorption on Cu-BTTri, using the dual-site Langmuir-Freundlich fits at 278 K, 288 K, and 298 K.

$$(\ln P)_n = -\frac{Q_{st}}{R} \left(\frac{1}{T} \right) + C \quad \text{Eq. (S4 – 6)}$$

Where, P is the pressure in any desired unit, n is the amount adsorbed mol/g, T is the temperature in K, R is the universal gas constant kJ/mol·K, and C is a constant. The isosteric heat of adsorption, Q_{st} , was obtained from the slope of plots of $(\ln P)_n$ as a function of inverse T . The isosteric heats of adsorption for CO₂ and N₂ as a function of loading of the adsorbate in Cu-BTTri can be found in Figure S4-7 and S4-9.

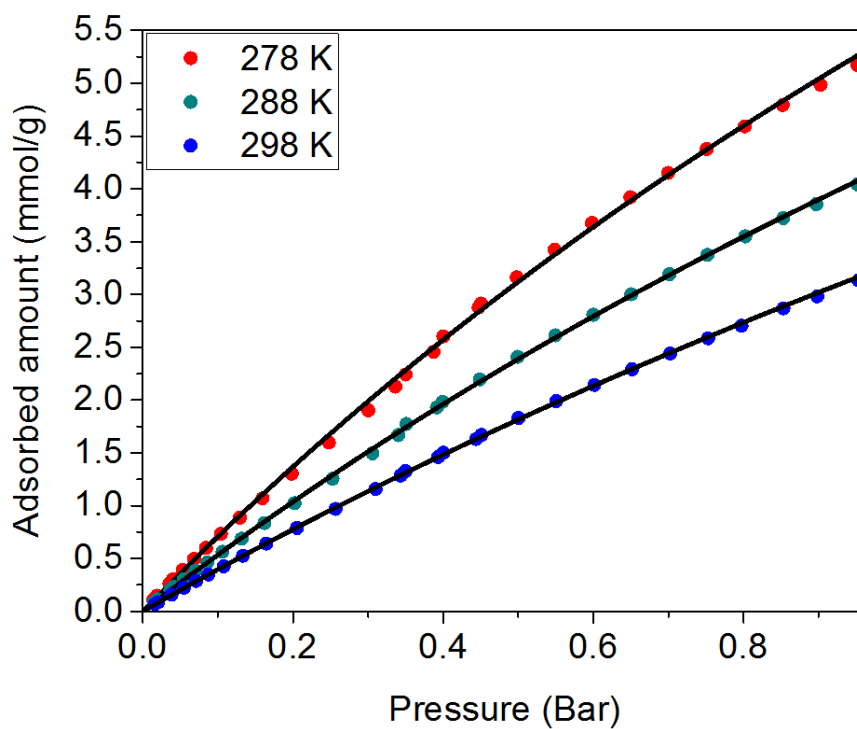


Figure S4-4. Dual-site Langmuir fits for CO₂ adsorption in Cu-BTtri at 278 K, 288 K, and 298 K.

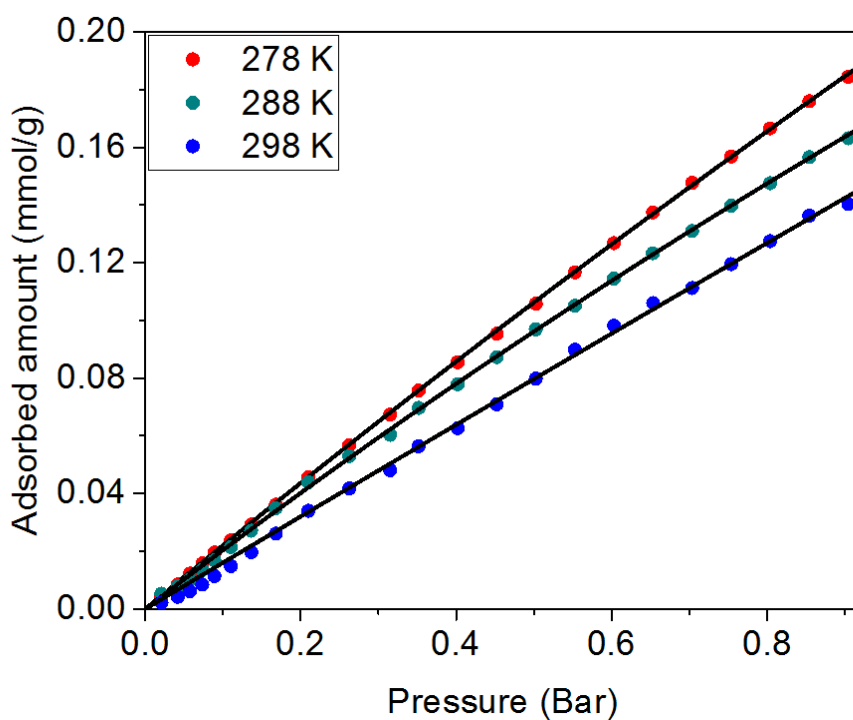


Figure S4-5. Dual-site Langmuir fits for N₂ adsorption in Cu-BTtri at 278 K, 288 K, and 298 K.

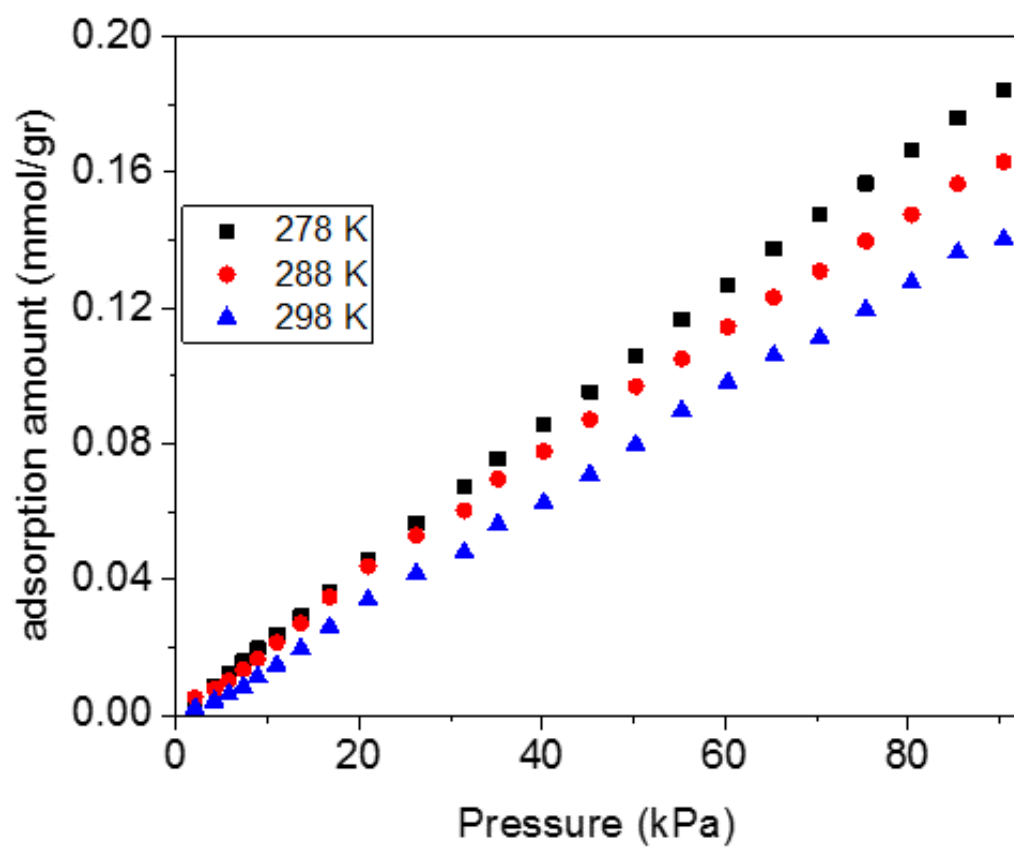


Figure S4-6. The measured N_2 adsorption isotherms for Cu-BTtri at different temperatures.

Table S4-1- Dual-site Langmuir parameters for CO₂ adsorption in Cu-BTTri at 278 K, 288 K, and 298 K.

	<i>a</i>	<i>b</i>	<i>c</i>	<i>d</i>
278 K	0.016748	3.927E-06	0.187684	3.967E-08
288 K	0.014541	3.415E-06	0.157244	3.406E-08
298 K	0.012518	2.800E-06	0.166689	3.343E-08

Table S4-2- Dual-site Langmuir parameters for N₂ adsorption in Cu-BTTri at 278 K, 288 K, and 298 K.

	<i>a</i>	<i>b</i>	<i>c</i>	<i>d</i>
278 K	2.622E-07	5.849E-06	2.379786	9.346E-07
288 K	2.961E-07	1.453E-06	1.331992	1.556E-06
298 K	1.275E-07	1.847E-06	9.005747	1.786E-07

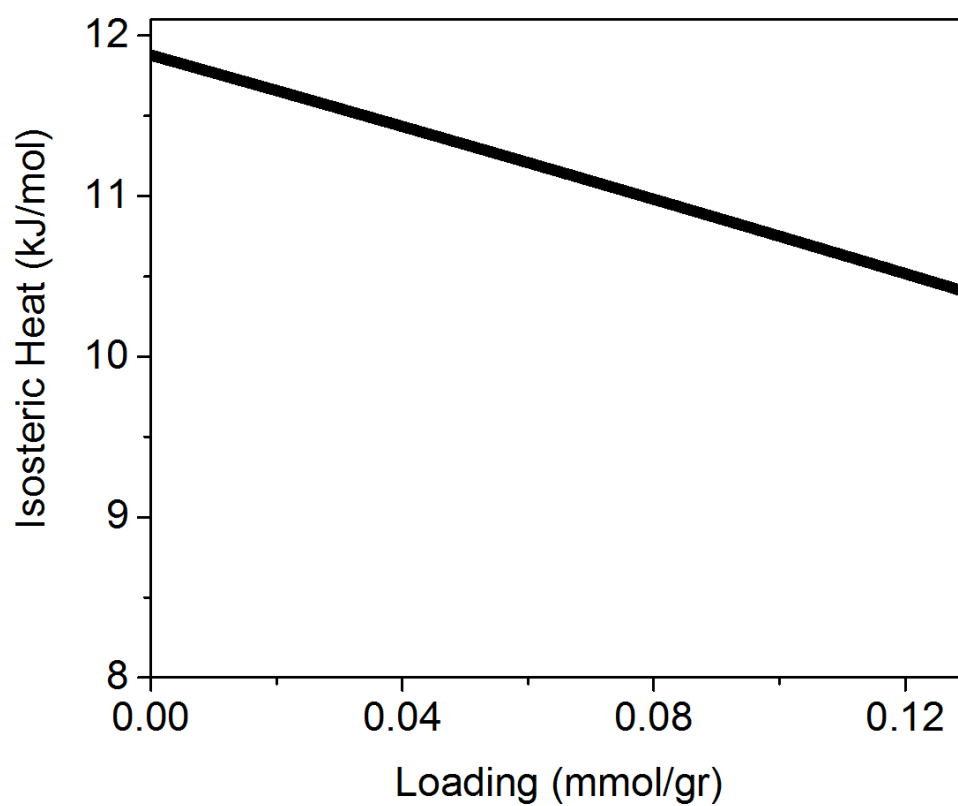


Figure S4-7. The N_2 isosteric heat of adsorption for Cu-BTTRI obtained from Clasius-Clapeyron equation.

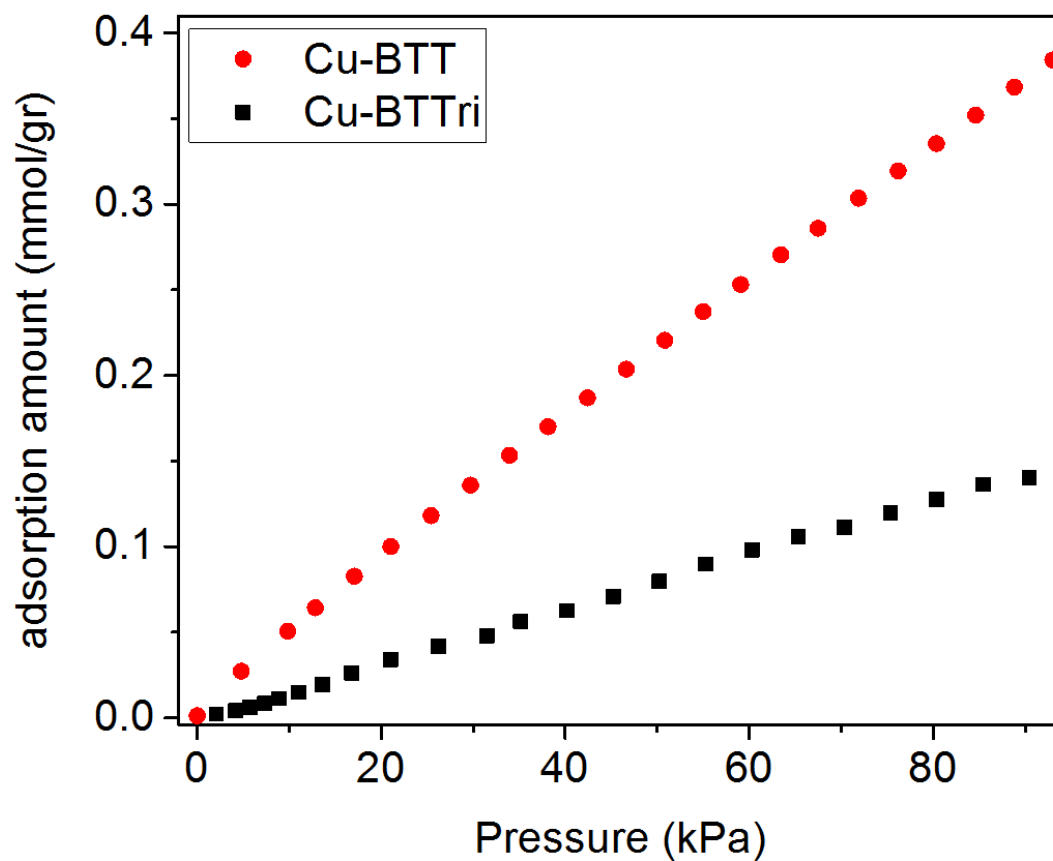


Figure S4-8. The comparison of nitrogen adsorption data for Cu-BTT and Cu-BTTri at 298K. The data for the adsorption data for Cu-BTT has been extracted from literature.³²³

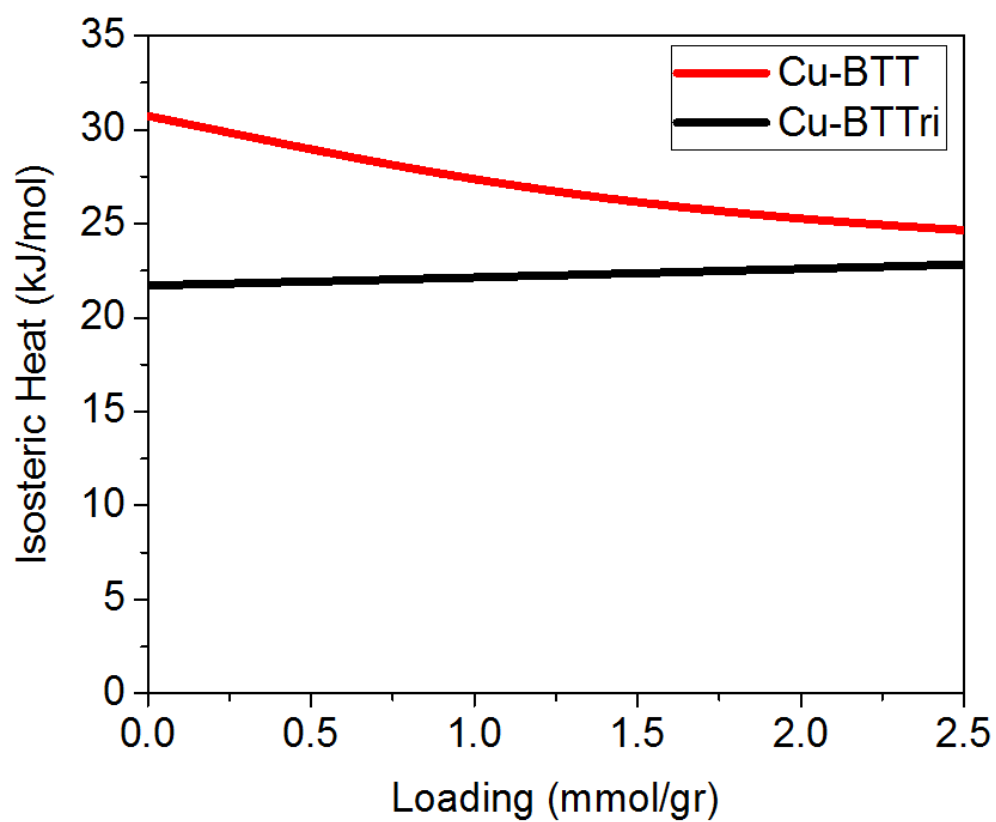


Figure S4-9. The comparison of CO₂ isosteric heat of adsorption for Cu-BTT and Cu-BTTri obtained by Clasiuss-Clapeyron equation. The data for the adsorption data for Cu-BTT has been extracted from literature.³²³

Table S4-3- Experimental and computed data for CO₂ adsorption sites in Cu-BTTri framework.

	Overall	Site I		Site II		Site III		Site IV	
	-Q _{st} (kJ/mol)	-H ₀ (kJ/mol)	Cu-O (CO ₂)	-H ₀ (kJ/mol)	N-O (CO ₂)	-H ₀ (kJ/mol)	C-O (CO ₂)	-H ₀ (kJ/mol)	O-N/C (triazole)
Experimental	21.7	-	2.86(7)	-	3.27(4)	-	2.8(1)	-	3.02(9) Å
DFT	-	25.0	2.96	26.5	3.16	17.0	3.42	15.8	≈ 3 Å

Table S4-4- Contributions to the binding energies for the four detected CO₂ adsorption sites in Cu-BTTri structure

Site No.	E _{PBE} (kJ/mol)	E _{Dispersion-D2} (kJ/mol)
1	-7.412	-17.606
2	3.792	-30.259
3	-1.605	-15.390
4	0.054	-15.837

7.3.6 Isosurfaces of the charge density plots for CO₂ adsorption sites

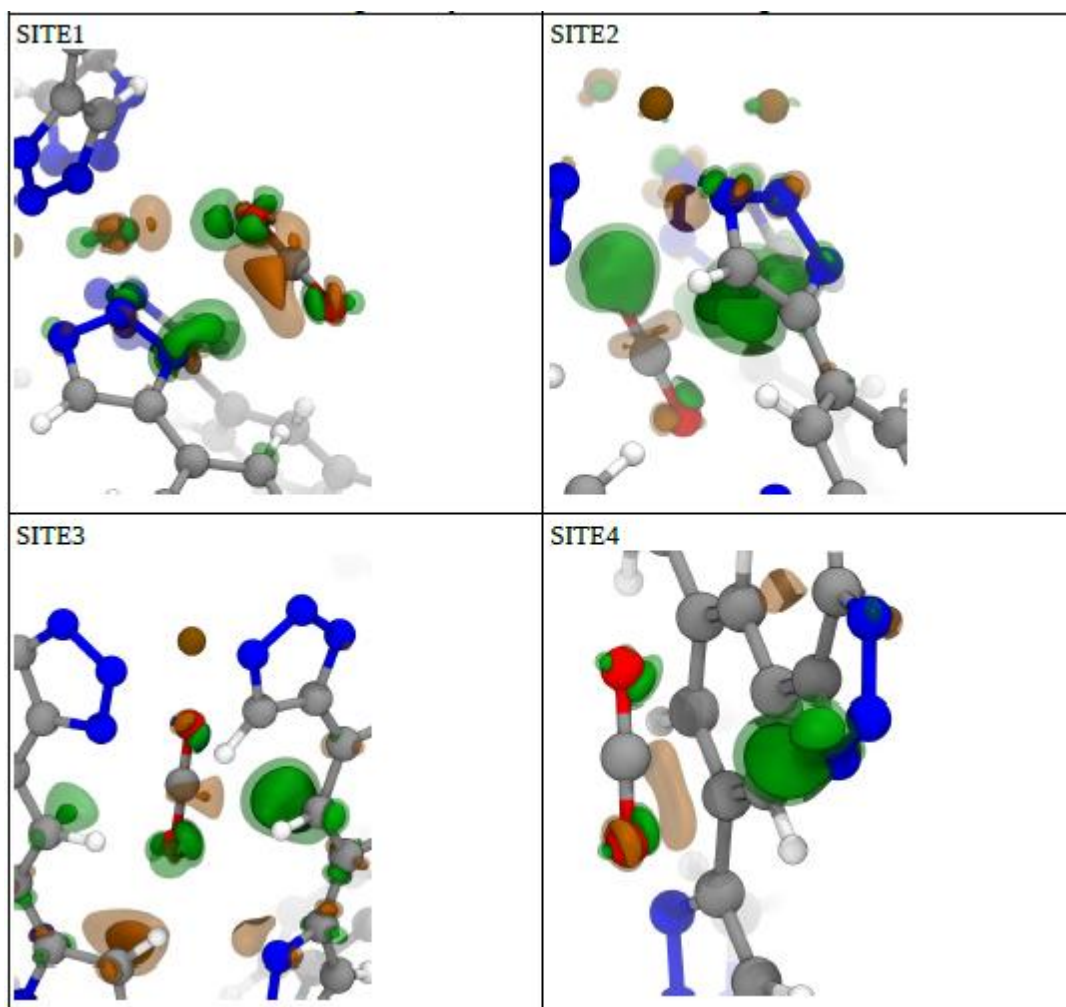


Figure S4-10. Schemes showing the four CO₂ adsorption sites and two isosurfaces of the charge density (negative=green, positive=orange) that are involved in the binding to Cu-BTtri.

Table S4-5. Contributions to the binding energies for the six detected N₂ adsorption sites in Cu-BTtri structure

Site No.	E _{PBE} (kJ/mol)	E _{Dispersion-D2} (kJ/mol)	Total binding energy (kJ/mol)
1	-1.983	-9.927	-11.9
2	1.506	-18.544	-17.0
3	2.447	-14.074	-11.6
4	-0.631	-5.475	-6.1
5	1.926	-8.979	-7.1
6	0.167	-4.618	-4.5

7.3.7 Isosurfaces of the charge density plots for N_2 adsorption sites

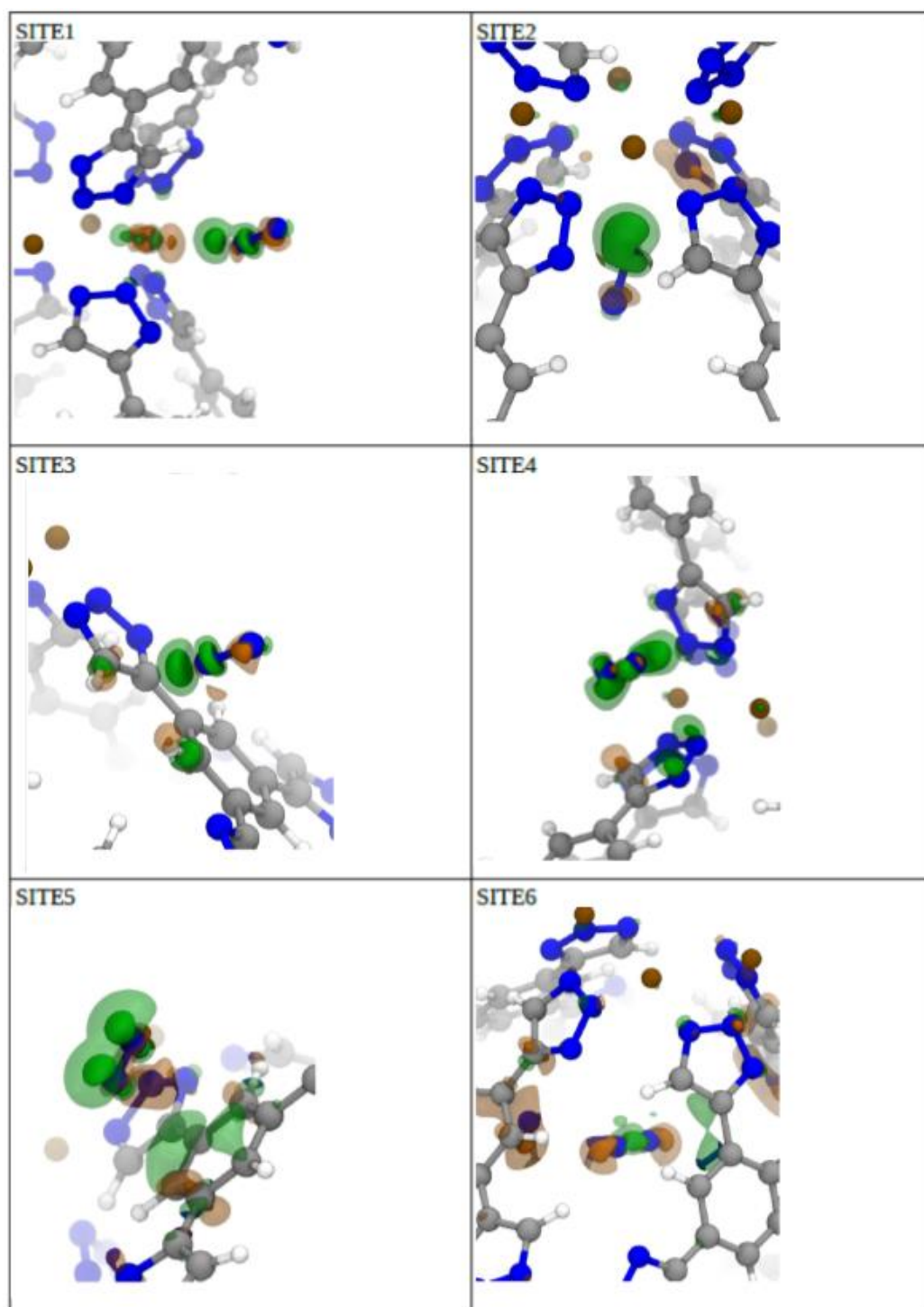


Figure S4-11. Schemes depicting the four N_2 adsorption sites and two isosurfaces of the charge density (negative=green, positive=orange) that are involved in the binding to Cu-BTtri.

7.3.8 Rietveld refinement of the framework loaded with 0.40 CO₂/Cu²⁺ (neutron diffraction data)

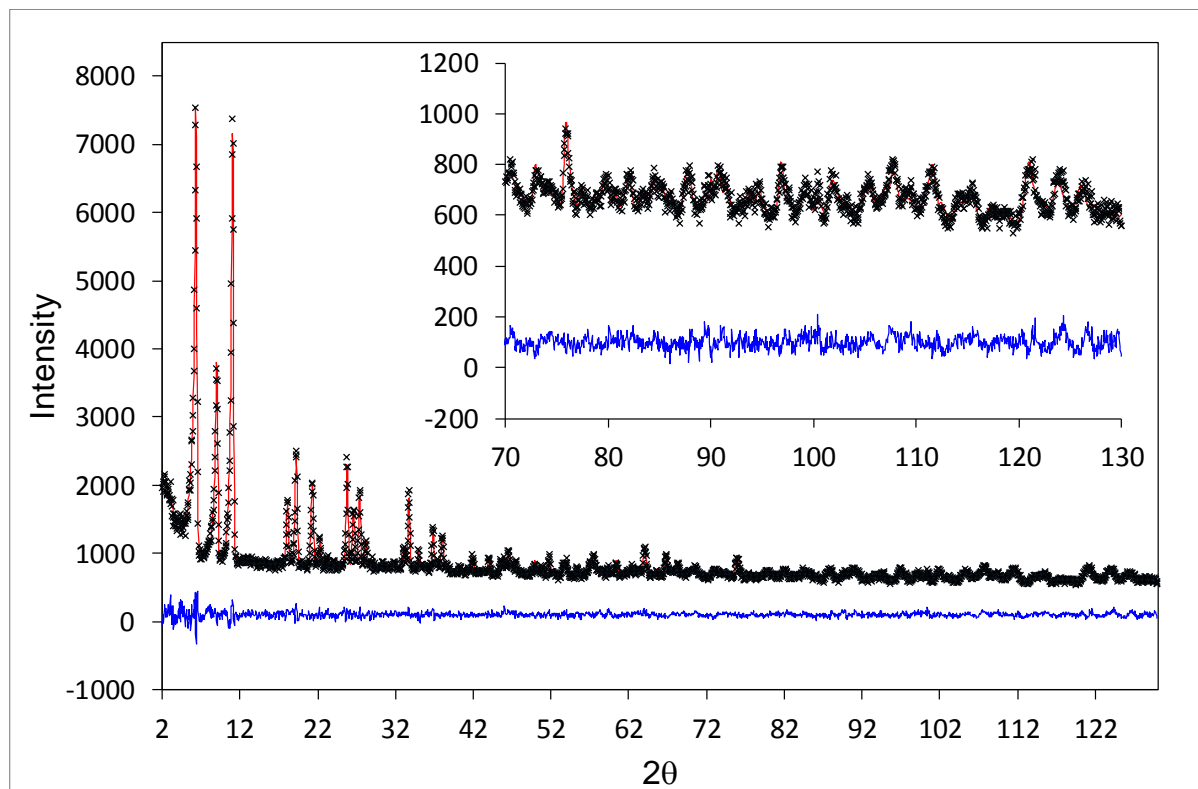


Figure S4-12. Neutron powder diffraction data collected at 10 K for a sample of Cu-BTTri loaded with 0.40 CO₂ per Cu site (38.4 CO₂ per unit cell). The green line, crosses, and red line represent the background, experimental, and calculated diffraction patterns, respectively. The blue line represents the difference between experimental and calculated patterns.

Table S4-6. Fractional atomic coordinates, occupancies, and isotropic displacement parameters obtained from Rietveld refinement of the structural model for Cu-BTTri loaded with 0.40 CO₂ per Cu site (38.4 CO₂ per unit cell) against diffraction data presented in Figure S4-12. The structure is cubic with *Fm-3c* space group, $a = 37.070(2)$ Å, and $V = 50942(7)$ Å³. Values in parentheses represent standard deviation. GOF parameters: wRp = 0.0418, Rp = 0.0327. (The number for corresponding CIF file in CCDC database: [1893609](#)).

Atom	x	y	z	occupancy	Biso (Å ²)
Cu1	0.5	0.3144(5)	0.7569(8)	1	1.0(6)
C1	0.3380(3)	0.6154(4)	0.3380(3)	1	1.9(3)
C3	0.3222(4)	0.6312(3)	0.3688(3)	1	1.9(3)
C2	0.3224(3)	0.5817(5)	0.3224(3)	1	1.9(3)
N1	0.2838(4)	0.5397(5)	0.3173(5)	1	1.9(2)
N2	0.3089(5)	0.5363(5)	0.2910(4)	1	1.9(2)
N3A	0.3336(6)	0.5624(6)	0.2933(7)	0.56038	1.9(2)
C1A	0.2924(8)	0.5672(7)	0.3389(7)	0.43962	1.9(2)
N3B	0.2924(8)	0.5672(7)	0.3389(7)	0.43962	1.9(2)
C1B	0.3336(6)	0.5624(6)	0.2933(7)	0.56038	1.9(2)
H1	0.301(1)	0.619(2)	0.380(2)	1	4.4(9)
H1A	0.282(4)	0.579(3)	0.362(4)	0.43962	4.4(9)
H1B	0.355(4)	0.570(3)	0.278(3)	0.56038	4.4(9)
O_new2a	0.391(3)	0.264(3)	0.75(1)	0.101(6)	6(8)
O_new2b	0.340(3)	0.299(3)	0.75(1)	0.101(6)	9(7)
C_new2c	0.366(3)	0.282(3)	0.75(1)	0.101(6)	9(7)
O_new1a	0.5	0.388(4)	0.760(4)	0.21(2)	8(6)
O_new1b	0.551(4)	0.418(8)	0.780(4)	0.106(9)	8(6)
C_new1c	0.525(2)	0.403(6)	0.770(4)	0.106(9)	8(6)

7.3.9 Rietveld refinement of the framework loaded with 1.25 CO₂/Cu²⁺ (neutron diffraction data)

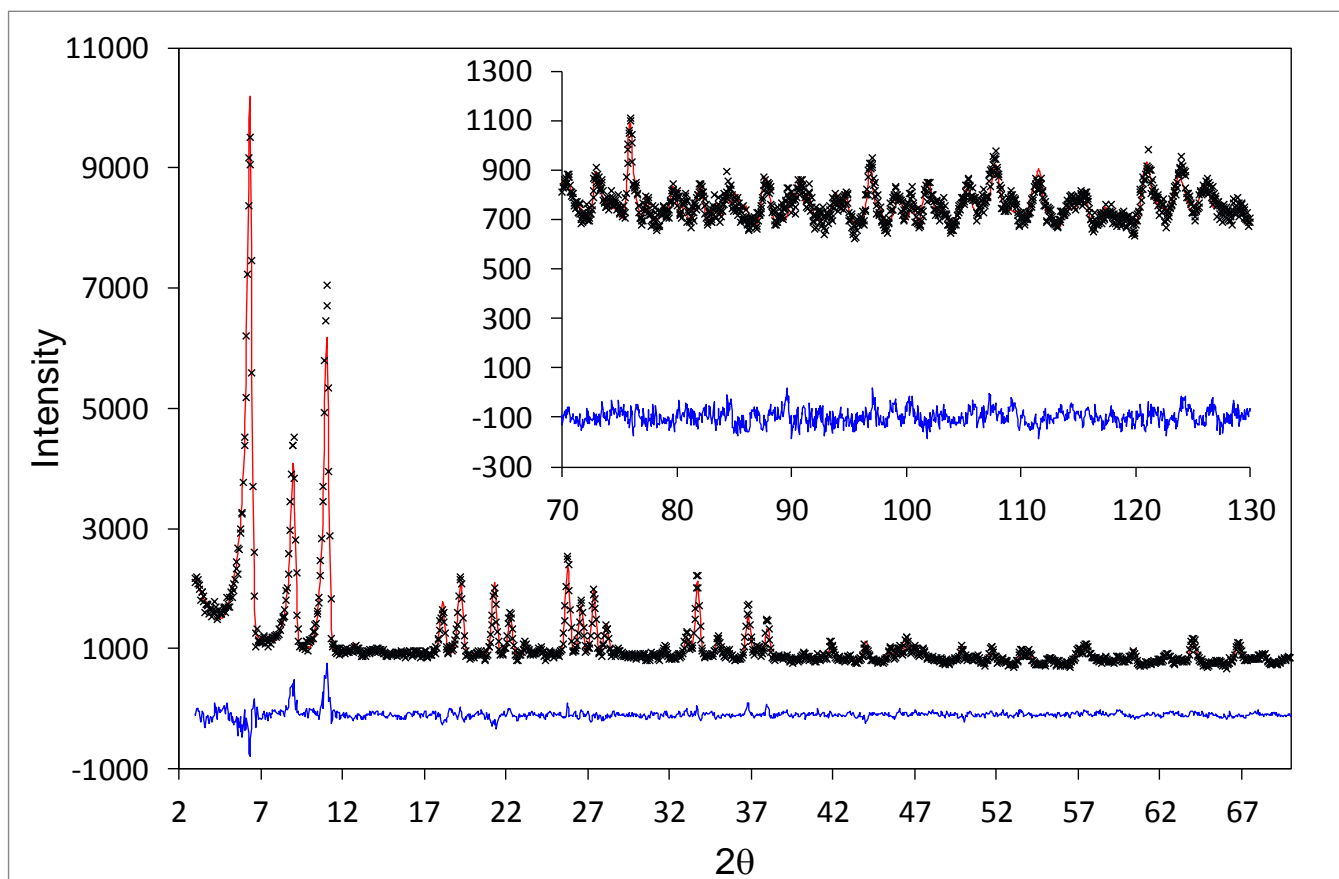


Figure S4-13. Neutron powder diffraction data collected at 10 K on a sample of Cu-BTtri loaded with 1.25 CO₂ per Cu site (120 CO₂ per unit cell). The green line, crosses, and red line represent the background, experimental, and calculated diffraction patterns, respectively. The blue line represents the difference between experimental and calculated patterns.

Table S4-7. Fractional atomic coordinates, occupancies, and isotropic displacement parameters obtained from Rietveld refinement of the structural model for Cu-BTTri loaded with 1.25 CO₂ per Cu site (120 CO₂ per unit cell) against diffraction data collected presented in Figure S4-13. The structure is cubic, space group *Fm-3c*, $a = 37.072(2)$ Å, $V = 50949(7)$ Å³. Values in parentheses represent standard deviation. GOF parameters: $wRp = 0.0474$, $Rp = 0.0369$. (The number for corresponding CIF file in CCDC database: 1893608).

Atom	x	y	z	occupancy	Biso (Å ²)
Cu1	0.5	0.3153(5)	0.7566(10)	1	1.2(6)
C1	0.3374(3)	0.6152(4)	0.3374(3)	1	1.1(2)
C3	0.3222(4)	0.6300(3)	0.3700(3)	1	1.1(2)
C2	0.3225(3)	0.5817(5)	0.3225(3)	1	1.1(2)
N1	0.2850(5)	0.5381(6)	0.3159(6)	1	1.7(1)
N2	0.3093(5)	0.5372(6)	0.2913(5)	1	1.7(1)
N3A	0.3345(6)	0.5634(7)	0.2928(7)	0.56038	1.7(1)
C1A	0.2928(8)	0.5665(8)	0.3386(8)	0.43962	1.7(1)
N3B	0.2928(8)	0.5665(8)	0.3386(8)	0.43962	1.7(1)
C1B	0.3345(6)	0.5634(7)	0.2928(7)	0.56038	1.7(1)
H1	0.3017(9)	0.6156(14)	0.3789(13)	1	3.1(9)
H1A	0.279(4)	0.578(3)	0.361(4)	0.43962	3.1(9)
H1B	0.357(4)	0.572(3)	0.277(3)	0.56038	3.1(9)
O_new2a	0.411(2)	0.25	0.75	0.48(3)	2
O_new2b	0.360(2)	0.284(2)	0.750(8)	0.120(6)	0.37858
C_new2c	0.386(2)	0.267(2)	0.750(8)	0.120(6)	0.37858
O_new1a	0.5	0.394(2)	0.767(2)	0.739(19)	8.45671
O_new1b	0.559(3)	0.413(3)	0.780(3)	0.369(10)	8.45671
C_new1c	0.530(2)	0.403(3)	0.773(3)	0.369(10)	8.45671
C_new3a	0.228(2)	0.3134(9)	0.771(2)	0.128(5)	19.92848
O_new3b	0.246(2)	0.2950(9)	0.754(2)	0.128(5)	19.92848
O_new3c	0.210(2)	0.3318(9)	0.789(2)	0.128(5)	19.92848

7.3.10 Rietveld refinement of the framework loaded with 1.60 CO₂/Cu²⁺ (neutron diffraction data)

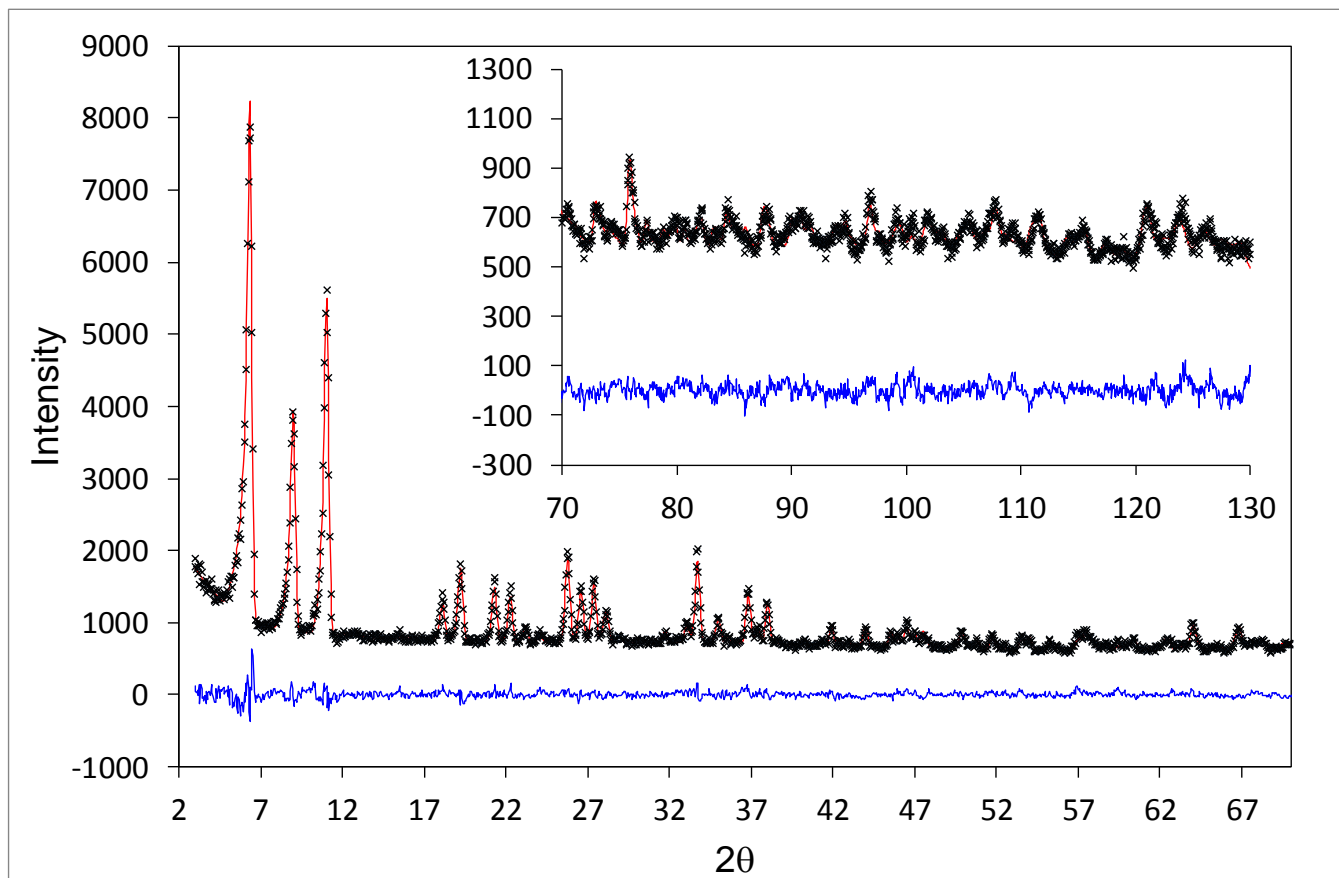


Figure S4-14. Neutron powder diffraction data collected at 10 K for a sample of Cu-BTTRI loaded with 1.60 CO₂ per Cu site (153.6 CO₂ per unit cell). The green line, crosses, and red line represent the background, experimental, and calculated diffraction patterns, respectively. The blue line represents the difference between experimental and calculated patterns.

Table S4-8. Fractional atomic coordinates, occupancies, and isotropic displacement parameters obtained from Rietveld refinement of the structural model for Cu-BTTr loaded with 1.60 CO₂ per Cu site (153.6 CO₂ per unit cell) against diffraction data collected presented in Figure S4-14. The structure is cubic, space group *Fm-3c*, $a = 37.070(1)$ Å, $V = 50943(5)$ Å³. Values in parentheses represent standard deviation. GOF parameters: wRp = 0.0460, Rp = 0.0362. (The number for corresponding CIF file in CCDC database: 1893610).

Atom	x	y	z	occupancy	Biso (Å ²)
Cu1	0.5	0.3156(5)	0.7566(8)	1	0.4(6)
C1	0.3366(3)	0.6162(4)	0.3366(3)	1	1.0(2)
C3	0.3224(4)	0.6306(3)	0.3694(3)	1	1.0(2)
C2	0.3218(3)	0.5823(5)	0.3218(3)	1	1.0(2)
N1	0.2848(5)	0.5385(5)	0.3175(5)	1	1.8(1)
N2	0.3077(5)	0.5363(5)	0.2915(4)	1	1.8(1)
N3A	0.3305(5)	0.5631(6)	0.2915(6)	0.56038	1.8(1)
C1A	0.2946(6)	0.5648(7)	0.3397(7)	0.43962	1.8(1)
N3B	0.2946(6)	0.5648(7)	0.3397(7)	0.43962	1.8(1)
C1B	0.3305(5)	0.5631(6)	0.2915(6)	0.56038	1.8(1)
H1	0.297(1)	0.625(2)	0.382(2)	1	6.0(1)
H1A	0.282(4)	0.577(4)	0.363(4)	0.43962	6.0(1)
H1B	0.349(4)	0.568(3)	0.272(3)	0.56038	6.0(1)
O_new2a	0.411(1)	0.25	0.75	0.67(3)	2
O_new2b	0.360(1)	0.284(2)	0.753(4)	0.168(8)	0.68754
C_new2c	0.386(2)	0.267(2)	0.752(4)	0.168(8)	0.68754
O_new1a	0.5	0.392(2)	0.766(2)	0.82(2)	5.4171
O_new1b	0.553(2)	0.418(2)	0.785(2)	0.411(9)	5.4171
C_new1c	0.527(2)	0.404(2)	0.775(2)	0.411(9)	5.4171
O_new4a	0.334(6)	0.983(6)	0.609(6)	0.09(2)	20
O_new4b	0.379(6)	0.983(6)	0.652(6)	0.09(2)	20
C_new4c	0.356(6)	0.983(6)	0.630(6)	0.09(2)	20
C_new3a	0.331(2)	0.313(2)	0.767(4)	0.124(8)	15.83856
O_new3b	0.348(2)	0.295(2)	0.749(4)	0.124(8)	15.83856
O_new3c	0.314(2)	0.332(2)	0.785(4)	0.124(8)	15.83856

7.3.11 Rietveld refinement of the framework loaded with 0.33 N_2/Cu^{2+} (neutron diffraction data)

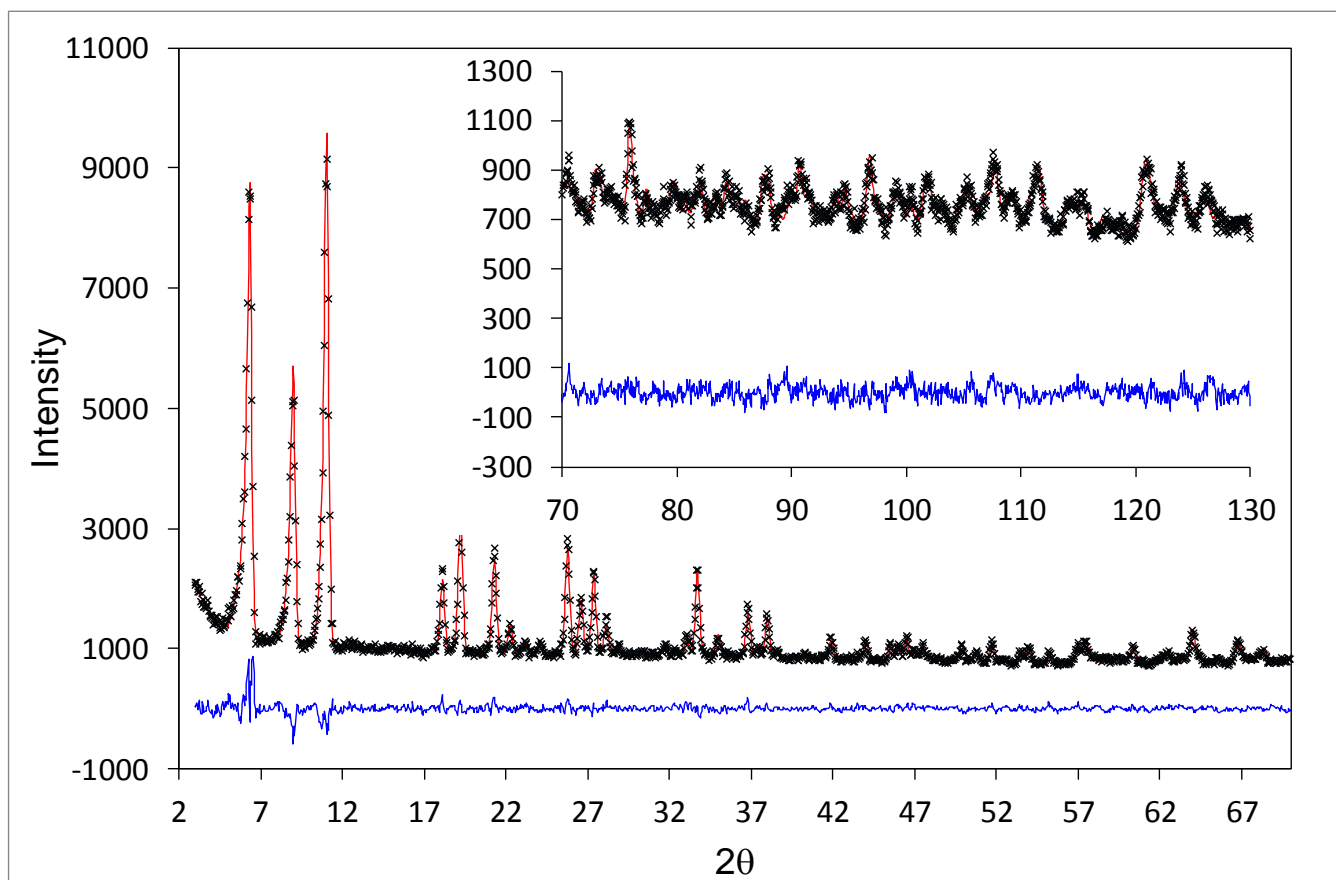


Figure S4-15. Neutron powder diffraction data collected at 10 K for a sample of Cu-BTTrI loaded with 0.33 N_2 per Cu site (31.7 N_2 per unit cell). The green line, crosses, and red line represent the background, experimental, and calculated diffraction patterns, respectively. The blue line represents the difference between experimental and calculated patterns.

Table S4-9. Fractional atomic coordinates, occupancies, and isotropic displacement parameters obtained from Rietveld refinement of the structural model for Cu-BTTr loaded with 0.33 N₂ per Cu site (31.7 N₂ per unit cell) against diffraction data collected presented in Figure S4-15. The structure is cubic, space group *Fm-3c*, $a = 37.078(1)$ Å, $V = 50974(6)$ Å³. Values in parentheses represent standard deviation. GOF parameters: wRp = 0.0407, Rp = 0.0348. (The number for corresponding CIF file in CCDC database: 1893610).

Atom	x	y	z	occupancy	Biso (Å ²)
Cu1	0.2446(6)	0.5	0.3158(5)	1	0.39406
C1	0.3370(2)	0.6162(3)	0.3370(2)	1	1.63372
C3	0.3219(3)	0.6312(2)	0.3688(2)	1	1.63372
C2	0.3220(2)	0.5831(4)	0.3220(2)	1	1.63372
N1	0.2838(4)	0.5389(4)	0.3161(4)	1	1.77941
N2	0.3090(4)	0.5344(4)	0.2913(3)	1	1.77941
N3A	0.3317(5)	0.5620(4)	0.2940(5)	0.56038	1.77941
C1A	0.2912(6)	0.5672(5)	0.3364(6)	0.43962	1.77941
N3B	0.2912(6)	0.5672(5)	0.3364(6)	0.43962	1.77941
C1B	0.3317(5)	0.5620(4)	0.2940(5)	0.56038	1.77941
H1	0.3015(9)	0.621(1)	0.383(1)	1	5.5799
H1A	0.276(4)	0.577(3)	0.359(3)	0.43962	5.5799
H1B	0.350(3)	0.570(3)	0.275(3)	0.56038	5.5799
N1_1	0.386(2)	0.509(3)	0.738(3)	0.145(7)	5.8349
N1_2	0.408(2)	0.512(3)	0.757(4)	0.145(7)	5.1375
N2_1	0.245(9)	0.605(6)	0.737(9)	0.020(4)	0.5
N2_2	0.229(9)	0.623(6)	0.755(9)	0.020(4)	0.5

7.3.12 Rietveld refinement of the framework loaded with 2.19 N_2/Cu^{2+} (neutron diffraction data)

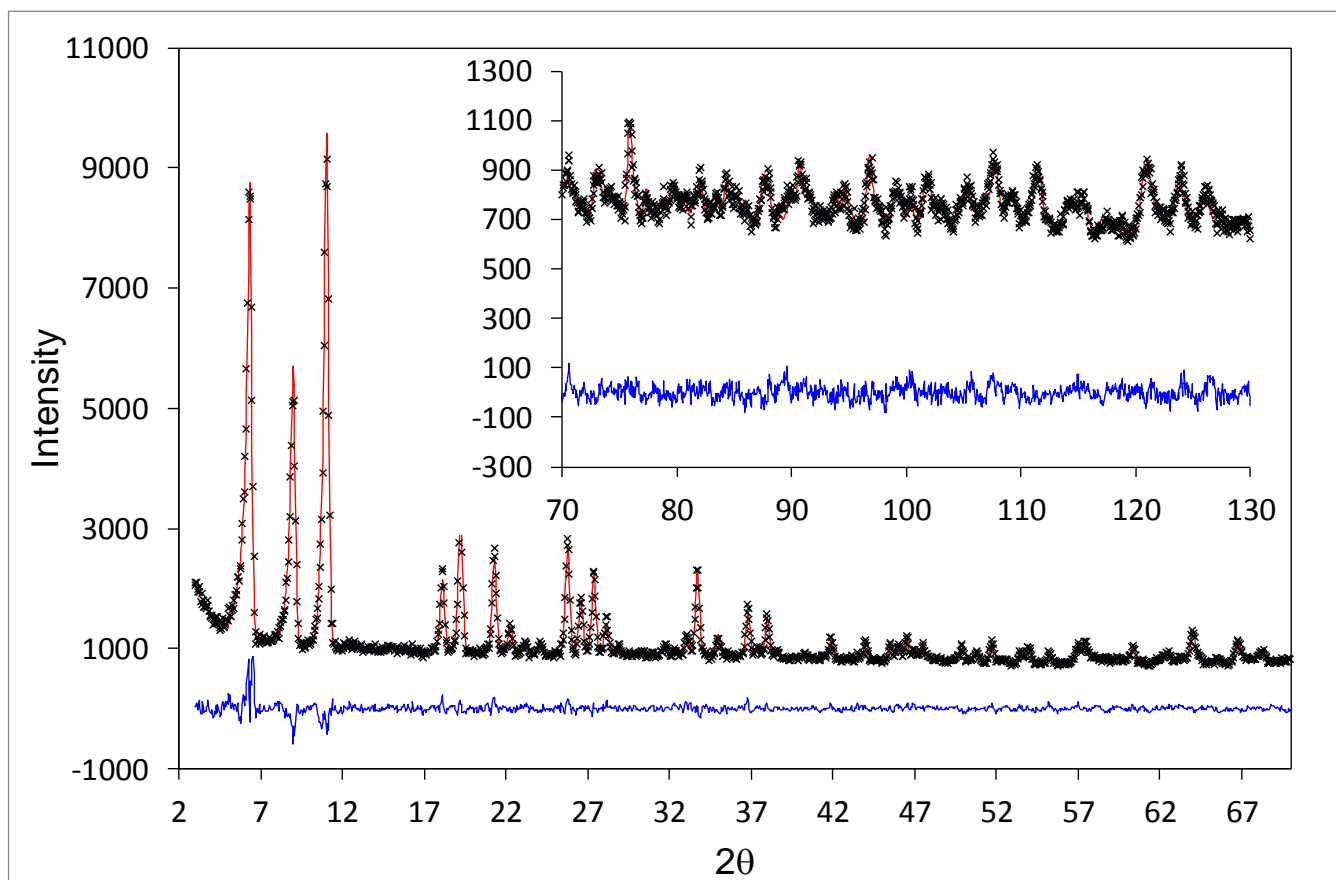


Figure S4-16. Neutron powder diffraction data collected at 10 K for a sample of Cu-BTTRI loaded with 2.19 N_2 per Cu site (210 N_2 per unit cell). The green line, crosses, and red line represent the background, experimental, and calculated diffraction patterns, respectively. The blue line represents the difference between experimental and calculated patterns.

Table S4-10. Fractional atomic coordinates, occupancies, and isotropic displacement parameters obtained from Rietveld refinement of the structural model for Cu-BTtri loaded with 2.19 N₂ per Cu site (210 N₂ per unit cell) against diffraction data collected presented in Figure S4-16. The structure is cubic, space group *Fm-3c*, $a = 37.098(2)$ Å, $V = 51057(7)$ Å³. Values in parentheses represent standard deviation. GOF parameters: wRp = 0.0420, Rp = 0.0356. (The number for corresponding CIF file in CCDC database: [1893606](#)).

Atom	x	y	z	occupancy	Biso (Å ²)
Cu1	0.2457(8)	0.5	0.3153(5)	1	0.69447
C1	0.3370(3)	0.6165(4)	0.3370(3)	1	1.4(2)
C3	0.3228(4)	0.6310(3)	0.3690(3)	1	1.4(2)
C2	0.3218(3)	0.5819(5)	0.3218(3)	1	1.4(2)
N1	0.2839(4)	0.5394(5)	0.3159(5)	1	1.8(2)
N2	0.3092(5)	0.5345(4)	0.2917(4)	1	1.8(2)
N3A	0.3327(5)	0.5614(5)	0.2934(6)	0.56038	1.8(2)
C1A	0.2911(7)	0.5674(6)	0.3360(7)	0.43962	1.8(2)
N3B	0.2911(7)	0.5674(6)	0.3360(7)	0.43962	1.8(2)
C1B	0.3327(5)	0.5614(5)	0.2934(6)	0.56038	1.8(2)
H1	0.302(1)	0.621(1)	0.383(1)	1	4.6(9)
H1A	0.277(3)	0.577(3)	0.360(3)	0.43962	4.6(9)
H1B	0.350(3)	0.570(3)	0.275(3)	0.56038	4.6(9)
N1_1	0.389(1)	0.501(7)	0.7380(1)	0.296(9)	2.71822
N1_2	0.412(1)	0.509(3)	0.751(5)	0.296(9)	13.27875
N6_1	0.180(4)	0.75	0.765(5)	0.041(10)	0.5
N2_1	0.2665(7)	0.607(2)	0.741(2)	0.149(8)	20
N2_2	0.2504(7)	0.624(2)	0.758(2)	0.149(8)	20
N3_1	0.503(5)	0.362(2)	0.854(2)	0.29(1)	5
N3_2	0.508(2)	0.343(1)	0.875(2)	0.29(1)	5
N4_1	0.452(3)	0.453(3)	0.670(2)	0.28(1)	16.33157
N4_2	0.437(3)	0.437(3)	0.690(2)	0.28(1)	16.33157
N5_1	0.413(4)	0.405(5)	0.895(4)	0.057(6)	1
N5_2	0.390(4)	0.419(5)	0.909(4)	0.057(6)	1

7.3.13 Rietveld refinement of the framework loaded with 1.09 CO₂/Cu²⁺ (synchrotron diffraction data)

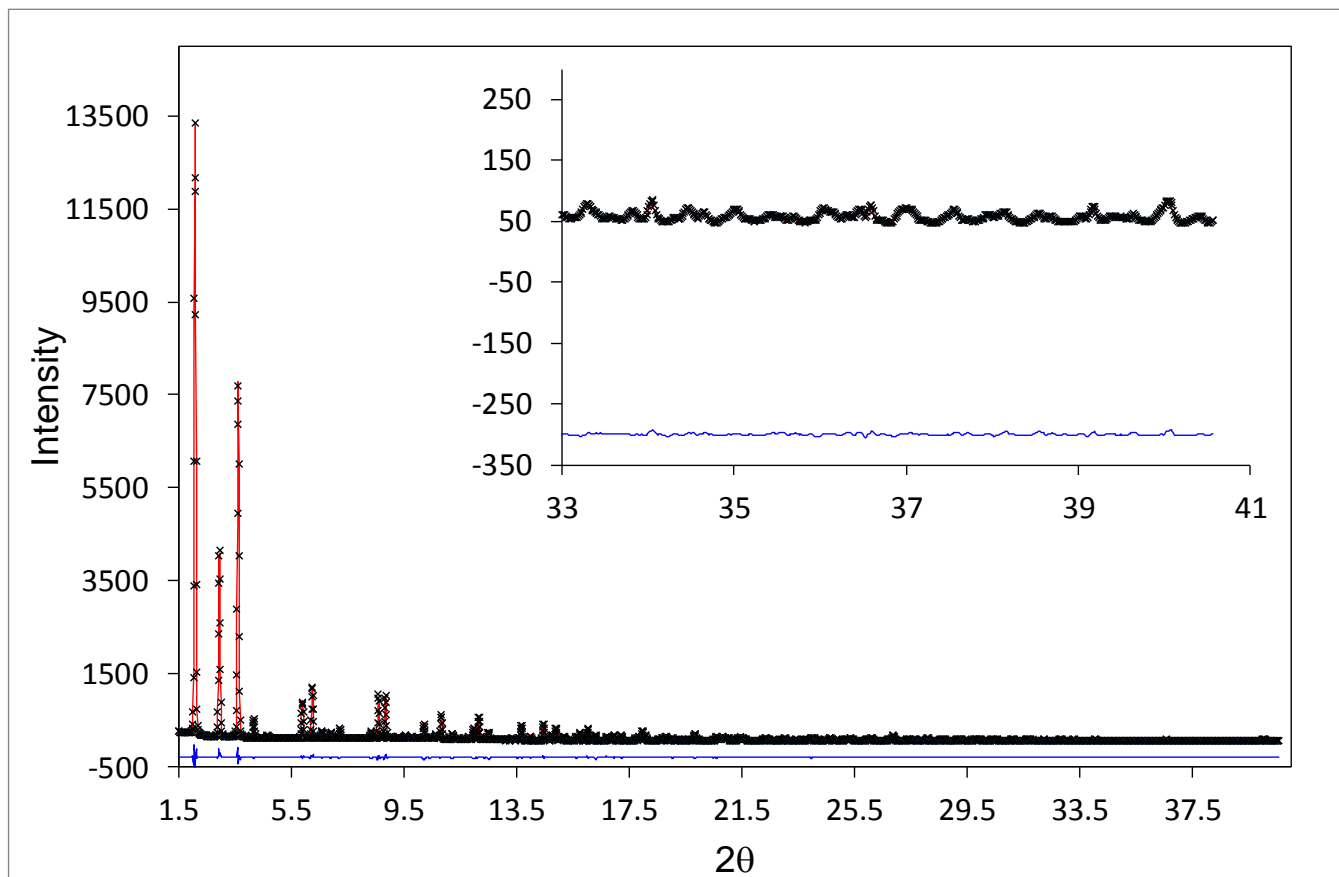


Figure S4-17. Synchrotron powder diffraction data collected at 100 K for a sample of Cu-BTTr loaded with 1.09 CO₂ per Cu site (104.6 CO₂ per unit cell). The green line, crosses, and red line represent the background, experimental, and calculated diffraction patterns, respectively. The blue line represents the difference between experimental and calculated patterns.

Table S4-11. Fractional atomic coordinates, occupancies, and isotropic displacement parameters obtained from Rietveld refinement of the structural model for Cu-BTtri loaded with 1.09 CO₂ per Cu site (104.6 CO₂ per unit cell) against diffraction data collected presented in Figure S4-17. The structure is cubic, space group *Fm-3c*, $a = 37.091(9)$ Å, $V = 51027(69)$ Å³. Values in parentheses represent standard deviation. GOF parameters: wRp = 0.0409, Rp = 0.0285. (The number for corresponding CIF file in CCDC database: 1894884).

Atom	x	y	z	occupancy	Biso (Å ²)
Cu1	0.5	0.31340(6)	0.75456(7)	1	1
C1	0.3369(2)	0.6163(3)	0.3369(2)	1	1
C3	0.3223(2)	0.63127(18)	0.36873(18)	1	1
C2	0.3226(2)	0.5854(3)	0.3226(2)	1	2
N1	0.2832(3)	0.5407(3)	0.3177(3)	1	1
N2	0.3086(3)	0.5356(3)	0.2927(3)	1	1
N3A	0.3333(4)	0.5633(3)	0.2955(3)	0.56038	1
C1A	0.2901(4)	0.5714(4)	0.3375(4)	0.43962	1
N3B	0.2901(4)	0.5714(4)	0.3375(4)	0.43962	1
C1B	0.3333(4)	0.5633(3)	0.2955(3)	0.56038	1
O_new2a	0.4079(11)	0.25	0.75	0.66(3)	12
O_new2b	0.3565(11)	0.284(3)	0.749(9)	0.165(8)	20
C_new2c	0.3824(11)	0.267(3)	0.748(9)	0.165(8)	20
O_new1a	0.5	0.390(2)	0.762(2)	0.472(9)	18
O_new1b	0.559(2)	0.409(2)	0.774(2)	0.236(5)	18
C_new1c	0.529(3)	0.400(4)	0.768(5)	0.236(5)	18
O_new4a	0.326(6)	1.0(6)	0.608(6)	0.032(6)	12
O_new4b	0.371(6)	1.0(6)	0.652(6)	0.032(6)	12
C_new4c	0.348(6)	1.0(6)	0.630(6)	0.032(6)	12
C_new3a	0.326(6)	0.293(9)	0.770(13)	0.111(7)	20
O_new3b	0.348(5)	0.280(5)	0.753(11)	0.111(7)	20
O_new3c	0.303(9)	0.305(15)	0.787(15)	0.111(7)	20

7.3.14 Fitting of unary isotherm data for transient breakthrough simulations

The unary isotherm data for CO₂ and N₂ in CuBTT and CuBTTri were fitted with good accuracy using the single-site Langmuir model

$$q = q_{\text{sat}} \frac{bp}{1 + bp} \quad \text{Eq. (S4 - 7)}$$

The fitted parameter values are presented in Table S4-12 and Table S4-13.

Table S4-12. Single-site Langmuir parameter fits for CO₂ and N₂ in CuBTT at 298 K.

	q_{sat} mol kg ⁻¹	b Pa ⁻¹
CO ₂	6.4	1.44E-05
N ₂	6.4	6.93E-07

Table S4-13. Single-site Langmuir parameter fits for CO₂ and N₂ in CuBTTri at 298 K.

	q_{sat} mol kg ⁻¹	b Pa ⁻¹
CO ₂	15	2.73E-06
N ₂	15	9.81E-08

7.3.15 References for the appendix to chapter 4

- (1) Brunauer, S.; Emmett, P. H.; Teller, E. Adsorption of gases in multimolecular layers. *Journal of the American chemical society* **1938**, 60 (2), 309-319.
- (2) Asgari, M.; Jawahery, S.; Bloch, E. D.; Hudson, M. R.; Flacau, R.; Vlasisavljevich, B.; Long, J. R.; Brown, C. M.; Queen, W. L. An experimental and computational study of CO₂ adsorption in the sodalite-type M-BTT (M= Cr, Mn, Fe, Cu) metal–organic frameworks featuring open metal sites. *Chemical science* **2018**, 9 (20), 4579-4588.
- (3) Mason, J. A.; Sumida, K.; Herm, Z. R.; Krishna, R.; Long, J. R. Evaluating metal–organic frameworks for post-combustion carbon dioxide capture via temperature swing adsorption. *Energy & Environmental Science* **2011**, 4 (8), 3030-3040.
- (4) Mathias, P. M.; Kumar, R.; Moyer, J. D.; Schork, J. M.; Srinivasan, S. R.; Auvel, S. R.; Talu, O. Correlation of multicomponent gas adsorption by the dual-site Langmuir model. Application to nitrogen/oxygen adsorption on 5A-zeolite. *Industrial & engineering chemistry research* **1996**, 35 (7), 2477-2483.
- (5) McDonald, T. M.; D'Alessandro, D. M.; Krishna, R.; Long, J. R. Enhanced carbon dioxide capture upon incorporation of N, N'-dimethylethylenediamine in the metal–organic framework CuBTTri. *Chemical Science* **2011**, 2 (10), 2022-2028.

7.4 Appendix to Chapter 5

7.4.1 Synchrotron powder X-ray diffraction pattern of Cu-TDPAT at 100K

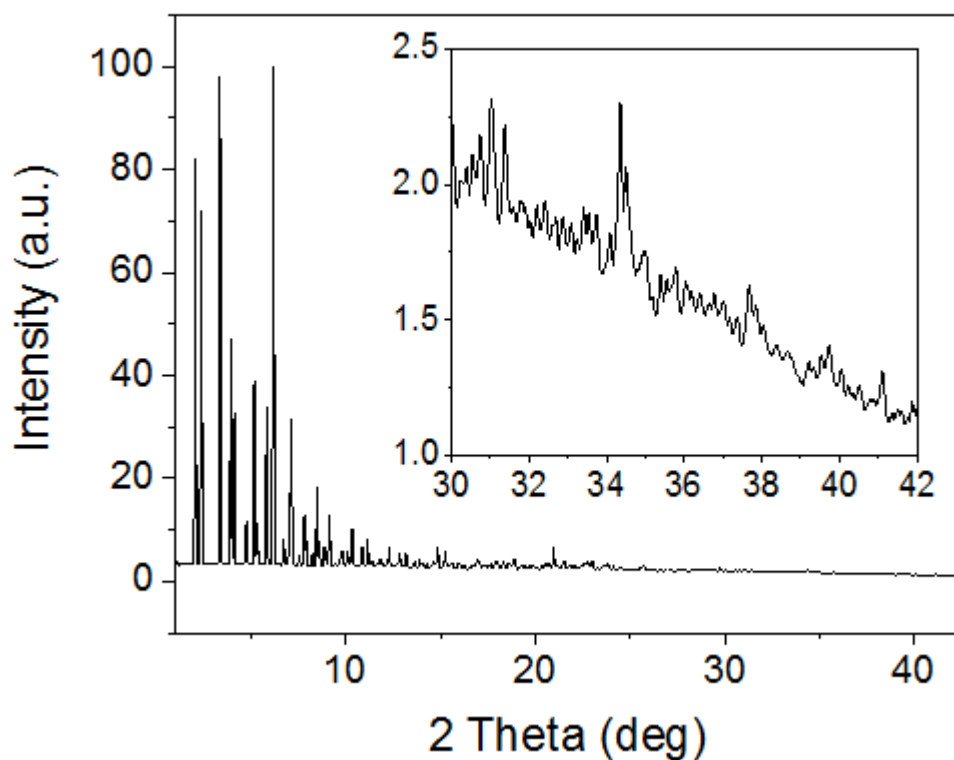


Figure S5-1. Synchrotron x-ray diffraction pattern collected on the bare Cu-TDPAT at 100 K in SNBL (BM01), ESRF. The wavelength is set to 0.78256 Å. The sample is diffracting up to two theta of 42 deg ($d \approx 1$ Å). The data confirms high crystallinity of the sample needed for obtaining the accurate lattice parameters.

7.4.2 Synchrotron powder X-ray diffraction pattern of Cu-TDPAT at 500K

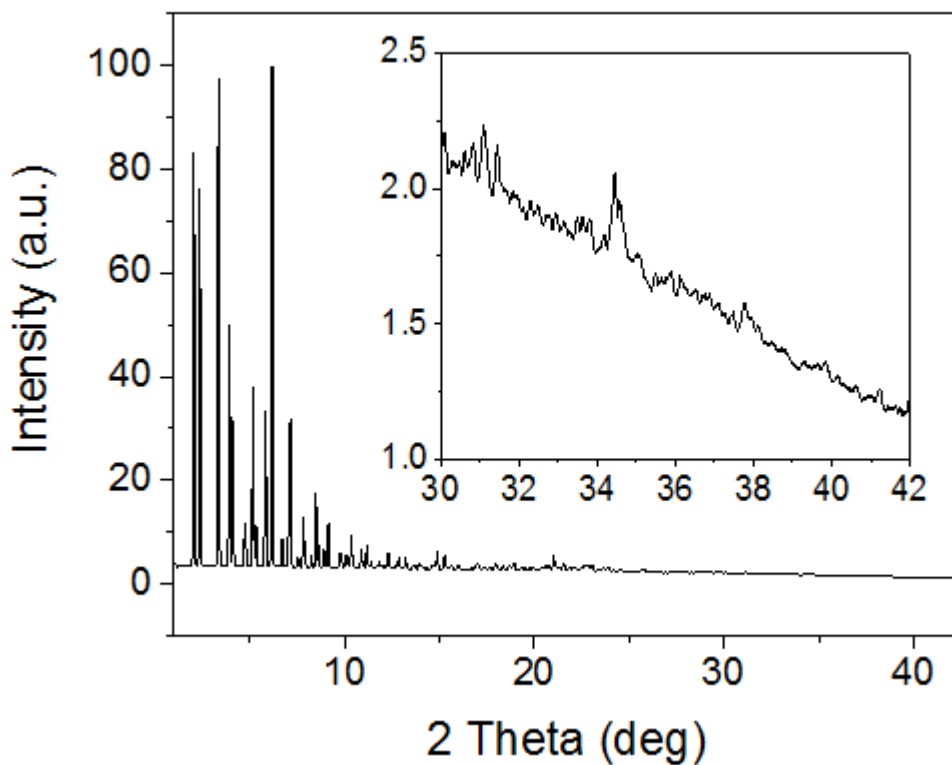


Figure S5-2. Synchrotron x-ray diffraction pattern collected on the bare Cu-TDPAT at 500 K in SNBL (BM01), ESRF. The wavelength is set to 0.78256 Å. The sample is diffracting up to two theta of 42 deg ($d \approx 1$ Å). The data confirms high crystallinity of the sample needed for obtaining the accurate lattice parameters.

7.4.3 Synchrotron single crystal X-ray diffraction pattern of Cu-TDPAT at 100 K

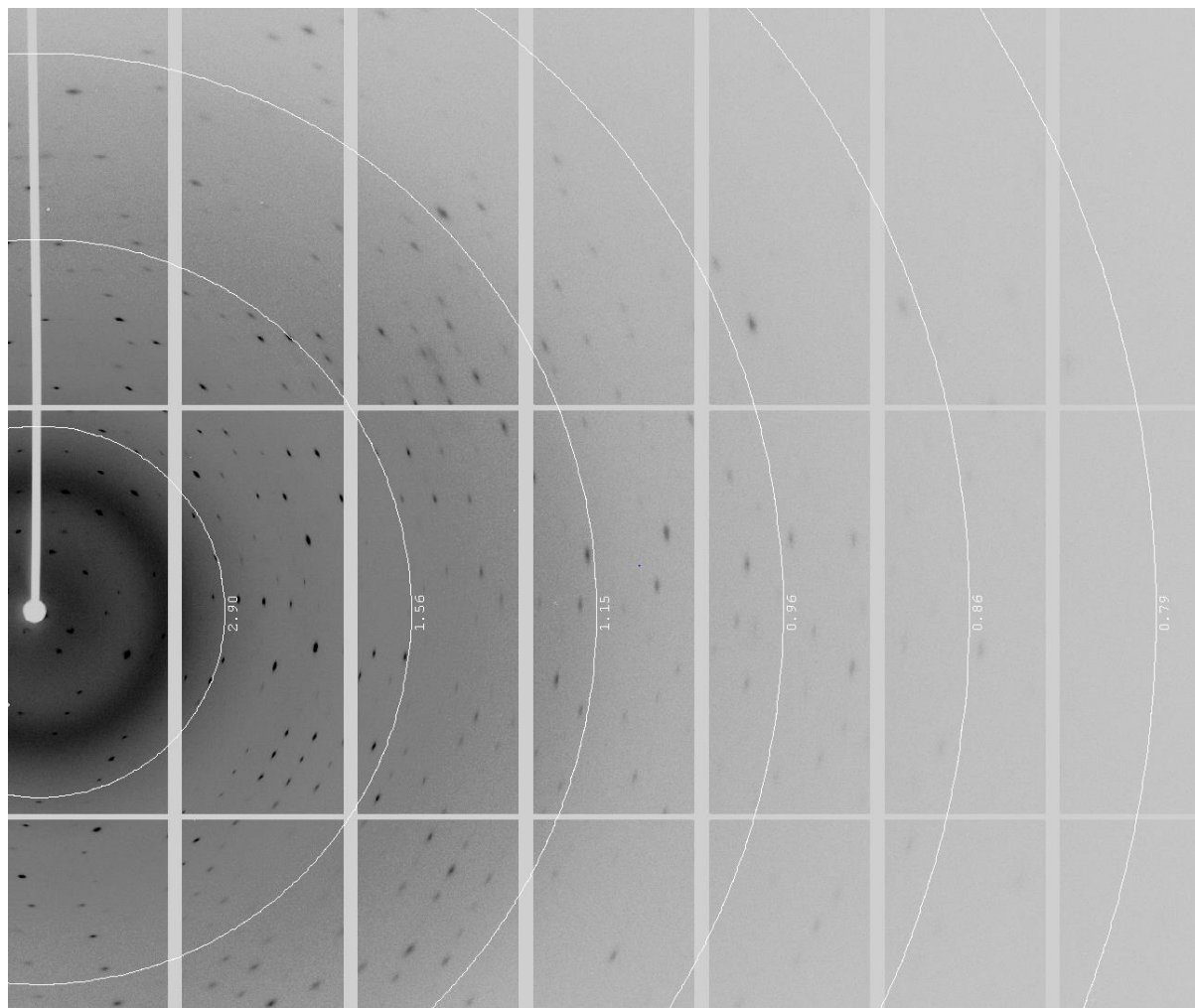


Figure S5-3. Single X-ray crystal diffraction pattern of Cu-TDPAT (T=100 K). The crystal quality is very good and is diffracting up to $d=0.8$ Å.

7.4.4 Sequential LeBail refinement

Table S5-1. Lattice parameters and unit cell volume obtained by *in-situ* sequential LeBail refinement performed on the variable temperature *in-situ* synchrotron powder X-ray diffraction patterns collected at SNBL (BM01), ESRF. ($\lambda = 0.78256 \text{ \AA}$)

Temperature	<i>a</i>	esd (<i>a</i>)	<i>C</i>	esd (<i>c</i>)	<i>V</i>	esd (<i>V</i>)
100.28	26.58714	0.00039	38.03369	0.00105	26885.094	1.077
103.3	26.58799	0.0004	38.03549	0.00120	26888.094	1.233
107.8	26.58837	0.00044	38.03409	0.00122	26887.869	1.240
112.09	26.58900	0.00045	38.03233	0.00125	26887.904	1.266
116.3	26.58806	0.00044	38.03147	0.00121	26885.384	1.231
120.54	26.58735	0.00044	38.02976	0.00121	26882.753	1.230
124.77	26.58592	0.00042	38.03004	0.00116	26880.054	1.179
128.89	26.58514	0.00042	38.02829	0.00115	26877.253	1.175
133.02	26.58229	0.00038	38.02759	0.00104	26870.983	1.071
137.12	26.58159	0.00038	38.02552	0.00102	26868.112	1.052
141.35	26.58141	0.00038	38.02243	0.00104	26865.563	1.070
145.44	26.58043	0.00038	38.02197	0.00102	26863.256	1.051
149.55	26.57996	0.00038	38.01914	0.00103	26860.312	1.057
153.67	26.57902	0.00038	38.01820	0.00103	26857.739	1.057
157.88	26.57858	0.00038	38.01747	0.00105	26856.330	1.077
161.97	26.57784	0.00038	38.01716	0.00103	26854.616	1.056
166.04	26.57687	0.00038	38.01673	0.00103	26852.367	1.052
170.29	26.57672	0.00039	38.01603	0.00107	26851.560	1.092
174.33	26.57622	0.00041	38.01571	0.00112	26850.327	1.142
178.47	26.57605	0.00041	38.01449	0.00114	26849.111	1.155
182.58	26.57369	0.00039	38.01207	0.00106	26842.638	1.081
186.78	26.57445	0.00045	38.01311	0.00125	26844.906	1.27
190.86	26.57267	0.00044	38.01321	0.00121	26841.386	1.231
194.95	26.57230	0.00043	38.01288	0.00120	26840.410	1.221
199.07	26.57090	0.00042	38.01125	0.00115	26836.428	1.167
203.26	26.56890	0.00039	38.01067	0.00107	26831.973	1.093
207.37	26.56739	0.00039	38.00889	0.00107	26827.668	1.089
211.48	26.56640	0.00038	38.00652	0.00105	26824.009	1.069
215.68	26.56535	0.00038	38.00408	0.00104	26820.167	1.060
219.76	26.56417	0.00037	38.00300	0.00102	26817.017	1.043
223.92	26.56293	0.00037	38.00271	0.00101	26814.313	1.032
227.99	26.56225	0.00038	38.00081	0.00103	26811.595	1.049
232.17	26.56154	0.00038	37.99875	0.00104	26808.702	1.064

236.32	26.55977	0.00037	37.99947	0.00100	26805.634	1.021
240.36	26.55925	0.00037	37.99722	0.00102	26803.002	1.040
244.48	26.55836	0.00038	37.99628	0.00103	26800.546	1.050
248.71	26.55691	0.00037	37.99619	0.00101	26797.550	1.029
252.72	26.55603	0.00037	37.99535	0.00101	26795.186	1.034
256.88	26.55553	0.00038	37.99345	0.00103	26792.832	1.051
261.04	26.55361	0.00037	37.99497	0.00101	26790.029	1.030
265.13	26.55279	0.00037	37.99371	0.00101	26787.497	1.027
269.3	26.55160	0.00037	37.99332	0.00101	26784.812	1.034
273.36	26.55061	0.00037	37.99206	0.00101	26781.936	1.030
277.63	26.55028	0.00037	37.98998	0.00100	26779.809	1.021
281.74	26.54914	0.00037	37.98990	0.00100	26777.449	1.026
285.73	26.54846	0.00037	37.98888	0.00100	26775.342	1.024
289.96	26.54803	0.00037	37.98665	0.00100	26772.914	1.021
294.04	26.54681	0.00037	37.98645	0.00100	26770.312	1.022
298.26	26.54622	0.00037	37.98530	0.00100	26768.311	1.019
302.22	26.54554	0.00037	37.98413	0.00100	26766.112	1.022
306.51	26.54469	0.00037	37.98345	0.00101	26763.924	1.032
311.74	26.54489	0.00037	37.98016	0.00101	26762.007	1.027
314.93	26.54497	0.00037	37.97784	0.00102	26760.542	1.041
319.09	26.54373	0.00037	37.97825	0.00100	26758.318	1.022
323.12	26.54362	0.00037	37.97632	0.00101	26756.744	1.027
327.16	26.54304	0.00037	37.97488	0.00100	26754.563	1.020
331.23	26.54231	0.00037	37.97459	0.00100	26752.873	1.020
335.45	26.54124	0.00037	37.97521	0.00101	26751.160	1.031
339.48	26.54140	0.00037	37.97194	0.00102	26749.170	1.037
343.59	26.54037	0.00037	37.97211	0.00102	26747.212	1.037
347.74	26.53984	0.00037	37.97058	0.00102	26745.066	1.037
351.91	26.53889	0.00036	37.96863	0.00099	26741.786	1.007
356.06	26.53920	0.00037	37.96420	0.00101	26739.299	1.034
360.05	26.53728	0.00036	37.96578	0.00098	26736.548	1.007
364.07	26.53679	0.00036	37.96452	0.00098	26734.667	1.003
368.35	26.53625	0.00036	37.96325	0.00099	26732.676	1.009
372.58	26.53602	0.00036	37.96178	0.00098	26731.187	1.006
376.67	26.53606	0.00036	37.95981	0.00099	26729.884	1.008
380.82	26.53496	0.00037	37.96052	0.00099	26728.162	1.016
384.82	26.53507	0.00036	37.95823	0.00099	26726.771	1.009
388.97	26.53437	0.00036	37.95745	0.00099	26724.811	1.011
393.08	26.53396	0.00036	37.95633	0.00099	26723.190	1.010
397.24	26.53331	0.00037	37.95562	0.00100	26721.379	1.026
401.42	26.53347	0.00036	37.95286	0.00098	26719.766	1.005
405.56	26.53372	0.00036	37.95000	0.00097	26718.249	0.996

409.66	26.53278	0.00036	37.95081	0.00099	26716.928	1.012
413.8	26.53280	0.00036	37.94893	0.00098	26715.654	1.000
417.93	26.53193	0.00037	37.94902	0.00100	26713.96	1.021
422.02	26.53205	0.00036	37.94631	0.00098	26712.301	1.001
426.22	26.53172	0.00036	37.94552	0.00098	26711.067	1.004
430.3	26.53096	0.00037	37.94550	0.00100	26709.533	1.023
434.38	26.53109	0.00036	37.94274	0.00100	26707.842	1.000
438.47	26.53052	0.00036	37.94171	0.00098	26705.968	1.001
442.65	26.53003	0.00036	37.94026	0.00098	26703.971	1.000
446.78	26.52966	0.00036	37.93844	0.00098	26701.946	0.998
450.81	26.52891	0.00036	37.93827	0.00098	26700.324	1.005
454.99	26.52786	0.00037	37.93805	0.00100	26698.034	1.022
459.27	26.52753	0.00037	37.93629	0.00100	26696.134	1.011
463.29	26.52738	0.00036	37.93415	0.00100	26694.341	1.001
467.37	26.52632	0.00037	37.93481	0.00100	26692.668	1.027
471.58	26.52633	0.00036	37.93169	0.00100	26690.484	1.000
475.6	26.52521	0.00037	37.93247	0.00100	26688.787	1.024
479.64	26.52470	0.00037	37.93100	0.00099	26686.736	1.014
483.8	26.52408	0.00037	37.93060	0.00100	26685.190	1.022
488.06	26.52318	0.00037	37.92964	0.00100	26682.710	1.034
492.14	26.52618	0.00043	37.92906	0.00120	26688.345	1.214
495.98	26.52205	0.00037	37.92797	0.00100	26679.264	1.032
500.07	26.52395	0.00044	37.92976	0.00120	26684.334	1.222
501.02	26.52072	0.00038	37.92712	0.00102	26675.994	1.054
500.6	26.52058	0.00037	37.92579	0.00100	26674.775	1.028
500.31	26.52056	0.00037	37.92521	0.00099	26674.322	1.022
500.15	26.52000	0.00037	37.92550	0.00100	26673.402	1.034

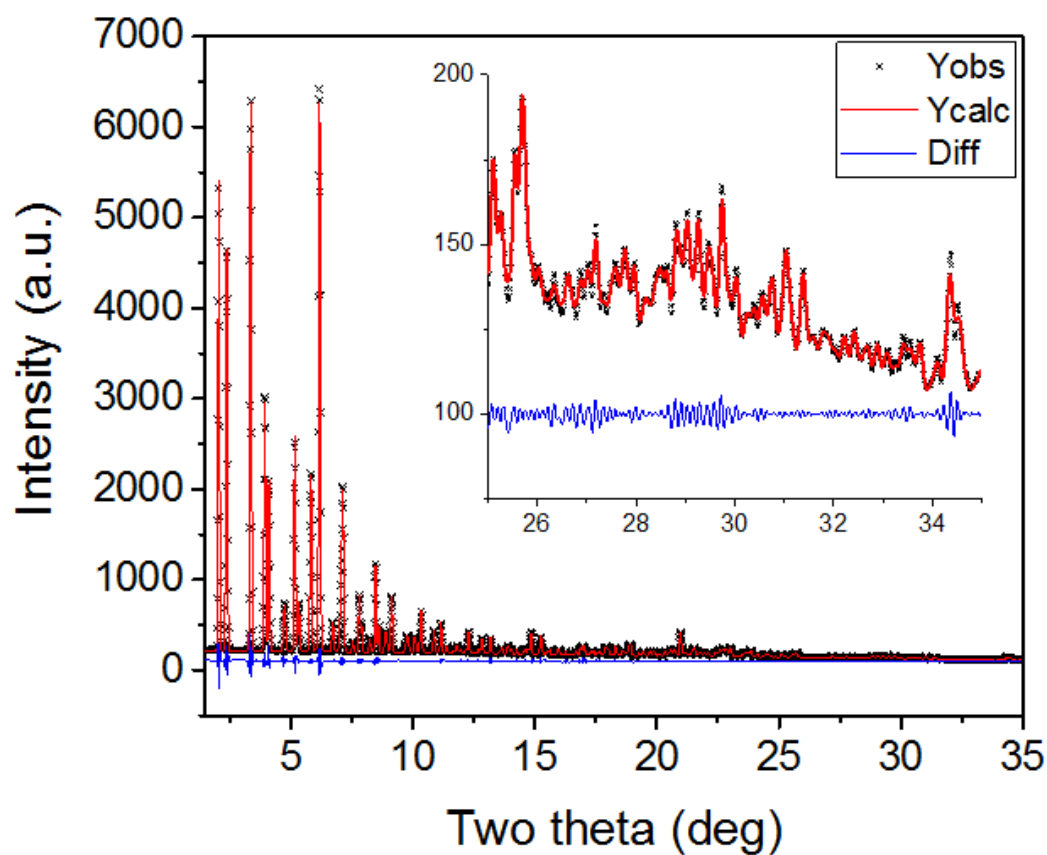


Figure S5-4. An example of Le Bail refinement performed on the synchrotron XRD data collected on Cu-TDPAT at 100 K ($R_p = 2.126\%$, $R_{wp} = 3.205\%$). The black crosses represent the experimental data, the red line is representing the pattern constructed based on the model and the blue line shows the difference.

7.4.5 Fitting of the lattice parameters and unit cell volume by 2nd degree polynomial

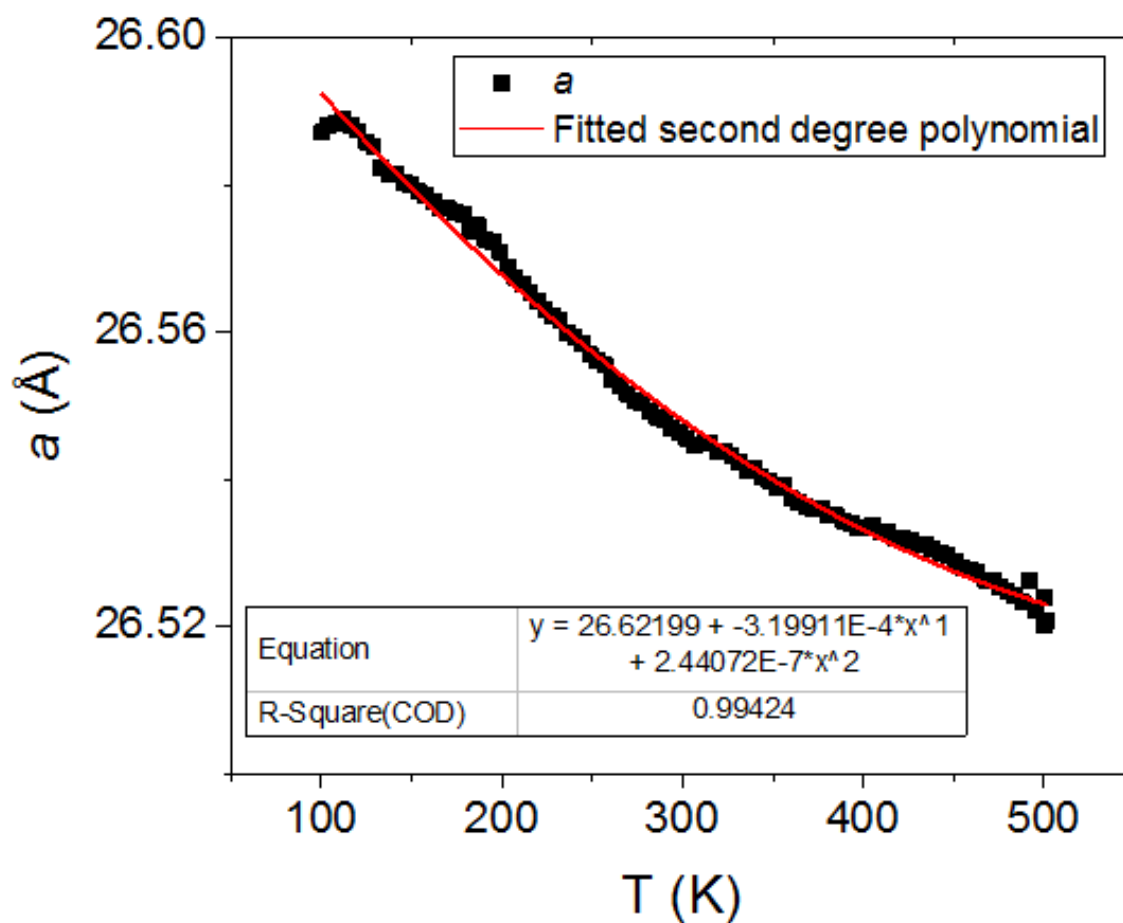


Figure S5-5. 2nd degree polynomial fitting of the lattice parameter a as a function of temperature. The standard deviations are smaller than the size of the points. Therefore, cannot be shown in this graph.

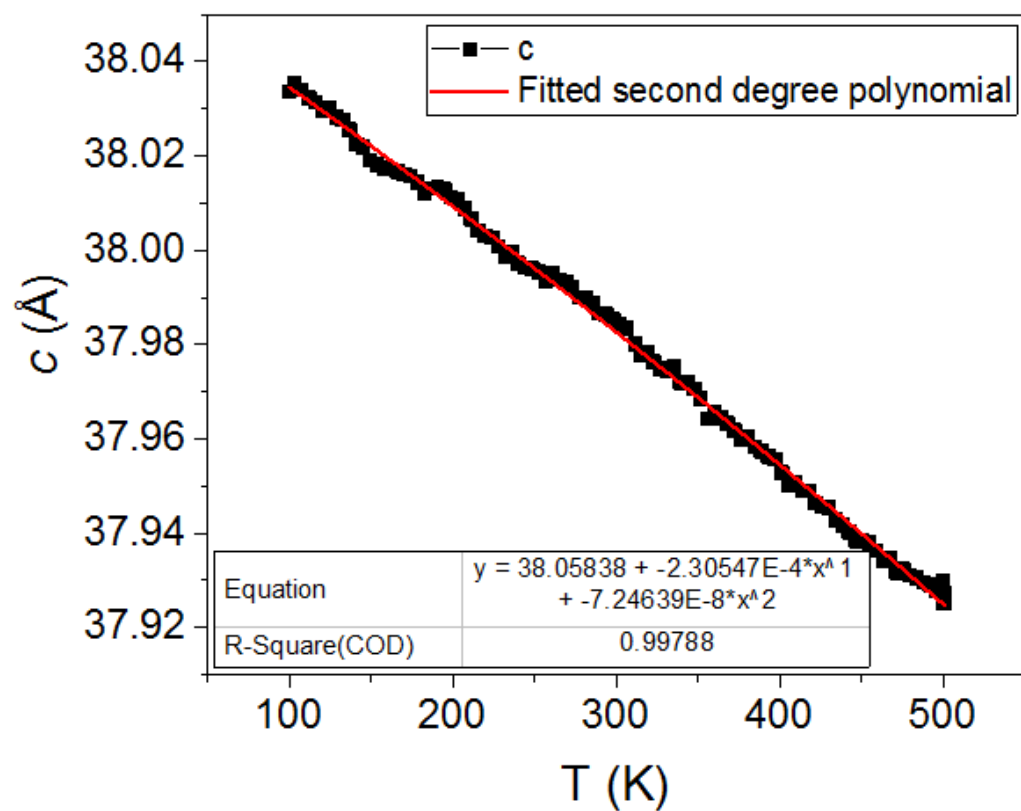


Figure S5-6. 2nd degree polynomial fitting of the lattice parameter c as a function of temperature. The standard deviations are smaller than the size of the points. Therefore, cannot be shown in this graph.

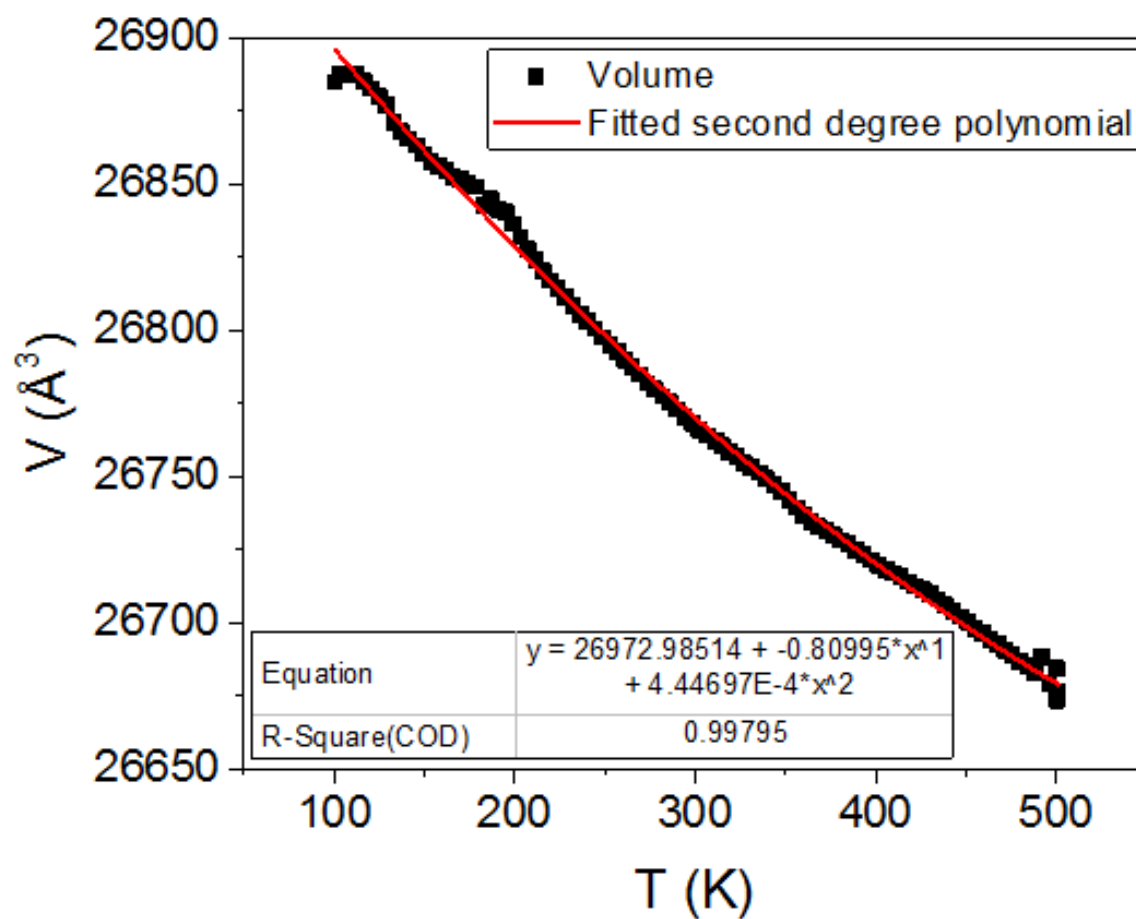


Figure S5-7. 2nd degree polynomial fitting of the unit cell volume as a function of temperature. The standard deviations are smaller than the size of the points. Therefore, cannot be shown in this graph.

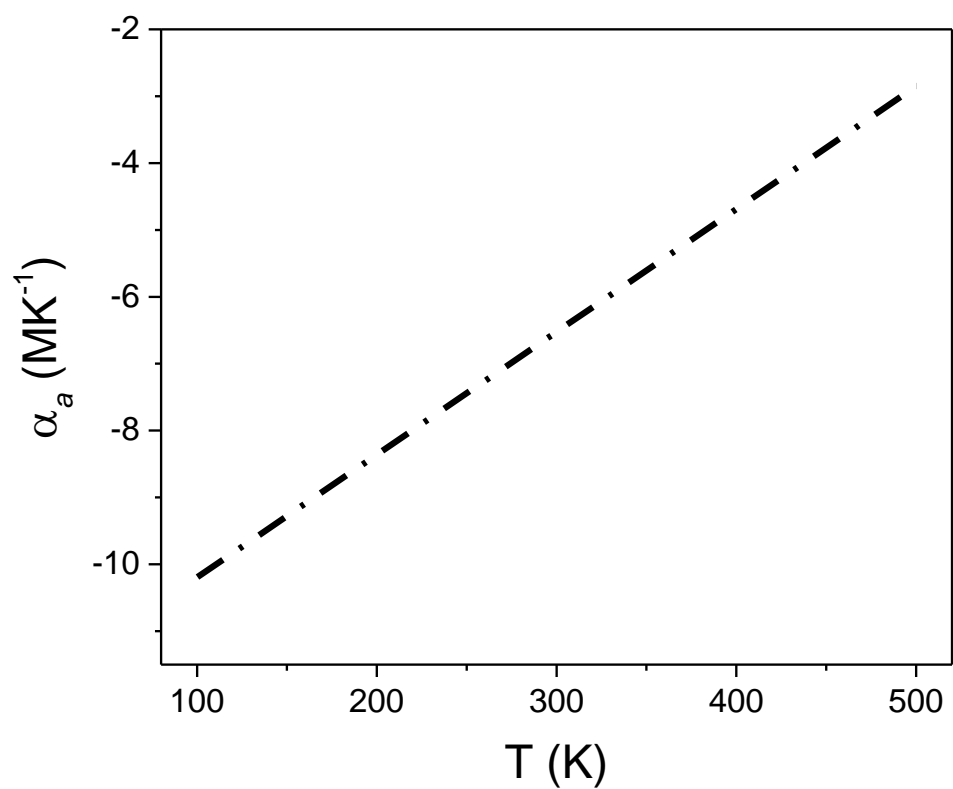


Figure S5-8. The temperature dependent linear thermal expansion coefficient obtained for the lattice parameter, a , by the second polynomial fitting of the data.

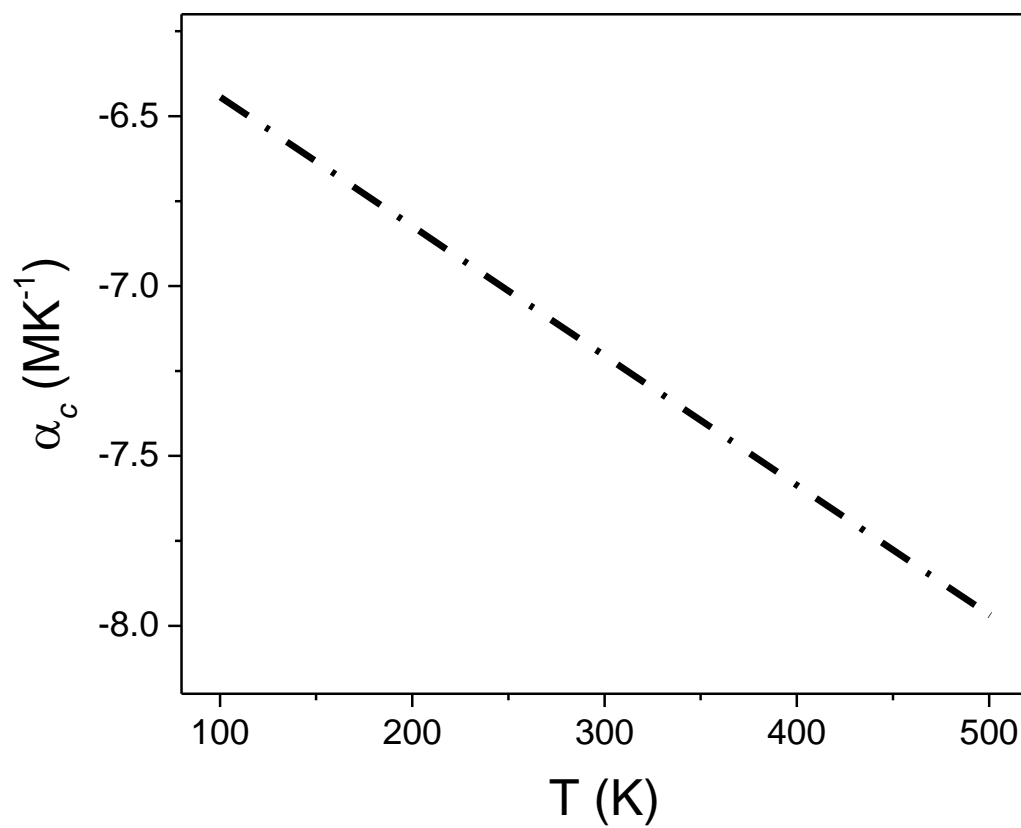


Figure S5-9. The temperature dependent linear thermal expansion coefficient obtained for the lattice parameter, c , by the second polynomial fitting of the data.

7.4.6 Lattice parameters from Single Crystal diffraction

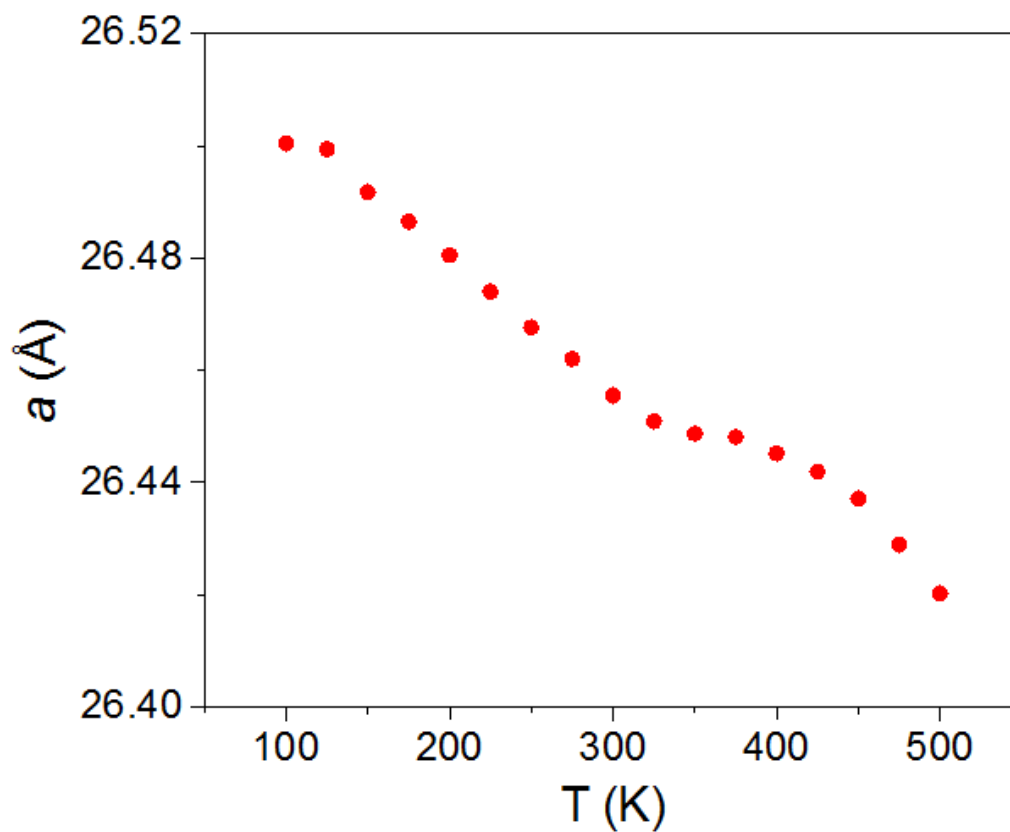


Figure S5-10. The lattice parameter (a) obtained based on the single crystal diffraction analysis. The average linear thermal expansion coefficient (obtained by the linear fitting of the data) is -7.2 (MK)^{-1} for the lattice parameter a , based on the single crystal diffraction data. The standard deviations are smaller than the size of the points. Therefore, cannot be shown in this graph.

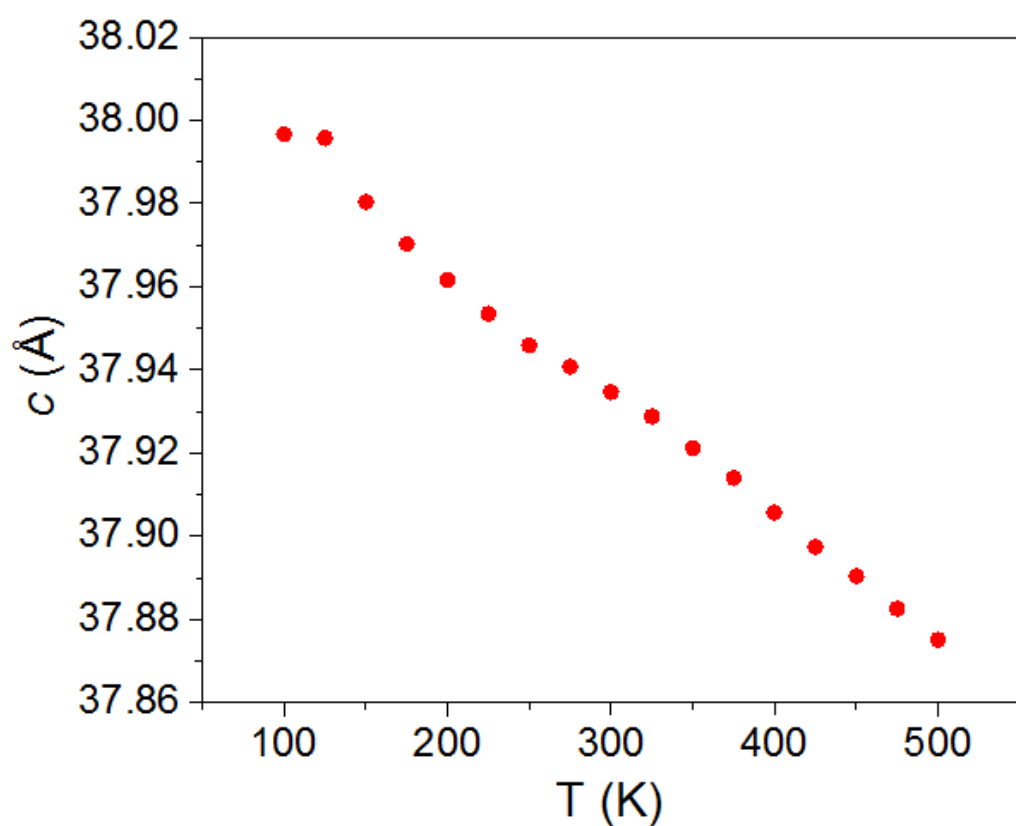


Figure S5-11. The lattice parameter (c) obtained based on the single crystal diffraction analysis. The average linear thermal expansion coefficient (obtained by the linear fitting of the data) is -7.9 (MK)^{-1} for the lattice parameter c , based on the single crystal diffraction data. The standard deviations are smaller than the size of the points. Therefore, cannot be shown in this graph.

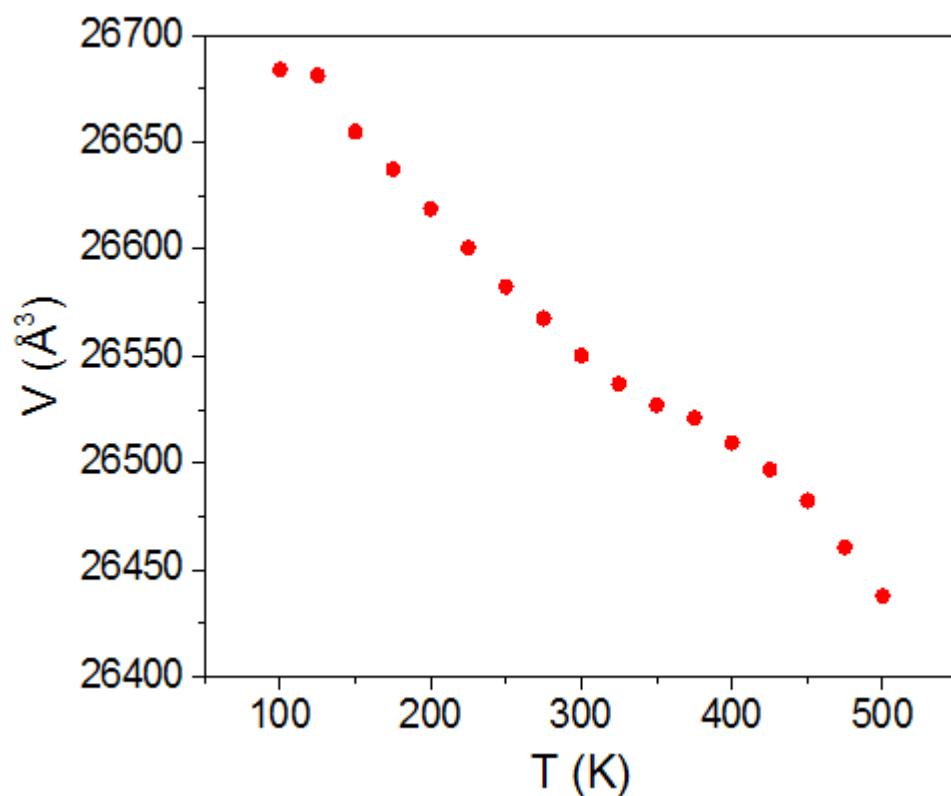


Figure S5-12. The unit cell volume (V) obtained based on the single crystal diffraction analysis. The average volumetric thermal expansion coefficient (obtained by the linear fitting of the data) is -22.1 (MK)^{-1} for the unit cell volume, based on the single crystal diffraction data. The standard deviations are smaller than the size of the points. Therefore, cannot be shown in this graph.

7.4.7 Naming of the atoms in the asymmetric unit of Cu-TDPAT

In the Figure S5-13, we report the naming conventions that will be later used to analyse the structural motions that were observed from single crystal diffraction refinement at different temperatures. In addition, the planes passing central rings (benzene rings and triazine ring) have been demonstrated in this picture.

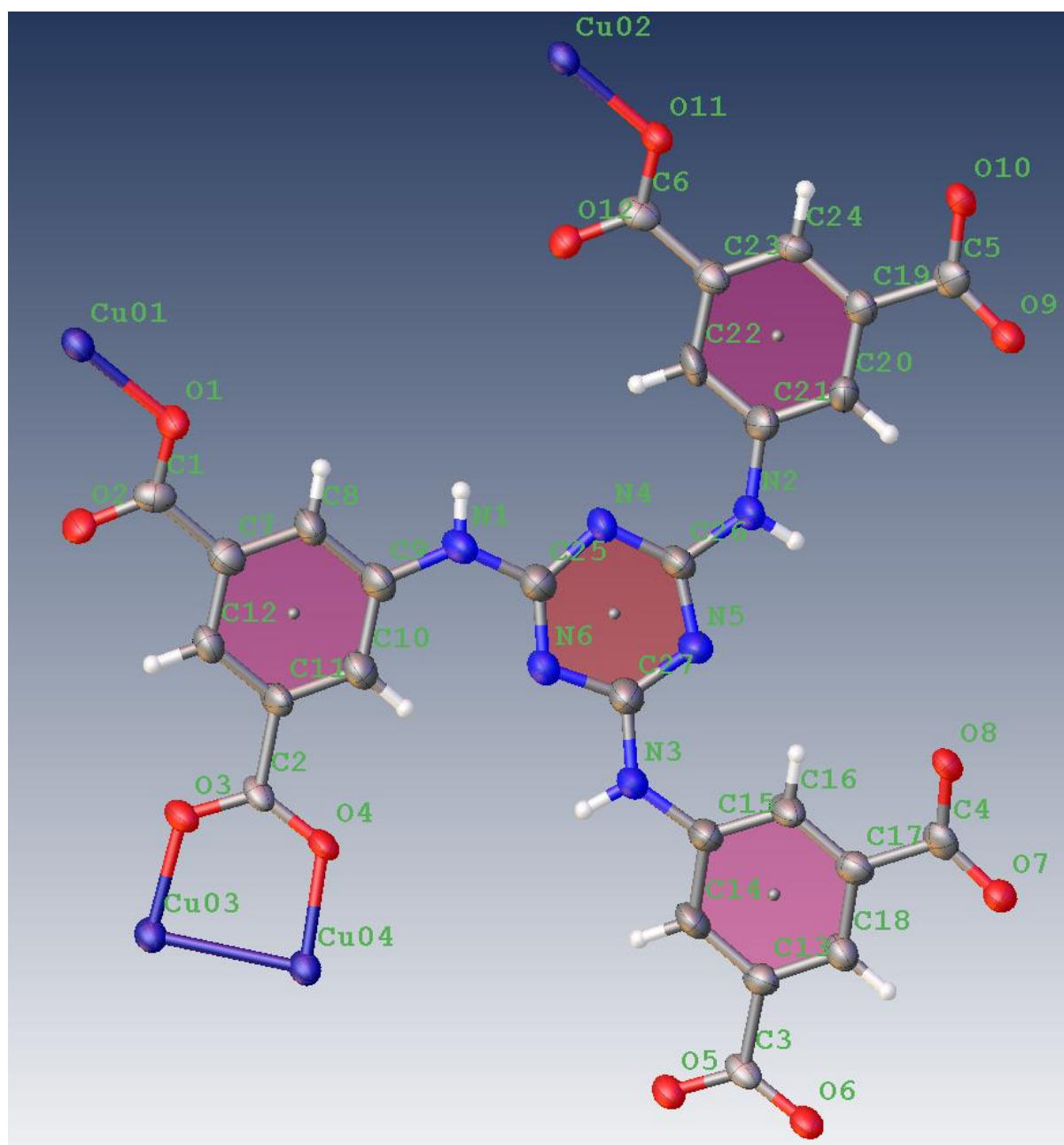


Figure S5-13. The asymmetric unit of Cu-TDPAT; the azine ring has been clarified by the brown color and the benzene rings by pink color.

7.4.8 The fold angle between the azine ring (N4, C26, N5, C27, N6, and C25) and the benzene ring (C15, C16, C17, C18, C13, and C14)

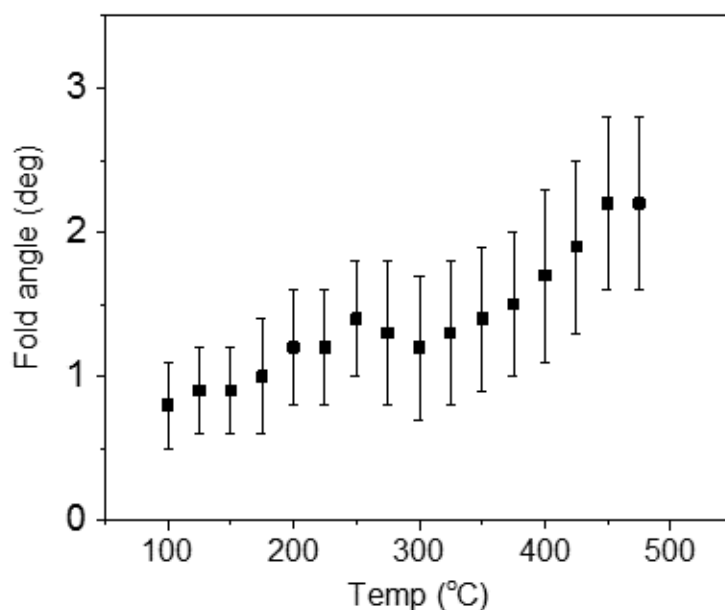


Figure S5-14. The fold angle between the central azine ring and the neighboring benzene ring, which is showing ligand bending. This fold angle has been defined as the angle between the brown plane and the pink lower-right rings in figure S5-13. Numerical values are reported in table S5-2.

Table S5-2. The fold angle (in deg) between the central azine ring and the neighboring benzene ring, which is showing ligand bending.

C15 C16 C17 C18 C13 C14 - N4 C26 N5 C27 N6 C25	
Temp (K)	Fold angle (deg)
100	0.8(3)
125	0.8(3)
150	0.9(3)
175	1.0(4)
200	1.2(4)
225	1.2(4)
250	1.4(4)
275	1.3(5)
300	1.2(5)
325	1.3(5)
350	1.4(5)
375	1.5(5)
400	1.7(6)
425	1.9(6)
450	2.2(6)
475	2.2(6)

7.4.9 Benzene rings rotating around the paddlewheel planes

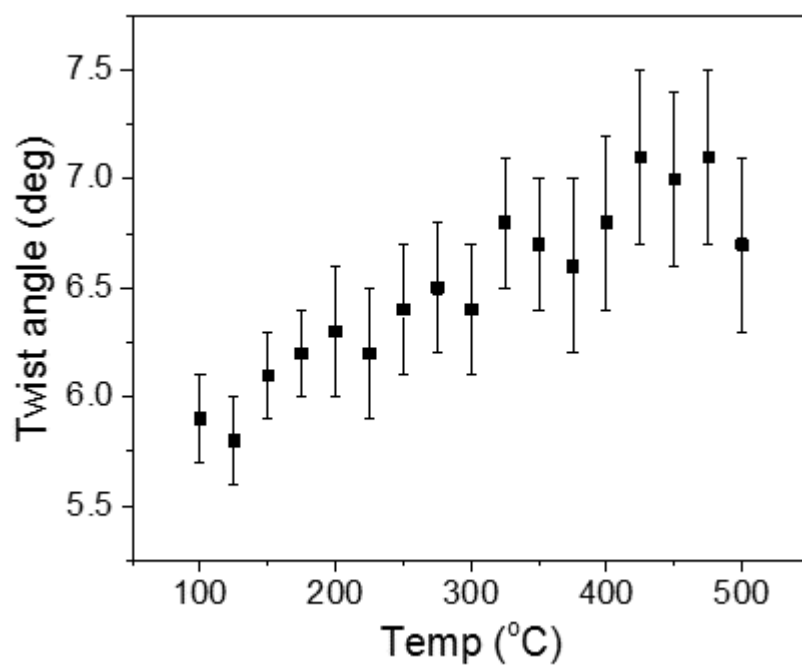


Figure S5-15. The twist angle between C22 C23 C24 C19 C20 C21 (benzene ring)- Cu03 Cu04 O9 O10 (Paddlewheel plane).

Table S5-3. The twist angle (in deg) between C22 C23 C24 C19 C20 C21 (benzene ring)- Cu03 Cu04 O9 O10 (Paddlewheel plane)

Temp (K)	Twist angle
100	5.9(2)
125	5.8(2)
150	6.1(2)
175	6.2(3)
200	6.3(3)
225	6.2(3)
250	6.4(3)
275	6.5(3)
300	6.4(3)
325	6.8(3)
350	6.7(3)
375	6.6(4)
400	6.8(4)
425	7.1(4)
450	7(4)
475	7.1(4)
500	6.7(4)

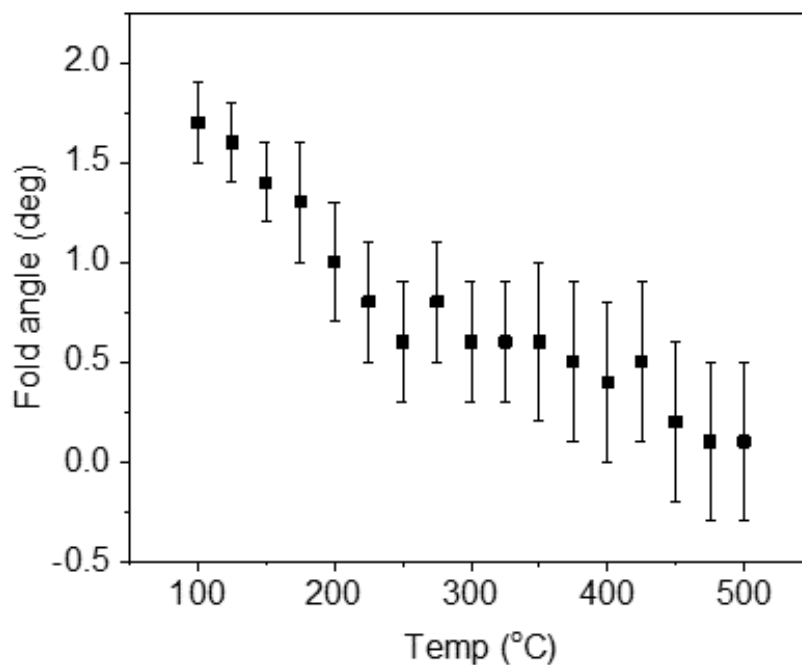
**Figure S5-16.** The fold angle between C15 C16 C17 C18 C13 C14 (benzene ring) - Cu03 O7 O8 Cu04 (paddlewheel plane).

Table S5-4. The fold angle (in deg) between C15 C16 C17 C18 C13 C14 (benzene ring)- Cu04 O5 O6 Cu03 (Paddlewheel plane)

Temp (K)	Fold angle
100	11.3(2)
125	11.4(2)
150	11.3(3)
175	11.2(3)
200	11.5(3)
225	11.6(3)
250	11.6(3)
275	11.5(3)
300	11.5(3)
325	11.7(4)
350	11.6(4)
375	11.7(4)
400	11.6(4)
425	11.7(4)
450	11.9 (4)
475	11.9 (5)
500	11.9 (5)

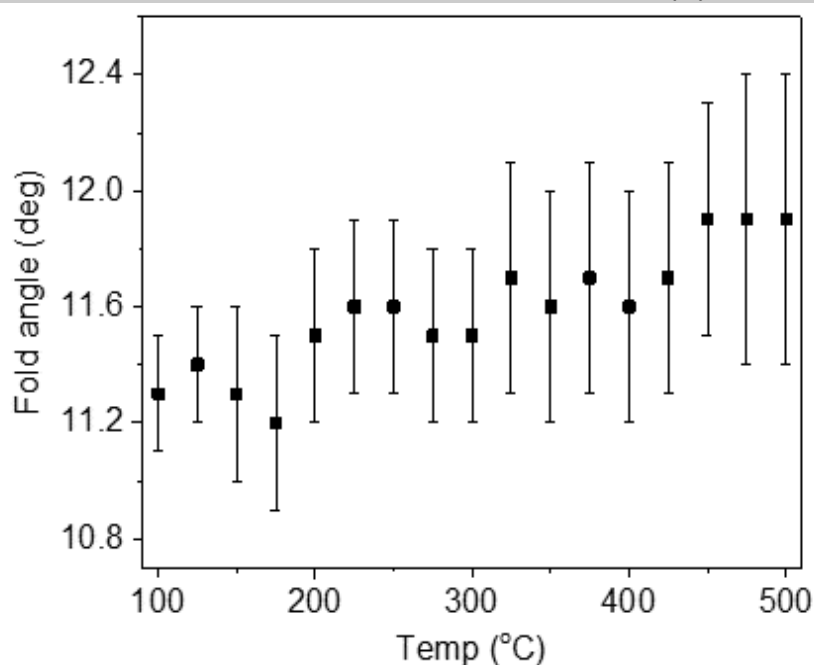


Figure S5-17. The fold angle between C15 C16 C17 C18 C13 C14 (benzene ring)- Cu04 O5 O6 Cu03 (Paddlewheel plane).

Table S5-5. The twist angle (in deg) between C15 C16 C17 C18 C13 C14 (benzene ring) - Cu03 O7 O8 Cu04 (paddlwheel plane)

Temp (K)	Twist angle
100	1.7(2)
125	1.6(2)
150	1.4(2)
175	1.3(3)
200	1.0(3)
225	0.8(3)
250	0.6(3)
275	0.8(3)
300	0.6(3)
325	0.6(3)
350	0.6(4)
375	0.5(4)
400	0.4(4)
425	0.3(4)
450	0.2(4)
475	0.1(4)
500	0.1(4)

7.4.10 Paddlewheels twisting

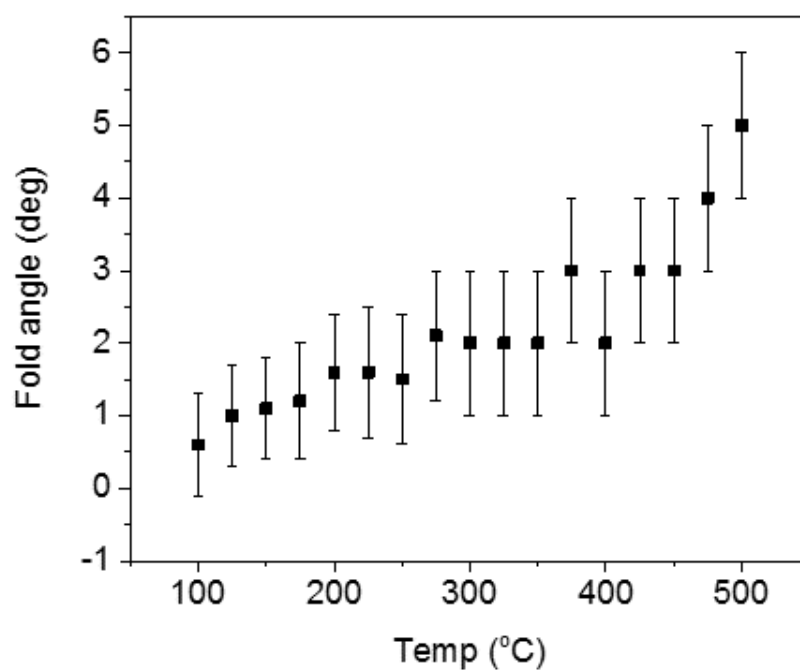


Figure S5-18. The fold angle between the planes C2 Cu4 Cu3 - O4 O3 C2.

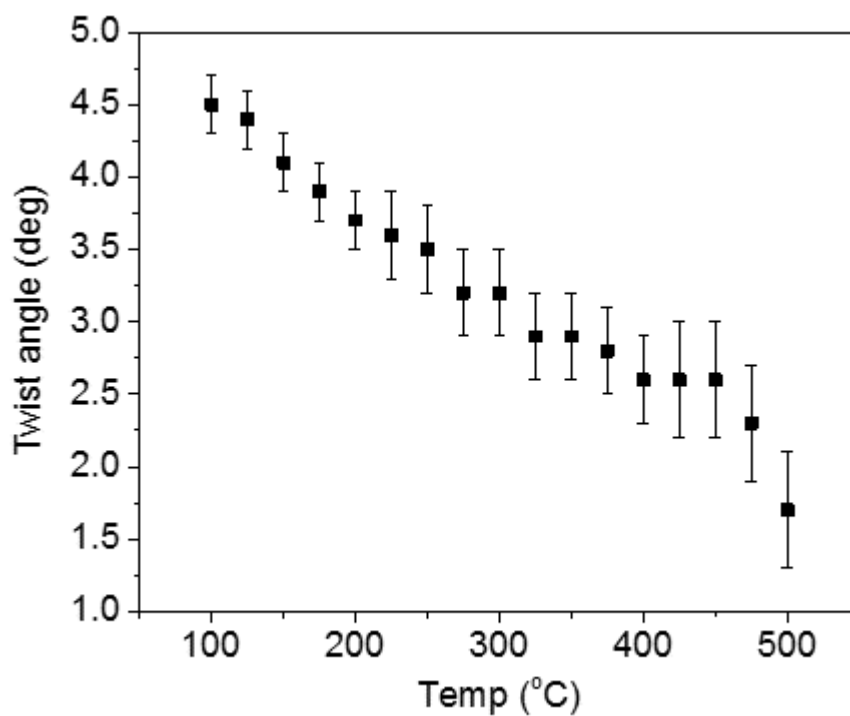


Figure S5-19. The twist angle between the planes C2 Cu4 Cu3 - O4 O3 C2.

Table S5-6. The twist and fold angles (in deg) between the planes C2 Cu4 Cu3 - O4 O3 C2

Temp (K)	Twist angle	Fold angle
100	4.5(2)	0.6(7)
125	4.4(2)	1.0(7)
150	4.1(2)	1.1(7)
175	3.9(2)	1.2(8)
200	3.7(2)	1.6(8)
225	3.6(3)	1.6(9)
250	3.5(3)	1.5(9)
275	3.2(3)	2.1(9)
300	3.2(3)	2(1)
325	2.9(3)	2(1)
350	2.9(3)	2(1)
375	2.8(3)	3(1)
400	2.6(3)	2(1)
425	2.6(4)	3(1)
450	2.6(4)	3(1)
475	2.3(4)	4(1)
500	1.7(4)	5(1)

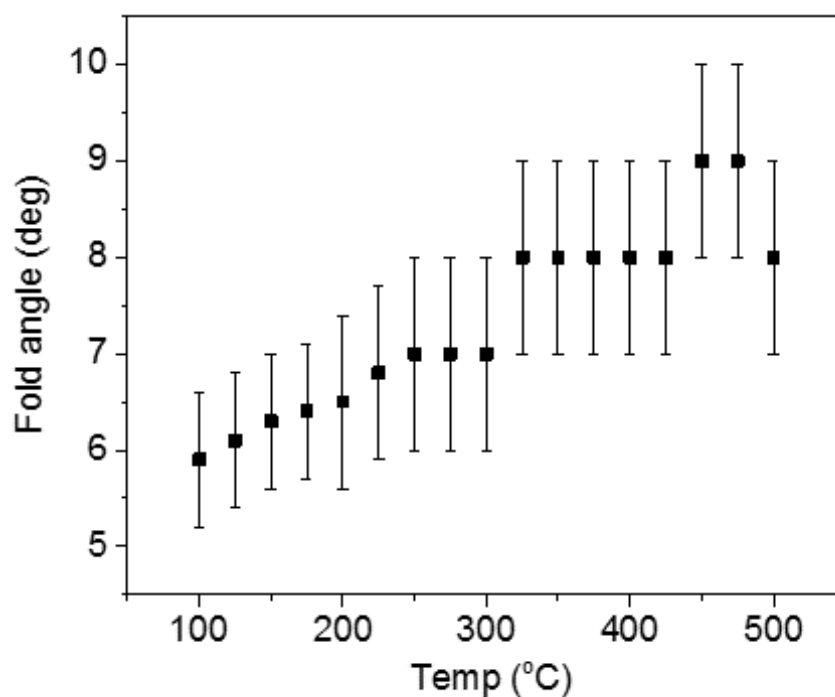


Figure S5-20. The fold angle between the planes C6 Cu01 Cu02 - O12 O11 C6.

Table S5-7. The twist angle (in deg) between the planes C6 Cu01 Cu02 - O12 O11 C6

Temp (K)	Fold angle
100	5.9(7)
125	6.1(7)
150	6.3(7)
175	6.4(7)
200	6.5(9)
225	6.8(9)
250	7(1)
275	7(1)
300	7(1)
325	8(1)
350	8(1)
375	8(1)
400	8(1)
425	8(1)
450	9(1)
475	9(1)
500	8(1)

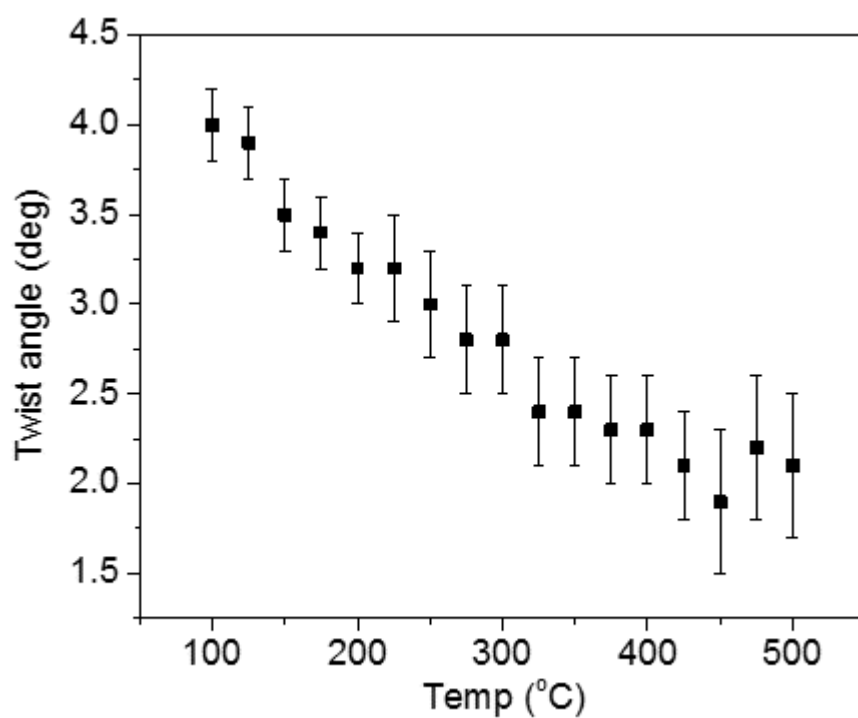


Figure S5-21. The twist angle between the planes C5 Cu03 Cu04 - O10 O9 C5.

Table S5-8. The twist angle (in deg) between the planes C5 Cu03 Cu04 - O10 O9 C5

Temp (K)	Twist angle
100	4.0(2)
125	3.9(2)
150	3.5(2)
175	3.4(2)
200	3.2(2)
225	3.2(3)
250	3.0(3)
275	2.8(3)
300	2.8(3)
325	2.4(3)
350	2.4(3)
375	2.3(3)
400	2.3(3)
425	2.1(3)
450	1.9(4)
475	2.2(4)
500	2.1(4)

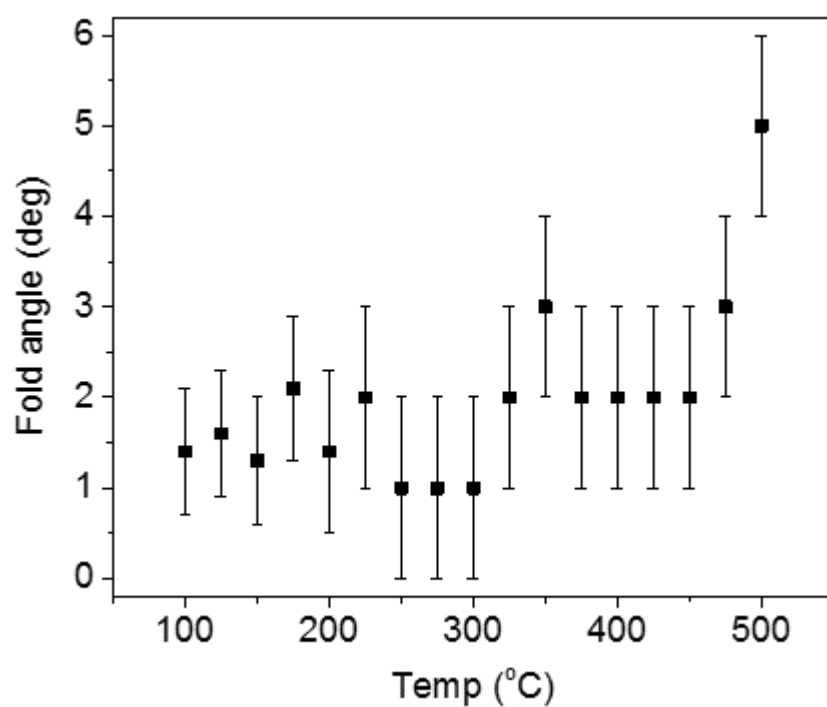


Figure S5-22. The fold angle between the planes C4 Cu04 Cu03 - O8 O7 C4.

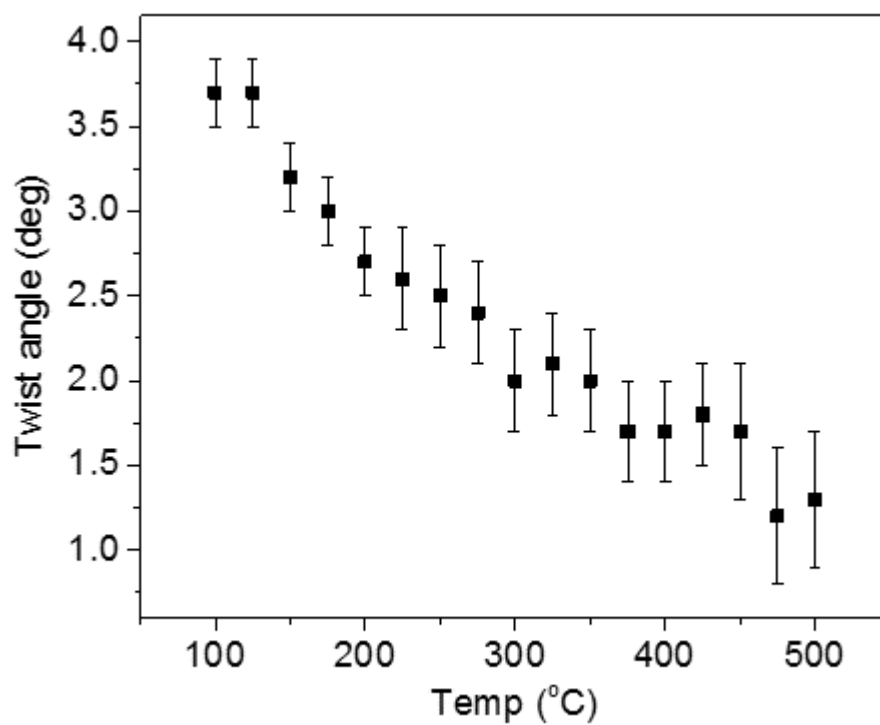


Figure S5-23. The twist angle between the planes C4 Cu04 Cu03 - O8 O7 C4.

Table S5-9. The twist and fold angles (in deg) between the planes C4 Cu04 Cu03 - O8 O7 C4

Temp (K)	Twist angle	Fold angle
100	3.7(2)	1.4(7)
125	3.7(2)	1.6(7)
150	3.2(2)	1.3(7)
175	3.0(2)	2.1(8)
200	2.7(2)	1.4(9)
225	2.6(3)	2(1)
250	2.5(3)	1(1)
275	2.4(3)	1(1)
300	2.0(3)	1(1)
325	2.1(3)	2(1)
350	2.0(3)	3(1)
375	1.7(3)	2(1)
400	1.7(3)	2(1)
425	1.8(3)	2(1)
450	1.7(4)	2(1)
475	1.2(4)	3(1)
500	1.3(4)	5(1)

7.4.11 Change in the Cu-Cu distance

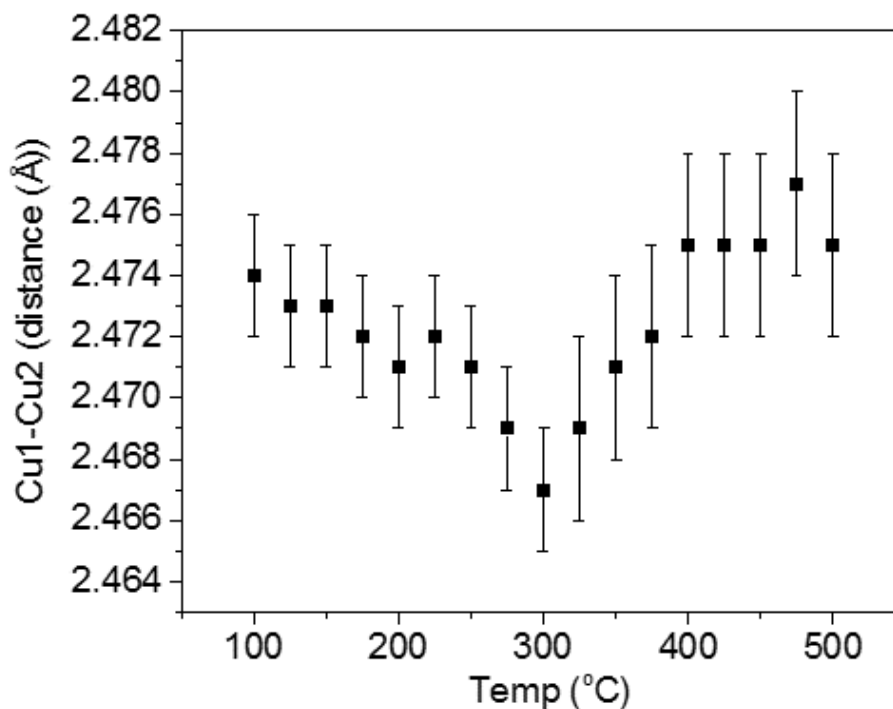


Figure S5-24. The distance of Cu1-Cu2 in one of the paddlewheel clusters as a function of temperature.

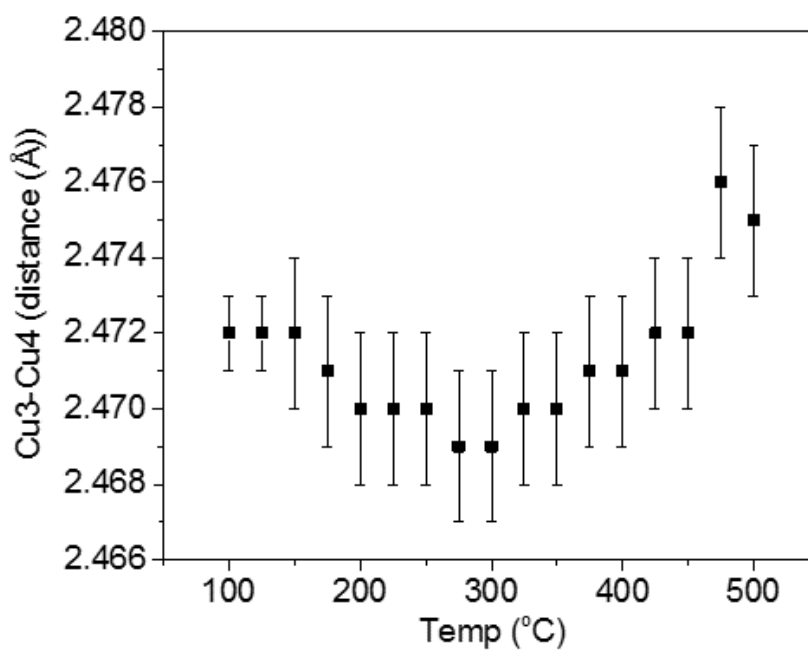


Figure S5-25. The distance of Cu3-Cu4 in one of the paddlewheel clusters as a function of temperature.

Table S5-10. The distance between Cu atoms in the Cu paddlewheel clusters (in Å)

Temp (K)	Distances between atoms	
	Cu1-Cu2	Cu3-Cu4
100	2.474(2) Å	2.472(1) Å
125	2.473(2) Å	2.472(1) Å
150	2.473(2) Å	2.472(2) Å
175	2.472(2) Å	2.471(2) Å
200	2.471(2) Å	2.470(2) Å
225	2.472(2) Å	2.470(2) Å
250	2.471(2) Å	2.470(2) Å
275	2.469(2) Å	2.469(2) Å
300	2.467(2) Å	2.469(2) Å
325	2.469(3) Å	2.470(2) Å
350	2.471(3) Å	2.470(2) Å
375	2.472(3) Å	2.471(2) Å
400	2.475(3) Å	2.471(2) Å
425	2.475(3) Å	2.472(2) Å
450	2.475(3) Å	2.472(2) Å
475	2.477(3) Å	2.476(3) Å
500	2.475(3) Å	2.475(3) Å

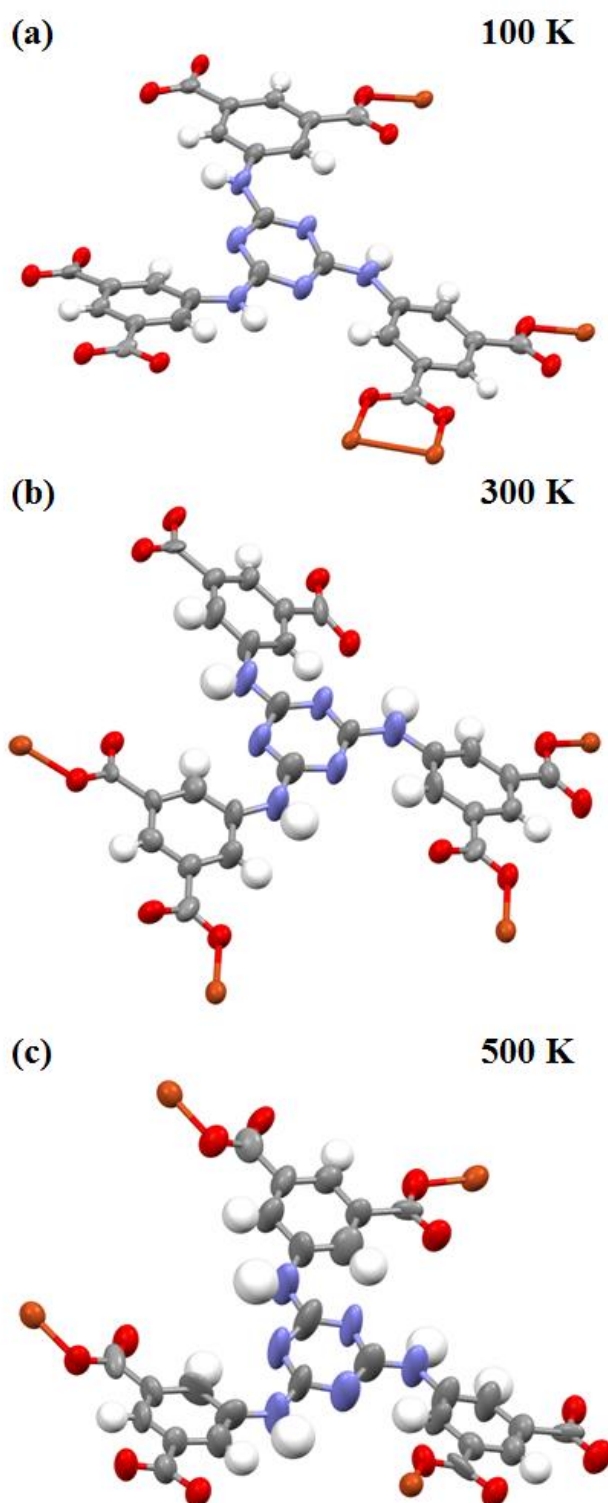


Figure S5-26. The asymmetric unit of Cu-TDPAT at 3 different temperatures of 100 K, 300 K, and 500 K. The size of ellipsoids are indicating the magnitude of ADPs. The picture clearly shows that the ADPs of the atoms in the central triazine ring and the adjacent benzene rings are growing in a direction perpendicular to that of the ring.

Table S5-11. The Uiso for all the atoms in the central triazine ring as a function of the temperature in the temperature range of 100 K-500 K

	100 K	125 K	150 K	175 K	200 K	225 K	250 K	275 K	300 K	325 K	350 K	375 K	400 K	425 K	450 K	475 K	500 K
C25	0.047(2)	0.048(2)	0.058(3)	0.058(3)	0.072(3)	0.070(4)	0.081(4)	0.089(5)	0.093(5)	0.059(3)	0.102(6)	0.106(6)	0.109(6)	0.115(7)	0.120(7)	0.129(8)	0.136(8)
C26	0.044(2)	0.044(2)	0.055(3)	0.055(3)	0.067(3)	0.079(4)	0.085(4)	0.088(4)	0.096(5)	0.098(5)	0.090(5)	0.096(5)	0.098(6)	0.104(6)	0.109(7)	0.118(8)	0.122(8)
C27	0.050(2)	0.050(2)	0.061(3)	0.061(3)	0.076(4)	0.076(4)	0.074(4)	0.079(4)	0.081(4)	0.098(5)	0.102(6)	0.106(6)	0.107(6)	0.112(7)	0.115(7)	0.120(8)	0.130(8)
N4	0.0463(19)	0.048(2)	0.058(2)	0.058(2)	0.072(3)	0.075(3)	0.082(3)	0.087(4)	0.091(4)	0.096(4)	0.101(5)	0.103(5)	0.107(5)	0.113(6)	0.120(6)	0.124(7)	0.137(7)
N5	0.050(2)	0.0478(19)	0.058(2)	0.058(2)	0.074(3)	0.077(3)	0.079(3)	0.085(4)	0.090(4)	0.095(4)	0.099(4)	0.106(5)	0.108(5)	0.112(5)	0.117(6)	0.122(6)	0.128(6)
N6	0.0470(19)	0.052(2)	0.062(2)	0.062(2)	0.070(3)	0.074(3)	0.084(4)	0.087(4)	0.091(4)	0.097(4)	0.098(4)	0.102(5)	0.110(5)	0.116(6)	0.122(6)	0.133(7)	0.127(6)

Table S5-12. The Uiso for all the atoms in a benzene ring of the ligand constituted by [C7 C8 C9 C10 C11 C12] (which is here called Benzene ring 1) as a function of the temperature in the temperature range of 100 K-500 K

	100 K	125 K	150 K	175 K	200 K	225 K	250 K	275 K	300 K	325 K	350 K	375 K	400 K	425 K	450 K	475 K	500 K
C10	0.043(2)	0.044(2)	0.050(2)	0.044(2)	0.061(3)	0.050(2)	0.056(3)	0.058(3)	0.064(3)	0.066(3)	0.082(4)	0.085(4)	0.089(5)	0.094(5)	0.099(5)	0.103(6)	0.110(6)
C11	0.0345(18)	0.0347(19)	0.041(2)	0.043(2)	0.047(2)	0.050(3)	0.055(3)	0.055(3)	0.061(3)	0.063(3)	0.062(3)	0.063(3)	0.065(3)	0.067(4)	0.068(4)	0.075(4)	0.077(4)
C12	0.0351(18)	0.0360(19)	0.042(2)	0.045(2)	0.048(2)	0.050(3)	0.050(3)	0.055(3)	0.055(3)	0.057(3)	0.063(3)	0.066(3)	0.069(4)	0.071(4)	0.073(4)	0.080(4)	0.081(4)
C7	0.0383(19)	0.039(2)	0.045(2)	0.048(2)	0.052(2)	0.056(3)	0.067(3)	0.079(4)	0.075(4)	0.078(4)	0.070(4)	0.070(4)	0.072(4)	0.075(4)	0.078(4)	0.080(5)	0.084(5)
C8	0.041(2)	0.042(2)	0.049(2)	0.058(3)	0.060(3)	0.066(3)	0.071(4)	0.075(4)	0.079(4)	0.086(5)	0.083(4)	0.090(5)	0.090(5)	0.098(6)	0.100(6)	0.107(6)	0.103(6)
C9	0.045(2)	0.044(2)	0.053(2)	0.056(3)	0.063(3)	0.068(3)	0.067(3)	0.067(3)	0.076(4)	0.082(4)	0.089(5)	0.089(5)	0.095(5)	0.100(6)	0.107(6)	0.113(7)	0.117(7)

Table S5-13. The Uiso for all the atoms in a benzene ring of the ligand constituted by [C13 C14 C15 C16 C17 C18] (which is here called *Benzene ring 2*) as a function of the temperature in the temperature range of 100 K-500 K

	100 K	125 K	150 K	175 K	200 K	225 K	250 K	275 K	300 K	325 K	350 K	375 K	400 K	425 K	450 K	475 K	500 K
C13	0.0350(18)	0.0346(19)	0.043(2)	0.060(3)	0.048(2)	0.070(4)	0.061(3)	0.072(4)	0.069(4)	0.074(4)	0.062(3)	0.063(3)	0.066(4)	0.069(4)	0.071(4)	0.075(4)	0.077(4)
C14	0.046(2)	0.046(2)	0.056(3)	0.057(3)	0.065(3)	0.067(3)	0.071(4)	0.077(4)	0.080(4)	0.082(4)	0.088(5)	0.094(5)	0.099(6)	0.101(6)	0.106(6)	0.112(7)	0.117(7)
C15	0.043(2)	0.045(2)	0.053(3)	0.052(3)	0.062(3)	0.059(3)	0.073(4)	0.072(3)	0.083(4)	0.085(5)	0.087(5)	0.088(5)	0.090(5)	0.096(6)	0.099(6)	0.102(6)	0.106(6)
C16	0.041(2)	0.042(2)	0.049(2)	0.047(2)	0.057(3)	0.053(3)	0.051(3)	0.053(3)	0.057(3)	0.058(3)	0.076(4)	0.079(4)	0.081(5)	0.087(5)	0.092(5)	0.095(6)	0.100(6)
C17	0.0385(19)	0.040(2)	0.045(2)	0.044(2)	0.051(2)	0.050(3)	0.051(3)	0.057(3)	0.056(3)	0.056(3)	0.065(3)	0.067(3)	0.068(4)	0.071(4)	0.073(4)	0.077(4)	0.076(4)
C18	0.0366(19)	0.0353(19)	0.042(2)	0.044(2)	0.049(2)	0.050(3)	0.056(3)	0.060(3)	0.061(3)	0.061(3)	0.061(3)	0.063(3)	0.062(3)	0.067(4)	0.070(4)	0.073(4)	0.078(4)

Table S5-14. The Uiso for all the atoms in a benzene ring of the ligand constituted by [C19 C20 C21 C22 C23 C24] (which is here called Benzene ring 3) as a function of the temperature in the temperature range of 100 K-500 K

	100 K	125 K	150 K	175 K	200 K	225 K	250 K	275 K	300 K	325 K	350 K	375 K	400 K	425 K	450 K	475 K	500 K
C19	0.0368(18)	0.0372(19)	0.044(2)	0.055(3)	0.049(2)	0.063(3)	0.072(4)	0.062(3)	0.081(4)	0.083(4)	0.062(3)	0.062(3)	0.066(4)	0.068(4)	0.070(4)	0.073(4)	0.073(4)
C20	0.0364(19)	0.0368(19)	0.043(2)	0.042(2)	0.053(2)	0.048(2)	0.070(4)	0.074(4)	0.078(4)	0.079(4)	0.070(4)	0.076(4)	0.078(4)	0.080(4)	0.083(5)	0.087(5)	0.087(5)
C21	0.045(2)	0.045(2)	0.055(3)	0.045(2)	0.064(3)	0.051(3)	0.058(3)	0.076(4)	0.066(3)	0.070(4)	0.082(4)	0.086(5)	0.090(5)	0.091(5)	0.093(5)	0.098(6)	0.098(6)
C22	0.044(2)	0.045(2)	0.052(3)	0.047(2)	0.063(3)	0.054(3)	0.054(3)	0.055(3)	0.059(3)	0.059(3)	0.086(5)	0.089(5)	0.094(5)	0.097(6)	0.099(6)	0.106(6)	0.106(6)
C23	0.0355(18)	0.0366(19)	0.042(2)	0.054(3)	0.049(2)	0.062(3)	0.053(3)	0.054(3)	0.058(3)	0.058(3)	0.061(3)	0.063(3)	0.067(4)	0.069(4)	0.071(4)	0.074(4)	0.074(4)
C24	0.0339(18)	0.0351(19)	0.041(2)	0.058(3)	0.047(2)	0.066(3)	0.053(3)	0.057(3)	0.057(3)	0.059(3)	0.059(3)	0.063(3)	0.065(3)	0.067(4)	0.071(4)	0.074(4)	0.074(4)

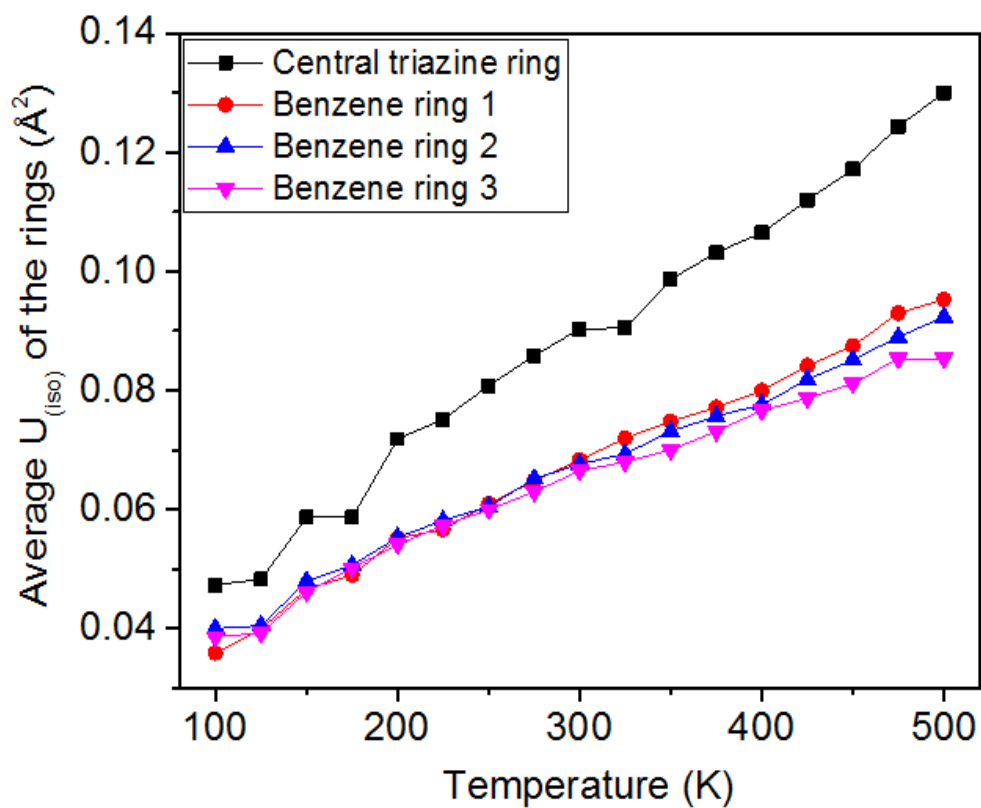


Figure S5-27. Average U_{iso} parameters for the atoms in each of central triazine ring and the adjacent benzene rings as a function of the temperature.

7.4.12 References for the appendix to chapter 5

1. S. L. Mayo, B. D. Olafson and W. A. Goddard, *Journal of Physical chemistry*, 1990, **94**, 8897-8909.
2. P. G. Boyd, S. M. Moosavi, M. Witman and B. Smit, *The journal of physical chemistry letters*, 2017, **8**, 357-363.
3. M. J. Frisch, G. W. Trucks, H. B. Schlegel, G. E. Scuseria, M. A. Robb, J. R. Cheeseman, G. Scalmani, V. Barone, G. A. Petersson, H. Nakatsuji, X. Li, M. Caricato, A. V. Marenich, J. Bloino, B. G. Janesko, R. Gomperts, B. Mennucci, H. P. Hratchian, J. V. Ortiz, A. F. Izmaylov, J. L. Sonnenberg, Williams, F. Ding, F. Lipparini, F. Egidi, J. Goings, B. Peng, A. Petrone, T. Henderson, D. Ranasinghe, V. G. Zakrzewski, J. Gao, N. Rega, G. Zheng, W. Liang, M. Hada, M. Ehara, K. Toyota, R. Fukuda, J. Hasegawa, M. Ishida, T. Nakajima, Y. Honda, O. Kitao, H. Nakai, T. Vreven, K. Throssell, J. A. Montgomery Jr., J. E. Peralta, F. Ogliaro, M. J. Bearpark, J. J. Heyd, E. N. Brothers, K. N. Kudin, V. N. Staroverov, T. A. Keith, R. Kobayashi, J. Normand, K. Raghavachari, A. P. Rendell, J. C. Burant, S. S. Iyengar, J. Tomasi, M. Cossi, J. M. Millam, M. Klene, C. Adamo, R. Cammi, J. W. Ochterski, R. L. Martin, K. Morokuma, O. Farkas, J. B. Foresman and D. J. Fox, *Gaussian 16*, 2016.
4. S. Plimpton, *Journal of computational physics*, 1995, **117**, 1-19.

References

- (1) McConnaughey, T. A.; Burdett, J.; Whelan, J. F.; Paull, C. K. Carbon isotopes in biological carbonates: respiration and photosynthesis. *Geochimica et Cosmochimica Acta* **1997**, *61* (3), 611-622.
- (2) Pierrehumbert, R. T. High levels of atmospheric carbon dioxide necessary for the termination of global glaciation. *Nature* **2004**, *429* (6992), 646-649.
- (3) D. G. Victor, D. Z., E. H. M. Ahmed, P.; K. Dadhich, J. G. J. O., H-H. Rogner, K. Sheikho, M. Yamaguchi *Mitigation of Climate Change. Contribution of Working Group III to the Fifth Assessment Report of the Intergovernmental Panel on Climate Change*; 2014.
- (4) Culp, J. T. Flexible Solid Sorbents for CO₂ Capture and Separation. *Novel Materials for Carbon Dioxide Mitigation Technology* **2015**, 149.
- (5) SCHULTZ, H. Climate change and viticulture: a European perspective on climatology, carbon dioxide and UV - B effects. *Australian Journal of grape and wine research* **2000**, *6* (1), 2-12.
- (6) Sims, R. E.; Schock, R. N.; Adegbululge, A.; Fenhann, J. V.; Konstantinaviciute, I.; Moomaw, W.; Nimir, H. B.; Schlamadinger, B.; Torres-Martínez, J.; Turner, C. Energy supply. In *Climate change 2007: Mitigation. Contribution of Working Group III to the fourth assessment report of the Intergovernmental Panel on Climate Change*; Cambridge University Press: 2007.
- (7) Eggleton, T. *A short introduction to climate change*, Cambridge University Press: 2012.
- (8) Ritter, S. K., Global CO₂ Breaches 400 PPM. AMER CHEMICAL SOC 1155 16TH ST, NW, WASHINGTON, DC 20036 USA: 2015.
- (9) WMO, W. Greenhouse Gas Bulletin No. 8. *World Meteorological Organization, Geneva* **2012**, 1-3.
- (10) *CO₂ emissions from fuel combustion*; IEA Publications: 9, rue de la Federation, 75739 Paris Cedex 15, France, 2015, 2015.
- (11) Metz, B.; Davidson, O.; De Coninck, H.; Loss, M.; Meyer, L. IPCC Special Report on Carbon Dioxide Capture and Storage Cambridge University Press. *Cambridge, United Kingdom, and New York, NY, USA* **2005**.
- (12) Rochelle, G. T. Amine scrubbing for CO₂ capture. *Science* **2009**, *325* (5948), 1652-1654.
- (13) Awais, M. Determination of the mechanism of the reaction between CO₂ and alkanolamines. **2013**.
- (14) Yu, C.-H.; Huang, C.-H.; Tan, C.-S. A review of CO₂ capture by absorption and adsorption. *Aerosol Air Qual. Res* **2012**, *12* (5), 745-769.
- (15) Kohl, A. L.; Nielsen, R. *Gas purification*, Gulf Professional Publishing: 1997.

- (16) Yang, J.; Tan, H.; Low, Q.; Binks, B.; Chin, J. CO₂ capture by dry alkanolamines and an efficient microwave regeneration process. *Journal of Materials Chemistry A* **2015**, 3 (12), 6440-6446.
- (17) Strelzoff, S.; Shen, W. W., Separation of carbon dioxide from ammonia. Google Patents: 1957.
- (18) LAROCHE, C. R.; Dowdle, J. R., Process for the removal of acid gases from gaseous mixtures using an aqueous solution of 2-dimethylamino-2-hydroxymethyl-1, 3-propanediol. Google Patents: 2016.
- (19) Songolzadeh, M.; Soleimani, M.; Takht Ravanchi, M.; Songolzadeh, R. Carbon dioxide separation from flue gases: a technological review emphasizing reduction in greenhouse gas emissions. *The Scientific World Journal* **2014**, 2014.
- (20) Stylianou, K. C.; Queen, W. L. Recent Advances in Carbon Capture with Metal–Organic Frameworks. *CHIMIA International Journal for Chemistry* **2015**, 69 (5), 274-283.
- (21) Liu, Y.; Wang, Z. U.; Zhou, H. C. Recent advances in carbon dioxide capture with metal - organic frameworks. *Greenhouse Gases: Science and Technology* **2012**, 2 (4), 239-259.
- (22) Mohamedali, M.; Nath, D.; Ibrahim, H.; Henni, A. Review of Recent Developments in CO₂ Capture Using Solid Materials: Metal Organic Frameworks (MOFs). **2016**.
- (23) D'Alessandro, D. M.; Smit, B.; Long, J. R. Carbon dioxide capture: prospects for new materials. *Angewandte Chemie International Edition* **2010**, 49 (35), 6058-6082.
- (24) Songolzadeh, M.; Ravanchi, M. T.; Soleimani, M. Carbon dioxide capture and storage: a general review on adsorbents. *World Academy of Science, Engineering and Technology* **2012**, 70, 225-232.
- (25) Kearley, G. J.; Peterson, V. K. *Neutron Applications in Materials for Energy*, Springer: 2015.
- (26) Li, H.; Eddaoudi, M.; Groy, T. L.; Yaghi, O. Establishing microporosity in open metal-organic frameworks: Gas sorption isotherms for Zn (BDC)(BDC= 1, 4-benzenedicarboxylate). *Journal of the American Chemical Society* **1998**, 120 (33), 8571-8572.
- (27) Li, H.; Eddaoudi, M.; O'Keeffe, M.; Yaghi, O. M. Design and synthesis of an exceptionally stable and highly porous metal-organic framework. *Nature* **1999**, 402 (6759), 276-279.
- (28) Janiak, C. Demonstration of permanent porosity in flexible and guest-responsive organic zeolite analogs (now called MOFs). *Chemical Communications* **2013**, 49 (62), 6933-6937.
- (29) Gallagher, A. T.; Kelty, M. L.; Park, J. G.; Anderson, J. S.; Mason, J. A.; Walsh, J. P.; Collins, S. L.; Harris, T. D. Dioxygen binding at a four-coordinate cobaltous porphyrin site in a metal–organic framework: structural, EPR, and O₂ adsorption analysis. *Inorganic Chemistry Frontiers* **2016**, 3 (4), 536-540.
- (30) Farha, O. K.; Eryazici, I.; Jeong, N. C.; Hauser, B. G.; Wilmer, C. E.; Sarjeant, A. A.; Snurr, R. Q.; Nguyen, S. T.; Yazaydin, A. O. z. r.; Hupp, J. T. Metal–organic framework materials with ultrahigh surface areas: is the sky the limit? *Journal of the American Chemical Society* **2012**, 134 (36), 15016-15021.
- (31) Farrusseng, D. *Metal-organic frameworks: applications from catalysis to gas storage*, John Wiley & Sons: 2011.

- (32) Czaja, A. U.; Trukhan, N.; Müller, U. Industrial applications of metal–organic frameworks. *Chemical Society Reviews* **2009**, *38* (5), 1284-1293.
- (33) Lu, W.; Yuan, D.; Zhao, D.; Schilling, C. I.; Plietzsch, O.; Muller, T.; Bräse, S.; Guenther, J.; Blümel, J.; Krishna, R. Porous polymer networks: synthesis, porosity, and applications in gas storage/separation. *Chemistry of Materials* **2010**, *22* (21), 5964-5972.
- (34) Schröder, M. *Functional metal-organic frameworks: Gas storage, separation and catalysis*, Springer: 2010; Vol. 293.
- (35) Mueller, U.; Schubert, M.; Teich, F.; Puetter, H.; Schierle-Arndt, K.; Pastre, J. Metal–organic frameworks—prospective industrial applications. *Journal of Materials Chemistry* **2006**, *16* (7), 626-636.
- (36) Li, J.-R.; Kuppler, R. J.; Zhou, H.-C. Selective gas adsorption and separation in metal–organic frameworks. *Chem. Soc. Rev.* **2009**, *38* (5), 1477-1504.
- (37) Chang, Z.; Zhang, D.-S.; Chen, Q.; Bu, X.-H. Microporous organic polymers for gas storage and separation applications. *Physical Chemistry Chemical Physics* **2013**, *15* (15), 5430-5442.
- (38) Lee, J.; Farha, O. K.; Roberts, J.; Scheidt, K. A.; Nguyen, S. T.; Hupp, J. T. Metal–organic framework materials as catalysts. *Chemical Society Reviews* **2009**, *38* (5), 1450-1459.
- (39) Gascon, J.; Corma, A.; Kapteijn, F.; Llabres i Xamena, F. X. Metal organic framework catalysis: Quo vadis? *ACS Catalysis* **2013**, *4* (2), 361-378.
- (40) Kuppler, R. J.; Timmons, D. J.; Fang, Q.-R.; Li, J.-R.; Makal, T. A.; Young, M. D.; Yuan, D.; Zhao, D.; Zhuang, W.; Zhou, H.-C. Potential applications of metal-organic frameworks. *Coordination Chemistry Reviews* **2009**, *253* (23), 3042-3066.
- (41) Liu, J.; Thallapally, P. K.; McGrail, B. P.; Brown, D. R.; Liu, J. Progress in adsorption-based CO₂ capture by metal–organic frameworks. *Chemical Society Reviews* **2012**, *41* (6), 2308-2322.
- (42) Sumida, K.; Hill, M. R.; Horike, S.; Dailly, A.; Long, J. R. Synthesis and hydrogen storage properties of Be₁₂(OH)₁₂(1, 3, 5-benzenetribenzoate)₄. *Journal of the American Chemical Society* **2009**, *131* (42), 15120-15121.
- (43) Peng, Y.; Krungleviciute, V.; Eryazici, I.; Hupp, J. T.; Farha, O. K.; Yildirim, T. Methane storage in metal–organic frameworks: current records, surprise findings, and challenges. *Journal of the American Chemical Society* **2013**, *135* (32), 11887-11894.
- (44) Furukawa, H.; Ko, N.; Go, Y. B.; Aratani, N.; Choi, S. B.; Choi, E.; Yazaydin, A. Ö.; Snurr, R. Q.; O’Keeffe, M.; Kim, J. Ultrahigh porosity in metal-organic frameworks. *Science* **2010**, *329* (5990), 424-428.
- (45) Tranchemontagne, D. J.; Hunt, J. R.; Yaghi, O. M. Room temperature synthesis of metal-organic frameworks: MOF-5, MOF-74, MOF-177, MOF-199, and IRMOF-0. *Tetrahedron* **2008**, *64* (36), 8553-8557, DOI: <http://dx.doi.org/10.1016/j.tet.2008.06.036>.

- (46) Bae, Y. J.; Cho, E. S.; Qiu, F.; Sun, D. T.; Williams, T. E.; Urban, J. J.; Queen, W. L. Transparent Metal–Organic Framework/Polymer Mixed Matrix Membranes as Water Vapor Barriers. *ACS Applied Materials & Interfaces* **2016**, 8 (16), 10098-10103, DOI: 10.1021/acsami.6b01299.
- (47) Sanchez-Sanchez, M.; Getachew, N.; Diaz, K.; Diaz-Garcia, M.; Chebude, Y.; Diaz, I. Synthesis of metal-organic frameworks in water at room temperature: salts as linker sources. *Green Chemistry* **2015**, 17 (3), 1500-1509, DOI: 10.1039/C4GC01861C.
- (48) Khan, N. A.; Jhung, S. H. Synthesis of metal-organic frameworks (MOFs) with microwave or ultrasound: Rapid reaction, phase-selectivity, and size reduction. *Coordination Chemistry Reviews* **2015**, 285, 11-23, DOI: <http://dx.doi.org/10.1016/j.ccr.2014.10.008>.
- (49) Friscic, T. Supramolecular concepts and new techniques in mechanochemistry: cocrystals, cages, rotaxanes, open metal-organic frameworks. *Chemical Society Reviews* **2012**, 41 (9), 3493-3510, DOI: 10.1039/C2CS15332G.
- (50) Crawford, D.; Casaban, J.; Haydon, R.; Giri, N.; McNally, T.; James, S. L. Synthesis by extrusion: continuous, large-scale preparation of MOFs using little or no solvent. *Chemical Science* **2015**, 6 (3), 1645-1649, DOI: 10.1039/C4SC03217A.
- (51) Rubio-Martinez, M.; Batten, M. P.; Polyzos, A.; Carey, K.-C.; Mardel, J. I.; Lim, K.-S.; Hill, M. R. Versatile, High Quality and Scalable Continuous Flow Production of Metal-Organic Frameworks. *Scientific Reports* **2014**, 4, 5443, DOI: 10.1038/srep05443
<http://www.nature.com/articles/srep05443#supplementary-information>.
- (52) Bayliss, P. A.; Ibarra, I. A.; Perez, E.; Yang, S.; Tang, C. C.; Poliakoff, M.; Schroder, M. Synthesis of metal-organic frameworks by continuous flow. *Green Chemistry* **2014**, 16 (8), 3796-3802, DOI: 10.1039/C4GC00313F.
- (53) Carné-Sánchez, A.; Imaz, I.; Cano-Sarabia, M.; Maspoch, D. A spray-drying strategy for synthesis of nanoscale metal–organic frameworks and their assembly into hollow superstructures. *Nat Chem* **2013**, 5 (3), 203-211, DOI: <http://www.nature.com/nchem/journal/v5/n3/abs/nchem.1569.html#supplementary-information>.
- (54) Jasuja, H. *Developing Design Criteria and Scale Up Methods for Water-Stable Metal-Organic Frameworks for Adsorption Applications*; DTIC Document: 2014.
- (55) Peplow, M. The hole story. *Nature* **2015**, 520 (7546), 148-150.
- (56) Peplow, M. Materials science: The hole story. *Nature, News Feature* **2015**, 520 (7546), 148-150, DOI: 10.1038/520148a.
- (57) Furukawa, H. *BASF Develops Method for Industrial-Scale MOF Synthesis; Trials Underway in Natural Gas Vehicle Tanks*; Green Car Congress: 2010.
- (58) Dhakshinamoorthy, A.; Alvaro, M.; Garcia, H. Commercial metal–organic frameworks as heterogeneous catalysts. *Chemical Communications* **2012**, 48 (92), 11275-11288.

- (59) Parkes, M. V.; Staiger, C. L.; Perry IV, J. J.; Allendorf, M. D.; Greathouse, J. A. Screening metal–organic frameworks for selective noble gas adsorption in air: effect of pore size and framework topology. *Physical Chemistry Chemical Physics* **2013**, *15* (23), 9093-9106.
- (60) Deniz, E.; Karadas, F.; Patel, H. A.; Aparicio, S.; Yavuz, C. T.; Atilhan, M. A combined computational and experimental study of high pressure and supercritical CO₂ adsorption on Basolite MOFs. *Microporous and Mesoporous Materials* **2013**, *175*, 34-42.
- (61) Yilmaz, B.; Trukhan, N.; MÜLLER, U. Industrial outlook on zeolites and metal organic frameworks. *Chinese Journal of Catalysis* **2012**, *33* (1), 3-10.
- (62) Mason, J. A.; Sumida, K.; Herm, Z. R.; Krishna, R.; Long, J. R. Evaluating metal–organic frameworks for post-combustion carbon dioxide capture via temperature swing adsorption. *Energy & Environmental Science* **2011**, *4* (8), 3030-3040.
- (63) Queen, W. L.; Hudson, M. R.; Bloch, E. D.; Mason, J. A.; Gonzalez, M. I.; Lee, J. S.; Gygi, D.; Howe, J. D.; Lee, K.; Darwish, T. A. Comprehensive study of carbon dioxide adsorption in the metal-organic frameworks M₂(dobdc) (M = Mg, Mn, Fe, Co, Ni, Cu, Zn). *Chemical Science* **2014**, *5* (12), 4569-4581.
- (64) Queen, W. L.; Bloch, E. D.; Brown, C. M.; Hudson, M. R.; Mason, J. A.; Murray, L. J.; Ramirez-Cuesta, A. J.; Peterson, V. K.; Long, J. R. Hydrogen adsorption in the metal–organic frameworks Fe₂(dobdc) and Fe₂(O₂)(dobdc). *Dalton Transactions* **2012**, *41* (14), 4180-4187.
- (65) Singh, S. How long will fossil fuels last?
- (66) Clemente, J. How Much Oil Does the World Have Left? <http://www.forbes.com/sites/judeclemente/2015/06/25/how-much-oil-does-the-world-have-left/#13416d395dc5>.
- (67) Reporter, S., World Energy Day 2014: How Much Oil is Left and How Long Will it Last? *International Business Times* October 22, 2014 10:14 BST, 2014.
- (68) Rao, A. B.; Rubin, E. S. A technical, economic, and environmental assessment of amine-based CO₂ capture technology for power plant greenhouse gas control. *Environmental science & technology* **2002**, *36* (20), 4467-4475.
- (69) Lu, W.; Verdegaal, W. M.; Yu, J.; Balbuena, P. B.; Jeong, H.-K.; Zhou, H.-C. Building multiple adsorption sites in porous polymer networks for carbon capture applications. *Energy & Environmental Science* **2013**, *6* (12), 3559-3564.
- (70) Leung, D. Y.; Caramanna, G.; Maroto-Valer, M. M. An overview of current status of carbon dioxide capture and storage technologies. *Renewable and Sustainable Energy Reviews* **2014**, *39*, 426-443.
- (71) Yang, H.; Li, J.-R. Metal-Organic Frameworks (MOFs) for CO₂ Capture. In *Porous Materials for Carbon Dioxide Capture*; Springer: 2014; pp 79-113.
- (72) Bloch, E. D.; Murray, L. J.; Queen, W. L.; Chavan, S.; Maximoff, S. N.; Bigi, J. P.; Krishna, R.; Peterson, V. K.; Grandjean, F.; Long, G. J. Selective binding of O₂ over N₂ in a redox–active metal–organic

- framework with open iron (II) coordination sites. *Journal of the American Chemical Society* **2011**, *133* (37), 14814-14822.
- (73) Lee, J. S.; Vlaisavljevich, B.; Britt, D. K.; Brown, C. M.; Haranczyk, M.; Neaton, J. B.; Smit, B.; Long, J. R.; Queen, W. L. Understanding Small - Molecule Interactions in Metal-Organic Frameworks: Coupling Experiment with Theory. *Adv. Mater.* **2015**, *27* (38), 5785-5796.
- (74) Millward, A. R.; Yaghi, O. M. Metal-organic frameworks with exceptionally high capacity for storage of carbon dioxide at room temperature. *Journal of the American Chemical Society* **2005**, *127* (51), 17998-17999.
- (75) Myers, A.; Prausnitz, J. M. Thermodynamics of mixed - gas adsorption. *AIChE Journal* **1965**, *11* (1), 121-127.
- (76) Mason, J. A.; McDonald, T. M.; Bae, T.-H.; Bachman, J. E.; Sumida, K.; Dutton, J. J.; Kaye, S. S.; Long, J. R. Application of a High-Throughput Analyzer in Evaluating Solid Adsorbents for Post-Combustion Carbon Capture via Multicomponent Adsorption of CO₂, N₂, and H₂O. *Journal of the American Chemical Society* **2015**, *137* (14), 4787-4803, DOI: 10.1021/jacs.5b00838.
- (77) Herm, Z. R.; Swisher, J. A.; Smit, B.; Krishna, R.; Long, J. R. Metal-organic frameworks as adsorbents for hydrogen purification and precombustion carbon dioxide capture. *Journal of the American Chemical Society* **2011**, *133* (15), 5664-5667.
- (78) Krishna, R.; van Baten, J. M. In silico screening of metal-organic frameworks in separation applications. *Physical Chemistry Chemical Physics* **2011**, *13* (22), 10593-10616.
- (79) Krishna, R.; van Baten, J. M. Investigating the potential of MgMOF-74 membranes for CO₂ capture. *Journal of membrane science* **2011**, *377* (1), 249-260.
- (80) Krishna, R.; van Baten, J. M. Maxwell-Stefan modeling of slowing-down effects in mixed gas permeation across porous membranes. *Journal of membrane science* **2011**, *383* (1), 289-300.
- (81) Cessford, N. F.; Seaton, N. A.; Düren, T. Evaluation of ideal adsorbed solution theory as a tool for the design of Metal-Organic Framework materials. *Industrial & Engineering Chemistry Research* **2012**, *51* (13), 4911-4921.
- (82) Ruthven, D. M. Fundamentals of adsorption equilibrium and kinetics in microporous solids. In *Adsorption and Diffusion*; Springer: 2006; pp 1-43.
- (83) Carrington, K. R.; Barcelo, S.; Karkamkar, A.; Purewal, J.; Ma, S.; Zhou, H.-C.; Dantzer, P.; Ott, K.; Burrell, T.; Semeslberger, T., Recommended Best Practices for the Characterization of Storage Properties of Hydrogen Storage Materials. US Department of Energy-Office of Energy Efficiency & Renewable Energy: 2012.
- (84) Farrusseng, D.; Daniel, C.; Gaudillère, C.; Ravon, U.; Schuurman, Y.; Mirodatos, C.; Dubbeldam, D.; Frost, H.; Snurr, R. Q. Heats of Adsorption for Seven Gases in Three Metal-Organic Frameworks: Systematic Comparison of Experiment and Simulation. *Langmuir* **2009**, *25* (13), 7383-7388, DOI: 10.1021/la900283t.

- (85) Wang, Q. M.; Shen, D.; Bülow, M.; Lau, M. L.; Deng, S.; Fitch, F. R.; Lemcoff, N. O.; Semanscin, J. Metallo-organic molecular sieve for gas separation and purification. *Microporous and Mesoporous Materials* **2002**, *55* (2), 217-230.
- (86) Britt, D.; Furukawa, H.; Wang, B.; Glover, T. G.; Yaghi, O. M. Highly efficient separation of carbon dioxide by a metal-organic framework replete with open metal sites. *Proceedings of the National Academy of Sciences* **2009**, *106* (49), 20637-20640.
- (87) Caskey, S. R.; Wong-Foy, A. G.; Matzger, A. J. Dramatic tuning of carbon dioxide uptake via metal substitution in a coordination polymer with cylindrical pores. *Journal of the American Chemical Society* **2008**, *130* (33), 10870-10871.
- (88) Hamon, L.; Llewellyn, P. L.; Devic, T.; Ghoufi, A.; Clet, G.; Guillerm, V.; Pirngruber, G. D.; Maurin, G.; Serre, C.; Driver, G.; Beek, W. v.; Jolimaître, E.; Vimont, A.; Daturi, M.; Férey, G. Co-adsorption and Separation of CO₂-CH₄ Mixtures in the Highly Flexible MIL-53(Cr) MOF. *Journal of the American Chemical Society* **2009**, *131* (47), 17490-17499, DOI: 10.1021/ja907556q.
- (89) Férey, G.; Latroche, M.; Serre, C.; Millange, F.; Loiseau, T.; Percheron-Guegan, A. Hydrogen adsorption in the nanoporous metal-benzenedicarboxylate M(OH)(O₂C-C₆H₄-CO₂) (M = Al³⁺, Cr³⁺), MIL-53. *Chemical Communications* **2003**, (24), 2976-2977, DOI: 10.1039/B308903G.
- (90) Mollmer, J.; Lange, M.; Moller, A.; Patzschke, C.; Stein, K.; Lassig, D.; Lincke, J.; Glaser, R.; Krautscheid, H.; Staudt, R. Pure and mixed gas adsorption of CH₄ and N₂ on the metal-organic framework Basolite[registered sign] A100 and a novel copper-based 1,2,4-triazolyl isophthalate MOF. *Journal of Materials Chemistry* **2012**, *22* (20), 10274-10286, DOI: 10.1039/C2JM15734A.
- (91) Xu, J.; Zha, X.; Wu, Y.; Ke, Q.; Yu, W. Fast and highly efficient SO₂ capture by TMG immobilized on hierarchical micro-meso-macroporous AlPO-5/cordierite honeycomb ceramic materials. *Chemical Communications* **2016**, *52* (38), 6367-6370.
- (92) Plaza, M. G.; Durán, I.; Querejeta, N.; Rubiera, F.; Pevida, C. Experimental and Simulation Study of Adsorption in Postcombustion Conditions Using a Microporous Biochar. 1. CO₂ and N₂ Adsorption. *Industrial & Engineering Chemistry Research* **2016**, *55* (11), 3097-3112.
- (93) Dietzel, P. D.; Besikiotis, V.; Blom, R. Application of metal-organic frameworks with coordinatively unsaturated metal sites in storage and separation of methane and carbon dioxide. *Journal of Materials Chemistry* **2009**, *19* (39), 7362-7370.
- (94) Kizzie, A. C.; Wong-Foy, A. G.; Matzger, A. J. Effect of humidity on the performance of microporous coordination polymers as adsorbents for CO₂ capture. *Langmuir* **2011**, *27* (10), 6368-6373.
- (95) Bhatt, P. M.; Belmabkhout, Y.; Cadiau, A.; Adil, K.; Shekhah, O.; Shkurenko, A.; Barbour, L. J.; Eddaoudi, M. A Fine-Tuned Fluorinated MOF Addresses the Needs for Trace CO₂ Removal and Air Capture Using Physisorption. *Journal of the American Chemical Society* **2016**, *138* (29), 9301-9307, DOI: 10.1021/jacs.6b05345.

- (96) Fracaroli, A. M.; Furukawa, H.; Suzuki, M.; Dodd, M.; Okajima, S.; Gándara, F.; Reimer, J. A.; Yaghi, O. M. Metal–Organic Frameworks with Precisely Designed Interior for Carbon Dioxide Capture in the Presence of Water. *Journal of the American Chemical Society* **2014**, *136* (25), 8863-8866, DOI: 10.1021/ja503296c.
- (97) Coelho, J. A.; Ribeiro, A. M.; Ferreira, A. F.; Lucena, S. M.; Rodrigues, A. E.; Azevedo, D. C. d. Stability of an Al-Fumarate MOF and Its Potential for CO₂ Capture from Wet Stream. *Industrial & Engineering Chemistry Research* **2016**, *55* (7), 2134-2143.
- (98) Nakagawa, K.; Tanaka, D.; Horike, S.; Shimomura, S.; Higuchi, M.; Kitagawa, S. Enhanced selectivity of CO₂ from a ternary gas mixture in an interdigitated porous framework. *Chemical Communications* **2010**, *46* (24), 4258-4260, DOI: 10.1039/C0CC00027B.
- (99) Mason, J.; Sumida, K.; Herm, Z.; Krishna, R.; Long, J. Energy Environ. Sci., 2011, 4, 3030 RSC;(b) JJ Perry, JA Perman and MJ Zaworotko. *Chem. Soc. Rev* **2009**, *38*, 1400.
- (100) Dietzel, P. D.; Morita, Y.; Blom, R.; Fjellvåg, H. An In Situ High - Temperature Single - Crystal Investigation of a Dehydrated Metal -Organic Framework Compound and Field - Induced Magnetization of One - Dimensional Metal -Oxygen Chains. *Angewandte Chemie* **2005**, *117* (39), 6512-6516.
- (101) Dietzel, P. D. C.; Johnsen, R. E.; Fjellvag, H.; Bordiga, S.; Groppo, E.; Chavan, S.; Blom, R. Adsorption properties and structure of CO₂ adsorbed on open coordination sites of metal-organic framework Ni₂(dhtp) from gas adsorption, IR spectroscopy and X-ray diffraction. *Chemical Communications* **2008**, (41), 5125-5127, DOI: 10.1039/B810574J.
- (102) Llewellyn, P. L.; Bourrelly, S.; Serre, C.; Vimont, A.; Daturi, M.; Hamon, L.; De Weireld, G.; Chang, J.-S.; Hong, D.-Y.; Kyu Hwang, Y. High Uptakes of CO₂ and CH₄ in Mesoporous Metal • Organic Frameworks MIL-100 and MIL-101. *Langmuir* **2008**, *24* (14), 7245-7250.
- (103) Valenzano, L.; Vitillo, J.; Chavan, S.; Civalieri, B.; Bonino, F.; Bordiga, S.; Lamberti, C. Structure–activity relationships of simple molecules adsorbed on CPO-27-Ni metal–organic framework: In situ experiments vs. theory. *Catalysis today* **2012**, *182* (1), 67-79.
- (104) Kontos, A. G.; Likodimos, V.; Veziri, C. M.; Kouvelos, E.; Moustakas, N.; Karanikolos, G. N.; Romanos, G. E.; Falaras, P. CO₂ Captured in Zeolitic Imidazolate Frameworks: Raman Spectroscopic Analysis of Uptake and Host–Guest Interactions. *ChemSusChem* **2014**, *7* (6), 1696-1702.
- (105) McDonald, T. M.; Mason, J. A.; Kong, X.; Bloch, E. D.; Gygi, D.; Dani, A.; Crocellà, V.; Giordanino, F.; Odoh, S. O.; Drisdell, W. S. Cooperative insertion of CO₂ in diamine-appended metal-organic frameworks. *Nature* **2015**, *519* (7543), 303-308.
- (106) Kong, X.; Scott, E.; Ding, W.; Mason, J. A.; Long, J. R.; Reimer, J. A. CO₂ dynamics in a metal–organic framework with open metal sites. *Journal of the American Chemical Society* **2012**, *134* (35), 14341-14344.
- (107) Lin, L. C.; Kim, J.; Kong, X.; Scott, E.; McDonald, T. M.; Long, J. R.; Reimer, J. A.; Smit, B. Understanding CO₂ dynamics in metal–organic frameworks with open metal sites. *Angewandte Chemie International Edition* **2013**, *52* (16), 4410-4413.

- (108) Drisdell, W. S.; Poloni, R.; McDonald, T. M.; Long, J. R.; Smit, B.; Neaton, J. B.; Prendergast, D.; Kortright, J. B. Probing adsorption interactions in metal–organic frameworks using X-ray spectroscopy. *Journal of the American Chemical Society* **2013**, *135* (48), 18183-18190.
- (109) Dietzel, P. D.; Georgiev, P. A.; Eckert, J.; Blom, R.; Strässle, T.; Unruh, T. Interaction of hydrogen with accessible metal sites in the metal–organic frameworks M₂(dhtp)(CPO-27-M; M= Ni, Co, Mg). *Chemical Communications* **2010**, *46* (27), 4962-4964.
- (110) Yan, Y.; Telepeni, I.; Yang, S.; Lin, X.; Kockelmann, W.; Dailly, A.; Blake, A. J.; Lewis, W.; Walker, G. S.; Allan, D. R. Metal–organic polyhedral frameworks: high H₂ adsorption capacities and neutron powder diffraction studies. *Journal of the American Chemical Society* **2010**, *132* (12), 4092-4094.
- (111) Yazaydin, A. O.; Benin, A. I.; Faheem, S. A.; Jakubczak, P.; Low, J. J.; Willis, R. R.; Snurr, R. Q. Enhanced CO₂ adsorption in metal–organic frameworks via occupation of open-metal sites by coordinated water molecules. *Chemistry of Materials* **2009**, *21* (8), 1425-1430.
- (112) Sumida, K.; Brown, C. M.; Herm, Z. R.; Chavan, S.; Bordiga, S.; Long, J. R. Hydrogen storage properties and neutron scattering studies of Mg₂(dobdc)—a metal–organic framework with open Mg²⁺ adsorption sites. *Chemical Communications* **2011**, *47* (4), 1157-1159.
- (113) Salles, F.; Kolokolov, D. I.; Jovic, H.; Maurin, G.; Llewellyn, P. L.; Devic, T.; Serre, C.; Ferey, G. Adsorption and diffusion of H₂ in the MOF type systems MIL-47 (V) and MIL-53 (Cr): A combination of microcalorimetry and QENS experiments with molecular simulations. *The Journal of Physical Chemistry C* **2009**, *113* (18), 7802-7812.
- (114) Chapman, K. W.; Halder, G. J.; Chupas, P. J. Guest-Dependent High Pressure Phenomena in a Nanoporous Metal–Organic Framework Material. *Journal of the American Chemical Society* **2008**, *130* (32), 10524-10526.
- (115) Chapman, K. W.; Halder, G. J.; Chupas, P. J. Guest-Dependent High Pressure Phenomena in a Nanoporous Metal–Organic Framework Material. *Journal of the American Chemical Society* **2008**, *130* (32), 10524-10526, DOI: 10.1021/ja804079z.
- (116) Xiao, D. J.; Bloch, E. D.; Mason, J. A.; Queen, W. L.; Hudson, M. R.; Planas, N.; Borycz, J.; Dzubak, A. L.; Verma, P.; Lee, K. Oxidation of ethane to ethanol by N₂O in a metal–organic framework with coordinatively unsaturated iron (II) sites. *Nature chemistry* **2014**, *6* (7), 590-595.
- (117) Bloch, E. D.; Hudson, M. R.; Mason, J. A.; Chavan, S.; Crocellà, V.; Howe, J. D.; Lee, K.; Dzubak, A. L.; Queen, W. L.; Zadrozny, J. M.; Geier, S. J.; Lin, L.-C.; Gagliardi, L.; Smit, B.; Neaton, J. B.; Bordiga, S.; Brown, C. M.; Long, J. R. Reversible CO Binding Enables Tunable CO/H₂ and CO/N₂ Separations in Metal–Organic Frameworks with Exposed Divalent Metal Cations. *Journal of the American Chemical Society* **2014**, *136* (30), 10752-10761, DOI: 10.1021/ja505318p.
- (118) Wu, H.; Simmons, J. M.; Srinivas, G.; Zhou, W.; Yildirim, T. Adsorption Sites and Binding Nature of CO₂ in Prototypical Metal–Organic Frameworks: A Combined Neutron Diffraction and First-Principles Study. *The Journal of Physical Chemistry Letters* **2010**, *1* (13), 1946-1951, DOI: 10.1021/jz100558r.

- (119) Serre, C.; Bourrelly, S.; Vimont, A.; Ramsahye, N. A.; Maurin, G.; Llewellyn, P. L.; Daturi, M.; Filinchuk, Y.; Leynaud, O.; Barnes, P. An explanation for the very large breathing effect of a metal–organic framework during CO₂ adsorption. *Advanced materials* **2007**, *19* (17), 2246-2251.
- (120) Furukawa, H.; Gándara, F.; Zhang, Y.-B.; Jiang, J.; Queen, W. L.; Hudson, M. R.; Yaghi, O. M. Water Adsorption in Porous Metal–Organic Frameworks and Related Materials. *Journal of the American Chemical Society* **2014**, *136* (11), 4369-4381, DOI: 10.1021/ja500330a.
- (121) Bloch, E. D.; Queen, W. L.; Hudson, M. R.; Mason, J. A.; Xiao, D. J.; Murray, L. J.; Flacau, R.; Brown, C. M.; Long, J. R. Hydrogen Storage and Selective, Reversible O₂ Adsorption in a Metal–Organic Framework with Open Chromium(II) Sites. *Angewandte Chemie International Edition* **2016**, *55* (30), 8605-8609, DOI: 10.1002/anie.201602950.
- (122) Kitaura, R.; Kitagawa, S.; Kubota, Y.; Kobayashi, T. C.; Kindo, K.; Mita, Y.; Matsuo, A.; Kobayashi, M.; Chang, H.-C.; Ozawa, T. C. Formation of a one-dimensional array of oxygen in a microporous metal-organic solid. *Science* **2002**, *298* (5602), 2358-2361.
- (123) Bloch, E. D.; Queen, W. L.; Chavan, S.; Wheatley, P. S.; Zadrozny, J. M.; Morris, R.; Brown, C. M.; Lamberti, C.; Bordiga, S.; Long, J. R. Gradual Release of Strongly Bound Nitric Oxide from Fe₂(NO)₂(dobdc). *Journal of the American Chemical Society* **2015**, *137* (10), 3466-3469, DOI: 10.1021/ja5132243.
- (124) Gygi, D.; Bloch, E. D.; Mason, J. A.; Hudson, M. R.; Gonzalez, M. I.; Siegelman, R. L.; Darwish, T. A.; Queen, W. L.; Brown, C. M.; Long, J. R. Hydrogen Storage in the Expanded Pore Metal–Organic Frameworks M₂(dobpdc) (M = Mg, Mn, Fe, Co, Ni, Zn). *Chemistry of Materials* **2016**, *28* (4), 1128-1138, DOI: 10.1021/acs.chemmater.5b04538.
- (125) Queen, W. L.; Bloch, E. D.; Brown, C. M.; Hudson, M. R.; Mason, J. A.; Murray, L. J.; Ramirez-Cuesta, A. J.; Peterson, V. K.; Long, J. R. Hydrogen adsorption in the metal-organic frameworks Fe₂(dobdc) and Fe₂(O₂)(dobdc). *Dalton Transactions* **2012**, *41* (14), 4180-4187, DOI: 10.1039/C2DT12138G.
- (126) Bourrelly, S.; Llewellyn, P. L.; Serre, C.; Millange, F.; Loiseau, T.; Férey, G. Different Adsorption Behaviors of Methane and Carbon Dioxide in the Isotypic Nanoporous Metal Terephthalates MIL-53 and MIL-47. *Journal of the American Chemical Society* **2005**, *127* (39), 13519-13521, DOI: 10.1021/ja054668v.
- (127) Loiseau, T.; Serre, C.; Huguenard, C.; Fink, G.; Taulelle, F.; Henry, M.; Bataille, T.; Férey, G. A Rationale for the Large Breathing of the Porous Aluminum Terephthalate (MIL - 53) Upon Hydration. *Chemistry -A European Journal* **2004**, *10* (6), 1373-1382.
- (128) Llewellyn, P. L.; Bourrelly, S.; Serre, C.; Filinchuk, Y.; Férey, G. How hydration drastically improves adsorption selectivity for CO₂ over CH₄ in the flexible chromium terephthalate MIL - 53. *Angewandte Chemie* **2006**, *118* (46), 7915-7918.
- (129) Plonka, A. M.; Banerjee, D.; Woerner, W. R.; Zhang, Z.; Nijem, N.; Chabal, Y. J.; Li, J.; Parise, J. B. Mechanism of Carbon Dioxide Adsorption in a Highly Selective Coordination Network Supported by Direct Structural Evidence. *Angewandte Chemie International Edition* **2013**, *52* (6), 1692-1695, DOI: 10.1002/anie.201207808.

- (130) Kwon, H. T.; Jeong, H.-K. In situ synthesis of thin zeolitic–imidazolate framework ZIF-8 membranes exhibiting exceptionally high propylene/propane separation. *Journal of the American Chemical Society* **2013**, *135* (29), 10763-10768.
- (131) Nijem, N.; Veyan, J.-F.; Kong, L.; Wu, H.; Zhao, Y.; Li, J.; Langreth, D. C.; Chabal, Y. J. Molecular hydrogen “pairing” interaction in a metal organic framework system with unsaturated metal centers (MOF-74). *Journal of the American Chemical Society* **2010**, *132* (42), 14834-14848.
- (132) Yao, Y.; Nijem, N.; Li, J.; Chabal, Y. J.; Langreth, D. C.; Thonhauser, T. Analyzing the frequency shift of physisorbed CO₂ in metal organic framework materials. *Physical Review B* **2012**, *85* (6), 064302.
- (133) Schloss, J. M. Infrared Spectroscopy of Trapped Gases in Metal-Organic Frameworks. Oberlin College Honors Theses, 2011.
- (134) Valenzano, L.; Civalieri, B.; Chavan, S.; Palomino, G. T.; Areán, C. O.; Bordiga, S. Computational and Experimental Studies on the Adsorption of CO, N₂, and CO₂ on Mg-MOF-74. *The Journal of Physical Chemistry C* **2010**, *114* (25), 11185-11191, DOI: 10.1021/jp102574f.
- (135) Zhang, Z.; Li, Z.; Li, J. Computational study of adsorption and separation of CO₂, CH₄, and N₂ by an rht-type metal–organic framework. *Langmuir* **2012**, *28* (33), 12122-12133.
- (136) Li, B.; Zhang, Z.; Li, Y.; Yao, K.; Zhu, Y.; Deng, Z.; Yang, F.; Zhou, X.; Li, G.; Wu, H. Enhanced binding affinity, remarkable selectivity, and high capacity of CO₂ by dual functionalization of a rht - type metal-organic framework. *Angewandte Chemie International Edition* **2012**, *51* (6), 1412-1415.
- (137) Li, B.; Zhang, Z.; Li, Y.; Yao, K.; Zhu, Y.; Deng, Z.; Yang, F.; Zhou, X.; Li, G.; Wu, H.; Nijem, N.; Chabal, Y. J.; Lai, Z.; Han, Y.; Shi, Z.; Feng, S.; Li, J. Enhanced Binding Affinity, Remarkable Selectivity, and High Capacity of CO₂ by Dual Functionalization of a rht-Type Metal–Organic Framework. *Angewandte Chemie International Edition* **2012**, *51* (6), 1412-1415, DOI: 10.1002/anie.201105966.
- (138) Chen, Y.; Wang, H.; Li, J.; Lockard, J. V. In situ spectroscopy studies of CO₂ adsorption in a dually functionalized microporous metal-organic framework. *Journal of Materials Chemistry A* **2015**, *3* (9), 4945-4953, DOI: 10.1039/C4TA05524A.
- (139) Demessence, A.; D'Alessandro, D. M.; Foo, M. L.; Long, J. R. Strong CO₂ binding in a water-stable, triazolate-bridged metal– organic framework functionalized with ethylenediamine. *J. Am. Chem. Soc.* **2009**, *131* (25), 8784-8786.
- (140) McDonald, T. M.; D'Alessandro, D. M.; Krishna, R.; Long, J. R. Enhanced carbon dioxide capture upon incorporation of N,N[prime or minute]-dimethylethylenediamine in the metal-organic framework CuBTTri. *Chemical Science* **2011**, *2* (10), 2022-2028, DOI: 10.1039/C1SC00354B.
- (141) Huck, J. M.; Lin, L.-C.; Berger, A. H.; Shahrak, M. N.; Martin, R. L.; Bhowan, A. S.; Haranczyk, M.; Reuter, K.; Smit, B. Evaluating different classes of porous materials for carbon capture. *Energy & Environmental Science* **2014**, *7* (12), 4132-4146.

- (142) Greenaway, A.; Gonzalez-Santiago, B.; Donaldson, P. M.; Frogley, M. D.; Cinque, G.; Sotelo, J.; Moggach, S.; Shiko, E.; Brandani, S.; Howe, R. F.; Wright, P. A. In situ Synchrotron IR Microspectroscopy of CO₂ Adsorption on Single Crystals of the Functionalized MOF Sc₂(BDC-NH₂)₃. *Angewandte Chemie International Edition* **2014**, *53* (49), 13483-13487, DOI: 10.1002/anie.201408369.
- (143) Yang, S.; Sun, J.; Ramirez-Cuesta, A. J.; Callear, S. K.; David, W. I.; Anderson, D. P.; Newby, R.; Blake, A. J.; Parker, J. E.; Tang, C. C. Selectivity and direct visualization of carbon dioxide and sulfur dioxide in a decorated porous host. *Nature Chemistry* **2012**, *4* (11), 887.
- (144) Stallmach, F.; Gröger, S.; Künzel, V.; Kärger, J.; Yaghi, O.; Hesse, M.; Müller, U. NMR Studies on the Diffusion of Hydrocarbons on the Metal - Organic Framework Material MOF - 5. *Angewandte Chemie International Edition* **2006**, *45* (13), 2123-2126.
- (145) Gassensmith, J. J.; Furukawa, H.; Smaldone, R. A.; Forgan, R. S.; Botros, Y. Y.; Yaghi, O. M.; Stoddart, J. F. Strong and reversible binding of carbon dioxide in a green metal-organic framework. *Journal of the American Chemical Society* **2011**, *133* (39), 15312-15315.
- (146) Lopez, M. G.; Canepa, P.; Thonhauser, T. NMR study of small molecule adsorption in MOF-74-Mg. *The Journal of Chemical Physics* **2013**, *138* (15), 154704, DOI: <http://dx.doi.org/10.1063/1.4800952>.
- (147) Lucier, B. E. G.; Zhang, Y.; Lee, K. J.; Lu, Y.; Huang, Y. Grasping hydrogen adsorption and dynamics in metal-organic frameworks using ²H solid-state NMR. *Chemical Communications* **2016**, *52* (48), 7541-7544, DOI: 10.1039/C6CC03205B.
- (148) Horike, S.; Matsuda, R.; Kitaura, R.; Kitagawa, S.; Iijima, T.; Endo, K.; Kubota, Y.; Takata, M. Motion of methanol adsorbed in porous coordination polymer with paramagnetic metal ions. *Chemical Communications* **2004**, (19), 2152-2153, DOI: 10.1039/B406883A.
- (149) Sutrisno, A.; Terskikh, V. V.; Shi, Q.; Song, Z.; Dong, J.; Ding, S. Y.; Wang, W.; Provost, B. R.; Daff, T. D.; Woo, T. K.; Huang, Y. Characterization of Zn-Containing Metal-Organic Frameworks by Solid-State ⁶⁷Zn NMR Spectroscopy and Computational Modeling. *Chemistry – A European Journal* **2012**, *18* (39), 12251-12259, DOI: 10.1002/chem.201201563.
- (150) Peterson, G. W.; Wagner, G. W.; Balboa, A.; Mahle, J.; Sewell, T.; Karwacki, C. J. Ammonia Vapor Removal by Cu₃(BTC)₂ and Its Characterization by MAS NMR. *The journal of physical chemistry. C, Nanomaterials and interfaces* **2009**, *113* (31), 13906-13917, DOI: 10.1021/jp902736z.
- (151) Stallmach, F.; Gröger, S.; Künzel, V.; Kärger, J.; Yaghi, O. M.; Hesse, M.; Müller, U. NMR Studies on the Diffusion of Hydrocarbons on the Metal-Organic Framework Material MOF-5. *Angewandte Chemie International Edition* **2006**, *45* (13), 2123-2126, DOI: 10.1002/anie.200502553.
- (152) Wehring, M.; Gascon, J.; Dubbeldam, D.; Kapteijn, F.; Snurr, R. Q.; Stallmach, F. Self-Diffusion Studies in CuBTC by PFG NMR and MD Simulations. *The Journal of Physical Chemistry C* **2010**, *114* (23), 10527-10534, DOI: 10.1021/jp102212w.
- (153) Hoffmann, H. C.; Debowski, M.; Müller, P.; Paasch, S.; Senkovska, I.; Kaskel, S.; Brunner, E. Solid-State NMR Spectroscopy of Metal-Organic Framework Compounds (MOFs). *Materials* **2012**, *5* (12), 2537-2572.

- (154) Klein, N.; Herzog, C.; Sabo, M.; Senkovska, I.; Getzschmann, J.; Paasch, S.; Lohe, M. R.; Brunner, E.; Kaskel, S. Monitoring adsorption-induced switching by ^{129}Xe NMR spectroscopy in a new metal-organic framework $\text{Ni}_2(2,6\text{-ndc})_2(\text{dabco})$. *Physical Chemistry Chemical Physics* **2010**, *12* (37), 11778-11784, DOI: 10.1039/C003835K.
- (155) Hoffmann, H.; Debowski, M.; Müller, P.; Paasch, S.; Senkovska, I.; Kaskel, S.; Brunner, E. Solid-State NMR Spectroscopy of Metal–Organic Framework Compounds (MOFs). *Materials* **2012**, *5* (12), 2537-2572.
- (156) Rosenbach, N.; Jobic, H.; Ghoufi, A.; Salles, F.; Maurin, G.; Bourrelly, S.; Llewellyn, P. L.; Devic, T.; Serre, C.; Férey, G. Quasi - Elastic Neutron Scattering and Molecular Dynamics Study of Methane Diffusion in Metal Organic Frameworks MIL - 47 (V) and MIL - 53 (Cr). *Angewandte Chemie International Edition* **2008**, *47* (35), 6611-6615.
- (157) Salles, F.; Jobic, H.; Maurin, G.; Koza, M.; Llewellyn, P.; Devic, T.; Serre, C.; Férey, G. Experimental evidence supported by simulations of a very high H_2 diffusion in metal organic framework materials. *Physical review letters* **2008**, *100* (24), 245901.
- (158) Salles, F.; Jobic, H.; Devic, T.; Llewellyn, P. L.; Serre, C.; Férey, G.; Maurin, G. Self and Transport Diffusivity of CO_2 in the Metal–Organic Framework MIL-47(V) Explored by Quasi-elastic Neutron Scattering Experiments and Molecular Dynamics Simulations. *ACS Nano* **2010**, *4* (1), 143-152, DOI: 10.1021/nn901132k.
- (159) Vieira Soares, C.; Damasceno Borges, D.; Wiersum, A.; Martineau, C.; Nouar, F.; Llewellyn, P. L.; Ramsahye, N. A.; Serre, C.; Maurin, G.; Leitão, A. A. Adsorption of Small Molecules in the Porous Zirconium-Based Metal Organic Framework MIL-140A (Zr): A Joint Computational-Experimental Approach. *The Journal of Physical Chemistry C* **2016**, *120* (13), 7192-7200, DOI: 10.1021/acs.jpcc.6b01428.
- (160) Prakash, M.; Jobic, H.; Ramsahye, N. A.; Nouar, F.; Damasceno Borges, D.; Serre, C.; Maurin, G. Diffusion of H_2 , CO_2 , and Their Mixtures in the Porous Zirconium Based Metal–Organic Framework MIL-140A(Zr): Combination of Quasi-Elastic Neutron Scattering Measurements and Molecular Dynamics Simulations. *The Journal of Physical Chemistry C* **2015**, *119* (42), 23978-23989, DOI: 10.1021/acs.jpcc.5b07253.
- (161) Tan, K.; Zuluaga, S.; Gong, Q.; Gao, Y.; Nijem, N.; Li, J.; Thonhauser, T.; Chabal, Y. J. Competitive Coadsorption of CO_2 with H_2O , NH_3 , SO_2 , NO , NO_2 , N_2 , O_2 , and CH_4 in M-MOF-74 ($\text{M} = \text{Mg}, \text{Co}, \text{Ni}$): The Role of Hydrogen Bonding. *Chemistry of Materials* **2015**, *27* (6), 2203-2217, DOI: 10.1021/acs.chemmater.5b00315.
- (162) Yang, S.; Sun, J.; Ramirez-Cuesta, A. J.; Callear, S. K.; DavidWilliam, I. F.; Anderson, D. P.; Newby, R.; Blake, A. J.; Parker, J. E.; Tang, C. C.; Schröder, M. Selectivity and direct visualization of carbon dioxide and sulfur dioxide in a decorated porous host. *Nat Chem* **2012**, *4* (11), 887-894, DOI: <http://www.nature.com/nchem/journal/v4/n11/abs/nchem.1457.html#supplementary-information>.

- (163) Wang, Q.; Bai, J.; Lu, Z.; Pan, Y.; You, X. Finely tuning MOFs towards high-performance post-combustion CO₂ capture materials. *Chemical Communications* **2016**, 52 (3), 443-452.
- (164) Poloni, R.; Lee, K.; Berger, R. F.; Smit, B.; Neaton, J. B. Understanding Trends in CO₂ Adsorption in Metal–Organic Frameworks with Open-Metal Sites. *The journal of physical chemistry letters* **2014**, 5 (5), 861-865.
- (165) Vaidhyanathan, R.; Iremonger, S. S.; Dawson, K. W.; Shimizu, G. K. An amine-functionalized metal organic framework for preferential CO₂ adsorption at low pressures. *Chemical communications* **2009**, (35), 5230-5232.
- (166) Couck, S.; Denayer, J. F.; Baron, G. V.; Rémy, T.; Gascon, J.; Kapteijn, F. An amine-functionalized MIL-53 metal– organic framework with large separation power for CO₂ and CH₄. *Journal of the American Chemical Society* **2009**, 131 (18), 6326-6327.
- (167) Arstad, B.; Fjellvåg, H.; Kongshaug, K. O.; Swang, O.; Blom, R. Amine functionalised metal organic frameworks (MOFs) as adsorbents for carbon dioxide. *Adsorption* **2008**, 14 (6), 755-762.
- (168) Gascon, J.; Aktay, U.; Hernandez-Alonso, M. D.; Van Klink, G. P.; Kapteijn, F. Amino-based metal-organic frameworks as stable, highly active basic catalysts. *Journal of Catalysis* **2009**, 261 (1), 75-87.
- (169) Landa, H. O. R.; Flockerzi, D.; Seidel - Morgenstern, A. A method for efficiently solving the IAST equations with an application to adsorber dynamics. *AIChE Journal* **2013**, 59 (4), 1263-1277.
- (170) Keskin, S.; van Heest, T. M.; Sholl, D. S. Can Metal–Organic Framework Materials Play a Useful Role in Large - Scale Carbon Dioxide Separations? *ChemSusChem* **2010**, 3 (8), 879-891.
- (171) Bae, Y. S.; Snurr, R. Q. Development and evaluation of porous materials for carbon dioxide separation and capture. *Angewandte Chemie International Edition* **2011**, 50 (49), 11586-11596.
- (172) Lin, Y.; Lin, H.; Wang, H.; Suo, Y.; Li, B.; Kong, C.; Chen, L. Enhanced selective CO₂ adsorption on polyamine/MIL-101(Cr) composites. *Journal of Materials Chemistry A* **2014**, 2 (35), 14658-14665, DOI: 10.1039/C4TA01174K.
- (173) McDonald, T. M.; Lee, W. R.; Mason, J. A.; Wiers, B. M.; Hong, C. S.; Long, J. R. Capture of Carbon Dioxide from Air and Flue Gas in the Alkylamine-Appended Metal–Organic Framework mmen-Mg₂(dobpdc). *Journal of the American Chemical Society* **2012**, 134 (16), 7056-7065, DOI: 10.1021/ja300034j.
- (174) Hu, Y.; Verdegaal, W. M.; Yu, S.-H.; Jiang, H.-L. Alkylamine-Tethered Stable Metal–Organic Framework for CO₂ Capture from Flue Gas. *ChemSusChem* **2014**, 7 (3), 734-737, DOI: 10.1002/cssc.201301163.
- (175) Wu, D.; Gassensmith, J. J.; Gouvêa, D.; Ushakov, S.; Stoddart, J. F.; Navrotsky, A. Direct Calorimetric Measurement of Enthalpy of Adsorption of Carbon Dioxide on CD-MOF-2, a Green Metal–Organic Framework. *Journal of the American Chemical Society* **2013**, 135 (18), 6790-6793, DOI: 10.1021/ja402315d.

- (176) Li, T.; Chen, D.-L.; Sullivan, J. E.; Kozłowski, M. T.; Johnson, J. K.; Rosi, N. L. Systematic modulation and enhancement of CO₂ : N₂ selectivity and water stability in an isorecticular series of bio-MOF-11 analogues. *Chemical Science* **2013**, *4* (4), 1746-1755, DOI: 10.1039/C3SC22207A.
- (177) Min Wang, Q.; Shen, D.; Bülow, M.; Ling Lau, M.; Deng, S.; Fitch, F. R.; Lemcoff, N. O.; Semanscin, J. Metallo-organic molecular sieve for gas separation and purification. *Microporous and Mesoporous Materials* **2002**, *55* (2), 217-230, DOI: [http://dx.doi.org/10.1016/S1387-1811\(02\)00405-5](http://dx.doi.org/10.1016/S1387-1811(02)00405-5).
- (178) Choi, J.-S.; Son, W.-J.; Kim, J.; Ahn, W.-S. Metal–organic framework MOF-5 prepared by microwave heating: Factors to be considered. *Microporous and Mesoporous Materials* **2008**, *116* (1–3), 727-731, DOI: <http://dx.doi.org/10.1016/j.micromeso.2008.04.033>.
- (179) Zhang, Z.; Xian, S.; Xia, Q.; Wang, H.; Li, Z.; Li, J. Enhancement of CO₂ Adsorption and CO₂/N₂ Selectivity on ZIF-8 via Postsynthetic Modification. *AIChE Journal* **2013**, *59* (6), 2195-2206, DOI: 10.1002/aic.13970.
- (180) Liu, Y.; Kabbour, H.; Brown, C. M.; Neumann, D. A.; Ahn, C. C. Increasing the density of adsorbed hydrogen with coordinatively unsaturated metal centers in metal-organic frameworks. *Langmuir* **2008**, *24* (9), 4772-4777.
- (181) Shultz, A. M.; Farha, O. K.; Hupp, J. T.; Nguyen, S. T. A catalytically active, permanently microporous MOF with metalloporphyrin struts. *Journal of the American Chemical Society* **2009**, *131* (12), 4204-4205.
- (182) Rosi, N. L.; Kim, J.; Eddaoudi, M.; Chen, B.; O'Keeffe, M.; Yaghi, O. M. Rod packings and metal-organic frameworks constructed from rod-shaped secondary building units. *Journal of the American Chemical Society* **2005**, *127* (5), 1504-1518.
- (183) Dietzel, P. D.; Panella, B.; Hirscher, M.; Blom, R.; Fjellvåg, H. Hydrogen adsorption in a nickel based coordination polymer with open metal sites in the cylindrical cavities of the desolvated framework. *Chemical communications* **2006**, (9), 959-961.
- (184) Zhou, W.; Wu, H.; Yildirim, T. Enhanced H₂ Adsorption in Isostructural Metal–Organic Frameworks with Open Metal Sites: Strong Dependence of the Binding Strength on Metal Ions. *Journal of the American Chemical Society* **2008**, *130* (46), 15268-15269.
- (185) Dincă, M.; Dailly, A.; Liu, Y.; Brown, C. M.; Neumann, D. A.; Long, J. R. Hydrogen Storage in a Microporous Metal–Organic Framework with Exposed Mn²⁺ Coordination Sites. *Journal of the American Chemical Society* **2006**, *128* (51), 16876-16883, DOI: 10.1021/ja0656853.
- (186) Dincă, M.; Han, W. S.; Liu, Y.; Dailly, A.; Brown, C. M.; Long, J. R. Observation of Cu²⁺–H₂ Interactions in a Fully Desolvated Sodalite-Type Metal–Organic Framework. *Angewandte Chemie International Edition* **2007**, *46* (9), 1419-1422, DOI: 10.1002/anie.200604362.
- (187) Sumida, K.; Horike, S.; Kaye, S. S.; Herm, Z. R.; Queen, W. L.; Brown, C. M.; Grandjean, F.; Long, G. J.; Dailly, A.; Long, J. R. Hydrogen storage and carbon dioxide capture in an iron-based sodalite-type

- metal-organic framework (Fe-BTT) discovered via high-throughput methods. *Chemical Science* **2010**, *1* (2), 184-191, DOI: 10.1039/C0SC00179A.
- (188) Biswas, S.; Maes, M.; Dhakshinamoorthy, A.; Feyand, M.; De Vos, D. E.; Garcia, H.; Stock, N. Fuel purification, Lewis acid and aerobic oxidation catalysis performed by a microporous Co-BTT (BTT3- = 1,3,5-benzenetristetrazolate) framework having coordinatively unsaturated sites. *Journal of Materials Chemistry* **2012**, *22* (20), 10200-10209, DOI: 10.1039/C2JM15592C.
- (189) Chui, S. S.-Y.; Lo, S. M.-F.; Charmant, J. P.; Orpen, A. G.; Williams, I. D. A chemically functionalizable nanoporous material [Cu₃ (TMA)₂ (H₂O)₃]_n. *Science* **1999**, *283* (5405), 1148-1150.
- (190) Kramer, M.; Schwarz, U.; Kaskel, S. Synthesis and properties of the metal-organic framework Mo₃(BTC)₂ (TUDMOF-1). *Journal of Materials Chemistry* **2006**, *16* (23), 2245-2248, DOI: 10.1039/B601811D.
- (191) Murray, L. J.; Dinca, M.; Yano, J.; Chavan, S.; Bordiga, S.; Brown, C. M.; Long, J. R. Highly-Selective and Reversible O₂ Binding in Cr₃(1,3,5-benzenetricarboxylate)₂. *Journal of the American Chemical Society* **2010**, *132* (23), 7856-7857, DOI: 10.1021/ja1027925.
- (192) Feldblyum, J. I.; Liu, M.; Gidley, D. W.; Matzger, A. J. Reconciling the discrepancies between crystallographic porosity and guest access as exemplified by Zn-HKUST-1. *Journal of the American Chemical Society* **2011**, *133* (45), 18257-18263.
- (193) Kozachuk, O.; Yussenko, K.; Noei, H.; Wang, Y.; Walleck, S.; Glaser, T.; Fischer, R. A. Solvothermal growth of a ruthenium metal-organic framework featuring HKUST-1 structure type as thin films on oxide surfaces. *Chemical Communications* **2011**, *47* (30), 8509-8511, DOI: 10.1039/C1CC11107H.
- (194) Wade, C. R.; Dincă, M. Investigation of the synthesis, activation, and isosteric heats of CO₂ adsorption of the isostructural series of metal-organic frameworks M₃ (BTC)₂ (M= Cr, Fe, Ni, Cu, Mo, Ru). *Dalton Transactions* **2012**, *41* (26), 7931-7938.
- (195) Queen, W. L.; Brown, C. M.; Britt, D. K.; Zajdel, P.; Hudson, M. R.; Yaghi, O. M. Site-specific CO₂ adsorption and zero thermal expansion in an anisotropic pore network. *The Journal of Physical Chemistry C* **2011**, *115* (50), 24915-24919.
- (196) Yu, D.; Yazaydin, A. O.; Lane, J. R.; Dietzel, P. D.; Snurr, R. Q. A combined experimental and quantum chemical study of CO₂ adsorption in the metal-organic framework CPO-27 with different metals. *Chemical Science* **2013**, *4* (9), 3544-3556.
- (197) Morris, W.; Leung, B.; Furukawa, H.; Yaghi, O. K.; He, N.; Hayashi, H.; Houndonougbo, Y.; Asta, M.; Laird, B. B.; Yaghi, O. M. A combined experimental- computational investigation of carbon dioxide capture in a series of isorecticular zeolitic imidazolate frameworks. *Journal of the American Chemical Society* **2010**, *132* (32), 11006-11008.
- (198) Salles, F.; Jobic, H.; Devic, T.; Llewellyn, P. L.; Serre, C.; Férey, G.; Maurin, G. Self and Transport Diffusivity of CO₂ in the Metal- Organic Framework MIL-47 (V) Explored by Quasi-elastic Neutron Scattering Experiments and Molecular Dynamics Simulations. *ACS nano* **2009**, *4* (1), 143-152.

- (199) Chen, Y.; Jiang, J. A Bio - Metal-Organic Framework for Highly Selective CO₂ Capture: A Molecular Simulation Study. *ChemSusChem* **2010**, 3 (8), 982-988.
- (200) Vaidhyanathan, R.; Iremonger, S. S.; Shimizu, G. K. H.; Boyd, P. G.; Alavi, S.; Woo, T. K. <div xmlns="http://www.w3.org/1999/xhtml">Direct Observation and Quantification of CO₂</sub> Binding Within an Amine-Functionalized Nanoporous Solid</div>. *Science* **2010**, 330 (6004), 650-653, DOI: 10.1126/science.1194237.
- (201) Vaidhyanathan, R.; Iremonger, S. S.; Dawson, K. W.; Shimizu, G. K. H. An amine-functionalized metal organic framework for preferential CO₂ adsorption at low pressures. *Chemical Communications* **2009**, (35), 5230-5232, DOI: 10.1039/B911481E.
- (202) House, K. Z.; Harvey, C. F.; Aziz, M. J.; Schrag, D. P. The energy penalty of post-combustion CO₂ capture & storage and its implications for retrofitting the US installed base. *Energy & Environmental Science* **2009**, 2 (2), 193-205.
- (203) Hwang, Y. K.; Hong, D. Y.; Chang, J. S.; Jhung, S. H.; Seo, Y. K.; Kim, J.; Vimont, A.; Daturi, M.; Serre, C.; Férey, G. Amine grafting on coordinatively unsaturated metal centers of MOFs: consequences for catalysis and metal encapsulation. *Angewandte Chemie International Edition* **2008**, 47 (22), 4144-4148.
- (204) Lee, W. R.; Hwang, S. Y.; Ryu, D. W.; Lim, K. S.; Han, S. S.; Moon, D.; Choi, J.; Hong, C. S. Diamine-functionalized metal-organic framework: exceptionally high CO₂ capacities from ambient air and flue gas, ultrafast CO₂ uptake rate, and adsorption mechanism. *Energy & Environmental Science* **2014**, 7 (2), 744-751.
- (205) Ciferno, J.; Litynski, J.; Plasynski, S.; Murphy, J.; Vaux, G.; Munson, R.; Marano, J. DOE/NETL carbon dioxide capture and storage RD&d roadmap. *National Energy Technology Laboratory, accessed September 2010*, 13, 2011.
- (206) McDonald, T. M.; Lee, W. R.; Mason, J. A.; Wiers, B. M.; Hong, C. S.; Long, J. R. Capture of carbon dioxide from air and flue gas in the alkylamine-appended metal-organic framework mmen-Mg₂ (dobpdc). *Journal of the American Chemical Society* **2012**, 134 (16), 7056-7065.
- (207) Song, H.-J.; Lee, S.; Park, K.; Lee, J.; Chand Spah, D.; Park, J.-W.; Filburn, T. P. Simplified estimation of regeneration energy of 30 wt% sodium glycinate solution for carbon dioxide absorption. *Industrial & Engineering Chemistry Research* **2008**, 47 (24), 9925-9930.
- (208) McDonald, T. M.; Mason, J. A.; Kong, X.; Bloch, E. D.; Gygi, D.; Dani, A.; Crocella, V.; Giordanino, F.; Odoh, S. O.; Drisdell, W. S.; Vlasisavljevich, B.; Dzubak, A. L.; Poloni, R.; Schnell, S. K.; Planas, N.; Lee, K.; Pascal, T.; Wan, L. F.; Prendergast, D.; Neaton, J. B.; Smit, B.; Kortright, J. B.; Gagliardi, L.; Bordiga, S.; Reimer, J. A.; Long, J. R. Cooperative insertion of CO₂ in diamine-appended metal-organic frameworks. *Nature* **2015**, 519 (7543), 303-308, DOI: 10.1038/nature14327
<http://www.nature.com/nature/journal/v519/n7543/abs/nature14327.html#supplementary-information>.

- (209) Wu, D.; Gassensmith, J. J.; Gouvea, D.; Ushakov, S.; Stoddart, J. F.; Navrotsky, A. Direct Calorimetric Measurement of Enthalpy of Adsorption of Carbon Dioxide on CD-MOF-2, a Green Metal–Organic Framework. *Journal of the American Chemical Society* **2013**, *135* (18), 6790–6793.
- (210) Bosch, M.; Zhang, M.; Zhou, H.-C. Increasing the Stability of Metal–Organic Frameworks. *Advances in Chemistry* **2014**, *2014*, 8, DOI: 10.1155/2014/182327.
- (211) Lee, K. B.; Sircar, S. Removal and recovery of compressed CO₂ from flue gas by a novel thermal swing chemisorption process. *AIChE Journal* **2008**, *54* (9), 2293–2302, DOI: 10.1002/aic.11531.
- (212) Huang, X. C.; Lin, Y. Y.; Zhang, J. P.; Chen, X. M. Ligand - Directed Strategy for Zeolite - Type Metal–Organic Frameworks: Zinc (II) Imidazoles with Unusual Zeolitic Topologies. *Angewandte Chemie* **2006**, *118* (10), 1587–1589.
- (213) Park, K. S.; Ni, Z.; Côté, A. P.; Choi, J. Y.; Huang, R.; Uribe-Romo, F. J.; Chae, H. K.; O’Keeffe, M.; Yaghi, O. M. Exceptional chemical and thermal stability of zeolitic imidazolate frameworks. *Proceedings of the National Academy of Sciences* **2006**, *103* (27), 10186–10191.
- (214) DeCoste, J. B.; Peterson, G. W.; Jasuja, H.; Glover, T. G.; Huang, Y.-g.; Walton, K. S. Stability and degradation mechanisms of metal–organic frameworks containing the Zr₆O₄(OH)₄ secondary building unit. *Journal of Materials Chemistry A* **2013**, *1* (18), 5642–5650, DOI: 10.1039/C3TA10662D.
- (215) Colombo, V.; Galli, S.; Choi, H. J.; Han, G. D.; Maspero, A.; Palmisano, G.; Masciocchi, N.; Long, J. R. High thermal and chemical stability in pyrazolate-bridged metal–organic frameworks with exposed metal sites. *Chemical Science* **2011**, *2* (7), 1311–1319.
- (216) Clingerman, D. J.; Morris, W.; Mondloch, J. E.; Kennedy, R. D.; Sarjeant, A. A.; Stern, C.; Hupp, J. T.; Farha, O. K.; Mirkin, C. A. Stabilization of a highly porous metal–organic framework utilizing a carborane-based linker. *Chemical Communications* **2015**, *51* (30), 6521–6523, DOI: 10.1039/C4CC09212K.
- (217) Decoste, J. B.; Peterson, G. W.; Smith, M. W.; Stone, C. A.; Willis, C. R. Enhanced Stability of Cu-BTC MOF via Perfluorohexane Plasma-Enhanced Chemical Vapor Deposition. *Journal of the American Chemical Society* **2012**, *134* (3), 1486–1489, DOI: 10.1021/ja211182m.
- (218) Yang, S. J.; Park, C. R. Preparation of Highly Moisture-Resistant Black-Colored Metal Organic Frameworks. *Advanced Materials* **2012**, *24* (29), 4010–4013, DOI: 10.1002/adma.201200790.
- (219) Carné-Sánchez, A.; Stylianou, K. C.; Carbonell, C.; Naderi, M.; Imaz, I.; Maspocho, D. Protecting Metal–Organic Framework Crystals from Hydrolytic Degradation by Spray-Dry Encapsulating Them into Polystyrene Microspheres. *Advanced Materials* **2015**, *27* (5), 869–873, DOI: 10.1002/adma.201403827.
- (220) Shearer, G. C.; Colombo, V.; Chavan, S.; Albanese, E.; Civalleri, B.; Maspero, A.; Bordiga, S. Stability vs. reactivity: understanding the adsorption properties of Ni₃(BTP)₂ by experimental and computational methods. *Dalton Transactions* **2013**, *42* (18), 6450–6458.
- (221) Wu, T.; Shen, L.; Luebbers, M.; Hu, C.; Chen, Q.; Ni, Z.; Masel, R. I. Enhancing the stability of metal–organic frameworks in humid air by incorporating water repellent functional groups. *Chemical communications* **2010**, *46* (33), 6120–6122.

- (222) Jasuja, H.; Huang, Y.-g.; Walton, K. S. Adjusting the stability of metal–organic frameworks under humid conditions by ligand functionalization. *Langmuir* **2012**, *28* (49), 16874–16880.
- (223) Padial, N. M.; Quartapelle Procopio, E.; Montoro, C.; López, E.; Oltra, J. E.; Colombo, V.; Maspero, A.; Masciocchi, N.; Galli, S.; Senkovska, I.; Kaskel, S.; Barea, E.; Navarro, J. A. R. Highly Hydrophobic Isorecticular Porous Metal–Organic Frameworks for the Capture of Harmful Volatile Organic Compounds. *Angewandte Chemie International Edition* **2013**, *52* (32), 8290–8294, DOI: 10.1002/anie.201303484.
- (224) Singh, M. P.; Dhumal, N. R.; Kim, H. J.; Kiefer, J.; Anderson, J. A. Influence of Water on the Chemistry and Structure of the Metal–Organic Framework Cu₃(btc) 2. *The Journal of Physical Chemistry C* **2016**, *120* (31), 17323–17333.
- (225) Lin, Y.; Yan, Q.; Kong, C.; Chen, L. Polyethyleneimine incorporated metal-organic frameworks adsorbent for highly selective CO₂ capture. *Scientific reports* **2013**, *3*, 1859.
- (226) Zhang, Z.; Nguyen, H. T. H.; Miller, S. A.; Ploskonka, A. M.; DeCoste, J. B.; Cohen, S. M. Polymer–Metal–Organic Frameworks (polyMOFs) as Water Tolerant Materials for Selective Carbon Dioxide Separations. *Journal of the American Chemical Society* **2016**, *138* (3), 920–925, DOI: 10.1021/jacs.5b11034.
- (227) Lipman, T. *An Overview of Hydrogen Production and Storage Systems with Renewable Hydrogen Case Studies*; Clean Energy States Alliance: 2011.
- (228) Shekhah, O.; Belmabkhout, Y.; Adil, K.; Bhatt, P. M.; Cairns, A. J.; Eddaoudi, M. A facile solvent-free synthesis route for the assembly of a highly CO₂ selective and H₂S tolerant NiSIFSIX metal-organic framework. *Chemical Communications* **2015**, *51* (71), 13595–13598, DOI: 10.1039/C5CC04487A.
- (229) Hamon, L.; Serre, C.; Devic, T.; Loiseau, T.; Millange, F.; Férey, G.; Weireld, G. D. Comparative Study of Hydrogen Sulfide Adsorption in the MIL-53(Al, Cr, Fe), MIL-47(V), MIL-100(Cr), and MIL-101(Cr) Metal–Organic Frameworks at Room Temperature. *Journal of the American Chemical Society* **2009**, *131* (25), 8775–8777, DOI: 10.1021/ja901587t.
- (230) Peng, Y.; Srinivas, G.; Wilmer, C. E.; Eryazici, I.; Snurr, R. Q.; Hupp, J. T.; Yildirim, T.; Farha, O. K. Simultaneously high gravimetric and volumetric methane uptake characteristics of the metal–organic framework NU-111. *Chemical Communications* **2013**, *49* (29), 2992–2994.
- (231) Grüner, R.; Bon, V.; Heerwig, A.; Klein, N.; Müller, P.; Stoeck, U.; Baburin, I. A.; Mueller, U.; Senkovska, I.; Kaskel, S. Dye Encapsulation Inside a New Mesoporous Metal–Organic Framework for Multifunctional Solvatochromic - Response Function. *Chemistry-A European Journal* **2012**, *18* (42), 13299–13303.
- (232) Cui, P.; Ma, Y.-G.; Li, H.-H.; Zhao, B.; Li, J.-R.; Cheng, P.; Balbuena, P. B.; Zhou, H.-C. Multipoint interactions enhanced CO₂ uptake: a zeolite-like zinc–tetrazole framework with 24-nuclear zinc cages. *Journal of the American Chemical Society* **2012**, *134* (46), 18892–18895.

- (233) Rowsell, J. L.; Millward, A. R.; Park, K. S.; Yaghi, O. M. Hydrogen sorption in functionalized metal-organic frameworks. *Journal of the American Chemical Society* **2004**, *126* (18), 5666-5667.
- (234) Farha, O. K.; Hupp, J. T. Rational design, synthesis, purification, and activation of metal-organic framework materials. *Accounts of chemical research* **2010**, *43* (8), 1166-1175.
- (235) Han, S. S.; Jung, D.-H.; Heo, J. Interpenetration of Metal Organic Frameworks for Carbon Dioxide Capture and Hydrogen Purification: Good or Bad? *The Journal of Physical Chemistry C* **2012**, *117* (1), 71-77.
- (236) Kang, Z.; Peng, Y.; Qian, Y.; Yuan, D.; Addicoat, M. A.; Heine, T.; Hu, Z.; Tee, L.; Guo, Z.; Zhao, D. Mixed Matrix Membranes (MMMs) Comprising Exfoliated 2D Covalent Organic Frameworks (COFs) for Efficient CO₂ Separation. *Chemistry of Materials* **2016**, *28* (5), 1277-1285.
- (237) Nandi, S.; De Luna, P.; Daff, T. D.; Rother, J.; Liu, M.; Buchanan, W.; Hawari, A. I.; Woo, T. K.; Vaidhyanathan, R. A single-ligand ultra-microporous MOF for precombustion CO₂ capture and hydrogen purification. *Science advances* **2015**, *1* (11), e1500421.
- (238) Choi, H. J.; Dinca, M.; Long, J. R. Broadly Hysteretic H₂ Adsorption in the Microporous Metal-Organic Framework Co (1, 4-benzenedipyrazolate). *Journal of the American Chemical Society* **2008**, *130* (25), 7848-7850.
- (239) Krishna, R.; Long, J. R. Screening metal-organic frameworks by analysis of transient breakthrough of gas mixtures in a fixed bed adsorber. *The Journal of Physical Chemistry C* **2011**, *115* (26), 12941-12950.
- (240) Herm, Z. R.; Krishna, R.; Long, J. R. Reprint of: CO₂/CH₄, CH₄/H₂ and CO₂/CH₄/H₂ separations at high pressures using Mg₂(dobdc). *Microporous and Mesoporous Materials* **2012**, *157*, 94-100.
- (241) Wu, H.; Yao, K.; Zhu, Y.; Li, B.; Shi, Z.; Krishna, R.; Li, J. Cu-TDPAT, an rht-type dual-functional metal-organic framework offering significant potential for use in H₂ and natural gas purification processes operating at high pressures. *The Journal of Physical Chemistry C* **2012**, *116* (31), 16609-16618.
- (242) Banu, A.-M.; Friedrich, D.; Brandani, S.; Düren, T. A multiscale study of MOFs as adsorbents in H₂ PSA purification. *Industrial & Engineering Chemistry Research* **2013**, *52* (29), 9946-9957.
- (243) Kakaras, E.; Koumanakos, A.; Doukelis, A.; Giannakopoulos, D.; Vorrias, I. Oxyfuel boiler design in a lignite-fired power plant. *Fuel* **2007**, *86* (14), 2144-2150, DOI: <http://dx.doi.org/10.1016/j.fuel.2007.03.037>.
- (244) Rezvani, S.; Huang, Y.; McIlveen-Wright, D.; Hewitt, N.; Wang, Y. Comparative assessment of sub-critical versus advanced super-critical oxyfuel fired PF boilers with CO₂ sequestration facilities. *Fuel* **2007**, *86* (14), 2134-2143, DOI: <http://dx.doi.org/10.1016/j.fuel.2007.01.027>.
- (245) KACST Technology and Innovation Center on Carbon Capture and Sequestration. <https://www3.kfupm.edu.sa/CCS/Oxy-fuel.html>.
- (246) *Oxy-fuel Combustion Systems (OCS)*; 4th Floor, B-Block, Building No. 14, Cyber City, DLF City Phase –III, Gurgaon, Haryana –122002, Jun-13, 2013.

- (247) Hoffman, A.; Collins, D.; Day, V.; Fleischer, E.; Srivastava, T.; Hoard, J. Crystal structure and molecular stereochemistry of μ -oxo-bis [α -, β -, γ -, δ -tetraphenylporphyrinatoiron (III)]. *Journal of the American Chemical Society* **1972**, *94* (10), 3620-3626.
- (248) Feng, D.; Chung, W.-C.; Wei, Z.; Gu, Z.-Y.; Jiang, H.-L.; Chen, Y.-P.; Darensbourg, D. J.; Zhou, H.-C. Construction of ultrastable porphyrin Zr metal–organic frameworks through linker elimination. *Journal of the American Chemical Society* **2013**, *135* (45), 17105-17110.
- (249) Anderson, J. S.; Gallagher, A. T.; Mason, J. A.; Harris, T. D. A Five-Coordinate Heme Dioxygen Adduct Isolated within a Metal–Organic Framework. *Journal of the American Chemical Society* **2014**, *136* (47), 16489-16492.
- (250) Babcock, H. D.; Herzberg, L. Fine Structure of the Red System of Atmospheric Oxygen Bands. *The Astrophysical Journal* **1948**, *108*, 167.
- (251) Cho, J.; Woo, J.; Nam, W. An “End-On” Chromium (III)-Superoxo Complex: Crystallographic and Spectroscopic Characterization and Reactivity in C–H Bond Activation of Hydrocarbons. *Journal of the American Chemical Society* **2010**, *132* (17), 5958-5959.
- (252) Zhang, W.; Banerjee, D.; Liu, J.; Schaef, H. T.; Crum, J. V.; Fernandez, C. A.; Kukkadapu, R. K.; Nie, Z.; Nune, S. K.; Motkuri, R. K. Redox - Active Metal-Organic Composites for Highly Selective Oxygen Separation Applications. *Advanced Materials* **2016**.
- (253) Mu, B.; Walton, K. S. Thermal Analysis and Heat Capacity Study of Metal–Organic Frameworks. *The Journal of Physical Chemistry C* **2011**, *115* (46), 22748-22754, DOI: 10.1021/jp205538a.
- (254) Colon, Y. J.; Snurr, R. Q. High-throughput computational screening of metal-organic frameworks. *Chemical Society Reviews* **2014**, *43* (16), 5735-5749, DOI: 10.1039/C4CS00070F.
- (255) Wilmer, C. E.; Leaf, M.; Lee, C. Y.; Farha, O. K.; Hauser, B. G.; Hupp, J. T.; Snurr, R. Q. Large-scale screening of hypothetical metal–organic frameworks. *Nat Chem* **2012**, *4* (2), 83-89, DOI: <http://www.nature.com/nchem/journal/v4/n2/abs/nchem.1192.html#supplementary-information>.
- (256) Geerts, B.; Linacre, E. Changes in Concentration of Atmospheric Carbon Dioxide, other Greenhouse Gases, and Aerosols. *Carbon* **2002**, *3*, 02.
- (257) Ainsworth, E. A. The importance of intraspecific variation in tree responses to elevated [CO₂]: breeding and management of future forests. *Tree physiology* **2016**, tpw039.
- (258) Trickett, C. A.; Helal, A.; Al-Maythalony, B. A.; Yamani, Z. H.; Cordova, K. E.; Yaghi, O. M. The chemistry of metal–organic frameworks for CO₂ capture, regeneration and conversion. *Nature Reviews Materials* **2017**, *2* (8), 17045.
- (259) Yan, J. *Handbook of Clean Energy Systems, 6 Volume Set*, Wiley: 2015.

- (260) Cabello, C. P.; Rumori, P.; Palomino, G. T. Carbon dioxide adsorption on MIL-100 (M)(M= Cr, V, Sc) metal–organic frameworks: IR spectroscopic and thermodynamic studies. *Microporous and Mesoporous Materials* **2014**, *190*, 234-239.
- (261) Huang, S.-L.; Zhang, L.; Lin, Y.-J.; Jin, G.-X. Discrepant gas adsorption in isostructural heterometallic coordination polymers: strong dependence of metal identity. *CrystEngComm* **2013**, *15* (1), 78-85.
- (262) Queen, W. L.; Hudson, M. R.; Bloch, E. D.; Mason, J. A.; Gonzalez, M. I.; Lee, J. S.; Gygi, D.; Howe, J. D.; Lee, K.; Darwish, T. A. Comprehensive study of carbon dioxide adsorption in the metal–organic frameworks M₂(dobdc)(M= Mg, Mn, Fe, Co, Ni, Cu, Zn). *Chemical Science* **2014**, *5* (12), 4569-4581.
- (263) Dinca, M.; Dailly, A.; Liu, Y.; Brown, C. M.; Neumann, D. A.; Long, J. R. Hydrogen storage in a microporous metal-organic framework with exposed Mn²⁺ coordination sites. *Journal of the American Chemical Society* **2006**, *128* (51), 16876-16883.
- (264) Dincă, M.; Han, W. S.; Liu, Y.; Dailly, A.; Brown, C. M.; Long, J. R. Observation of Cu²⁺–H₂ Interactions in a Fully Desolvated Sodalite - Type Metal-Organic Framework. *Angewandte Chemie International Edition* **2007**, *46* (9), 1419-1422.
- (265) Sumida, K.; Horike, S.; Kaye, S. S.; Herm, Z. R.; Queen, W. L.; Brown, C. M.; Grandjean, F.; Long, G. J.; Dailly, A.; Long, J. R. Hydrogen storage and carbon dioxide capture in an iron-based sodalite-type metal–organic framework (Fe-BTT) discovered via high-throughput methods. *Chemical Science* **2010**, *1* (2), 184-191.
- (266) Biswas, S.; Maes, M.; Dhakshinamoorthy, A.; Feyand, M.; De Vos, D. E.; Garcia, H.; Stock, N. Fuel purification, Lewis acid and aerobic oxidation catalysis performed by a microporous Co-BTT (BTT 3–= 1, 3, 5-benzenetristetrazolate) framework having coordinatively unsaturated sites. *Journal of Materials Chemistry* **2012**, *22* (20), 10200-10209.
- (267) Bloch, E. D.; Queen, W. L.; Hudson, M. R.; Mason, J. A.; Xiao, D. J.; Murray, L. J.; Flacau, R.; Brown, C. M.; Long, J. R. Hydrogen Storage and Selective, Reversible O₂ Adsorption in a Metal–Organic Framework with Open Chromium (II) Sites. *Angewandte Chemie* **2016**, *128* (30), 8747-8751.
- (268) Dietzel, P. D.; Johnsen, R. E.; Blom, R.; Fjellvåg, H. Structural changes and coordinatively unsaturated metal atoms on dehydration of honeycomb analogous microporous metal–organic frameworks. *Chemistry–A European Journal* **2008**, *14* (8), 2389-2397.
- (269) Dietzel, P. D.; Blom, R.; Fjellvåg, H. Base - Induced Formation of Two Magnesium Metal - Organic Framework Compounds with a Bifunctional Tetratopic Ligand. *European Journal of Inorganic Chemistry* **2008**, *2008* (23), 3624-3632.
- (270) Sanz, R.; Martínez, F.; Orcajo, G.; Wojtas, L.; Briones, D. Synthesis of a honeycomb-like Cu-based metal–organic framework and its carbon dioxide adsorption behaviour. *Dalton Transactions* **2013**, *42* (7), 2392-2398.

- (271) Pato - Doldán, B.; Rosnes, M. H.; Dietzel, P. D. An In - Depth Structural Study of the Carbon Dioxide Adsorption Process in the Porous Metal-Organic Frameworks CPO - 27 - M. *ChemSusChem* **2017**, *10* (8), 1710-1719.
- (272) Gygi, D.; Bloch, E. D.; Mason, J. A.; Hudson, M. R.; Gonzalez, M. I.; Siegelman, R. L.; Darwish, T. A.; Queen, W. L.; Brown, C. M.; Long, J. R. Hydrogen storage in the expanded pore metal-organic frameworks M2(dobpdc)(M= Mg, Mn, Fe, Co, Ni, Zn). *Chem. Mater.* **2016**, *28* (4), 1128-1138.
- (273) Reed, D. A.; Keitz, B. K.; Oktawiec, J.; Mason, J. A.; Runčevski, T.; Xiao, D. J.; Darago, L. E.; Crocellà, V.; Bordiga, S.; Long, J. R. A spin transition mechanism for cooperative adsorption in metal-organic frameworks. *Nature* **2017**, *550* (7674), 96.
- (274) Kapelewski, M. T.; Geier, S. J.; Hudson, M. R.; Stüch, D.; Mason, J. A.; Nelson, J. N.; Xiao, D. J.; Hulvey, Z.; Gilmour, E.; FitzGerald, S. A. M2(m-dobdc)(M= Mg, Mn, Fe, Co, Ni) metal-organic frameworks exhibiting increased charge density and enhanced H₂ binding at the open metal sites. *Journal of the American Chemical Society* **2014**, *136* (34), 12119-12129.
- (275) Kramer, M.; Schwarz, U.; Kaskel, S. Synthesis and properties of the metal-organic framework Mo₃(BTC)₂ (TUDMOF-1). *Journal of Materials Chemistry* **2006**, *16* (23), 2245-2248.
- (276) Murray, L. J.; Dinca, M.; Yano, J.; Chavan, S.; Bordiga, S.; Brown, C. M.; Long, J. R. Highly-selective and reversible O₂ binding in Cr₃(1, 3, 5-benzenetricarboxylate)₂. *Journal of the American Chemical Society* **2010**, *132* (23), 7856-7857.
- (277) Kozachuk, O.; Yusenko, K.; Noei, H.; Wang, Y.; Walleck, S.; Glaser, T.; Fischer, R. A. Solvothermal growth of a ruthenium metal-organic framework featuring HKUST-1 structure type as thin films on oxide surfaces. *Chemical Communications* **2011**, *47* (30), 8509-8511.
- (278) Mukherjee, S.; Manna, B.; Desai, A. V.; Yin, Y.; Krishna, R.; Babarao, R.; Ghosh, S. K. Harnessing Lewis acidic open metal sites of metal-organic frameworks: the foremost route to achieve highly selective benzene sorption over cyclohexane. *Chemical Communications* **2016**.
- (279) Sumida, K.; Stüch, D.; Mino, L.; Chai, J.-D.; Bloch, E. D.; Zavorotynska, O.; Murray, L. J.; Dincă, M.; Chavan, S.; Bordiga, S. Impact of metal and anion substitutions on the hydrogen storage properties of M-BTT metal-organic frameworks. *Journal of the American Chemical Society* **2013**, *135* (3), 1083-1091.
- (280) Allendorf, M. D.; Foster, M. E.; Léonard, F.; Stavila, V.; Feng, P. L.; Doty, F. P.; Leong, K.; Ma, E. Y.; Johnston, S. R.; Talin, A. A. Guest-Induced Emergent Properties in Metal-Organic Frameworks. *The journal of physical chemistry letters* **2015**, *6* (7), 1182-1195.
- (281) Zhang, T.; Lin, W. Metal-organic frameworks for artificial photosynthesis and photocatalysis. *Chemical Society Reviews* **2014**, *43* (16), 5982-5993.
- (282) Zhang, Z.; Yao, Z.-Z.; Xiang, S.; Chen, B. Perspective of microporous metal-organic frameworks for CO₂ capture and separation. *Energy & Environmental Science* **2014**, *7* (9), 2868-2899.

- (283) Lindner, H.; Schneider, E. Review of cost estimates for uranium recovery from seawater. *Energy Economics* **2015**, *49*, 9-22.
- (284) Larson, A. C.; Von Dreele, R. B. Gsas. *General Structure Analysis System. LANSCE, MS-H805, Los Alamos, New Mexico* **1994**.
- (285) Toby, B. H. EXPGUI, a graphical user interface for GSAS. *Journal of applied crystallography* **2001**, *34* (2), 210-213.
- (286) Dion, M.; Rydberg, H.; Schröder, E.; Langreth, D. C.; Lundqvist, B. I. Van der Waals density functional for general geometries. *Physical review letters* **2004**, *92* (24), 246401.
- (287) Lee, K.; Murray, É. D.; Kong, L.; Lundqvist, B. I.; Langreth, D. C. Higher-accuracy van der Waals density functional. *Physical Review B* **2010**, *82* (8), 081101.
- (288) Hamada, I. van der Waals density functional made accurate. *Physical Review B* **2014**, *89* (12), 121103.
- (289) Liechtenstein, A.; Anisimov, V.; Zaanen, J. Density-functional theory and strong interactions: Orbital ordering in Mott-Hubbard insulators. *Physical Review B* **1995**, *52* (8), R5467.
- (290) Lee, K.; Howe, J. D.; Lin, L.-C.; Smit, B.; Neaton, J. B. Small-molecule adsorption in open-site metal–organic frameworks: a systematic density functional theory study for rational design. *Chemistry of Materials* **2015**, *27* (3), 668-678.
- (291) Wang, L.; Maxisch, T.; Ceder, G. Oxidation energies of transition metal oxides within the GGA+ U framework. *Physical Review B* **2006**, *73* (19), 195107.
- (292) Blöchl, P. E. Projector augmented-wave method. *Physical Review B* **1994**, *50* (24), 17953.
- (293) Poloni, R.; Smit, B.; Neaton, J. B. Ligand-assisted enhancement of co₂ capture in metal–organic frameworks. *Journal of the American Chemical Society* **2012**, *134* (15), 6714-6719.
- (294) Campaná, C.; Mussard, B.; Woo, T. K. Electrostatic potential derived atomic charges for periodic systems using a modified error functional. *Journal of chemical theory and computation* **2009**, *5* (10), 2866-2878.
- (295) Dubbeldam, D.; Calero, S.; Ellis, D. E.; Snurr, R. Q. RASPA: molecular simulation software for adsorption and diffusion in flexible nanoporous materials. *Molecular Simulation* **2016**, *42* (2), 81-101.
- (296) Martin, M. G.; Siepmann, J. I. Transferable potentials for phase equilibria. 1. United-atom description of n-alkanes. *The Journal of Physical Chemistry B* **1998**, *102* (14), 2569-2577.
- (297) Rappé, A. K.; Casewit, C. J.; Colwell, K.; Goddard Iii, W.; Skiff, W. UFF, a full periodic table force field for molecular mechanics and molecular dynamics simulations. *Journal of the American chemical society* **1992**, *114* (25), 10024-10035.
- (298) Gave, M. A.; University, M. S. *Synthesis and Characterization of Novel Chalcophosphate Materials*, Michigan State University: 2007.
- (299) Goreshnik, E.; Slyvka, Y. I.; Mys'kiv, M. The first example of a direct Cu⁺–bond. Synthesis and crystal structure of two closely related copper (I) hexafluorosilicate π -complexes with 1-allylbenzotriazole

- of [Cu₂(C₆H₄N₃(C₃H₅))₂(H₂O)₂SiF₆]. 2H₂O and [Cu₂(C₆H₄N₃(C₃H₅))₂(CH₃OH)₂(H₂O)₂]SiF₆ composition. *Inorganica Chimica Acta* **2011**, 377 (1), 177-180.
- (300) Hulvey, Z.; Vlaisavljevich, B.; Mason, J. A.; Tsivion, E.; Dougherty, T. P.; Bloch, E. D.; Head-Gordon, M.; Smit, B.; Long, J. R.; Brown, C. M. Critical Factors Driving the High Volumetric Uptake of Methane in Cu₃(btc) 2. *Journal of the American Chemical Society* **2015**, 137 (33), 10816-10825.
- (301) Dinca, M.; Long, J. R. High-enthalpy hydrogen adsorption in cation-exchanged variants of the microporous metal-organic framework Mn₃[(Mn₄Cl)₃(BTT)₈(CH₃OH)₁₀]₂. *Journal of the American Chemical Society* **2007**, 129 (36), 11172-11176.
- (302) Mason, J. A.; Veenstra, M.; Long, J. R. Evaluating metal-organic frameworks for natural gas storage. *Chemical Science* **2014**, 5 (1), 32-51.
- (303) Rosi, N. L.; Eckert, J.; Eddaoudi, M.; Vodak, D. T.; Kim, J.; O'keeffe, M.; Yaghi, O. M. Hydrogen storage in microporous metal-organic frameworks. *Science* **2003**, 300 (5622), 1127-1129.
- (304) Rowsell, J. L.; Yaghi, O. M. Strategies for hydrogen storage in metal-organic frameworks. *Angew. Chem.* **2005**, 44 (30), 4670-4679.
- (305) Asgari, M.; Queen, W. L. Carbon Capture in Metal-Organic Frameworks. *Materials and Processes for CO₂ Capture, Conversion, and Sequestration* **2018**, 1-78.
- (306) Férey, G.; Serre, C.; Devic, T.; Maurin, G.; Jobic, H.; Llewellyn, P. L.; De Weireld, G.; Vimont, A.; Daturi, M.; Chang, J.-S. Why hybrid porous solids capture greenhouse gases? *Chem. Soc. Rev.* **2011**, 40 (2), 550-562.
- (307) Van de Voorde, B.; Bueken, B.; Denayer, J.; De Vos, D. Adsorptive separation on metal-organic frameworks in the liquid phase. *Chem. Soc. Rev.* **2014**, 43 (16), 5766-5788.
- (308) Kochetygov, I.; Bulut, S.; Asgari, M.; Queen, W. L. Selective CO₂ adsorption by a new metal-organic framework: synergy between open metal sites and a charged imidazolinium backbone. *Dalton Transactions* **2018**, 47 (31), 10527-10535, DOI: 10.1039/C8DT01247D.
- (309) Tan, Y.-X.; He, Y.-P.; Zhang, J. Microporous Metal-Organic Framework Based on Mixing Nanosized Tris ((4-carboxyl)-phenylduryl) amine and 4, 4' -Bipyridine Ligands for Gas Storage and Separation. *Crystal Growth & Design* **2012**, 12 (5), 2468-2471 % @ 1528-7483.
- (310) Corma, A.; García, H.; Llabrés i Xamena, F. Engineering metal organic frameworks for heterogeneous catalysis. *Chem. Rev.* **2010**, 110 (8), 4606-4655.
- (311) Kreno, L. E.; Leong, K.; Farha, O. K.; Allendorf, M.; Van Duyne, R. P.; Hupp, J. T. Metal-organic framework materials as chemical sensors. *Chem. Rev.* **2011**, 112 (2), 1105-1125.
- (312) Horcajada, P.; Serre, C.; Vallet - Regí, M.; Sebban, M.; Taulelle, F.; Férey, G. Metal-organic frameworks as efficient materials for drug delivery. *Angew. Chem.* **2006**, 118 (36), 6120-6124.

- (313) Bloch, E. D.; Queen, W. L.; Hudson, M. R.; Mason, J. A.; Xiao, D. J.; Murray, L. J.; Flacau, R.; Brown, C. M.; Long, J. R. Hydrogen storage and selective, reversible O₂ adsorption in a metal–organic framework with open chromium (II) sites. *Angew. Chem.* **2016**, *55* (30), 8605-8609.
- (314) Férey, G. Hybrid porous solids: past, present, future. *Chemical Society Reviews* **2008**, *37* (1), 191-214.
- (315) Suh, M. P.; Park, H. J.; Prasad, T. K.; Lim, D.-W. Hydrogen storage in metal–organic frameworks. *Chemical reviews* **2011**, *112* (2), 782-835.
- (316) Dincă, M.; Long, J. R. Hydrogen storage in microporous metal–organic frameworks with exposed metal sites. *Angew. Chem.* **2008**, *47* (36), 6766-6779.
- (317) Murray, L. J.; Dincă, M.; Long, J. R. Hydrogen storage in metal–organic frameworks. *Chem. Soc. Rev.* **2009**, *38* (5), 1294-1314.
- (318) Zhou, H.-C.; Long, J. R.; Yaghi, O. M. Introduction to Metal–Organic Frameworks. *Chem. Rev.* **2012**, *112* (2), 673-674, DOI: 10.1021/cr300014x.
- (319) Ren, J.; North, B. C. Shaping porous materials for hydrogen storage applications: a review. *Journal of Technology Innovations in Renewable Energy* **2014**, *3* (1), 12.
- (320) Tong, M.; Lan, Y.; Yang, Q.; Zhong, C. High-throughput computational screening and design of nanoporous materials for methane storage and carbon dioxide capture. *Green Energy & Environment* **2018**, *3* (2), 107-119.
- (321) Sagara, T.; Klassen, J.; Ganz, E. Computational study of hydrogen binding by metal-organic framework-5. *The Journal of chemical physics* **2004**, *121* (24), 12543-12547.
- (322) Mueller, T.; Ceder, G. A density functional theory study of hydrogen adsorption in MOF-5. *The Journal of Physical Chemistry B* **2005**, *109* (38), 17974-17983.
- (323) Asgari, M.; Jawahery, S.; Bloch, E. D.; Hudson, M. R.; Flacau, R.; Vlasisavljevich, B.; Long, J. R.; Brown, C. M.; Queen, W. L. An experimental and computational study of CO₂ adsorption in the sodalite-type M-BTT (M= Cr, Mn, Fe, Cu) metal–organic frameworks featuring open metal sites. *Chemical science* **2018**, *9* (20), 4579-4588.
- (324) Dinca, M.; Dailly, A.; Liu, Y.; Brown, C. M.; Neumann, D. A.; Long, J. R. Hydrogen storage in a microporous metal– organic framework with exposed Mn²⁺ coordination sites. *J. Am. Chem. Soc.* **2006**, *128* (51), 16876-16883.
- (325) Xiao, D. J.; Gonzalez, M. I.; Darago, L. E.; Vogiatzis, K. D.; Haldoupis, E.; Gagliardi, L.; Long, J. R. Selective, tunable O₂ binding in cobalt (II)–triazolate/pyrazolate metal–organic frameworks. *Journal of the American Chemical Society* **2016**, *138* (22), 7161-7170.
- (326) Reed, D. A.; Xiao, D. J.; Gonzalez, M. I.; Darago, L. E.; Herm, Z. R.; Grandjean, F.; Long, J. R. Reversible CO scavenging via adsorbate-dependent spin state transitions in an iron (II)–triazolate metal–organic framework. *Journal of the American Chemical Society* **2016**, *138* (17), 5594-5602.

- (327) Liu, Y.; Kabbour, H.; Brown, C. M.; Neumann, D. A.; Ahn, C. C. Increasing the density of adsorbed hydrogen with coordinatively unsaturated metal centers in metal– organic frameworks. *Langmuir* **2008**, *24* (9), 4772-4777.
- (328) Yang, S.; Peng, L.; Oveisi, E.; Bulut, S.; Sun, D. T.; Asgari, M.; Trukhina, O.; Queen, W. L. MOF - Derived Cobalt Phosphide/Carbon Nanocubes for Selective Hydrogenation of Nitroarenes to Anilines. *Chemistry -A European Journal* **2018**, *24* (17), 4234-4238.
- (329) Bloch, E. D.; Queen, W. L.; Krishna, R.; Zadrozny, J. M.; Brown, C. M.; Long, J. R. Hydrocarbon separations in a metal-organic framework with open iron (II) coordination sites. *science* **2012**, *335* (6076), 1606-1610.
- (330) Coelho, A. A. TOPAS and TOPAS - Academic: an optimization program integrating computer algebra and crystallographic objects written in C++. *Journal of Applied Crystallography* **2018**, *51* (1), 210-218.
- (331) Larson, A.; Von Dreele, R. General Structure Analysis System, LANSCE, MS-H805, Los Alamos, New Mexico 1994; b) BH Toby. *J. Appl. Crystallogr* **2001**, *34*, 210-213.
- (332) Perdew, J. P.; Burke, K.; Ernzerhof, M. Generalized gradient approximation made simple. *Physical review letters* **1996**, *77* (18), 3865.
- (333) Giannozzi, P.; Baroni, S.; Bonini, N.; Calandra, M.; Car, R.; Cavazzoni, C.; Ceresoli, D.; Chiarotti, G. L.; Cococcioni, M.; Dabo, I. QUANTUM ESPRESSO: a modular and open-source software project for quantum simulations of materials. *Journal of physics: Condensed matter* **2009**, *21* (39), 395502.
- (334) Vanderbilt, D. Soft self-consistent pseudopotentials in a generalized eigenvalue formalism. *Physical Review B* **1990**, *41* (11), 7892.
- (335) Garrity, K. F.; Bennett, J. W.; Rabe, K. M.; Vanderbilt, D. Pseudopotentials for high-throughput DFT calculations. *Computational Materials Science* **2014**, *81*, 446-452.
- (336) Dal Corso, A. Pseudopotentials periodic table: From H to Pu. *Computational Materials Science* **2014**, *95*, 337-350.
- (337) Grimme, S. Semiempirical GGA - type density functional constructed with a long - range dispersion correction. *Journal of computational chemistry* **2006**, *27* (15), 1787-1799.
- (338) Lin, X.; Telepeni, I.; Blake, A. J.; Dailly, A.; Brown, C. M.; Simmons, J. M.; Zoppi, M.; Walker, G. S.; Thomas, K. M.; Mays, T. J. High capacity hydrogen adsorption in Cu (II) tetracarboxylate framework materials: the role of pore size, ligand functionalization, and exposed metal sites. *Journal of the American Chemical Society* **2009**, *131* (6), 2159-2171.
- (339) Savage, M.; Da Silva, I.; Johnson, M.; Carter, J. H.; Newby, R.; Suyetin, M.; Besley, E.; Manuel, P.; Rudić, S.; Fitch, A. N. Observation of binding and rotation of methane and hydrogen within a functional metal–organic framework. *J. Am. Chem. Soc.* **2016**, *138* (29), 9119-9127.

- (340) Kong, L.; Cooper, V. R.; Nijem, N.; Li, K.; Li, J.; Chabal, Y. J.; Langreth, D. C. Theoretical and experimental analysis of H₂ binding in a prototypical metal-organic framework material. *Physical Review B* **2009**, *79* (8), 081407.
- (341) Lee, H.; Choi, Y. N.; Choi, S. B.; Kim, J.; Kim, D.; Jung, D. H.; Park, Y. S.; Yoon, K. B. Liquid-Like Hydrogen Stored in Nanoporous Materials at 50 K Observed by in Situ Neutron Diffraction Experiments. *The Journal of Physical Chemistry C* **2013**, *117* (6), 3177-3184.
- (342) Brown, C. M.; Liu, Y.; Yildirim, T.; Peterson, V. K.; Kepert, C. J. Hydrogen adsorption in HKUST-1: a combined inelastic neutron scattering and first-principles study. *Nanotechnology* **2009**, *20* (20), 204025.
- (343) Catalan, J.; Elguero, J. Basicity and acidity of azoles. In *Advances in heterocyclic chemistry*; Elsevier: 1987; pp 187-274.
- (344) Matta, C. F.; Hernández - Trujillo, J.; Tang, T. H.; Bader, R. F. Hydrogen-hydrogen bonding: a stabilizing interaction in molecules and crystals. *Chemistry -A European Journal* **2003**, *9* (9), 1940-1951.
- (345) Abramov, Y. A.; Brammer, L.; Klooster, W. T.; Bullock, R. M. Experimental Charge Density and Neutron Structural Study of cis-HMn (CO) 4PPh₃: Comprehensive Analysis of Chemical Bonding and Evidence for a C–H \cdots H–Mn Hydrogen Bond. *Inorg. Chem.* **1998**, *37* (24), 6317-6328.
- (346) Sutor, D. J. 204. Evidence for the existence of C–H \cdots O hydrogen bonds in crystals. *Journal of the Chemical Society (Resumed)* **1963**, 1105-1110.
- (347) Zheng, B.; Bai, J.; Duan, J.; Wojtas, L.; Zaworotko, M. J. Enhanced CO₂ binding affinity of a high-uptake rht-type metal–organic framework decorated with acylamide groups. *J. Am. Chem. Soc.* **2010**, *133* (4), 748-751.
- (348) Al-Janabi, N.; Hill, P.; Torrente-Murciano, L.; Garforth, A.; Gorgojo, P.; Siperstein, F.; Fan, X. Mapping the Cu-BTC metal–organic framework (HKUST-1) stability envelope in the presence of water vapour for CO₂ adsorption from flue gases. *Chemical Engineering Journal* **2015**, *281*, 669-677.
- (349) Simon, C. M.; Mercado, R.; Schnell, S. K.; Smit, B.; Haranczyk, M. What are the best materials to separate a xenon/krypton mixture? *Chem. Mater.* **2015**, *27* (12), 4459-4475.
- (350) Witman, M.; Ling, S.; Jawahery, S.; Boyd, P. G.; Haranczyk, M.; Slater, B.; Smit, B. The influence of intrinsic framework flexibility on adsorption in nanoporous materials. *J. Am. Chem. Soc.* **2017**, *139* (15), 5547-5557.
- (351) Banerjee, D.; Simon, C. M.; Plonka, A. M.; Motkuri, R. K.; Liu, J.; Chen, X.; Smit, B.; Parise, J. B.; Haranczyk, M.; Thallapally, P. K. Metal–organic framework with optimally selective xenon adsorption and separation. *Nature communications* **2016**, *7*, ncomms11831.
- (352) Mitxelena, I.; Piris, M. Molecular electric moments calculated by using natural orbital functional theory. *The Journal of chemical physics* **2016**, *144* (20), 204108.
- (353) Van Groenigen, K. J.; Qi, X.; Osenberg, C. W.; Luo, Y.; Hungate, B. A. Faster decomposition under increased atmospheric CO₂ limits soil carbon storage. *Science* **2014**, *344* (6183), 508-509.

- (354) Beleggia, R.; Fragasso, M.; Miglietta, F.; Cattivelli, L.; Menga, V.; Nigro, F.; Pecchioni, N.; Fares, C. Mineral composition of durum wheat grain and pasta under increasing atmospheric CO₂ concentrations. *Food Chemistry* **2018**, *242*, 53-61.
- (355) Drage, T. C.; Snape, C. E.; Stevens, L. A.; Wood, J.; Wang, J.; Cooper, A. I.; Dawson, R.; Guo, X.; Satterley, C.; Irons, R. Materials challenges for the development of solid sorbents for post-combustion carbon capture. *Journal of Materials Chemistry* **2012**, *22* (7), 2815-2823.
- (356) Samanta, A.; Zhao, A.; Shimizu, G. K.; Sarkar, P.; Gupta, R. Post-combustion CO₂ capture using solid sorbents: a review. *Industrial & Engineering Chemistry Research* **2011**, *51* (4), 1438-1463.
- (357) Zuluaga, S.; Canepa, P.; Tan, K.; Chabal, Y. J.; Thonhauser, T. Study of van der Waals bonding and interactions in metal organic framework materials. *Journal of Physics: Condensed Matter* **2014**, *26* (13), 133002.
- (358) Pettinari, C.; Tăbăcaru, A.; Galli, S. Coordination polymers and metal–organic frameworks based on poly (pyrazole)-containing ligands. *Coord. Chem. Rev.* **2016**, *307*, 1-31.
- (359) Aromí, G.; Barrios, L. A.; Roubeau, O.; Gamez, P. Triazoles and tetrazoles: Prime ligands to generate remarkable coordination materials. *Coord. Chem. Rev.* **2011**, *255* (5-6), 485-546.
- (360) Howarth, A. J.; Liu, Y.; Li, P.; Li, Z.; Wang, T. C.; Hupp, J. T.; Farha, O. K. Chemical, thermal and mechanical stabilities of metal–organic frameworks. *Nature Reviews Materials* **2016**, *1* (3), 15018.
- (361) Asgari, M.; Semino, R.; Schouwink, P.; Kochetygov, I.; Trukhina, O.; Tarver, J.; Bulut, S.; Yang, S.; Brown, C.; Ceriotti, M. An in - situ neutron diffraction and DFT study of hydrogen adsorption in a sodalite - type metal-organic framework, Cu - BTri. *European Journal of Inorganic Chemistry*.
- (362) Dyadkin, V.; Pattison, P.; Dmitriev, V.; Chernyshov, D. A new multipurpose diffractometer PILATUS@ SNBL. *Journal of synchrotron radiation* **2016**, *23* (3), 825-829.
- (363) Tkatchenko, A.; Scheffler, M. Accurate molecular van der Waals interactions from ground-state electron density and free-atom reference data. *Physical review letters* **2009**, *102* (7), 073005.
- (364) Li, X.-H.; Xia, F.-Y.; Xiao, H.-P.; Hu, M.-L. Hexaaquacopper (II) diperchlorate dihydrate. *Acta Crystallographica Section E: Structure Reports Online* **2004**, *60* (3), i31-i32.
- (365) Rulíšek, L. r.; Vondrášek, J. Coordination geometries of selected transition metal ions (Co²⁺, Ni²⁺, Cu²⁺, Zn²⁺, Cd²⁺, and Hg²⁺) in metalloproteins. *Journal of inorganic biochemistry* **1998**, *71* (3-4), 115-127.
- (366) Morosin, B. The crystal structures of copper tetrammine complexes. A. Cu (NH₃)₄SO₂. H₂O and Cu (NH₃)₄SeO₄. *Acta Crystallographica Section B* **1969**, *25* (1), 19-30.
- (367) Greenwood, N. N.; Earnshaw, A. *Chemistry of the Elements*, Elsevier: 2012.

- (368) Lu, Z.; Godfrey, H. G.; Da Silva, I.; Cheng, Y.; Savage, M.; Tuna, F.; McInnes, E. J.; Teat, S. J.; Gagnon, K. J.; Frogley, M. D. Modulating supramolecular binding of carbon dioxide in a redox-active porous metal-organic framework. *Nature Communications* **2017**, *8*, 14212.
- (369) Giacobbe, C.; Lavigna, E.; Maspero, A.; Galli, S. Elucidating the CO₂ adsorption mechanisms in the triangular channels of the bis (pyrazolate) MOF Fe₂ (BPEB)₃ by in situ synchrotron X-ray diffraction and molecular dynamics simulations. *Journal of Materials Chemistry A* **2017**, *5* (32), 16964-16975.
- (370) Dubbeldam, D.; Walton, K. S.; Ellis, D. E.; Snurr, R. Q. Exceptional negative thermal expansion in isorecticular metal-organic frameworks. *Angewandte Chemie* **2007**, *119* (24), 4580-4583.
- (371) Han, S. S.; Goddard, W. A. Metal-Organic Frameworks Provide Large Negative Thermal Expansion Behavior. *The Journal of Physical Chemistry C* **2007**, *111* (42), 15185-15191.
- (372) Wu, Y.; Kobayashi, A.; Halder, G. J.; Peterson, V. K.; Chapman, K. W.; Lock, N.; Southon, P. D.; Kepert, C. J. Negative Thermal Expansion in the Metal-Organic Framework Material Cu₃ (1, 3, 5 - benzenetricarboxylate)₂. *Angewandte Chemie International Edition* **2008**, *47* (46), 8929-8932.
- (373) Fogler, H. S. Elements of chemical reaction engineering. **1999**.
- (374) Saha, P.; Chowdhury, S. Insight into adsorption thermodynamics. In *Thermodynamics*; InTech: 2011.
- (375) Mason, J. A.; Sumida, K.; Herm, Z. R.; Krishna, R.; Long, J. R. Evaluating Metal-Organic Frameworks for Post-Combustion Carbon Dioxide Capture via Temperature Swing Adsorption. *Energy Environ. Sci.* **2011**, *4*, 3030-3040.
- (376) Krishna, R. The Maxwell-Stefan Description of Mixture Diffusion in Nanoporous Crystalline Materials. *Microporous Mesoporous Mater.* **2014**, *185*, 30-50.
- (377) Krishna, R. Methodologies for Evaluation of Metal-Organic Frameworks in Separation Applications. *RSC Advances* **2015**, *5*, 52269-52295.
- (378) Myers, A. L.; Prausnitz, J. M. Thermodynamics of Mixed Gas Adsorption. *A.I.Ch.E.J.* **1965**, *11*, 121-130.
- (379) Krishna, R. Screening Metal-Organic Frameworks for Mixture Separations in Fixed-Bed Adsorbers using a Combined Selectivity/Capacity Metric. *RSC Advances* **2017**, *7*, 35724-35737.
- (380) Krishna, R. Methodologies for Screening and Selection of Crystalline Microporous Materials in Mixture Separations. *Sep. Purif. Technol.* **2018**, *194*, 281-300, DOI: <https://doi.org/10.1016/j.seppur.2017.11.056>.
- (381) Miller, W.; Smith, C.; Mackenzie, D.; Evans, K. Negative thermal expansion: a review. *Journal of materials science* **2009**, *44* (20), 5441-5451.
- (382) Lock, N.; Wu, Y.; Christensen, M.; Cameron, L. J.; Peterson, V. K.; Bridgeman, A. J.; Kepert, C. J.; Iversen, B. B. Elucidating negative thermal expansion in MOF-5. *The Journal of Physical Chemistry C* **2010**, *114* (39), 16181-16186.

- (383) Evans, J. S. Negative thermal expansion materials. *Journal of the Chemical Society, Dalton Transactions* **1999**, (19), 3317-3326.
- (384) Wang, L.; Wang, C.; Sun, Y.; Shi, K.; Deng, S.; Lu, H. Large negative thermal expansion provided by metal-organic framework MOF-5: a first-principles study. *Materials Chemistry and Physics* **2016**, *175*, 138-145.
- (385) Closmann, C.; Sleight, A.; Haygarth, J. Low-Temperature Synthesis of ZrW₂O₈ and Mo-Substituted ZrW₂O₈. *Journal of Solid State Chemistry* **1998**, *139* (2), 424-426.
- (386) Versluis, A.; Douglas, W. H.; Sakaguchi, R. L. Thermal expansion coefficient of dental composites measured with strain gauges. *Dental materials* **1996**, *12* (5-6), 290-294.
- (387) Sleight, A. W. Negative thermal expansion materials. *Current Opinion in Solid State and Materials Science* **1998**, *3* (2), 128-131.
- (388) Mary, T.; Evans, J.; Vogt, T.; Sleight, A. Negative thermal expansion from 0.3 to 1050 Kelvin in ZrW₂O₈. *Science* **1996**, *272* (5258), 90-92.
- (389) Ernst, G.; Broholm, C.; Kowach, G.; Ramirez, A. Phonon density of states and negative thermal expansion in ZrW₂O₈. *Nature* **1998**, *396* (6707), 147.
- (390) Lightfoot, P.; Woodcock, D. A.; Maple, M. J.; Villaescusa, L. A.; Wright, P. A. The widespread occurrence of negative thermal expansion in zeolites. Basis of a presentation given at Materials Discussion No. 3, 26-29 September, 2000, University of Cambridge, UK. *Journal of materials Chemistry* **2001**, *11* (1), 212-216.
- (391) Phillips, A. E.; Goodwin, A. L.; Halder, G. J.; Southon, P. D.; Kepert, C. J. Nanoporosity and Exceptional Negative Thermal Expansion in Single - Network Cadmium Cyanide. *Angewandte Chemie* **2008**, *120* (8), 1418-1421.
- (392) Chapman, K. W.; Chupas, P. J.; Kepert, C. J. Compositional dependence of negative thermal expansion in the prussian blue analogues MIIPTIV (CN)₆ (M= Mn, Fe, Co, Ni, Cu, Zn, Cd). *Journal of the American Chemical Society* **2006**, *128* (21), 7009-7014.
- (393) Goodwin, A. L.; Kepert, C. J. Negative thermal expansion and low-frequency modes in cyanide-bridged framework materials. *Physical Review B* **2005**, *71* (14), 140301.
- (394) Wu, Y.; Peterson, V. K.; Luks, E.; Darwish, T. A.; Kepert, C. J. Interpenetration as a Mechanism for Negative Thermal Expansion in the Metal-Organic Framework Cu₃ (btb)₂ (MOF - 14). *Angewandte Chemie International Edition* **2014**, *53* (20), 5175-5178.
- (395) Asgari, M.; Semino, R.; Schouwink, P.; Kochetygov, I.; Trukhina, O.; Tarver, J. D.; Bulut, S.; Yang, S.; Brown, C. M.; Ceriotti, M. An In - Situ Neutron Diffraction and DFT Study of Hydrogen Adsorption in a Sodalite - Type Metal-Organic Framework, Cu - BTTri. *European Journal of Inorganic Chemistry* **2019**, *2019* (8), 1147-1154.

- (396) Moghadam, P. Z.; Li, A.; Wiggin, S. B.; Tao, A.; Maloney, A. G.; Wood, P. A.; Ward, S. C.; Fairen-Jimenez, D. Development of a Cambridge Structural Database subset: a collection of metal–organic frameworks for past, present, and future. *Chemistry of Materials* **2017**, 29 (7), 2618-2625.
- (397) Hönicke, I. M.; Senkovska, I.; Bon, V.; Baburin, I. A.; Bönisch, N.; Raschke, S.; Evans, J. D.; Kaskel, S. Balancing Mechanical Stability and Ultrahigh Porosity in Crystalline Framework Materials. *Angewandte Chemie International Edition* **2018**, 57 (42), 13780-13783.
- (398) Zhou, W.; Wu, H.; Yildirim, T.; Simpson, J. R.; Walker, A. H. Origin of the exceptional negative thermal expansion in metal-organic framework-5 Zn 4 O (1, 4- benzenedicarboxylate) 3. *Physical Review B* **2008**, 78 (5), 054114.
- (399) Chen, Y.; Wang, H.; Li, J.; Lockard, J. V. In situ spectroscopy studies of CO₂ adsorption in a dually functionalized microporous metal–organic framework. *Journal of Materials Chemistry A* **2015**, 3 (9), 4945-4953.
- (400) Burtch, N. C.; Baxter, S. J.; Heinen, J.; Bird, A.; Schneemann, A.; Dubbeldam, D.; Wilkinson, A. P. Negative Thermal Expansion Design Strategies in a Diverse Series of Metal–Organic Frameworks. *Advanced Functional Materials* **2019**, 1904669.
- (401) Starvin, A.; Rao, T. P. Solid phase extractive preconcentration of uranium (VI) onto diarylazobisphenol modified activated carbon. *Talanta* **2004**, 63 (2), 225-232.
- (402) Brunauer, S.; Emmett, P. H.; Teller, E. Adsorption of gases in multimolecular layers. *Journal of the American chemical society* **1938**, 60 (2), 309-319.
- (403) Mathias, P. M.; Kumar, R.; Moyer, J. D.; Schork, J. M.; Srinivasan, S. R.; Auvil, S. R.; Talu, O. Correlation of multicomponent gas adsorption by the dual-site Langmuir model. Application to nitrogen/oxygen adsorption on 5A-zeolite. *Industrial & engineering chemistry research* **1996**, 35 (7), 2477-2483.
- (404) McDonald, T. M.; D'Alessandro, D. M.; Krishna, R.; Long, J. R. Enhanced carbon dioxide capture upon incorporation of N, N'-dimethylethylenediamine in the metal-organic framework CuBTri. *Chemical Science* **2011**, 2 (10), 2022-2028.

Curriculum vitae

Personal information

Date of birth: March 22, 1989
Working address: EPFL Valais Wallis, EPFL SB ISIC LFIM
Rue de l'Industrie, 17 Case postale 440, 1951 Sion, Switzerland.
Mobile: +41788859656
Living address: Route de Vissigen 22b, 1950 Sion, Switzerland.
E-mail: mehrdad.asgari@epfl.ch
Researcher ID: [Google scholar](#)

Education

Doctor of Philosophy; 2015-2019

LFIM, Institut des Sciences et Ingenierie Chimiques (ISIC), Swiss Federal Institute of Technology in Lausanne (EPFL), Sion, Switzerland.

GPA: The evaluation is based on pass and fail system in the courses.

Thesis title: "Characterization of metal organic frameworks of interest for post-combustion carbon capture" under supervision of **Prof. Wendy Queen**.

Starting date: Oct 1st 2015

Master of Science; 2011-2014

Department of Chemical Engineering, University of Tehran, Tehran, Iran

GPA: 19.23/20

Thesis title: "Synthesis of Core Shell Nano-Particles and Investigation of Its Effect on the Performance of Chemical Gas Sensor" under supervision of Prof. Abbas Ali Khodadadi and Prof. Yadollah Mortazavi.

Bachelor of Science; 2007-2011

Department of Chemical Engineering, University of Tehran, Tehran, Iran

GPA: 17.58/20

Thesis title: "Design and construction of an experimental reactor setup in order to conduct multiphase atmospheric reactions" under supervision of Prof. Shohreh Fatemi.

High School Diploma; 2003-2007

NODET (National Organization for Development of Exceptional Talents), Qom, Iran

GPA: 19.00/20

Employment history

1- Doctoral assistant

EPFL Valais Wallis, Rue de l'Industrie, 17, 1951 Sion, Switzerland (**Oct 2015-Present**)

2- Process Design Engineer

R&D Department, Fan Niroo Co., No.36, Vali Asr St, Tehran, Iran (**July 2011-Sep 2015**)

3- Process Design Engineer

R&D Department, Avin Palayesh Niroo Co., Amirabad, Tehran, Iran (**Summer 2009**)

Approved research projects

Research projects during PhD

- Synthesis of MOF-nanoparticle composite for efficient hydrocarbon separation (**June 2018-present**)
- Revealing the mechanism of observed anisotropic negative thermal expansion in metal organic frameworks using *in-situ* single crystal x-ray diffraction technique. (**Mar 2018-Present**)
- Investigation of the efficiency of metal organic frameworks materials for noble gas separation (**Jan 2018-Present**)
- The use of mixed MOF and zeolite matrix as efficient adsorbents with enhanced capacity, selectivity and stability for one-pot hydrogen purification and carbon dioxide capture (**Aug 2017-Present**)
- Designing effective MOF-based adsorbents for simultaneous hydrogen purification and CO₂ capture (in collaboration with the group of Prof. Mazzotti in ETH Zurich) (**Aug 2017-Present**)
- Dry post-combustion CO₂ capture: the effect of ligand properties on the efficiency of M-BTtri family of frameworks. (**Feb 2017-Present**)
- Investigation of the structural changes inside the framework by conduction of sequential LeBail and Rietveld refinement on *in-situ* synchrotron x-ray data (**Jan 2016-Present**)
- Computing isosteric heat of adsorption by having variable temperature adsorption isotherm data (**Jan 2016-Present**)
- Investigation of the Lewis acidity of the porous frameworks by *in-situ* IR spectroscopy (**Jan 2016-Present**)
- Using metal organic frameworks as catalyst for biomass conversion reactions (**Jun 2016-Dec 2018**)
- An *in-situ* neutron diffraction and DFT study of hydrogen adsorption in a sodalite-type metal-organic framework, Cu-BTtri (**Feb 2017-Nov 2018**)
- An experimental and computational study of CO₂ adsorption in the sodalite-type M-BTT (M = Cr, Mn, Fe, Cu) metal-organic frameworks featuring open metal sites (**Sep 2016-Apr 2018**)

Research projects before PhD

- Design, simulation and optimization of the Multi Effect Desalination, Zero Liquid Discharge (ZLD) and fresh water distiller units (**July 2011-Sep 2015**)
- Synthesis of core shell nano-particles and investigation of their effect on the performance of chemical gas sensor (**Sep 2012-March 2015**)
- Synthesizing different composite and heterostructured semiconductor nanoparticle sensors for detection of ethanol and acetone (**Sep 2012-Mar 2015**)
- Deep oxidative desulfurization of dibenzothiophene with homogeneous and heterogeneous catalyst (**Feb 2011-Jan 2013**)
- Design and construction of an experimental reactor setup in order to conduct multiphase atmospheric reactions (**June 2010-Feb 2011**)

Supervision of students/junior researchers

- Matthieu Porchet, "Synthesis and characterization of Metal Organic Framework for hydrogen purification by pressure swing adsorption". Master semester project. (**Feb 2018- June 2018**)
- Hassan Abedini, "Location of small gas molecules inside metal organic frameworks by *in-situ* single crystal x-ray diffraction technique". Visiting PhD student. (**June 2018-Dec 2018**)

Teaching activities

1- **Title of the course: The engineering of chemical reactions.**

ISIC, EPFL, Lausanne, Switzerland. Fall semester. B.Sc course. (**Sep 2017- Feb 2018**)

2- Title of the course: Chemical process control.

ISIC, EPFL, Lausanne, Switzerland. Fall semester. B.Sc course. (Sep 2017- Feb 2018)

3- Title of the course: Introduction to transport phenomena.

ISIC, EPFL, Lausanne, Switzerland. Spring semester. B.Sc course. (Feb 2017- July 2017)

4- Workshop lecturer (Desalination units)

R&D department, Fan Niroo Co, Tehran, Iran. (Aug 2012- Sep 2015)

5- Title of the course: Unit Operations 2

Department of Chemical Engineering, University of Tehran. (Dec 2011 – June 2015)

6- Title of the course: Advanced Reactor Design

Department of Chemical Engineering, University of Tehran. (Sep 2014 – Jan 2015)

7- Title of the course: Computer Aided Process Simulation

Department of Chemical Engineering, University of Tehran. (Jan 2011 - July 2011)

Prizes, awards, fellowships

- **Chemistry travel award of Swiss Chemical Society, Switzerland.**

ISIC, EPFL Valais, Sion, Switzerland, 2019

- **Ranked 1st in Master of Science program in chemical engineering among more than 80 students in class of 2011.**

Department of Chemical Engineering, University of Tehran, 2014

- **Ranked 4th among the best chemical engineering students from different universities in final stage of 16th National Chemical Engineering Olympiad in Iran (2011)**

Iran, 2011

- **Graduated with a Bachelor Degree, ranked 5th in class of 2007 and was exempted from taking Entrance Exam for Master of Science program in Chemical Engineering (2011)**

Department of Chemical Engineering, University of Tehran, 2011

- **The top student among more than 100 students in class of 2007 in the last 2 years of Bachelor's program in chemical engineering (GPA: 18.83/20)**

Department of Chemical Engineering, University of Tehran, 2009-2011

- **Award (FOE) for the top student in school year of 2009-2010 among more than 100 students in class of 2007**

Department of Chemical Engineering, University of Tehran, 2010

- **Admitted in the 1st stage of High School Mathematics and Physics Olympiad of Iran**

NODET, Qom, Iran, 2006

- **Admitted in the entrance exam of National Organization for Development of Exceptional Talents (NODET)**

Dr Hesabi Elementary School, Qom, Iran, 2000

Academic Service and memberships

- **A member of Swiss Chemical Society (SCS).**

ISIC, EPFL, Lausanne, Switzerland. (May 2018-Present)

- **President of the board of student representatives**

Department of Chemical Engineering, University of Tehran. (Sep 2008-Sep 2009)

- **Representative of the students of class**

Department of Chemical Engineering, University of Tehran. (Sep 2007-Sep 2009)

Organizing programs

- **Organization of the third anniversary of chemical engineering students**

Department of Chemical Engineering, University of Tehran. (Sep 2009-Feb 2010)

Personal skills

Computer Programs:

Microsoft Office, Origin, Matlab, , Olex 2, TOPAS, EXPGUI and GSAS, HYSYS & ASPEN Plus.

Languages:

Persian:	Native
English:	Fluent
Spanish:	Beginner (A2)
French:	Beginner (A2)

Publication list

Publications in peer-reviewed scientific journals

- 1- Peng, L., Yang, S., Jawahery, S.; Moosavi, S. M.; Huckaba, A. J., **Asgari, M.**, Oveisi, A., Nazeeruddin, M. K., Smit, B., and Queen, W. Preserving porosity of metal-organic frameworks by introducing polymer guest into hierarchical micro- and mesoporous MOFs. (2019). *Journal of the American Chemical Society (JACS)*, 141(31), pp. 12397-12405. **(Featured cover article)**. ([Link](#))
- 2- Yang, S., Peng, L., Sun, D.T., **Asgari, M.**, Oveisi, E., Trukhina, O., Bulut, S., Jamali, A. and Queen, W.L., 2019. A new post-synthetic polymerization strategy makes metal-organic frameworks more stable. *Chemical Science*. 10(17), pp. 4542-4549. **(Featured cover article)** ([Link](#))
- 3- **Asgari, M.**, Semino, R., Schouwink, P., Kochetygov, I., Trukhina, O., Tarver, J.D., Bulut, S., Yang, S., Brown, C.M., Ceriotti, M. and Queen, W.L., (2019). An In-Situ Neutron Diffraction and DFT Study of Hydrogen Adsorption in a Sodalite-Type Metal–Organic Framework, Cu-BTTri. *European Journal of Inorganic Chemistry*, 2019(8), pp.1147-1154. ([Link](#))
- 4- Peng, L., Yang, S., Sun, D.T., **Asgari, M.** and Queen, W.L., (2018). MOF/polymer composite synthesized using a double solvent method offers enhanced water and CO₂ adsorption properties. *Chemical Communications*, 54(75), pp.10602-10605. ([Link](#))
- 5- **Asgari, M.**, Jawahery, S., Bloch, E.D., Hudson, M.R., Flacau, R., Vlaisavljevich, B., Long, J.R., Brown, C.M. and Queen, W.L., (2018). An experimental and computational study of CO₂ adsorption in the sodalite-type M-BTT (M= Cr, Mn, Fe, Cu) metal–organic frameworks featuring open metal sites. *Chemical science*, 9(20), pp.4579-4588. **(Featured cover article)** ([Link](#))
- 6- Kochetygov, I., Bulut, S., **Asgari, M.** and Queen, W.L., (2018). Selective CO₂ adsorption by a new metal–organic framework: synergy between open metal sites and a charged imidazolium backbone. *Dalton Transactions*. 47(31), pp10527-10535. ([Link](#))
- 7- Yang, S., Peng, L., Oveisi, E., Bulut, S., Sun, D.T., **Asgari, M.**, Trukhina, O. and Queen, W.L., (2017). MOF-derived cobalt phosphide/carbon nanocubes for selective hydrogenation of nitroarenes to anilines. *Chemistry-A European Journal*. 24(17), pp4234-4238. **(Featured cover article)** ([Link](#))
- 8- **Asgari, M.**, Saboor, F. H., Mortazavi, Y., & Khodadadi, A. A. (2017). SnO₂ decorated SiO₂ chemical sensors: Enhanced sensing performance toward ethanol and acetone. *Materials Science in Semiconductor Processing*, 68, 87-96. ([Link](#))
- 9- Peng, L., **Asgari, M.**, Mievile, P., Schouwink, P., Bulut, S., Sun, D.T., Zhou, Z., Pattison, P., Van Beek, W. and Queen, W.L., (2017). Using Predefined M₃ (μ₃-O) Clusters as Building Blocks for an Isostructural Series of Metal–Organic Frameworks. *ACS applied materials & interfaces*, 9(28), pp.23957-23966. ([Link](#))
- 10- Saboor, F. H., Khodadadi, A. A., Mortazavi, Y., & **Asgari, M.** (2017). Microemulsion synthesized silica/ZnO stable core/shell sensors highly selective to ethanol with minimum sensitivity to humidity. *Sensors and Actuators B: Chemical*, 238, 1070-1083. ([Link](#))
- 11- Alamolhoda, F., R. KouhiKamali, and **M. Asgari**. Parametric simulation of MED–TVC units in operation. *Desalination and Water Treatment* 57.22 (2016): 10232-10245. ([Link](#))
- 12- Sagharichiha, M., Jafarian, A., **Asgari, M.**, & Kouhikamali, R. (2014). Simulation of a forward feed multiple effect desalination plant with vertical tube evaporators. *Chemical Engineering and Processing: Process Intensification*, 75, 110-118. ([Link](#))
- 13- Kouhikamali, R., FallahRamezani, Z., & **Asgari, M.** (2013). Investigation of thermo-hydraulic design aspects in optimization of MED plants. *Desalination and Water Treatment*, 51(28-30), 5501-5508. ([Link](#))
- 14- Kouhikamali, R., Kojidi, A. S., **Asgari, M.**, & Alamolhoda, F. (2012). The effect of condensation and evaporation pressure drop on specific heat transfer surface area and energy consumption in MED–TVC plants. *Desalination and Water Treatment*, 46(1-3), 68-74. ([Link](#))

- 15- Haghighat Mamaghani, A., Fatemi, S., & **Asgari, M.** (2013). Investigation of influential parameters in deep oxidative desulfurization of dibenzothiophene with hydrogen peroxide and formic acid. *International Journal of Chemical Engineering*, 2013. ([Link](#))

Contribution to the conferences

• Oral presentation

- 16- **Asgari, M.**, Schouwink, P., Jawahery, S., Smit, B., Bulut, S., and Queen, W. In-situ neutron diffraction study of carbon dioxide adsorption on M-BTT frameworks, a series of highly crystalline MOFs. Annual meeting of the Swiss Society of Crystallography in Geneva (2017), Geneva. Oral Presentation. ([Link](#))
- 17- **Asgari, M.**, and Queen, W. Obtaining a molecular level view of CO₂ adsorption in a series of isostructural Metal Organic Frameworks (MOFs). Challenges & Opportunities in Energy Research NRG2018, (2018), Crans-Montana. Oral Presentation. ([Link](#))
- 18- Trukhina, O., Karve, V., **Asgari, M.**, Dapsens, P. Y., and Queen, W. Glucose conversion with metal-organic frameworks in water. Swiss Chemistry Fall Meeting, September 2018, EPFL Lausanne. Oral Presentation. ([Link](#))

• Poster presentation

- 19- **Asgari, M.**, Jawahery, S., Semino, R., Schouwink, P., Ceriotti, M., and Queen, W. In-situ diffraction study of carbon dioxide adsorption on M-BTT(ri) frameworks. Advanced sorption seminar, May 2018, empädubendorf, Poster presentation. ([Link](#))
- 20- **Asgari, M.**, Jawahery, S., Semino, R., Schouwink, P., Ceriotti, M., and Queen, W. In situ neutron diffraction study of carbon dioxide adsorption on M-BTT frameworks, a series of highly crystalline MOFs. Swiss Chemistry Fall Meeting, September 2018, EPFL Lausanne. Poster Presentation. ([Link](#))
- 21- Hooriabad Saboor, F., **Asgari M.**, Mortazavi, Y., Khodadadi A. A. Enhanced gas sensing performance of nanostructured ZnO/SnO₂ nanoparticles via micro-emulsion synthesis method. Asian Nano Forum Congress 2015. / Kish Island, Iran.\ ([Link](#))
- 22- **Asgari, M.**, Mortazavi, Y., Khodadadi, A. A., Hooriabad Saboor, F. Enhanced sensitivity of chemical gas sensors to ethanol using SnO₂ decorated SiO₂ nanoparticles. 5th International Congress on Nanoscience & Nanotechnology (ICNN2014) / Tehran, Iran.\ ([Link](#))
- 23- Kouhikamali, R., Alamolhoda, F., **Asgari, M.**. Thermo-Hydraulic design aspects of MED-TVC units. The International Desalination Association World Congress on Desalination and Water Reuse 2013 / Tianjin, China.\ ([Link](#))

Peer-reviewed books

- 24- **Asgari, M.**, & Queen, W. L. (2018). Carbon Capture in Metal–Organic Frameworks. *Materials and Processes for CO₂ Capture, Conversion, and Sequestration*, 1-78. ([Link](#))
- 25- **Asgari, M.**, Saboor, F. H., and Vahdatifar, S. (2019) Advances in Microelectronics: Reviews. Volume 2. Chapter 13. Fabrication and Characterization of Silica/Metal Oxide Semiconductor Nanostructures to Improve Gas Sensing Performance, 425-505. ([Link](#))

Patents and licenses

- Khodadadi, A. A., Mortazavi, Y., Hooriabad Saboor, F., **Asgari, M.**, (2017). *Iranian patent Application, No. 93270*. ([Link in Persian](#))

Developed characterization tools and experimental setups

- Gas dosnig manifold for in-situ diffraction and spectroscopy experiments (Figure 1)

- In-situ powder diffraction cell (mountable on goniometer head, used and tested in synchrotron radiation facilities) for in-situ powder diffraction experiments (Figure 2)
- In-situ single crystal diffraction cell (mountable on goniometer head, used and tested in synchrotron radiation facilities) for in-situ single crystal diffraction experiments (Figure 3)
- In-situ IR spectroscopy chamber on the external bench of IR instrument (Figure 4)
- Fixed bed adsorption setup (breakthrough apparatus) (Figure 5)



Figure 1- Gas dosing manifold



Figure 2- In-situ powder diffraction cell

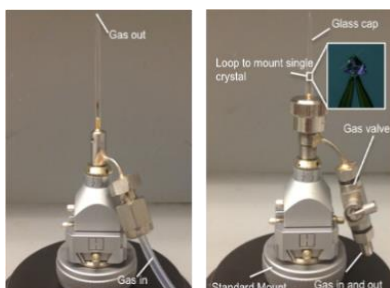


Figure 3- In-situ single crystal diffraction cell



Figure 4-In-situ IR cell mounted on the external bench



Figure 5- Breakthrough apparatus